Mechanistic studies of photoactivatable fluorescent proteins: a combined approach by crystallography and spectroscopy

Virgile Adam

UNIVERSITY JOSEPH FOURIER – GRENOBLE 1
SCIENCES, TECHNOLOGY, MEDICINE

THESIS
To obtain the degree of
DOCTOR FROM THE UNIVERSITY JOSEPH FOURIER

Specialty: Structural Biology & Nanobiology
Doctoral school: Chemistry and Life Sciences

Publicly presented and defended by

Virgile ADAM

The 20th May 2009

MECHANISTIC STUDIES OF PHOTOACTIVATABLE FLUORESCENT PROTEINS: A COMBINED APPROACH BY CRYSTALLOGRAPHY AND SPECTROSCOPY

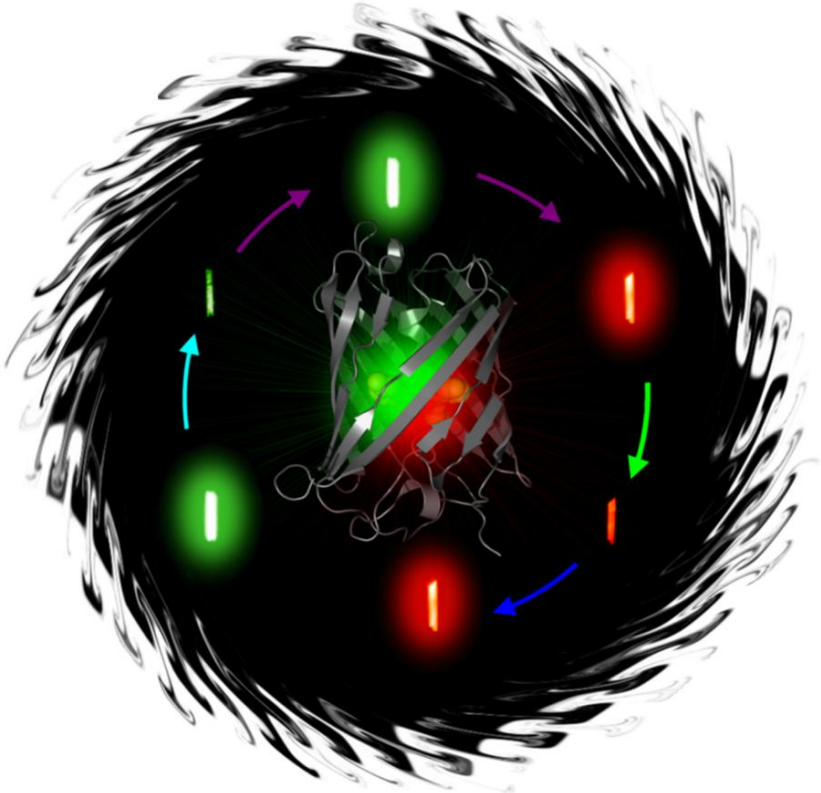

Examining board

Chairman	Pr. Michel ROBERT-NICOUD	Institut Albert Bonniot, Grenoble, FR
Reporters	Dr. Catherine ROYER	Centre de Biochimie Structurale, Montpellier, FR
	Dr. Daniel PICOT	Institut de Biologie Physico-Chimique, Paris, FR
Examiners	Pr. Gerd Ulrich NIENHAUS	Institut für Biophysik, Ulm, DE
	Pr. Johan HOFKENS	Afdeling Moleculaire en Nanomaterialen, Leuven, BE
Thesis supervisors	Dr. Dominique BOURGEOIS	Institut de Biologie Structurale, Grenoble, FR
	Dr. Seán McSWEENEY	European Synchrotron Radiation Facility, Grenoble, FR

Doctoral thesis prepared at the European Synchrotron Radiation Facility (ESRF)

The cover picture represents the fluorescent protein IrisFP described in this thesis and which undergoes multiple color changes, making of it a powerful tool for bioimaging and biotechnological applications. The X-ray structure of IrisFP is shown in the center (gray ribbons) and the green and red rays represent multi-color light-emission by the protein. Pictures of crystals of IrisFP in its different forms (switched on/off, green/red) are shown around the central image, linked by arrows representing the colors of the lasers needed to operate the color changes.

UNIVERSITE JOSEPH FOURIER – GRENOBLE 1
SCIENCES, TECHNOLOGIE, MEDECINE

THESE
Pour obtenir le grade de
DOCTEUR DE L'UNIVERSITE JOSEPH FOURIER

Discipline : Biologie Structurale et Nanobiologie
Ecole Doctorale : Chimie et Sciences du Vivant

Présentée et soutenue publiquement par

Virgile ADAM

Le 20 Mai 2009

ETUDES MECANISTIQUES DES PROTEINES FLUORESCENTES PHOTOACTIVABLES : UNE APPROCHE COMBINEE PAR CRISTALLOGRAPHIE ET SPECTROSCOPIE

Composition du jury

Président	Pr. Michel ROBERT-NICOUD	Institut Albert Bonniot, Grenoble, FR
Rapporteurs	Dr. Catherine ROYER	Centre de Biochimie Structurale, Montpellier, FR
	Dr. Daniel PICOT	Institut de Biologie Physico-Chimique, Paris, FR
Examinateurs	Pr. Gerd Ulrich NIENHAUS	Institut für Biophysik, Ulm, DE
	Pr. Johan HOFKENS	Afdeling Moleculaire en Nanomaterialen, Leuven, BE
Directeurs de thèse	Dr. Dominique BOURGEOIS	Institut de Biologie Structurale, Grenoble, FR
	Dr. Seán McSWEENEY	European Synchrotron Radiation Facility, Grenoble, FR

Thèse préparée à l'Installation Européenne de Rayonnement Synchrotron (ESRF) en collaboration avec le département de biophysique de l'Université de Ulm, Allemagne

Addresses of the examining board members

Pr. Michel ROBERT-NICOUD
Institut Albert Bonniot
CRI INSERM/UJF U823
Rond-point de la Chantourne
F-38706 La Tronche Cedex
E-mail: michel.robert-nicoud@ujf-grenoble.fr
Tel: +33(0)4 76 51 40 91
Fax: +33(0)4 76 51 40 92

Pr. Gerd Ulrich NIENHAUS
Universität Ulm
Institut für Biophysik
Albert-Einstein-Allee 11
D-89081 Ulm
E-mail: uli@uiuc.edu
Tel: +49(0)731 23050
Fax: +49(0)731 23059

Pr. Johan HOFKENS
Katholieke Universiteit Leuven
Afdeling Moleculaire en Nanomaterialen
Celestijnenlaan 200f - bus 02404
B-3001 Heverlee
E-mail: johan.hofkens@chem.kuleuven.be
Tel: +32(0)1 6327 804
Fax: +32(0)1 6327 990

Current address:
Institut für Angewandte Physik
Universität Karlsruhe
Wolfgang Gäde Str. 1
D-76131 Karlsruhe

Dr. Catherine ROYER
Centre de Biochimie Structurale
29, route de Navacelles
F-34090 Montpellier Cedex
E-mail: catherine.royer@cbs.cnrs.fr
Tel: +33(0)4 67 41 79 02
Fax: +33(0)4 67 41 79 13

Dr. Daniel PICOT
Institut de Biologie Physico-Chimique
13, rue Pierre et Marie Curie
F-75005 Paris
E-mail: daniel.picot@ibpc.fr
Tel: +33(0)1 58 41 51 03
Fax: +33(0)1 58 41 50 24

Dr. Dominique BOURGEOIS
Institut de Biologie Structurale J.P. Ebel
41, rue Jules Horowitz
F-38027 Grenoble Cedex 1
E-mail: dominique.bourgeois@ibs.fr
Tel: +33(0)4 38 78 96 44
Fax: +33(0)4 38 78 51 22

Dr. Seán McSWEENEY
European Synchrotron Radiation Facility
6, rue Jules Horowitz BP 220
F-38043 Grenoble Cedex
E-mail: seanmcs@esrf.fr
Tel: +33(0)4 76 88 23 62
Fax: +33(0)4 76 88 21 60

"Chacun sait que dans les rêves on ne voit jamais le soleil, bien qu'on ait souvent la perception d'une clarté beaucoup plus vive. Les objets et les corps sont lumineux par eux-mêmes"

Gérard de Nerval (Aurélia), 1855

"They are ill discoverers that think there is no land, when they can see nothing but sea"

Francis Bacon (The advancement of learning), 1605

This page intentionally left blank

Table of Contents

List of Figures

List of Tables

List of abbreviations

$AmSO_4$: ammonium sulphate
B-factor: temperature factor $B = 8\pi^2 \times \bar{u}^2$ (expressed in Å²) related to $\bar{u}^2$, the mean square displacement of the atomic vibration in the plane perpendicular to the plane $h\ k\ l$ where atoms diffract in phase
Bicine: N,N-Bis(2-hydroxyethyl)glycine
CALI: Chromophore Assisted Light Inactivation
CCD: Coupled Charge Device
CCP4: Collaborative Computational Project, number 4 (www.ccp4.ac.uk)
CNS: Crystallography and NMR System (http://cns-online.org)
CP: Chromo-Protein
EC: Enzyme Commission numbers
ESRF: European Synchrotron Radiation Facility (www.esrf.eu)
F_{calc}: calculated structure factors
F_{obs}: observed structure factors
FIONA: Fluorescence Imaging with One-Nanometer Accuracy
FLIP: Fluorescence Loss In Photobleaching
FP: Fluorescent Protein
FRAP: Fluorescence Recovery After Photobleaching
FRET: Förster Resonance Energy Transfer
FWHM: Full Width at Half Maximum
GFP: Green Fluorescent Protein
HBDI: 4-hydroxybenzylidene-1,2-dimethylimidazoline (model compound of the GFP chromophore)
p-HBI: *p*-hydroxybenzylidene-imidazolinone
HEPES: 4-(2-hydroxyethyl)-1-piperazineethanesulfonic acid
I: Intensity
IBS: Institut de Biologie Structurale (www.ibs.fr)
IR: Infrared
LD, MD, HD: Low Dose, Moderate Dose, High Dose
λ^{act} : Actinic wavelength
$\lambda^{em.}_{max}$: Maximal wavelength of emission
$\lambda^{ex.}_{max}$: Maximal wavelength of excitation
MW: Molecular Weight
NCBI: National Center for Biotechnology Information (www.ncbi.nlm.nih.gov)
NCS: Non-Crystallographic Symmetry
PAFP: Photo-Activatable Fluorescent Protein
PALM: PhotoActivated Localization Microscopy
PDB: Protein Data Bank (www.pdb.org)
PEG: PolyEthylene Glycol
PSB: Partnership for Structural Biology (http://psb.esrf.eu)
R_{cryst}: $\frac{\sum_{hkl}|F_{obs} - F_{calc}|}{\sum_{hkl}|F_{obs}|}$, Reliability factor indicating the crystallographic correctness of a model

R_{free}: $\frac{\sum_{hkl\subset T}|F_{obs} - F_{calc}|}{\sum_{hkl\subset T}|F_{obs}|}$ The Free R-factor is similar to the R_{cryst} but is calculated with a small fraction (i.e. 5%) of reflections randomly chosen to be part of test group T. This R factor, thus, is not biased by the refinement process.

R_{sym}: $\frac{\sum_{hkl}\sum_{i}|I_i(hkl) - \overline{I(hkl)}|}{\sum_{hkl}\sum_{i}|I_i(hkl)|}$, reliability factor comparing the intensity of symmetry-related reflections
RCFP: Reef Coral Fluorescent Protein
rms: Root Mean Square, $rms = \sqrt{\frac{1}{n}\sum_{i=1}^{n} X_i^2} = \sqrt{\frac{x_1^2 + x_2^2 + \cdots + x_n^2}{n}}$ for n values $\{x_1, x_2, \ldots, x_n\}$
RSFP: Reversibly Switchable Fluorescent Protein
STED: STimulated Emission Depletion
STORM: STochastic Optical Reconstruction Microscopy
TCSPC: Time Correlated Single Photon Counting
TIRF: Total Internal Reflection Fluorescence
Tris: tris-(hydroxymethyl)aminomethane
UV : Ultra-Violet
wt: Wild type

Remerciements / Acknowledgements

EH bien voilà, une page se tourne… la thèse est terminée et clôt ces années d'études et d'efforts pour réaliser un rêve d'enfance qui se concrétise aujourd'hui. J'aurais tellement de gens à remercier qui ont tellement compté pour moi durant des années que toutes les pages de cette thèse (pourtant nombreuses !) n'y suffiraient pas. J'espère que tous ceux dont j'oublierai le nom ne m'en tiendront pas trop rigueur. Je tenais tout de même à remercier un certain nombre nommément pour ces merveilleux moments, parfois difficiles mais de toute façon inoubliables.

Dominique Bourgeois, mon directeur de thèse, vers qui je suis arrivé seulement armé de ma sincérité, mon ignorance et ma bonne volonté et qui m'a offert sa confiance et un avenir. Depuis mon tout premier stage auprès de lui il y a maintenant presque huit ans, travailler à ses côtés a été un plaisir qui m'a mené à prendre plus confiance en moi, à devenir meilleur scientifique et à peut-être pouvoir me vanter d'avoir gagné son amitié. Je ne lui ai probablement pas assez dit à quel point je lui suis reconnaissant d'avoir joué un rôle si important pour moi et donc j'en profite ici pour lui dire un simple mais si profond « merci ». Ce n'est qu'un au revoir et certainement pas un adieu.

Je tiens à remercier les membres du jury m'ayant fait l'honneur d'examiner ce travail :

A mes rapporteurs, Dr. Catherine Royer et Dr. Daniel Picot, merci pour ces rapports si élogieux !

Dr. Catherine Royer, dont l'expertise en corrélation croisée de fluorescence, en spectroscopie sur molécule unique et en anisotropie de fluorescence permet de juger les résultats contenus dans ce rapport et d'apprécier la portée de ces résultats dans leurs futures applications. Merci d'avoir accepté de donner son avis certainement très juste sur ce travail.

Dr. Daniel Picot, que j'ai eu l'occasion de croiser à plusieurs reprises lors de congrès de biologie structurale et dont les capacités en cristallographie ne sont plus à prouver. De par son expérience en cristallographie des protéines photosensibles, son jugement sur ce rapport est précieux pour moi. Je ne saurai certainement pas me passer de cristallographie et donc nos chemins devraient se recroiser.

Pr. Michel Robert-Nicoud, que j'ai eu le plaisir et l'honneur d'avoir eu comme enseignant et qui m'a fait découvrir les merveilles de la fluorescence appliquée à la recherche avec les "*F-techniques*" que je ne suis pas prêt d'oublier. Merci à lui d'avoir accepté d'être le président de mon jury, et d'avoir jugé mon travail avec l'œil afuté d'un microscopiste. J'espère que mon travail servira à la communauté des microscopistes et acquérir dans les années à venir plus de connaissances me permettant d'apporter une nouvelle pierre à cet édifice.

Herr Dr. Prof. Uli Nienhaus und Frau Dr. Karin Nienhaus dafür, daß ich in Ihrer Arbeitsgruppe (Abteilung Biophysik) in Ulm immer so herzlich willkommen war, Ihre Hilfe im Kampf mit der deutschen Bürokratie, daß Sie es mir ermöglicht haben mit diesen wundervollen Proteinen zu Arbeiten und daß Sie immer alles gegeben haben um unserere Projekte erfolgreich voranzubringen.

Professor Hofkens, die niet alleen deze thesis nauwgezet beoordeeld heeft en daarbij hartelijk in de omgang was, maar mij, door me de komende jaren welkom te heten in zijn team in Leuven, ook het volste vertrouwen gaf. Ik hoop van ganser harte dat onze samenwerking bijzonder vruchtbaar zal zijn!

Dr. Sean McSweeney, director of the Macromolecular Crystallography (MX) group, for his continuous support during these years spent among the MX group. Thanks for having accepted me, for having integrated me so fast in the group and for all the last-minute details for the organisation of the defense!

I also wanted to thank Sine Larsen, scientific director at the ESRF, who was always available for me and trusted me and the project when we proposed it at the beginning of the thesis, as were very nice people with me all along these years, either at the MX group (Joanne McCarthy, David Flot, Dave Hall, Gordon Leonard and all the scientists and students) or elsewhere at the ESRF (Guillaume Potdevin and his gas detectors, Adeline Buffet and her alloys topographs, Sylvain Petitgirard and his high-pressure diamond-anvil cells…), IBS, EMBL and ILL… thanks for all this kindness and all those soft moments. I just can't forget members of the PSB wetlabs: Samira Acajjaoui, Meike Stelter, Hayretin Yumerefendi, Tomaso Tosi, Sofia Caria, Ganesh Natrajan, Maxime Cuypers, Laurent Terradot, Cyril Dian, Amandine Lallemand and all the others who all participated to the nice ambience in which I evolved. All this wonderful period wouldn't have been the same without those who shared the office with me: Charles Sabin, Wendy Rénier, Bernhard Pätzold, Therese Johansson and Isabel Baker... thanks for all these good moments!

Ma famille qui m'a bien sûr construit pour me permettre d'être celui que je suis, et au tout premier plan ma petite maman, merci pour tout ce que tu représentes à mes yeux, pour avoir été à toi seule pendant dix belles années (et toujours !) mes deux parents et assumé contre vents et marées. Je compte sur toi plus que jamais pour être à mes côtés durant toutes celles à venir. Merci d'avoir toujours cru en moi et avoir tout simplement fait qui je suis. Cette thèse t'est bien évidemment dédiée.

Bien sûr ma tendre épouse Marie, qui depuis des années n'a eu de cesse de me donner son amour et de croire en moi et en nous. Six ans après nos fiançailles et trois ans après notre mariage, je suis le plus heureux à tes côtés et tu as été ma force pour faire toujours mieux. Désormais nous allons continuer ce chemin avec notre petit Gabriel, merveilleux petit ange que tu viens de nous offrir il y a quelques semaines et qui représente la preuve par trois que l'avenir nous appartient.

Ma sœur et sa jolie famille : Didier, Marion, Laurie et Emmanuelle, famille soudée par-delà les saisons qui passent.

Un grand grand merci à tous ceux qui m'ont rencontré, aidé ou accompagné sur ce chemin rocailleux qu'est celui de la recherche scientifique. Je pense à tous ceux de l'équipe de cristallographie cinétique : Emanuela Fioravanti e la sua amicizia preziosa, che conosco dai miei primi giorni di tirocinio e che ho seguito sul cammino oscuro della tesi, Antoine Royant pour son amitié, tout ces bons moments au fil des années et ses précieux conseils et discussions scientifiques que j'ai toujours apprécié au plus haut point et n'oublierai pas, Philippe Carpentier pour toute la gentillesse dans la vie et lors des manips de photoblanchiment qui nous ont donné mal à la tête, mais aussi Jeremy Ohana, Guillaume Durin, Gergely Katona, Martin Weik, Jacques Colletier, Benoît Sanson… vous avez tous été une part très importante de mon chemin de tout petit stagiaire et de petit doctorant.

Un grand merci également à tous ceux qui m'ont aidé avec des techniques spécialisées à un moment ou à un autre de mon travail et sans qui j'aurais été vite bloqué : Alexeï Grichine de l'IAB (microscopie de fluorescence), Monika Budayova-Spano de l'UVHCI (neutrons), Mickael Wulff, Marco Cammarata et Friederike Ewald de l'ESRF (diffraction Laue), Yvain Nicolet et Xavier Vernède de l'IBS…

Mickaël Lelimousin, mon cher *« très très bientôt docteur »* de ces années de doctorat, qui en plus d'avoir été dans la même promo de DEA, a partagé avec moi les stress, joies, cafés, travaux et espoirs déçus ou récompensés de l'avancée de ce projet sur lequel il a également fait sa thèse soutenue à quelques jours de la mienne !

Anne Martel… la p'tite Anne, docteur ès-fil-de-soie, ce fut un réel plaisir de faire nos thèses côte à côte et de boire tous ces litres de thé. Je te souhaite de réussir et surtout d'être toujours au moins aussi motivée par ton travail, quelle que soit la voie dans laquelle tu t'engageras.

Charles Sabin, pote depuis si longtemps, nos chemins ne cessent de se croiser depuis le lycée, rien n'y fait on se ressemble finalement trop pour ne pas nous retrouver ensemble à nous poser des questions similaires sur tout et n'importe quoi. Merci d'avoir été présent aussi souvent (en particulier au déjeuner !) et d'avoir partagé avec moi les doutes et reprises de motivation, inhérents à la recherche.

Avoir passé toutes ces années dans ce cadre unique a été une superbe expérience pour moi. Quel plaisir enrichissant et rare de pouvoir partager chaque jour de la semaine des temps avec des gens de nationalités et de domaines scientifiques si différents, quel bonheur de pouvoir travailler aussi librement dans une variété de laboratoires aussi bien équipés que le synchrotron européen, le laboratoire de biologie moléculaire européen, l'institut Laue-Langevin, l'institut de biologie structurale, le commissariat à l'énergie atomique, l'institut Albert Bonniot… A l'orée de cette nouvelle vie qui s'ouvre à moi, je prie pour pouvoir dans l'avenir être amené à connaître de nouveau toute cette ouverture culturelle et scientifique.

Merci à tous, merci pour tout !

Résumé général en français

La production de lumière par des êtres vivants comme les lucioles trouble les humains depuis la nuit des temps. Des premiers écrits chinois aux études des savants du 19ème siècle, en passant par les philosophes grecs, tous ont tenté de percer ce mystère qui sera successivement appelé phosphorescence puis bioluminescence. Il y a moins de 50 ans, la première production de lumière par un animal, non pas uniquement par réaction chimique mais également par fluorescence, était découverte avec l'identification de la protéine fluorescente verte (GFP) chez la méduse *Æquorea victoria*. L'isolation et le clonage de cette protéine il y a moins de 20 ans a permis à la fin des années 1990 un bond phénoménal en biologie cellulaire et recherche biomédicale, en permettant de marquer et suivre des protéines ou des organelles d'intérêts dans des cellules ou des organismes. Les efforts de génie génétique ont même permis les mutations de cette protéine, créant une véritable palette de couleurs disponibles pour la microscopie de fluorescence.

La recherche d'autres animaux marins générant des protéines fluorescentes (FP) a permis la découverte de molécules de couleurs et brillances variées, mais au début du 21ème siècle, la découverte des protéines fluorescentes photoactivables (PAFPs), notamment chez les anthozoaires, a initié une révolution dans le domaine de la technologie des FP. Ces protéines fluorescentes sont en effet capables d'être irréversiblement photoconverties d'une forme fluorescente verte à une forme fluorescente rouge ou encore d'être réversiblement commutées entre des formes allumées ou éteintes, selon des longueurs d'onde d'excitation spécifiques. Les PAFPs sont actuellement intensivement employées dans les techniques de microscopie optique, particulièrement en "nanoscopie", qui permet d'atteindre une résolution optique 10 fois meilleure que la limite théorique d'Abbe.

Tout au long de ce volume de thèse, nous présenterons d'abord l'état de l'art des protéines fluorescentes, depuis la découverte du phénomène de fluorescence jusqu'à celle des protéines fluorescentes photoactivables. Les résultats des travaux présentés couvrent trois grandes problématiques actuellement débattues dans le domaine des PAFPs : les mécanismes de la photoconversion du vert au rouge, de la photocommutation réversible entre un état lumineux et un état non-fluorescent, et du photoblanchiment menant à l'extinction définitive des marqueurs biofluorescents.

Grâce à une approche combinée de diffraction des rayons X, de microspectrophotométrie en solution et sur cristaux, et de calculs de mécanique quantique et moléculaire, nous sommes parvenus à proposer un nouveau mécanisme réactionnel menant à la photoconversion du vert au rouge de EosFP, une PAFP photoconvertible du vert au rouge, issue d'un corail constructeur de récif, ainsi que la structure tridimensionnelle et la caractérisation de Dendra2, autre PAFP photoconvertible du vert au rouge, issue d'un corail mou et aux propriétés particulières. Les interfaces se formant dans les cristaux entre des

chaines protéiques n'interagissant normalement pas en solution nous a permis d'aborder la question de l'oligomérisation des protéines fluorescentes et de proposer des mutations que nous pensons importantes afin d'améliorer leur stabilité sous forme monomérique, étape essentielle pour l'obtention de biomarqueurs efficaces.

Nous avons également découvert la première protéine fluorescente photoactivable regroupant à la fois les propriétés de photoconversion du vert au rouge et de photocommutation réversible entre des états lumineux et non fluorescents, à la fois sous forme verte et sous forme rouge. Une telle protéine devrait se montrer utile en microscopie à super-résolution à deux couleurs où des protéines non phototransformées (vertes) et phototransformées (rouges) pourraient être localisées très précisément en même temps. Une application futuriste intéressante est celle de l'utilisation de ces protéines pour stocker des données soit de manière irréversible en utilisant les propriétés de photoconversion du vert au rouge, soit en permettant l'effacement et la réécriture en utilisant les propriétés de photocommutation réversibles. Même si de telles applications dans la vie courante sont pour l'instant irréalistes, une preuve de principe pour ces deux types de stockage est fournie dans cette thèse.

Enfin, nous nous sommes intéressés au photoblanchiment, étape irrémédiable et délétère menant à la perte du signal en imagerie de fluorescence. Nous avons étudié le photoblanchiment des PAFPs induit par les UV, la lumière visible et les rayons X et nous avons obtenu et caractérisé les déformations du chromophore associées à la formation d'un état radicalaire induit par les rayons X et probablement impliqué dans la voie de photoblanchiment des PAFPs.

Les perspectives essentielles de ce travail sont l'amélioration des PAFPs pour leur utilisation en biotechnologie et en nanoscopie mais de nombreuses études initiées durant cette thèse restent à faire : diffraction de neutrons, diffraction de rayons X Laue, mutagénèse...

I. STATE OF THE ART

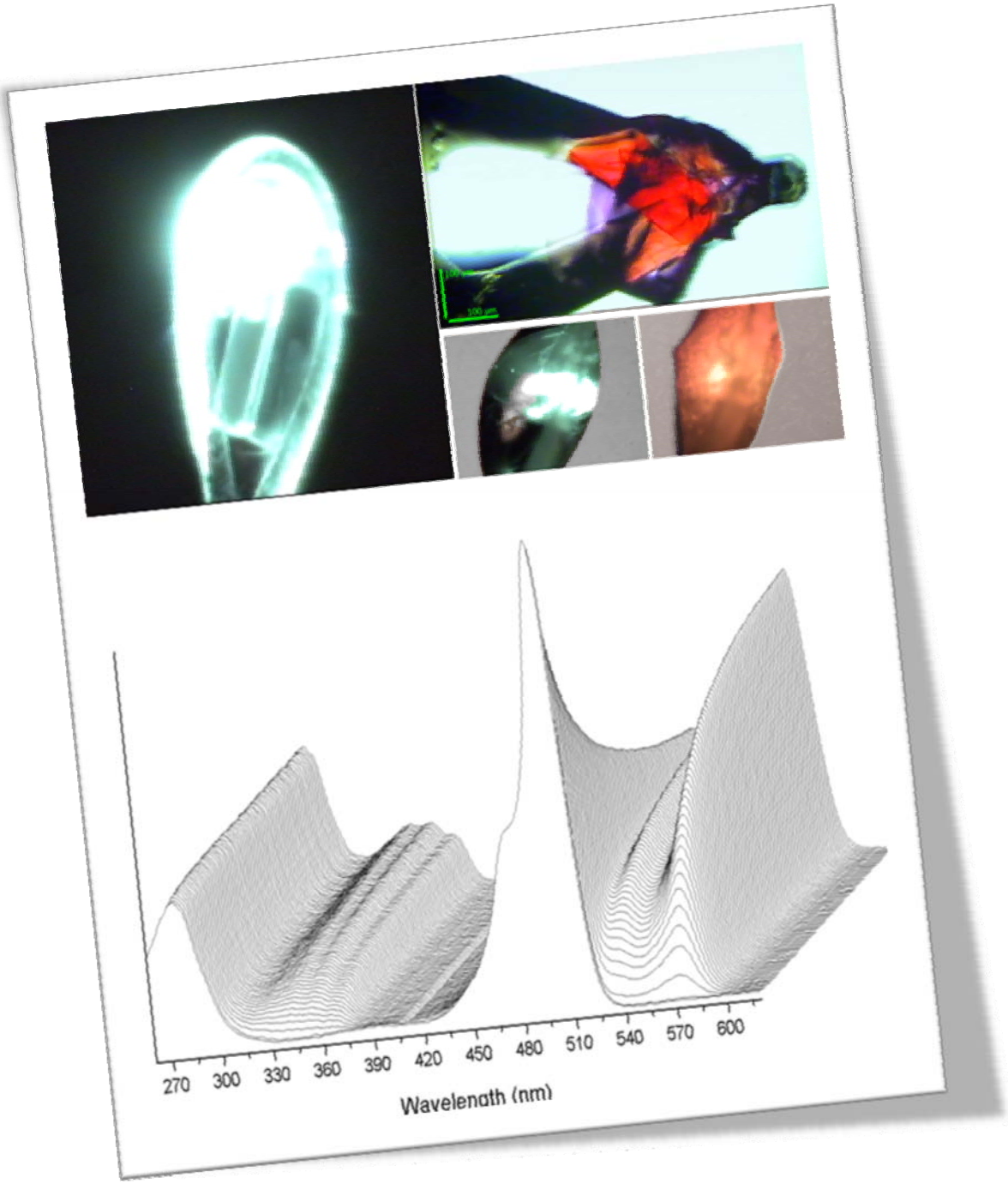

The illustration represents an assemblage of several examples of green-to-red photoconvertible fluorescent proteins and experiments presented in this thesis. From left to right and from top to bottom: a green crystal of Dendra2, a red crystal of EosFP, green and red forms of EosFP, and a 3D evolution of absorption spectra of EosFP during green-to-red photoconversion.

Chapter 1 - History of the fluorescence discovery

Résumé en français

Par une approche historique, ce chapitre introductif permet d'appréhender et de différencier les termes et notions complexes de phosphorescence, fluorescence et luminescence. Depuis la découverte des premières pierres émettant de la lumière dans le noir jusqu'aux animaux luminescents, les phénomènes physiques d'absorption, de fluorescence, de phosphorescence, de relaxation non radiative et de fluorescence retardée seront expliqués au travers d'exemples.

Nous nous intéresserons en particulier aux deux premiers systèmes enzymatiques menant à la bioluminescence qui ont été découverts : le système Luciférase/luciférine présent par exemple chez les lucioles et le système Æquorine/cœlentérazine, présent chez certains animaux marins.

Part 1 - Phosphorescence, fluorescence or luminescence?

1 - Matter shining by its own: a story of phosphorescence

NEAR Bologna, in 1603, the alchemist Vincenzo Cascariolo studied stones that he exposed under sunlight and noticed that they were shining by themselves in the dark (Licetus 1640). Thinking that he just found something close to the philosopher's stone, he named this compound able to generate light in the dark after having been illuminated "phosphorus of Bologna", phosphorus meaning "light carrier" (from the Greek words φως [phos] meaning "light" and φερειν [pherein] meaning "to carry"). However, this compound was actually barium sulphide (baryte: $BaSO_4$) and not the real phosphorus element, which was discovered by the alchemist Hennig Brandt in 1669 from urine phosphates, and described eight years later by the chemist Johann von Löwenstern-Kunckel (von Löwenstern-Kunckel 1678). This phenomenon of light emission by an object without incandescence (sometimes called "cold light"), whatever the involved process, was thus qualified by the term of **phosphorescence** until late 19^{th} century.

Between 1839 and 1841, Alexandre Edmond Becquerel studied the emission of visible light by calcium sulphur after samples were exposed to the ultraviolet (UV) part of the sunlight spectrum. He showed that this light was emitted at longer wavelengths than the one used to excite the object (Becquerel 1839). However, he qualified all the events of cold light production (by minerals or living organisms) by the term "phosphorescence".

Five years later, Sir Georges Gabriel Stokes studied the emission of visible light produced by quinine sulphate and crystals of fluorine (CaF_2) under a UV irradiation. At the difference of calcium sulphur, this light emission ceased when the exposure to UV light was stopped. He proposed for this phenomenon the term **fluorescence** (Stokes 1852) whose etymology is a neologism from the words fluorine and opalescence. In fact, more than forty years later, it was found that this fluorescence did not actually come from fluorine itself but from impurities inside, like yttrium or dysprosium (Lenard & Wolf 1889).

From then, it seemed that two different ways of producing light could coexist and the term **luminescence** (from the Latin *lumen* meaning "light") was proposed in 1888 by Eilhardt Wiedemann to refer to both phenomena of fluorescence and phosphorescence (Wiedemann 1888). Today, the phenomenon of luminescence is defined as being a "spontaneous emission of radiation from an electronically or vibrationally excited species not in thermal equilibrium with its environment"[1]. The phenomenon of fluorescence is defined as a "luminescence which occurs essentially only during the irradiation of a substance by electromagnetic radiation"[2] and the phenomenon of phosphorescence is described as follow: "the luminescence involves a change in spin multiplicity, typically from triplet to singlet or vice versa. The luminescence from a quartet state to a doublet state is also phosphorescence"[3].

2 - The physics behind luminescence phenomena

In spite of all those works and progresses, the phenomena of molecular absorption of photons (A), fluorescence (F) and phosphorescence (P) remained poorly understood until the 20th century.

In 1929, Francis Henri Jean Siegfried Perrin during his second PhD thesis, made a physical distinction between fluorescence and phosphorescence (Perrin 1926; 1929). The various transitions between the electronic ground state (S_0), the singlet excited states ($S_{n>0}$) and the triplet excited states ($T_{n>0}$) were all represented and summarized in a single chart by Aleksander Jabłoński (Jablonksi 1935), known today as Perrin-Jabłoński diagram (Figure I.1.1).

[1] Glossary of terms used in photochemistry, IUPAC recommendations 1996, 68, p.2252
[2] Nomenclature for radioanalytical chemistry, IUPAC recommendations 1994, 66, p.2519
[3] Glossary of terms used in photochemistry, IUPAC recommendations 1996, 68, p.2258

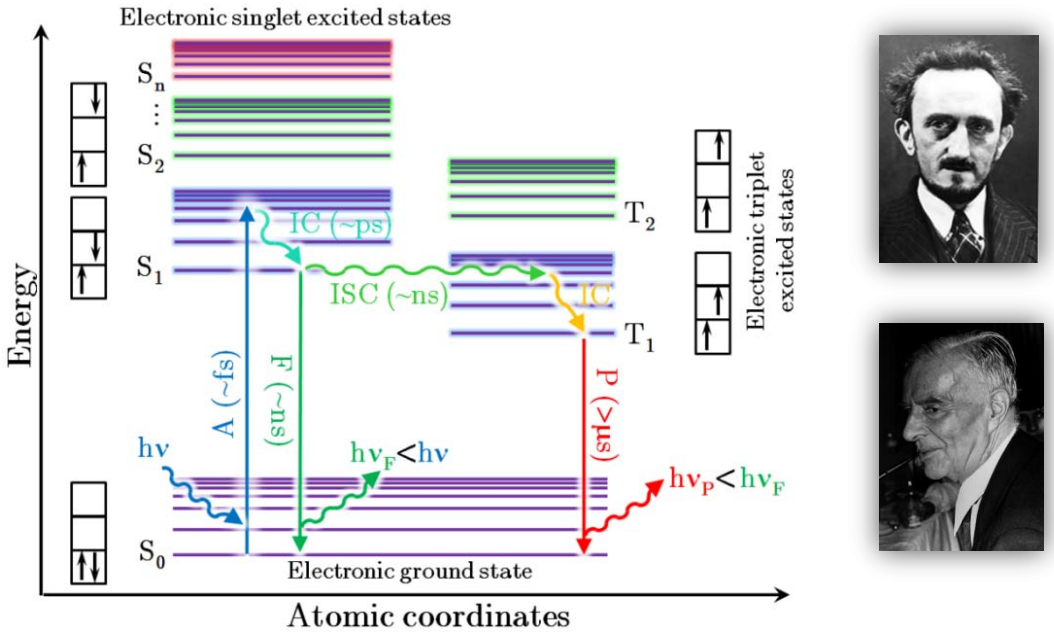

Figure I.1.1 - Simplified Perrin-Jabłoński diagram and photographs of Francis Perrin (up) & Aleksander Jabłoński (bottom)

This diagram must be seen as the graphical representation of the various possible transitions that a system in its ground state[4] can exhibit once excited by an electromagnetic wave. For sake of clarity, the version represented here is simplified and does not represent for example the rotational levels between the vibrational levels, but it allows getting a pretty accurate idea of the phenomena of absorption, radiative relaxations (like fluorescence and phosphorescence), or non radiative relaxations.

a - Absorption

The molecular absorption of a photon that has the same energy than the energy difference between the lowest vibrational level of the ground state (S_0) and one of the vibrational levels of an excited state ($S_{n>0}$) of a molecule, allows an electron to cross this energy barrier and travel from the ground state to one of the excited state levels. This absorption is faster (about 10^{-15} s)

[4] "The state of lowest Gibbs energy of a system" - Glossary of terms used in physical organic chemistry, IUPAC recommendations 1994, 66, p.1118 (Gibbs energy was previously called free enthalpy or free energy)

compared to the timescale of the motion of atomic nuclei so that it is classically considered as being instantaneous (Franck-Condon principle).

The molecule relaxation, which will lead to the loss of the energy quantum that was absorbed, occurs in two steps. First, by relaxing to the lowest vibrational level of the excited state S_1 by internal conversion (IC) in a time range comprised between 10^{-13} and 10^{-11} seconds, thanks to the interactions of the molecule with its environment. Depending on the molecules and their environment, the lifetime τ of this excited state can vary from 10^{-12} to 10^{-9} seconds. In a second step, there will be a relaxation of the molecule either by direct return to the ground state S_0 with fluorescence emission or by phosphorescence emission with intersystem crossing to an excited state called triplet state (T_1) (Lewis & Kasha 1944). Alternatively, heat dissipation may occur (non-radiative relaxation to the ground state) with a new internal conversion without photons emission.

b - Fluorescence

In the case of fluorescence, the return to the ground state S_0 is preceded by the relaxation from the excited vibrational level that was reached to the lowest vibrational level of the S_1 excited state. For most fluorophores, the vibrational energy level spacing for S_0 and for S_1 is about the same size, which makes that excitation and emission spectra resemble a lot (this is not true anymore for higher excited states). The probability that an electron in S_1 returns to a given vibrational level of S_0 is proportional to the overlap between these states, as represented by the Franck-Condon energy diagram (Figure I.1.2). The return to S_0 will thus be generally achieved through an elevated vibrational level, which will then relax by internal conversion to the lowest vibrational level, relax to the equivalent elevated vibrational level of S_0 and finally relax again by internal conversion to the lowest vibrational level of S_0. Those particular

transitions produce a typical mirror image of the fluorescence spectrum compared to the absorption spectrum; this is called the mirror image rule (Franck & Livingston 1941).

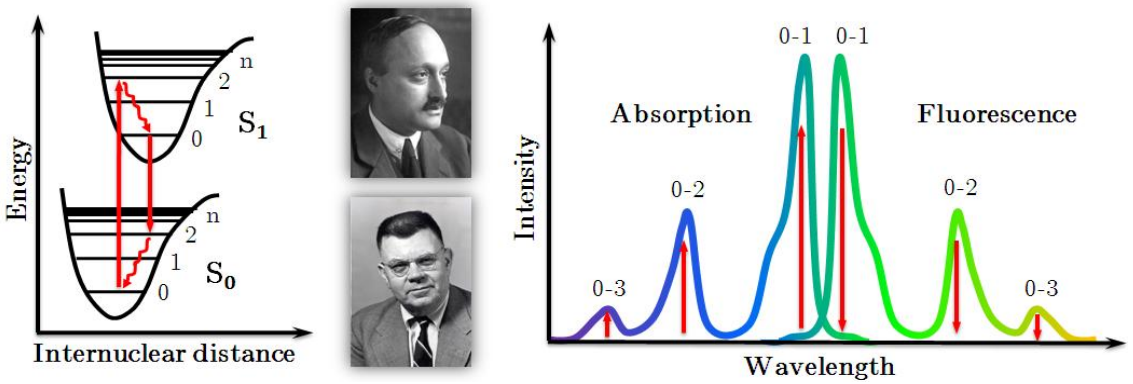

Figure I.1.2 - The mirror image rule. Left: Franck-Condon diagram showing the example of the 0-2 absorption/relaxation; Middle: photographs of James Franck (top) and Edward Condon (bottom); Right: the probability of the transitions creates the mirror image structure between the absorption and fluorescence spectra

Since there is a loss of energy during this process, the fluorescence spectrum will be shifted toward less energetic wavelengths (bathochromic or red shift) than the ones that were used for the excitation: this is called the Stokes shift. In solution, this shift is even more pronounced because of a solvent relaxation phenomenon in the S_1 state. The influence of the solvent is indeed far from being negligible since the motion of solvent molecules is much faster (~ps) than the fluorescence lifetime (~ns). This has the consequence that solvent molecules can rearrange around the excited-state dipole in about 10^{-10} s (Lakowicz 2006). This solvent relaxation lowers the excited molecule energy and thus here again a bathochromic shift is observed.

c - Phosphorescence

In the case of phosphorescence, a crossing from the singlet excited state S_1 to a triplet excited state T_1 is qualified as intersystem crossing (ISC). This isoenergetic non-radiative transition reverses the excited electron spin. The probability of an ISC is increased if the vibrational levels of the two states involved (singlet excited and triplet) overlap. Finally, after

an internal conversion to the lowest vibrational level of the triplet state, a last ISC conversion will allow the return to the (singlet) ground state. Because of the spin flippings, such ISC are very improbable and even qualified as "forbidden transitions" and for this reason, the lifetime (τ) of the triplet state T_1 is way longer than the one of S_1 (10^{-6} to 10^4 seconds, several hours for e.g. europium compounds) and the shortest phosphorescence lifetimes are close to the longest fluorescence lifetimes. However, lifetimes are not sufficient to distinguish between fluorescence and phosphorescence; since the lowest vibrational level of T_1 is lower than the one of S_1, the internal conversions and intersystem crossings will result in a smaller loss of energy compared to the simple relaxation from a singlet excited state. A phosphorescence emission spectrum will thus be more shifted to high wavelengths (red shift) than a fluorescence emission spectrum.

d - Non-radiative relaxations and delayed fluorescence

It is worthwhile noting that the phosphorescence lifetime is often so long that a number of collisions between the excited molecules and solvent or oxygen molecules favor the relaxation toward the ground state S_0 without any photon emission (non-radiative relaxation) (Kautsky 1939). This quenching leads to the fact that most of the time, the phosphorescence is not observable in liquid phase (unless the molecule is in a hydrophobic solution or is protected from the solvent by its close environment) but only in rigid, crystal-like media. Finally, instead of directly relaxing from the triplet state toward the ground state, the inter-system crossing can be reversed from T_1 to S_1, leading to a delayed fluorescence.

e - A wide variety of luminescence events

Since the definition of Wiedemann, quoting fluorescence and phosphorescence under the single term of luminescence, several other kinds of luminescence have been discovered (Figure I.1.3). The luminescence phenomena have thus been classified by their physical mechanisms. For example, the luminescence that needs the prior absorption of a photon (fluorescence and

phosphorescence) has been named "photoluminescence" while the one that needs a chemical reaction has been called "chemiluminescence".

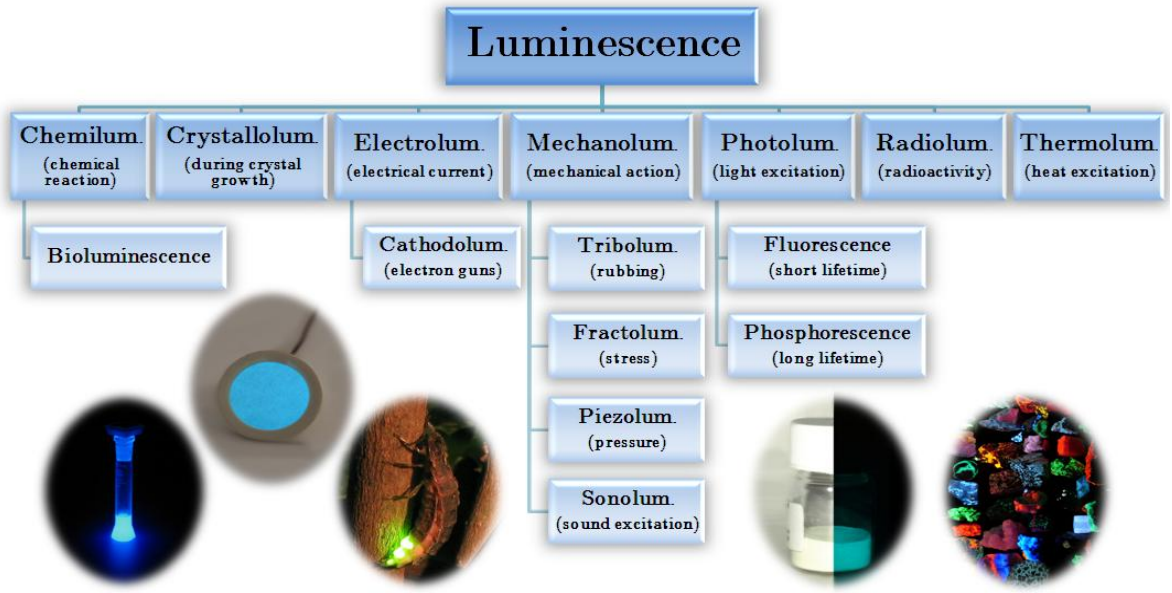

Figure I.1.3 - The different kind of luminescence phenomena illustrated by some photographs. From left to right examples are shown of: chemiluminescence with the reaction of luminol with blood; electroluminescence with a nightlight; bioluminescence with a glow-worm; phosphorescence with a bottle containing a strontium/europium compound shown under ambient light and total darkness, and fluorescence with a collection of fluorescent minerals.

Part 2 - The explanation of an ancestral mystery

When luminescence is produced by a living organism as a consequence of a chemical reaction, one talks of bioluminescence (hybrid word made of the Greek word βιος [bios] meaning "life" and the Latin word *lumen* meaning "light"). The first observation that some plants or animals can glow in the dark is lost in History but the best known example of bioluminescence is of course the luminescence produced by "glow-worms" and especially fireflies (*Lampyris noctiluca*) during summer nights. This animal production of light is actually the most ancient written testimony of bioluminescence since some Chinese texts dated 1000-1500

BC describe this fact. No real explanations for this phenomenon were given during centuries. Naturally, some well-reads tried to understand this extraordinary phenomenon, but most of them ended with the somewhat useless conclusion that those organisms were glowing by nature. It is reported in the book "Aglow in the dark" (Pieribone & Gruber 2005) that Aristotle for example wrote *"it is the nature of smooth things to shine in the dark"* and Gaius Plinius Secundus (Pliny the Elder) wrote *"it is the nature of these fishes to shine in darkness with a bright light when other light is removed"*. During the 17th century, Robert Boyle understood that the bioluminescent light was cold and required air (Boyle 1672; 1680) but the biggest advancements in the study of bioluminescence only occurred during the 19th century.

Alessandro Volta had just invented his electric pile battery and the efforts to develop the electric light made scientists of this period, like Alexandre Edmond Becquerel, Edmund Newton Harvey or Victor Audoin, highly interested in understanding how light is created. They were especially paying a lot of attention to organisms capable of emitting what they were still calling phosphorescence or "phosphoric glow", like some annelids, fungi and glow-worms (Audoin 1840). Raphaël Horace Dubois was one of those scientists. He studied the West Indian firefly *Pyrophorus* and discovered the components and the origin of this enigmatic light emission: an enzyme and its substrate that he respectively called Luciferase and luciferin (Dubois 1887), from "Lucifer" meaning literary "light carrier" (from the Latin words *lux* (gen. *lucis*) meaning "light" and *ferre* meaning "carry").

1 - The Luciferase and luciferin system

The mechanism involved in this bioluminescence system is the oxidation of luciferin into oxyluciferin by the Luciferase, which is an ATP-hydrolyzing mono-oxygenase (EC 1.13.12.7). Along with ATP hydrolysis, the Luciferase will excite the luciferin molecule. Its relaxation is achieved through the formation of a radical form and finally to the luciferin decarboxylation into oxyluciferin, accompanied with the emission of a photon (Figure I.1.4).

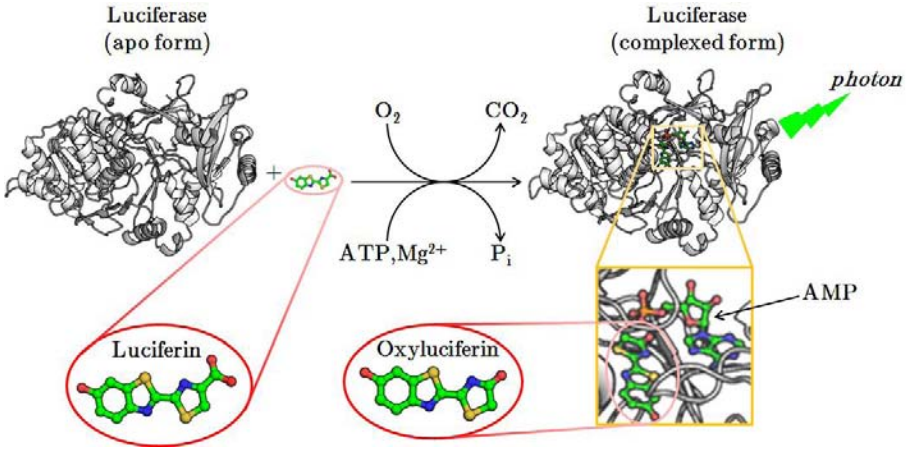

Figure I.1.4 - Mechanism of the firefly bioluminescence involving Luciferase (PDB:1LCI,2D1R) & luciferin

Dubois, however, did not really explain this biochemical mechanism. It was made by Edmund Newton Harvey, one of the most important contradictors of Dubois, who preferred to call Luciferase "photogenin" and luciferin "photophelein" but spent almost all his career on the topic of animal bioluminescence, working especially on the luciferin and Luciferase from the crustacean *Cypridina* (EC 1.13.12.5). He allowed major improvements in the understanding of bioluminescence (Harvey 1917; 1919; 1920; 1924) until the end of his career in the 1950's (he died in 1959), at which date his team became world leading in bioluminescence research. His student Franck Johnson and himself, though, remained unable to crystallize *Cypridina* luciferin... this will be achieved by Osamu Shimomura, who joined their team.

2 - The Æquorin and cœlenterazine system

We know today that more than 700 animal genera use chemical molecules very similar to the couple luciferin/Luciferase to create light signals in the whole visible spectrum. Most of those species, though, are not terrestrial but live in oceans, like some fishes, bacteria or zooplankton. In the 1960's, Osamu Shimomura, working on the extraction of a new

bioluminescent protein from the jellyfish *Æquorea victoria*[5] (Shimomura *et al.* 1962) discovered a new enzyme involved in bioluminescence that he naturally called Æquorin. This enzyme (EC 1.13.12.5) once activated by a calcium atom, works in a very similar way than the already known Luciferase, by exciting a prosthetic luciferin-like molecule called cœlenterazine, since it is found in cœlenterates organisms. Like in the case of the oxyluciferin (excited form of the luciferin), the activated form of the cœlenterazine, the cœlenteramide, will be decarboxylated along with the emission of a blue photon ($\lambda_{\text{max}}^{\text{em.}} = 470$ nm).

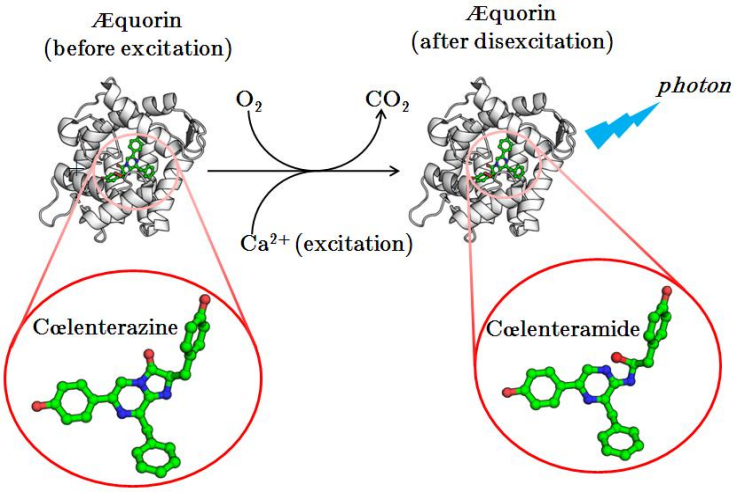

Figure I.1.5 - Mechanism of Æquorea bioluminescence involving Æquorin (PDB code: 1EJ3) and cœlenterazine

During this work, he also discovered another protein that he characterized later as being the very first protein capable of green light production (maximal emission at 507 nm) without any associated biochemical reaction. This protein was the first ever discovered that only needed a light excitation to produce its luminescence (maximal excitation at 475 nm). From what we said previously, we see that this kind of luminescence, even though being of a biological origin, should not be qualified of bioluminescence but of biofluorescence. This photoprotein was

[5] After having sucessively been called *Æquorea æquorea* (Forsskål, 1775) and *Æquorea forskalea* (Péron 1809) & Lesueur, 1810), Murbach and Shearer (1902) identified individuals with morphological differences that they separated from the species *forskalea* to create the new species *victoria*. This distinction is today debated, but it seems that the gleaming properties of these jellyfishes (and other animals) were known from a long time (Péron 1809; Lamarck (de Monet de) 1816; Jourdan 1837; Pieribone & Gruber 2005)

logically and simply called GFP, standing for green fluorescent protein (Hastings & Morin 1969) and will initiate the big revolution of biofluorescence.

Figure I.1.6 - Æquorea victoria (the light does not actually come from a luminescence but from external reflections) and a photograph of Osamu Shimomura (holding a tube filled with GFP)

Chapter 2 - Fluorescent proteins shed a new light on a bioluminescent world

Résumé en français

Dans ce chapitre, nous parlons de la protéine fluorescente verte (GFP) et de la révolution qu'elle a apportée dans le monde de la recherche biomédicale. La structure particulière de cette protéine est décrite ainsi que son mécanisme de formation et de fluorescence. La notion de systèmes conjugués et la dépendance en pH de la fluorescence de cette protéine sont exposées. Très rapidement, l'utilisation de la GFP en imagerie biomédicale a donné lieu à des efforts de bioingénierie et cette utilisation a été confrontée à des phénomènes photochimiques comme le photoblanchiment ou la photoactivation, qui sont également expliqués ici.

Ce chapitre décrit également la découverte des premières protéines fluorescentes découvertes dans d'autres animaux marins comme les coraux ou les anémones de mer, ce qui a permis d'accroître considérablement la gamme des couleurs disponibles pour la microscopie de fluorescence. Parmi ces nouvelles protéines, nous nous intéresserons particulièrement à des protéines fluorescentes qualifiées de photoactivables. Plusieurs exemples de ces protéines fluorescentes, soit capables d'être réversiblement éteintes, soit d'être irréversiblement converties d'une couleur d'émission à une autre sont discutés.

Part 1 - The Green Fluorescent Protein

1 - Of bioluminescence and biofluorescence

FOLLOWING Shimomura's discovery of GFP, it was found how to purify it and that it functions together with the Æquorin thanks to a Resonance Energy Transfer (Morin & Hastings 1971; Wampler *et al.* 1971; Morise *et al.* 1974). Indeed, if, *in-vitro*, the excitation of Æquorin by Ca^{2+} produces the final release of a blue photon, *in-vivo* this excitation acts as a donor by transferring the equivalent energy to GFP, whose excitation will release a green photon (Figure I.2.1).

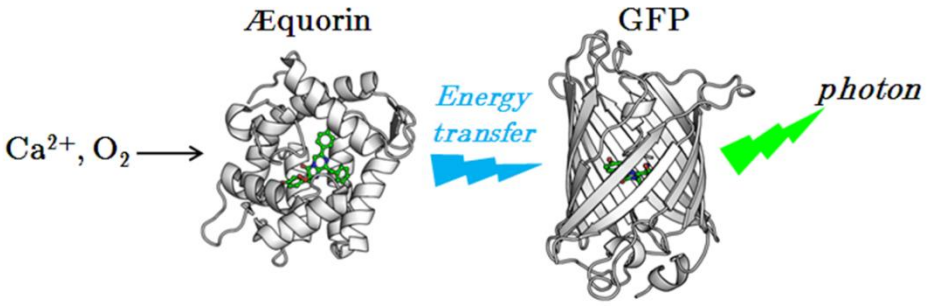

Figure I.2.1 - Mechanism of the energy transfer between the Æquorin and the GFP in the jellyfish Æquorea

After several years of work (Shimomura 1985), the gene of the GFP could be isolated and cloned by Douglas Prasher and its sequence was determined (Prasher *et al.* 1992). A lot of efforts were made to understand the structural origin of this fluorescence, that was determined to be an endogenous chromophore made from the protein peptidic chain itself (Cody *et al.* 1993).

2 - Biological applications of the GFP

The achievement of those major steps opened the way to the first real applications of GFP in molecular biology, with the proposals by Martin Chalfie to use fluorescent proteins as biological markers (Chalfie *et al.* 1994). The team of Roger Yonchien Tsien quickly created a brighter version of the GFP by mutating the first residue of the chromophore (S65T) and called it EGFP for Enhanced GFP (Heim *et al.* 1995).

Figure I.2.2 - Photographs of Douglas Prasher, Martin Chalfie and Roger Y. Tsien

A remarkably high number of applications in molecular biology bloomed the same year (Prasher 1995) with the effective tagging of proteins of interest with GFP, in organisms as diversified as Amoeba (Hodgkinson 1995), insects (Brand 1995), superior organisms like plants (Haseloff & Amos 1995) and mammalian cells (Pines 1995) and even transgenic organisms (Ikawa *et al.* 1995).

In parallel, there was strong competition to crystallize and obtain the first three-dimensional structure of GFP. This structural information would indeed bring a better understanding on where the chromophore is located and on the novel autofluorescence mechanism of this protein. Those efforts led to the release of two X-ray structures the next year: one of wild-type GFP (Ormö *et al.* 1996) and one of its enhanced version EGFP (Yang *et al.* 1996).

O. Shimomura, M. Chalfie and R. Y. Tsien have been awarded the Nobel Prize in Chemistry 2008 for the discovery and development of the green fluorescent protein.

3 - The structure of GFP

a - Implications of a peculiar structure

The three dimensional structures of the green fluorescent protein, revealed a new β-barrel fold in which eleven antiparallel β-strands form a single β-sheet that is rolled in a tube shape. This β-barrel fold is completed at both ends with short α-helices and loops, which play the role of lids and protect even more the inner of the β-barrel from the outer medium. Resemblances of this closed structure with a soda can, made people qualify it as "β-can". The carboxyl- and amino-termini sides of the protein clearly show long ends that allow the tagging by fusion at either ends with proteins of interest.

As already anticipated by previous biochemical studies (Cody *et al.* 1993), the β-can of the GFP shelters a chromophore, said to be endogenous and made of aminoacids contained in the protein (Figure I.2.3). Strictly speaking, this compound should be called chromophore when it only absorbs light without emission and fluorophore when fluorescence is emitted. However, for sake of simplicity, it will always be called "chromophore" from now, since its fluorescent or non fluorescent behavior will be specified each time. This component has quickly been identified as the origin of the fluorescence emission but unexpectedly revealed to be non fluorescent when isolated in solution (Niwa *et al.* 1997). The cylindrical folding of the protein provides indeed a wonderful milieu for the chromophore since it is kept planar owing to the strong interactions with the surrounding sidechains. This locking allows a rigid conformation of the chromophore and hence a greater fluorescence quantum yield. The chromophore is also protected from fluorescence quenching by collisions with external solvent molecules that cannot easily reach the chromophore due to the almost perfectly closed barrel structure. However, a study (Follenius-Wund *et al.* 2003) has shown that the removal of oxygen in a solution containing the isolated chromophore does not increase significantly the fluorescence quantum yield. This result tends to show that the main reason for the loss of fluorescence in solution is mostly due to the degrees of freedom the chromophore acquires by not being in the protein matrix. This also

indicates that the chromophore has a natural tendency to move and distort and that its protein environment is finely tuned to constraint it very tightly.

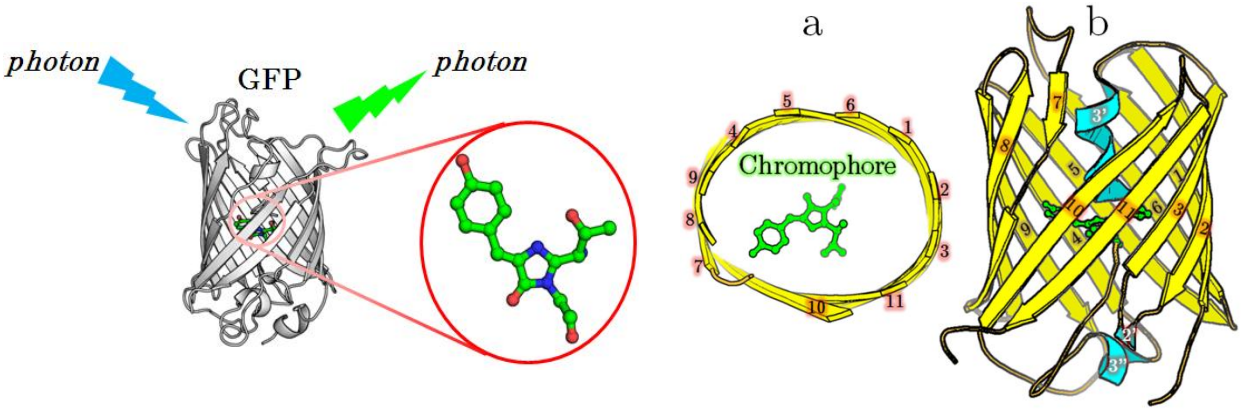

Figure I.2.3 - Overall structure of GFP. Left: scheme of the green fluorescence produced by GFP after excitation by a blue photon. Right: top (a) and side (b) schematic views of the GFP β-can structure. The 11 β-strands are shown in yellow, the α-helices in cyan and the chromophore in green balls & sticks

Although being a rare folding, the β-barrel is not a unique property of fluorescent proteins since it is also found in at least four other types of proteins: Porins, G2F domain of Nidogen (Entactin), Retinol-binding proteins (RBP) and Streptavidin (Figure I.2.4). Porins are membrane proteins found in Gram-negative bacteria and endosymbiotic organelles like mitochondria and chloroplasts. Their barrel is not made of 11 β-strands but 16, which makes it wide enough to form a channel that allows the transmembrane passive diffusion of some molecules. Nidogen is a type of protein that binds to laminin in the extracellular matrix and mediates its formation. The number of β-strands in the G2F (globular-2 fragment) domain of Nidogen is the same as GFP but instead of protecting a chromophore between two short α-helices, the barrel only shelters a long α-helix. RBP is found in mammals and helps the regulation of retinol (vitamin A) by encapsulation and release of this compound, which is allowed by the open shape of its small (8 strands) barrel. Streptavidin is produced by the bacterium *Streptomyces* and has the same role of binding biotin (vitamin B8) as hen egg white Avidin but with a higher affinity. Streptavidin also comprises 8 strands to form its β-barrel but its tight shape does not allow anything to enter within the protein's core.

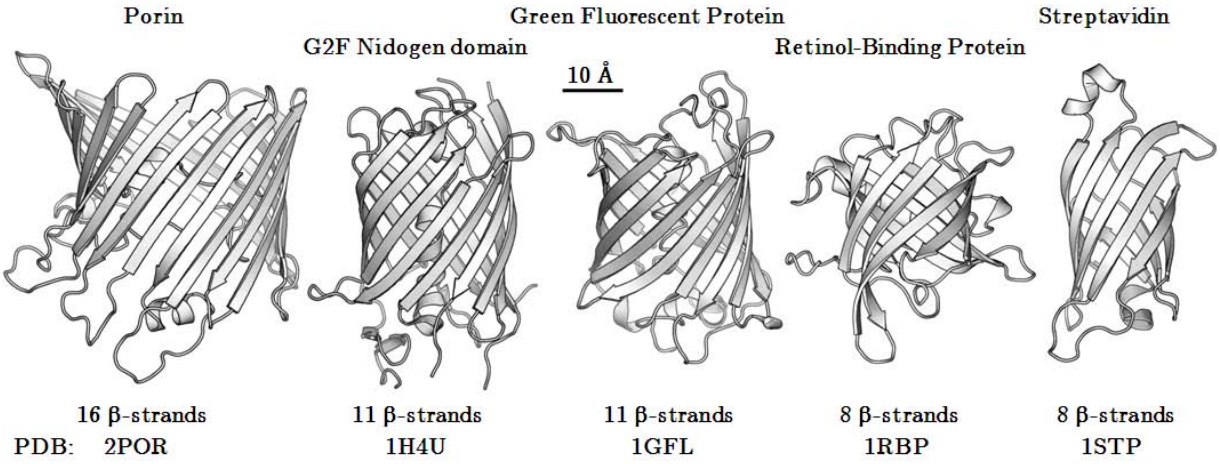

Figure I.2.4 - The different types of β-barrel foldings in Porin, GFP and RBP

Interestingly, although those proteins are found in very different types of organisms, their structures are remarkably similar and it is tempting to think that it is a case of divergent evolution where proteins are folded in a similar way in order to either encapsulate/protect a compound or allow its channeling but without necessarily emitting fluorescence. This theory has been partially supported by a work considering GFP homologs like the GF2 domain of Nidogen proteins as being members of a superfamily that rapidly derived from the fluorescent proteins (Shagin *et al.* 2004).

b - Maturation and mechanism

During the *in-vivo* synthesis, GFP undergoes a series of transformations in a subtle process called maturation (Figure I.2.5) that leads to the formation of the chromophore. This chromophore is formed by three aminoacids that autocatalytically reorganize in post-translation stages to form a compound made of an imidazolinone ring and a hydroxybenzylidene (or hydroxyphenylmethylene) ring. This compound, called 4-(*p*-hydroxybenzylidene)5-imidazolinone is covalently bound to the protein mainchain and stands in the center of the β-barrel.

It has been shown that the crucial aminoacid that is always conserved to yield a mature chromophore is a glycine in the sequence X-Tyr-Gly forming the triad of the chromophore (with X=Ser for the wild-type GFP and X=Thr for the EGFP). However, if this sequence is indeed absent in the very similar but uncolored G2F domain of Nidogen shown above, it is widespread in proteins that do not form any chromophore, showing that the sole presence of this sequence is obviously not sufficient to produce a chromophore. Infact, the steric constraints imposed by the β-barrel shape, induce a quick cyclization of the glycine (residue n+2) with the residue X (residue n), to form a compound called imidazolin-5-one (Heim *et al.* 1994) that undergoes a slow aerial oxidation and is dehydrogenated to form the mature chromophore (Figure I.2.5). Noteworthily, this last step produces hydrogen peroxide (H_2O_2) that can potentially be toxic for the cell in case of overexpression.

These last maturation steps have been recently discussed though, by Rebekka Wachter's group. The production of a hydrogen peroxide molecule for each mature GFP (Zhang *et al.* 2006) seems accepted and has only been debated with an alternative possibility where an environment-mediated elimination of $2H^+$, $2e^-$ has been proposed by Elizabeth Getzoff's group (Barondeau *et al.* 2003), but for a mutant forming a triad Gly-Gly-Gly displaying very different steric conformations. It has been shown that the formation of a first reaction intermediate (Figure I.2.5, step 5) can form a second intermediate either by first being dehydrated and then being oxidized, along with the production of the H_2O_2 molecule (Cubitt *et al.* 1995) or by first being oxidized along with the production of the H_2O_2 molecule and then being dehydrated (Rosenow *et al.* 2004).

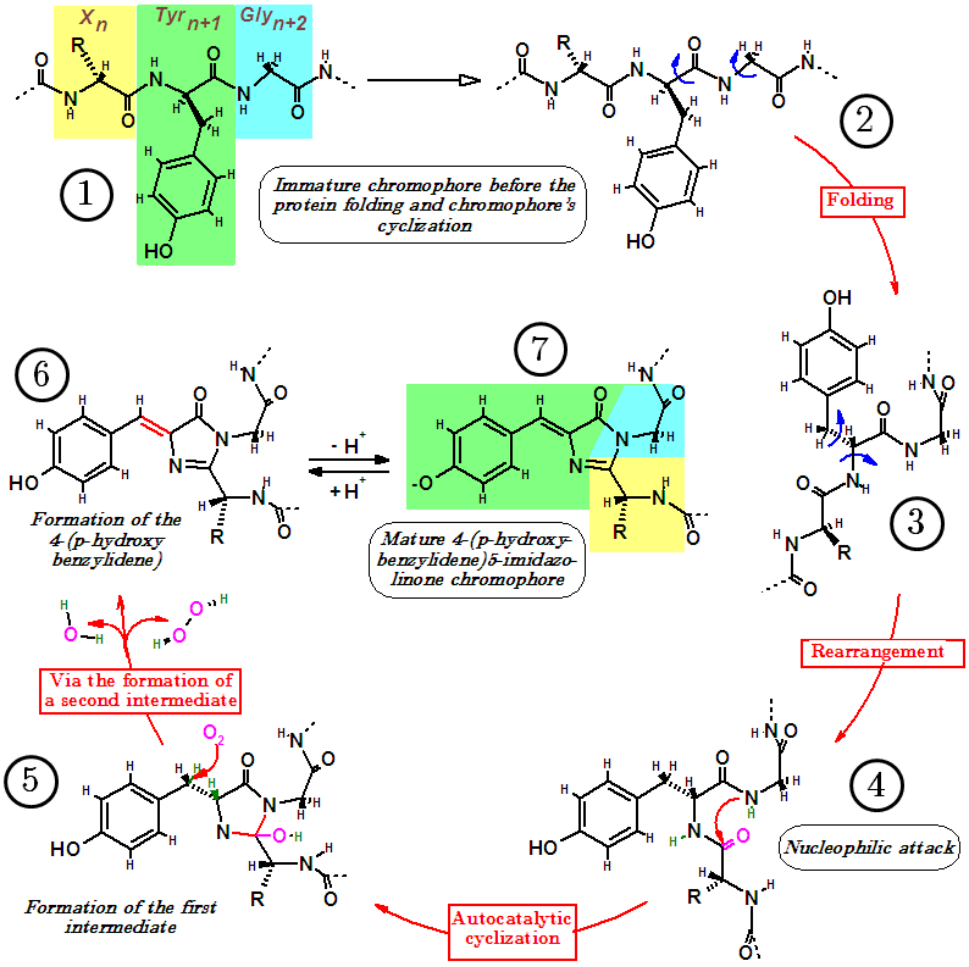

Figure I.2.5 - Post-translational formation of green fluorescent proteins chromophores

Those post-translational modifications lead to the dehydrogenation of the tyrosine to dehydrotyrosine (consisting of a phenol group and a methylene bridge), and the formation of an aromatic five-carbon cycle called imidazolinone ring. This system allows electron delocalization on a wide part of the chromophore (see after) and its properties of photon absorption as explained by the Perrin-Jabłoński diagram (pages 6-8). Within the protective environment of the β-barrel, the chromophore exposed to light having an energy that matches a possible electronic transition ($\lambda_{max}^{exc.} = 395$ nm for the wt-GFP while $\lambda_{max}^{exc.} = 475$ nm for the enhanced mutant EGFP) will be excited and relax with emission of green fluorescence ($\lambda_{max}^{em.} = 508$ nm).

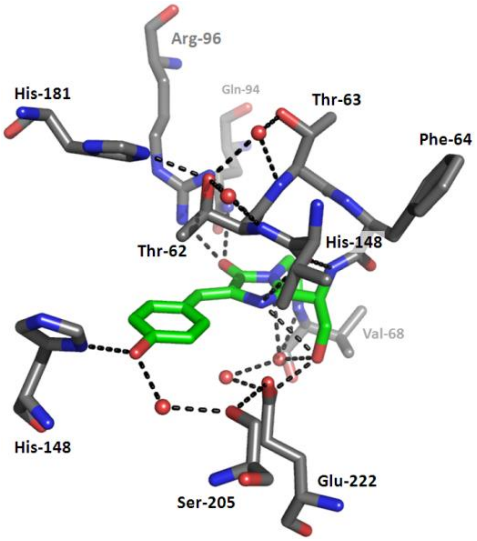

Figure I.2.6 - Illustration of the tight constraints imposed to the GFP chromophore by its environment and the hydrogen bond network.

Hydrogen bonds are represented by black dashes. The chromophore is depicted with green carbons while its surrounding residues have grey carbons. Water molecules are represented by red balls. Nitrogen and oxygen atoms are colored in blue and red respectively

The constraints imposed to the chromophore by its microenvironment not only force this compound to be a planar system, which increases the fluorescence quantum yield, but also draws tight hydrogen bonds (Figure I.2.6) that are very important for its fluorescence activity.

4 - The chromophore: a conjugated system

The hydroxybenzylidene moiety of the GFP chromophore is a crucial element that can be either protonated (phenol) or anionic (phenolate). Depending on the protonation state and the delocalization, the spectroscopic properties of the chromophore can be drastically modified.

a - Conjugated systems

The electronic configuration of a carbon atom in its ground state is [$1s^2$, $2s^2$, $2p^2$]. In an alkene-like structure such as carbon atoms in a phenol group, a double bond is formed between two adjacent carbons. This is achieved by the raising of one of the electrons 2s to a vacant atomic orbital p, the detailed valence shell configuration becoming [$2s^1$, $2p_x^1$, $2p_y^1$, $2p_z^1$]. The hybridization of three of those orbitals will give rise to three hybrid orbitals sp^2 in a planar

trigonal organization and to a non-hybridized orbital p that will be localized above and below this plan (Figure I.2.7). Each of those orbitals contains one electron.

The axial overlap of an orbital sp^2 with another orbital sp^2 (from another carbon atom for example) or with an orbital s (from a hydrogen atom) will give rise to a molecular orbital σ forming a simple covalent bond thanks to the pooling of two electrons. The partial lateral overlap of a non-hybridized orbital or the lone pair of an oxygen atom for example will lead to the formation of a molecular orbital π above and below the molecular plan, forming, with a molecular orbital σ, a double bond. Because the lateral overlap is not as good as the axial overlap of two p orbitals, the energy of a π orbital is weaker (264 $kJ.mol^{-1}$) than a σ one (348 $kJ.mol^{-1}$) and thus, although a double bond (σ+π) is shorter than a single σ bond, its energy is lower than twice that of a single bond.

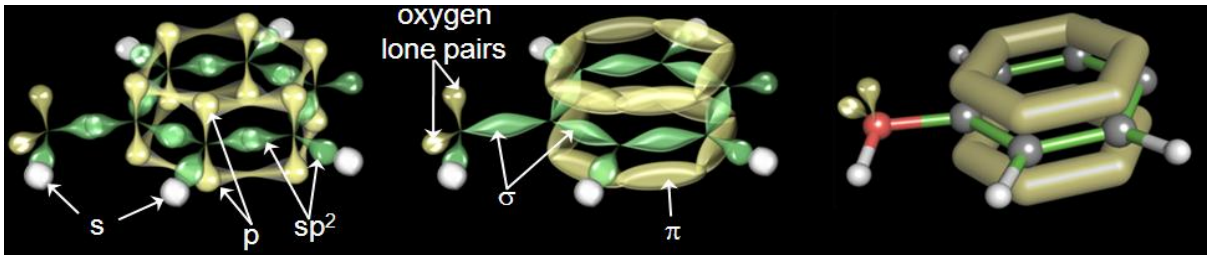

a – atomic orbitals in phenol | b – hybridized molecular orbitals in phenol | c – 3D representation of phenol and its electron delocalization

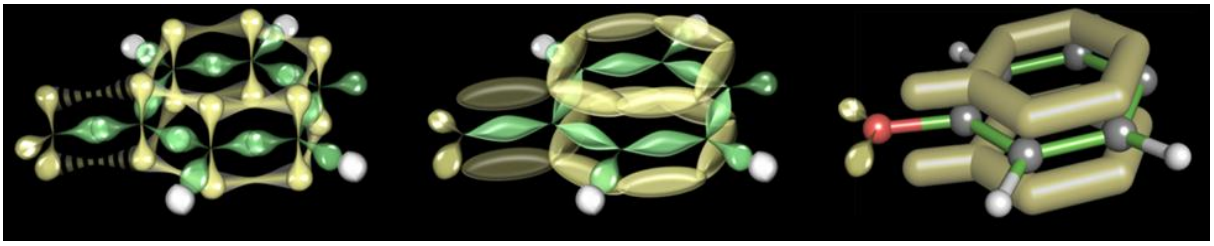

d – atomic orbitals in phenolate | e – hybridized molecular orbitals in phenolate | f – 3D representation of phenolate and its electron delocalization

Figure I.2.7 - Hybridization and electron delocalization in phenol (a-c) and phenolate (d-f)

When a molecule consists of alternated single and double bonds, the system is said to be conjugated with its electrons delocalized on several adjacent atoms. This delocalization implies that the bond order cannot be well described by Lewis representations of resonance structures

(also known as mesomeric structures). It must be seen instead as an average structure of the most probable resonance structures (those having the best charge repartitions) called resonance hybrid, where all the delocalized bonds are longer than a double bond and shorter than a single bond. A delocalized system can be linear and/or cyclic. In this last case, the sequence of unsaturated bonds, lone pairs or empty orbitals is named aromatic ring.

In the particular case of fluorescent proteins chromophores, the electrons are delocalized on a wide region composed of successions of conjugated bonds and aromatic rings, which give the chromophores their strong UV-Vis absorbance properties and specific absorbance spectra. The hydroxybenzylidene, the imidazolinone ring and the methylene bridge in between form the conjugated part of the chromophore. Depending on whether the chromophore is protonated or not and as seen above (Figure I.2.7), the hydroxybenzylidene moiety can be in its phenolic or phenolate form.

Considering the chromophore moiety alone (the protein matrix might have a strong effect), this protonation has the consequence of modifying the charge within this group and of favoring one or several resonance structures (Figure I.2.8). The resulting resonance hybrids of the protonated and unprotonated forms of the chromophore alone will thus be also slightly different.

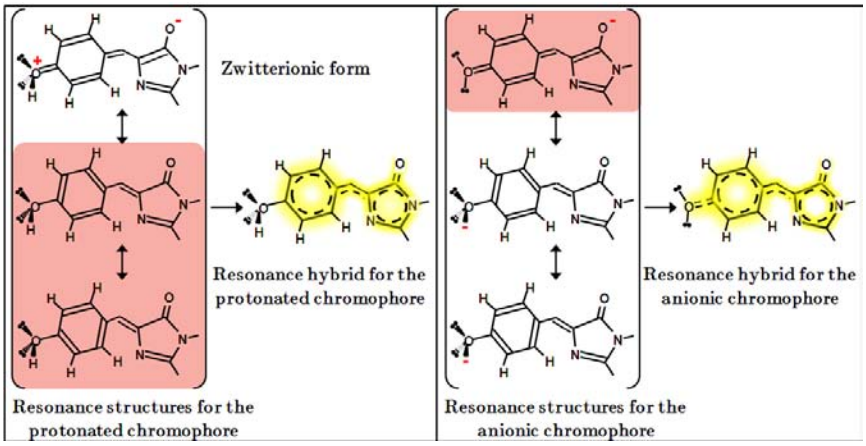

Figure I.2.8 - Resonance structures of the protonated and anionic chromophores with their respective resonance hybrids. The resonance structures displaying the best charge repartitions (pink background) are favored

Interestingly, the bond lengths for the two conjugated bonds involved in the methylene bridge between the imidazolinone and hydroxybenzylidene moieties, a bond (A) bound to the imidazolinone ring and a bond (B) bound to the phenol, have been calculated (Helms *et al.* 2000) as not having identical values. In its ground state indeed, the neutral chromophore displays bond lengths that are typical of a single bond for A and of a double bond for B. This becomes less clear in the anionic form and has a tendency to be the contrary in the excited state. This demonstrates once again that the global behavior of the chromophore is different depending on its protonation and excitation states.

b - Proton transfer and pH-dependent fluorescence

The wt-GFP chromophore absorbs light mainly at 395 nm (extinction coefficient = 30000 $M^{-1}.cm^{-1}$), with a minor absorption peak at 475 nm (extinction coefficient = 7000 $M^{-1}.cm^{-1}$). However, when excited at 395 nm, a conversion occurs that leads to a decrease of this absorption peak and the increase of the peak at 475 nm. A similar effect is observed when the pH is increased (Kneen *et al.* 1998).

As we said above, the conjugation within the chromophore is different depending on the protonation state, and its spectroscopic properties should also be different. It has been postulated, thus, that the protonated form (neutral) of the chromophore absorbs mainly at 395 nm and that its deprotonated (anionic) form absorbs mainly at 475 nm. By the way, the brighter mutant EGFP only displays a major absorption peak characteristic of the anionic chromophore with a slight bathochromic shift at 488 nm.

Another observation is that there is no fluorescence obtained when the chromophore is in its neutral form (peak at 395 nm) and only the deprotonated form gives rise to fluorescence emission, with the exception of the phenomenon of ESPT described below. Interestingly, several mutants of the Tyr66 residue have been produced with substitutions by other aromatic residues like His, Trp and Phe (Heim *et al.* 1994). Following what we said concerning the delocalization, one can expect that the substitution by a phenylalanine should result in the same conjugation as a protonated tyrosine, without the involvement of the oxygen in the

delocalization. However, while the Y66W and Y66H mutants exhibit a weaker and modified fluorescence, shifted in the cyan and blue, respectively, the Y66F mutant revealed to be almost non-fluorescent (only very weakly when excited by UV light). These fluorescence modifications can be explained by the fact that when the tyrosine is substituted with a phenylalanine, the electron delocalization looks like the one of the non-fluorescent protonated form of a tyrosine-containing chromophore, where the hydroxyl moiety is very unlikely to be involved in the electron delocalization.

For a molecule such as a chromophore to absorb a wavelength λ, the energy E corresponding to this wavelength ($E = h.c/\lambda = h.\nu$) must correspond to the energy ΔE between the initial and final absorbing molecular orbitals. In the case of π systems where a molecular orbital π is formed via the overlap of two non-hybridized atomic orbitals p_z^1 and p_z^2, the energy ΔE is equal to the energy between the frontier orbitals HOMO (highest occupied molecular orbital) and LUMO (lowest unoccupied molecular orbital) and is called band gap. The absorption of a photon allows the transition of an electron from the HOMO to the LUMO and the smaller the band gap, the lower the energy to excite the molecule is needed (Figure I.2.9).

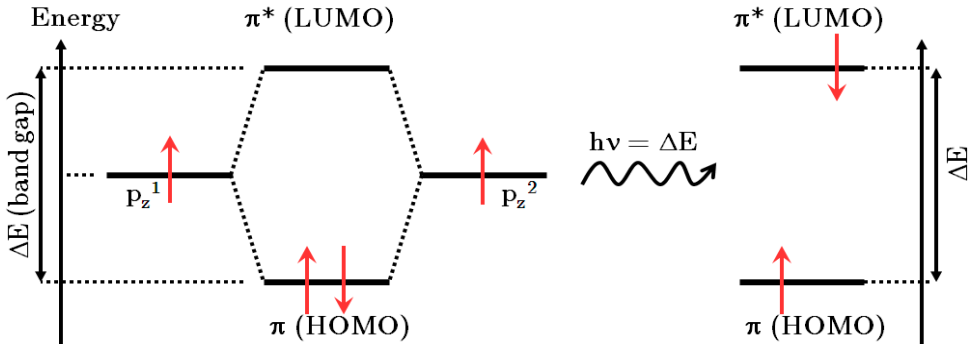

Figure I.2.9 - Diagram representing the HOMO and LUMO frontier orbitals

When the chromophore is excited, the energy absorption required to cross the band gap and promote an electron to the LUMO will thus give it its spectroscopic properties (absorption spectrum). The de-excitation from the LUMO will generate either a non-radiative relaxation (heat dissipation or conformational change) or a radiative relaxation (fluorescence).

Calculations by quantum mechanics methods of those frontier orbitals for the chromophore will thus allow the prediction of the molecule behavior during its photoexcitation. A representation of the neutral and anionic chromophores in their ground state (HOMO) for example, reveals a clear change indicating that the two molecules will not absorb light in the same way (Figure I.2.10).

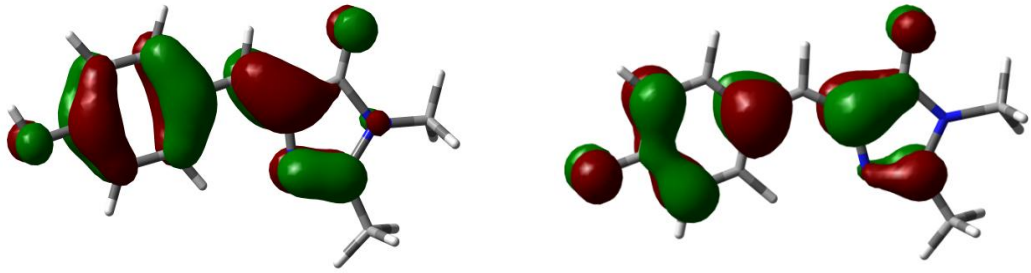

Figure I.2.10 - Representations of the HOMO for the neutral (left) and anionic (right) forms of the GFP chromophore, reproduced with courtesy of M. Lelimousin (IBS, Grenoble, France)

The strong change between the HOMO and the LUMO in the neutral GFP chromophore (Figure I.2.11) shows that the charges are withdrawn from the hydroxybenzylidene and redistributed to the methylene bridge and the imidazolinone moiety. The localization of the charges on the phenol ring of chromophoric tyrosine has indeed been evaluated to 67% in HOMO and 25% in LUMO (Voityuk *et al.* 1998).

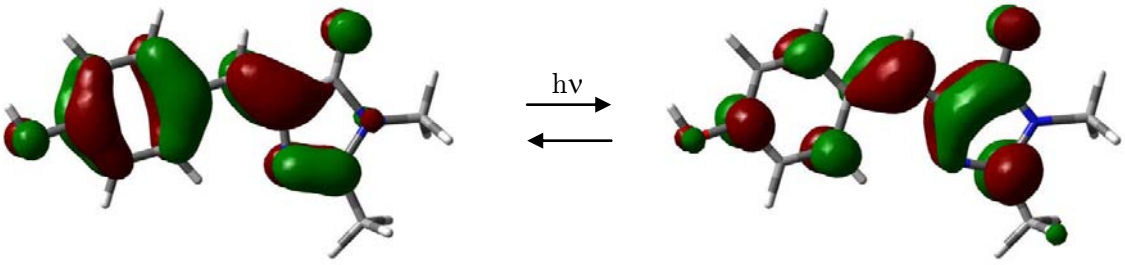

Figure I.2.11 - Representations of the HOMO and LUMO of the GFP neutral chromophore, reproduced with courtesy of M. Lelimousin (IBS, Grenoble, France)

The redistribution of the π electron cloud involves an intramolecular charge transfer (ICT) that weakens the hydroxyl electron density (Agmon 2005). This has the direct consequence that the acidity constant (pKa) of the hydroxybenzylidene decreases so drastically that it easily

deprotonates once in the excited state. It has been described, by the way, that the hydroxyphenyl acidity is much higher in the excited state than in the ground state (Chattoraj *et al.* 1996; Fron *et al.* 2007). Moreover, it has also been shown that the acidity is lower in triplet state T_1 than in singlet excited state S_1 (Turro 1991). This proton transfer is induced under illumination and is thus called Excited State Proton Transfer (ESPT).

The network of interactions established between the chromophore (and especially the hydroxybenzylidene), surrounding residues and water molecules in GFP (Figure I.2.6), governs a proton transfer between the chromophore and neighboring side chains. It has been proposed (Brejc *et al.* 1997) on the basis of the structural analysis that Glu-222 is the key residue that, with hydrogen bonding via a bound water molecule and Ser-205, is a proton acceptor during the mechanism of ESPT.

The anionic form (basic form, B) of the chromophore can be obtained either by ESPT (irradiating the protein at 395 nm) or by increasing the pH. Since the neutral form (acidic form, A) can be re-obtained by decreasing the pH, the equilibrium and interconversion between the neutral and anionic forms of the chromophore can be described by a cycle, nowadays called Förster Cycle (Figure I.2.12).

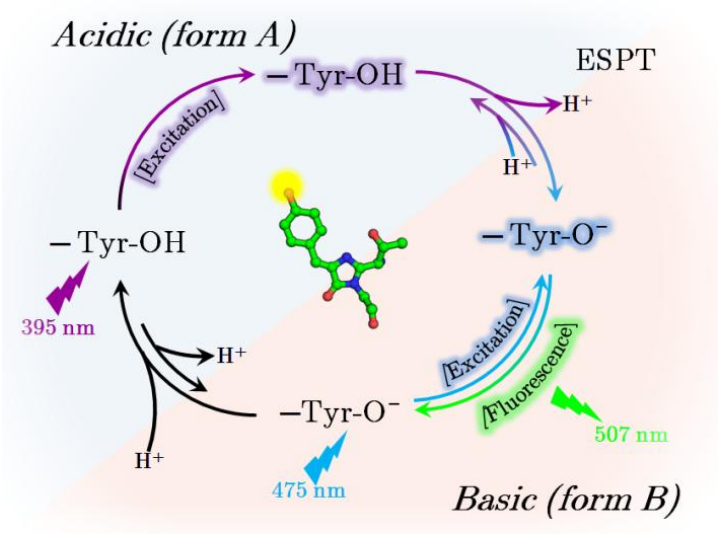

Figure I.2.12 - Scheme of the GFP Förster cycle involving an excited state proton transfer (ESPT)

This type of cycle has been proposed by Theodor Förster (Förster 1949; 1950) to describe the changes in acidity of certain molecules upon excitation. Noteworthily, the GFP was the first protein in which such a cycle has been observed (Youvan & Michel-Beyerle 1996).

In reality, the proton transfer from the hydroxybenzylidene moiety is probably mediated by an intermediate state (I). The fact that this intermediate state and the basic form (B) are slightly different make that the fluorescence emission is also slightly different if the form A is excited at 395 nm (ESPT involved) or the form B is excited at 475 nm (no ESPT involved).

5 - The photobleaching phenomenon

In addition to the events already described, the parasitic event of irreversible photobleaching (or fading), this loss of fluorescence (and thus of information) that ultimately happens when a FP is repeatedly excited, is a problem that often has to be avoided. Certain techniques have taken advantage of this phenomenon such as the so-called fluorescence recovery after photobleaching (FRAP) technique. In this technique, a small region of a fluorescent sample is photobleached and the molecular diffusion of unbleached molecules within the bleached area will lead to the recovery of fluorescence and the determination of the diffusion coefficient (Figure I.2.13).

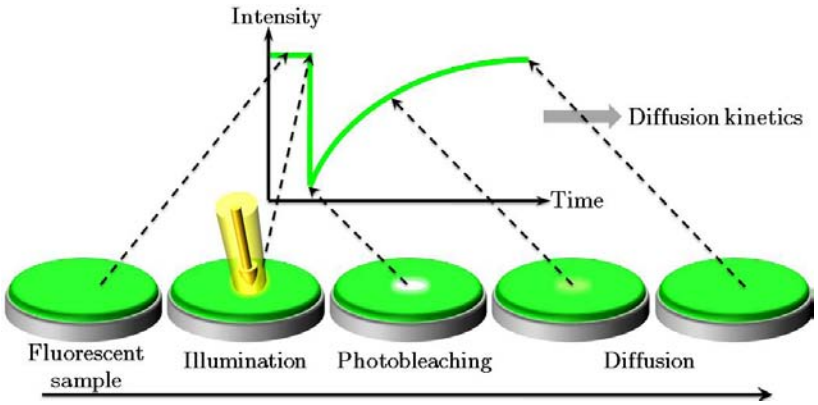

Figure I.2.13 - The FRAP technique uses the photobleaching phenomenon as an advantage

This phenomenon of irreversible photobleaching though, has to be understood in order to avoid it and further improve the photostability of fluorescent proteins.

6 - The photoactivation phenomenon

Evidences of a photoinduced decarboxylation of Glu-222 using UV-light have been found in wtGFP (van Thor *et al.* 2002; Bell *et al.* 2003). This reaction produces an irreversible bleaching of the main excitation peak typical of the protonated form (395 nm) and an increase of the peak typical of the deprotonated form (475 nm), showing that light absorption not only excites the chromophore but can also alter its environment. The importance of Glu-222 and the spectroscopic properties of GFP has also been shown with the mutant E222G that displays the same effect (Ehrig *et al.* 1995).

A very weakly fluorescent GFP variant called PA-GFP (for "photo-activatable" GFP) has been designed to take advantage of such a decarboxylation at lower energies (488 nm), resulting in a 100-fold brighter fluorescence once photoactivated by this decarboxylation (Patterson & Lippincott-Schwartz 2002). This property allows new kind of experiments in cell biology using probes that can be activated on demand (Post *et al.* 2005; Schneider *et al.* 2005; Stark & Kulesa 2005). A cyan-to-green photoactivatable variant of a GFP-like protein from *Æquorea cœrulescens*, called PS-CFP, for photoswitchable cyan fluorescent protein (Chudakov *et al.* 2004) uses this same effect to be irreversibly transformed upon actinic irradiation at 405 nm. Recently, a new photoactivatable fluorescent protein, called PAmCherry1 (Subach *et al.* 2009), has been designed from the red fluorescent protein mCherry (Shaner *et al.* 2004). This fluorescent protein, as well as two other variants called PAmCherry2 and PAmCherry3 (each containing at least 10 mutations compared to mCherry), can be photoactivated by violet light from a non-fluorescent form to a red fluorescent form.

As we have seen, those last years the *Æquorea victoria* GFP has been (and is still) widely studied for its major interest as a biological marker. Several mutants have been designed to

widen the color palette and possibilities offered by this tool, like for example a cyan-emitting variant called CFP, in which the chromophoric tyrosine has been mutated to a tryptophan, which is responsible of an hypsochromic shift from 507 to 476 nm. Another example is a yellow emitting variant called YFP, in which a π-stacking between the chromophoric tyrosine and another tyrosine produces a bathochromic shift from 507 to 527 nm. This kind of mutants allowed conducting more complicated experiments such as imaging using Förster Resonance Energy Transfer (FRET). If CFP and YFP molecules are close enough (about 5 nm), since there is a spectral overlap between the emission spectrum of the donor CFP and the excitation spectrum of the acceptor YFP, a transfer of the excitation energy will occur so that the yellow emission from YFP will be observable (Figure I.2.14).

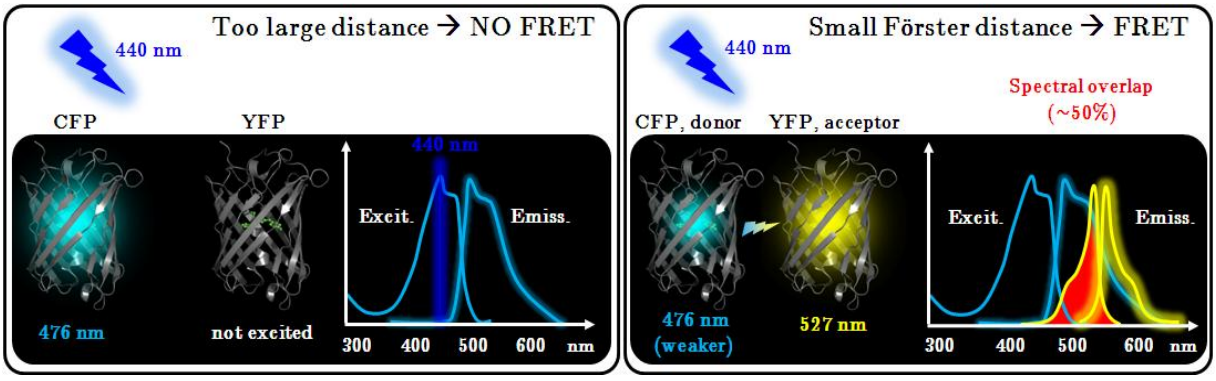

Figure I.2.14 - The FRET pair formed by CFP and YFP

In spite of all these improvements, recent discoveries in anthozoan animals brought shattering news to this field by widely expanding this color palette and our understanding of the complex photoactivation processes involved.

Part 2 - The discovery of anthozoan fluorescent proteins

1 - Fluorescent-like proteins are common in oceans

At the beginning of the 2000's, the discovery of GFP-like proteins in other animals than the jellyfish *Æquorea* initiated a wide search to expand the fluorescent proteins toolbox. This search led to the conclusion that GFP-like proteins are rather common in ocean animals; however, their late discovery can be explained by the fact that the animals producing those proteins are anthozoans which are essentially non-fluorescent organisms.

Although anthozoans are categorized in a huge independent class composed of corals and sea anemones, they have a common ancestor with hydrozoans (of whom the jellyfish *Æquorea* is a representative) since they are all classified in the phylum of cnidarians (Cf. p.264, Appendix IV - Phylogeny of cnidarians producing FPs & CPs). However, if the fluorescent properties of *Æquorea victoria* were rather obvious to observe (the bioluminescence was produced in darkness), this was not the case at all for anthozoans since the high diversity of colors they display does not necessarily originate from GFP-like proteins.

a - DsRed, first member of a large family

These discoveries started with the naturally red fluorescent protein (RFP) drFP583, also known as DsRed, found in the coral *Discosoma striata* (Matz *et al.* 1999; Baird *et al.* 2000). Compared to GFP, a supplementary maturation step of the 4-(*p*-hydroxybenzylidene)5-imidazolinone chromophore (Cf. p.25; Figure I.2.5, step 7) occurs. This step involves the oxidation of a mainchain bond next to the chromophore into an acylimine bond [—C(=O)N=C—] that extends the electron delocalization to a larger zone (Figure I.2.18, b). This has the consequence to shift the fluorescence emission toward less energetic (longer) wavelengths (Tubbs *et al.* 2005). The crystallographic structure of the protein revealed a tetrameric organization of the β-barrels (Yarbrough *et al.* 2001) unlike GFP, which is a common property of anthozoan GFP-like proteins. Although being red fluorescent

($\lambda_{max}^{em.}$ = 583 nm), both the chromophore (Gln-Tyr-Gly) and the β-barrel structure displayed high similarities with those of GFP (Gross *et al.* 2000) and, interestingly, the chromophore maturation is very long, passing through an intermediate green state, which provides further evidence for a common origin with the classical GFP. This long maturation even allowed the creation of a mutant of drFP583 that slowly maturates from the green to the red form, allowing it to act as a "fluorescent timer" when produced in cells (Terskikh *et al.* 2000). An interesting point about DsRed, as well as all the other anthozoan GFP-like proteins that were discovered later, is that it can be considered as being intrinsically fluorescent (Heikal *et al.* 2000). Indeed, at the difference of GFP, those proteins are not involved in a bioluminescence pathway and the excitation is directly provided by the sunlight since anthozoans are organisms that live in shallow waters.

While GFP is found in a dimeric form, DsRed (as the other anthozoan FPs) adopts a tetrameric organization. Although, it took several years and a lot of mutations, DsRed could be produced in a monomeric form, which is the most useful form of a fluorescent protein (because it is easier to use and disturbs less the tagged system). The big efforts in mutating the GFP (Tsien 1999) were also applied to DsRed in order to change its fluorescence properties. This gave rise to a series of new monomeric variants named after fruits (m-Honeydew, m-Banana, m-Strawberry, m-Tomato...) and emitting their fluorescence in a wide range of colors, from light orange to red (Fradkov *et al.* 2000; Shaner *et al.* 2004).

b - Glowing by nature?... Fluoroproteins & chromoproteins

After this finding, the classis of anthozoans was deeply studied in order to find other members of the GFP family. It was found that although colors in corals and anemones mainly came from small dye molecules, some animals like for example the sea anemone *Anemonia sulcata*, produce non-fluorescent but colored GFP-like proteins called chromoproteins (CP), which participate to their colorful aspect (Lukyanov *et al.* 2000). These chromoproteins only absorb certain wavelengths, giving their colors, but relax by a non-radiative way so that they emit extremely low fluorescent signals, if any. Several other FPs and CPs of various colors have

been found in *A. sulcata* (Wiedenmann *et al.* 2000) as well as in other organisms. The biological role of such proteins is of course puzzling and even if some photoprotective actions have been proposed (Salih *et al.* 2000) as well as the possibility that colorations induced by GFP-like proteins may attract/repel fishes (Matz *et al.* 2006), their functions remain rather mysterious.

Many other reef coral FPs and CPs were found in other anthozoans genera (*Montipora*, *Montastraea*, *Favia*, *Zoanthus*...) like for example the tetrameric RFP eqFP611 from *Entacmea quadricolor*. Concerning the resemblances and common origins of FPs and CPs, a very interesting property of chromoproteins is that very few mutations are sufficient to transform a chromoprotein into a fluorescent protein. This was the case for example with the red chromoprotein from *Heteractis crispa* (HcCP) that was transformed thanks to a single point mutation into HcRed, a dimeric red fluorescent protein (Gurskaya *et al.* 2001a) whose green to red maturation of the chromophore is identical to that of DsRed and eqFP611, involving the formation of an acylimine bond (Figure I.2.18, b).

c - Under which form are chromophores the most stable?

Surprisingly, the chromophore of eqFP611 is stable and fluorescent in a trans conformation (stereoisomer Z) and not in cis conformation (stereoisomer E) like for most FPs. Chromophores of FPs are indeed more often in a cis planar conformation and when in trans, they are generally more distorted (Quillin *et al.* 2005). However, non-coplanar cis conformations for the CP Rtms5 (Prescott *et al.* 2003) and coplanar trans conformations for eqFP611 (Petersen *et al.* 2003) have already been described. The choice between cis and trans conformation probably depends on the steric constraints driving the chromophore formation (Barondeau *et al.* 2003; Nienhaus *et al.* 2008) and the energy difference between both conformations has been calculated as being very small (He *et al.* 2003). It has been proposed recently that chromophores of FPs could stay in a resting distorted conformation until being excited and becoming planar (Pletnev *et al.* 2008). The same authors propose that chromophores could undergo cis/trans isomerizations induced by pH changes only. The variation of protonation

state induced by pH modifications could then be sufficient to alter the interactions between the chromophore and its environment, leading to cis/trans isomerizations.

In a similar way, it was found that some mutations around the chromophore of fluorescent proteins could either bleach the fluorescence, transforming them into chromoproteins (Bulina *et al.* 2002), or even modify the fluorescence spectrum, and thus the color of the emitted light (Gurskaya *et al.* 2001b). In all those FPs and CPs, it is important to notice that the chromophore sequence is always X-Tyr-Gly, the first aminoacid varying a lot from a protein to another. Since the β-barrel structure is always conserved, the spectroscopic properties are thus strongly related to the chromophore configurations and its environment, whose slight modifications create cyan, green, orange or red fluorescent proteins.

2 - Photochromic reversibly switchable fluorescent proteins

Recently, our perception of fluorescent proteins' behavior has been drastically changed by the discovery of the so-called photoactivatable fluorescent proteins (PAFP). In particular, the discovery of reversibly switchable fluorescent proteins (RSFP) has shown that the phenomenon of photobleaching was not inevitably an irreversible phenomenon. Those proteins can indeed be either in a bright (on) state or a dark (off) state, depending on the actinic wavelength they are submitted to. Such a property is called photochromism and is defined as "a photoinduced transformation of a molecular structure, photochemically or thermally reversible, that produces a spectral change, typically, but not necessarily, of visible color"[6].

The observation of compounds being able to change their spectral properties in a reversible way under illumination was made for the very first time more than 140 years ago (Fritzsche 1867) on orange tetracene. It was noticed that when this chemical was illuminated, it underwent a reversible transformation to a colorless material. This kind of reversible

[6] Glossary of terms used in photochemistry, IUPAC recommendations 1996, 68, p.2259

photoreaction generally occurs between a colored form and a colorless form called leuco (from the Greek word λευκος [leukos] meaning "white, clear").

This phenomenon was first named "phototropy" (Marckwald 1899) and although this term is still valid in chemistry, it created confusion with the word phototropism being nowadays understood as the phenomenon by which some plants and fungi grow toward a light source. Therefore, in 1950 the photochemist Yehuda Hirschberg (Figure I.2.15) proposed the term "photochromism" (from the Greek words φῶς [phos] meaning "light" and χρωμα [chroma] meaning "color").

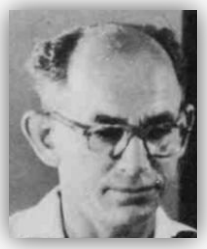

Figure I.2.15 - Photograph of Yehuda Hirschberg

Hirschberg defined the photochromism as being the reversible transformation of a single chemical species being induced in one or both directions by electromagnetic radiation between two states having distinguishable absorption spectra (Dürr 1990). Generally, the back conversion toward the most stable form is photo-induced but is very often in competition with a thermal back conversion. This causes most photochromic molecules to also display a thermochromic behavior (from the Greek word θέρμη [thermai] meaning "heat").

a - Dronpa

The first discovered fluorescent protein exhibiting photochromic switching between a green fluorescent form and a leuco non-fluorescent form after an actinic illumination was called Dronpa. This engineered PAFP was isolated by the groups of Atsuchi Miyawaki and Johan Hofkens from the scleractinian "chalice coral" *Pectiniidae sp.* (Habuchi *et al.* 2005a). To create Dronpa, the wild-type form called 22G was engineered by six mutations to form a monomeric form (22Gm3). Dronpa is the first discovered member of the reversibly switchable fluorescent proteins (RSFP): its green fluorescence signal can be rapidly bleached under cyan light ($\lambda^{act.} = 488$ nm) and very efficiently restored when irradiated by violet light

($\lambda^{act.}$ = 405 nm). The name Dronpa is composed from the ninja term ドロン [d(o)ron] meaning "vanishing, disappearing" in reference to the behavior of fluorescence fading and the two letters PA standing for Photo-Activation.

The crystal structures of Dronpa (Habuchi *et al.* 2005a; Wilmann *et al.* 2006) revealed that the photochromism was accompanied by a photoinduced isomerization of its chromophore (Figure I.2.18, a). In its cis conformation, the chromophore is indeed characteristic of the protein in its bright form while the dark (non-fluorescent) form is produced when the chromophore is in its trans conformation. This reversible photoisomerization can be repeated many times. However, Atsuchi Miyawaki's group in a recent NMR study on Dronpa (Mizuno *et al.* 2008), has found that an essential step for the reversible bleaching of the protein is induced by the loss of a hydrogen bond between the chromophoric tyrosine and the β-barrel. This would increase the flexibility of the chromophore, probably the first step to allow the photoswitching, which loses most of its energy by vibrating instead of emitting fluorescence.

Several mutants of Dronpa with higher photoswitching quantum yields have been recently successfully obtained, in order to increase the photoactivation efficiency of RSFP-based microscopy experiments (Figure I.2.16).

Miyawaki's and Hofken's groups created two variants of Dronpa that exhibit an enhanced switch-off conversion when illuminated at 490 nm. The first mutant, containing the mutation M159T, was called Dronpa-2 and the second, containing the mutations V157I and M159A, was called Dronpa-3 (Ando *et al.* 2007). Dronpa-2 and Dronpa-3 revealed bright-to-dark conversion quantum yields ~150 times and ~18 times higher than Dronpa, respectively. If fluorescence recoveries photo-induced at 400 nm look similar for the three proteins Dronpa, Dronpa-2 and Dronpa-3, thermal recoveries are much faster for Dronpa-2 and Dronpa-3 (faster for Dronpa-3) than for the parent protein Dronpa.

In parallel, Hell's group also produced fast-switching mutants of Dronpa (Stiel *et al.* 2007) also involving the two residues Val-157 and Met-159. The mutant Dronpa-V157G, called rsFastLime (rs: reversible switchable, lime: visible color of the protein in a highly concentrated

water solution in the daylight[7]), displays for example a switch-off half-time of <5 s (~50 times faster than Dronpa). The mutant Dronpa-M159T, (identical to Dronpa-2) has been described as exhibiting an even faster switch-off half-time of 230 ms (~1150 times faster than Dronpa).

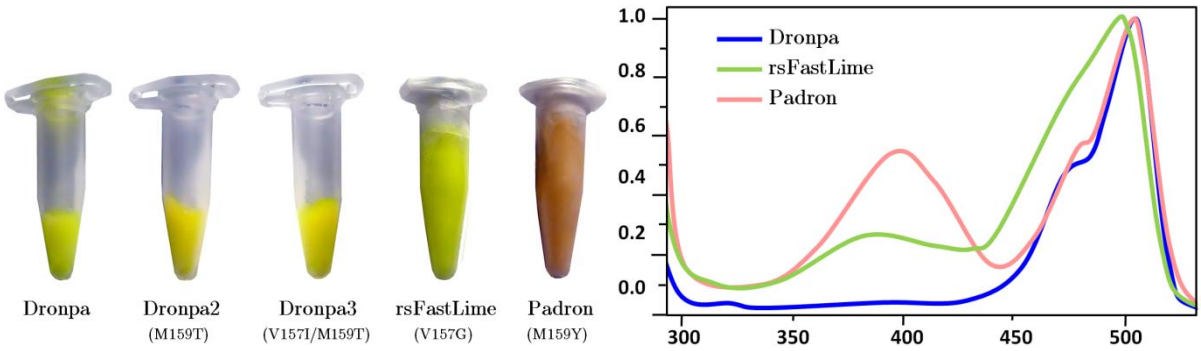

Figure I.2.16 - The color of Dronpa variants - Left: frozen concentrated solutions of Dronpa and its variants Dronpa-2, Dronpa-3, rsFastLime and Padron are shown. Samples provided by P. Dedecker and J. Hofkens . Right: absorption spectra of Dronpa, rsFastLime and Padron reproduced from (Dedecker et al. 2006; Stiel et al. 2007; Andresen et al. 2008)

The mutation of Met-159 in Dronpa (described above) revealed that this residue is instrumental for photoswitching properties of RSFPs and several other mutants have been created by Hell's group, using this property. The mutation M159Y in rsFastLime led, after several other rounds of mutations, to a RSFP that was called Padron (Andresen *et al.* 2008) and which, as indicated by its name, works in a reversed way compared to Dronpa. This means that instead of inducing a negative-switching like in all the other RSFPs, blue-light switches on the fluorescence and UV light switches it off (positive switching). This protein almost keeps the fast-switching properties of its parent rsFastLime. Along the process for the creation of Padron, the same authors found that the mutation M159C produced, after several other rounds of mutations, a protein that had a blue-shifted and broader absorption spectrum. This negative-switching RSFP called bsDronpa (bs standing for broad-absorption spectrum) can thus be switched-off with a broad range of wavelengths and displays a larger Stokes shift than Dronpa.

[7] Details provided in (Hofmann 2007)

b - mTFP0.7

mTFP0.7 is one of the intermediate variant that was obtained along the series of mutations performed on the cyan fluorescent protein cFP484 from the "brown star polyp" coral *Clavularia sp.* to produce the protein mTFP1 (Figure I.2.17). Although cFP484 is naturally a tetramer (like all the other coral FPs), mutagenesis efforts produced dimeric and then monomeric forms called dTFPs and mTFPs, the prefixes "d" and "m" standing for "dimeric" and "monomeric" respectively and "TFP" standing for "Teal Fluorescent Protein" (Ai *et al.* 2006). The name of the protein comes from the color teal, a dark cyan color whose coding is 0, 128, 128 in standard RGB format (cyan being 0, 255, 255). This name was chosen because teal fluorescent proteins emit their fluorescence in a range of wavelengths a bit shifted (from 485 to 492 nm) compared to the cyan cFP484.

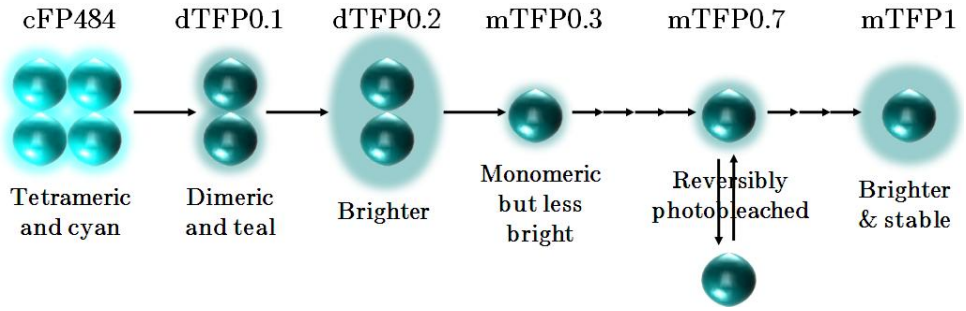

Figure I.2.17 - Engineering of cFP484 into teal fluorescent proteins

The authors were surprised to find that one of the monomeric teal FP, mTFP0.7, rapidly lost its fluorescence upon illumination at 450-488 nm but recovered it by its own within minutes or within seconds if illuminated at about 400 nm. The structural characterization of mTFP0.7 revealed here again that a cis/trans isomerization of the chromophore was involved in the reversible photobleaching properties of this protein (Henderson *et al.* 2007). In its trans, non-fluorescent form, the chromophoric phenol moiety establishes few hydrogen bonds (one with a glutamate and one with a water molecule) with residues that could stabilize an anionic form so that the chromophore is most probably neutral in its dark form (Figure I.2.18, a). This trans state was also shown to be non-coplanar and rather disordered, which could also play a role in the loss of fluorescence.

c - asFP595

Another photochromic fluorescent protein is known: asFP595 which name is composed of the two letters "a" and "s" referring to the host animal *Anemonia sulcata*, a sea anemone (now officially called *Anemonia viridis*) and 595 which is the value in nanometers of the maximum fluorescence peak of the activated fluorescent form (Andresen *et al.* 2005). This tetrameric protein isolated from the sea anemone *Anemonia sulcata* is originally a deep purple colored chromoprotein called asCP or asulCP. Crystallographic structures revealed an autocatalytic cleavage of the mainchain acylimine bond between the chromophore and the preceding residue (Wilmann *et al.* 2005; Henderson & Remington 2006) which is a further maturation step of DsRed-like FPs. The consequence of this cleavage is that a ketone becomes involved in a broader electron delocalization of the chromophore. The degree of FPs' maturation is probably linked with their structures that were accommodated along evolution to allow or prevent the next maturation steps. However, this phenomenon is not fully understood yet. Under green light excitation ($\lambda^{act.} \sim 550$ nm) this non-fluorescent protein is switched to a red fluorescent form (called "kindled" state). This process is reversible under illumination by blue light ($\lambda^{act.} \sim 450$ nm), giving to this protein a photochromic behavior (Ando *et al.* 2004; Schafer *et al.* 2008), although functioning in the reverse way compared to Dronpa since the most stable state is non-fluorescent (Figure I.2.18, c). Like Dronpa and mTFP0.7, the protein is in its non-fluorescent state when the chromophore is in trans conformation and switches to the fluorescent state via a photoinduced reversible trans/cis isomerization. A mutant (A143G) of this protein called KFP1 (for "kindling fluorescent protein") has been engineered to irreversibly photoactivate the protein in a fluorescent state (Chudakov *et al.* 2003; Quillin *et al.* 2005).

d - Other RSFPs

Recently, other reversibly switchable fluorescent proteins have been engineered, both in a negative-switching way like in Dronpa or mTFP0.7, and in a reversible positive-switching way like in asFP595 or Padron. For example, the red fluorescent mCherry (Shaner *et al.* 2004) was mutated to obtain two RSFPs called rsCherry and rsCherryRev (Stiel *et al.* 2008). While

rsCherry (mCherry E144V, I161S, V177F, K178W) displays a positive-switching mode (which means that the excitation wavelength, 550 nm, also turns the protein to a brighter state), rsCherryRev (with the supplementary mutations S146C, Q163M) shows a more classical negative-switching mode (the excitation wavelength turns the protein to its dark state).

To summarize, reversibly switchable fluorescent proteins (RSFPs) constitute a PAFP family that contains only three recently discovered members: Dronpa, mTFP0.7 and asFP595. The excitation of these proteins at the maximum excitation peak of their chromophore allows the photoinduced isomerization of this compound. In their cis conformation, proteins are able to emit fluorescence (with a color depending on the maturation and environment of the protein's chromophore) and in their trans conformation, the fluorescence is bleached. Although this is far from being clear, the photoisomerization does not seem to be the only cause of photobleaching and both a change in planarity and in protonation of the chromophore seem involved. All the studies on those proteins indeed, tend to show that in their cis (bright) conformation, the chromophores are mainly in a planar anionic form whereas a distorted neutral form is reported when the chromophore is in its trans (dark state).

Looking at all the FPs that are known, it looks rather clear that chromophores are very often more distorted and non-fluorescent in the trans conformation and more planar in the cis conformation (Quillin *et al.* 2005). However, this is not always the case as already seen with the trans fluorescent chromophore of HcRed, and examples of non-planar cis chromophores have already been reported in bright FPs (Prescott *et al.* 2003; Pletnev *et al.* 2008) as well as cases of planar trans chromophores (Petersen *et al.* 2003). We can thus propose that the planarity is maybe not that crucial in the phenomenon of transient loss of fluorescence compared to the change of protonation state concomitant with the chromophore isomerization.

The most exciting property of such proteins is their reversible nature, since the very fast photoinduced back-isomerization of the chromophore will rescue the protein's initial spectroscopic properties. Because Dronpa is the first member of the RSFPs, such photochromic

FPs will be referred to in this thesis as being part of the "Dronpa-like family". Like most of the already known photochromic molecules, these proteins are also thermochromic, meaning that even without excitation, the most stable conformation of the chromophore (cis for Dronpa or mTFP0.7 and trans for KFP) will be slowly restored; this phenomenon is accelerated as the temperature is increased. The photoswitchings between "on" and "off" states in the photochromic FP Dronpa have also been shown to be dependent on the protonation states of its chromophore (Habuchi *et al.* 2006) and calculations on asFP595 revealed that its photoswitchings are also related to its protonation states (Andresen *et al.* 2005).

Another family, however, gathers fluorescent proteins that exhibit photoinduced processes that are no less impressive: the green-to-red photoconvertible fluorescent proteins.

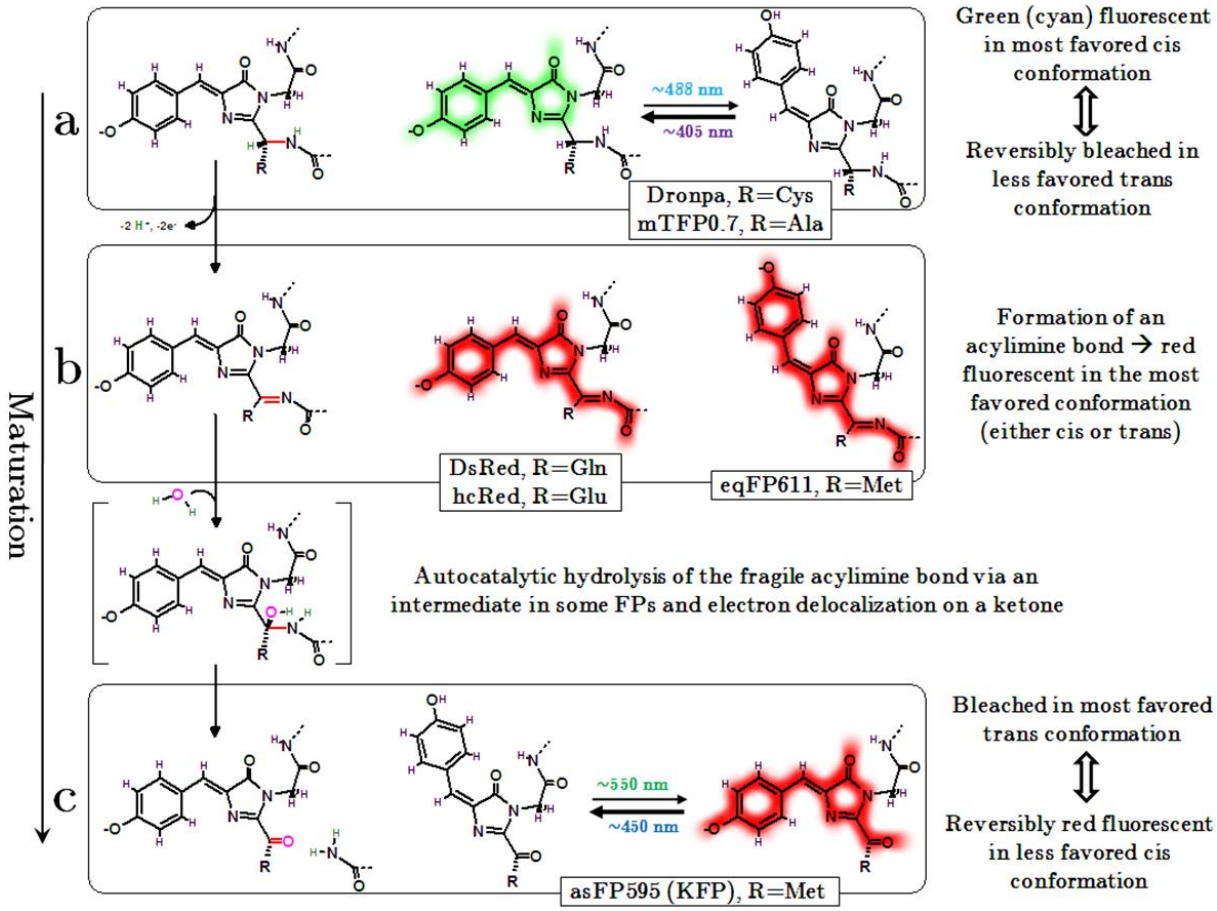

Figure I.2.18 - Maturation of some chromophores of anthozoans FPs. Three types of chromophores are represented: reversibly photoswitchable GFP-type chromophores like for Dronpa or mTFP0.7 (a), acylimine-containing chromophores of red FPs like DsRed, HcRed or eqFP611 (b) and reversibly switchable ketone-containing chromophores like for KFP (c)

3 - Green-to-red photoconvertible fluorescent proteins

In parallel with the discovery of Dronpa-like PAFPs, other reef coral fluorescent proteins have been discovered that demonstrate the possibility of having their fluorescence irreversibly photoconverted from an initial green fluorescent form to an orange/red fluorescent form.

a - Kaede

The first member of this PAFP family, named Kaede (Ando *et al.* 2002). This fluorescent protein contains a chromophore made of the three modified aminoacids His-Tyr-Gly and is the first discovered member of a family of PAFPs that we will call in this thesis "photoconvertible fluorescent proteins" (PCFPs) to distinguish with the RSFPs that have been described above. The members of this family irreversibly photoconvert from a green fluorescent form to a red fluorescent form after an actinic illumination. Kaede was isolated in 2002 by the group of Atsushi Miyawaki (Figure I.2.20) from the scleractinian (stony) "open brain coral" *Trachyphyllia geoffroyi (Veron 2000f)*. It shows excitation and emission maxima at 508 nm and 518 nm, respectively but when submitted to an (actinic) irradiation at $\lambda^{act.} = 400$ nm, it irreversibly photoconverts to a red form with excitation and emission maxima at 572 nm and 582 nm, respectively. The name Kaede originates from the Japanese maple tree *Acer palmatum* whose Japanese name カエデ [kaede] is the protein's eponym. This name was chosen as a comparison with the protein's colors since the color of the tree's foliage drastically turns from tender green to crimson red in autumn.

The crystal structure of Kaede confirmed that the green-to-red photoconversion was due to a UV-induced cleavage of the backbone between the first residue of the chromophore (His62) and the previous one (Mizuno *et al.* 2003). This breakage transforms at one side the residue 61 into an amide residue and forms at the other side a double bond between C_α and C_β of His-62. The formation of this double bond allows the spreading of the delocalized π-system formed by

the chromophoric tyrosine and the imidazolinone moiety with the involvement of the histidine imidazole ring in the electron delocalization (Figure I.2.19).

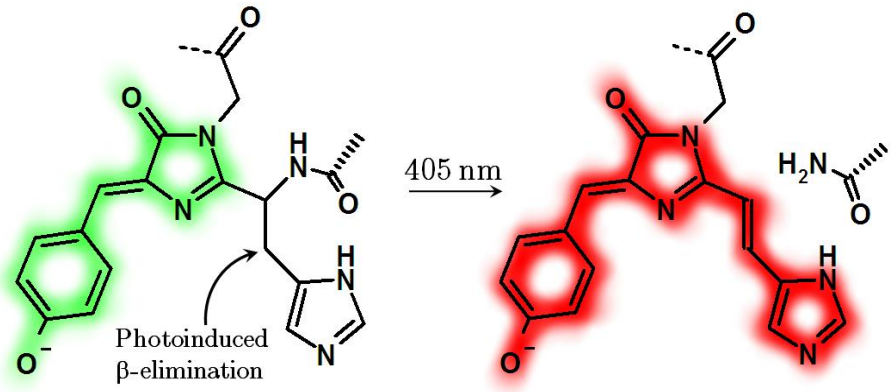

Figure I.2.19 - Photoinduced backbone cleavage of the chromophore in Kaede-like PAFPs

Chemically, the region on which the electron delocalization extends is called 2-[(1E)-2-(5-imidazolyl)ethenyl] (or 2-(amino-2-(5-imidazolyl)ethyl)-1-carboxymethyl) and thus, the newly formed chromophore is called 2-[(1E)-2-(5-imidazolyl)ethenyl]-4-(*p*-hydroxybenzylidene)5-imidazolinone. The consequence is that following the excitation of the protein, the emitted photons are of a lower energy than those emitted when only the chromophore formed by the hydroxybenzylidene and the imidazolinone moieties are excited (i.e. the fluorescence is shifted toward longer wavelengths), which results in a red fluorescence.

b - KikGR

Based on those findings, Miyawaki's group mutated KikG, a fluorescent protein isolated from the scleractinian "pineapple coral" *Favia favus* (Veron 2000b), to insert the chromophore His-Tyr-Gly and to adapt its environment. This had the consequence of turning this protein into a PCFP called KikGR (Tsutsui *et al.* 2005) and also known by its commercial name "Kikume". This engineered PAFP has similar spectroscopic properties than those of Kaede since the excitation and emission maxima in its green form are 506 nm and 517 nm respectively. Upon actinic excitation at 400 nm, the photoconversion occurs, giving rise to the red form with $\lambda_{max}^{ex.}$ = 583 nm and $\lambda_{max}^{em.}$ = 593 nm. The name Kikume comes from the word キクメイシ[kikume-ishi] which is simply the Japanese name for the coral *Favia favus*.



Figure I.2.20 - Photographs of Atsushi Miyawaki, G. Ulrich Nienhaus and Sergey Lukyanov

c - EosFP

Around the same years, the group of Gerd Ulrich Nienhaus (Figure I.2.20) isolated and described another wild-type PCFP from the scleractinian "carpet brain coral" *Lobophyllia hemprichii* (Veron 2000c). This Kaede-like protein named EosFP can be irreversibly photoconverted with an actinic illumination at ~400 nm from green to red with excitation and emission maxima of 506 nm and 516 nm respectively in the green form, and 571 nm and 581 nm respectively in the red form (Wiedenmann *et al.* 2004). The chromophore has the same sequence His62-Tyr63-Gly64 than Kaede, providing the protein with its photoconversion properties.

It has been proposed (Nienhaus *et al.* 2005) that, like for Kaede, the neutral chromophore of EosFP absorbs wavelengths around 400 nm, causing an indirect photoinduced proton transfer from the hydroxyl group of the hydroxybenzylidene moiety to the chromophoric histidine (His-62). Finally, this charged histidine would easily give its β hydrogen (β-elimination) to the nearby acceptor Glu-212, producing the formation of a double bond, the breakage of the covalent bond linking the chromophore with the residue 61 and the extension of the conjugated system on the histidine. The crystal structures of the green and red forms of EosFP revealed here again the same kind of backbone cleavage (between residues 61 and 62) that Kaede undergoes, stretching the electron delocalization on a broader region of the chromophore and red-shifting the fluorescence emission.

The mechanism of this light-driven cleavage has been proposed by Nienhaus' group (Nienhaus *et al.* 2005) as involving a β-elimination reaction (Figure I.2.21). The anionic form of the chromophore is in equilibrium with its neutral, protonated form. This state absorbs light at ~400 nm, which would have the consequence to induce the β-elimination of one of the (-CH_2) hydrogen atoms of the chromophoric histidine. The acceptor of this atom has been proposed to be the strictly conserved Glu-212 (equivalent to Glu-222 in GFP) since its mutation produces a non-photoconvertible FP. Following this proton transfer, the reorganization of the electronic repartition leads to the cleavage of the peptide bond between the chromophore and the previous residue, and the formation of a double bond between Cα and Cβ of the chromophoric histidine. Finally, the newly formed π-bonds would involve the histidine in the electron delocalization, which produces a modified chromophore that can be excited at longer wavelengths.

This proposition is based on structural and mass spectrometry evidences of photocleavage, the obvious implication of protonation modifications and the need for the nearby glutamate. However, the reaction itself as well as the acceptors and donors still need to be proven or invalidated.

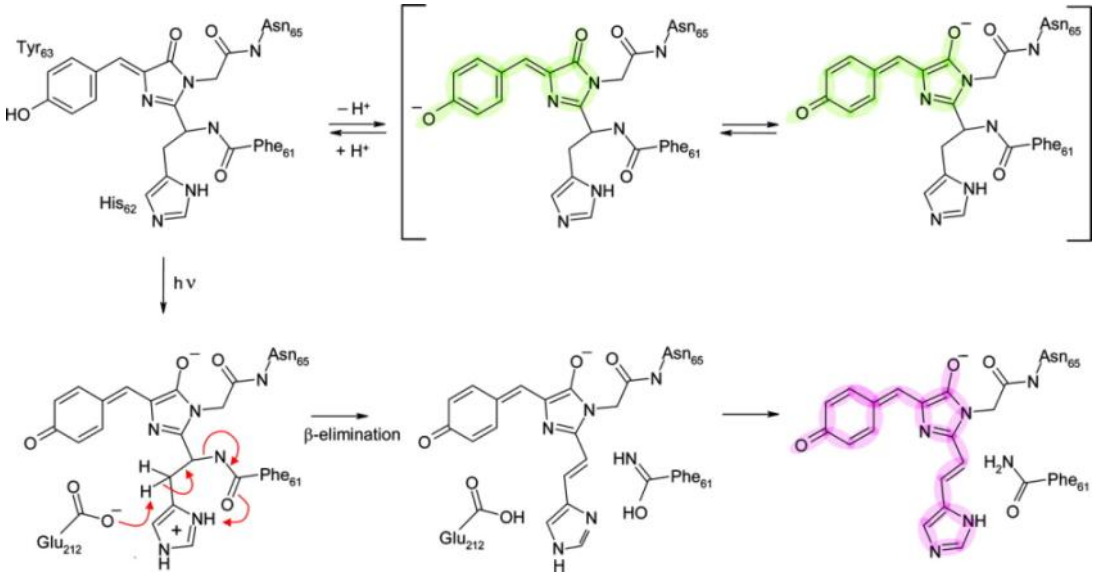

Figure I.2.21 - Proposed mechanism for the green-to-red photo-induced conversion of EosFP [reproduced from (Nienhaus et al. 2005)]

The name EosFP comes from the Greek goddess of dawn Ηως [Eos] whose infidelity, according to the mythology, was discovered, making her blush with shame when she wakes up every morning: rosy dawn, hence the analogy with the protein's property to be photoconvertible to a red color.

EosFP has naturally a homotetrameric organization but several variants have been made by Nienhaus' group that exhibit various degrees of oligomerization. The single mutation of a residue involved in the interface between the two dimers (V123T) has been shown to be sufficient to split this interface, forming a dimeric form called d1EosFP. At the other interface, the single point mutation T158H is sufficient to split the wild-type form into another dimeric form called d2EosFP. The double mutant V123T/T158H logically induces the splitting of both interfaces, producing a monomeric form called mEosFP easier to be used for protein fusion applications. The wild-type form of EosFP as well as the monomeric form (mEosFP) and one of the dimeric forms (d1EosFP) have been studied during this thesis work.

d - Dendra

At the same period, the group of Sergey Lukyanov (Figure I.2.20) isolated and studied another PCFP, called Dendra, from the azooxanthelate non-scleractinian soft "tree coral" *Dendronephthya sp.* Dendra is a monomeric engineered variant of a green-to-red photoconvertible fluorescent protein called dendGFP or dendFP (Pakhomov *et al.* 2004). Similarly to Kaede and EosFP, the protein displays excitation and emission maxima at 488 nm and 505 nm respectively in its green form, but after an actinic illumination at ~400 nm it irreversibly photoconverts to its red form with excitation and emission maxima at 556 nm and 575 nm respectively (Gurskaya *et al.* 2006). Despite the absence of crystal structure, the same chromophore His-Tyr-Gly was identified and recognized as being the origin of the photoconversion capabilities. The name Dendra is made of the apocope of the genus *Dendronephthya* and of the two letters RA standing for Red-Activatable. A brighter

commercial version is available and called Dendra2. This protein (Dendra2) has also been studied during this thesis (Adam *et al.* 2009b), as an example of an irreversibly photoconvertible PAFP from a non-scleractinian coral.

e - Other PCFPs

Recently, new green-to-red photoconvertible fluorescent proteins have been discovered and engineered. For example cjarRFP, mcavRFP and lhemOFP (Oswald *et al.* 2007) found in the stony corals *Catalaphyllia jardinei*, *Montastrea cavernosa* and *Lobophyllia hemprichii*, respectively. All have been described as containing a chromophore made of the sequence His-Tyr-Gly. The reaction mechanism of those proteins, thus, is probably the same as the one of the other PCFPs described above.

To summarize what is written above, some fluorescent proteins display incredible properties of photoconversion from a color to another. These PAFPs all contain a chromophore composed of the triad of aminoacids His-Tyr-Gly, essential for the photoinduced extension of the conjugated system. Currently, few irreversibly photoconvertible FPs of this type are known: the wild-type Kaede, EosFP (and its monomeric and dimeric versions), DendFP (and its monomeric variants Dendra and Dendra2) and the engineered KikGR. Since the first discovered member of those proteins is Kaede, this type of PAFP will be referred in this thesis as members of the "Kaede-like family".

Together with the Reversibly Switchable Fluorescent Proteins, the PhotoConvertible Fluorescent Proteins are part of an always bigger family of PhotoActivatable Fluorescent Proteins (Table I.2.1) that can undergo a wide variety of phototransformations by changing their emission color, switching reversibly of irreversibly between bright and dark states… All those transformations are very useful for numerous applications, especially in protein tracking within cells and high-resolution microscopy.

			Before photoactivation						After photoactivation					
Ref.	Protein name	Type of PAFP	λ_{max} ex/em (nm)	Φ_{fluo}	Bright.	pKa	ε ($M^{-1}.cm^{-1}$)	Actinic light (nm)	λ_{max} ex/em (nm)	Φ_{fluo}	Bright.	pKa	ε ($M^{-1}.cm^{-1}$)	Thermal Stability
1	EGFP (weak D)	Reference	488 / 507	0.60	33.6=100%	6.0	56 000	NA	NA	NA	NA	NA	NA	NA
2	PA-GFP (M)	Irreversibly photo-activatable FPs	400 / 515	0.13	8%	4.5	20 700	413 →	504 / 517	0.79	41%	ND	17 400	NA
3	PS-CFP (M)		402 / 468	0.16	17%	4..0	34 000	400 →	498 / 511	0.19	15%	6.0	27 000	NA
4	KFP1 (T)		580 / 600	<0.001	<0.4%	ND	123 000	532 →	580 / 600	0.07	12%	ND	59 000	NA
5	PAmCherry1 (M)		404 / NA	NA	NA	ND	6 500	400 →	564 / 595	0.46	25%	6.5	18 000	NA
6	asFP595 (T)	Reversibly switchable FPs (RSFPs)	572 / NA	NA	NA	ND	56 200	550→/←450	572 / 595	ND	ND	ND	ND	ND
7	mTFP0.7 (M)		453 / 488	0.50	89%	4.0	60 000	453→/←370	376 / NA	NA	NA	ND	ND	minutes
8	Dronpa (M)		503 / 517	0.85	240%	5.0	95 000	503→/←400	400 / 517	<0.02	NA	5.0	57 000	hours
9	Dronpa-2 (M)		489 / 515	0.23	42%	ND	61 732	489→/←400	400 / NA	NA	NA	ND	ND	ND
9	Dronpa-3 (M)		487 / 514	0.33	57%	ND	58 000	487→/←400	400 / NA	NA	NA	ND	ND	minutes
10	rsFastLime (M)		496 / 518	0.77	89%	ND	39 094	496→/←400	384 / NA	NA	NA	ND	ND	seconds
11	bsDronpa (M)		460 / 504	0.50	67%	ND	45 000	490→/←400	385 / NA	NA	NA	ND	ND	ND
11	Padron (M)		505 / NA	NA	NA	ND	ND	490→/←400	503 / 522	0.64	82%	ND	43 000	ND
12	rsCherry (M)		572 / NA	NA	NA	ND	ND	550→/←450	572 / 610	ND	ND	ND	ND	sec. / min.
12	rsCherryRev (M)		572 / 608	ND	ND	ND	ND	550→/←450	572 / NA	NA	NA	ND	ND	seconds
13	Kaede (T)	Green-to-red photo-convertible FPs (PCFPs)	508 / 518	0.88	259%	5.6	98 800	400 →	572 / 582	0.33	59%	5.6	60 400	NA
14	KikGR (T)		506 / 517	0.70	112%	7.8	53 700	400 →	583 / 593	0.65	68%	5.5	35 100	NA
15	EosFP (T)		506 / 516	0.70	150%	5.8	72 000	400 →	571 / 581	0.55	67%	ND	41 000	NA
15	mEosFP (M)		506 / 516	0.64	128%	5.5	67 200	400 →	569 / 581	0.62	68%	5.5	37 000	NA
15	d1EosFP (D)		505 / 516	0.68	151%	ND	74 800	400 →	571 / 581	0.62	74%	ND	40 000	NA
15	d2EosFP (D)		506 / 516	0.66	165%	ND	84 000	400 →	569 / 581	0.60	59%	ND	33 000	NA
16	DendFP (T)		492 / 508	0.65	174%	6.5	90 000	400 →	557 / 575	0.68	71%	6.9	35 000	NA
17	Dendra (M)		488 / 505	0.72	44%	6.6	21 000	400 →	556 / 575	0.70	43%	6.9	20 000	NA
4	Dendra2 (M)		490 / 507	0.50	45%	6.6	45 000	400 →	553 / 573	0.55	39%	6.9	35 000	NA
18	mcavRFP (T)		504 / 517	0.60	95%	ND	53 100	400 →	571 / 582	0.60	107%	ND	60 000	NA
18	cjarRFP (T)		509 / 517	0.55	172%	ND	105 000	400 →	573 / 582	0.56	90%	ND	53 800	NA
18	lhemOFP (T)		507 / 517	0.58	163%	ND	94 200	400 →	543 / 574	0.65	70%	ND	36 300	NA

M: monomer, D: dimer, T: tetramer, λ_{max} ex/em: max. excitation and emission wavelengths, Φ_{fluo}: fluorescence quantum yield, NA: not applicable, ND: not determined, Bright.: brightness (product of $\varepsilon * 10^{-3}$ and Φ_{fluo}) in % of EGFP, ε: extinction coefficient

Table I.2.1 - The different types & spectroscopic properties of photoactivatable fluorescent proteins

References: 1-(Prasher et al. 1992); 2-(Patterson & Lippincott-Schwartz 2002); 3-(Chudakov et al. 2004); 4-Evrogen website; 5-(Subach et al. 2009); 6-(Lukyanov et al. 2000); 7-(Ai et al. 2006); 8-(Ando et al. 2004); 9-(Ando et al. 2007); 10-(Stiel et al. 2007); 11-(Andresen et al. 2008); 12-(Stiel et al. 2008); 13-(Ando et al. 2002); 14-(Tsutsui et al. 2005); 15-(Nienhaus et al. 2006a); 16-(Pakhomov et al. 2004); 17-(Gurskaya et al. 2006); 18-(Oswald et al. 2007)

Chapter 3 - Applications of PAFPs and aim of the thesis

Résumé en français

Ce chapitre discute de l'utilisation des protéines fluorescentes photoactivables et en particulier le suivi de protéines d'intérêt dans les cellules vivantes et leur utilisation en microscopie de fluorescence à super-résolution. Après un court rappel sur la microscopie conventionnelle, les récentes techniques de nanoscopie seront introduites : STED, PALM et STORM.

Enfin, le but de ce travail de thèse sera explicité : étudier les phénomènes de phototransformations subies par les protéines fluorescentes photoactivables : photoconversion, photocommutation et photoblanchiment, grâce à l'utilisation de trois protéines modèles.

Part 1 - Tracking elements within living cells

THE irreversible photoconversion capabilities of Kaede-like proteins such as EosFP make them very interesting fluorescent probes for following dynamical events (Figure I.3.1). Indeed, the high contrast between the initial green emitting state and the photoconverted red state of the protein allows to follow the motion of photoconverted elements such as fusion proteins moving from a cellular compartment to another, growing cytoskeleton...

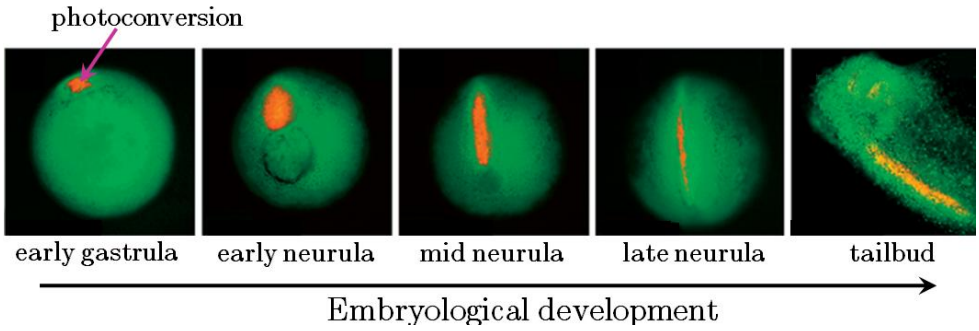

Figure I.3.1 - An example of application of EosFP in dynamical microscopy. An embryo of Xenopus laevis at its early stage is marked with EosFP and a small area, corresponding to the future neural cells, is photoconverted from green to red. Upon embryological development, the motion of the photoconverted cells is clearly visible due to the high contrast between green and red emissions [Reproduced and adapted from (Nienhaus et al. 2006a)]

The photoinduced transformations from one state to another of a fluorescent biomarker such as a fluorescent protein is indeed of major interest in cell biology and biotechnologies, to allow the development of new kinds of dynamical experiments and technologies. The recent discovery of the new photoconvertible and photoswitchable fluorescent proteins described previously has already allowed the spatio-temporal labeling and dynamical study of proteins of interest in an unprecedented manner compared to the somewhat static studies permitted by more simple types of fluorescent probes (Lukyanov *et al.* 2005).

Like for the GFP and its variants, researchers quickly used the red fluorescent protein DsRed (Ayoob *et al.* 2001) and its "timer" variant (Mirabella *et al.* 2004) in cell tracking experiments. The use of the newly discovered PCFPs though, offered great new perspectives by expanding the toolbox of fluorescent biomarkers in transcriptional reporting, tag fusion or biosensing experiments, such as the dynamical track of events within cells. This was the case

for Kaede (Mutoh *et al.* 2006; Sato *et al.* 2006; Leung & Holt 2008; Tomura *et al.* 2008), EosFP (Ivanchenko *et al.* 2005; Nienhaus *et al.* 2006a; Wiedenmann & Nienhaus 2006) or Dendra (Chudakov *et al.* 2007a; b) for example. It was also the case for photochromic switchable PAFPs like Dronpa (Flors *et al.* 2007) or asFP595 and its variant KFP (Henderson & Remington 2006). However, one of the most exciting and promising function of PAFPs is their use in the recent super-resolution microscopy techniques.

Part 2 - Super-resolution microscopy using PAFPs

One of the most promising and exciting application of PCFPs and RSFPs is their use in nanoscopy. Indeed, thanks to techniques newly developed, those proteins can be used as efficient fluorescent probes, in a way that allows to defeat the resolution limitation imposed by diffraction.

1 - The resolution is limited by diffraction in far-field visible microscopy

The resolution of a microscope refers to the resolving power of the lenses that compose this microscope. The resolving power is the ability of an apparatus to measure the angular distance between two points (i.e. distinguish two points) of an object, and is limited by the phenomenon of diffraction. In far-field microscopy, the waves emitted by a light source in a microscope do not focus in an infinitely small point but interfere together near the image plane to form a so-called Fraunhofer diffraction pattern. As a consequence, this pattern at the focal plane will resemble a disc surrounded by concentric blurred rings called first, second... order maxima (Figure I.3.2) and separated by minima called first, second... zeros; this pattern is called the Airy disc. The Airy disc is characterized by an intensity distribution function called the point-spread function (PSF) of the microscope. The point spread function is thus the instrumental response of the imaging of a point object and the image is a convolution of the object and the PSF. The degree of spreading (blurring) is a measure for the quality of an imaging system.

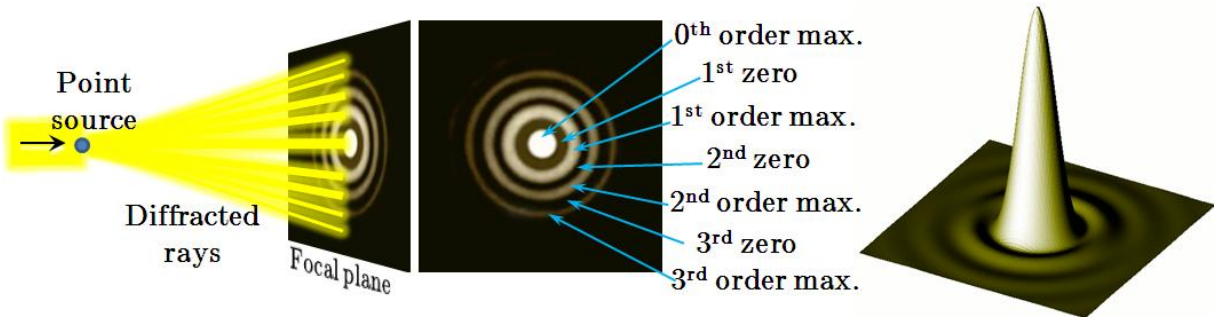

Figure I.3.2 - The parasitic phenomenon of diffraction causes the formation of an Airy disc (left). The corresponding point-spread function (right)

a - The Abbe's relation

The physicist Ernst Abbe (Figure I.3.3) found (Abbe 1873) that in far-field microscopy, using visible light, the smallest distance between two objects that can be distinguished defines the resolving power (r) of the apparatus. He described this value as being: $r \sim \lambda/2n$

Where λ is the wavelength that is used and n is the refractive index of the medium in which the light rays travel. For example, with $n=1$ (air) and $\lambda=500$ nm, we find that the best resolution equals $r \sim 250$ nm.

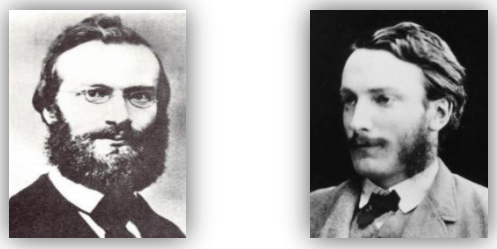

Figure I.3.3 - Photograph of Ernst Karl Abbe and John William Strutt Rayleigh

b - The Rayleigh criterion

In reality, two objects start to be undistinguishable when their Airy discs are separated by an Airy radius. Below this distance, the objects will be unresolved. This expression that approaches very much the Abbe's relation is known as the Rayleigh criterion (Figure I.3.4) and is expressed by:

$$r = 0.61\frac{\lambda}{NA} \quad \text{or} \quad r = \frac{1.22\,\lambda}{2\,NA} = \frac{1.22\,\lambda}{2\,n \cdot sin(\alpha)}$$

Equation I.1

Where NA and α are the numerical aperture and the half aperture of the microscope, respectively. For example, with NA=1.2 and λ=500 nm, we find a resolution of $r \approx 254$ nm.

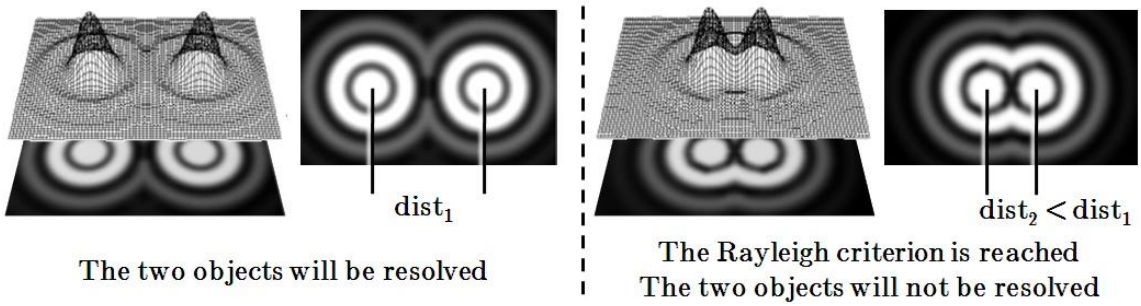

Figure I.3.4 - The Rayleigh criterion. When the distance between two objects is too close for the microscope resolution, they cannot be distinguished

This relation shows that the resolution of a microscope depends on two parameters: the wavelength (the resolution is worse when the wavelength increases) and NA (the resolution is better when the numerical aperture increases). The optical resolution is a complex topic.

Since state of the art air objectives in visible microscopy allow a numerical aperture of 0.95, the best resolution that can be achieved with such microscopes is r=λ/1.5. With oil immersion objectives, numerical aperture values up to 1.65 can be reached so that the best resolutions with such microscopes are about r=λ/2.7. Overall, it is admitted that for conventional optical

microscopy the resolution is limited to values around λ/2 or 250 nm for visible light (James 1976) and is never better than λ/3. The observation of a real specimen made of many punctual objects gives rise to a high number of Airy patterns whose PSF can be resolved or not (Figure I.3.5). This is a major problem in fluorescence microscopy because the smallest cellular structures cannot be detailed and there are always doubts concerning the co-localizations of elements of interest.

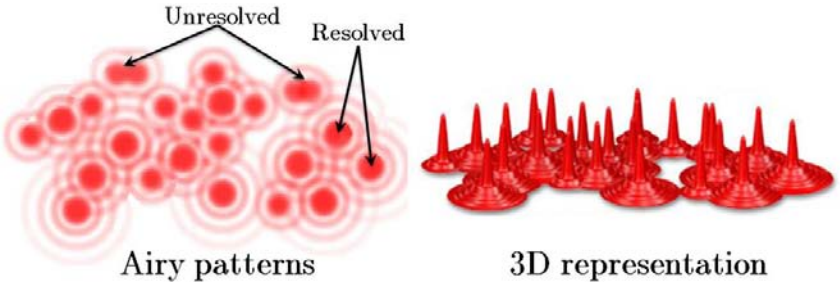

Figure I.3.5 - Resolution in far-field microscopy. The observed elements give rise to Airy patterns that can only be resolved if the objects are separated enough - Reproduced from Olympus Microscopy Resource Center[8]

2 - Defeating the resolution limit, the quest for nanoscopy

The Abbe-Rayleigh relation stood as the golden rule in microscopy for almost 130 years, up until recent advances allowed breaking it for UV-Vis fluorescence microscopy, which have allowed the development of diffraction-unlimited resolution techniques.

a - Localization of fluorescent objects with high accuracy

Watt Webb (Figure I.3.7) at Cornell University, USA, discovered that fitting the PSF and calculating their centroid, an improved localization of individual fluorescent particles, and thus, their precise tracking (Thompson *et al.* 2002) could be obtained compared to conventional microscopy. This fitting procedure is made by simple gaussian curves instead of Airy functions because fluorescent images are rarely precise enough to distinguish between those alternatives.

[8] www.olympusmicro.com

This method reveals that if enough fluorescent photons are integrated from an individual fluorescent spot, its PSF fitting allows a greater resolution by an order of magnitude!

The authors found that while conventional diffraction-limited imaging of a fluorescent object only allows a resolution of ~250 nm FWHM, the precise localization of its center can be estimated with an accuracy given by the FWHM divided by the signal to noise $\sqrt{N_{ph}}$ (with N_{ph} the number of photons integrated). Basically, if the total number of integrated photons for a single spot is 10^4, the localization of a fluorescent object can be:

$$\frac{FWHM}{\sqrt{N_{ph}}} = \frac{250}{\sqrt{10^4}} \cong \pm 1.3\ nm$$

Equation I.2

This discovery gave rise to the development of the technique called FIONA, standing for Fluorescence Imaging with One-Nanometer Accuracy (Selvin *et al.* 2007). This technique allows the precise localization of single fluorescent molecules in the *x,y* plane with only using a sample fixed on a coverslip and excited by a total internal reflection fluorescence (TIRF) microscope (Yildiz *et al.* 2003; Yildiz & Selvin 2005).

b - Stimulated emission depletion (STED)

The first high resolution fluorescence microscopy technique was developed by Stefan Hell (Figure I.3.7) and colleagues at Göttingen, Germany (where Ernst Abbe obtained his doctorate in 1861) and is called STED (STimulated Emission Depletion).

The principle of STED (Hell & Wichmann 1994; Klar *et al.* 2001) is based on PSF engineering, increasing the fluorescence microscopy resolution by depleting the signal coming from molecules located in a ring-shaped light pulse. In practice, two synchronized laser pulses separated by a very short delay are sent on a fluorescent sample. The first pulse uses the excitation wavelength. A second doughnut-shaped and red-shifted pulse is applied at the

circumference, immediately after the first one, during the excitation lifetime. The excited state comes back to the ground state without fluorescence emission by stimulated emission. The consequence is that the resulting PSF that is really observed is much narrower than what would have been expected following the conventional diffraction-limited rule (Figure I.3.6).

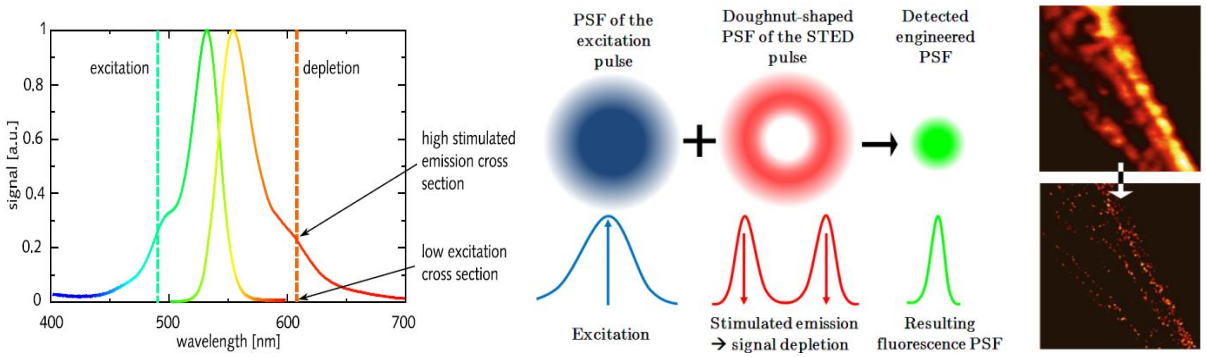

Figure I.3.6 - The principle of STED microscopy. Left: a depletion wavelength is chosen so that a good stimulation emission is achieved without re-excitation of the fluorophore [reproduced from (Kellner 2007)]; Middle: by stimulating molecules at the periphery of the excitation spot with a longer wavelength, a doughnut-shaped STED pulse acts like a carving knife on the excitation PSF's tails so that the effective PSF is shrunk. Right: example of resolution improvement between confocal fluorescence microscopy and STED microscopy on neurofilaments (source: MPI-BPC Göttingen website[9])

The resolution is thus greatly improved (about λ/20 instead of λ/2) and it is possible to reconstruct details of the smallest structures inside cells at unprecedented resolutions of 15-30 nm (150-300 Å), approaching resolutions of standard scanning electron microscopes (SEM). The STED technique is based on the principle of RESOLFT (REversible Saturable Optically Linear Fluorescence Transitions)(Hell 2003; 2007). This principle claims that the Abbe-Rayleigh formula (Equation I.1) can be developed and approximated by :

$$r = \frac{\lambda}{2NA \cdot \sqrt{1 + \frac{I}{I_{sat}}}}$$

Equation I.3

[9] http://www.mpibpc.mpg.de

Where I is the intensity of the depletion excitation light and I_{sat} is the intensity needed to saturate the transition (half of the molecules excited are stimulated to return to S_0). In theory, thus, one can improve the optical resolution by increasing the intensity I, and as the intensity of the STED pulse is increased, the detected (engineered) PSF shrinks further.

Figure I.3.7 - Photographs of Watt W. Webb, Stefan W. Hell, Eric Betzig and Xiaowei Zhuang

c - Photoactivated localization microscopy (PALM)

Very recently, the use of Kaede-like PAFPs in microscopy found an impressive application with the development of the PhotoActivated Localization Microscopy by Eric Betzig (Figure I.3.7) and colleagues at the Howard Hughes Medical Institute, USA (Betzig *et al.* 2006). Basically, this technique uses a sample marked with green-to-red PAFPs. A short pulse at ~400 nm induces the irreversible photoconversion of a few, well separated individual molecules whose localization can determined with extreme precision with the method described above, p.61. Those molecules are finally bleached by this light and the photoconversion step can be renewed, photoconverting other elements in the sample. This iterative method ultimately allows the reconstruction of stochastically photoconverted individual elements with a very high accuracy, which produces a diffraction-unlimited fluorescence microscopic image (Figure I.3.8).

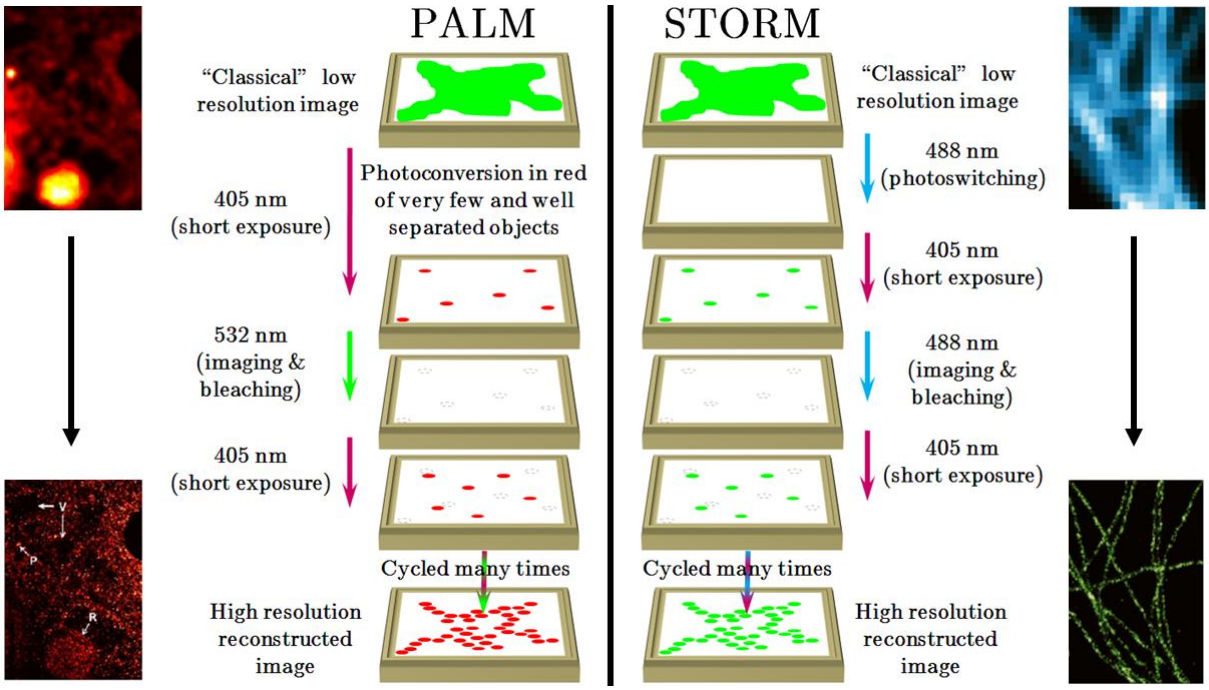

Figure I.3.8 - Principles of PALM and STORM sub-diffraction microscopy techniques allowed by PAFPs and RSFPs. Thumbnail images show the improvement of resolution allowed by both techniques [inset images reproduced from (Betzig et al. 2006) and (Bates et al. 2007)]

d - Stochastic optical reconstruction microscopy (STORM)

The same stochastic approach has been used by Xiaowei Zhuang (Figure I.3.7) and colleagues at Harvard University, USA, to develop the STochastic Optical Reconstruction Microscopy technique the same year (Rust *et al.* 2006). This technique is strictly comparable to the PALM technique but was initially developed using photochromic dyes. First, all the RSFP molecules are turned "off", then a short pulse at 405 nm randomly turns "on" very few and separated objects that can be precisely imaged and bleached before the activation of other molecules to be recycled (Figure I.3.8). The fast trans to cis isomerization of Dronpa-like RSFPs permits a faster acquisition time although the iterative process and reconstruction is still a slow process.

PALM and STORM are thus two extremely similar techniques that use the photoactivation properties of PAFPs or RSFPs to individually image all the points within an object with a very high accuracy and then obtain an image superposing all the points in order to reconstruct a

diffraction-unlimited high-resolution image that reveals the smallest details of the studied sample (Figure I.3.9).

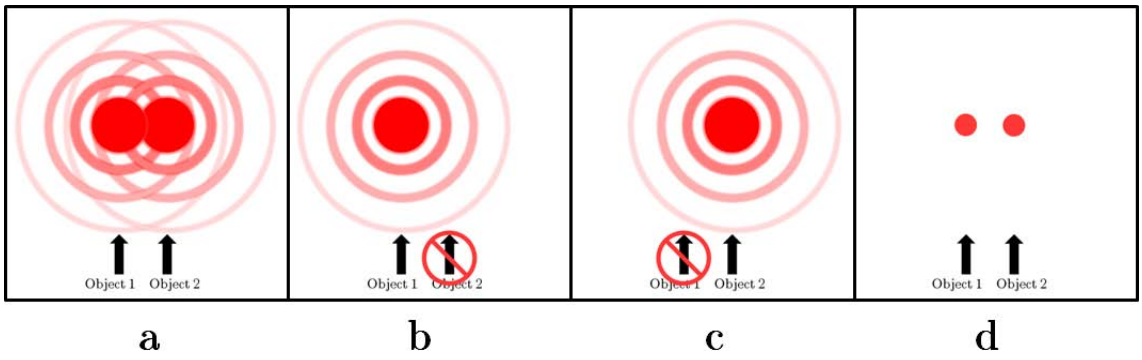

Figure I.3.9 - The idea behind the PALM/STORM super-resolution techniques. Two objects are too close each other to be resolved since the Rayleigh criterion is reached (a). The precise localization of only one object by temporarily bleaching the other one (b) and then of only the second one by the reverse action (c) allow the positioning of both objects with a very high accuracy (d)

e - Fast and three-dimensional PALM/STORM microscopies

The main drawbacks of PALM/STORM methods compared to STED are that the iterative pulse/reconstruction steps make them time-consuming techniques and also that they only can be used in TIRF-based (surface bound) systems. The recent use of fast RSFPs such as Dronpa mutants (Flors *et al.* 2007) in PALM/STORM-like experiments now allows solving the first problem. The development of 3D-PALM and 3D-STORM techniques now makes possible the fast super-resolutive microscopy of objects in solution. If, as we said previously, the lateral resolution is limited by the Airy radius $r_{x,y} \approx 0.61 \cdot \lambda/NA$ in conventional visible microscopy (and a bit better in confocal microscopy: $r_{x,y} \approx 0.46 \cdot \lambda/NA$), the axial resolution is really worse: $r_{x,z} \approx 2 \cdot \lambda/NA^2$ (and $r_{x,z} \approx 1.4 \cdot \lambda/NA^2$ in confocal microscopy) because of an elongated PSF.

The use of 4Pi-microscopy (Hell *et al.* 1994) along with sample sectioning allowed axial resolutions to be reached <80 nm in STED (Punge *et al.* 2008). In parallel, the development of the PALM technique with the so-called biplane detection (Juette *et al.* 2008) recently allowed an axial resolution of 75 nm to be reached and the development of the STORM technique with

elliptical astigmatism permitted the enhancement of the axial resolution up to 50-60 nm (Huang *et al.* 2008). The 3D visible far-field nanoscopy with axial resolutions of λ/6 to λ/10 is thus a reality.

To summarize, super-resolution techniques represent a revolution in visible far-field microscopy by allowing us to have detailed information on the smallest cellular structures. They also provide direct and precise information on objects that colocalize without requesting mathematical tricks or beads calibrations.

Part 3 - Aim of this thesis work

This Ph.D. thesis project is focused on understanding at the near atomic level how photoactivatable fluorescent proteins function. More precisely, we are interested in this study to better understand the phototransformations that a photoactivatable fluorescent protein can undergo during experiments in microscopy: photoconversion, photoswitching, photobleaching, but also the delicate questions of protonation and pH dependency of fluorescent proteins. Ultimately, those studied are expected to lead to further improvements of fluorescent biomarkers.

Photobiochemistry is an extremely complex topic, since during an excitation, a panel of photoinduced events can occur, producing unexpected reactions that may have dramatic effects on the spectral properties of proteins. Those effects are strongly dependent on the wavelengths and powers that are used and on the protonation states of the chromophore.

In order to improve fluorescent proteins for their use as biological probes, one has to understand how those reactions happen and why. The difficulty of this task is increased by the fact that all the fluorescent proteins that are known, although their sequence identity is often quite low compared to GFP (<25%), display the same folding, consisting in an eleven-stranded β-barrel protecting an endogenous chromophore from the solvent (Figure I.3.10). This means that very often, in spite of strong differences in spectroscopic properties, the structural explanations will reside in very slight changes in the chromophore environment.

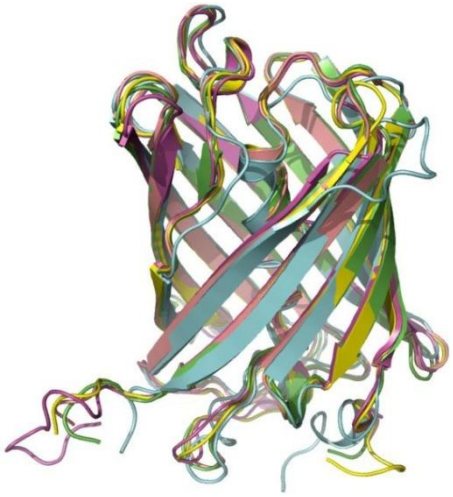

Figure I.3.10 - Superimposition demonstrating the common β-barrel structure of different FPs: EosFP (green), GFP (cyan), KFP (magenta), DsRed (salmon), eqFP611 (yellow)

Finally, another challenge for having fluorescent proteins suitable for live cell applications is to produce those proteins in their monomeric form. As said previously indeed, the wtGFP is naturally found in its dimeric form and all the anthozoans FPs are found as tetramers and the monomerization of such proteins often requires mutating several aminoacids at protein interfaces.

This thesis work is aimed at studying all those phenomena by combining X-ray crystallography experiments, with various types of spectroscopies (UV-Vis, fluorescence, Raman...) either in solution or directly in protein crystals thanks to the microspectrophotometry installations of the ESRF Cryobench laboratory and with molecular mechanics to model photochemical events. Such a multidisciplinary approach has allowed the study of a wide range of possible phototransformations on two different representative green-to-red PAFPs: the wild-type version of EosFP (wtEosFP) and the monomeric commercial version of dendGFP: Dendra2. A monomeric variant and a dimeric variant of wtEosFP (mEosFP and d1EosFP, respectively) were also studied to understand the influence of FPs oligomerization states. These studies are part of current worldwide efforts to better understand and improve the unique properties of reversible and irreversible photoactivations of the photoactivatable fluorescent proteins.

During this thesis, we also discovered the first PAFP displaying multiple phototransformations. This protein, named IrisFP, is a mutant of wtEosFP with a modified chromophore environment and that displays the surprising ability to be both photoconvertible from green to red, like its wild-type parent, but also to display on/off photochromic properties. This protein can be reversibly photoswitched between a green fluorescent and a non-fluorescent state, irreversibly photoconverted from a green fluorescent to a red fluorescent state and finally reversibly photoswitched between a red fluorescent and a non-fluorescent state. IrisFP, thus, represents the first PAFP that gathers both the properties of the Kaede-like family and the Dronpa-like family and allows a better understanding of photoconversion and photochromic behaviors in PAFPs.

II. RESULTS AND DISCUSSION

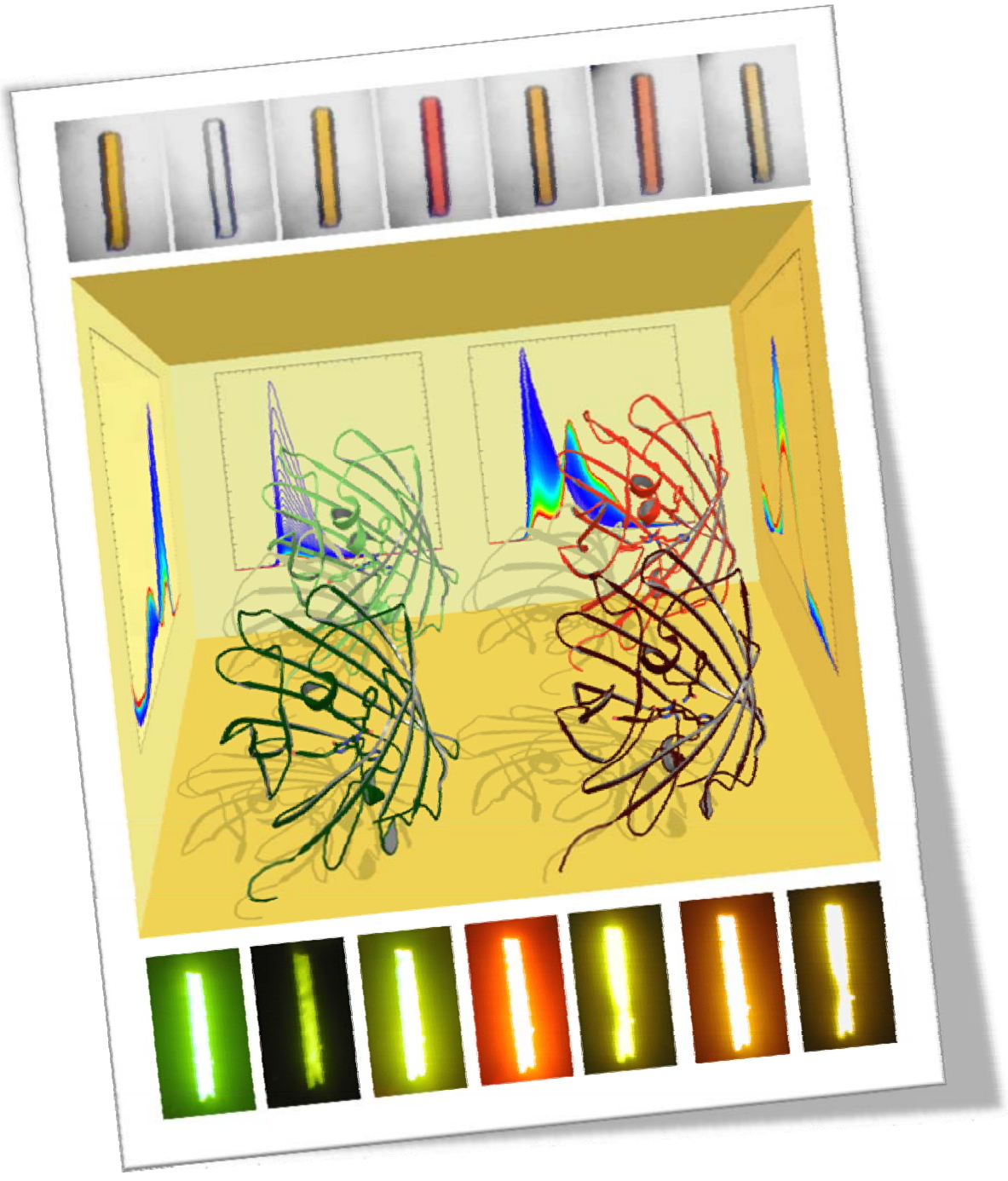

The illustration represents the 3D structures for the four states of the fluorescent protein IrisFP described in this thesis: green cis, green trans, red cis, red trans. The structures are surrounded by absorption and emission spectra of the different phototransformations studied in this thesis: reversible green-to-dark conversion (left), photobleaching and green-to-red conversion in fluorescence (back) and green-to-red conversion in absorbance (right). Top and bottom parts represents the multiple color conversion occurring in a single crystal of IrisFP

Chapter 1 - Photoconversion from green to red

Résumé en français

Dans ce premier chapitre des résultats sont présentés les travaux réalisés sur l'étude du phénomène de photoconversion irréversible du vert au rouge de certaines protéines fluorescentes photoactivables. Grâce à l'étude de la protéine EosFP, qui a été cristallisée et dont la structure et l'analyse spectroscopique ont été réalisées, ainsi que grâce à l'obtention de la première structure tridimensionnelle d'une autre de ces protéines : Dendra2, les études présentées, couplées à des simulations de mécanique quantique et moléculaire, ont permis de proposer un nouveau mécanisme réactionnel de photoconversion du vert au rouge.

Les propriétés particulières de Dendra2, en tant que protéine fluorescente démontrant une grande facilité de photoconversion, ont été étudiées et comparées à celles d'EosFP. Comparée à EosFP, Dendra2 est en effet plus facilement convertible mais présente également un pKa plus important, des spectres d'absorption et d'émission plus décalées dans le bleu et une forme super-rouge.

Enfin, les structures des formes monomérique et dimérique d'EosFP ont également été obtenues et ont permis, en complément de celle de Dendra2, d'étudier les interfaces entre chaînes protéiques. Sous forme cristalline, en effet, la concentration en protéine est telle que les protéines fluorescentes anthozoaires mutées afin d'avoir un comportement monomérique ou dimérique en solution, reforment un tétramère dans le cristal. Cette propriété permet donc d'étudier quels acides aminés sont impliqués dans les interfaces et de proposer des mutations afin d'améliorer la stabilité de ces protéines sous forme monomérique.

AMONG very rare green-to-red photoconvertible fluorescent proteins (PCFPs) known to date (Kaede (Ando *et al.* 2002), Dendra (Labas *et al.* 2002), EosFP (Wiedenmann *et al.* 2004), KikGR (Tsutsui *et al.* 2005), mcavRFP, cjarRFP and lhemOFP (Oswald *et al.* 2007)), only the green and red structures of EosFP were available when I started this Ph.D. thesis (PDB accession codes: 1ZUX and 2BTJ, respectively). The green and red structures of KikGR (PDB accession codes: 2DDD and 2DDC, respectively) and Kaede (PDB accession codes: 2GW3 and 2GW4, respectively) were only released in March 2006 (KikGR) and November 2007 (Kaede).

In order to better understand the fascinating phenomenon of photoconversion, we decided to study EosFP as a model PCFP. Since there was no known structure for the PCFP Dendra (Gurskaya *et al.* 2006), we also tried to obtain the 3D structure of the monomeric bright commercial version of this protein, called Dendra2 (Evrogen, Moscow, Russia). This PCFP is interesting since its photoconversion yield has been reported to be higher than PCFPs such as EosFP. Finally, we also studied the interfaces formed in the crystal structures, especially by using a monomeric and a dimeric variant of EosFP, in order to better target which residues are involved in these interfaces, which could indicate what mutations could be useful to engineer stable monomeric PCFPs.

Part 1 - Study of the photoconversion of EosFP

1 - Crystallization of EosFP

We started our work by trying to reproduce the results that were obtained on the already well-described fluorescent protein EosFP. This PCFP has been thoroughly studied both spectroscopically (Wiedenmann *et al.* 2004) and structurally (Nienhaus *et al.* 2005) but we wanted to seek for a better comprehension of the photoconversion mechanism thanks to the analysis of spectroscopic modifications induced at several temperatures both in solution and crystal, at the Cryobench laboratory.

EosFP crystals were obtained in hanging drops with the vapor diffusion method (Cf. material and methods, p. 199) and using the crystallization protocol already published (Nienhaus *et al.* 2005). Probably because of different crystallization kinetics, the protein crystallizes in different crystal shapes, of which five have been identified (Figure II.1.1, left).

Thanks to the easy access to the ESRF beamlines, all those forms have been tested and appear to belong to the same orthorhombic spacegroup $P2_12_12_1$. However, if most of those crystal forms (Figure II.1.1, a-d) contain four molecules (a tetramer) per asymmetric unit, one form (Figure II.1.1, e) is made of a more complicated packing with three tetramers inside the asymmetric unit (Figure II.1.1, right).

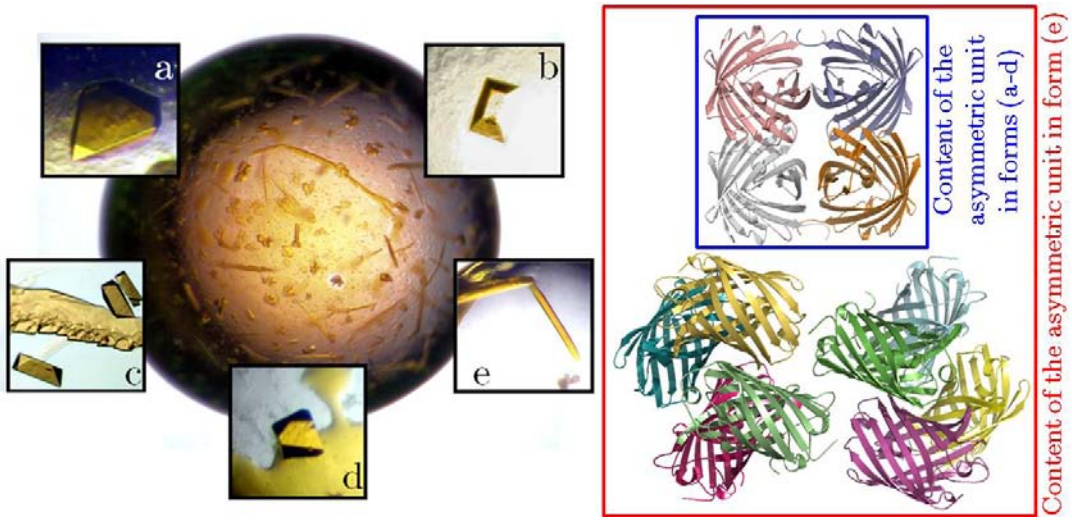

Figure II.1.1 - The different crystal shapes of EosFP. In a single crystallization drop, diameter=2.5 mm (left), up to five different crystal forms have been identified (a-e), all belonging to the same spacegroup. While in most crystal forms, a tetramer is present per asymmetric unit (AU), one form (e) comprises 12 molecules/AU (right)

Instead of simply reproducing the crystal structures obtained and published before, it was more interesting to try to obtain better resolutions and get the structure of a protein photoconverted directly in the crystal. Indeed, since we reproduce those crystals mainly in order to study *in-crystallo* the green-to-red photoconversion spectroscopically, it seems essential to first check whether the peptide bond cleavage responsible for the photoconversion is present not only when the protein is photoconverted prior to crystallization but also after. Crystal

parameters and data collection statistics for both EosFP green and red forms are compiled in Table II.1.3, p.93.

2 - Structures of the green and red forms of EosFP

X-ray data collections were performed at the ESRF beamline ID14-3 ($\lambda = 0.931$ Å) and ID23-2 ($\lambda = 0.873$ Å) for the green and red forms of EosFP, respectively. Because of the very focused beam on the microfocus beamline ID23-2, the diffraction patterns of EosFP red form degraded after a few images and a composite dataset approach had to be chosen: five partial datasets were collected and merged in a single data set according to the method described in (Berglund *et al.* 2002; Adam *et al.* 2004).

The microfocus beamline ID23-2 is certainly not the ideal beamline for relatively big crystals because the high beam flux provokes the creation of many reactive species that stay trapped in the crystal bulk and lead to a strong radiation damage; but this choice was led by the available and allocated beamtime. Six partial datasets were collected, of which five were merged to form a single complete dataset. Contrary to the structure of EosFP green form, that could be obtained at 1.55 Å, the structure of the red form could not be obtained at a higher resolution (2.0 Å) than the one published from data collection with an X-ray generator, probably because the crystal suffered during the laser illumination at 405 nm that was used in order to photoconvert it (direct illumination at room temperature in the crystallization drop during 5 minutes at 0.5-1 W/cm²). However, this structure is interesting since it comes from a protein that was photoconverted directly in its crystalline form rather than in solution prior to crystallization. The data treatment was performed as described in material & methods, p.215.

Chromophore restraints were generated from idealized coordinates found in the Hic-Up database (Kleywegt *et al.* 2003) and adjusted as explained in material & methods (Chapter 4 - Restraints on the chromophores, p. 243). Refinement statistics are compiled in Table II.1.4.

Although very few movements are observed between the red and green forms, the peptide cleavage is clearly visible in the $2F_{obs}$-F_{calc} electron density map (Figure II.1.2) and some details

are important to notice: firstly, a water molecule near the chromophoric histidine (W1) present in the green form, disappears in the red form and secondly, the carboxamide of Phe-61 in the red form rotates, compared to the green form so that its NH_2 group moves away from the chromophore.

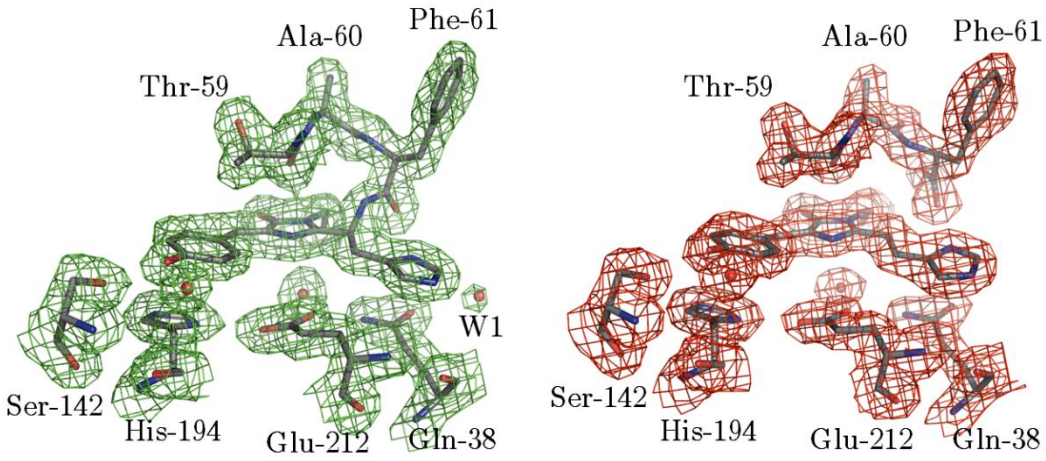

Figure II.1.2 - The chromophore environment in green and red forms of EosFP. $2F_{obs}$-F_{calc} electron density maps contoured at 1σ are shown

These observations are also visible in the deposited structure obtained from a protein that has been photoconverted in solution, before crystallization. This result suggests that the structural modifications that occur in crystallo during the photoconversion are the same than those happening in solution. This point is crucial since the original goal of those studies was to find intermediate states of the reaction by initiating the photoconversion reaction within crystals at low temperatures. The observed modifications also give us essential clues that we will correlate with those observed in the structures of other PCFPs and with quantum mechanics calculations, in order to elucidate the photoconversion mechanism.

3 - Observation of the photoconversion phenomenon

The interest of green-to-red photoconvertible fluorescent proteins is that high contrast dual color fluorescence microscopy becomes possible with only one fluorescent tag instead of two such as when GFP and DsRed are used together (Figure II.1.3)

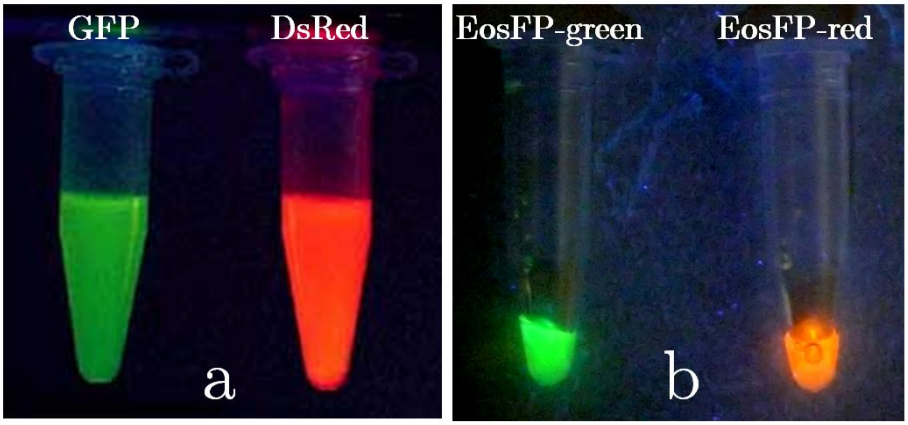

Figure II.1.3 - The interest of PCFPs: instead of tagging proteins of interest with two FPs such as GFP and DsRed (a)[10] a single protein can produce the same level of contrast (b)

The photoconversion mechanism studied in detail during this thesis thanks to the instruments provided at the Cryobench laboratory (Cf. material & methods, Chapter 2 , p.217) was investigated in absorption and in fluorescence modes either in solution or directly within protein crystals (Figure II.1.4).

Bright field photographs of the photoconversion were obtained by illumination at 405 nm of a solution contained in an Eppendorf tube (Figure II.1.4, a) or in crystals in their crystallization drop (Figure II.1.4, b). For fluorescence photographs, the photoconversion was achieved by illumination at 405 nm of a solution contained in a cuvette held in a cuvette holder (Figure II.1.4, c), in a crystal mounted in a microloop (Figure II.1.4, d) or in onion epidermal cell expressing a cytoskeleton labeled with EosFP (Figure II.1.4, e). The experiment shown in row (Figure II.1.4, e) is reproduced from (Schenkel et al. 2008), all the other experiments were performed at the Cryobench laboratory. The series of absorption and emission spectra presented in Figure II.1.4, f shows typical green-to-red photoconversion at room temperature either in solution or crystal form.

[10] From Marc Zimmer's GFP website (http://www.conncoll.edu/ccacad/zimmer/GFP-ww/lukyanov.html)

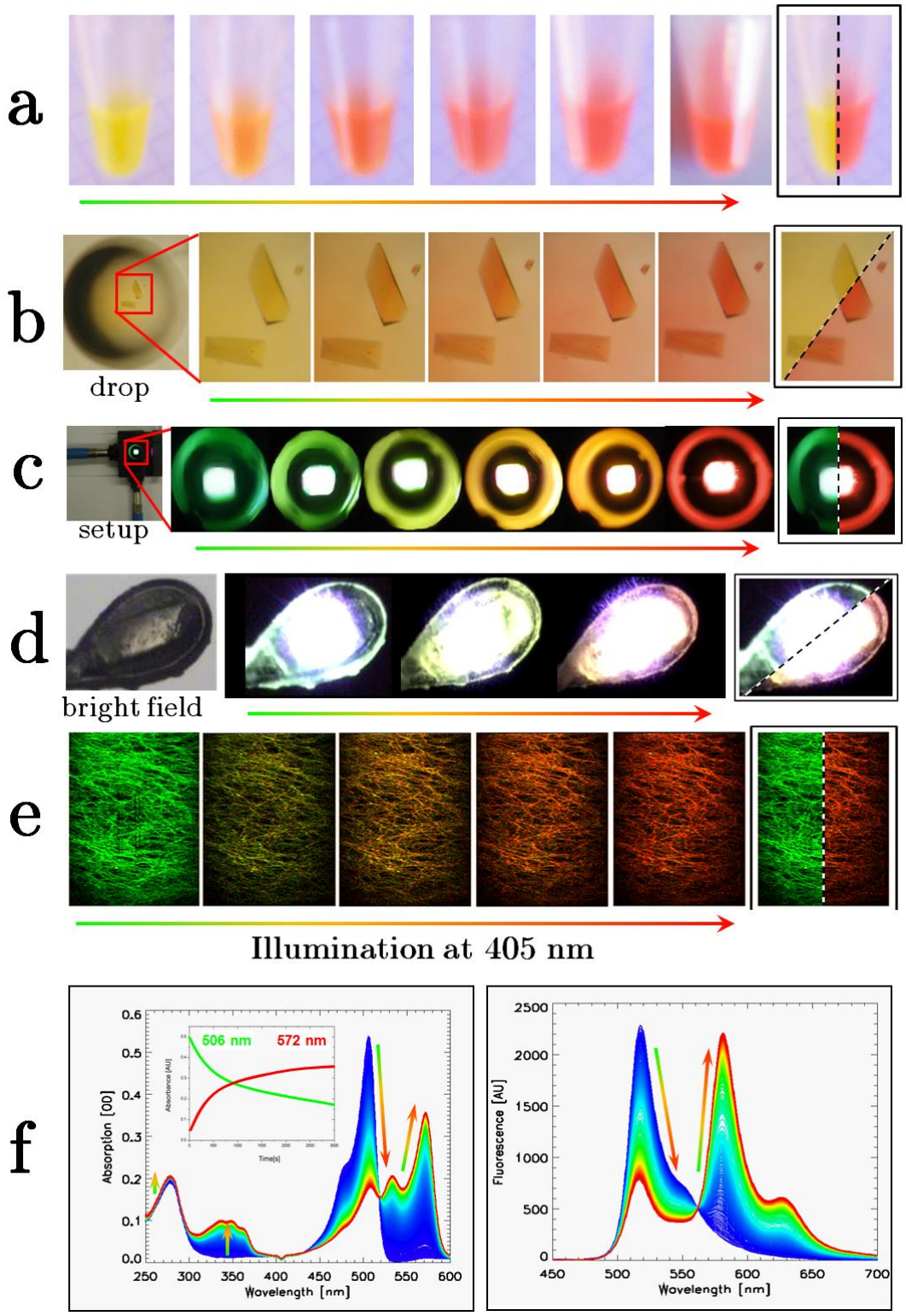

Figure II.1.4 - The color of EosFP. Green to red photoconversion of EosFP observed in bright field (a, b) and in fluorescence (c,d,e) either in solution (a, c), in crystals (b, d) or as a tag fusion application (e). The last boxed pictures represent composite images of initial and final states. The last row (f) represents the overlay of hundreds of absorption (left) and fluorescence (right) spectra during the photoconversion at room temperature (a simple baseline correction was only applied).

The migration on a SDS-PAGE of an EosFP sample that has been photoconverted in solution shows three bands (Figure II.1.5). A band at 26 kDa that is due to the still unphotoconverted protein and two bands at 18 kDa and 8 kDa that are due to the two parts of the cleaved protein. These bands are also visible when crystals are photoconverted and dissolved before running the electrophoresis, which proves once again that we can produce the same reaction either in solution or in crystals. This photoconversion is directly dependent on the exposure time to 405 nm light and, when photoconverting more and more the protein, we can see on the gels that the intensity of the band at 26 kDa decreases while that of the other bands is increasing.

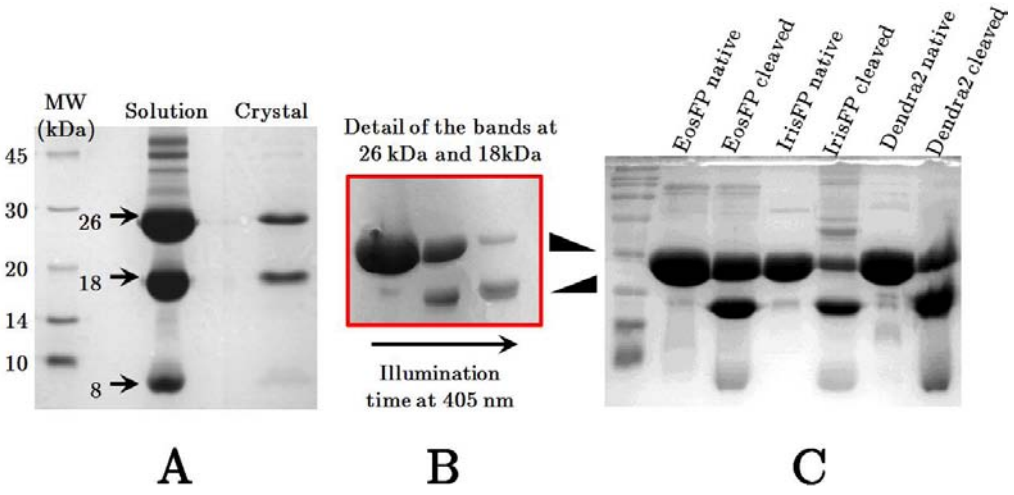

Figure II.1.5 - Electrophoresis gels showing the photo-induced cleavage of PCFPs. (A) SDS-PAGE showing partially cleaved EosFP in solution and in melted/washed crystals. The band at 26 kDa is specific of the uncleaved protein and the bands at 18 kDa and 8 kDa are specific of the cleaved protein. (B) Upon illumination at 405 nm, the band at 26 kDa decreases in intensity while the band at 18 kDa increases in intensity. An overall decrease in band intensity is observable, which can be attributed to an alteration of the protein during the process. (C) Comparison between several PCFPs presented in this thesis, native or partially cleaved in solution

Interestingly, while the photoconversion was described as occurring when the protonated form of the chromophore is excited, we see from the gel above that a cleavage is clearly observable also in crystals, for which the pH is rather basic (pH 8.0). This is due to an exchange between the protonated and anionic forms of the chromophore within the crystals (as it also happens in solution) so that the anionic form is constantly pumped to the neutral form that is cleaved by the laser.

The protein can be photoconverted in a few minutes using laser light at 405 nm (~1 W/cm²) but only at temperatures higher than 180K. At 100K the crystal can be irradiated without any conversion to occur and barely suffers from photobleaching. Additionally, an irradiation at 100K followed by an increase of the temperature in the dark does not lead to any photoconversion, which suggests that the system needs both a light excitation and a sufficient temperature for either allowing the crossing of an activation barrier or enough solvent flexibility for the photoconversion to occur. However, as we will see, the associated structural movements are really subtle and a high solvent flexibility does not seem *a priori* necessary.

4 - Is there an intermediate state forming?

It is very difficult answering such a question since we are working on samples containing many molecules that are not synchronized and may respond differently to light excitation, leading to a population mixing. Moreover, we are not equipped with instruments allowing measurements at the single molecule level. Looking at the spectral series measured at room temperature during the photoconversion (Figure II.1.4, f), no intermediate state seems possible as there is an isobestic point between the peaks specific of the green and red states. However, it is still possible that a putative intermediate state forms extremely rapidly, that we miss because of insufficient time resolution. To study this possibility, we measured the fluorescence lifetime of EosFP and performed the green-to-red photoconversion in temperature controlled experiments.

a - TCSPC experiments

Fluorescence lifetime was measured at room and cryogenic temperatures both on solution and crystals of EosFP in its green and red forms (Figure II.1.6) thanks to the time correlated single photon counting (TCSPC) technique, which is available at the Cryobench laboratory (Cf. material & methods, Chapter 2 p.232). The aim of these studies was to finely examinate the spectroscopic signature of the green and red forms thanks to their respective fluorescent lifetimes, and see whether it is possible to determine any potential reaction intermediate. For further information, refer to (Royant *et al.* 2007) in which those results have been published.

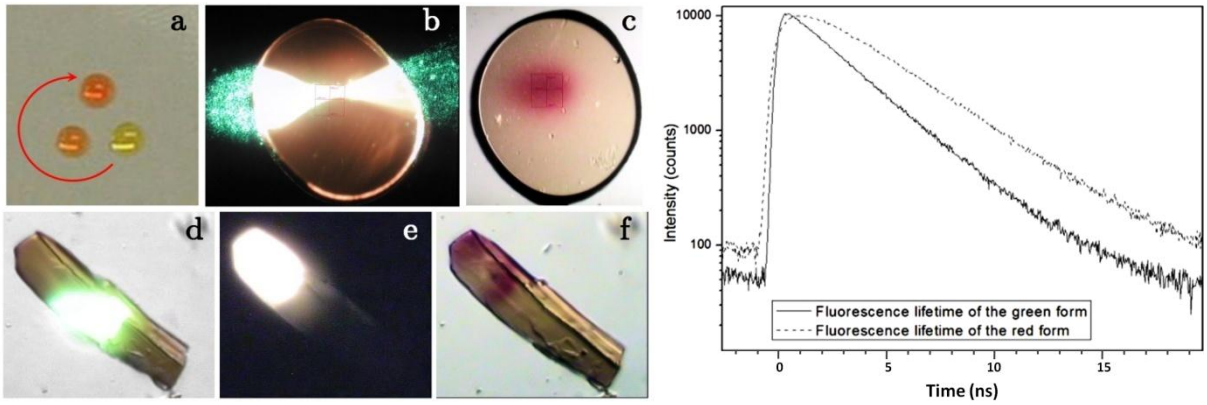

Figure II.1.6 - Left: samples of EosFP used for TCSPC measurements. Solutions (a-c) and crystals (d-f) were analyzed either in their initial green state of in their photoconverted red state. Right: fluorescence decays of green and red forms of EosFP

Both samples in crystalline and solution forms were studied with this extremely sensitive technique to detect differences in fluorescence lifetime depending of the protein state and sample phase. Our results corroborate those already published (Ivanchenko *et al.* 2005), yielding a fluorescence lifetime of about 3 ns for the green form, best fitted by a monoexponential decay. During our experiments at room temperature (setup explained in material & methods, Chapter 2 p.232), we noticed that, very often, the protein volume where the 440 nm laser used for TCSPC measurements was focused, was photoconverted in red.

We took advantage of this drawback to measure several interesting things (Table II.1.2). First, we thought that we could probably follow the photoconverted state of a sample thanks to its fluorescence lifetime since the amplitude of the green state (filter at 510 nm) decreases when the sample is being photoconverted and since the fluorescence lifetime of the red state is longer than that of the green state. Secondly, we always noticed the presence of a steep decrease upon illumination in the green fluorescence lifetime reaching a minimum around 1.8 ns and best fitted by a biexponential decay (around 90% relaxing in 1.5 ns and around 10% in 4 ns) instead of the initial single exponential decay. This result suggests that a second population is forming during the photoconversion. After a transient increase (Table II.1.2, spectra 40-50), this second population decreases again (Table II.1.2, spectra 50-120) when the illumination at 440 nm is prolonged. This species seems to have a longer lifetime than the green species, since it increases up to ~9 ns before finally dropping to ~4 ns (not shown), which is close to the lifetime of the

final red form. In diluted solution, the values we found are very close to the ones published, showing that fluorescent lifetime properties are kept both in solution and crystal forms.

Spectra	Best fitted by a	χ^2	$\tau 1$ (ns)	%($\tau 1$)	$\tau 2$ (ns)	%($\tau 2$)
0 to 20	monoexponential	1.95	3.08	100	0	0
40 to 50	biexponential	2.4	1.83	87.6	4.21	12.4
50 to 70	biexponential	1.9	2.58	88.2	9.02	11.8
100 to 120	biexponential	1.9	2.32	94	7.39	6

Table II.1.2 - Results of TCSPC measurements performed on EosFP crystals at room temperature using a 440-nm laser and an interferential filter at 510 nm to follow the fluorescence lifetime of the green form

This observation is still mysterious and we are not really able to understand it, but the transient evolution of both the fluorescence lifetime and population homogeneity during the illumination correlates with an observation that we made several times. Indeed, we very often saw that when crystals of EosFP are irradiated around 400 nm, the main fluorescence peak evolves from 516 nm to around 520-530 nm where it stays quite stable before being photoconverted to red. Our results would suggest that we can detect an intermediate state of the photoconversion mechanism. If it does exist, this intermediate state would be formed at early stages of the photoconversion mechanism. Indeed, when we illuminate the green protein with an efficient wavelength such as 405 nm (that only excites the neutral form), we see that an isobestic point is present both in absorption and in fluorescence spectral series measured during photoconversion (Figure II.1.4, f), suggesting that if an intermediate state forms, it forms quickly and is not observable later. On the other hand, when a 440-nm light irradiation is used, both the neutral and anionic forms can be partially excited, which can produce an unidentified process that can be at the origin of the observed phenomenon.

At the difference of experiments led at room temperature, if we keep the crystals 100 K during illumination at 440 nm, the fluorescence lifetime is fitted by a monoexponential decay both in the green and red forms. This suggests that the intermediate state cannot form at low temperatures.

b - Temperature-controlled fluorescence experiments

The results detailed above resemble an observation that we have made several times. When a crystal of EosFP is excited at 440 nm at 100 K, only green fluorescence is observed... but intriguingly, when a short annealing (short excursion at room temperature) is performed, still under illumination, we often noticed that the crystal turns visually orange-red but immediately turns back to the green form as soon as we come back to 100 K. This strange process can be repeated several times and only a small fraction of the molecules will turn red irreversibly.

This phenomenon, along with observations made in TCSPC, suggests the existence of a transient red-like intermediate that only shows up at temperatures higher than 180 K. To study further this phenomenon that we initially observed accidentally, we performed temperature-controlled experiments at the Cryobench where a crystal of EosFP was illuminated by a laser light at 440 nm (we did not control this phenomenon on diluted solutions) while slowly ramping the temperature from 100 K to 270 K.

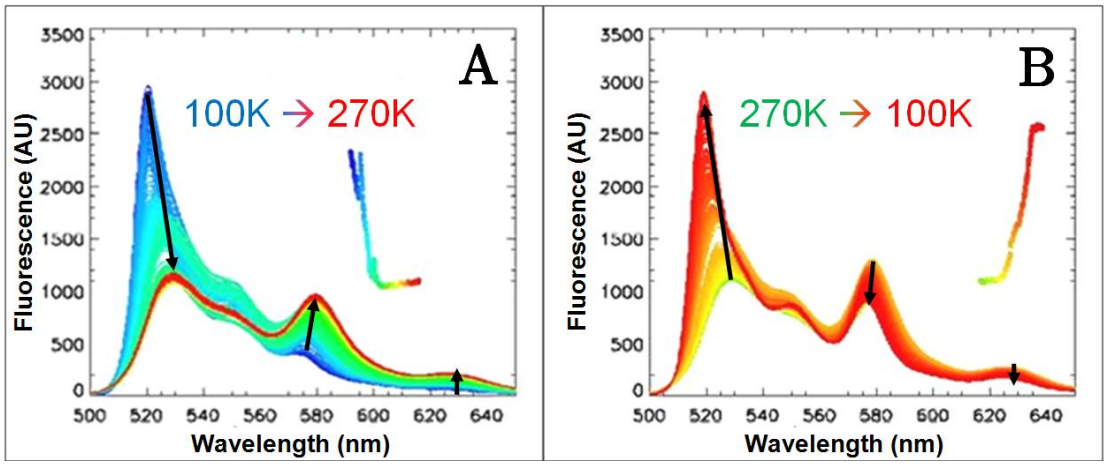

Figure II.1.7 - Fluorescence spectra of EosFP being photoconverted (λ=440 nm) with temperature varying from 100K to 270K (A) and from 270K to 100K (B), passing through a yellow state – Insets represent the evolution of the main fluorescence peak.

The results (Figure II.1.7) show that, as expected, the photoconversion process is very slow compared to the use of a 405 nm laser but also that while the temperature is increasing, the maximum peak of emission shifts from 516 to 530 nm, forming a kind of yellow form that we

never observed before. The most striking observation, however, is that this species is almost completely reversible to the initial green form as soon as we come back to 100 K, and this can also be repeated a number of times. Finally, if the laser exposure is prolonged at room temperature, the molecules irreversibly turn red.

This "yellow form" is rather intriguing since at room temperature, the protein is characterized as emitting its green fluorescence at a maximum wavelength of 516 nm and not 530 nm. By decreasing the power of the laser at 440 nm and limiting the increase of temperature to 260 K instead of 270 K, the photoconversion to the red form could be avoided and the "yellow form" at 530 nm isolated spectroscopically (Figure II.1.8). Here again, as soon as the temperature is ramped back to 100 K, the signal comes back to the initial green state.

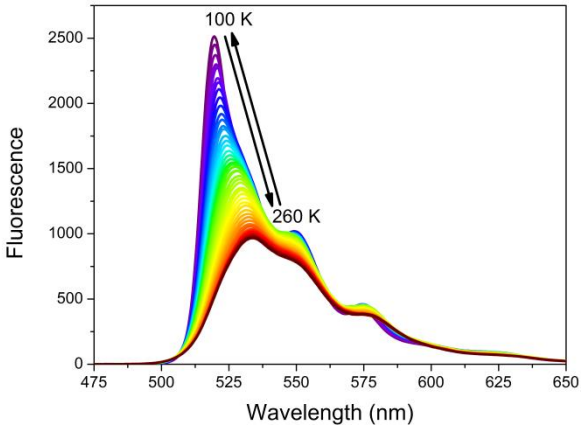

Figure II.1.8 - Spectroscopic isolation by temperature of a reversible yellow-emitting form in a crystal of EosFP

We cannot conclude, thus, on this wavelength shift that can be due to strange optical effects existing in the particular and highly concentrated media that are protein crystals. Despite many efforts, we were unable to perform a data collection under higher temperatures than 180 K and under illumination without provoking too much radiation damages to the protein crystals. If we could perform this experiment, it would be realized with the help of the online microspectrophotometer, under laser exposure at 440 nm, in order to trap the putative yellow intermediate state and solve its structure. It would also be interesting to study the

apparition of this form excited at 440 nm at different pH values, in order to see if this wavelength excites the neutral band or the anionic peak, or both.

Currently, we cannot conclude on the origin of the phenomenon described above but taken together, the TCSPC and temperature-controlled spectroscopic measurements on EosFP crystals suggest that a reaction intermediate can form at the beginning of the green-to-red photoconversion and that this species, although resembling the red state, can be reversible to the initial green state. Most likely, if this state really exists, it is a state in which the peptide bond close to the chromophore is extended but not cleaved, or a state in which the cleavage can be reversed as soon as an energy barrier leading to the final red state is not crossed.

5 - Toward a better comprehension of the photoconversion mechanism

One of the main goals of this thesis was to gather enough experimental evidences to indicate whether or not the proposed photoconversion mechanism is valid. As already explained, following the irradiation of the protein at around 400 nm, the photocleavage of a peptide bond between the chromophore and the prior residue (F61) was explained by a putative β-elimination reaction (Nienhaus *et al.* 2005). This mechanism (Cf. Figure I.2.21, p.50) would be initiated thanks to the protonated state of the chromophore which absorbs light at ~400 nm and which subsequently would transfer an H^+ to the chromophoric histidine (H62). This unstable biprotonated histidine is proposed to relax thanks to a β-elimination whose acceptor is a glutamate (E212) and the concerted cleavage of the peptide bond between the histidine and the previous residue (F61).

a - New proposition for the photoconversion mechanism

Based on the structures of the green and red forms of EosFP and the experimental results of the photoconversion, Mickael Lelimousin (IBS, Grenoble) during his Ph.D. thesis, could calculate potential energy surfaces (PES) at the ground (S_0), excited (S_1) and triplet (T_1)

states. The minimum energy pathway shows two conical intersections that allow two intersystem crossings between the PES at S_1 & T_1 and the PES at T_1 & S_0, called ISC_1 and ISC_2, respectively (Figure II.1.9). The transient passage via the triplet state seems necessary for the reaction to occur, because an energy barrier of more than 100 kJ/mol has been calculated to cleave the mainchain at the singlet excited state S_1, which is far too much for the reaction to occur at this state (since the Arrhenius relation would predict a reaction timescale longer than a second, which is way too long for the excited state lifetime, a few nanoseconds). The intersystem crossing between S_1 and T_1 (ISC_1) allows having a much lower energy barrier to cross (~45 kJ/mol). Those results will be submitted for publication (Lelimousin *et al.* 2009).

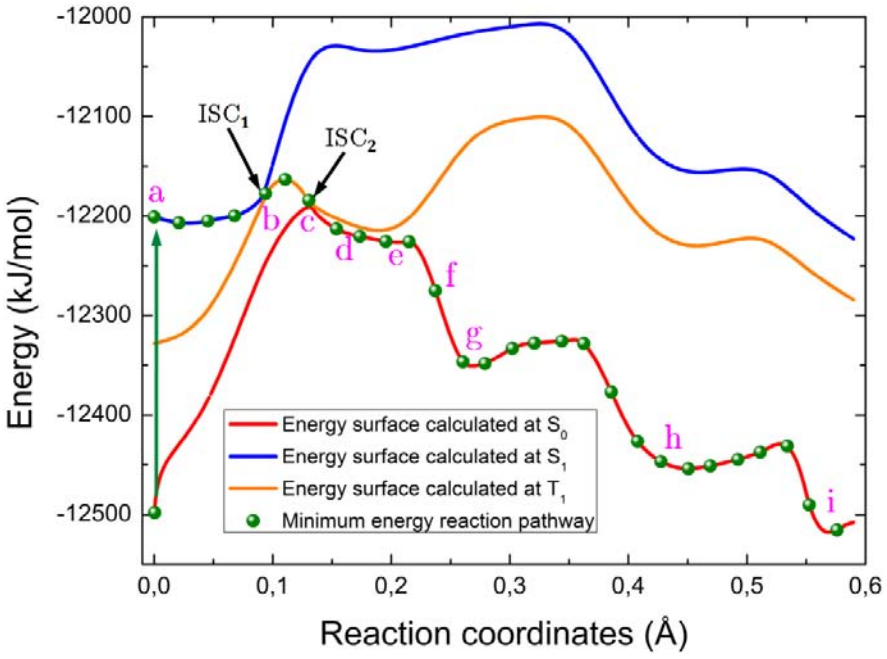

Figure II.1.9 - Calculated reaction pathway for the green-to-red photoconversion mechanism of EosFP. The two intersystem crossings (ISC) allow the reaction to occur by transiently passing through the triplet state.

Thanks to the quantum chemistry calculations, a new reaction mechanism for the photoconversion of EosFP can be proposed (Figure II.1.10) that completes and modifies the one that has been proposed initially (Figure I.2.21, page 50).

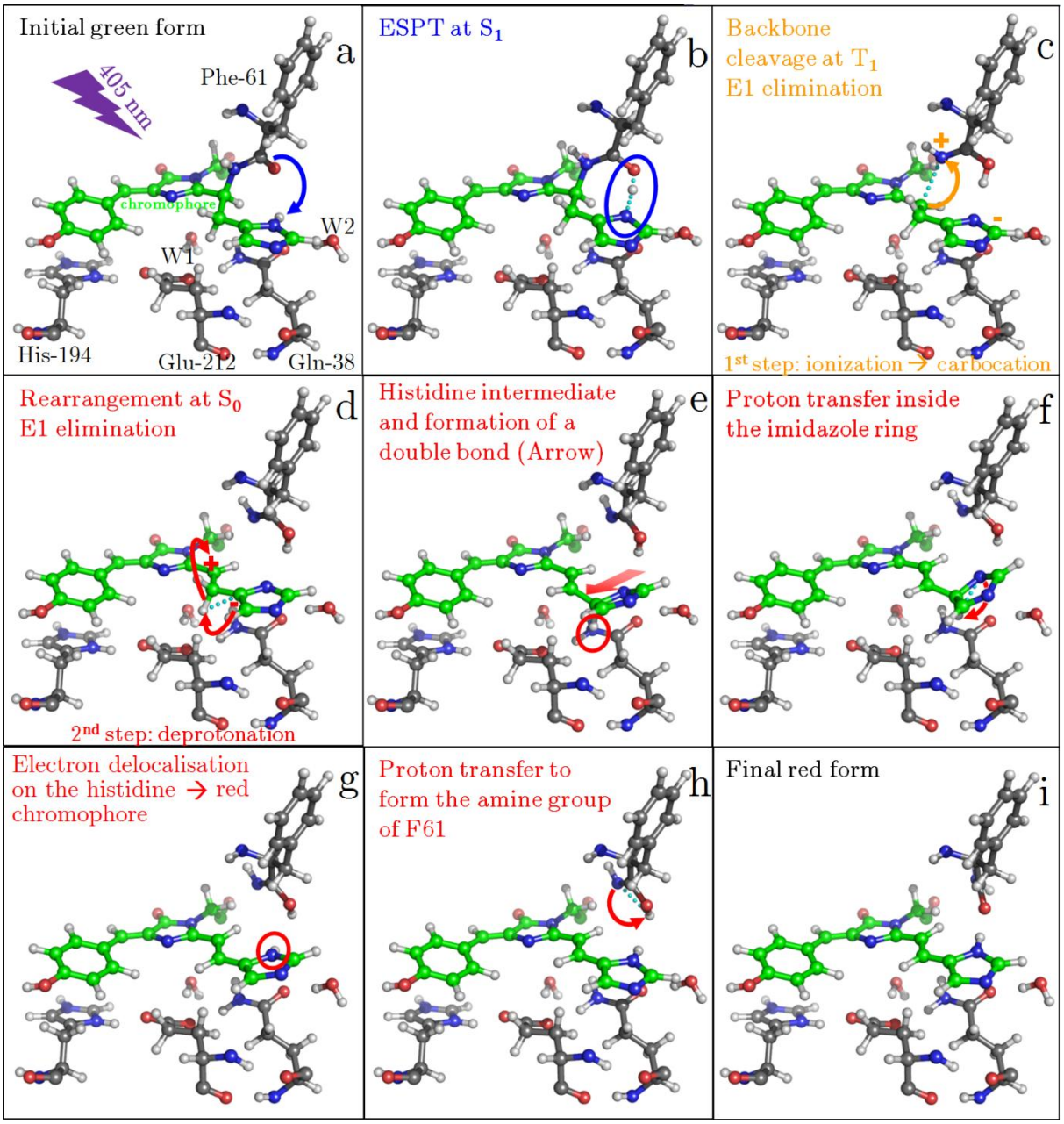

Figure II.1.10 - The new photoconversion mechanism proposed for EosFP

After the Franck-Condon excitation of the neutral chromophore at ~400 nm, the excited state S_1 is reached and an excited state proton transfer (ESPT) is induced from the chromophoric histidine (His62) to the carbonyl moiety of the neighboring Phe61. This protonation induces the first step of a β-elimination of the first order (E1) by forming a carbocation. As stated above, this step can be only achievable at the triplet state and the

subsequent intersystem crossing to S_0 allows the second step of the β-elimination by inducing a deprotonation of the His62-Cβ to the His62-Cγ. This carbon (His62-Cγ), thus, becomes hybridized sp^3 along with the formation of a double bond between His62-Cβ and His62-Cγ. The transfer of this unstable proton to the His62-Nδ allows the imidazole ring to regain its aromatic character along with the electron delocalization on the whole chromophoric triad, forming a red chromophore. Finally, the carbonyl moiety of Phe61 is restored by a proton transfer to its nitrogen, forming the final carboxylamide moiety. Further information detailing this mechanism involving multiple intersystem crossings can be found in (Lelimousin *et al.* 2009).

b - An odd isomerization of the chromophoric histidine in KikGR

Recently, the crystallographic structures of both green and red forms of the KikGR protein (PDB accession codes: 2DDD and 2DDC respectively) have been released. The structures of this green-to-red photoconvertible protein formed from the green light-emitting protein KikG (kikume) by mutating its chromophore (Asp-Tyr-Gly) to the one of Kaede-like proteins (His-Tyr-Gly) show an interesting flip of the chromophore's histidine sidechain in the photoconverted form. This unique isomerization of the chromophoric histidine seems intriguing but can be easily explained looking at the structures and the reaction scheme shown above. During the reaction steps, while a proton is transferred within the imidazole ring of the chromophoric histidine (Figure II.1.10, steps d to f), this ring is non coplanar with the rest of the chromophore and a double bond is formed. These steps allow an enhanced flexibility of the chromophoric histidine that can isomerize from its initial trans conformation to a cis conformation, given that it has enough space to do so.

While the chromophore environment of EosFP and Kaede can be almost perfectly superimposed, we can notice some clear differences between the superimposition of EosFP and KikGR (Figure II.1.11). In EosFP and Kaede, the superimposition of three residues in the vicinity of the chromophore: M40, I196 and L210 is almost perfect both in the green and red forms and van der Waals interactions between I196 and L210 are clearly present. In KikGR, the equivalent of M40 is a valine (V40) and the equivalent of I196 is a methionine (M198).

This has the consequence to reverse the van der Waals interactions that are now formed between the equivalent of L210 (L212) and the residue 40. M198, thus, freed from its interaction with L210, can freely move and rotate, leaving space for the chromophoric histidine to isomerize while the double bond is formed.

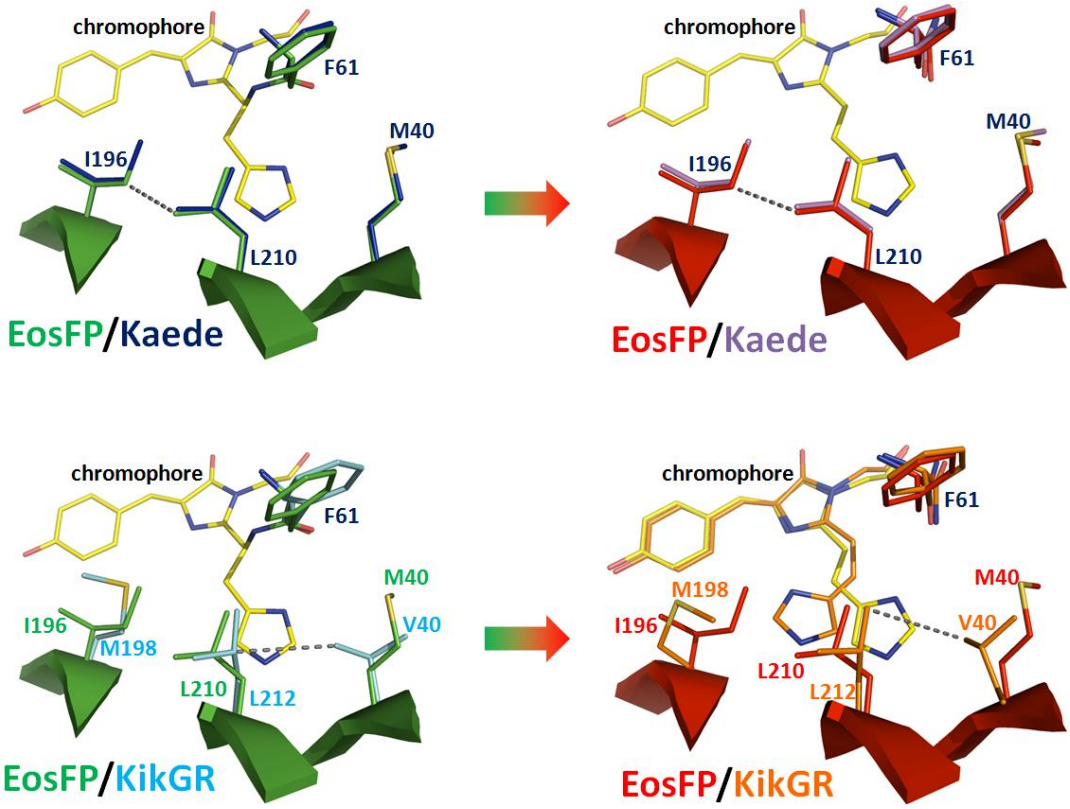

Figure II.1.11 - The trans-to-cis isomerization of the chromophoric histidine of KikGR in its red form can be explained by the influence of the chromophore environment - Top: superimposition of the chromophore and some surrounding residues between EosFP and Kaede, both in the green and red forms. Bottom: superimposition of the chromophore and some surrounding residues between EosFP and KikGR, both in the green and red forms. Van der Waals interaction between I196 and L210 (top) or between V40 and L210 (bottom) are depicted by dashes.

Part 2 - Dendra2: an efficient PCFP

1 - Crystallization of Dendra2

Crystallizing the protein Dendra2 required much more efforts than for EosFP and rather unusual techniques that are detailed in material & methods (Part 2, p.202). The difficulty of this task compared to the other fluorescent proteins described in this thesis can be explained by the fact that Dendra2 is a rather stable monomer that does not easily oligomerize, which generally helps forming crystal contacts during crystallization.

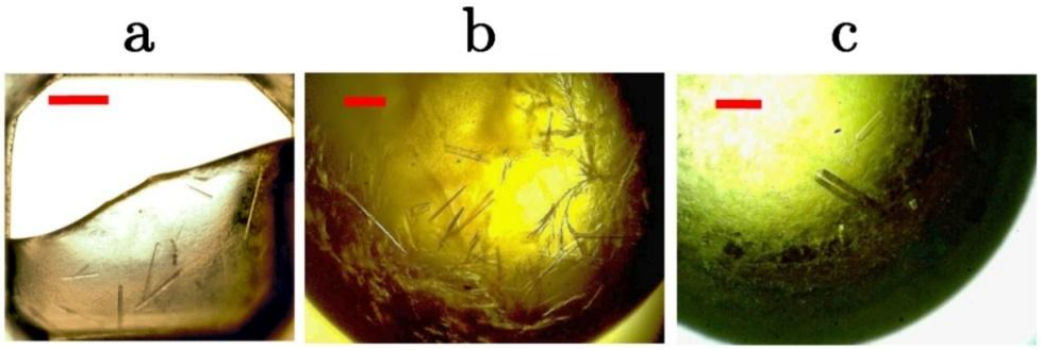

Figure II.1.12 - Crystals of Dendra2 obtained in magnesium nitrate. A condition from the salt screening gave nice crystals in magnesium nitrate but too small for data collection (a). After repurification and once reproduced on a bigger scale, the crystals were still too small (b). Once crystals were crushed and seeded, two crystals of a sufficient size grew (c). The red scales represent 200 µm.

The final crystals were obtained in 32% PEG 3350, 0.1 M magnesium nitrate, 0.1 M Tris-HCl pH 8.8 (Figure II.1.12) and crystal parameters and data collection statistics are compiled in Table II.1.3.

Because of the difficulties experimented during crystallization, we could not obtain more than two single crystals that were suitable for data collection. Only data collections on green crystals were then performed and obtaining the structure of the red form would require to obtain more crystals, which was not made during the time of this thesis.

Crystal parameters and data collection statistics			
Protein	**EosFP green**	**EosFP red**	**Dendra2 green**
Crystallization			
Crystallization conditions	30% PEG 4000, 0.2 M sodium acetate, 0.1 M Tris-HCl pH 8.5	30% PEG 4000, 0.2 M sodium acetate, 0.1 M Tris-HCl pH 8.5	32% PEG 3350, 0.1 M magnesium nitrate, 0.1 M Tris-HCl pH 8.8
Initial protein concentration (mg/mL)	10.7	10.7	17.4
Protein:precipitant ratio	1:1	1:1	1:1 and then seeding
Cryoprotectant	10% glycerol	10% glycerol	10% glycerol
Post-crystallization treatments	None	Irradiation at 405 nm	None
Content of the unit cell			
Space group	$P\ 2_12_12_1$	$P\ 2_12_12_1$	P 1
Cell dimensions			
a; *b*; *c*, Å	73.70; 106.33; 122.38	72.98; 105.46; 123.68	71.26; 76.85; 92.50
α; β; γ, °	90; 90; 90	90; 90; 90	90.05; 108.17; 106.58
Solvent content, %	47.0	46.6	44.1
Monomers/asymmetric unit	4	4	8

Table II.1.3 - Crystallization data for green and red forms of EosFP and green form of Dendra2

2 - Structure of Dendra2

We have measured the X-ray structure of the green species of Dendra2 and performed a comprehensive characterization of the optical absorption and fluorescence properties of the protein in both its green and red forms. The structure, which is very similar to those reported for the closely related proteins EosFP and Kaede, revealed a local structural change involving mainly Arg66 and a water molecule (W4), which are part of a charged and hydrogen-bonded cluster of amino acids and water molecules next to the chromophore.

Unlike in EosFP and Kaede, Arg66 of Dendra2 does not contribute to negative charge stabilization on the imidazolinone ring by hydrogen bonding to the imidazolinone carbonyl. This structural change may explain the blue shift of the absorption and emission bands, as well as the markedly higher pKs of the hydroxyphenyl moiety of the chromophore, which were determined as 7.1 and 7.5 for the green and red species, respectively. The 20-fold enhancement of the neutral species in Dendra2 at physiological pH accounts for the observed higher photoconversion yield of this protein in comparison to EosFP.

X-ray data collections were performed on two single crystals at the ESRF beamline ID14-4 (X-ray wavelength $\lambda = 0.939$ Å). Dendra2 crystals were kept at 100 K during data collection by using a nitrogen stream. The diffraction quality of the crystals rapidly decreased during data

collection so that, similarly to the red structure of EosFP, a composite data collection approach was chosen to maximize the completeness required by the spacegroup in which Dendra2 crystallized (P1). Data reduction and refinement were performed as described in material & methods, p.215. Refinement statistics are compiled in Table II.1.4.

Chromophore restraints were generated from idealized coordinates found in the Hic-Up database (Kleywegt *et al.* 2003) and adjusted as explained in material & methods (Chapter 4 - Restraints on the chromophores, p.243).

	Crystal parameters and data collection statistics		
Protein	**EosFP green**	**EosFP red**	**Dendra2 green**
PDB accession code	Not deposited	Not deposited	2VZX
Data collection			
Beamline	ESRF / ID14-3	ESRF / ID23-2	ESRF / ID14-4
Wavelength, Å	0.931	0.873	0.939
Temperature, K	100	100	100
Data collection statistics			
Number of datasets (crystals)	1 (1)	5 (1)	2 (2)
Resolution, Å	48.7-1.55 (1.7-1.55)	47.2-2.0 (2.11-2.0)	33.5-2.0 (2.1-2.0)
R_{merge}, %[a]	6.8 (47.2)	13.0 (40.7)	4.7 (17.4)
Mean $I/\sigma(I)$	17.7 (4.3)	15.1 (6.5)	12.15 (4.42)
Completeness, %	97.1 (95.8)	100 (100)	94.1 (94.5)
No. of total reflections	849,308 (137,416)	875,394 (126,594)	220,830 (30,255)
No. of unique reflections	123,433 (20,063)	65,241 (9,389)	113,213 (16,379)
	Data refinement statistics		
R_{cryst} [b] / R_{free}[c]	0.156 / 0.183	0.184 / 0.228	0.212 / 0.269
Nonhydrogen atoms			
Protein	7168	7,768	15,867
of which, chromophore	100	96	200
Water	741	640	1,280
rms deviation from ideality			
Bond lengths, Å	0.01	0.008	0.009
Bond angles, °	1.493	1.425	1.415
Ramachandran plot			
Most favored, %	93.5	93.4	91.6
Allowed region, %	6.2	6.3	8.2
Generously allowed region, %	0.1	0.3	0.2
Disallowed, %	0.1	0.0	0.0
Average B factor, Å²			
All atoms	13.8	20.2	21.8
Chromophore	12.9	15.9	15.7

$$^{a}R_{merge} = \frac{\sum_{hkl}\sum_{i}\left|I_i(hkl) - \overline{I(hkl)}\right|}{\sum_{hkl}\sum_{i}\left|I_i(hkl)\right|} \qquad ^{b}R_{cryst} = \frac{\sum_{hkl}\left|F_{obs} - F_{calc}\right|}{\sum_{hkl}F_{obs}} \qquad ^{c}R_{free} = \frac{\sum_{hkl\subset T}\left|F_{obs} - F_{calc}\right|}{\sum_{hkl\subset T}F_{obs}}$$

The R_{free} is calculated with a small fraction (5%) of reflections randomly chosen to be part of test group T. This R factor, thus, is not biased by the refinement process

Table II.1.4 - Data collection, data processing and structure quality statistics for green and red forms of EosFP and green form of Dendra2. Values between brackets refer to the highest resolution shell

a - General description of the structure

The unit cell contains eight protein chains (Figure II.1.13 right), with little deviation between them (the average rmsd between two protomers in the asymmetric unit is 0.72 ± 0.21 Å). All 225 amino acids are visible in the electron density, unlike the hexahistidine tag preceding the N-terminus, which apparently is highly disordered.

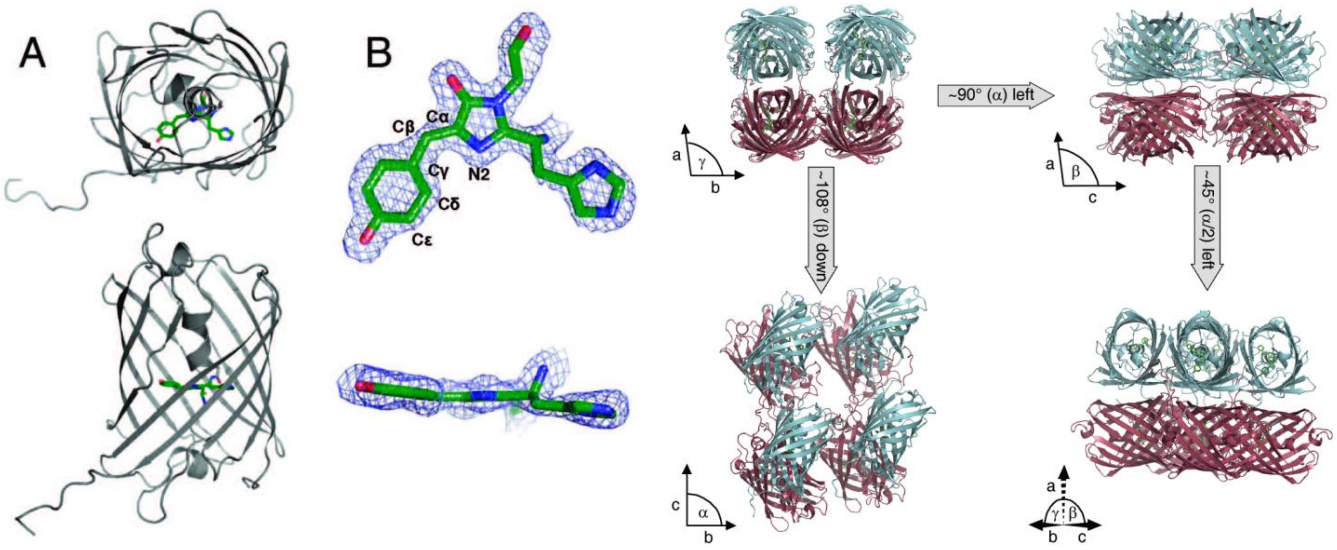

Figure II.1.13 - The structure of Dendra2

Left: Overview of a monomer of Dendra2 and detail of its chromophore. (A) Top and side views of the overall fold of a monomer, in cartoon representation with the embedded chromophore shown in sticks. (B) Top and side views of the chromophore with the final 2Fo-Fc electron density map, contoured at 1.5 σ. Right: Crystal packing of Dendra2. The molecular packing is shown along (a) the unit cell axis c, (b) the axis b, (c), the axis a, and (d) the median between the axis b and c. The unit cell content consists in eight molecules arranged in four weak dimers, whose molecules are colored in cyan and prune respectively. Chromophores are shown as green sticks.

The amino acid preceding the chromophoric triad is a phenylalanine in many FPs including EosFP, Kaede, eqFP611 and avGFP. Interestingly, it is a valine (Val61) in Dendra2. Multiple hydrogen bonds and van-der-Waals interactions restrain the chromophore in the center of the β-can in an essentially co-planar arrangement of the aromatic imidazolinone and phenyl rings (Figure II.1.15, Table II.1.4). The cis conformation of the *p*-HBI chromophore is stabilized by hydrogen bonds from the tyrosine oxygen atom to the Ser142 oxygen (2.7 Å) and to a water

molecule (2.8 Å). The carbonyl oxygen of the imidazolinone ring hydrogen-bonds with the side chain of Arg91 (2.9 Å). Glu144, His193, Glu211, Arg66, water molecule (W4), and Tyr177 form a planar network beneath the chromophore stabilized by hydrogen bonds and Coulomb interactions (Figure II.1.14). Similar polar networks, which may provide a rigid scaffold restricting chromophore dynamics, have been noticed for a variety of anthozoan FPs including DsRed (Wall *et al.* 2000; Yarbrough *et al.* 2001), eqFP611 (Nienhaus *et al.* 2003; Petersen *et al.* 2003), zFP538 (Remington *et al.* 2005) and amFP486 (Henderson & Remington 2005). The Arg66 side chain is held in place by a salt bridge from Nη1 to Glu211, a hydrogen bond between Nη1 and a water molecule and another hydrogen bond from Nη2 to water molecule W4. It is further stabilized by a weak hydrogen bond between its Nε and the side chain hydroxyl of Thr69 (Figure II.1.15).

b - Comparison with EosFP

The structure of Dendra2 (Figure II.1.13) is very close to that of EosFP with which it shares 69% identical amino acid residues and the 11-strand β-barrel shape of all known fluorescent proteins. However, at the difference of EosFP for which the tetramer is present in the asymmetric unit, eight molecules per asymmetric unit, under the form of four dimers, are found for Dendra2. If EosFP is naturally under its tetrameric form in solution, Dendra2 is a monomer but the high concentration present in the crystal helps the reformation of those dimers. The electron density defines a chromophore that can be modeled in full cis conformation (Figure II.1.13, left).

When observing more closely the chromophore and its environment, however, we can notice some differences as compared with the structure of EosFP. The most striking difference between EosFP and Dendra2 resides in its arginine 66 that is in direct interaction with the strictly conserved glutamate 211 (Glu212 in EosFP numbering, Glu222 in GFP numbering) as shown in Figure II.1.14. In EosFP, this arginine interacts with the carbonyl group of the chromophoric imidazolinone ring. Based on the structure, we may speculate that the tight salt-bridge interaction between Arg66 and Glu211 in Dendra2 creates a more rigid environment

that maintains the neutral, highly fluorescent red chromophore (QY=0.45 at pH5) as well as its anionic form (QY=0.61 at pH 9) in a coplanar conformation, which is essential for a high fluorescence quantum yield.

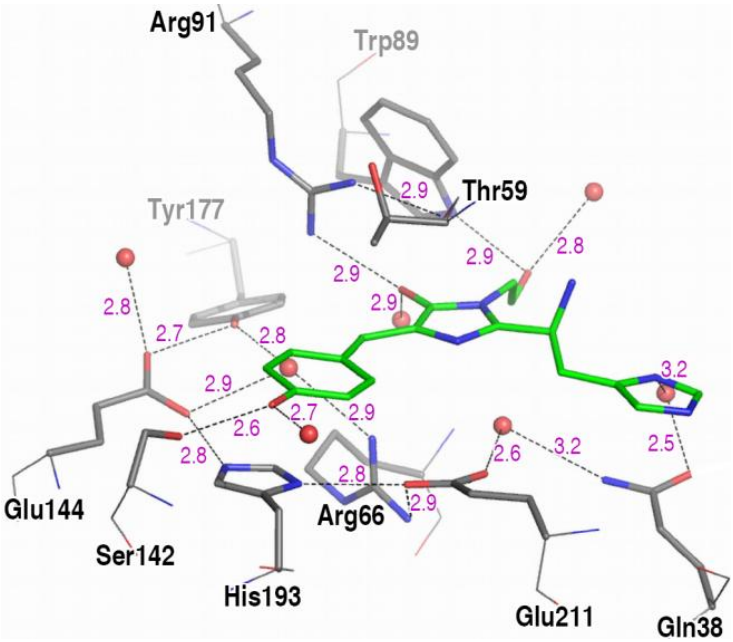

Figure II.1.14 - Close-up of the interactions between the chromophore and its environment. The backbone atoms are represented as thin lines and the sidechains atoms as sticks. Color coding: grey carbons = non-chromophore, green carbons = chromophore, blue = nitrogen, red = oxygen. Water molecules are represented by red spheres. Distances in purple are given in Å and correspond to significant values averaged over all the monomers.

Comparing the chromophore environment of EosFP and Dendra2 we see that a significant structural difference in the immediate chromophore environment is obvious (Figure II.1.14 and Figure II.1.15, left). Water W4 and the Arg66 guanidino group have exchanged their locations. The completely different orientation of the Arg66 side chain in EosFP may originate from the replacement of Thr69 by Ala69 (Figure II.1.15, right). The small aliphatic side chain cannot form a hydrogen bond to Nε of Arg66. This interaction is also absent in Kaede and KikGR; their Arg66 side chains also adopt the EosFP-like position. As a consequence, the carbonyl oxygen of the imidazolinone is only 2.9 Å away from the Nη1 atom of Arg66 in EosFP, so that an additional hydrogen bond is established. In contrast, the distance between the Arg66 side guanidine moiety and the carbonyl oxygen is 3.9 Å in Dendra2 and thus too long for hydrogen

bonding. As will be described below, this structural finding bears consequences for the particular optical properties of Dendra2.

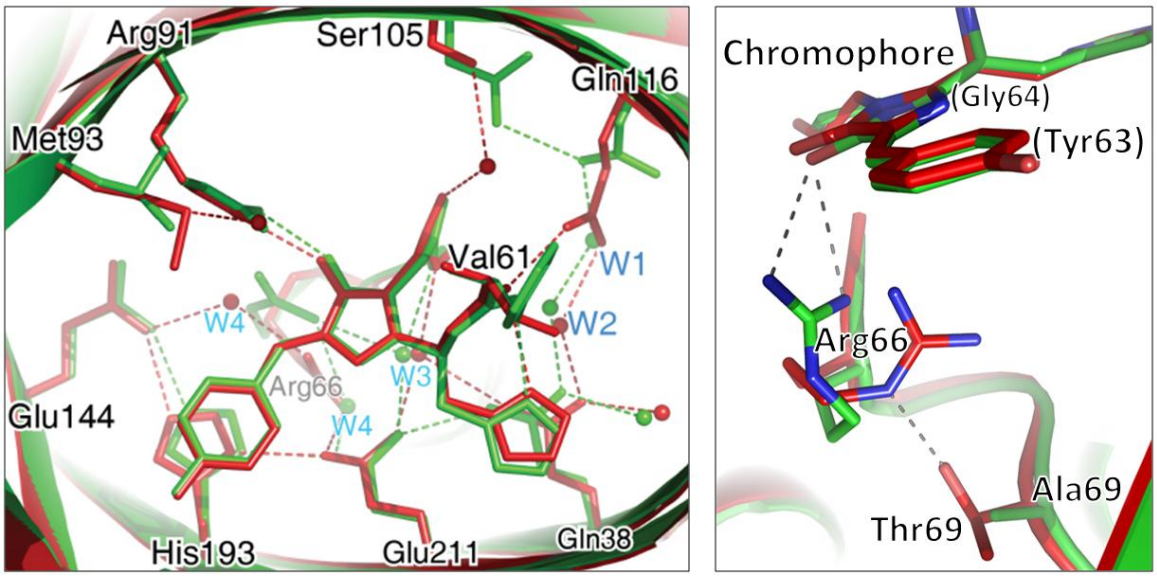

Figure II.1.15 - Superimposition of the chromophore environment in EosFP (green) and Dendra2 (red). Left: Despite a similar folding, the aminoacid composition is different and a very slight but global change in the proteins organization is observable and especially around the chromophore, finally affecting the highly conserved glutamate close to the chromophore. Right: View showing how a threonine at position 69 interacts with Arg66(Nε), preventing the interaction between Arg66 and the chromophore carbonyl. The residue numbering corresponds to that of Dendra2, dashes depict hydrogen bonds (<3Å)

Based on the X-ray structures of green and red EosFP, we suggested that the His62 imidazolium may donate a proton to the Phe61 carbonyl, thus rendering the peptide group between Phe61 and His62 an ideal carboximidic leaving group in the β-elimination reaction, which leads to the generation of the red 2-[(1E)-2-(5-imidazolyl)ethenyl]-4-(*p*hydroxybenzylidene)-5-imidazolinone chromophore (cf. chapter on the green-to-red photoconversion, p. 73). The distances between His62-Nδ and the Phe61 carbonyl are 3.3 Å in EosFP (Nienhaus *et al.* 2005) and 3.2 Å in Kaede (Hayashi *et al.* 2007). In the Dendra2 structure, the corresponding distance between the His62-Nδ and the Val61 carbonyl is significantly larger, 3.8 Å. However, structural readjustments could occur in the excited state that strengthen the interaction and allow proton transfer to take place.

3 - Unraveling the particular properties of Dendra2

a - The explanation of a higher pK value

The green-to-red photoconvertibility of PCFPs scales directly with the proportion of neutral chromophore during excitation. An efficient PAFP, thus, should have an important fraction of its population in its protonated form at the pH of the experiment. The pH-dependent absorption spectra of green Dendra2 (Figure II.1.16) show that two bands are present at ~385 and ~493 nm and that are denoted as A and B bands, respectively. These bands are associated with the neutral (phenol) and anionic (phenolate) forms of the chromophore (Chattoraj *et al.* 1996; Tsien 1998; Elsliger *et al.* 1999). The exact peak positions vary with pH and are compiled in Table II.1.5. With increasing pH, the B band gains amplitude at the expense of the A band.

		Neutral chromophore		Anionic chromophore	
	pH	$\lambda_{max, abs.}$ (nm)	$\lambda_{max, em.}$ (nm)	$\lambda_{max, abs.}$ (nm)	$\lambda_{max, em.}$ (nm)
Green form	1	381.7	–	–	–
	4	378.8	454	–	–
	7	383.1	–	460.8 ; 492.6	504.5 ; 542.0
	9	387.6	–	463.0 ; 495.1	504.5 ; 542.0
	13	–	–	446	–
Red form	1	381.7	–	–	–
	4	393.7 ; 414.9 ; 440.5 ; 471.7	480.8 ; 516.8 ; 561.8 ; 609.7	–	–
	10	–	–	478.5 ; 515.5 ; 555.6	570.5 ; 619.2 ; 675.7
	12	–	–	347.0 ; 499.0	–

Table II.1.5 - Optical properties of Dendra2

When comparing absorbance spectra of green forms of EosFP and Dendra2, it is obvious that the protonated form of the chromophore (absorbing at ~390 nm) is much higher for Dendra than for EosFP, even at basic pH values (Figure II.1.16). The apparent association constant pK between the chromophore and the labile proton of the hydroxyl group is indeed found to be much higher for Dendra2, pK=7.1 (Adam *et al.* 2009b) than for EosFP, pK=5.8

(Wiedenmann *et al.* 2004) or Kaede, pK=5.6 (Ando *et al.* 2002). Thus, Dendra2 reveals as being a very efficient green-to-red photoconvertible probe.

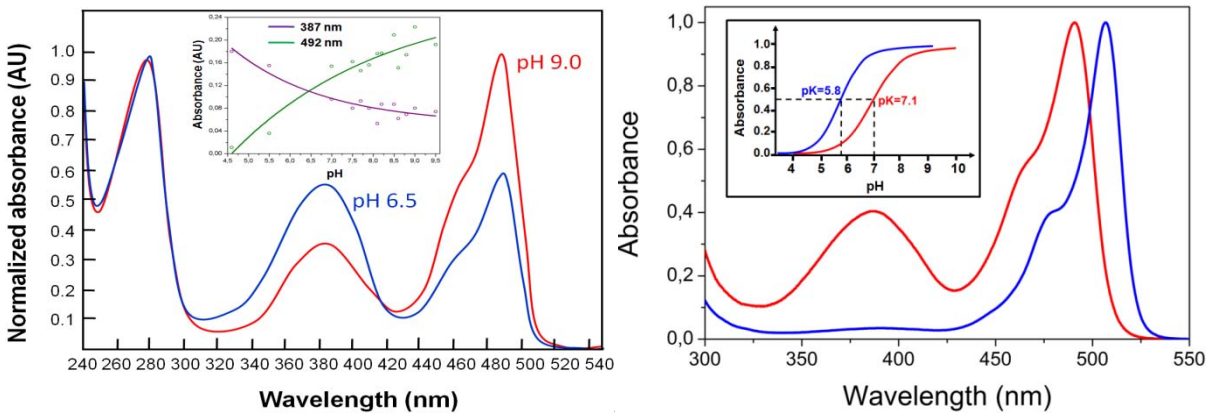

Figure II.1.16 - Left: Spectroscopic signature of Dendra2 depending on its protonation state. The two main absorption peaks at ~390 nm and ~490 nm, specific of the neutral and anionic chromophore, respectively are followed on a pH range from 4.5 to 9.5 and shown in inset. Right: Absorbance spectra of EosFP (blue) and Dendra2 (red), both at pH 8.0.- Inset: titration curves showing that Dendra2 has a chromophore that behaves as a stronger base than the one of EosFP.

The fact that Dendra2 has inherently a more acidic character than EosFP can be explained thanks to the crystallographic structure presented here. The stabilization of the proton on the phenyl moiety in Dendra2, which amounts to ~7.5 kJ/mol, may arise from the altered Arg66 side chain conformation due to its interaction with Thr69 (Figure II.1.15, right). The lack of hydrogen bonding between Arg66 and the carbonyl oxygen of the imidazolinone ring results in reduced negative charge stabilization on the ring. The concomitantly enhanced charge density on the hydroxyphenyl moiety is expected to cause stronger binding of the proton. In EosFP, we observed that replacement of Ala69 by threonine shifted the chromophore pK to ~7 (data not shown). Presumably, this mutation produced structural changes in EosFP that made it similar to Dendra2.

The reorganization of Arg66 in Dendra2 compared to EosFP can also be favored by the global structural differences between the two proteins. When looking at the chromophore environment more closely (Figure II.1.15, left), we can notice that there is a Gln at position 116 in Dendra2 instead of an Asn in EosFP. The steric constraints of this longer aminoacid makes the two water molecules (W1 and W2) bonding Asn116 and Gln38 in EosFP to be substituted

in Dendra2 only by the equivalent of the second water molecule (W2). This water molecule W2 is displaced because of a hydrogen bond with Gln116 that is a bit longer (3.0 +/- 0.2 Å) and it compresses Gln38 via a short hydrogen bond (2.5 +/- 0.1 Å). This molecule was too disordered in two out of eight chains (B and F) to be modeled.

Gln38 being moved away from Glu211, the hydrogen bond that exists between these two residues in EosFP (2.9 +/- 0.1 Å) does not exist in Dendra2 (3.6 +/- 0.2 Å). A water molecule (W3) bonding Glu212 and Arg66 in EosFP, bonds this same glutamate (Glu211) and Gln38 in Dendra2. Glu211 is thus freed from its interaction with Gln38 compared to EosFP and makes that Arg66 in Dendra2 finds a much stronger position by directly binding Glu211. The different position of Arg66 in EosFP and Dendra2 is accompanied by the different location of a water molecule (W4).

The direct interaction between Arg66 and Glu211 is very clear in the electron density maps of Dendra2 in each of the eight protein chains of the asymmetric unit and should also prevent this residue to move in alternate conformations like establishing an interaction with the imidazolinone ring as observed in other fluorescent proteins. This interaction has already been described in the literature, for example concerning the fluorescent protein mKO. A very similar interaction between the equivalent residues Glu212 and Arg69 in the fluorescent protein mKO has indeed been described and display a similar pattern of differences with another orange fluorescent protein called mOrange than between Dendra2 and EosFP (Figure II.1.17).

mOrange is a blue-shifted variant of the red fluorescent protein DsRed, being part of the so-called mFruits variants (Shu *et al.* 2006). In this variant, the first amino acid of the chromophore triad (Gln66) was mutated to a threonine whose cyclization forms a third chromophoric five-membered heterocycle (2-hydroxy-dihydrooxazole) responsible for the color shift. This cyclization is not a unique phenomenon since in the protein Zs Yellow (zFP538) found in the "button" polyp *Zoanthus sp.*, the cyclization of the chromophoric Lys66 forms a third six-membered tetrahydropyridine heterocycle (Remington *et al.* 2005). In mKO (Kikuchi *et al.* 2008), the autocatalytic cyclization of the first amino acid of the chromophore triad (Cys65) forms a new five-membered heterocycle (2-hydroxy-3-thiazoline) that provides it with

very similar orange emission properties. mKO (Kikuchi *et al.* 2008) is the monomeric version of the orange fluorescent protein Kusabira Orange, KO (Karasawa *et al.* 2004) which name comes from the word クサビライシ [Kusabira-ishi] that is the Japanese name of the stony "mushroom" coral *Fungia concinna* producing the protein.

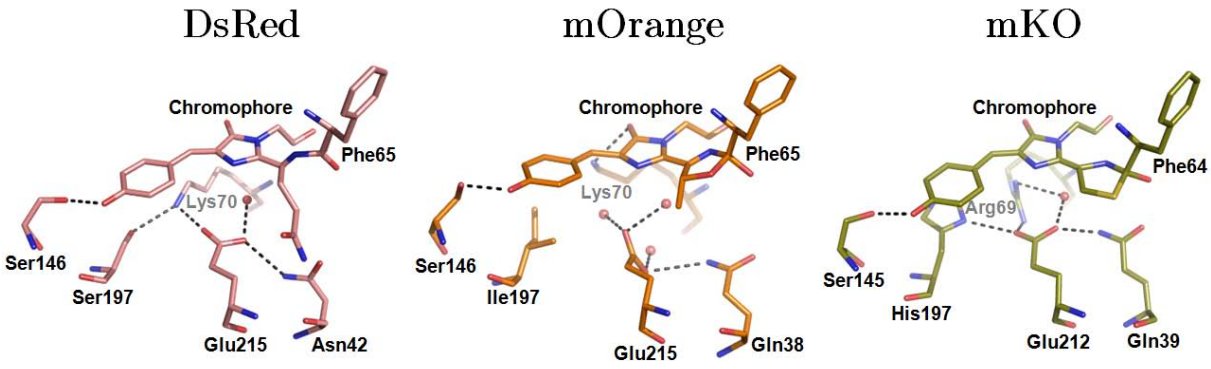

Figure II.1.17 - Comparison of the chromophore environments of DsRed, mOrange and mKO. Hydrogen bonds (<3Å) are represented by dashed lines.

In mKO thus, a direct interaction between Arg69 and the conserved glutamate is observed while this is not the case in mOrange where the equivalent of Arg69 is a lysine. The authors claim that such a direct interaction in mKO1 stabilizes a negative charge on the glutamate and establishes a π-cation interaction between Arg69 and the chromophore, both favoring pH tolerance.

Because of the higher pK of Dendra2 compared to other similar PCFPs, both the neutral and anionic species coexist in comparable proportions at physiological conditions, and the 20-fold higher concentration of the neutral species as compared with EosFP enhances the green-to-red photoconversion yield by the same factor. Consequently, Dendra2 can be photoconverted with 488-nm light more efficiently than EosFP in confocal imaging applications (Gurskaya *et al.* 2006). Infact, a few single molecules of EosFP also changed their emission wavelengths from green to red while scanned with 488-nm light [(Wiedenmann *et al.* 2004), Fig.5A]. In Dendra2, the red chromophore formed after conversion fluoresces efficiently in both its neutral and anionic forms. In fluorescence imaging applications, both green and red Dendra2 species can be excited efficiently between 450 and 500 nm, e.g., with 473-nm or 488-nm laser lines, and

selective excitation of the red species is achieved by excitation above ~510 nm, e.g., with 532-nm laser lines.

b - Blue-shifted absorption and emission spectra

Another interesting feature of Dendra2 compared to the very similar protein EosFP is that its emission spectrum is blue-shifted by more than 15 nm (Figure II.1.16). The difference between EosFP and Dendra2 concerning the reorganization of Arg66 can also explain this blue shift and the blue shift of the absorption maximum of the anionic green chromophore (492 nm) in Dendra2 with respect to EosFP (506 nm). Upon electronic excitation of the *p*-HBI chromophore, the electron density is known to shift from the phenyl to the imidazolinone (Tsien 1998; Voityuk *et al.* 1998). The missing charge stabilization on the imidazolinone by Arg66 in Dendra will, therefore, raise the energy of the excited state with respect to the ground state, resulting in a blue shift of the transition. Based on the comparison on many fluorescent proteins having this arginine (Arg66) and whose structure is known, we could separate those FPs in two groups that we named Eos-like and Dendra-like proteins. The Dendra-like proteins have their conserved glutamate in interaction with the equivalent residue of Arg66 in Dendra2, while the Eos-like proteins display the same pattern of interactions than in EosFP.

Eos-like proteins are Kaede (Hayashi *et al.* 2007), mKiKGR (Tsutsui *et al.* 2005) and Dronpa (Wilmann *et al.* 2006) while Dendra-like proteins are mTFP1 (Ai *et al.* 2008), amFP486 (Henderson & Remington 2005), mKO (Kikuchi *et al.* 2008), zFP538 (Remington *et al.* 2005) and cmFP512 (Nienhaus *et al.* 2006c). We propose that, once again, the swapping of Arg66 between the structures of Eos-like and Dendra-like proteins is the key point to explain this blue-shifted emission (Adam *et al.* 2009b). A comparison of the excitation and emission maxima of these proteins reveals that the bands of the Dendra-like proteins are blue-shifted by ~10 nm compared to the Eos-like proteins. The only exception in the Dendra-like group of proteins is cmFP512, which does not have the conserved serine at position 142 (in interaction with the hydroxybenzylidene moiety) but an alanine whose mutation to a serine leads to a blue-shifted protein (Nienhaus *et al.* 2006c).

Interestingly, in the high-pH regime (pH >10), the population ratio between the neutral and the anionic chromophore is observed to shift back to the protonated species. Most likely, the water molecule (Figure II.1.14) that, together with Ser142, stabilizes the negative charge on the phenolate oxygen is exchanged by a hydroxyl ion at high pH, so that the protonated hydroxyphenyl ring becomes energetically favored. The acid-denatured protein at pH 1 shows an absorption band at 381.7 nm, which is essentially identical to the A band, implying that the neutral green chromophore remains intact even under harsh acidic conditions. HBDI has an absorption maximum at 389 nm upon acidification, which further supports this assertion (Webber & Meech 2007). More information about the spectroscopic characterization of the photoconversion and of the degradation of Dendra2 can be found in (Adam *et al.* 2009b).

Based on mutational studies on amFP486, the cationic character of the His193 side chain was suggested to be the main determinant of the blue-shift because it stabilizes the charge on the *p*-hydroxybenzyl ring of the chromophore and thus reduces the extent of charge delocalization upon excitation (Henderson & Remington 2005). Based on the present study, we believe that the pronounced red-shift of the His193Thr mutant of amFP486 is predominantly caused by a hydrogen bonding interaction of the most likely neutral Glu211 with the imidazolinone nitrogen, as is also observed for a few other FPs (Nienhaus *et al.* 2006b; Adam *et al.* 2008). Upon replacement of His193, the Arg66 side chain adopts a position where it can best mimic the missing histidine side chain. Concomitantly, the Glu211 side chain, no longer stabilized by a salt bridge to Arg66, rotates by ~90° around the Cγ-Cδ bond, which places its Oε only 2.5 Å away from the imidazolinone nitrogen.

a - A super red species

In the absorption spectra of red Dendra2, we noticed a broad tail toward the red side of the spectrum, which may indicate an additional band at 586 nm (Figure II.1.18). To further investigate this feature, we collected an emission spectrum with excitation on the red edge of this band. The excitation of this band gives rise to a red-shifted emission spectrum, compared

to the normal red form (λ_{max}=600 nm), suggesting that a super red species is forming, similar to that already observed in the case of DsRed (Cotlet *et al.* 2001; Habuchi *et al.* 2005b).

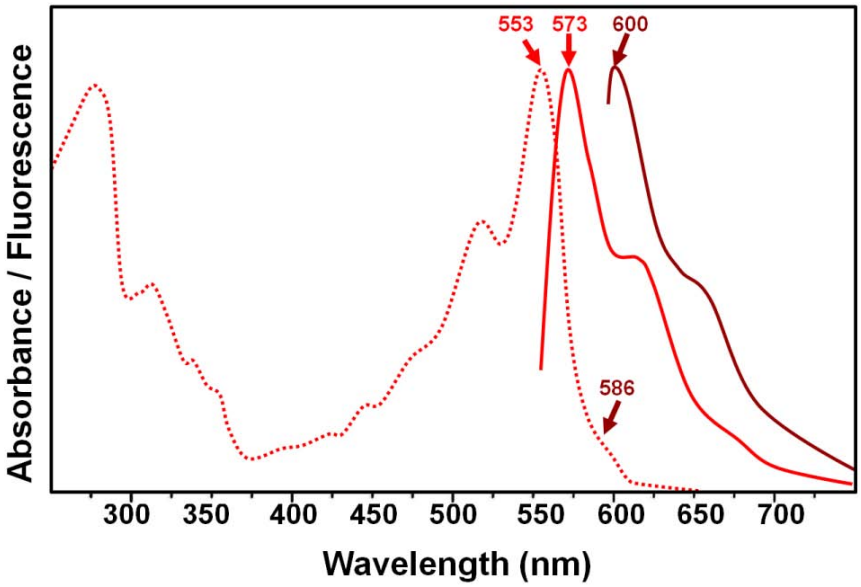

Figure II.1.18 - Absorbance and emission spectra of red Dendra2 at pH 10 showing emission spectra of its normal and super red species

The excitation of the anionic species at 553 nm gives rise to an emission spectrum peaking at 573 nm but the excitation of the broad weak shoulder at 586 nm with strong illumination gives rise to an emission spectrum peaking at 600 nm

In DsRed, this species was attributed to a weakly fluorescent intermediate species forming in the pathway toward the bleached protonated form. This phenomenon was explained to be due to a cis/trans isomerization of the red chromophore along with its twisting and the decarboxylation of the very conserved glutamate Glu-215 (Glu-211 in the case of Dendra2) upon intense laser irradiation (40 W/cm²) of the initial red anionic form (Habuchi *et al.* 2005b) and also required intense illumination to be observed in the case of Dendra2.

This interpretation is comforted by calculations made on model chromophores resembling the one of DsRed, and showing that the most important extensions of the π-conjugated electronic system are obtained for red anionic model chromophores (Boyé *et al.* 2003). According to the authors, the anionic form induces a much more delocalized system to the carbonyl oxygen atom of the chromophore. Looking at the structure of the green form of

Dendra2 that we obtained and comparing it to the one of DsRed (Figure II.1.19), we can notice that, at the difference of most fluorescent proteins, the structures of DsRed and Dendra2 display the striking common point that the residue which is commonly in interaction with the carbonyl atom of the chromophore (Lys70 for DsRed, Arg66 for Dendra2) is bonding instead the very conserved glutamate 215 (Glu211 for Dendra2). This interaction, leads to a modified electron density on the chromophore as compared to other fluorescent proteins and, even if badly understood for now, may give rise to super red species once the red chromophores are in their excited state.

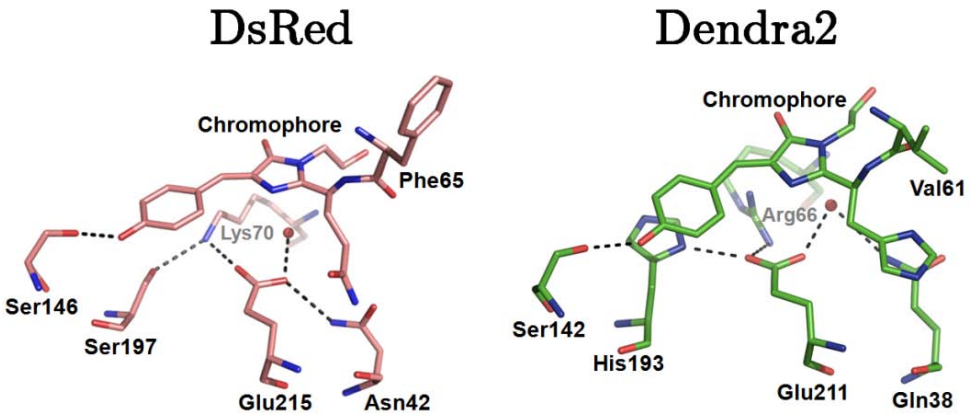

Figure II.1.19 - Comparison of the hydrogen bonds led by the residues in the vicinity of the chromophore for DsRed and Dendra2

Since we were unable, during the time of this thesis, to obtain a sufficient number of crystals of Dendra2 to solve the structure of its red form, we cannot conclude on this point, but it seems reasonable to suggest that upon intense light irradiation, the red chromophore of Dendra2 behaves like that of DsRed, undergoing a torsional motion, most likely accompanied with a modification of its hydrogen bonds with the nearby residues and solvent, leading to the observed super red species. It could be interesting, to support this idea, to compare in detail the absorbance spectra of Dendra-like proteins and see if weak shoulders are also present in red forms and whose excitation could lead to super red species.

Part 3 - Improving the monomerization of PCFPs

All the anthozoan fluorescent proteins that are known are obligate homotetramers in their wild-type form (Miyawaki 2002). As we said, PCFPs are excellent tools to visualize and track objects dynamically within cells, but in order to efficiently use them as fluorescent tags, they should be monomeric to avoid aggregation effects, bad folding and bad targeting in cell imaging applications. In spite of mutagenesis efforts, the tendency of fluorescent proteins to form oligomers is so high that many fluorescent proteins that were monomerized finally re-assemble their oligomeric interfaces when the concentration is high enough, which can be locally the case in the cell when fluorescent proteins are targeted to specific compartments[11]. This problem also concerns the PCFPs we are interested in, and the oligomeric state of monomers and dimers increase when concentration is increased (Figure II.1.20).

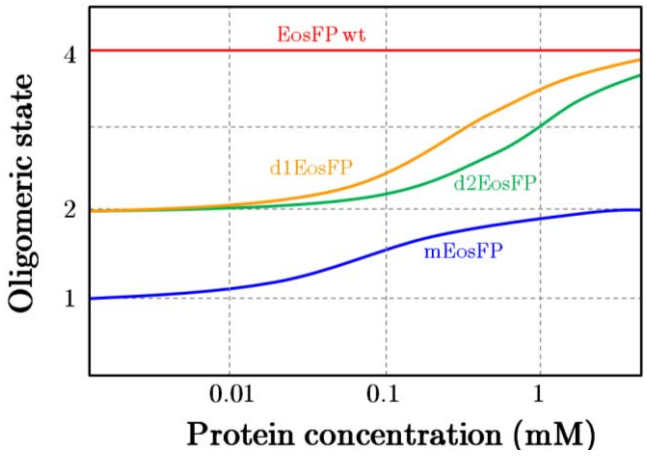

Figure II.1.20 - Concentration-dependent oligomerization of EosFP. Figure reproduced from (Wiedenmann et al. 2004)

In order to investigate and better understand which residues are crucial to the oligomerization process, we studied two mutants of the tetrameric wt-EosFP that form in dilute conditions either a dimer (d1EosFP) or a monomer (mEosFP) but that form tetrameric arrangements in a highly concentrated medium such as a protein crystal. We also analyzed the

[11] http://www.microscopyu.com/articles/livecellimaging/fpintro.html

weak interface that is formed in the crystallographic structure of the monomeric PCFP Dendra2.

In a typical tetrameric anthozoan FP, each protomer, denoted A, B, C, D, is in contact with two neighboring ones so that two subunit interfaces can be distinguished (denoted by A/B and A/C) (Nienhaus *et al.* 2003). The A and B barrels are oriented in an antiparallel fashion, which produces a mesh-like layering of the β-sheets in the A/B interface that is mainly stabilized by hydrophobic interactions. By contrast, in the more hydrophilic A/C interface, the neighboring barrels are rotated against each other to allow for perfect stacking of their β-sheets.

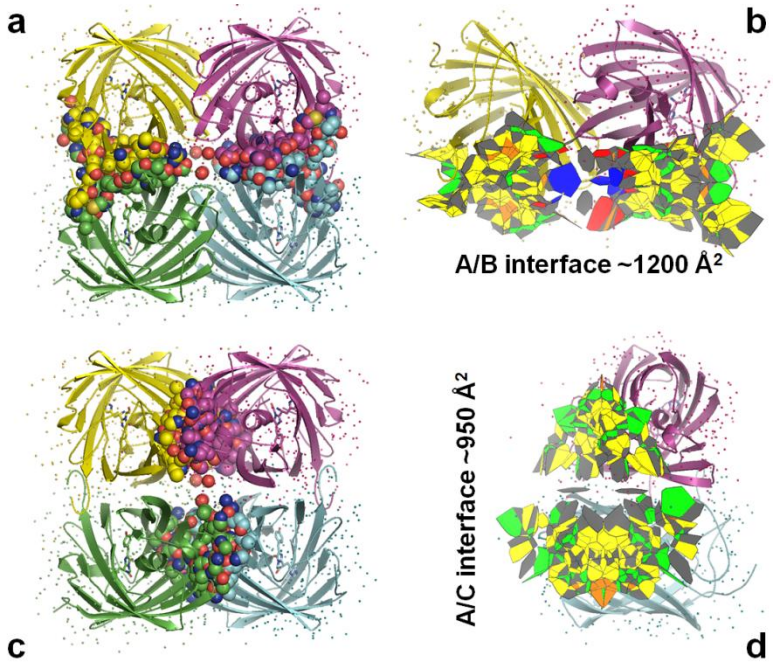

Figure II.1.21 - Interfaces present in a typical tetrameric anthozoan FP

The residues forming the A/B interface (a) and the A/C interface (c) are represented in spheres. A Voronoi tessellation (b, d) is represented and shows that the hydrophobic A/B interface has a bigger surface than the hydrophilic A/C interface.

Nienhaus *et al.* have mutated EosFP so that the homotetramer (ABCD) can be split either into two dimers AC and BD (d1EosFP), or into two dimers AB and CD (d2EosFP) or into four monomers A, B, C and D (mEosFP). The crystal structures of both the monomeric form

(mEosFP) and a dimeric form (d1EosFP) have been solved during this thesis and presented here. This study is aimed at understanding better how the interfaces structurally interact and eventually at finding better mutation alternatives to create enhanced monomers. We will compare these results with the interfaces observed in the 3D structure of Dendra2.

1 - Dimeric (V123T) and monomeric (V123T/T158H) mutants of EosFP

a - Dimeric EosFP

Crystals of d1EosFP were obtained as detailed in material & methods (Part 2, p.207). Small and numerous lenticular-shaped crystals appear in a clear drop within a few days. The crystallization is slowed-down by adding 10% glycerol to the mother liquor, which has the consequence to produce fewer and bigger crystals.

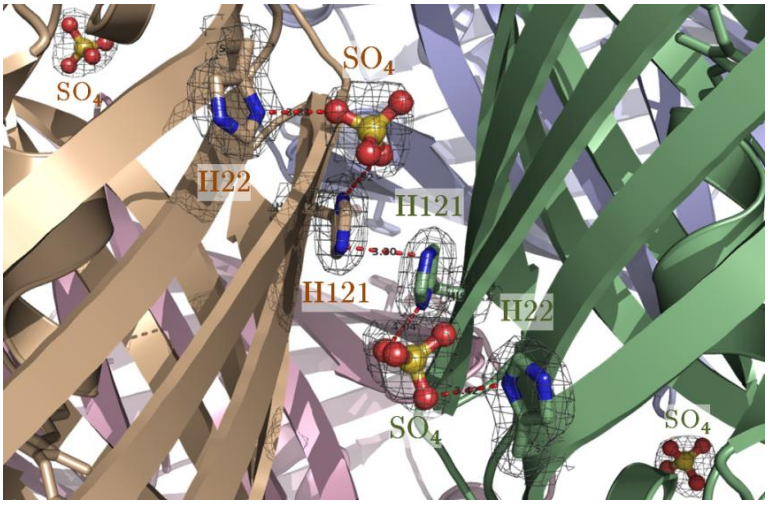

Figure II.1.22 - Structural details of the dimeric interface A/B in d1EosFP showing the participation of sulphate molecules. The electron density map is represented as a black mesh.

The crystal structure, solved on the MX beamline ID14-3 at the ESRF (Table II.1.6), revealed a tetrameric organization. The single mutation present in d1EosFP being V123T, this mutation is not directly observable in the 3D structure because valines and threonines look almost the same in X-ray crystallography. However, very well defined sulfate molecules are

present in the structure and form the pattern described for mEosFP, by interacting with pairs of histidines 22 and 121 (Figure II.1.22). The presence of this pattern seems to be the signature of a need for ammonium sulfate to re-form the interface A/B (C/D) and clearly identifies the fact that the molecule was dimeric prior being crystallized.

b - Monomeric EosFP

Crystals of mEosFP were obtained as detailed in material & methods (Part 2, p.207). In a few days, the protein forms a precipitate that could not be avoided and in which long rod-shaped crystals (Figure II.1.23) appeared within a week due to the so-called Ostwald ripening phenomenon (crystal formation from a precipitate).

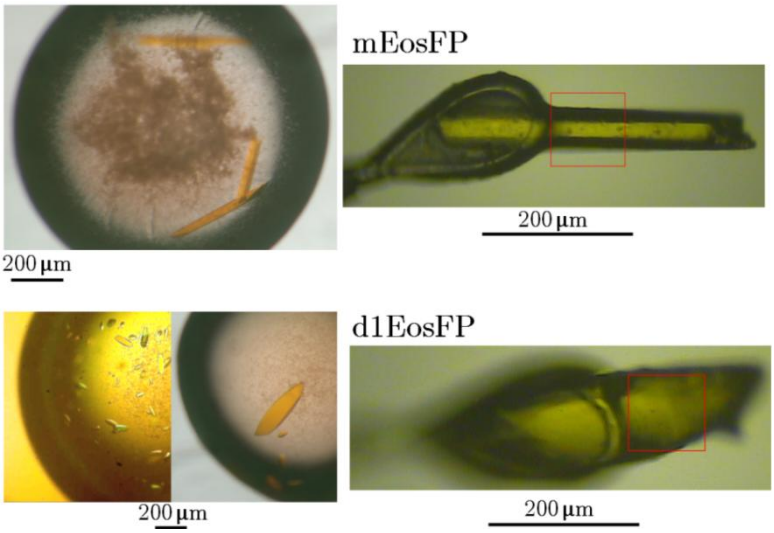

Figure II.1.23 - mEosFP and d1EosFP crystals in their crystallization drops (left) and single crystals mounted on the MX beamline ID14-3 (right) - For d1EosFP, the improvement of the crystal size allowed by the addition of 10% glycerol is illustrated

Although the protein has been described to be a monomer in solution (Nienhaus *et al.* 2006a), its crystal structure, solved at the MX beamline ID14-3 at the ESRF (Table II.1.6), here again revealed a tetrameric arrangement similar to that of wtEosFP. mEosFP is formed by two mutations of its wild-type parent EosFP: V123T and T158H that separate the interfaces A/B and A/C, respectively.

Concerning the interface A/C, the mutation T158H is very obvious to observe in the electron density maps (Figure II.1.24). Interactions between several residues situated in β-strands number 8 and 9 (as described in Figure I.2.3) are involved in this interface. While in the wild-type EosFP threonines 158 of each protomers interact via a single H-bond, the arginines 170 are also instrumental. They interact indeed with the carbonyl of Met159 and carboxyl of Asp172 of their respective chains, but also with the carboxyl of Asp156 of the other chain (Figure II.1.24). In contrast, in mEosFP, the mutation T158H induces a π-staking between histidines 158 in the crystal but their steric occupancy pushes the arginines 170 away. The consequence is that none of the H-bonds led by arginines 170 in wt-EosFP at this interface occurs in mEosFP (Figure II.1.24).

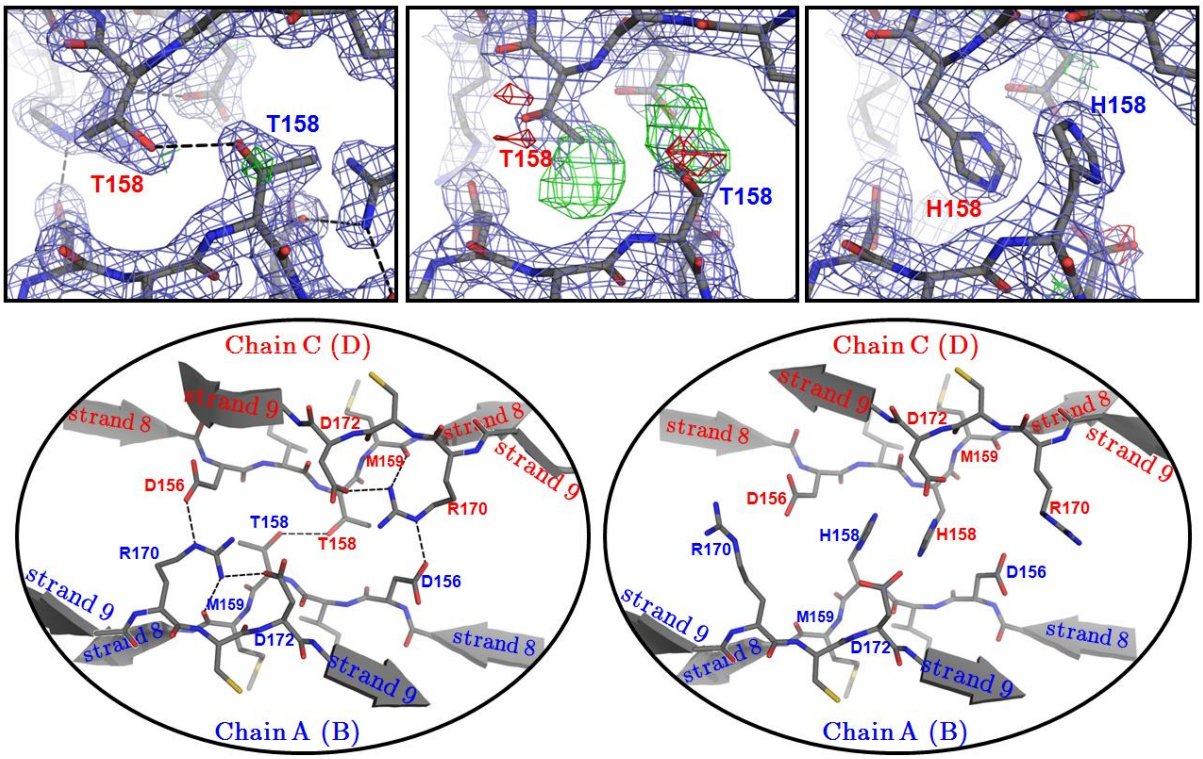

Figure II.1.24 - Zoom on the A/C interface of mEosFP. Top: difference maps residuals (middle) show that, at the difference of wtEosFP (left) position 158 is clearly not a threonine but a histidine (right) – $2F_{obs}$-F_{calc} and F_{obs}-F_{calc} maps are contoured at 1 σ and ±3 σ, respectively. Bottom: H-bond interactions present at the A/C interface of wtEosFP (left) are broken in mEosFP and replaced by a π-stacking between histidines 158 (right)

The π-stacking between histidines 158 in mEosFP seems to be a parasitic effect to the desired separation of the interface A/C and could, at least partially, explain why this interface re-assemble when concentration is increased in d2EosFP and mEosFP. The problem is that this mutation T158H has been made (Wiedenmann *et al.* 2004) to reproduce the one that permitted to separate the equivalent interface in Rtms5 (Prescott *et al.* 2003). However, in this case, the very hydrophobic phenylalanine 158 was mutated to a rather hydrophilic threonine, which is not the case in EosFP since T158 and H158 are two polar amino acids. Looking at the interactions between residues 158 in wt-EosFP and mEosFP in the crystal and looking at the central role of arginine 170, this structure allows to postulate that a better possibility to separate the A/C interface in EosFP and its mutants, would be to mutate the arginine 170 and/or the aspartate 156, in addition to the threonines 158.

Concerning the interface A/B (C/D), as for the structure of d1EosFP, the mutation V123T is less obvious to observe because of the resemblance between since valines and threonines in X-ray crystallography. However, if we compare mEosFP with its wild-type parent, we notice that the hydrophobic interactions that existed between Ile-102 of protomer A (B) & Val-123 of protomer B (A) and between Ile-102 of protomer C (D) & Val-123 of protomer D (C) in wtEosFP, are clearly broken in mEosFP (Figure II.1.26). However, the π-staking between His-121 of protomers A & B and of protomers C & D is present in both proteins. This stacking was already present in the structure of the wild-type form of EosFP but is not sufficient by its own to maintain an interface between monomers in solution. However, it is re-enforced in the crystal by the presence of two sulfate molecules bridging the chains A & B and C & D by interacting both with the histidines 121 and the histidines 22 (Figure II.1.22). This pattern is very clear in the structures of both mEosFP and d1EosFP, which contain the very same mutation at position 123. It can also explain why the protein crystallizes only with ammonium sulfate while the wtEosFP does not.

Crystal parameters and data collection statistics		
Protein	**mEosFP**	**d1EosFP**
Data collection		
Beamline	ESRF / ID14-3	ESRF / ID14-3
Wavelength, Å	0.931	0.931
Temperature, K	100	100
Data collection statistics		
Resolution, Å	48.4-2.25 (2.5-2.25)	48.3-2.2 (2.3-2.2)
R_{sym}, %[a]	7.9 (51.3)	8.1 (58.2)
Mean $I/\sigma(I)$	15.7 (3.1)	15.4 (2.9)
Completeness, %	99.5 (99.4)	99.8 (99.4)
No. of total reflections	274,651 (73,708)	334,594 (40,782)
No. of unique reflections	56,351 (15,034)	60,242 (7,361)
Data refinement statistics		
R_{cryst} [b]/ R_{free}[c]	0.232 / 0.289	0.236 / 0.285
Nonhydrogen atoms		
Protein	7425	7556
of which, chromophore	100	100
Water	297	357
rms deviation from ideality		
Bond lengths, Å	0.008	0.009
Bond angles, °	1.301	1.236
Ramachandran plot		
Most favored, %	90.4	88.5
Allowed region, %	9.5	11.1
Generously allowed region, %	0.1	0.4
Disallowed, %	0.0	0.0
Average B factor, Å^2		
All atoms	29.2	24.3
Chromophore	24.2	19.5

$$^{a}R_{sym} = \frac{\sum_{hkl}\sum_{i}\left|I_i(hkl) - \overline{I(hkl)}\right|}{\sum_{hkl}\sum_{i}\left|I_i(hkl)\right|} \qquad ^{b}R_{cryst} = \frac{\sum_{hkl}\left|F_{obs} - F_{calc}\right|}{\sum_{hkl}F_{obs}} \qquad ^{c}R_{free} = \frac{\sum_{hkl\subset T}\left|F_{obs} - F_{calc}\right|}{\sum_{hkl\subset T}F_{obs}}$$

The R_{free} is calculated with a small fraction (5%) of reflections randomly chosen to be part of test group T.

This R factor, thus, is not biased by the refinement process

Table II.1.6 - Data collection, data processing and structure quality statistics for monomeric and dimeric variants of EosFP. Values between brackets refer to the highest resolution shell

Looking at the crystal structures of both mEosFP and d1EosFP, it is very obvious that the mutation of His-121 could very efficiently help to break the interface A/B, leading to a most stable monomeric form of EosFP. This point is important since stable monomers of PCFPs such as Dendra2, whose structure is presented in this thesis, are crucial for their use as precise fusion tags in nanoscopy techniques. Very recently, this mutation of His-121 has finally been performed in mEosFP, creating a new variant called mEos2 (McKinney *et al.* 2009) which, as expected, behaves as a very stable monomeric form of EosFP.

2 - Dendra2

Dendra2 was reported to be monomeric in solution (Gurskaya *et al.* 2006), and its monomeric state may be responsible for the enormous difficulties we encountered in growing crystals. In crystals, the Dendra2 protomers are observed to form A/C dimers because residual stabilizing interactions promote interface formation at the high protein concentrations present during crystal growth. Two salt bridges exist between Arg149 and Glu96 of each monomer (Figure II.1.26, bottom), as in the EosFP A/C interface (Nienhaus *et al.* 2006a). Additional interface stabilization is provided by hydrogen bonds within a cluster consisting of Thr143, Asn158 and Arg216 of both monomers. In EosFP, there is also a hydrogen-bonded cluster consisting of Thr143, Arg170 and Asp156. In EosFP, DsRed and eqFP611, three aromatic residues at positions 188, 190 and 212 of the A and C chains form an additional hydrophobic patch. To generate the monomeric variant Dendra2, one of these residues (Tyr188) was replaced by alanine in the dendGFP sequence, which apparently was sufficient to destabilize the interface at low protein concentrations (Gurskaya *et al.* 2006).

An A/B-type interface is absent in the Dendra2 crystal. Compared with the wild-type protein, Dendra2 has two point mutations that were introduced to disrupt this interface, Asn121Lys and Met123Thr. The same residues were also modified to destroy the A/B interface in other anthozoan FPs, for example, Val123Thr in EosFP (Nienhaus *et al.* 2006a) and Thr121Arg and Val123Thr in eqFP611 (Wiedenmann *et al.* 2005). The sequence alignment of EosFP and Dendra2 (cf. EosFP and Dendra sequences in Appendices, p.259) shows that the interface-forming residues of these two proteins are identical except for position 121, at which the histidine of EosFP is replaced by a lysine in Dendra2. In EosFP, the His121 side chain of protomers A and B are π-stacked and, thereby, help stabilize the interface. In Dendra2, the long lysine side chain may generate steric conflicts (Figure II.1.25) and, moreover, the charged amino groups repel each other, so that the interface is completely destabilized.

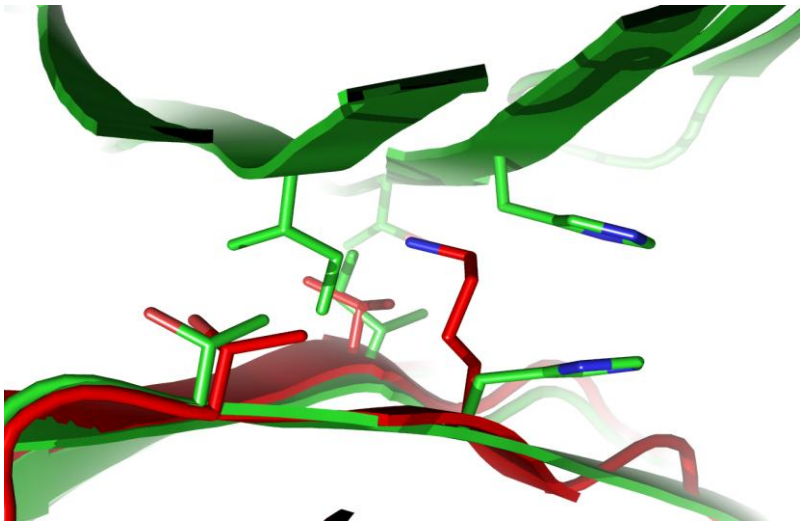

Figure II.1.25 - Superposition of EosFP (green) and Dendra2 (red) showing that the formation of the interface A/B is not possible in Dendra since the position 121 is not a histidine in Dendra2 but a lysine

3 - Discussion and conclusion

To summarize, the crystal structures of monomeric or dimeric forms of fluorescent proteins can be used to analyze the interfaces that they are forming in crystalline phase, even if they are not forming in diluted solutions. The interfaces and residues involved in their formation for EosFP, mEosFP and Dendra2 are summarized in Figure II.1.26.

The analysis of these interfaces allows the proposition of supplementary mutations to further destabilize them and create more stable monomers for their use in cell imaging applications.

This method allows proposing the mutation of residues H121, H158 or R170 in mEosFP for example and residues E96, T143, R149, T158 and R216 for example in Dendra2. The position 121 in mEosFP that we propose to mutate and disturbs the formation of the A/B interface in Dendra2 has been mutated to a tyrosine and led to the creation of a much more stable monomer called mEos2.

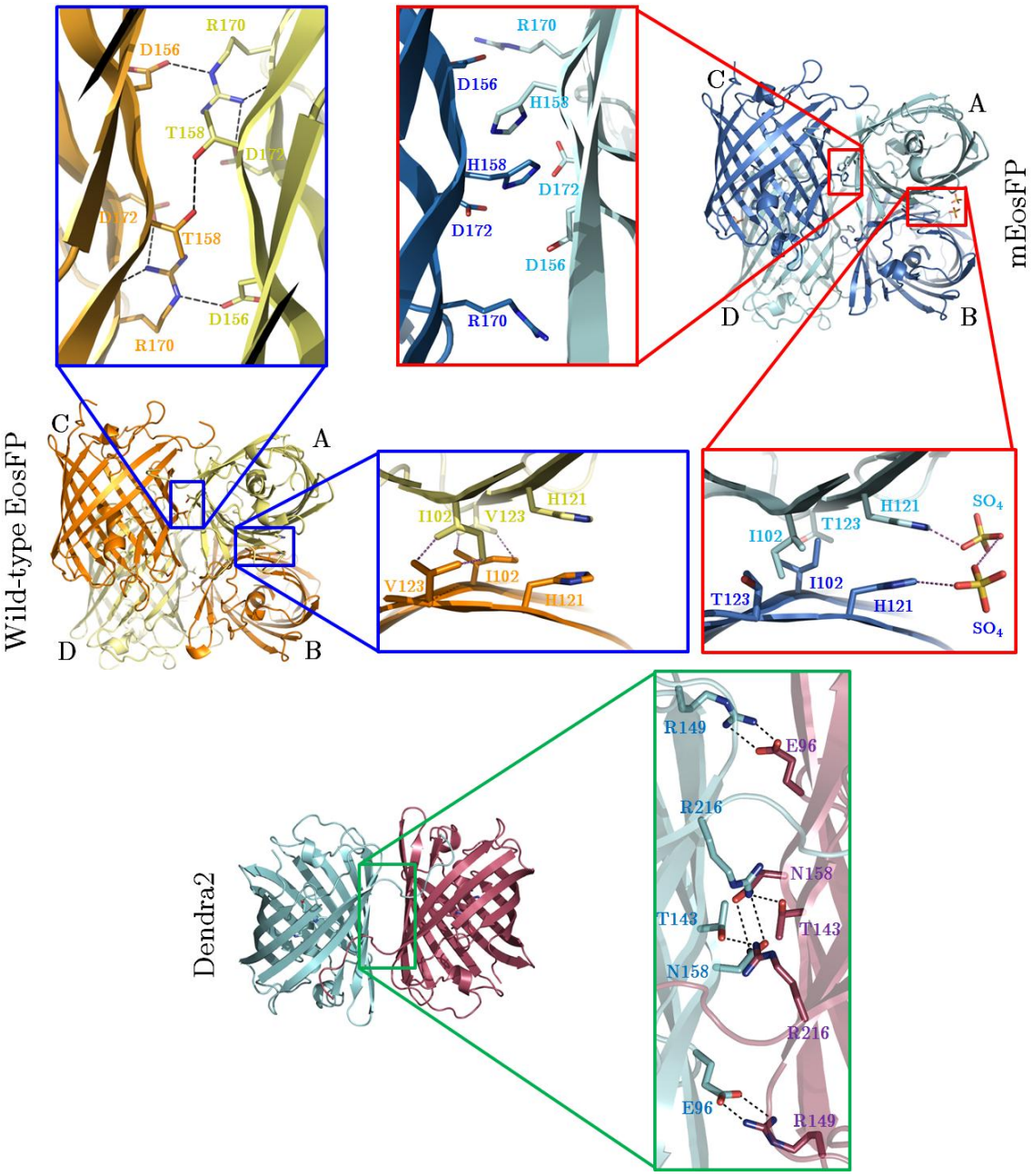

Figure II.1.26 - Comparison between the interfaces formed in the crystal structures of EosFPwt and mEosFP (top) and Dendra2 (bottom) with the detail of the residues involved in the strongest interactions

Chapter 2 - Photoswitching: a reversible bleaching event

Résumé en français

Ce chapitre regroupe les résultats obtenus lors de l'étude du phénomène de photocommutation réversible de certaines protéines fluorescentes photoactivables. En étudiant un variant de EosFP, protéine décrite dans le chapitre précédent, nous avons découvert des propriétés photochromiques, c'est-à-dire que la fluorescence de cette protéine peut-être réversiblement éteinte à loisir. Ce comportement a été étudié sur cette protéine que nous avons appelé IrisFP, et nous avons quantifié l'efficacité de conversion vers l'état éteint, ainsi que celle de son retour à l'état fluorescent, soit thermique, soit induit par illumination. Cette isomérisation a été caractérisée par diverses méthodes : cristallographie, spectroscopie Raman, spectroscopie UV/Vis… et la question actuellement très débattue de l'ordre entre les événements de protonation et d'isomérisation du chromophore est traitée.

Les raisons de cet impressionnant phénomène sont expliquées grâce à la structure tridimensionnelle de la protéine, que nous avons obtenue, et qui montre clairement une photoisomérisation du chromophore. Cette découverte est très différente de celle d'autres protéines fluorescentes photochromiques, en ce que la capacité de photoconversion du vert au rouge possédée par la protéine parente EosFP, a été conservée chez ce variant, faisant d'IrisFP la première protéine fluorescente activable découverte regroupant les deux types de photoactivation en même temps.

Nous pensons que ce troisième type de protéine fluorescente photoactivable permettra dans un avenir proche le développement de nouvelles méthodes de microscopie de fluorescence à super-résolution dynamique en deux couleurs. Une autre application pouvant se révéler intéressante est celle de l'encodage de données irréversible ou réversible au sein de l'assemblage compact que représente un cristal de protéines. Si l'application réelle d'une telle technique est loin d'exister à l'heure actuelle, une preuve de principe est fournie dans ce chapitre, pour les deux modes d'encodage.

ANOTHER major phototransformation we have thoroughly studied during this thesis is the photoinduced reversible loss of fluorescence that occurs in some FPs. As we said in the introduction, some fluorescent proteins called RSFPs (reversibly switchable fluorescent proteins), have the property of being reversibly switchable between a bright and a dark state. The most popular representative is Dronpa. These proteins are currently used in nanoscopy with the STORM technique in pretty much the same way as PCFPs are used with the PALM technique. Thus, their study is another important topic in the field of PAFPs.

When we started these studies, we did not focus of RSFPs but rather on PCFPs such as EosFP and Dendra, but a discovery on the mutant F173S of EosFP redirected our research in a fascinating way.

Part 1 - Spectroscopic characterization of a reversible switching

1 - Discovery of a strange phenomenon

a - Autorecovery of a coloration loss

We started to work on the mutant EosFP-F173S that had been obtained by random mutagenesis by Nienhaus' group (Ulm, Germany) in attempts to design better variants of EosFP. When we started to study the poorly characterized properties of this mutant, we performed very rough photoconversion trials by exposing tubes containing small amounts of the protein directly under the sunlight. The observations were very strange since, depending on the day and the weather, the protein either kept its initial color, or bleached or took a more reddish color. The more logical explanation seemed to be that clouds and changing weather played a role on the wavelengths and intensities shone onto the samples, provoking different spectroscopic behaviors.

In order to study in more detail the surprising photosensitivity of EosFP-F173S, fresh crystals of the protein (see crystallization procedure in material & methods p. 207) were

submitted to illumination from each of the lasers available at the Cryobench laboratory. The most dramatic change was observed with the wavelength 488 nm, since at moderate power densities (~1 W/cm^2), crystals became transparent within seconds. Intriguingly, the day after the experiment, crystals looked as if they had never lost their color. A more controlled experiment was made by using new crystals, reduced laser intensity (30 mW/cm^2) and monitoring visually changes along time (Figure II.2.1). The divergent beam of the 488-nm laser was directed toward a crystallization drop containing crystals of EosFP-F173S (Cf. material & methods, p. 236).

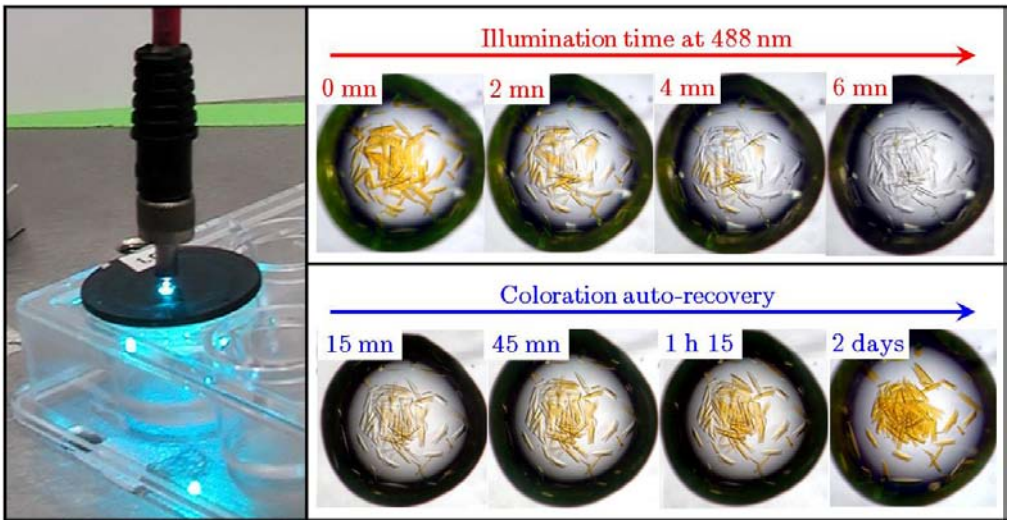

Figure II.2.1 - First experiment in which a drop containing crystals of EosFP-F173S is submitted to a filtered laser illumination at 488 nm (left panel). Crystals become more and more translucent when exposed to cyan light (top panel) and a complete slow auto-recovery of the coloration occurs when leaving the crystals in the dark (bottom panel)

The crystals were regularly photographed thanks to quick snapshots of the drop, making obvious that the protein became quickly transparent. This non-absorbing state slowly reversed (27 hours) by just keeping the crystals in the dark at room temperature.

EosFP-F173S, thus, revealed to have a very different behavior than its wild-type parent since it is capable to undergo a reversible color extinction between a green and a dark state.

To further study this phenomenon, a solution of the protein was placed in a cuvette and exposed to a continuous light irradiation at 488 nm until it became transparent (several

minutes of illumination with manual mixing of the solution every 30 seconds). The initial absorbance peak at 488 nm quickly decreased in intensity while a peak at 390 nm increased. This solution was then left in the dark and quick absorption spectra were measured from time to time in order to probe recovery to the initial state as observed in the crystals. The results (Figure II.2.2) show that the recovery to the initial state reaches a completion of 90% (see inset) after 14 hours 30 minutes.

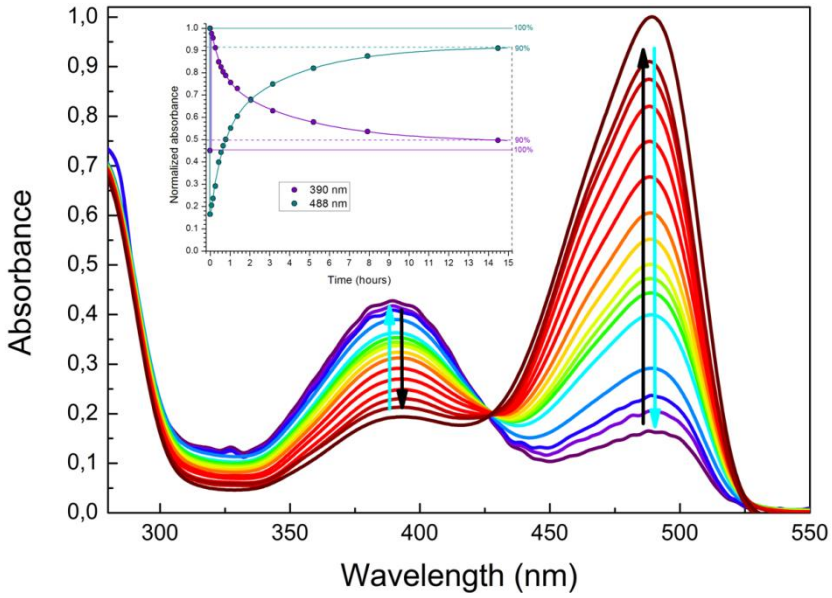

Figure II.2.2 - Reversible thermal absorbance recovery of a solution of EosFP-F173S. The cyan arrows represent the evolution of the absorption spectra upon illumination at 488 nm, the black arrows represent the evolution of the absorption spectra during thermal relaxation. Inset: evolution of the absorbance peaks at 390 and 488 nm along the experiment.

This reversible color extinction is very similar to the already reported cases of RSFPs such as Dronpa, suggesting that this recovery could also be photostimulated.

b - The back-switching to the green state can be stimulated by light

After on/off conversion with 488 nm light, the absorbance of a diluted solution of EosFP-F173S was followed while being continuously exposed to a laser emitting at 405 nm (~30 mW/cm²) to achieve the dark-to-bright conversion. The results clearly show a huge acceleration of the recovery to the initial state upon illumination at 405 nm with a time of a few seconds instead of tens of hours (Figure II.2.3)

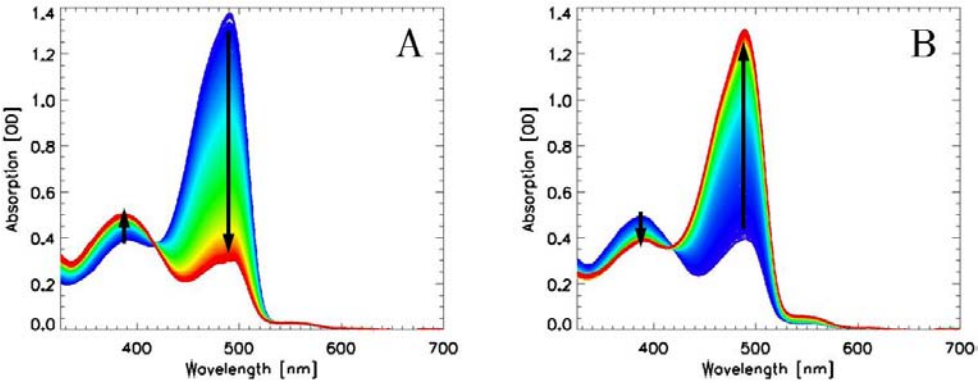

Figure II.2.3 - Series of absorbance spectra showing the light-induced reversible on/off conversion in a green solution of EosFP-F173S. A laser at 488 nm (~30 mW/cm²) allowed the conversion from a bright to a dark state in ~5 seconds (A) and laser at 405 nm (~30 mW/cm²) allowed the back-conversion from the dark to the bright state in ~1.2 seconds

The mutation F173S in EosFP, thus, allowed to give to this PCFP a photochromic property but since this protein is a single mutant of EosFP, it was anticipated that it would also keep green-to-red photoconversion characteristic of the wild-type EosFP.

2 - The first protein being both a PCFP and a RSFP

Two crystals of EosFP-F173S were mounted in microloops and kept at room temperature thanks to special loop bases that can be covered by plastic capillaries (Figure III.2.2, p.221). They were then submitted to laser lights at 488 nm for one crystal and 405 nm for the other one. The results clearly show that not only the protein can be switched off transiently when irradiated at 488 nm but also keeps the properties of its parent by being irreversibly photoconverted to a red form when irradiated at 405 nm (Figure II.2.4).

Both the reversible switching and the irreversible photoconversion can be obtained either in solution or in crystals. This surprising discovery suggested that EosFP-F173S is the first fluorescent protein exhibiting both properties of photochromism (between a bright colored state and a dark transparent state, like in the RSFP Dronpa) and photoconversion (from green to red, as described in the previous chapter with the PCFPs EosFP or Dendra).

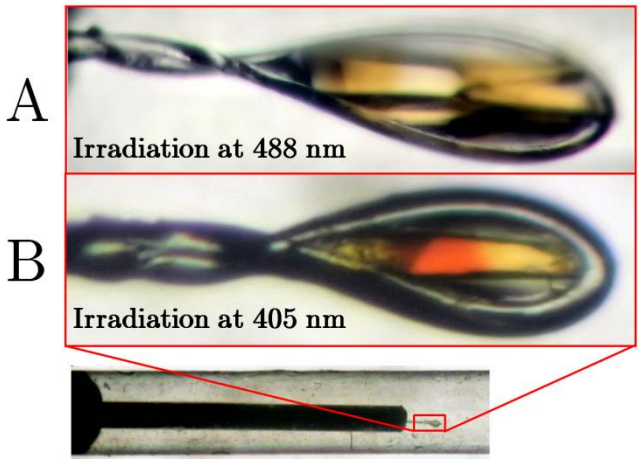

Figure II.2.4 - Phototransformations on a part of EosFP-F173S crystals kept at room temperature. (A) loss of color induced by an illumination at 488 nm. (B) green-to-red photoconversion induced by an illumination at 405 nm

3 - Reversible switching of the red form

The most exciting discovery was that, once the protein was converted in its red form, its illumination at 532 nm, close to the peak absorbance (anionic chromophore) of the red form of EosFP, turned the protein to a kind of green state. This state revealed to be poorly fluorescent and was very surprising since the green-to-red photoconversion was supposed to be an irreversible reaction.

This green-like state was slowly reversing by its own to a brighter red state in several hours, similarly to what was observed between the initial green and dark forms. It seems logical, then, to think that the same phenomenon is taking place in the green-to-dark and red-to-green reversible switchings and that this latter green-like form can also be stimulated by light excitation of the neutral form of the red chromophore. After conversion of the crystalline protein to the red state (with 405-nm light) and subsequent photoswitching of this red state to the green-like state (with 532-nm light), we illuminated our sample at either 405 nm or 440 nm. The choice for these two wavelengths was guided by what we had learnt from the switching of the green state. 405 nm was indeed the wavelength we used to stimulate the back-switching of

the green state. The illumination at 440 nm was also tried because the difference between the wavelengths of the lasers used at 532 nm and 440 nm (92 nm) is similar to the 98-nm difference between the peaks specific of the anionic (390 nm) and neutral forms (488) of the chromophore in the absorbance spectrum of the green form. Since the absorbance spectrum of the red species peaks at 551 nm (anionic chromophore), it seems logical to think that we excite the neutral form around 440 nm.

When the green-like state was submitted to laser excitations at 405 nm or 440 nm, a dramatic increase in the recovery of the red state was observable both in absorbance and fluorescence. The illumination with our laser emitting at 440 nm revealed to be much more efficient than the one at 405 nm, which confirmed that we probably excited the neutral form of the red form, as we did with the green form at 405 nm. Timecourses of the maximum red fluorescence peak at 580 nm as a function of time ("shark fins") were recorded by switching the red fluorescence on and off in a crystal (Figure II.2.5).

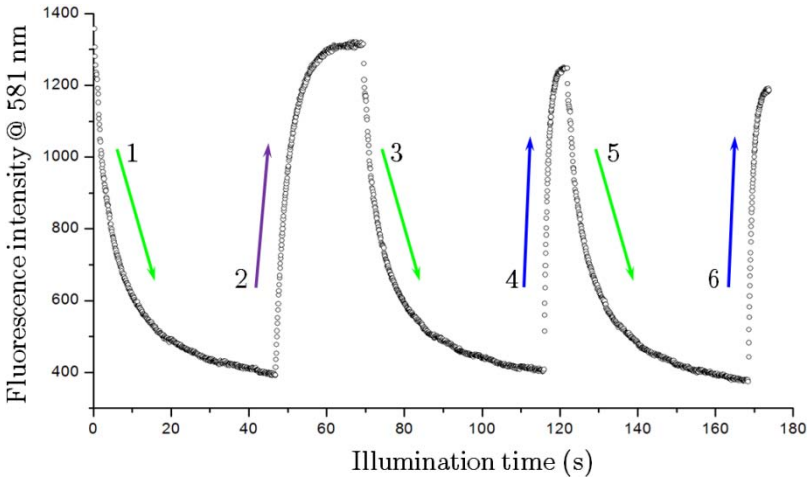

Figure II.2.5 - Wavelength dependency on the efficiency of the fluorescence recovery for a crystal of red EosFP-F173S. The shark fins represent the maximum of fluorescence intensity of the red protein, followed when converted to a dark state by illumination at 532 nm (1,3,5) and back-switched to a bright state by illumination either at 405 nm (2) or 440 nm (4,6)

The protein was switched off with pulses of laser light at 532 nm (50 mW/cm², 90 ms/pulse) and back-switched to the bright state either by pulses at 405 or 440 nm (50 mW/cm², 50 ms/pulse). The process could be repeated several times.

We discovered, hence, a photochromic property of the protein in its red state, similar to what is observed in the RSFP asFP595 but instead of having a positive switching like in asFP595, EosFP595 exhibits a negative switching behavior both in the green and in the red states.

A surprising phenomenon was noticed, though: instead of switching between a red and dark state, we observed either in solution or crystals a switching from the red state to a green-like state. To better understand this strange observation and study the phenomenon of multiple photoinduced color changes (green, red, dark...) in comparison to the parent protein EosFP, a crystal of wt-EosFP and a crystal of EosFP-F173S were placed in a crystallization drop and submitted to a sequence of light illumination with wavelengths described above.

4 - An intramolecular FRET effect

The results presented in Figure II.2.6 show that if the crystal of EosFP was essentially not sensitive to any other wavelength than 405 nm (which converted it from its initial green state to its final red state), EosFP-F173S showed dramatic and very contrasted color changes both in bright field and in fluorescence mode.

As observed in Figure II.2.6, once the crystal of EosFP-F173S is turned red and then irradiated at 532 nm, instead of becoming transparent in bright field and less fluorescent, the crystal seems to come back to its state prior being converted to red. This red-to-green photoconversion seems very unlikely to occur based on what we have said in the chapter about photoconversion. Most likely, a fraction of the protein was not photoconverted to red during the illumination at 405 nm but became only visible as green fluorescent when we switched off the fraction that was photoconverted to red. The very same observation can be made both in crystal or in solution.

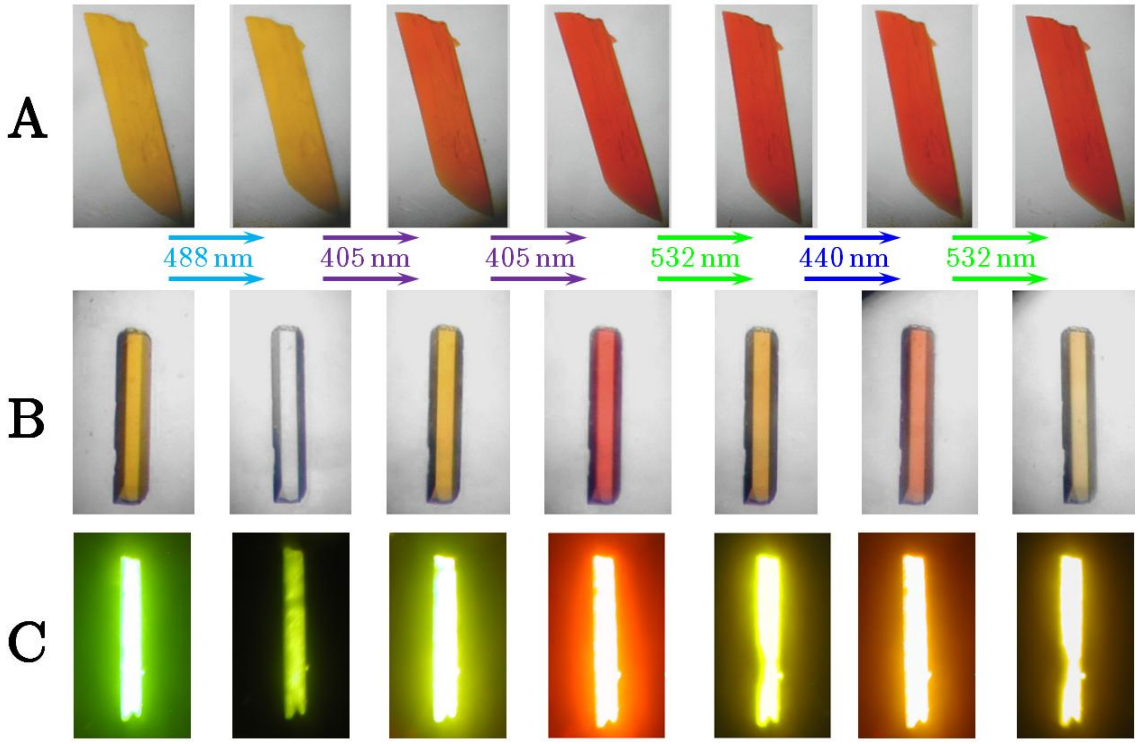

Figure II.2.6 - Comparison between photoinduced transformations in wt-EosFP (A) and EosFP-F173S (B, C). While EosFP only shows a single photoconversion by turning red, the mutant EosFP-F173S clearly undergoes multiple wavelength-dependent phototransformations both in bright field (B) and fluorescence (C).

This phenomenon can be explained by intramolecular FRET effect between the four monomers of the tetrameric structure. The strong FRET coupling between the chromophores in the tetramer leads to red fluorescence emission upon excitation of the green chromophores even if only one of the four chromophores is converted into its red fluorescent form. Off switching of the red form then results in the reappearance of green emission because the neutral red chromophore does not absorb green light.

Thus, the partially red-converted tetramer effectively shows an interconversion between two bright states, red and green (Figure II.2.7). Partial green-to-red photoconversion of the IrisFP tetramer, indeed, leads to predominantly red fluorescence, even when excited at 488 nm, because of intramolecular FRET from green to red monomers. Actinic illumination of these partially red tetramers with green light (λ=532 nm) reversibly photoswitches the red monomers to their nonfluorescent form. As a consequence, excitation at 488 nm does not result in FRET anymore and hence generates an increase in green fluorescence.

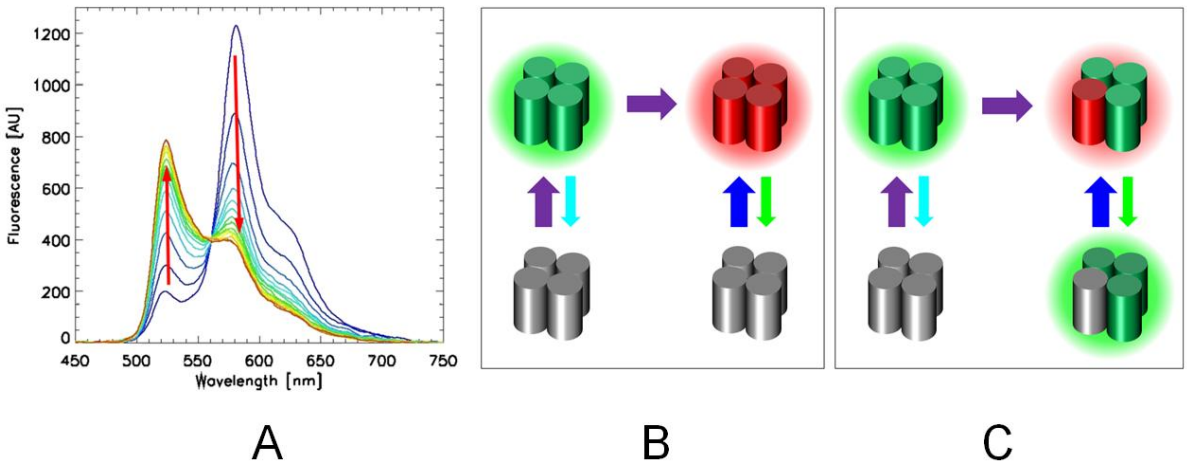

Figure II.2.7 - Red-to-green photoswitching due to the intramolecular FRET effect in tetrameric EosFP-F173S

(A) Red-to-green conversion as observed in fluorescence when irradiating at 532 nm a sample of EosFP-F173S partially photoconverted to the red form. (B) Complete photoconversion of the tetramer from green to red is assumed, resulting in the "normal" photoswitching behavior between a red bright state and a dark state. (C) Because of intramolecular FRET, partial photoconversion of the tetramer can be used to generate reversible photoswitching between two bright states. Colored halos represent the emission colors

Such a mechanism is reminiscent of a technique used in DsRed to induce a color change (Marchant *et al.* 2001) and also relates to the recently designed protein Phamret (Matsuda *et al.* 2008). It could be exploited further in tandem dimer constructs.

5 - When EosFP-F173S becomes IrisFP

EosFP-F173S, thus, displays a very different spectroscopic behavior as compared to its wild-type parent EosFP. The protein can indeed be irreversibly photoconverted from a green to a red state but each of these forms can be reversibly switched off and on by exciting the anionic and neutral forms of the chromophore, leading to dramatic changes in both the absorption and emission spectra of the four possible forms (Figure II.2.8).

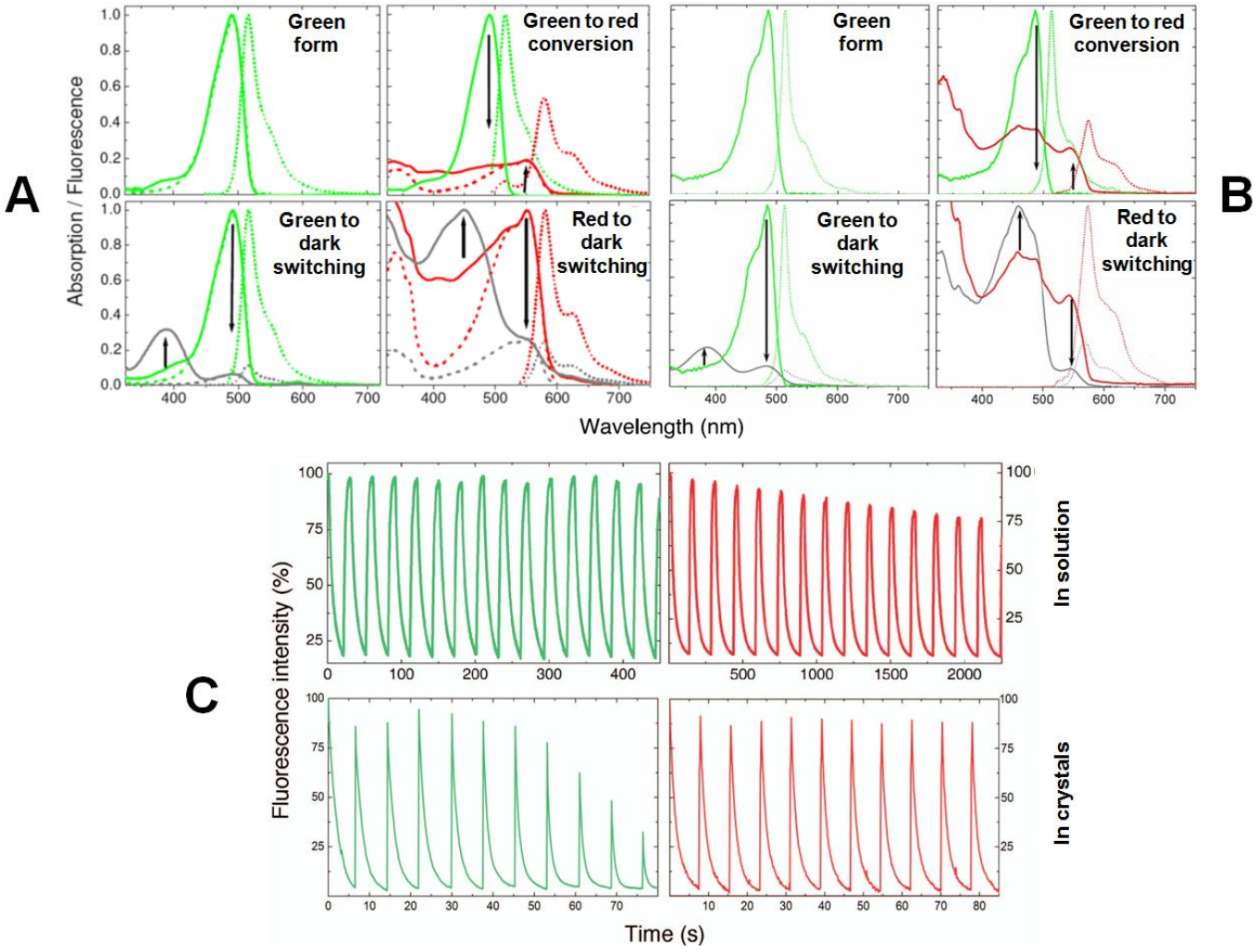

Figure II.2.8 - Spectroscopic characterization of the reversible and irreversible phototransformations of EosFP-F173S.

Absorption, excitation, and emission spectra of EosFP-F173S are depicted by solid, dashed, and dotted lines, respectively both in solution (A) and in crystals (B). Green and red lines represent the color of the protein, gray lines represent the dark states. Emission spectra of the green (red) protein were obtained by exciting at 488 (532) nm and the photoconversion was achieved at 405 nm. "Shark fins" measured in solution and in crystals of EosFP-F173S in their green and red forms are also shown (C).

In the experiment shown as "shark fins" in Figure II.2.8, the solution of the green sample was exposed to continuous illumination with 488-nm light (50 mW/cm^2), while 405 nm light (37 mW/cm^2) was switched on every 30 s during 10 s. The red form of the protein was exposed to continuous illumination with 561 nm light (49 mW/cm^2), while 440-nm light (31 mW/cm^2) was switched on every 120 s for 30 s. For studies in the crystalline state, a crystal of the green form of EosFP-F173S was mounted in a modified loop covered by a plastic capillary and

allowing to keep it at room temperature (see material and methods, Figure III.2.2, p.221) and exposed to continuous illumination with 488 nm light (2.5 W/cm²), while 405 nm light (1 W/cm²) was switched on every 7.5 s for 25 ms. Crystal drying was observed at the end of the series, explaining the faster decay as compared with the solution state. After green-to red photoconversion, the crystal was exposed to continuous illumination with 532 nm light (7.5 W/cm²), while 440 nm light (1 W/cm²) was switched on every 7.5 s for 200 ms. This work has been published and further details can be obtained by referring to (Adam *et al.* 2008).

The spectroscopic properties of EosFP-F173S have been characterized in all forms and compared to the ones of the wild-type protein (Table II.2.7). For further details about the calculation of photoswitching quantum yields, refer to material & methods, Part 2 - Calculating photoswitching quantum yields, p. 239.

Parameter	EosFP F173S		EosFP wild-type	
	Green form	Red form	Green form	Red form
λ_{max}, ex/em (nm)	488/516	551/580	506/516	571/581
ε ($M^{-1}.cm^{-1}$)	52200	35400	72000	41000
$QY_{fluorescence}$	0.43 ± 0.02	0.47 ± 0.02	0.70 ± 0.02	0.62 ± 0.03
$QY_{off\ switching}$	0.014	0.0020	NA	NA
$QY_{on\ switching}$	0.5	0.047	NA	NA
$QY_{green\text{-}to\text{-}red}$	0.0018	NA	0.0008	NA
$t^1/_2$ thermal recovery (hours)	5.5	3.2	NA	NA

Table II.2.7 - Spectroscopic properties of EosFP-F173S as compared to its wild-type parent EosFP. λ_{max}: peak wavelength; ex: excitation; em: emission; ε: extinction coefficient; QY: quantum yield; $t^1/_2$: half-life.

This mutant can be set to either a green or a red forms but also reversibly switched to a dark state from each of those forms, making of it the equivalent of three photoactivatable fluorescent proteins at once: a green-to-dark RSFP, a green-to-red PCFP and a red-to-dark RSFP. Those great properties, thus, offer new exciting possibilities for dual-color nanoscopy techniques.

Because of those new possibilities, to refer to its parent protein EosFP and because the protein can undergo multiple photoinduced color changes, this third type of PAFP was named IrisFP, whose name comes from the Greek goddess Iris (Ἶρις) who personifies the rainbow.

Part 2 - Structural characterization of the reversible switching

1 - Structure solution of IrisFP

We performed X-ray structure analyses on crystals that were exposed to light conditions chosen to enhance particular species. X-ray data were collected at 100 K at the ESRF. To induce phototransformations, crystals were illuminated in their crystallization drops before flash-cooling, using optical fibers. The reversible switching of the green form was induced by exposing crystals for ~2 min to 488-nm laser light at ~1 W/cm². The non-reversible photoconversion from green to red was induced by exposing crystals for ~30 min to 405-nm laser light at ~2.4 W/cm². Reversible switching of the red form was induced by illuminating crystals of the green form at 405 nm until they turn red and then for ~10 min with laser light at 532 nm (~370 mW/cm²). Crystal structures were solved by molecular replacement and refined as explained in material and methods p.211. The chromophore restraints were generated as for the structures of mEosFP, d1EosFP and Dendra2, as described in material and methods p.243. Data collection and refinement statistics are compiled in Table II.2.8.

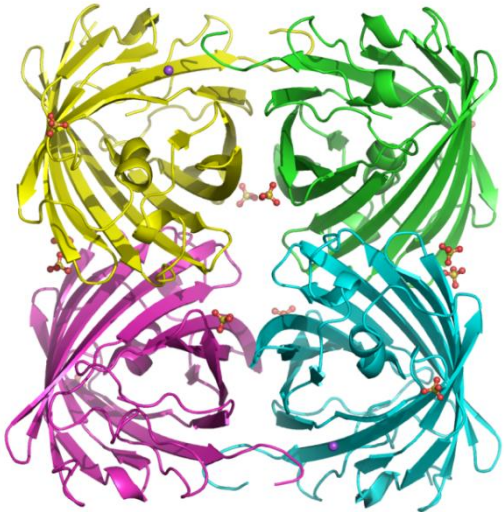

Figure II.2.9 - Overall structure of IrisFP. The protein is present as a tetramer in the asymmetric unit and a number of sulfate molecules participate to the interfaces between the four chains

The X-ray structure of the green form of IrisFP, crystallized in the dark, was determined at a resolution of 1.8 Å without prior light exposure. The asymmetric unit consists of a well-defined tetramer. The individual subunits of IrisFP show the classical β-can fold, with no major deviation from the EosFP structure (Nienhaus *et al.* 2005), as indicated by the backbone rms deviation of 0.36 Å calculated with the program Superpose (Maiti *et al.* 2004) between the two models.

The anionic chromophore is slightly nonplanar (Table II.2.8), which may account for the lower fluorescence quantum yield as compared with EosFP (Table II.2.7). The phenolate moiety is stabilized by a hydrogen bond to Ser-142 and two water molecules (W2188 and W2017, Figure II.2.10 and Figure II.2.13, A).

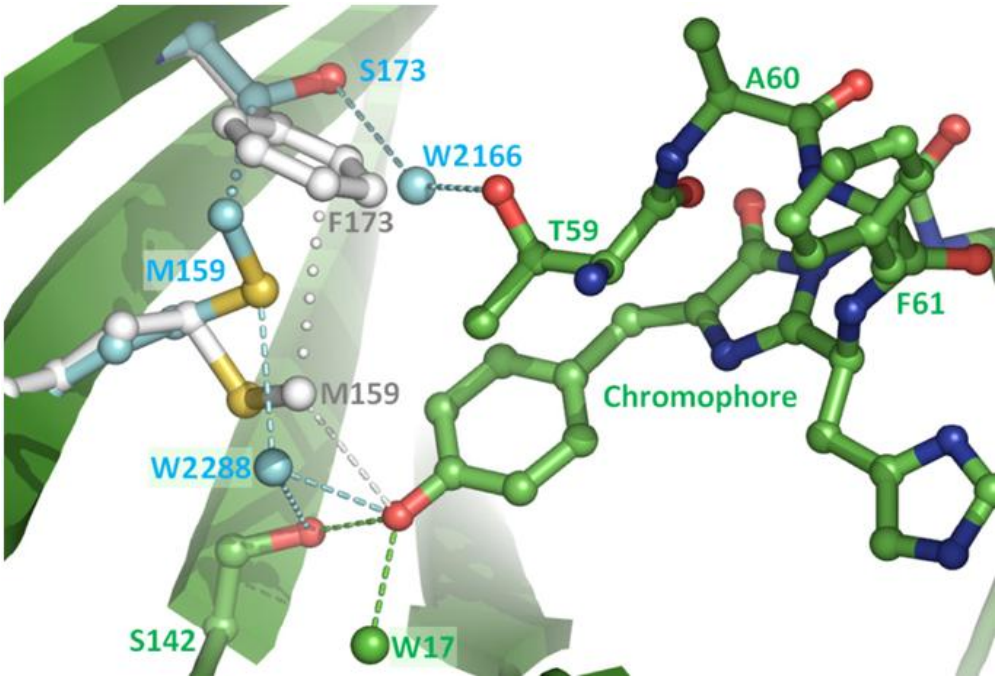

Figure II.2.10 - Changes in the chromophore environment induced by the F173S mutation in EosFP.

Common structural elements of EosFP and IrisFP are represented with green carbon atoms. Residues Phe-173 and Met-159 in EosFP are represented with gray carbon atoms, whereas the mutated residue Ser-173 and residue Met-159 in IrisFP are represented with cyan carbon atoms. The two water molecules (W-2188 and W-2166) are represented with cyan spheres, and W-2017 is represented with a green sphere. Hydrogen bonds are shown with dashed lines and van der Waals interactions with dotted lines

	Data set			
	Green cis	Green trans	Red cis	Red trans
PDB accession code	2VVH	2VVI	2VVJ	-
Data collection				
Beamline	ESRF / ID14-3	ESRF / ID14-3	ESRF / ID23-1	ESRF / ID29
Wavelength, Å	0.931	0.931	0.816	0.979
Space group	P $2_12_12_1$	P $2_12_12_1$	P $2_12_12_1$	P $2_12_12_1$
Cell dimensions				
a, Å	86.34	81.31	85.67	81.29
b, Å	96.55	96.38	96.62	96.60
c, Å	139.83	140.61	140.17	141.10
Resolution, Å	45.6-1.8 (1.9-1.8)	46.6-2.0 (2.2-2.0)	45.7-2.0 (2.1-2.0)	42.3-2.2 (2.5-2.2)
R_{sym}, %*	5.9 (42.8)	10.3 (46.8)	6.7 (43.6)	8.2 (54.7)
Mean $I/\sigma(I)$	19.06 (3.46)	10.1 (2.8)	15.37 (3.44)	12.30 (2.82)
Completeness, %	99.6 (99.6)	97.3 (98.6)	99.1 (99.0)	98.4 (99.4)
Redundancy	4.7 (4.6)	3.7 (3.7)	4.0 (3.9)	4.0 (4.0)
No. of unique reflections	108316 (15990)	73301 (18250)	78543 (10568)	56167 (17806)
Wilson B factor, Å²	29.6	33.9	35.8	42.1
Refinement				
Observations/parameters	3.22	2.22	2.35	-
R_{work}/R_{free}†	0.185 / 0.218	0.193 / 0.251	0.186 / 0.232	-
No. of atoms				
Total	8444	8189	8217	-
Protein	7166	7086	7159	-
Other	91	96	91	-
Water	1187	1007	967	-
Mean B factor, Å²	23.1	27.4	30.4	-
Rmsd				
Bond lengths, Å	0.009	0.011	0.008	-
Bond angles, °	1.209	1.322	1.163	-
Chromophore planarity				
Dihedral angle 1, °	5.7 ± 1.9	-176.4 ± 0.8	14.8 ± 2.3	-
Dihedral angle 2, °	12.3 ± 0.7	40.3 ± 8.4	21.6 ± 2.7	-
Ramachandran plot, %§				
Most favored	93.7	93.3	93.5	-
Additionally allowed	6.3	6.7	6.5	-
Generously allowed	0.0	0.0	0.0	-
Disallowed	0.0	0.0	0.0	-

*$R_{sym} = \Sigma j \Sigma h |I_{h,j} - \langle Ih \rangle| / \Sigma j \Sigma h\ I_{h,j}$

†$R_{work} = \Sigma h |F_{obs} - F_{calc}| / \Sigma h\ F_{obs}$. R_{free} is calculated with a small fraction (5%) of reflections chosen to be part of a test group.

§Determined by PROCHECK (Laskowski *et al.* 1993).

Table II.2.8 - Data collection, refinement and structure quality statistics of the different forms of IrisFP reported in this work. Values in parentheses refer to the highest resolution shell

2 - The green-to-dark reversible switching is due to cis/trans isomerization

Cis/trans photoisomerization is a well known mechanism for radiationless decay in organic molecules and is implicated for example in the photo cycle of retinal in bacteriorhodopsin and

of the photoactive yellow protein (PYP) chromophore. To examine the structural basis of photoswitching of the green form of IrisFP, we illuminated a green crystal with 488-nm laser light and flash-cooled it immediately afterward. A diffraction dataset was collected to a resolution of 2.0 Å. $2F_{obs}$-F_{calc} electron density composite omit maps, calculated with the program OMIT (Vellieux & Dijkstra 1997) using phases from the green structure of IrisFP, are shown in Figure II.2.13. From the superposition of the refined models of the fluorescent and nonfluorescent forms in Figure II.2.11, A, it is evident that off switching is accompanied by a cis/trans isomerization of the chromophore, as was earlier reported for Dronpa (Andresen *et al.* 2007) and mTFP0.7 (Henderson *et al.* 2007). The trans isomer of the chromophore is nonplanar (Table II.2.8). Substantial rearrangements of residues Ser-142, His-194, Glu-212, Arg-66, and Ile-157 in the chromophore cavity are also apparent (Figure II.2.11, A).

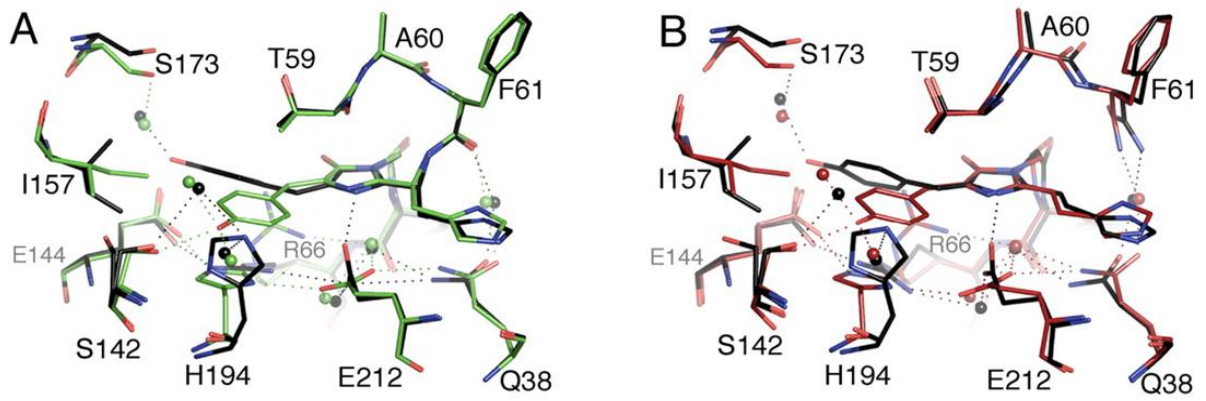

Figure II.2.11 - Structural changes of the chromophore pocket upon phototransformation of IrisFP. (A) Superposition of the native green state (green) and the first reversibly switched state (black) obtained upon illumination at 488 nm. (B) Superposition of the red state (red) obtained after illumination at 405 nm, with the second reversibly switched state (black) obtained upon illumination at 405 nm, followed by illumination at 532 nm. Hydrogen bonds are shown as dotted lines. Water molecules are shown as spheres.

The hydrogen bond between the phenolate oxygen of the cis chromophore and the Ser-142 hydroxyl side chain is removed and Ser-142 achieves a double conformation, either reorienting toward the solvent or H-bonding to His-194 and W2188. The trans chromophore hydrogen-bonds to the presumably deprotonated carboxylate group of Glu-144 and to W2032, most probably assuming a protonated phenolic form consistent with the observed loss of fluorescence and the increased absorption at 390 nm. The hydrogen-bonding network linking Glu-212 and

Glu-144 via His-194 in the cis conformation involves Arg-66 in the trans conformation, implying large conformational rearrangements of the latter two residues similar to those observed in Dronpa or mTFP0.7. In addition, the side chain of Ile-157 undergoes a flip of ~145°, possibly because of transient repulsion during chromophore isomerization. Based on these structures, the enthalpy difference between the two isomeric forms of green IrisFP was estimated from QM/MM molecular dynamics as 68 kJ/mol. This value is substantially smaller than the one estimated for EosFP (114 kJ/mol), assuming a similar trans structure. Calculations performed with null atomic charges for Ser-142 suggest that the stability of the trans isomeric state largely depends on the electrostatic interactions between this residue and its environment. These interactions are much more favorable in IrisFP than in EosFP [see supplementary material in (Adam *et al.* 2008)].

The remarkable photoactivation properties of IrisFP result from the replacement of Phe-173 by serine. In EosFP, Phe-173 forces the side chain of Met-159 to establish van der Waals contact with the hydroxybenzylidene moiety (Figure II.2.10). The smaller Ser-173 side chain in IrisFP reduces these steric constraints, and the Met-159 side chain rotates away from the chromophore. Two cavities are created and were determined by using the program CASTp (Dundas *et al.* 2006) as having a total volume ~13 Å^3. These Cavities are filled with water molecules (W2166 and W2288, Figure II.2.12).

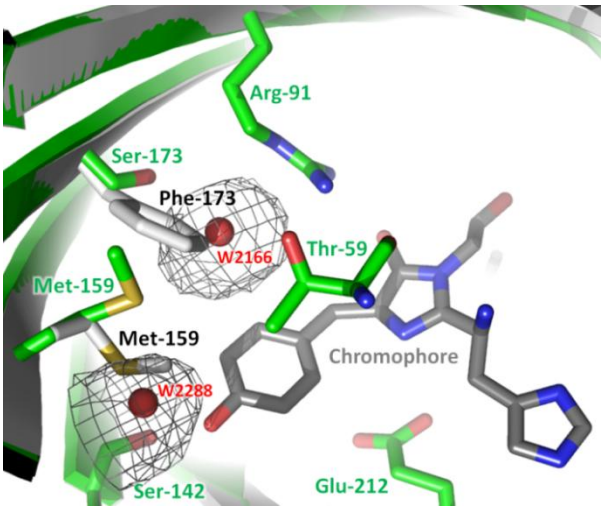

The chromophore of IrisFP is represented in grey sticks, a selection of neighboring residues are represented in green sticks (labeled in green) and the most important differences in the structure of EosFP are represented in white sticks (labeled in black). The space gained because of the F173S mutation and the subsequent rearrangement of Met-159 forms cavities represented in black mesh) that are filled in IrisFP by two new water molecules labeled W2166 and W2288.

Figure II.2.12 - Space gained around the chromophore of IrisFP due to the F173S mutation in EosFP

The less-densely packed chromophore environment of IrisFP may lead to the observed photoswitching due to enhanced flexibility of the chromophore, which is in line with the spectroscopic observations that compared with EosFP the absorption and emission bands are broader and the fluorescence quantum yield is reduced.

Diffraction data collected on a green IrisFP crystal after recovery in the dark from the off state confirmed the reversibility of the cis/trans isomerization, as the resulting structure was indistinguishable from the one of the initial fluorescent state (data not shown).

3 - Photoisomerization in the red state is also possible

To determine the structure of red IrisFP, a green crystal was illuminated by 405-nm light and flash-cooled to collect a diffraction dataset at 2.0 Å resolution. Backbone cleavage between Phe-61 and His-62 was firmly established on the basis of omit electron density maps (Figure II.2.13, C). Except for this modification, the superposition of the modeled chromophore environments of the green and red forms in Figure II.2.11, B shows a nearly unperturbed chromophore pocket, as was observed earlier for red EosFP (Nienhaus *et al.* 2005). A water molecule proximal to His-62 is dislocated in the red form, as was recently also reported for Kaede (Hayashi *et al.* 2007). These results support the hypothesis of identical green-to-red photoconversion mechanisms for IrisFP and EosFP. Signs of radiation damage that could be caused by the long violet-light exposure of the sample, such as decarboxylation of Glu-212, were not noticeable.

To investigate the structural basis of reversible photoswitching of the red form of IrisFP, a green crystal was irreversibly photoconverted to the red form by illumination with 405-nm light and subsequently exposed to 532-nm light to induce reversible switching. After flash-cooling, diffraction data were collected to 2.2 Å resolution. In addition to the features characteristic of green-to-red photoconversion of IrisFP, the electron density map shows the *p*-hydroxybenzylidene ring in both the cis and trans conformations (Figure II.2.13, D). This

observation suggests a partial cis/trans isomerization of the chromophore, with features similar to those displayed by green off-switched IrisFP (Figure II.2.11, A).

However, the multiple conformations coexisting in the crystal, possibly as a result of limited penetration of green light within the crystal, made a reliable structural refinement difficult. Thus, assuming a trans conformation of the chromophore, only a tentative, energy-minimized model of the off-switched state could be produced (Figure II.2.11, C and Figure II.2.13, C). Based on this model, the enthalpy difference between the two isomeric states of red IrisFP was calculated to be 62 kJ/mol. As for the green form, this difference is much higher for wild-type EosFP (122 kJ/mol) because of the less-favorable interactions of Ser-142 with its environment.

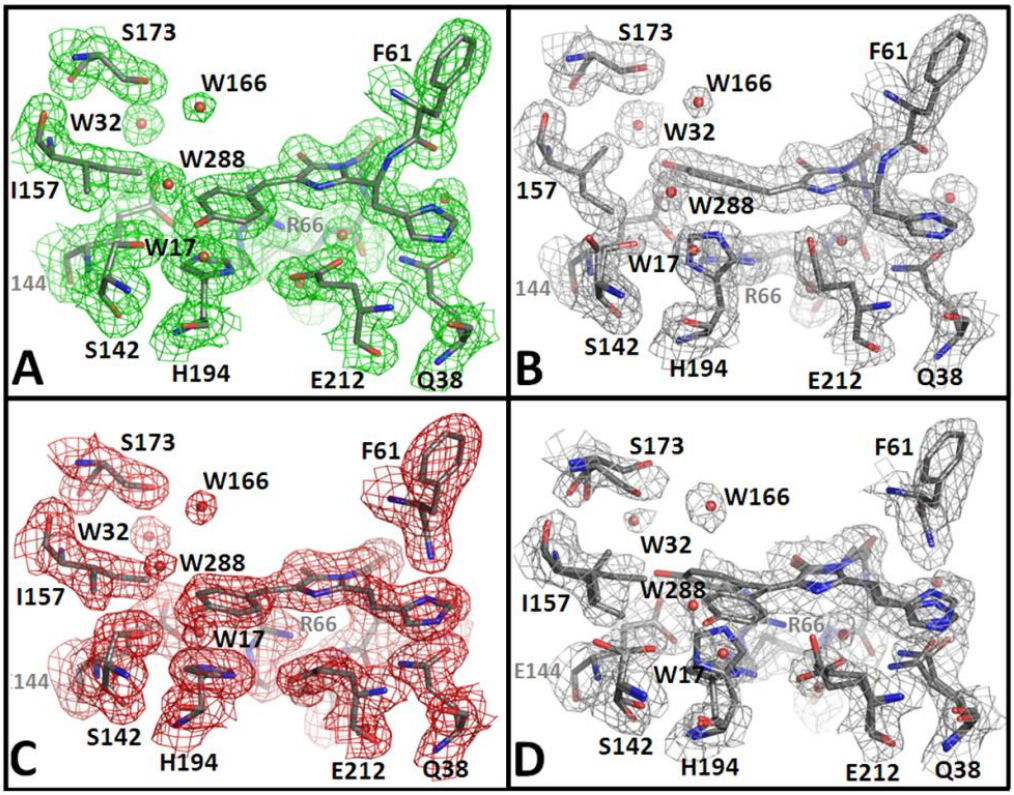

Figure II.2.13 - Omit electron density maps contoured at 1.0 σ of the various states of IrisFP

(A) Green state. (B) First reversibly switched state (green "off"). (C) Red state. (D) Second reversibly switched state (red "off"). All structures unambiguously show the conformation of the chromophore triad. After the first reversible switching (B), isomerization is essentially complete in the crystal. No increased disorder is noticed in the trans state. (C and D) For red IrisFP, the maps clearly indicate backbone cleavage between Phe-61 and His-62. In D, the density map suggests a mixed occupation by the cis and trans states of the chromophore

4 - Which kind of isomerization is involved?

The relaxation from an excited state can either be achieved by a radiative pathway along with fluorescence (or phosphorescence) emission or via non-radiative pathways such as nonadiabatic transitions. Photoisomerizations (occurring for example in small molecules, in vision process...) are known to proceed from nonadiabatic transitions (Ohmine 1985; Garavelli *et al.* 1996; Kim *et al.* 2001; Voliani *et al.* 2008). In such transitions, a crossing between the excited state and the ground state will allow the excited system to relax by "sliding" on a potential energy surface (PES) of the ground state as shown in Figure II.2.14. For details about nonadiabatic transitions, refer to Appendix II, p.260.

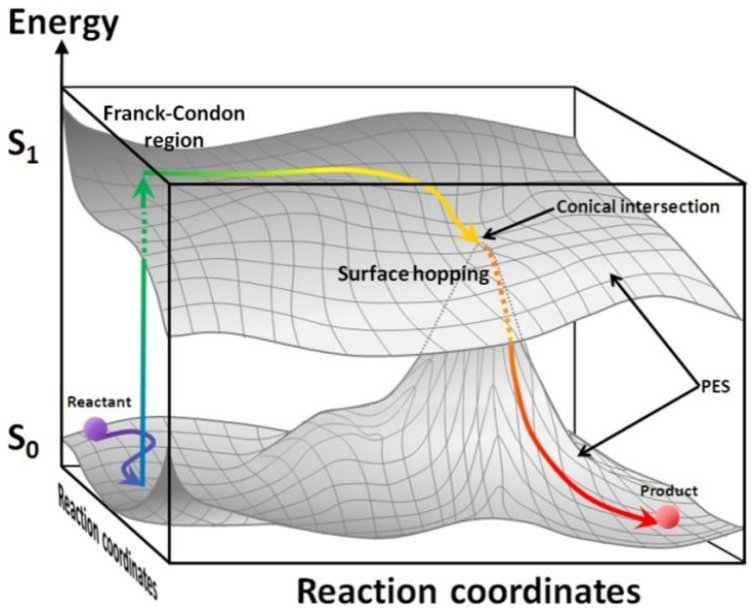

Figure II.2.14 - Schematic depiction of a photochemical system relaxing from its excited state via a nonadiabatic transition

Photoisomerization engages relatively important coordinates movements and can proceed, *a priori*, either by a rotation mechanism or a Hula-twist (HT) mechanism. The rotation mechanism would involve a single rotation around the dihedral angle τ (Figure II.2.15), which is a space-consuming process for the hydroxyphenyl ring that can potentially undergo steric clashes with the protein environment. The HT mechanism implies the simultaneous rotation around both dihedral angles φ and τ, which results in smaller displacements of the chromophore.

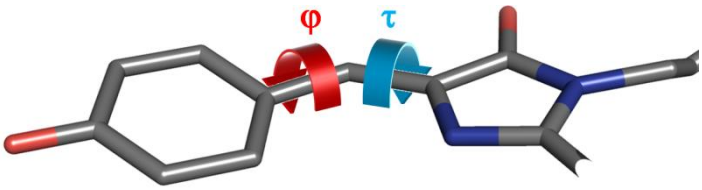

Figure II.2.15 - Hula-twist and rotation mechanisms. The Hula-twist proceeds from the simultaneous rotations of the dihedral angles φ and τ while the rotation is due to the single rotation around τ.

The HT mechanism has been first proposed (Liu & Asato 1985) to explain the Z/E isomerization of the 11-cis-retinyl (cis-s-trans) bound to the opsin via a Schiff base, into a trans-s-cis conformation under a light excitation and was proposed to be an extremely fast volume conserving reaction that is generally preferred to the rotation mechanism.

Quantum mechanics calculations performed by Mickael Lelimousin during his thesis seem to favor a HT mechanism rather than a rotation of the chromophore. In FPs, the simultaneous rotation around the two central bonds (methylene bridge) has been reported to be the most probable volume-conserving pathway for photoisomerization. For example in the photochromic protein asFP595, calculations reported that a HT mechanism was favored both for the chromophore embedded in the protein matrix and for the chromophore considered in a protein-free environment (Andresen *et al.* 2005). The higher probability for the occurrence of the HT mechanism involves less atomic movements than a rotation, was confirmed by quantum mechanics calculations on a GFP model chromophore, in three different protonation states: neutral, anionic, and the recently suggested zwitterionic form (Voityuk *et al.* 1998).

5 - Discussion and conclusion

From the spectroscopic and crystallographic data presented here, it is evident that two photoactivation mechanisms occur in IrisFP: reversible photoswitching between a fluorescent and a nonfluorescent state, based on cis/trans isomerization of the chromophore, and irreversible green-to-red photoconversion between two different fluorescent forms of the chromophore. Figure II.2.16 summarizes the different optical states of IrisFP, highlighting the richness of its photophysics.

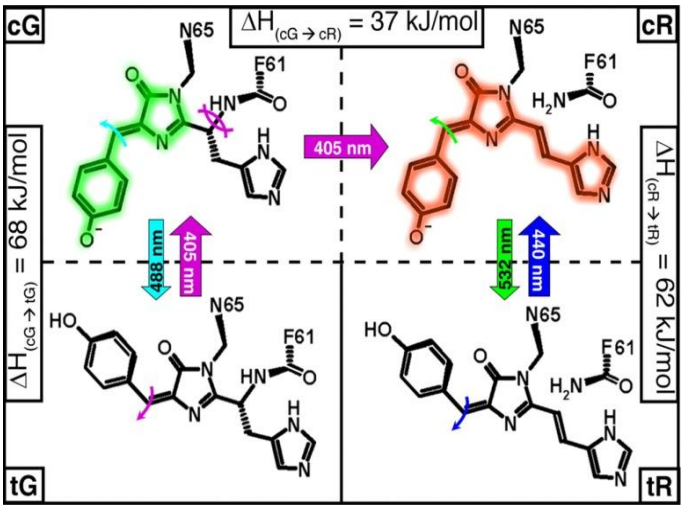

Figure II.2.16 - Photoinduced transformations in IrisFP. Structural motions induced by light are represented by curved arrows of the same color as those used to represent light illumination at specific wavelengths. CG, cis-green Iris; tG, trans-green Iris; cR, cis-red

Superposition of the structures of IrisFP, Dronpa, and mTFP0.7 in their fluorescent cis and nonfluorescent trans states (Figure II.2.17) suggests that reversible photoisomerization in these proteins proceeds by similar mechanisms. In all three proteins, rotation of the chromophore is coupled to concerted motions of His-194 and Arg-66. Glu-212 and Glu-144 act as nanotweezers, providing hydrogen bonds to His-194 in the cis configuration and to Arg-66 in the trans configuration and, thereby, stabilizing both conformations. However, this common configuration is clearly not sufficient to enable photoswitching, as it is also found in the cis state of nonphotoswitchable FPs such as EosFP or Kaede (Ando *et al.* 2002). Stabilization of the trans conformation of the chromophore requires additional interactions that, in particular, compensate for the cost of breaking the hydrogen bond linking the phenolate oxygen of the benzylidene group to Ser-142 in the cis state.

Comparison between EosFP and IrisFP allows a precise identification of these additional interactions. Our enthalpy calculations [see supplementary information in (Adam *et al.* 2008)] suggest that an essential factor is the availability of a polar environment around Ser-142 in the trans state. In IrisFP, such an environment is provided by the repositioning of Met-159 and by the introduction of water molecule W2188. As a consequence, Ser-142 may either hydrogen-bond to His-194 and W2188 or reorient toward the solvent. Our molecular dynamics simulations suggest that these two options are prohibited in EosFP because of the hydrophobic

character of Met-159 residing in close vicinity of Ser-142. In Dronpa and mTFP0.7, Ser-142 is also observed to find hydrogen bonding partners inside the barrel or to reorient toward the solvent in the trans configuration of the chromophore. Thus, there are several structural solutions to the problem of stabilizing Ser-142 (Figure II.2.17): in comparison with EosFP, Dronpa has a valine instead of Ile-157, mTFP0.7 a histidine instead of Met-159, and IrisFP a serine instead of Phe-173.

Another factor contributing to the stability of the trans state is the network of interactions available around the phenolic oxygen of the chromophore's benzylidene moiety in this state. In IrisFP, the phenolic oxygen is stabilized by Glu-144 and water molecule W2032, which both provide hydrogen bonding. Therefore, in contrast to Dronpa and mTFP0.7, the chromophore environment in the trans conformation appears largely polar.

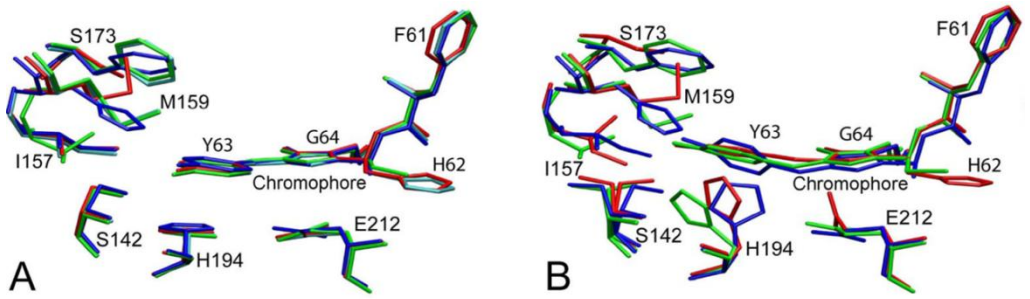

IrisFP	F61	H62	Y63	G64	S142	I157	M159	S173	H194	E212
EosFP	F61	H62	Y63	G64	S142	I157	M159	F173	H194	E212
Dronpa	F61	C62	Y63	G64	S142	V157	M159	F173	H193	E211
mTFP0.7	F65	A66	Y66	G68	S146	I161	H163	F177	H197	E215

Figure II.2.17 - Superposition of the chromophores and close environments of IrisFP, EosFP, Dronpa, and mTFP0.7. (A) Chromophores and surrounding side chains of monomer B of green IrisFP, green EosFP (PDB ID code: 1ZUX), Dronpa (PDB ID code: 2IOV) and mTFP0.7 (PDB ID code: 2OTB) are shown in the cis conformation in red, cyan, green, and blue colors, respectively. (B) Trans conformations of IrisFP, Dronpa, and mTFP0.7. Residues are labeled according to IrisFP

Whereas bistability is an essential property of photoswitchable FPs, efficient photoswitching requires a low transition barrier between the two isomeric states. Free space around the *p*-hydroxybenzylidene moiety of the chromophore (Figure II.2.12) can clearly influence the photoswitching kinetics. The superposition of the cis forms of EosFP, Dronpa, and mTFP0.7 (Figure II.2.17, A) reveals that these proteins provide rather similar steric

environments around the chromophore. In contrast, in IrisFP, the mutation Phe-173-Ser creates significantly more space around the chromophore, notably by displacing Met-159 (Figure II.2.10). This observation might relate to the exceptional switching quantum yields measured for this protein. Interestingly, the Dronpa mutant M159T shows substantially faster photoswitching kinetics than Dronpa (Stiel *et al.* 2007). Presumably, even more space is freed around the chromophore in this variant, further lowering the transition barrier at the expense of a much reduced fluorescence quantum yield.

It is interesting to note that the three proteins compared in Figure II.2.17 have a different first amino acid in the chromophore-forming triad, namely cysteine in Dronpa, histidine in IrisFP, and alanine in mTFP0.7. Therefore, on/off switching by photoisomerization apparently does not depend on the nature of this amino acid. We also noticed that the carboxylate group of Glu-212 in IrisFP rotates by 90° upon isomerization and forms a hydrogen bond to the presumably unprotonated nitrogen of the chromophore's imidazolinone moiety, contrary to what is observed in Dronpa or mTFP0.7. Therefore, Glu-212 in the neutral trans chromophore configuration appears to be protonated.

One could be concerned that the presence of multiple phototransformations in IrisFP would result in poor yields for each of them and in a high susceptibility to photobleaching. However, reversible photoswitching in green IrisFP displays a remarkable efficiency compared with other Dronpa-like proteins. The yield of green-to-red photoconversion is also slightly increased compared with its parent protein EosFP, although red IrisFP appears more susceptible to photobleaching than EosFP. However, upon illumination with violet light, no chromophore photodamage is apparent in our crystal structures. Our structural data suggest that the mechanisms for reversible photoswitching are essentially the same for green and red IrisFP, although the inhomogeneous chromophore conformation in the X-ray structure of photoswitched red IrisFP still leaves some possibility that isomerization may not be strictly required for switching in this state, as suggested for Dronpa (Mizuno *et al.* 2008). From the backbone breakage next to the chromophore in red IrisFP, which has also been noticed for the photoisomerizable marker protein asFP595 (Andresen *et al.* 2005), one may expect an enhanced conformational flexibility of the chromophore and thus a facilitated light-induced isomerization.

We noticed, on the contrary, that red IrisFP can be photoswitched to the nonfluorescent trans form slightly less efficiently than green IrisFP.

To turn IrisFP into a widely applicable highlighter protein, we aim to develop a monomeric version by introducing similar modifications as in EosFP (Wiedenmann *et al.* 2004), hoping that it will exhibit the same multiple photoactivation processes that we have observed here for the tetramer. PAFPs hold great promises for applications in cell biology. However, reversibly photoswitchable FPs are not visible in their off state, and photoconvertible FPs are limited by the non-reversible nature of photoconversion. These drawbacks may be alleviated with new highlighters such as IrisFP, which combine the two modes of photoactivation. Other applications taking advantage of the multiple phototransformations displayed by IrisFP will undoubtedly emerge, including two-color nanoscopy and sequential photoactivation schemes that can be beneficial for unraveling complex protein–protein interactions. IrisFP also hints at the possibility to combine read-only and rewritable capabilities in future mass storage media.

Part 3 - Further studies about the photoswitching

1 - The chicken and the egg dilemma: which is the first to occur between protonation and isomerization?

It is intriguing to notice that the fluorescence and absorption spectra measured during illumination at 488 nm and acidification of IrisFP and other RSFPs, are extremely similar and it is tempting to think that the same phenomenon is involved. Upon acidification, the absorbance peak corresponding to the anionic form of the chromophore decreases while the absorbance peak corresponding to the neutral form, always blue-shifted compared to the first one, increases. The fluorescence signal decreases in intensity while the protein gets protonated and increases in basic conditions. The phenomenon of pH-dependent conversion of the absorbance spectra is depicted in Figure II.2.18 with series measured on EosFP and IrisFP and is extremely similar for all known green PAFPs.

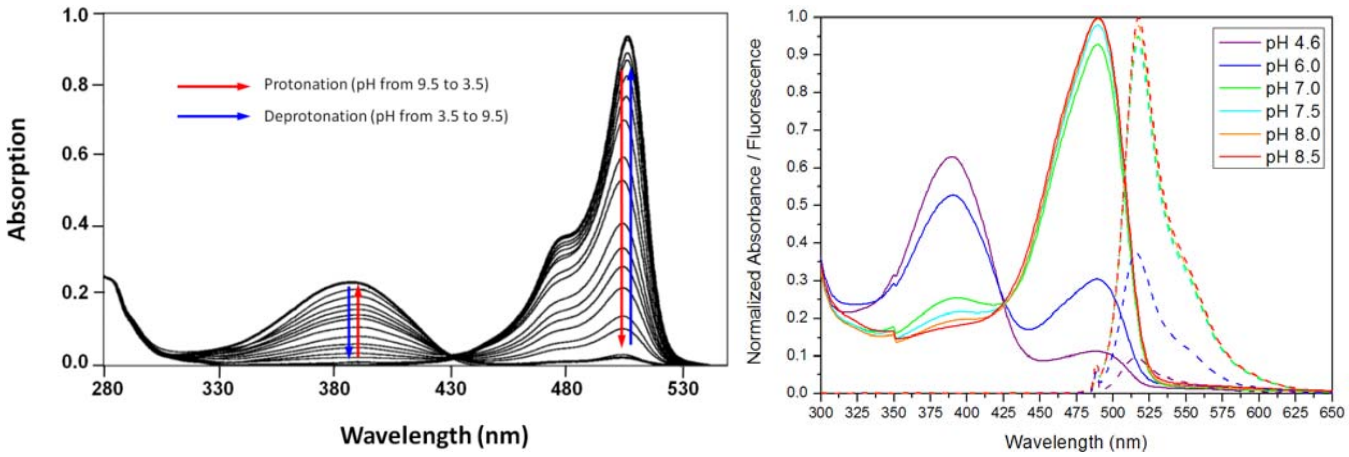

Figure II.2.18 - Evolution of the absorption spectra of EosFP (left) and the evolution of the absorption and fluorescence spectra of IrisFP (right) depending on their protonation state.

If the protonation of the chromophore is implicated in the cis/trans isomerization, this could mean that the sole protonation of the chromophore is sufficient to initiate isomerization, which would not necessitate photoexcitation to occur. The recent case of a FP being crystallized in a wide pH range has shown a cis conformation of the chromophore induced by high pH values, a trans conformation induced by low pH values and a mixed conformation for values in between (Pletnev *et al.* 2008).

To verify this hypothesis on our samples, we would need to obtain the X-ray structure of one of them in acidic conditions and compare its chromophore geometry with the ones obtained in cis and trans conformations. Unfortunately, we could not obtain suitable crystals at any pH value lower than 7.0 and soaking methods always produced cracks in the crystals that destroyed their diffractive power. We therefore cannot conclude on a potential pH influence on the isomerization state of the chromophore based on the structure.

As an alternative to progress on this ongoing debate, we used Raman spectroscopy and measured absorption and fluorescence spectra of an IrisFP sample illuminated by visible light both in solution and in the crystalline form at cryogenic temperature.

a - Raman spectroscopy

Raman spectroscopy is a powerful tool to observe (pre)resonance peaks of the chromophore in a given state, even in cracked crystals that do not diffract. This is of great interest since our crystals soaked in acidic buffers exhibit cracks that prevent them from diffracting. To compare the effect of light-induced and acidification-induced off-switching of IrisFP, we used this technique on a crystal of IrisFP before and after laser induced isomerization and on a second crystal before and after pH-induced acidification. To avoid any thermal relaxation, the crystals were flash-frozen straight after the laser irradiation or acidification. The cis-to-trans isomerization was achieved by the irradiation of an IrisFP crystal at 488 nm (0.9 kW/cm²) directly in a crystallization drop during 26 mn. The acidification was achieved by soaking a crystal of IrisFP either in a dilute solution of chlorhydric acid or in a dilute solution of acetic acid (pH 4.0) until the color of the crystal disappeared and it became transparent.

The results (Figure II.2.19) show very similar Raman spectra for the crystals exposed to an illumination at 488 nm and for the crystals soaked in an acidic buffer. The most spectacular differences reside in the region around the very resonant peak at 1545 cm^{-1}, which is the strongest resonantly enhanced band in GFP (Schellenberg *et al.* 2001). The spectrum shown in Figure II.2.19, A, however, may have suffered from photobleaching prior to the experiment as seen from the low intensity of the bands at ~1545 cm^{-1} related to the rest of the spectrum and compared to the spectrum shown in Figure II.2.19, B. Nevertheless, interesting features are clearly observable and, thanks to a previous study combining calculations and isotopic labeling experiments (He *et al.* 2002), we can tentatively assign the main changes observed in these experiments. We can especially notice the disappearance of the two peaks at 1503 cm^{-1} and 1540 cm^{-1}, assigned predominantly to the resonance of a phenol ring mode and of a stretching mode of the C_α-C_5 exocyclic double bond of the anionic chromophore, respectively.

Symmetrically to the decrease of these two peaks, two other peaks appear at 1564 cm^{-1} and 1604 cm^{-1} that correspond to a stretching mode of the C_α-C_5 exocyclic double bond and to the resonance of a phenol ring mode of the neutral chromophore, respectively. In other words, the

fraction of the anionic chromophore decreased while the fraction of the neutral chromophore increased, both for the crystal illuminated at 488 nm and for the crystal soaked in an acidic buffer.

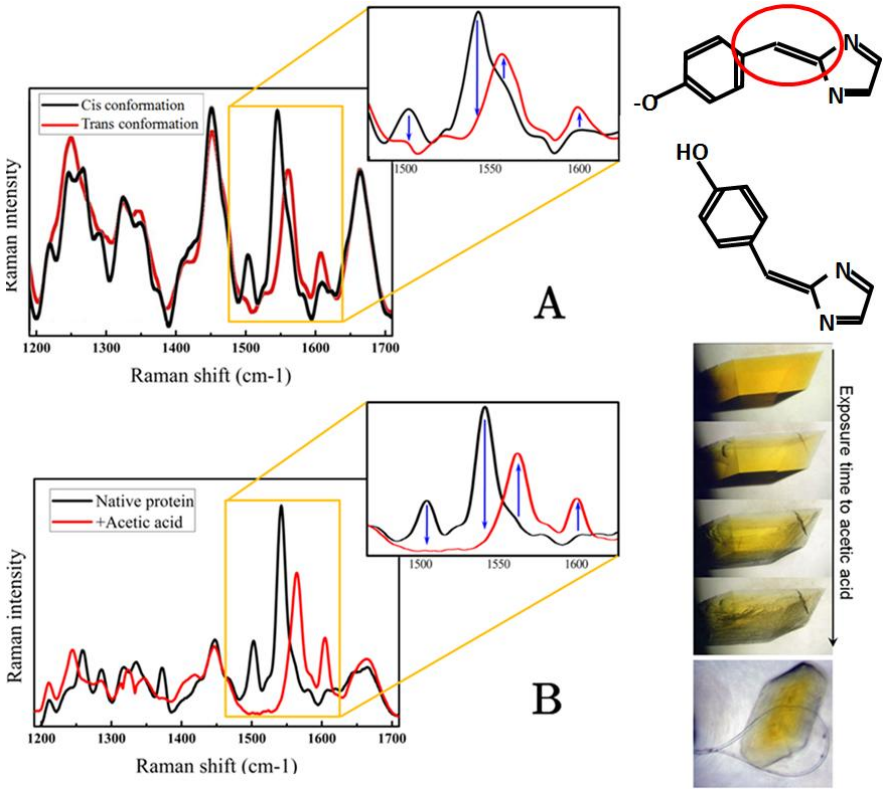

Figure II.2.19 - Raman spectra of IrisFP crystals measured at 100K before & after light-induced isomerization (A) and before & after protonation induced by addition of acetic acid at pH 4.0 (B) - Insets represent a zoom of the main bands specific of the methylene exocyclic bridge (circled in red on the sketch). The color loss of crystals soaked in acetic acid (C) clearly shows that the acid is entering the solvent channels, making the outer crystal shells transparent while the core of the crystal keeps its coloration. One can also notice the cracks in the crystals that appear and prevent from obtaining a crystallographic structure of this protonated form.

These results prove that the chromophores, after irradiation at 488 nm or after acidification are not only extremely similar in terms of absorbance and fluorescence spectra but are also extremely similar chemically, since the Raman signatures of both species are almost identical. Most importantly, they show that both experiments lead to the conversion from an anionic chromophore to a neutral chromophore. From the combination of the results obtained by crystallography and by Raman spectroscopy, we can propose that both chromophores of IrisFP illuminated at 488 nm and acidified (even without illumination) are protonated and in trans conformation.

b - Crystals exposed to visible light at cryogenic temperature

Both the absorption and fluorescence of a crystal of IrisFP at 100 K illuminated at 488 nm (~1.5 kW/cm^2 on the sample) have been recorded at the Cryobench laboratory. For absorption measurements, because of the very high optical density at this wavelength in crystals of IrisFP, a rod-shaped crystal with a very thin section (15x15x100 µm) was mounted in a microloop containing the crystallization mother liquor to which 20% glycerol was added. The crystal was flash-frozen and kept at 100 K. For fluorescence measurements, another rod-shaped crystal with a bigger section (50x50 µm) was mounted as previously at 100 K and submitted to a constant illumination at 488 nm that was used both as the actinic and the probe light.

Probably due to mechanical instability of the shutter controlling the lamp and the very thin crystal section that was illuminated, the absorbance spectra measured were rather unstable so that the baseline was hopping a bit from a spectrum to another. However, despite this instability, the results (Figure II.2.20, A) are clear and show a decrease of the anionic peak at 488 nm that can be well fitted by a biexponential decay. On the other hand, the absorbance of the neutral peak at 390 nm quickly increases and then remains rather stable with a slight decrease in time (Figure II.2.20, B).

The fast step ($t^1/_2$ = 193 sec) seems to be due to protonation since it correlates with the decrease of the anionic peak. The slower step ($t^1/_2$ = 5170 sec, i.e. ~1h43) could be associated to a process of degradation, since both peaks are slowly decreasing. The neutral form is less affected than the anionic peak but also decays either because it displays residual absorbance at 488 nm or because there is a constant slow exchange between neutral and anionic forms, which leads to the consumption of both species. Most likely this degradation is provoked through the same laser-induced intersystem crossing to the triplet state that permitted the chromophore protonation.

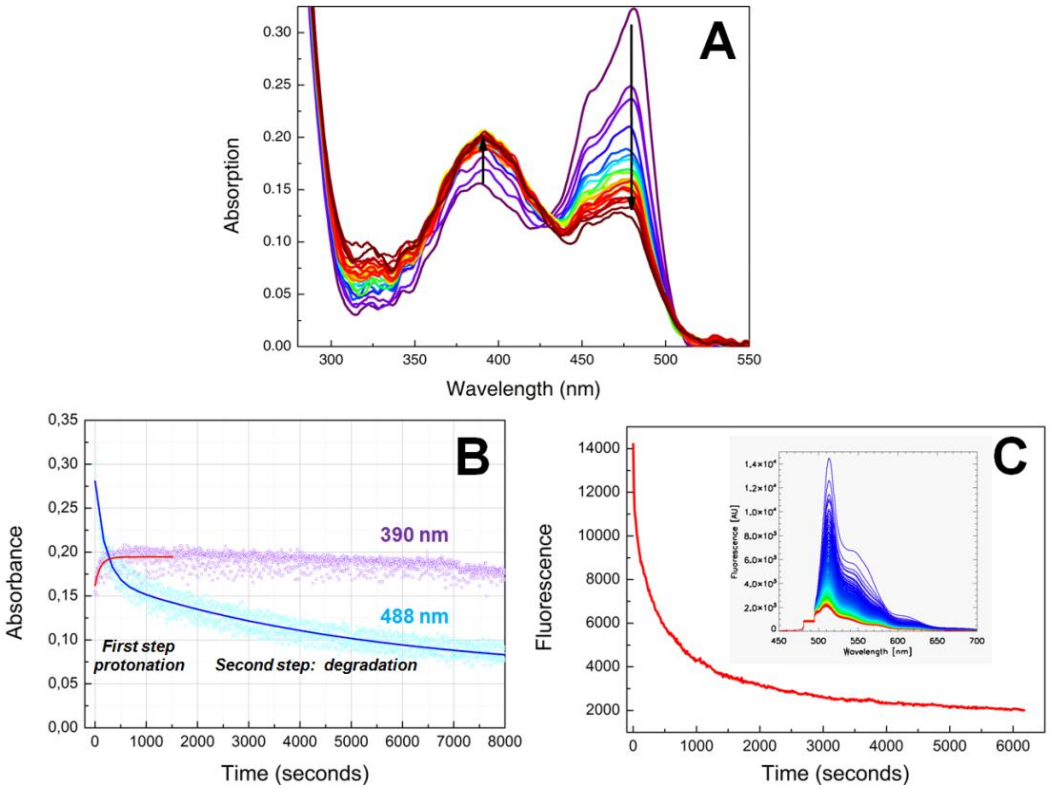

Figure II.2.20 - Photo-induced protonation and degradation at 100 K of IrisFP

During such an experiment, the fluorescence signal is decreasing with a decay that can be well fitted by a biexponential function (Figure II.2.20, C) having a fast phase with a $t^1/_2$ = 151 sec and slow phase with a $t^1/_2$ = 5160 sec (i.e. ~1h43), both values coherent with those observed in absorbance mode. This decay seems logical since two mixed phenomena occur, protonation and photobleaching, which both lead to a fluorescence decrease.

c - Solution exposed to visible light at cryogenic temperature

The experiment detailed above was reproduced with a solution instead of a crystal of IrisFP. A thin film of IrisFP solution mixed with 30% glycerol was flash-frozen in a microloop and maintained at 100 K. A series of alternate illumination at 488 nm (~0.4 kW/cm² on the sample) during 4 seconds, followed by measurement of the absorbance spectrum, allowed to record more stable spectra than those previously described. Probing the absorption signal regularly during ~7 mn, the results (Figure II.2.21, A) revealed to be extremely close to those

obtained on the crystalline form and, qualitatively, to those obtained at room temperature (Figure II.2.2). The anionic peak at 488 nm shows a biexponential decay with a fast step which is associated with a fast increase of the neutral peak at 390 nm (an isobestic point is clearly observable). Both evolutions (Figure II.2.21, B) can be fitted by a monoexponential ($t^1/_2$ = 180 sec) that we can assign to the protonation (first) step observed in the experiment detailed previously on a crystal.

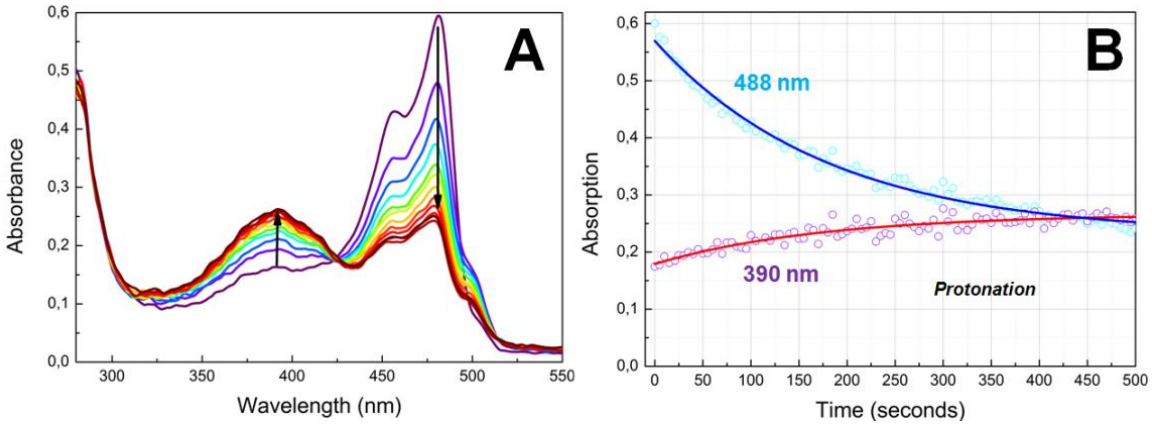

Figure II.2.21 - Photo-induced protonation at 100 K of a solution of IrisFP

When pursuing longer the illumination, here again the two peaks start to slowly decrease, indicating a photodestruction of the chromophore. We can better notice in this experiment the increase of the peak at 390 nm probably because the protein used was more anionic than the one in the crystal.

d - Discussion and conclusion

Considered together, these results strongly suggest that protonation is the initiating step of the isomerization mechanism. Indeed, our data show that protonation of the chromophore can be photoinduced at 100 K, a temperature at which the large movements associated with photoisomerization are very unlikely to occur. The change in protonation, even at 100 K, suggests that the exchanged proton is very close from the hydroxyl moiety of the chromophoric tyrosine. We propose that this labile proton could be the one of the conserved Ser-142 that is H-bonded (2.7 Å) to the hydroxybenzylidene. During light excitation of the anionic

chromophore, it has been shown (Voityuk *et al.* 1998) that the electron density delocalizes to the imidazolinone ring (Cf. repartition of the charges density at S_0, p.31), which is in disfavor of a protonation at the excited state. However, a recent study on Dronpa (Mizuno *et al.* 2008) proposed that upon intersystem crossing, both the long lifetime of T_1 and the less acidic character of the hydroxybenzylidene in T_1 as compared to S_1 (Turro 1991) would promote protonation of the chromophore. Once in this neutral form, the chromophore could isomerize to a trans conformation. Absorption of light at 390 nm would then lead back to the anionic form via ESPT.

Based on this suggestion and on the results presented above and as an analogy with the photosynthesis reaction having a dark phase and a light phase, we can propose a dark reaction and a light reaction for the protonation/isomerization mechanism of RSFPs (Figure II.2.22). In such a mechanism, the light reaction would be initiated by the absorption of cyan light by the chromophore, leading to an excited state that can either de-excite (by emission of fluorescence or non-radiatively) or cross to the triplet state T_1. The acidity of the chromophore being lower in this triplet state than in the excited state, its protonation becomes possible via the deprotonation of Ser-142 for example. This protonation would break the interactions between the hydroxybenzylidene and the barrel, loosening the chromophore that would finally become able to isomerize from its cis conformation to a more favorable trans conformation, depending on the chromophore environment and temperature. In such process, serine 142 may reprotonate via the network of water molecules identified near this residue in IrisFP. Finally, the violet light-induced or slow thermal recovery to the initial anionic cis conformation occurs as previously described: the thermal back-switching of the chromophore is most likely due to the fact that the protonated trans state of the chromophore is slightly less stable than the anionic cis state at neutral to basic pH values, so that the protonation is transient and slowly reversed. When the recovery from the trans state is photoinduced by a violet light illumination, it is due to an ESPT provoking the deprotonation of the trans chromophore, as shown by a deuteration experiment on Dronpa (Fron *et al.* 2007).

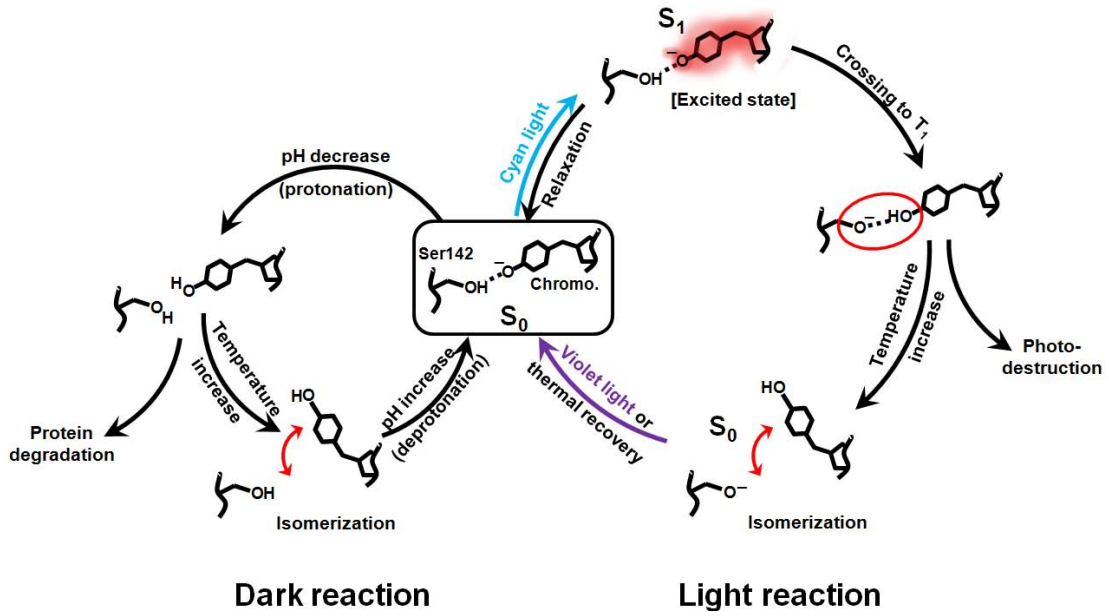

Figure II.2.22 - Proposition for the mechanism of a light induced and a pH induced reaction involving the change of protonation and isomerization states of RSFPs chromophores

Isomerization could be possible in proteins having a favorable chromophore environment such as Dronpa or IrisFP and if the temperature is high enough to allow those major conformational changes. Environmental constraints could explain the differences in bright-to-dark conversion efficiency (quantum yields) between proteins such as Dronpa, having a quantum-yield of 0.00032 (Ando *et al.* 2004) and IrisFP, having a quantum yield more than 43 times higher (0.014) as reported in Table II.2.7. However, in the structures of Dronpa illuminated by green light and obtained by NMR, the authors observed several agitated cis conformations but no trans conformation. This result is rather intriguing since the isomerization has been observed by X-ray crystallography for several RSFPs crystallized in different spacegroups and it seems improbable that the crystalline contacts favor the trans conformation. Moreover, several calculations (Weber *et al.* 1999; Usman *et al.* 2005) showed that the neutral (protonated) chromophore of green fluorescent proteins is inherently easily switchable to a trans conformation. Anyhow, cis-trans isomerization can be one of the different possible reactions occurring after the protonation of the chromophore and it is possible that this conformation can be favored in crystals, or upon cooling. Another possibility than we currently cannot exclude without further studies is that the direct isomerization may occur first, followed by protonation. These two possibilities may even coexist.

2 - Can non-switchable FPs be switched anyway?

When exposing a solution of EosFP wild-type to high laser power densities at 502 nm, we noticed that the spectra provided intriguing results. The initial goal of these experiments was to check the spectral changes of a non-photoswitchable fluorescent protein such as wt-EosFP, associated to photobleaching at room temperature. Surprisingly, the protein exhibited weak photoswitchable abilities with spectroscopic signatures resembling those of the on and off forms of RSFPs. Although it is difficult to characterize wt-EosFP as a RSFP, since the quantum yield for the on/off switching seems very low compared to Dronpa-like proteins (such as IrisFP), intense illumination at 502 nm results in an increase of the absorbance peak at 390 nm (neutral form) accompanying the decrease of the absorbance peak at 506 nm (anionic form). These results relate to the proposal that any fluorescent protein might be, at least partially, photoswitchable (Voliani et al. 2008).

To study whether this phenomenon could be due to a photoisomerization as observed in IrisFP at room temperature or to a photoprotonation as probably observed at cryogenic temperature, we tried to reproduce on a diluted solution of EosFP the same kind of illumination protocols used to photoswitch IrisFP at room temperature. Both the absorption and fluorescence spectra (excited at 502 nm) were measured and both a thermal recovery and a photoinduced recovery (405 nm) of the partially photoswitched state were followed.

a - Thermal relaxation of the off state

The on/off conversion was performed by irradiating continuously the protein solution in a standard quartz cuvette, made airtight with a plastic cover, at 502 nm (30 mW/cm^2) while recording a spectrum every 10 seconds for fluorescence measurements or by pulsing the laser at 1Hz with 600 ms/pulse followed by a pulse from a deuterium/halogen lamp with 200 ms/pulse for absorption measurements (Figure II.2.23, A).

The relaxation from the state stimulated by the 502-nm laser was followed by leaving in the dark the solution in its airtight cuvette for 5 hours and recording a spectrum every

10 minutes with a pulse from the 502-nm laser (80 ms/pulse) for fluorescence measurements or the deuterium/halogen lamp (200 ms/pulse) for absorption measurements (Figure II.2.23, B).

The absorbance peaks at 390 and 506 nm as well as the fluorescence peak at ~520 nm clearly show a conversion from the anionic form to the neutral form (Figure II.2.23) since the peak at 506 nm decreases while the peak at 390 nm increases. This conversion is accompanied by a loss of fluorescence. An isobestic point is observable at 430 nm, similar to what was already observed for absorbance spectra during the photoswitching of IrisFP at room temperature or photoprotonation or IrisFP at cryogenic temperature. However, this conversion is much more limited than in the case of IrisFP and a too long irradiation leads to a decrease of the whole spectrum (mostly for the peak at 506 nm that is excited) and to the disappearance of the isobestic point, indicating a degradation of the protein (data not shown). The absorbance spectra show an initial evolution that can be well fitted by a monoexponential function ($t^1/_2$ = ~1500 sec *i.e.* ~25 min) both for the increase of the peak at 390 nm and the decrease of the peak at 506 nm.

The fluorescence signal was measured during a longer time than the absorbance signal. Its timecourse can be well fitted by a biexponential function that correlates with the two-step behavior already described in the experiments performed on IrisFP at cryogenic conditions. Based on what we said, the fast phase ($t^1/_2$ = ~627 sec *i.e.* ~11 min) could be attributed to a protonation step and the much slower phase ($t^1/_2$ = ~3467 sec *i.e.* ~57 min) can be assigned to photobleaching. This second phase was not visible in absorbance because the acquisition time was not long enough. The irreversible degradation is confirmed by thermal relaxation experiments. Back-conversion to the initial state is evident since the peak at 390 nm decreases while both the peak at 506 nm and the fluorescence signal increase, but the final intensities of those peaks are much lower the initial ones. The intensity of the absorbance band at 280 nm remains intact, indicating that the damage is most likely limited to the chromophore and that the global integrity of the protein is maintained.

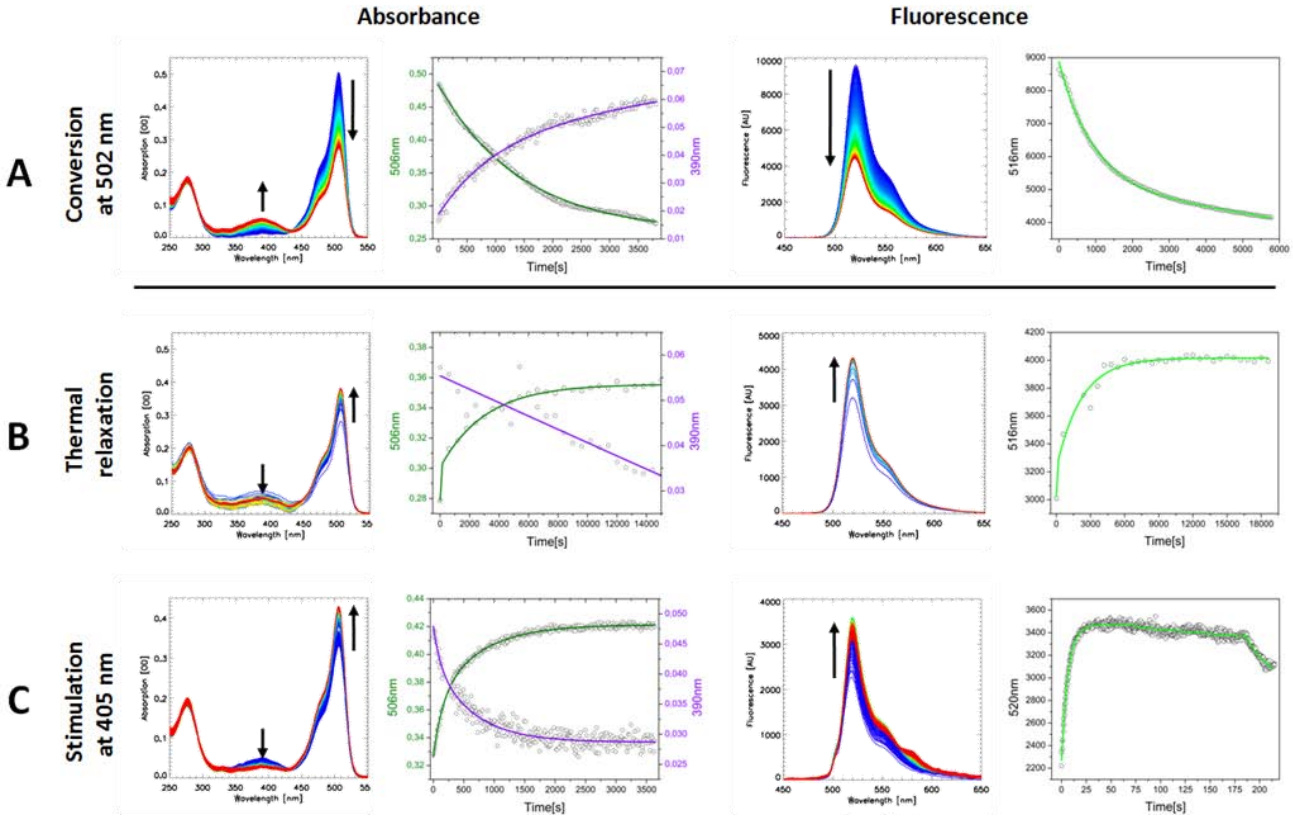

Figure II.2.23 - Spectral series and evolutions in absorption and fluorescence of a solution of EosFP being photoprotonated with a 502-nm laser (A) and exhibiting thermal autodeprotonation (B) or photostimulated deprotonation at 405 nm (C)

Following the absorbance peak at 506 nm during thermal relaxation led to a growing curve that can be fitted by a single exponential function ($t^1/_2$ = ~2200 sec *i.e.* ~36 min). Instabilities of the absorbance signal at 390 nm (most likely due to the instability of the shutter of the lamp used to measure the spectrum and the very low signal at this wavelength) prevented us to properly fit the evolution of the neutral species. However, its decay with time is very obvious. The fluorescence signal also increased monoexponentially during this relaxation ($t^1/_2$ = ~1980 sec *i.e.* ~33 min). It is interesting to note that this recovery is much faster than the trans-to-cis thermal recovery in IrisFP and that in spite of the long measuring time, this increase does not need to be fitted by a biexponential curve as in the fluorescence decay induced by illumination at 502 nm. This seems logical since no photoinduced degradation of the chromophore is possible during this thermal recovery.

b - Photostimulated relaxation of the off state

The conversion to the off state was made on a solution of EosFP at the same concentration and with the same method as described previously and was perfectly reproducible (Figure II.2.23, A). The photostimulation of the relaxation from the off state was performed by pulsing the 405-nm laser at 2 Hz with 5 ms/pulse and 1.5 mW/cm². The effect of an increased power density (11 mW/cm²) was also tested in fluorescence mode. The acquisition was made using either the excitation from the 502-mn laser (5 ms/pulse) for fluorescence measurements or pulses from a deuterium/halogen lamp (200 ms/pulse) for absorption measurements. The evolution of the absorbance spectra during this experiment could here again be well fitted by a monoexponential function ($t^1/_2$ = ~490 sec *i.e.* ~8 min) both for the decrease of the peak at 390 nm and the increase of the peak at 506 nm (Figure II.2.23, C).

Type of conversion	Absorbance		Fluorescence		
	$t^1/_2$ (de)protonation	$t^1/_2$ (degradation)	$t^1/_2$ (de)protonation	$t^1/_2$ (decay-1)	$t^1/_2$ (decay-2)
On/off conversion	25 min (502 nm) 30 mW/cm²	ND	11 min (502 nm) 30 mW/cm²	57 min (502 nm) 30 mW/cm²	-
Thermal relaxation	36 min	NA	33 min	NA	-
Stimulated relaxation	8 min (405 nm) 1.5 mW/cm²	ND	7 sec (405 nm) 11 mW/cm²	7.5 min (405 nm) 11 mW/cm²	20 sec (405 nm) 76 mW/cm²

Table II.2.9 - Values of the halftimes for reactions of photoprotonation and photoinduced or thermal deprotonations, depending on laser power densities. Blue and green colors represent the absorbance and fluorescence modes, respectively. Grey and pink colors represent the phenomena of degradation and photoconversion that occur upon long laser irradiations.

The fluorescence signal also increased according to a single exponential process ($t^1/_2$ = ~7.0 sec) but was followed by a second phase that consists in a monoexponential slow decrease ($t^1/_2$ = ~450 sec *i.e.* ~7.5 min). The increase of the 405-nm laser intensity between the measurement in absorbance (1.5 mW/cm2) and this experiment (11 mW/cm2) was probably too high, producing a beginning of green-to-red photoconversion as observed in the series of fluorescence spectra (Figure II.2.23, C). The intensity of the 405-nm laser was further increased (76 mW/cm2), resulting in a new abrupt monoexponential decay of green fluorescence ($t^1/_2$ =

~20 sec). All the values are compiled in Table II.2.9 and allow to see that the photoinduced relaxation from the off state is much faster than the thermal relaxation, consistent with a photoinduced protonation in the triplet state and a photoinduced deprotonation in the excited state S_1 by ESPT.

c - Conclusion

The results on EosFP at room temperature are pretty close to those obtained during photoswitching or acidification of IrisFP. It is not possible to discriminate on the sole basis of the spectra between isomerization or protonation but we cannot exclude that after the photoinduced protonation of EosFP, a small fraction may photoswitch from a cis conformation to a trans conformation. A fast decrease of the anionic form correlating with a fast increase of the neutral form occurs to a level comparable to that obtained in experiments performed on IrisFP at cryogenic temperatures (Figure II.2.20 & Figure II.2.21), and further illumination only lead to the degradation of the protein. At such low temperatures, the chromophore is extremely unlikely to isomerize and the spectral changes can be attributed to a photoinduced protonation of the chromophore. The same phenomenon (photoprotonation) can be proposed as an alternative explanation (rather than isomerization) to the observed switching when EosFP is exposed to light excitation at 502 nm at room temperature.

The observed degradation is proposed to occur mostly from the anionic form of the chromophore, the neutral form being constantly in weak equilibrium with the anionic form thanks to an ESPT produced by the weak absorption of the neutral form at 488 nm.The newly designed stable monomeric variant of EosFP, called mEos2, is also reported as having a very minor part of its population able to convert from an anionic form to a neutral form (McKinney *et al.* 2009) which is, most likely, the same phenomenon than the one we just described. This conversion of the absorption spectra in PAFPs may probably be generalized to many if not all FPs. The phenomenon can be considered as marginal for fluorescent proteins that are not designed especially to be photoswitchable, due to its slow rate, but it should not be underestimated, as it may be problematic for some single molecule or STED-like experiments.

Part 4 - PAFPs as optical data storage devices?

This part presents results obtained at the Institut Albert Bonniot, Grenoble, with the help of Dr. Alexeï Grichine and at the ESRF. These results should be considered as a preliminary proof of principle of the idea of using photoactivatable fluorescent proteins as data storage devices. This concept has been raised by several publications and patents, although no real practical evidence has been shown yet. Despite the interest of the experiments presented here, practical applications remain pretty much unrealistic as of today and it should be kept in mind that the principal applications of PAFPs concern the developments in super-resolution microscopy.

1 - The interest of biophotonics in data storage

a - Introduction

Current optical data storage devices (CD, DVD, Blu-ray...) are limited to a two-dimensional storage array (surface). Although during last years, efforts have been made to use smaller and smaller wavelengths to write more data on the same surface, an obvious physical limitation is going to happen (for a brief summary of existing 2D optical memories and how they work, refer to Appendix III, p.262). A solution to this problem is to use the thickness of the storage medium and holographic methods (Haw 2003). Another possibility would be to use a 3D arrangement of photoactivatable elements to store data in a three-dimensional array. This idea led Stefan W. Hell (Figure I.3.7) to deposit a patent (Hell *et al.* 2007) about the possibility of using crystals of GFP-like PAFPs in which each molecule would represent a data bit. Such a bit could be seen as a binary encoded element depending on the state of the PAFP, either fluorescent or switched off. Of course, this idea seems difficult to apply in reality because of several limitations imposed by biological matter (non-reversible photobleaching, need for a solvated state, sample aging...), and because photoactivating a single molecule within the highly concentrated 3D crystalline lattice is currently not achievable. However, recent amazing

developments of biophotonics, PAFP technology and nanotechnology make such a principle interesting to study.

b - DVDs made of protein crystals... an impossible dream?

In a condensed medium such as crystalline sample, a small volume representing a bit could only be addressed anywhere in the crystal depth at the condition that volumes located out of the focal volume are not excited. This precise tridimensional optical targeting is possible thanks to the two-photon effect.

If we consider a protein crystal of IrisFP of dimension 100 x 100 x 100 μm^3 (1 nL) formed by 1.37×10^{13} individual molecules (bits of about 10 x 10 x 10 nm^3 each), the data storage capacities of such a crystal would represent ~148 GB (gigabytes), which is the equivalent of more than 30 DVDs. Let's now imagine that we could create with such crystals a medium with the size of a DVD. The volume V of such a medium can be calculated by Equation II.4.

$$V = (\pi r_1^2 h) - (\pi r_2^2 h) = \pi h \times (r_1^2 - r_2^2)$$

Equation II.4

Where r_1 is the radius of the DVD, r_2 is the radius of the central hole and h is the thickness of the DVD.

For a standard DVD, r_1=60 mm, r_2=20 mm, h=1.1 mm, so that we find V=11058 mm^3 = 11 mL = 11×10^6 nL. The capacity of an "IrisDVD" would thus represent more than 16 EB (exabytes) which is equivalent to more than 3 billions of standard DVDs! Of course, our calculation is completely unrealistic since the minimum volume of excitation that is achievable nowadays is about a femtoliter, so that it is currently completely impossible to address a single molecule in a crystal and, thus, to consider such a single molecule as a bit.

With the best optics available, we can consider that we can probe a minimal confocal volume of the order of a femtoliter. Considering our single crystal having a volume of 1 nL, the minimal excitable volume would thus not be a single molecule but a millionth of the crystal volume. This means that the crystal would contain a maximum of one million bits (122 kilobytes). The total volume of a DVD made of such crystals would thus represent a total maximum storage capacity of 1.25×10^6 TB (terabytes) which is equivalent to more than 270 standard DVDs. Such a storage capacity is far below the 3 billions of DVDs that we calculated above, but still represents a considerable amount of data. The creation of such a DVD would of course be confronted to a number of difficulties and we hardly can consider the conception of this kind of data storage devices to be really feasible nowadays.

The easy and reproducible crystallization of IrisFP that forms big regular crystals, as well as the parallelipipedic morphology of these crystals makes this PAFP a potential good candidate for such a project. High-throughput crystallization robots allow the growth of a high number of crystals and these robots will undoubtedly make more progresses in the next years. The technology, possibly based on spin coating, that would allow the creation of the recording medium itself from these crystals as a regular layer has still to be developed, even if some experiments showed that it is practically possible to embed and preserve protein crystals in a plastic matrix as shown in Figure II.2.24.

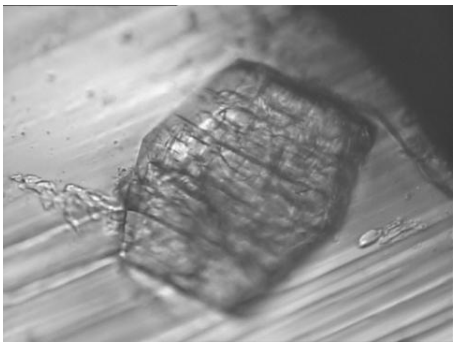

Figure II.2.24 - Single crystal of lysozyme embedded inside a plastic matrix. Photograph reproduced from (Ravelli et al. *2007)*

In a condensed medium such as a crystalline sample, a small volume located within the depth of the crystal and representing a bit would need to be addressed without excitation of the surrounding layers of molecules, notably along the optical axis. This precise tridimensional optical targeting is possible thanks to the two-photon effect.

c - The two-photon effect

Maria Göppert-Mayer predicted during her Ph.D. thesis in Göttingen the phenomenon of the simultaneous absorption of two photons (Göppert 1929; Göppert-Mayer 1931). This effect called the two-photon absorption (TPA) effect needs so powerful lasers that it could only be experimentally proven thirty years later with the first experiment using biphotonic excitation (Kaiser & Garrett 1961).

Figure II.2.25 - Photograph of Maria Göppert-Mayer

Biphotonic excitation (also called two-photon excitation, TPE) is defined [12] as "the simultaneous absorption of two photons, the energy of excitation being the sum of the energies of the two photons". For TPE to occur, two photons have to excite a molecule within a short enough time so that the molecule cannot relax in between. Even with powerful laser sources though, this event is so rare that two-photon (2P) absorption only occurs at the focal point where the photon concentration is the highest while single photon (1P) absorption occurs all along the illuminated optical path with a linear dependency on the photon concentration (Figure II.2.26).

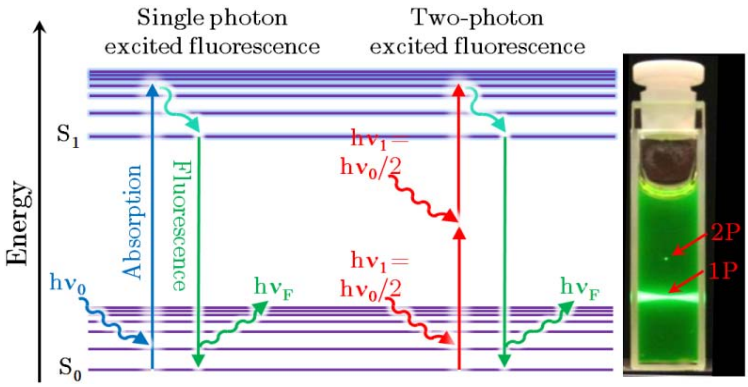

Figure II.2.26 - Single photon excitation versus two-photon excitation. Left: Perrin-Jablonski diagram showing the differences between single and two-photon excited fluorescence. Right: OPE (1P) and TPE (2P) of a fluorescein solution[13]

[12] Glossary of terms used in photochemistry, IUPAC recommendations 1996, 68, p.2230

[13] http://belfield.cos.ucf.edu/one vs two-photon excitation.html

Compared to standard optical microscopy, TPE allows a very precise excitation within a sample without interacting with other molecules in planes out of focus. This has a clear advantage for 3D imaging of samples and was first used by the group of Watt W. Webb (Figure I.3.7, p. 64) for microscopy purposes in 1990.

2 - Protein crystals as write-only 3D mass storage devices

We started our experiments by trying to image and visualize in three dimensions single crystals of IrisFP and d1EosFP, using confocal and two-photon microscopies. Crystals were placed in a drop of their crystallization mother liquors in Lab-Tek® chambered borosilicate coverglass trays. This setup is the same for all experiments presented below, with the exception of the one shown in Figure II.2.31.

3D images of crystals of IrisFP and d1EosFP have been obtained by confocal microscopy with an excitation wavelength ~488 nm (Figure II.2.27, a & b).

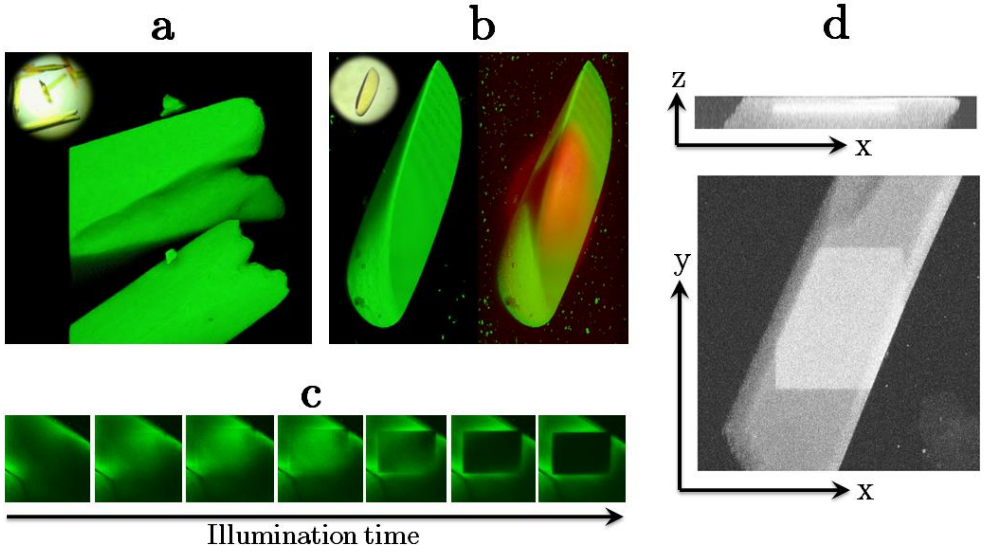

Figure II.2.27 - Confocal microscopy 3D reconstructions of crystals of IrisFP (a) and d1EosFP (b) before and after the partial 1P photoconversion at ~400 nm (insets show photographs of the crystals observed in bright field). (c) Progressive 2P photoconversion (observed in green) of the bottom layer of an IrisFP crystal, due to an irradiation at ~800 nm. (d) 2P green-to-red photoconversion (represented in gray levels) of a layer inside an IrisFP crystal by irradiation at ~800 nm

The green-to-red photoconversion could also be obtained and visualized on both proteins with a classical single photon actinic excitation at ~400 nm or with a two-photon actinic excitation at ~800 nm (Figure II.2.27, b, c & d). When we used the illumination at 400 nm, a UV lamp was focused on a large area (diameter = 350 μm) of the crystal and we could clearly see the cone formed by the light entering the crystal depth, defining the fraction of the crystal that was photoconverted. At the opposite, when we used TPE with the 800-nm line of a Ti:Sa laser, we could photoconvert a narrow layer inside the crystal depth. The laser used for TPE in the experiments presented below is a Tsunami Ti:Sa laser, pumped by a Millenia VII solid state laser (80 MHz, 120 fs), and tunable between 690 and 1100 nm.

We used the results shown in Figure II.2.27 to perform, in a second step, the irreversible green-to-red photoconversion using actinic TPE at 800 nm on several layers inside the depth of a crystal of IrisFP. In the control software (LSM, Zeiss, Germany) we drew masks of letters forming the words “IAB”, “ESRF” and “ULM”, standing for the names of the institutes involved in this project (the IBS was unduly forgotten on that day!). Inside these regions of interest, the 800-nm line of the Ti:Sa laser delivered a power of ~10 mW on the sample (Airy disc surface = 0.38 μm²) with a pixel dwell time of 1.6 μs. Each pixel measuring 70 x 70 nm and the array being made of 512x512 pixels, the total array surface is 1284 μm². This setup allowed to write the three words on three different planes inside the crystal of IrisFP with a very appreciable spatial resolution of 0.6 x 0.7 x 1.5 μm³ (0.63 femtoliter). This experiment was reproduced on another crystal several weeks later with an even better contrast Figure II.2.28. This contrast, however, could probably have been further enhanced if we had followed the green channel instead of the red channel, as we did.

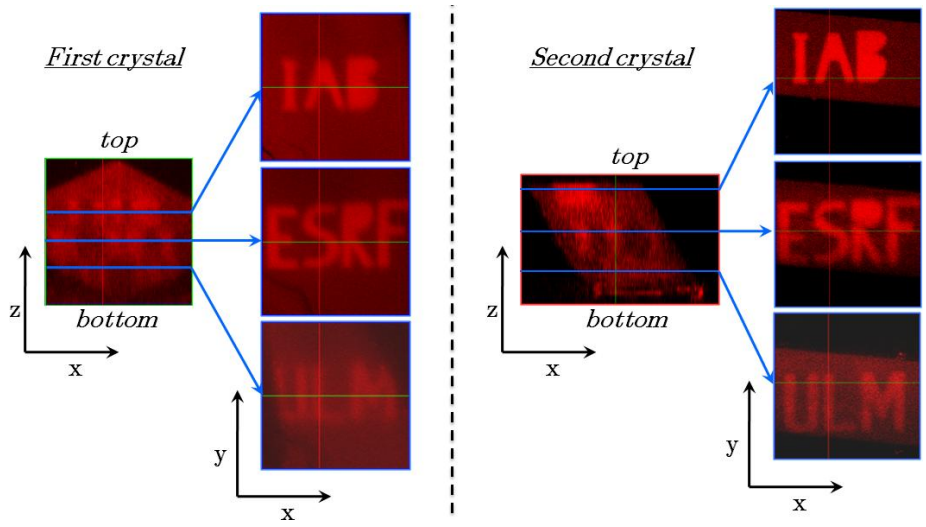

Figure II.2.28 - In-crystallo burning. An irreversible green-to red photoconversion is performed within two different IrisFP crystals at three different depths (blue horizontal lines) using TPE at ~800 nm to write the words "IAB", "ESRF" and "ULM". Fluorescent signals are then observed by 1P excitation at 543 nm and detection in the red channel

Although being highly perfectible, this first experiment unambiguously shows that we can irreversibly encode data at different locations within the core of a single protein crystal using TPE at ~800 nm, using the photoconversion property of a PCFP such as IrisFP. The photoconversion was also tried at 760 nm and 840 nm and no obvious differences could be observed, as the photoconversion seemed to occur as efficiently at all those wavelengths. This suggests that the biphotonic action spectrum for IrisFP photoconversion is probably very broad.

Since we know that IrisFP is not only a PCFP but also a RSFP, we wanted to check if we could use the photochromic properties of this PAFP to encode data, erase it and burn another information at the very same location. In other words: creating a rewritable biological storage device.

3 - Protein crystals as rewritable biophotochromic 3D mass storage devices

a - Introduction

The potential use of photochromic dyes as compounds for reversible 3D optical data storage was already (and first) suggested by Y. Hirschberg (Cf. Figure I.2.15, p. 40) in 1956 with the case of spiropyrans and bianthrone (Hirschberg 1956). He wrote: *"The cycle of the appearance of the color on ultraviolet irradiation and the disappearance of the color by irradiation with visible light is proposed for the first time as a photochemical memory model"*. While Hirschberg has shown that most photochromic molecules can exhibit their reversible behavior at room temperature, others demonstrated that some molecules can do the same in a rigid medium (Lewis & Lipkin 1942) and even that photochromism can be produced by two-photon excitation (Mandzhikov *et al.* 1973). Knowing that two-photon absorption is a rare event that allows the excitation of only the "in-focus" part of a bulk material, the idea has been proposed twenty years ago to use two-photon excitation of photochromic dyes to create real rewritable 3D data storage devices (Parthenopoulos & Rentzepis 1989). The recent development of biotechnology engineering of fluorescent proteins and especially photochromic FPs led to the recurrent references to their potential use as data storage devices (Dickson *et al.* 1997; Andresen *et al.* 2005; Sauer 2005; Schafer *et al.* 2008).

b - Results

We used the same experimental setup as described above to perform these experiments. To avoid the detection of a fluorescence signal coming from another crystal shell, the photoconversion was made on the bottom surface of a crystal of IrisFP (Figure II.2.29-a). First, by irradiating at ~800 nm (10 iterations, 10 mW on the sample), a 2P-induced on-to-off switching was performed inside a mask forming the letters "IAB" standing for Institut Albert Bonniot (Figure II.2.29-b). Then, the fluorescence was recovered by 5 seconds of wide field illumination with a mercury arc lamp in order to reinitialize the crystal shell (Figure II.2.29-c). Some weak remanence was observed though, because of either an insufficient illumination or a

fraction of the proteins that was irreversibly photobleached by the photoswitching step. Finally, a new mask was prepared and, using the same 2P photoswitching parameters, the word "IBS" (standing for Institut de Biologie Structurale) was written on the very same crystal shell (Figure II.2.29-d). Between each step, the images were obtained by exciting the sample with a 1P weak (~40 nW on the sample) illumination at 488 nm. The total area for each word was about 260 μm².

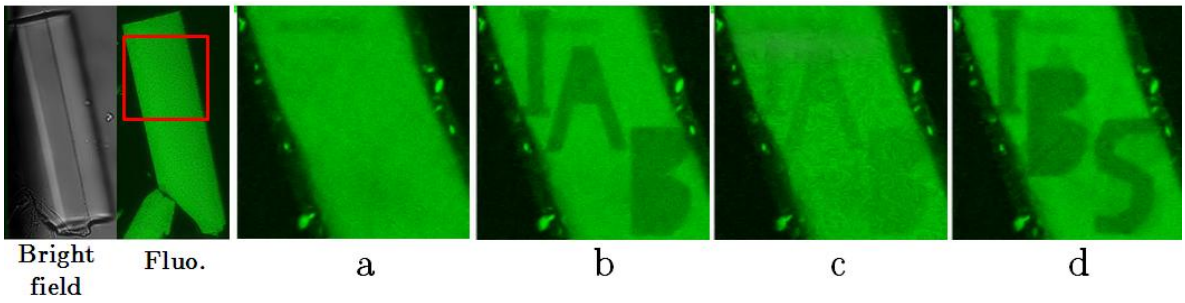

Figure II.2.29 - In crystallo rewritable burning using 2P photoswitching. A reversible photoswitching is performed on the surface of an IrisFP crystal (a) The word "IAB" is first written (b). The fluorescence is then recovered by 1P back-switching (c). Finally, the word "IBS" is written on the same layer (d)

c - Same wavelength but different effects

We were puzzled to notice that the same wavelength at 800 nm seemed to create two different effects: photoconversion as shown in Figure II.2.28 or photoswitching as shown in Figure II.2.29. The first point that we can address is that we worked using two-photon excitations and we can reasonably think that the action spectra for photoconversion and photoswitching are different using one photon (1P) and two photon (2P) excitations. The comparison between 1P and 2P excitation spectra of several dyes show major differences. If for some fluorescent dyes (Lucifer yellow, Coumarin 307, Cascade blue), the wavelengths of TPE peaks roughly fit with twice those of OPE peaks, the TPE spectra are generally more complicated, broader and blue-shifted as compared as OPE (Figure II.2.30). In reality, as written on Molecular expressions website[14]: "there is no fundamental basis for quantitatively predicting the two-photon excitation spectrum of a complex fluorophore simply by examining the single-photon cross section".

[14] http://micro.magnet.fsu.edu/primer/techniques/fluorescence/multiphoton/multiphotonintro.html

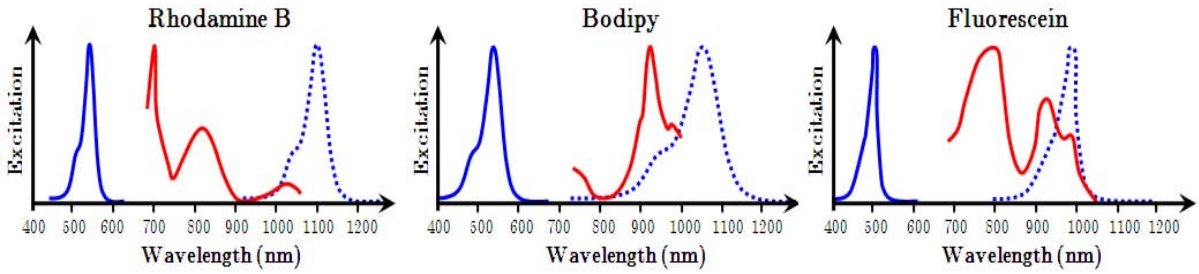

Figure II.2.30 - Difference between 1P and 2P excitation spectra. OPE spectra for three dyes (rhodamine B, bodipy and fluorescein) are shown as plain blue lines, TPE spectra for those three dyes are shown as plain red lines and differ notably from excitation spectra that could have been expected by simply multiplying by two the OPE spectra (dotted blue lines). Figure prepared with data from Molecular probes[15] and (Xu & Webb 1996)

The difference between these spectra suggests that the occurrence of photoconversion and photoswitching in IrisFP could be dramatically changed when we use TPE, as compared to the experiments described up-to-now with 1P excitations, and that these events could even be provoked by the same wavelength. However, we can wonder what was the determining criterion that decided, upon the same excitation, to rather initiate a photoconversion in one case and a photoswitching in another case. During our experiments, we noticed that our crystals were much more dried in the photoconversion experiment than in the photoswitching one. Moreover, the photoconversion revealed to be much more efficient on crystals that were let in the dark during several weeks and that were really dry (Cf. Figure II.2.28, right). On the other hand, wet crystals show a very poor susceptibility to photoconversion but were easily photoswitched.

We tried to study further this phenomenon by submitting crystals of IrisFP to the flow of a newly developed humidifier control device (Juan Sanchez-Weatherby, EMBL, Grenoble). Green fluorescent crystals of IrisFP were mounted on the goniometer head of the beamline ID14-2 at the ESRF thanks to MicroMesh mounts (MiTeGen, Ithaca, NY, USA). Crystals were first slowly dehydrated and then slowly re-hydrated. The fluorescence and the absorption were probed by regularly taking snapshots of the crystals during the experiments. This is done by switching on a backlight (fluorescence) or a frontlight (bright field) and switching them off immediately after the snapshot is taken, in order to avoid any photobleaching.

[15] http://www.invitrogen.com

The results (Figure II.2.31) are very reproducible and unambiguously show that the drying, even controlled and weak, is accompanied by a permanent loss of fluorescence and absorption.

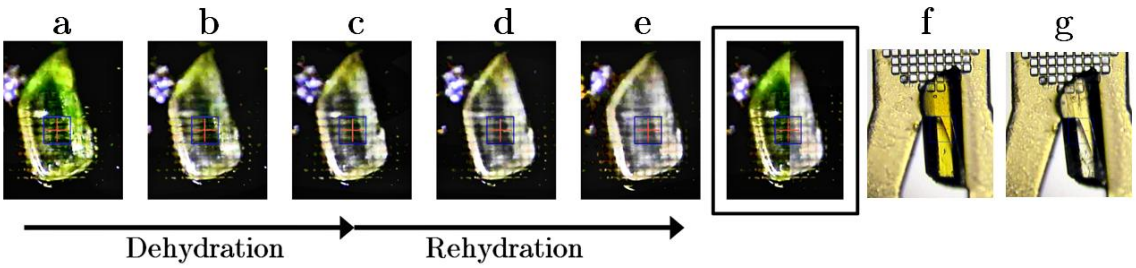

Figure II.2.31 - Controlled drying/humidifying of an IrisFP crystal – The influence of the drying process and subsequent rehydration on fluorescence is depicted from pictures a to e. The framed picture represents the difference between pictures a and e. Pictures f and g show a crystal observed in bright field, before and after controlled drying

These results do not allow to easily conclude on the role of humidity on the above-mentioned effects. Indeed, we could not solve the structure of a partially dried crystal, since these crystals do not diffract anymore once dried, even lightly, so that a structural hint to explain the efficient photoconversion by TPE could not be obtained.

We can propose, however, that under dry conditions, crystals of IrisFP are more efficiently photoconverted from green to red by TPE at 800 nm, due to some irreversible protonation of the chromophore. Using dry crystals is probably an advantage if plastic-like embedding of the crystals is the chosen solution. However, results presented in Figure II.2.31 suggest that the overall fluorescence signal is weak under these conditions. Moreover, we noticed that residual cross-talk between green and red fluorescence channels reduced the visual contrast of the encoded information compared to the background.

On the other hand, under wet conditions, the photoswitching seems favored in TPE experiments. The very good contrast and the possibility to write and erase the encoded data are clear advantages. However, the requirement of a wet conditioning and the thermal autorecovery (erasing) of the information are major hindrances to the development of rewritable biological storage devices and more studies would be required to find a solution.

Chapter 3 - Photobleaching: an intriguing problem

Résumé en français

Ce dernier chapitre des résultats traite du troisième grand phénomène de transformation photoinduite d'une protéine fluorescente : le photoblanchiment. Ce phénomène inévitable d'extinction définitive des sondes fluorescentes lors de l'excitation est encore très mal compris. Après un court état de l'art, les résultats de diverses expériences ayant mené au photoblanchiment des protéines fluorescentes photoactivables EosFP et IrisFP sont présentées. Le photoblanchiment de ces protéines, provoqué par illumination UV, visible, ou par les rayons X produits par le synchrotron européen est étudié tant en fluorescence qu'en absorbance, sur solution ou dans les cristaux. Des données structurales permettent en outre de caractériser un état fortement déformé du chromophore, correspondant à un état radicalaire probablement impliqué dans la voie de photoblanchiment des protéines fluorescentes.

Part 1 - About photobleaching

1 - What do we know about photobleaching?

PHOTOBLEACHING or fading is defined as the loss of absorption or emission intensity[16]. It occurs when a fluorophore permanently loses its ability to emit fluorescence due to photon-induced chemical damage resulting in covalent modifications[17]. Photobleaching of fluorescent probes may complicate their observation, since they will ultimately be destroyed by the light source necessary to excite them.

All fluorescent probes are subject to such a phenomenon and will emit a certain number of photons before definitely ceasing to do so. It is reported for example that a single fluorescein molecule emits about $3x10^5$ photons[18] and GFP-like molecules emit about 10^5 photons before being destroyed by photobleaching (Kubitscheck *et al.* 2000). Two-photon irradiation seems to be even more destructive to fluorescent proteins since higher order interactions occur and irreversibly photobleach proteins with higher quantum yields (Patterson & Piston 2000). Photobleaching, thus, seems to be an unavoidable event that may happen, at any moment of the illumination of a fluorescent protein.

Some techniques use photobleaching at their advantage (White & Stelzer 1999) such as Fluorescence Loss In Photobleaching (FLIP) or Fluorescence Recovery After Photobleaching (FRAP), that allow the determination of molecular diffusion rates. In super-resolution microscopy techniques such as PALM (Betzig *et al.* 2006), the role of photobleaching is also crucial since molecules are imaged until they are bleached, which terminates a cycle allows imaging of other molecules during the following cycle. However, in most cases, photobleaching represents a strong limitation in microscopy that one tries to avoid or at least reduce as much as possible.

[16] *Glossary of terms used in photochemistry (IUPAC Recommendations 1996)* on page 2231
[17] http://www.stratagene.com/lit/faq/faq.aspx?fqid=323
[18] http://www.microscopyu.com/articles/fluorescence/fluorescenceintro.html

2 - What are the factors influencing photobleaching?

a - The involvement of the triplet state and singlet oxygen

Although photobleaching is still poorly understood, the triplet state T_1 is generally recognized, due to its long lifetime, to be the most likely starting point for deleterious reactions leading to chromophore destruction (Donnert *et al.* 2007). Once in the triplet state, chromophores may either relax and re-populate the ground state, or the long living triplet state can allow reactions between excited chromophores and other molecules to occur, producing irreversible covalent modifications[19]. Other photobleaching pathways have been suggested to occur from the singlet excited state S_1 or even from higher orders of excited states such as S_2, that can be reached by illuminations with UV light (Bell *et al.* 2003; Kong *et al.* 2007).

One of the causes often proposed for the occurrence of photobleaching is when a fluorophore reacts with singlet oxygen. Singlet oxygen ($^1O_2$) is, at the opposite of most molecules, the unstable form of molecular oxygen, which, in its stable form, is actually in a triplet state ($^3O_2$). $^3O_2$ can be converted to $^1O_2$ by reacting with another molecule that is in its triplet state, following the general scheme: $\begin{matrix} {}^3O_2 \longrightarrow {}^1O_2 \\ T_1 \rightsquigarrow S_0 \end{matrix}$

It has been recently shown that the GFP chromophore produces $^1O_2$ when excited (Jimenez-Banzo *et al.* 2008), by monitoring the specific phosphorescence band of $^1O_2$ at 1275 nm (Nonell & Braslavsky 2000). However, at the exception of the engineered protein KillerRed which has been reported to produce major quantities of $^1O_2$ (Bulina *et al.* 2006a; Bulina *et al.* 2006b; Remington 2006), the usual production of singlet oxygen by fluorescent proteins seems to be low. Interestingly, whereas this protein produces high quantities of $^1O_2$, its bleaching rate is not particularly important, probably because there is a kind of tunnel allowing the efficient outflow of the reactive oxygen species (ROS) from the β-barrel. The technique of chromophore-assisted light inactivation (CALI) has been developed to permit, via the excitation of chromophores such as the one of KillerRed, the major production of ROS that

[19] http://www.olympusmicro.com/primer/java/fluorescence/photobleaching

inactivate the function of neighboring molecules (Bulina *et al.* 2006b; Jacobson *et al.* 2008). However, this technique, and more generally the production of $^1O_2$ did not obviously reveal being very efficient to photobleach GFP-like proteins and it seems that there is no clear evidence of the effect of molecular oxygen or quenchers on GFP bleaching (Swaminathan *et al.* 1997), most likely because of a shielding effect by the β-barrel. Even if it is one of the possible pathways implicated, the chromophore's photoxidation by $^1O_2$, thus, is probably not the main pathway leading to photobleaching.

Photobleaching, reveals to be a very complex phenomenon and has certainly more than a single origin. Many pathways probably coexist, such as the interaction between the chromophore and singlet oxygen, but also deleterious reactions occurring at the triplet state or at the singlet excited states, that lead to the photodestruction of fluorophores. We propose, in this work, to study one of these pathways.

b - The implication of a radical state?

A number of studies focusing on organic dyes have pointed to the possibility of radical formation from T_1 as an important pathway for photobleaching (Zondervan *et al.* 2003; Hoogenboom *et al.* 2005) and we can logically think that such a radical formation may also be involved in the photobleaching process of FPs. The strong acidity of the excited chromophore may for example promote electron transfer from the conserved Glu222 (GFP numbering), leading to decarboxylation of this residue via a bi-radical intermediate state [Photo-Kolbe reaction (Kraeutler *et al.* 1978; Sato 1983; Habibi & Farhadi 1998; Yanga *et al.* 2008)] and resulting in fluorescence activation (van Thor *et al.* 2002; Bell *et al.* 2003; Lukyanov *et al.* 2005) or bleaching (McAnaney *et al.* 2005). Contrary to small molecule dyes, the details of the underlying molecular mechanisms have remained largely unexplored for FPs. In particular, the structural distortions of the chromophore induced by radical formation have not yet been elucidated and the development of FPs with superior photostability has mainly followed empirical approaches to date (Ai *et al.* 2006; Shaner *et al.* 2008).

Part 2 - Effects of UV-light and X-rays on a fluorescent protein

1 - Bleaching of a FP with UV light

When crystals of EosFP are irradiated with UV light (e.g. 266 nm), the molecules are irreversibly photobleached within a few minutes, even at 100 K (Figure II.3.1).

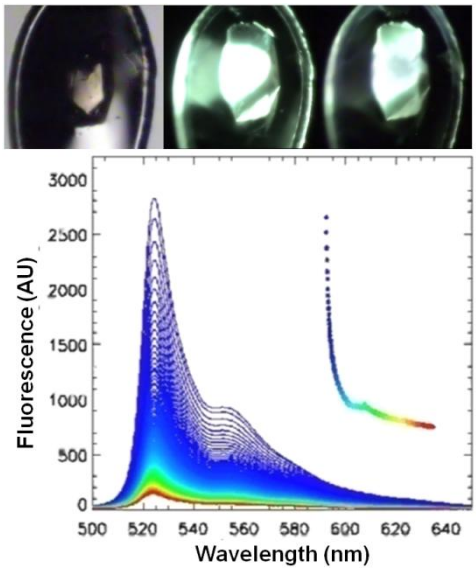

Figure II.3.1 - Photobleaching of a crystal of EosFP at 100 K by illumination at 266 nm. Top: the crystal is observed in bright field (left), in fluorescence at the beginning of the experiment (middle) and at the end of the experiment (right) - Bottom: Fluorescence spectra measured during the experiment, the inset shows the evolution of the highest peak

When IrisFP crystals submitted to a strong UV illumination during several minutes at 100 K are thawed, we can notice that they break apart with the clear emission of a bubbling coming from the irradiated volume (Figure II.3.2, D). This suggests the massive production of a gas, such as CO_2 that could come from UV-induced decarboxylations, presumably of Glu212 (equivalent to Glu222 in GFP). Surprisingly, the very same phenomenon occurs when IrisFP crystals that were irradiated by X-rays with a dose equivalent to a standard diffraction data collection at 100 K are thawed. The crystal volume where X-rays were focused is destroyed once the crystal is brought back to room temperature, along with the emission of bubbles (Figure II.3.2, C). This kind of burst subsequent to X-irradiation from synchrotron sources has already been observed as a sign of radiation damage for several proteins but the similarity of

this macroscopic effect of X-rays and UV light on IrisFP crystals is striking. We cannot exclude, thus, that this phenomenon has a common origin, which could be the photodestruction of the chromophore and its environment. In order to check whether this damage could come from the crystal being frozen and thawed, a crystal was flash-frozen and thawed several times (without illuminating it) and did not show any sign of degradation, even after 5 cycles of this treatment (Figure II.3.2, B).

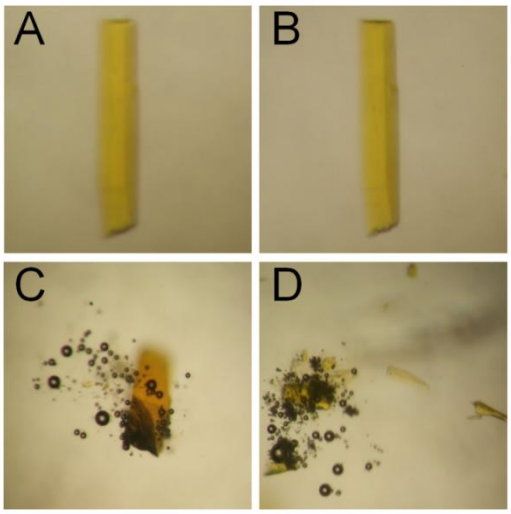

Figure II.3.2 - Macroscopic aspect of an IrisFP crystal submitted or not to a strong X-ray or UV irradiation

(A) crystal before any manipulation. (B) same crystal after five cycles of freezing and thawing but without irradiation. (C) Crystal frozen once, submitted to an X-irradiation equivalent to a normal data collection and thawed. (D) Crystal frozen once, submitted to a strong UV burning and thawed. When crystals are thawed, no degradation can be seen in B, while in C and D one can observe a bubbling when crystals are breaking apart.

The phenomenon of bleaching by UV/Vis light is known to be general for all fluorescent molecules. During experiments on crystals of several of the fluorescent proteins studied in our team, we noticed that the fluorescence emission exhibited very rapid decay under irradiation by the synchrotron X-ray beam, even at 100 K. This decay occurred much faster than the time needed to collect a complete diffraction data set. This phenomenon, together with the macroscopic degradation of crystals of IrisFP submitted to X-rays raised questions about the real effect of X-rays on the bleaching of fluorescent proteins. We tried to study this influence of

X-rays and compare it with the phenomenon of UV/Vis bleaching, by combining spectroscopic and crystallographic studies on IrisFP and EosFP as model fluorescent proteins.

2 - Fluorescence of FPs is lost under X-rays

To better study the damages created by X-rays and UV/Vis light on fluorescent proteins, a long rod-shaped crystal of IrisFP was mounted at the ESRF beamline ID14-2 equipped with the online microspectrophotometer (Cf. material & methods p.225 and (McGeehan *et al.* 2009)) and irradiated at 100 K on two different segments by either the X-ray beam or a 440-nm laser light (Figure II.3.3, A). This wavelength is very weakly absorbed by the protein but, under rather strong power density (760 W/cm^2), the fluorescence signal clearly slowly decreases, victim of photobleaching (Figure II.3.3, B & C).

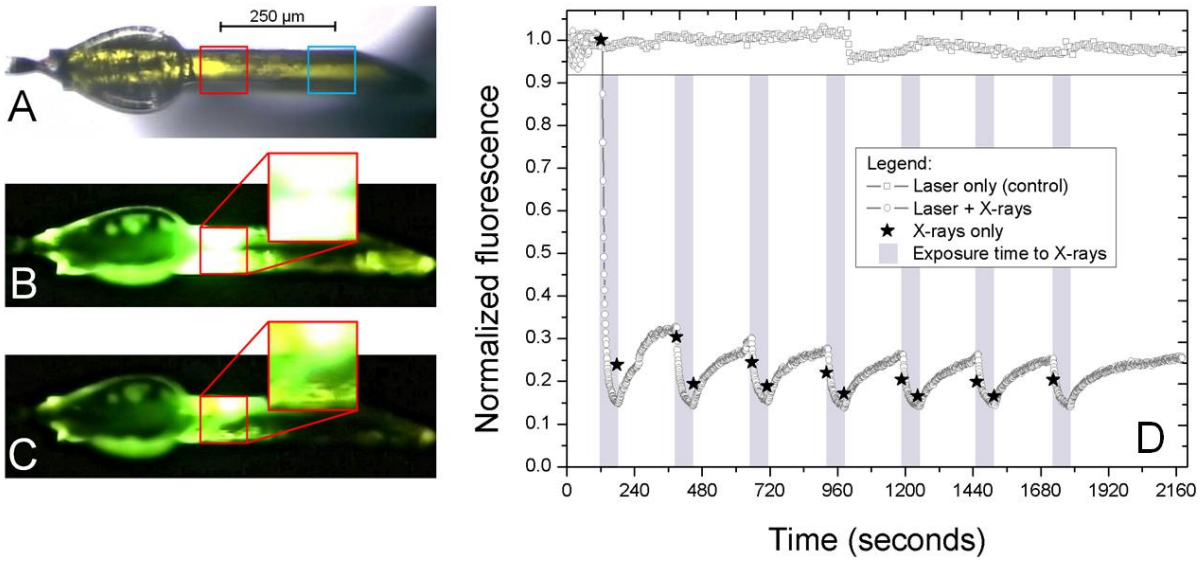

Figure II.3.3 - Study of damages induced by X-rays and 440-nm light on IrisFP at 100 K

A long crystal of IrisFP is burnt on two different segments by X-rays and 440-nm light, shown as blue and red squares respectively (A). The initial level of fluorescence in the segment hit by 440-nm light with a strong intensity (B) is decreased after a long exposure (C). The experiment (D) shows the evolution of the fluorescence signal (○) excited at 440 nm during periods (60 sec.) of exposure to X-irradiation (gray bars) and during periods (200 sec.) of relaxation. During identical exposures to X-irradiation only (without laser excitation), the fluorescence signal was probed before and after each period of exposure to X-rays (★).In the upper part, a control (□) shows that the continuous weak laser excitation at 440 nm (780 mW/cm²) does not influence the X-ray induced bleaching

In contrast, when the power density is weak (780 mW/cm^2), no sign of photobleaching is observed, even after a long exposure time (36 mn of continuous illumination). However, as soon as we open the X-ray shutter, the fluorescence signal shows a steep decrease, showing that the protein is obviously being bleached by the X-rays (Figure II.3.3, D). Surprisingly, when the X-ray shutter is closed, a partial slow recovery of the fluorescence signal occurs. This phenomenon can be cycled several times. During this X-ray photobleaching, short laser pulses (~20 ms) were used to excite fluorescence emission at 1 Hz.

It seems, thus, that major spectroscopic modifications produced by photobleaching either induced by UV/Vis light or X-rays take place far below the Henderson limit[20] (Henderson 1990) and even below the dose corresponding to a classical X-ray data set. We decided to investigate these modifications in more details both spectroscopically and structurally.

Part 3 - Structural basis of photobleaching

1 - UV-light induced photobleaching

The original goal of the experiment presented below was not the study of the photobleaching. We wanted to see if we could obtain the structure of EosFP during its excitation by UV-light, in order to trap a putative intermediate state along the photoconversion mechanism. The results, however, showed evident signs of photobleaching, which redirected our efforts toward this poorly understood topic.

We used the online microspectrophotometer (see material & methods, p.225) to illuminate a crystal of EosFP that was cryoprotected by adding 10% glycerol to the crystallization mother liquor and flash frozen. In order to efficiently illuminate the crystal within its depth, a UV laser emitting at 355 nm was preferred to the 266 nm-laser we had used previously. We could clearly

[20] Henderson limit: 2 × 10^7 Gy "the X-ray dose (energy per unit mass) a cryo-cooled crystal can absorb before the diffraction pattern decays to half of its original intensity"

see the cone formed by the laser entering the crystal and we collected X-ray diffraction images within the area containing the highest concentration of photons (Figure II.3.4, left). Two data sets were measured on different crystal volumes, with and without laser illumination, and a difference electron density map was calculated between these two data sets so that the effect of X-rays is subtracted (Figure II.3.4, right).

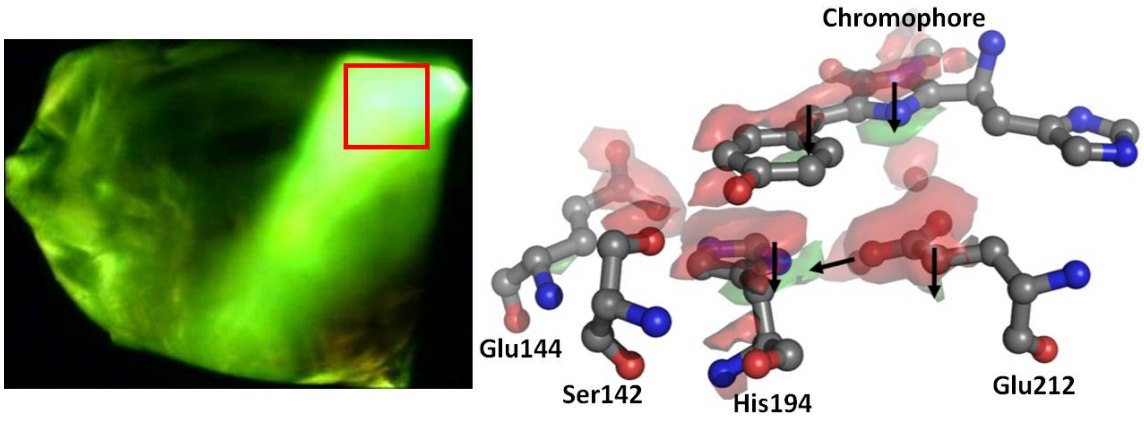

Figure II.3.4 - Crystal of EosFP being illuminated by a 355 nm laser source (fluorescent cone). A data collection is taken before the illumination and during this illumination (red square). Right: Structure of EosFP chromophore and some of its surrounding residues and water molecules showing negative (red) and positive (green) difference electron density maps between illuminated and non-illuminated states

The main advantage of such maps is their ability to highlight tiny electron movements (even in a small percentage of the molecules) in a much more accurate way than the more classical "F_{obs}-F_{calc}" difference maps.

The strongest peaks (negative) in the maps are located around the chromophore and on three residues: Glu144, His194 and Glu212. They suggest that the two glutamates decarboxylated and that His194 moved during the illumination. This structural change is probably concerted since His194 is biprotonated (confirmed by QM/MM) and binds the two glutamates 144 and 212 in the green emitting form. This hoop of aminoacids forms a cradle for the chromophore that rests on it via π-stacking of the tyrosine with the histidine 194 and via two water molecules (shown as red spheres) binding to the glutamate 212. These two water molecules are very stable (low B-factors) in the green form of EosFP, and that are dislocated together with Glu212. The consequence of this cradle movement is that the whole chromophore

"falls" (as seen with the negative and positive peaks on the chromophore). The crystallographic statistics for both data sets (non-illuminated and illuminated states of EosFP) are shown in Table II.3.10.

	Non-illuminated	Illuminated
Space group	P $2_12_12_1$	P $2_12_12_1$
Cell dimensions		
a, Å	72.80	72.52
b, Å	105.50	105.59
c, Å	121.07	121.04
Resolution, Å	1.4	1.6
R_{sym}, %*	6.7 (52.3)	10.8 (53.7)
Mean $I/\sigma(I)$	14.9 (2.9)	11.6 (3.8)
Completeness, %	99.1 (96.6)	100 (100)

Table II.3.10 - Crystallographic statistics of datasets for non-illuminated and illuminated states of EosFP

The results show that a dramatic modification of the chromophore with its close environment is occurring during the illumination of the protein. However, this experiment was not initially designed to study photobleaching so that the experimental setup prevented us to know the photobleaching state. We would have needed in particular to measure the fluorescence and/or absorbance signal during light exposure. Also, the wavelength was not properly chosen and visible light should have been used instead of UV light to match the experimental conditions used.

2 - X-ray induced photobleaching

To perform X-ray photobleaching, a portion of a needle shaped crystal was irradiated by the X-ray beam of the ESRF beamline ID14-2 (average flux: ~6.2×10^{10} ph/sec/$0.1 \times 0.1 mm^2$, wavelength: 0.931 Å).

a - Absorbance and fluorescence evolutions

The loss of absorbance induced by the exposure of an IrisFP crystal to X-rays revealed to be rather slow and composed of a rapid phase followed by a slower phase (Figure II.3.5, A).

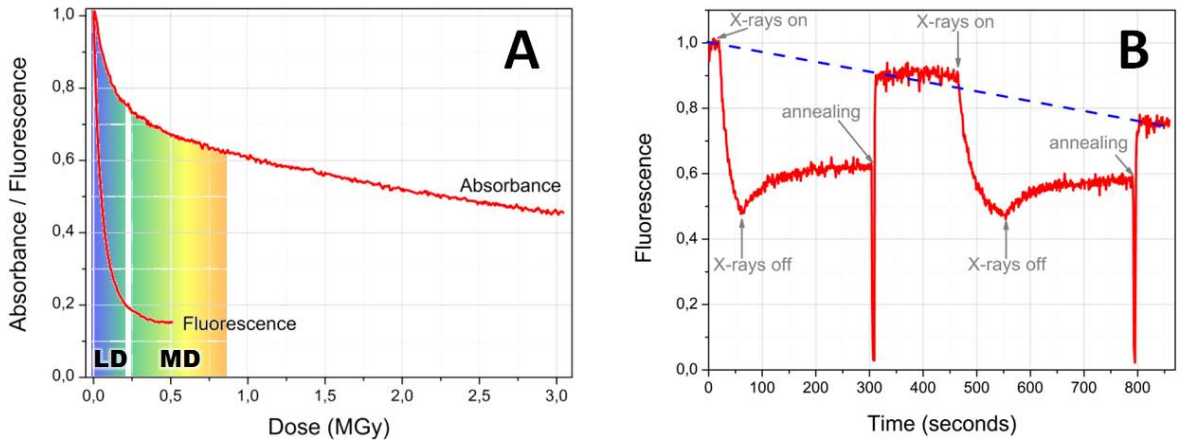

Figure II.3.5 - Comparison between the absorbance and fluorescence decays induced by the exposure to X-rays (A). Partially reversible fluorescence decay under X-irradiation (B). The red curves show the fast fluorescence and absorbance decay occurring under X-irradiation and that is slowly recovered at 100 K (and quickly after an annealing). The blue-dashed line depicts the X-ray induced irreversible photobleaching also occurring.

The corresponding fluorescence decay is much faster and displays a much bigger amplitude at comparable doses than in absorbance mode (Figure II.3.5, A). This decay is mostly reversible and only a small irreversible component is observed (Figure II.3.5, B).

The apparent discrepancy between the absorption and fluorescence decays in Figure II.3.5, A is most likely due to the fact that fluorescence decay kinetics are accelerated by quenching effects attributable to radical species generated by X-ray-induced water radiolysis. Even chemically intact chromophores may thus lose their ability to emit fluorescence, and the observed absorbance decay is judged more relevant to quantitatively evaluate the results. Under X-irradiation, the absorbance loss (Figure II.3.6, A) is also partly reversible. It decreases in two steps and shows a slow monophasic recovery in the absence of X-rays (Figure II.3.6, B).

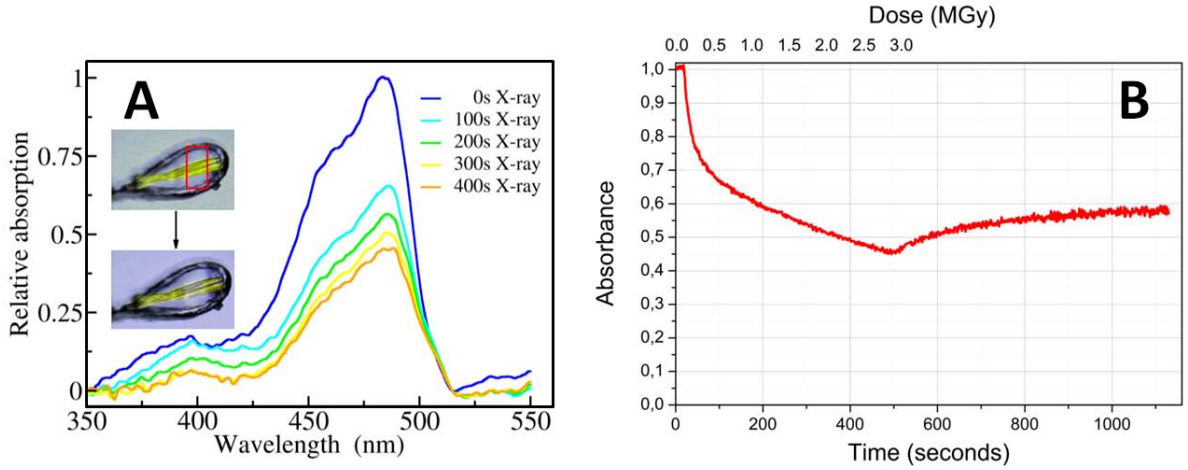

Figure II.3.6 - Absorbance decay of an IrisFP crystal under an X-ray beam (4.2 10^{10} ph/s) at 100 K (A). A selected set of baseline corrected spectra are shown and the loss of color of the crystal is shown in the inset. The absorbance decay kinetics at 485 nm (showing a clear biphasic behavior) and recovery in the absence of X-rays are displayed (B). Attempts to record absorbance recovery after excursion to room temperature failed, due to strong distortions of the baseline induced by the annealing procedure

b - Structure of a PAFP being bleached by X-rays

To obtain a structural view of the observed transient spectroscopic changes, we collected composite X-ray data sets (Berglund *et al.* 2002; Adam *et al.* 2004), i.e., subsets of diffraction data using different parts of an IrisFP crystal, so as to reconstruct two complete data sets acquired at low and moderate X-ray doses, respectively (Figure II.3.5, A). Data collection statistics for the LD and MD data sets are compiled in Table II.3.10.

	LD	MD
Median absorbed dose, MGy	0.09	0.50
Beamline	ESRF / ID14-2	ESRF / ID14-2
Wavelength, Å	0.933	0.933
Space group	P $2_12_12_1$	P $2_12_12_1$
Cell dimensions		
a, Å	85.54	85.51
b, Å	96.47	96.47
c, Å	139.81	139.80
Resolution, Å	50.0-2.00 (2.11-2.00)	50.0-1.86 (1.97-1.86)
R_{sym}, %*	10.1 (42.9)	7.9 (40.4)
Mean $I/\sigma(I)$	10.3 (3.1)	13.9 (3.2)
Completeness, %	95.6 (94.4)	93.3 (70.7)
Redundancy	3.8 (3.8)	4.8 (3.9)
No. of unique reflections	75305 (10884)	91100 (10786)
Wilson B factor, Å^2	19.9	19.0

*Table II.3.11 - Data collection statistics for the LD and MD data sets. Values in parentheses refer to the highest resolution shell. *$R_{sym} = \Sigma j \Sigma h | I_{hj} - \langle Ih \rangle | / \Sigma j \Sigma h \, I_{hj}$*

The LD data set corresponded to a total exposure of 32 sec under a non-attenuated X-ray beam (4.2×10^{10} ph/s, 0.1×0.1 mm^2), whereas the MD data set corresponded to a total exposure of 140 sec under the same flux.

The LD and MD data sets were each obtained from six subsets of 20 images (1° oscillation per frame), collected at different locations of the crystal, translating the latter by 50 μm and rotating it by 15° between subsequent subsets (overlap of 5°) so as to scan the entire reciprocal space. Only the 16 first images of each subset were used to reconstruct the LD data set, whereas all 20 images were utilized to reconstruct the MD data set. The absorbed dose during the LD data set was very small, running from 0 to 0.18 MGy (the median dose corresponded to 0.05 % of the Henderson limit (Henderson 1990)), and it was still small during the MD data set running from 0.23 to 0.80 MGy (*i.e.* 2 % of the Henderson limit). Hence, no sensible degradation of the diffractions patterns could be noticed. Based on an estimation of the crystal content, the approximate number of photons absorbed per unit cell was evaluated with the program Raddose (Murray *et al.* 2005).

Assuming that a single absorbed X-ray photon generates a cascade of up to ~500 e^-, ~30 e^- and ~160 e^- (on average) per unit cell may eventually be guided to the chromophores in the LD and MD cases, respectively. Therefore, with 16 chromophores per unit cell, these findings are consistent with very small and moderate photobleaching of the chromophores in the LD and MD data sets, respectively. Experimental difference electron density maps ($F_{obs, MD}$-$F_{obs, LD}$) were calculated with CNS (Brunger *et al.* 1998), using phases from the green structure of IrisFP (PDB accession ID 2VVH) and Bayesian q-weighting of the difference structure factor amplitudes (Ursby & Bourgeois 1997).

We also compared these results with experimental difference electron density maps ($F_{obs, HD}$-$F_{obs, Standard}$) where HD stands for "high dose" and corresponds to much higher (~20 MGy) X-ray doses than the ones used for LD & MD datasets, and $F_{obs, Standard}$ stands for a normal data set. We estimate that the doses employed for $F_{obs, Standard}$ and $F_{obs, HD}$ are ~2 times and ~8 times

that used for the MD data set, respectively. Due to dose accumulation on the crystal and associated expansion of the crystal unit-cell, the quality of the ($F_{obs, HD}$-$F_{obs, Standard}$) map is lower than that of the ($F_{obs, MD}$-$F_{obs, LD}$) map. NCS averaged ($F_{obs, MD}$-$F_{obs, LD}$) and ($F_{obs, HD}$-$F_{obs, Standard}$) maps are presented in Figure II.3.7. The (HD-Standard) dataset is mostly representative of structural changes associated with the slow absorbance decay phase (Figure II.3.5, A) and the electron difference density maps show a strongly tilted chromophore and a clear decarboxylation of Glu212 (Figure II.3.7, B). These structural data are indicative of a permanently bleached state.

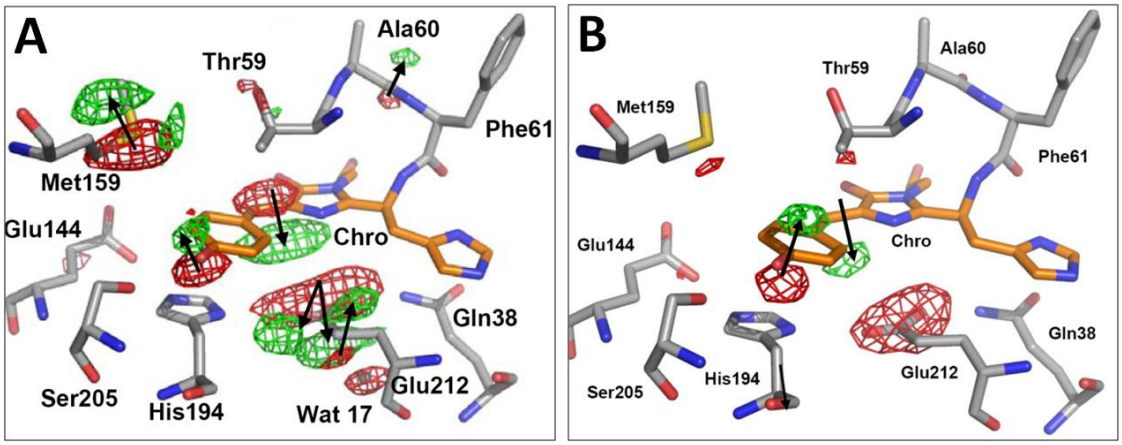

Figure II.3.7 - Experimental electron difference density map (red, -9.5σ; green: +9.5σ) between the LD and MD data sets, overlaid on the structure of IrisFP (left) and experimental electron difference density map (red, -8.0σ ; green: 8.0σ) between the HD and standard data sets, overlaid on the model of IrisFP (right). The chromophore is shown in orange, while neighboring residues are shown in grey. Arg66, in contact with the chromophore, is omitted for clarity.

Initial model refinement of IrisFP against LD and MD data did not give significant modifications as compared to the deposited model of IrisFP, which was collected under standard synchrotron conditions (Adam *et al.* 2008). Thus, model refinement was not further attempted.

The first (median dose: ~0.1 MGy) and second (~0.5 MGy) data sets correspond to the beginning and end of the fast absorbance decay phase, respectively (Figure II.3.5, A). At 0.5 MGy, the loss of fluorescence is almost entirely reversible (Figure II.3.5, B). The difference

electron density map between the two data sets revealed structural changes induced by X-irradiation, localized on the chromophore and its immediate environment (Figure II.3.7, A).

Experimental electron difference density maps are extremely sensitive to conformational changes by only a small fraction of the molecules in the crystal (cf. material & methods, p. 213) and from Figure II.3.5, A, we estimate that ≤ 20 % of the molecules in the crystal caused the changes between the LD, MD and "standard" data sets. Such a low value is observable in the maps but does not allow for a reliable refinement at the resolution of our data. Pairs of negative and positive difference density features show a downward motion of the chromophore's bridging methylene moiety and an upward motion of the benzylidene phenolate oxygen, resulting in a loss of planarity of the chromophore. The motion of the methylene bridge induces a displacement of Glu212, which seems to explore two conformations, with the carboxylate group H-bonding either to His194 or to Gln38. Glu212, however, does not decarboxylate noticeably. The motion of the chromophore phenolate oxygen is accompanied by a shift of the Met159 side chain, clearly visible due to the heavy sulfur atom. Other structural changes typically observed upon X-ray exposure of protein crystals are not visible at doses employed here.

Interestingly, when the electron difference density map is extended on an entire monomer, we can notice that the only big differences are only located at the position of the chromophore and its direct environment (see NCS-averaged map in Figure II.3.8). Moreover, these features are clearly visible on each of the four monomers present in the crystal asymmetric unit (Figure II.3.8, A-D)

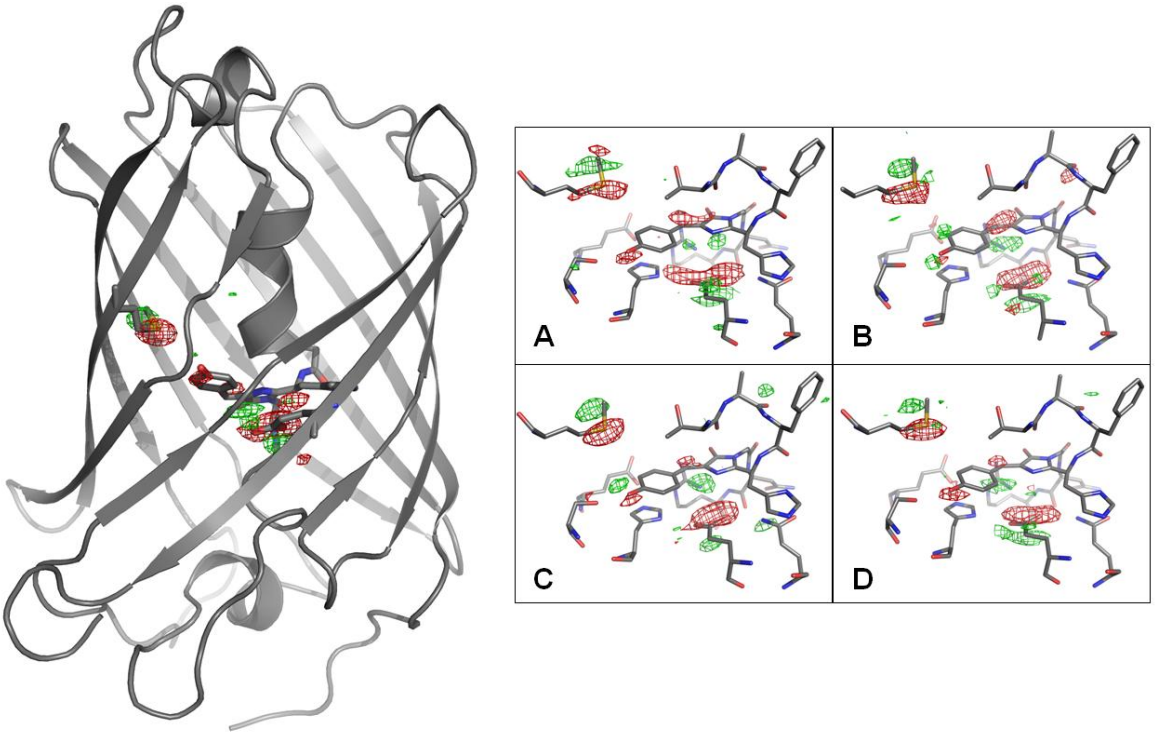

Figure II.3.8 - NCS-averaged experimental electron difference density map (red, -4σ; green: +4σ) between the LD and MD data sets, overlaid on the overall structure of a monomer of IrisFP. To demonstrate that the difference peaks are observed in each of the four monomers A, B, C and D, a close-up of the chromophore's environment is depicted on the right panel.

c - Raman spectroscopy

We also used Raman spectroscopy to probe the slight modifications of the chromophore signatures upon irradiation by X-rays and potentially correlate them to what we have observed during our Raman experiments described in the previous chapter.

In crystallo Raman spectra of IrisFP were collected online (ESRF beamline ID23-1) with 785-nm excitation before and immediately after 180 s exposure to an attenuated X-ray beam (4.4×10^{10} ph/s, 1 % transmission), equivalent to a 0.9 MGy absorbed dose. For recording full spectra (200-2000 cm^{-1}), a total exposure time of 15 min was used. Data-smoothing, baseline subtraction and cosmic ray removal were carried out with the program Wire[21]. The results showed a clear decay of the band at 1545 cm^{-1} (Figure II.3.9, red spectrum) after exposure to

[21] http://www.renishaw.com

X-rays. This band was already referred to in the chapter about Photoswitching (p.144) and was described to be the major resonant band assigned predominantly to a stretching mode of the C_α-C_5 exocyclic double bond of the anionic chromophore (He *et al.* 2002).

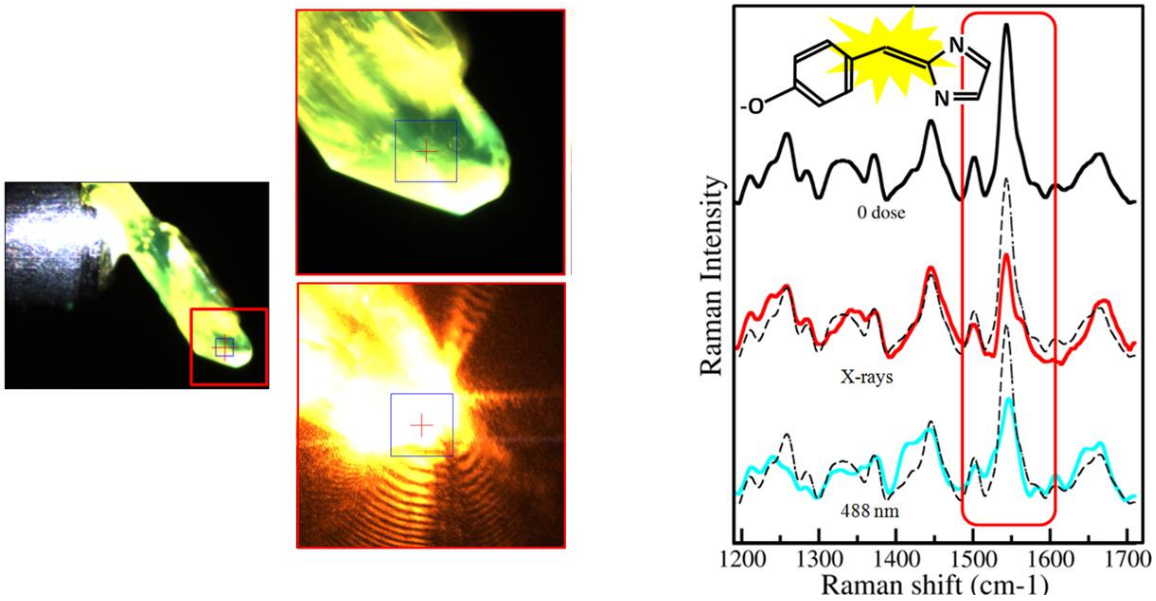

Figure II.3.9 - In crystallo Raman spectra of IrisFP at 100K before and after bleaching.

Left: experimental setup, a crystal of IrisFP is mounted on a crystallography pin. A zoom of the red-squared region is shown without and with the illumination of the Raman-laser. The blue square represents the size of the X-ray beam (100x100 µm). Right: Raman spectra before bleaching (top and dashed line), after X-ray bleaching (0.9 MGy, middle), and after 488 nm bleaching (26 min at 0.9 kW/cm², bottom). The main resonant band assigned to the methylene bridge (depicted in yellow on the chromophore sketch) is squared in red.

At the difference of what was observed in the Raman spectra of IrisFP before and after photoswitching (Figure II.2.19, p. 145) in which we saw the disappearance of the main peaks assigned to the anionic chromophore (1503 cm^{-1} and 1540 cm^{-1}) and the simultaneous appearance of the main peaks assigned to the neutral chromophore (1564 cm^{-1} and 1604 cm^{-1}), these spectra only show a decay of the band at 1545 cm^{-1}, with no obvious growing peak as a counterpart. This suggests that the C_α-C_5 π-bond of the methylene bridge is damaged by the exposure of the fluorescent protein to X-rays. No other change in the Raman spectra is judged significant, suggesting that the phenol moiety remains chemically intact and that the chromophore does neither isomerize nor change its protonation state (Luin *et al.* 2009).

Together with the diffraction and UV-Vis absorbance data, these Raman spectra strongly suggest that the C_α-C_5 π-bond is removed upon moderate X-ray exposure, implying that the conjugated π-electron system is reversibly disrupted. We can attribute this disruption to the formation of a chromophore radical species formed by the hydrated electrons and electron holes that are formed by the X-ray beam and that migrate onto the chromophore. The other radical species formed by the ionization of the solvent by the X-rays (secondary radiation damage) are unable to move at cryogenic conditions. Under high doses, this reversible disruption becomes mainly irreversible and accompanied by other modifications, such as the decarboxylation of Glu-212, leading to photobleaching.

3 - Visible light induced photobleaching

We mentioned earlier in this chapter that for studying the phenomenon of photobleaching as it occurs in real imaging applications, we need to focus on using visible light rather than UV light. Even if UV wavelengths are very efficient to photobleach FPs, the use of lights from UVC (such as 266 nm) to UVA (such as 355 nm) are not relevant for the actual use of FPs as fluorescent highlighters, and may produce non-specific damages on the proteins that could be very difficult to interpret. Since we know that IrisFP has its excitation peak at 488 nm but that this wavelength switches the protein to a dark state at room temperature, we finally concentrated on using 488 nm light (1.2 kW/cm²) at 100 K to generate the photobleaching. In this way, we tried to relate the observations made up on X-ray induced photobleaching of IrisFP with the mechanism of photobleaching induced by visible light.

Bleaching with visible light was carried out in IrisFP crystals in absorption and fluorescence mode. Experiments were also performed with frozen IrisFP solution samples containing 30 % glycerol and showed similar results than in crystals. A clear irreversible loss of fluorescence and absorbance as well as a reversible rise of the 390-nm absorbance band were observed. We can assign this weak reversible behavior to a probable photoinduced protonation

of the chromophore as discussed in the previous chapter (p. 151-155) and as previously suggested for Dronpa (Mizuno *et al.* 2008).

Due to the high optical density of IrisFP crystals at 488 nm, light is not evenly distributed throughout the crystal volume, making it difficult to study the changes by subsequent X-ray diffraction experiments. Here again, we used Raman spectroscopy to collect spectra on a crystal after illumination. Raman spectra were collected offline, before and after 1560 sec exposure to the 488-nm laser (1.7 kW/cm² at sample) and were obtained and treated as described previously. As in the X-ray case, the results showed a clear decrease of the band at ~1545 cm^{-1} (Figure II.3.9, cyan spectrum) and the same explanation can be proposed. A prolonged visible light illumination on the protein kept at 100 K (making photoisomerization impossible to occur) seems to photodamage the chromophore non-reversibly. This photodamage involves once again the C_α-C_5 π-bond of the methylene bridge, but at the difference of the bleaching provoked by X-rays, it is accompanied by further modifications of the chromophore and/or its immediate environment as assessed by other significant modifications in the Raman spectrum, for example at 1250 cm^{-1}, 1425 cm^{-1} and 1600 cm^{-1} (Figure II.3.9). These supplementary features suggest different mechanisms when we use X-rays and visible light but that ultimately lead to very resembling photobleached states.

Part 4 - Discussion and conclusion

In this chapter, we have described experiments in which we have used X-rays and visible light as tools to generate photobleached states in IrisFP in crystalline form and in solution. The results obtained by irradiation with visible light showed strong similarities with the X-ray case. Combining crystallography with *in crystallo* UV-Vis absorption, fluorescence and Raman spectroscopy (Carpentier *et al.* 2007), we have characterized the associated structural modifications of the chromophore and its environment. Altogether, these experiments showed reversible loss of absorbance and fluorescence as well as a probable disruption of the methylene

bridge between the imidazolinone and the phenyl rings of the chromophore. This work has been submitted to publication (Adam *et al.* 2009a) and the results as discussed below.

1 - A radical state is probably forming when FPs are submitted to X-rays

Reversible loss of absorbance and fluorescence in the crystal is achieved with a number of absorbed X-ray photons that is orders of magnitude smaller than the number of protein molecules within the diffracting volume. Consequently, absorption of a single X-ray photon results in transient bleaching of hundreds of chromophores. Therefore, X-ray bleaching of IrisFP at 100 K results predominantly from electrons released by water radiolysis. The observed structural changes suggest that these electrons (and electron holes) can migrate into the chromophore pocket, where they react with the chromophore to form a non-fluorescent radical.

The data suggest that, upon X-ray exposure, this intermediate state rapidly builds up, reaching a steady state level of ~20 %. The associated structural changes are those seen in Figure II.3.7, A. This intermediate or the initial state infrequently converts to a permanently bleached state, which corresponds to the slow phase in the absorbance decay and yields the structural changes of Figure II.3.7, B. The biphasic decay of absorbance observed when IrisFP is exposed to X-rays at 100 K (experiment presented in Figure II.3.6) can be explained by an equilibrium between the non-radical state (A) and the radical state (R) according to one of the two kinetic models presented in Equation II.5.

$$A \underset{k_{-1}}{\overset{k_1}{\rightleftarrows}} R \xrightarrow{k_2} B \qquad\qquad B \xleftarrow{k_2} A \underset{k_{-1}}{\overset{k_1}{\rightleftarrows}} R$$

Equation II.5

This equilibrium exists because while the powerful X-rays radiolyse water molecules, they create many radical species. Electrons and holes migrate onto the chromophore, and X-rays both induce radiation damage (forming the R state) but also continuously pump back to the A

state by reducing (or oxidizing) the chromophores that were oxidized (or reduced). In other words, the X-ray radiation not only provokes radiation damage but also fixes the damages it produces. The kinetic constants shown in Equation II.5 could be calculated for the transition A → R (k_1 = 0.013 s^{-1} → $t_{1/2}$ = 51 s (0.32 MGy)) and for the transition R → A (k_{-1} = 0.023 s-1 → $t_{1/2}$ = 24 s (0.19 MGy)).

When the X-rays are shut off, the absorbance is slowly autorecovering (k_{-1} = 0.0048 s^{-1} → $t_{1/2}$ = 146 s) because the fast X-ray induced recovery is abolished and only the slow relaxation of radicals at 100 K is possible. All along the experiment presented in Figure II.3.6, each molecule at the state R has the possibility to relax to the state A or being (irreversibly) bleached to the so-called state B, phenomenon that is slow (k_2 = 0.0032 s^{-1} → $t_{1/2}$ = 216 s) compared to the equilibrium between the relaxed state A and the radical state R.

When comparing absorbance and fluorescence decays induced by X-rays (Figure II.3.5, A), we can notice that the absorbance signal loses 50% of its initial level with an X-irradiation of 2.25 MGy while only 0.05 MGy (45 times less) are needed to produce the same effect in fluorescence. This very fast loss of fluorescence can be explained by the fluorescence quenching of chromophores by X-ray induced radicals. The chromophores are still healthy and capable of absorbing light and a much higher dose will be necessary to alter them.

2 - Photobleaching by visible light

Absorption of a visible photon in FPs may induce radical states arising from intramolecular electron transfer, preferentially in the triplet state. Therefore, radical formation by X-rays and visible light proceeds by different mechanisms. We propose that, upon absorption of a visible photon, charge transfer from Glu212 to the chromophore may occur in IrisFP, as in GFP (van Thor *et al.* 2002), leaving an unpaired electron on the latter residue. Relaxation of this bi-radical state may then lead back to the ground state or to decarboxylation of Glu212. In the latter case, a complete breakdown of the H-bonding network linking Glu212 to Glu144 (Adam

et al. 2008) may follow, accompanying destruction of the chromophore. A similar radical appears to be stabilized when a moderate dose of X-rays is employed at 100 K, probably because Glu212 remains chemically intact at such dose. At higher doses, however, the susceptibility of Glu212 to decarboxylation is evident (Figure II.3.7, B). Our Raman data indicate that the C_α-C_5 double bond, key to the chromophore's optical properties, is primarily affected along the bleaching pathways induced by X-rays or visible light. Thus, the observed X-ray induced structural changes are relevant to the mechanisms of bleaching by visible light. We propose that the transient structure observed in Figure II.3.7, A represents an early radical intermediate along a photobleaching pathway, trapped before the chromophore environment collapses. This radical may also be related to the reversible dark states observed in numerous single-molecule studies (Moerner 2002). We suggest that the strongly reducing electrons and oxidizing holes generated by X-ray-induced water radiolysis provide an effective shunt pathway to populate a radical state directly from the ground state (Figure II.3.10).

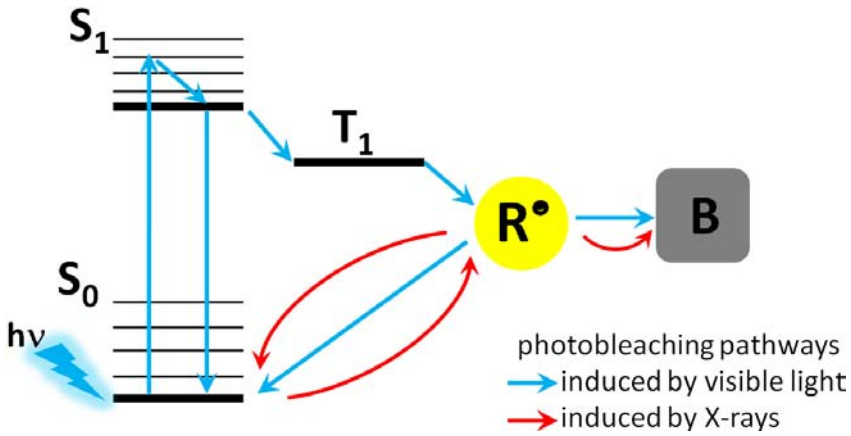

Figure II.3.10 - Proposed mechanism for X-ray induced radical generation in IrisFP, and implication in photobleaching pathway. Cyan and red arrows show photobleaching pathways induced by visible light and X-rays, respectively. R•: radical; B: bleached

X-ray structure analyses have revealed that chromophores in fluorescent proteins may not be strictly planar due to constraints imposed by the protein matrix (Maddalo & Zimmer 2006). However, the additional distortion induced by moderate X-irradiation observed here for IrisFP indicates that great caution has to be practiced so as to avoid such radiation-induced structural

changes when determining crystal structures of other FPs using synchrotron X-ray radiation. In conclusion, the reversible loss of π-conjugation directly observed in IrisFP may help unraveling the mechanisms of blinking and/or photobleaching in (PA)FPs, which is of considerable importance in the rational design of more photostable variants.

3 - Bleaching and blinking phenomena at the single molecule level

Under continuous illumination, a single FP molecule blinks, meaning that it displays a stochastic behavior between bright (fluorescent) and dark (non-fluorescent) states. In 2000, the authors of an experiment (Garcia-Parajo *et al.* 2000) described how single molecules of GFP were embedded in a gel and submitted to a strong continuous illumination (14 kW/cm²), which provoked the blinking of the molecules between bright and dark states. The average time of residence in the dark state (time gap between two consecutive photon bursts) was 1.6 s, which was much longer than both the average time in which the proteins are in the bright state (80 ms) and the reported GFP triplet state lifetime of 25-30 µs (Haupts *et al.* 1998; Jimenez-Banzo *et al.* 2008). However, the authors calculated a quantum yield for the transition to the dark state of 0.5×10^{-5}, which fits with the values generally found for photobleaching quantum yields between 10^{-5} and 10^{-6} (Griesbeck *et al.* 2001), which is about ten times higher than values reported for organic dyes such as coumarin (Peterman *et al.* 1999). The blinking phenomenon, thus, had to involve something else than simple crossing to the triplet state. We can propose that several pathways are possible after the excitation of a fluorescent protein to the triplet state and that, if one of them can be the direct photodestruction of the chromophore (photobleaching), another way can be attributed to phenomena such as photoisomerizations described in the previous chapter.

If the phenomena of photobleaching, photoisomerization and photoconversion are difficult to understand and distinguish in a bulk sample made of many molecules, they pose major problems of interpretation in single-molecule experiments. Part of the molecules that are considered to be photobleached could be infact only switched to a dark state during a long time

and we can propose that the higher sensibility to photobleaching for fluorescent proteins compared to organic dyes can be partially attributed to supplementary phenomena such as photoisomerizations. The more flexible structure of FPs chromophores compared to the robust architecture of most organic dyes may indeed involve photoisomerization processes and in the short timescales of microscopy experiments, the two processes (photoisomerization and photobleaching) would both appear as irreversible effects.

4 - Perspectives

This work proposes an explanation for the mechanism of one possible photobleaching pathway. An important point that can be noticed is that the X-ray structures of FPs obtained by X-ray crystallography using synchrotron sources may be altered by the chromophoric distortions described in the results and resulting in slightly overbent geometries of the chromophores.

Although being comforted by several evidences such as similar macroscopic aspects of PAFPs exposed to X-rays and UV/Vis light or similar Raman spectra between the protein exposed to visible light and X-irradiation, missing information have still to be obtained. In particular, we still have to make efforts to find a proper setup allowing obtaining the structure of IrisFP bleached by visible light. These experiments will undoubtedly guide us toward a better comprehension of photobleaching and toward the design of more stable and photoresistant mutants.

III. MATERIAL & METHODS

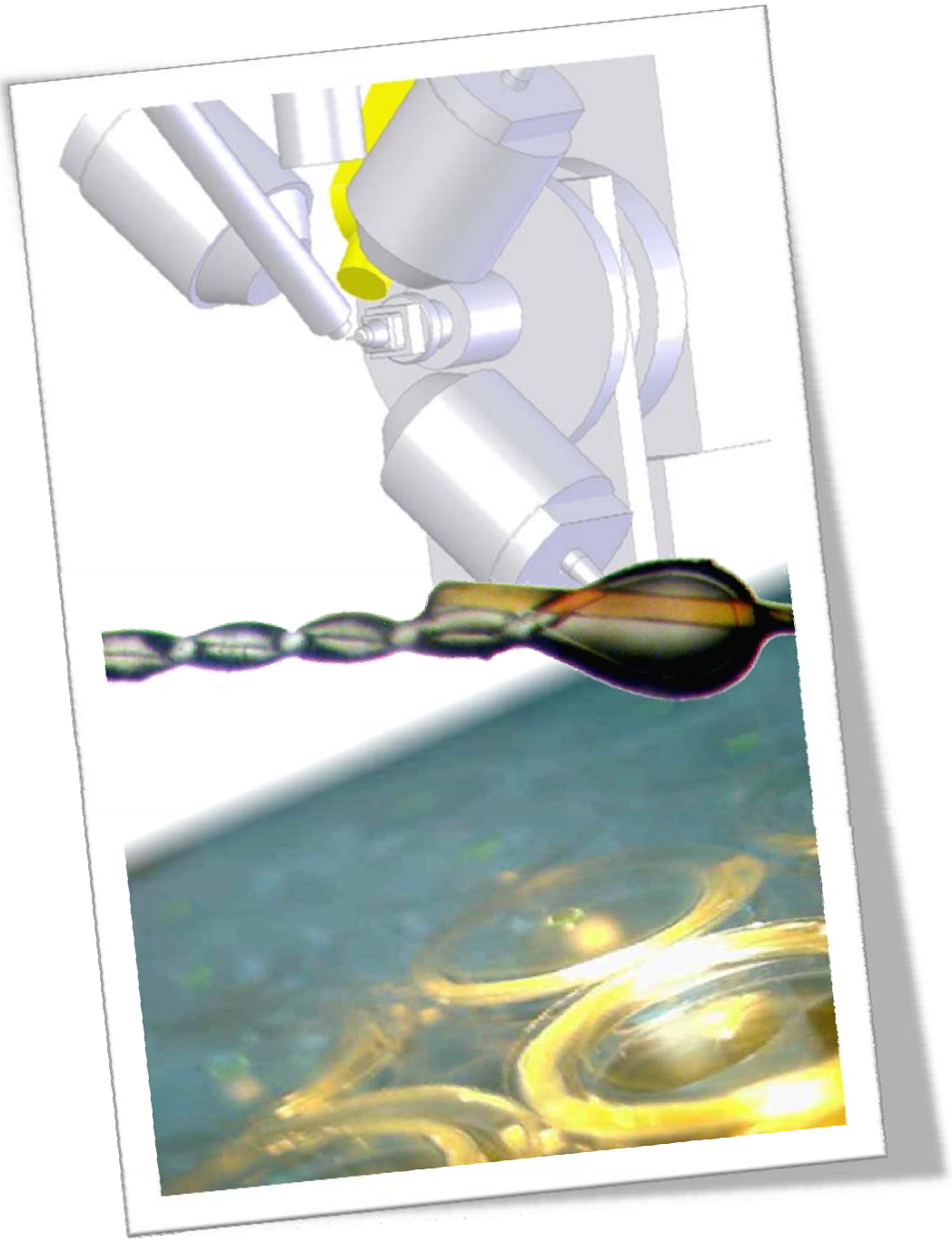

The illustration represents a collage of a sketch representing the Cryobench microspectrophotometer, a nylon microloop holding a crystal of IrisFP and a zoom on the surface of a crystallization tray containing drops of EosFP

Chapter 1 - Crystallogenesis and crystallography

Résumé en français

Dans ce chapitre, les notions de cristal et de cristallisation sont définies. Plusieurs méthodes sont abordées : diffusion de vapeur en goutte suspendue, technique d'ensemencement ou encore différence entre cristallisation manuelle ou automatique.

Le détail des protocoles de cristallisation de plusieurs protéines est donné : Dendra2, d1EosFP, mEosFP et IrisFP.

Les notions basiques de cristallographie des rayons X sont également rappelées dans ce chapitre ainsi que celles permettant le calcul de cartes de densité électronique et le traitement de données de diffraction.

Part 1 - Principle of crystallogenesis and crystal growth

1 - Definition of a crystal

CRYSTALS (from the Greek word κρυσταλος [krystallos] meaning ice; Figure III.1.1, a) are objects that form in a solid phase with a geometry defined by one of the 230 space groups belonging to one of the 7 crystal systems (orthorhombic, cubic...) itemized in the International Tables for Crystallography[22] and sorted according to the symmetry complexity. These objects are constituted by a series of smaller and identical units called unit cells (Figure III.1.1, b) that are aligned along one axis (1D crystal), two axes (2D crystal) or three axes (3D crystal), forming a lattice. Unit cells contain a defined number of subunits called asymmetric units, according to the space group crystals belong to, from 1 for the most simple space group P1 to 96 for the most complicated space group Ia3d). Asymmetric units are linked by symmetry relations. Molecules are not linked by any symmetric relations imposed by the crystal inside the asymmetric units (Figure III.1.1, c). Because proteins are chiral molecules, they will only crystallize in one of the 65 space groups having no symmetry planes

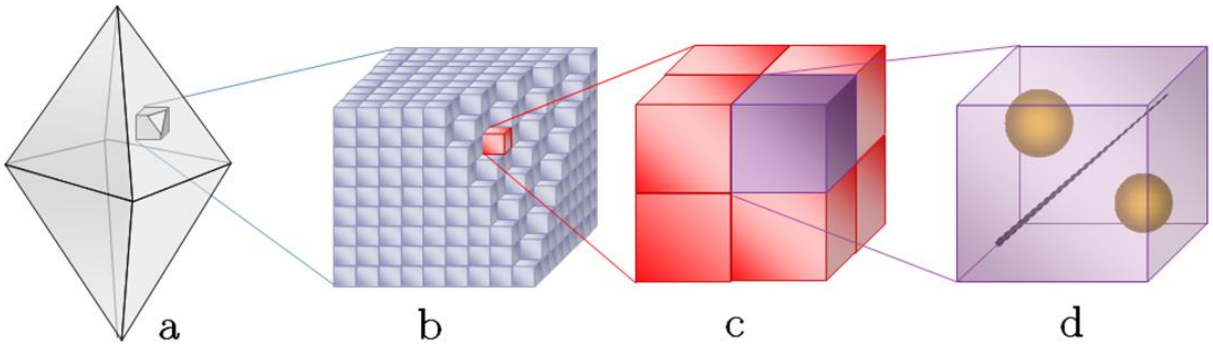

Figure III.1.1 - Representation of a crystal (a) made of unit cells (b). Each unit cell is constituted of asymmetric units (c, purple) and each asymmetric unit contains one or several molecules (d, spheres) that can be related by a non-crystallographic symmetry axis (dashed line)

The asymmetric units contain a certain number of entities (proteins for a protein crystal) that can be related by endogenous symmetry via some so-called non crystallographic symmetry (NCS) axis (Figure III.1.1, d). These molecules usually mostly behave like they would do in

[22] Edited by the International Union of Crystallography (IUCr), http://it.iucr.org

solution, but this is not always the case since some crystal contacts can be formed with adjacent symmetric entities

2 - Protein crystal growth

The principle of protein crystal growth is based on the fact that one should slowly push the protein solution to its solubility limit, gently enough so that the solution does not violently precipitate. In a small region of crystallization, the protein molecules helped by precipitating agents (polymers, salts...) start being close enough to each other so that they minimize their energy by adopting the same orientation, forming a crystal. This change of phase from liquid (solution) to solid (crystal) can be represented by a solubility diagram that represents the evolution of a protein solution at a given concentration according to the concentration in precipitating agents (Figure III.1.2) with initial and final concentrations depending on each particular protein.

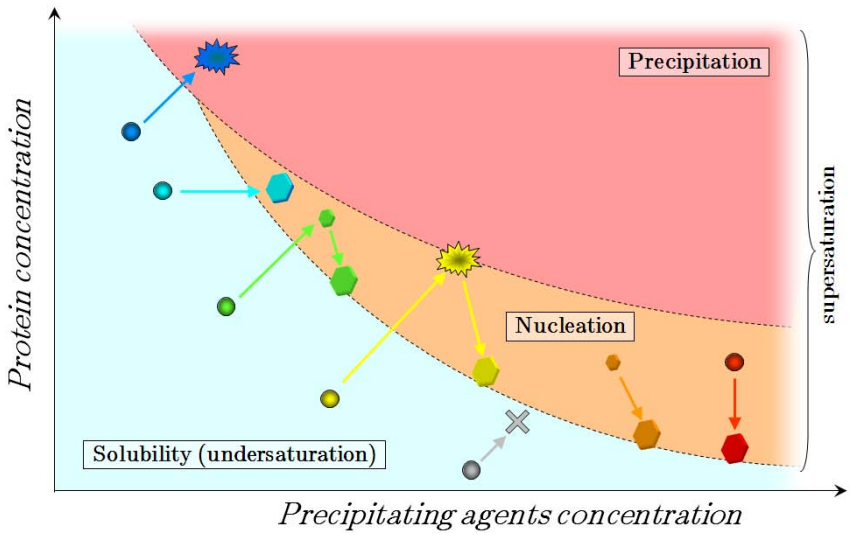

Figure III.1.2 - Simplified solubility diagram showing the possible consequences of crystallization trials.

Precipitation (blue), dialysis (cyan), crystal growth in vapor diffusion (green), crystal growth after partial precipitation (yellow), solubility (grey), crystal seeding (orange) and batch crystallization (red) are represented

Several techniques exist to achieve protein crystallization (dialysis, batch...) but the most common is the so-called vapor diffusion technique that was mainly used in this work.

a - Vapor diffusion technique

Although there are several different methods of crystallization by vapor diffusion, such as the sitting drop method, all the crystals that were obtained during this thesis were obtained thanks to the hanging drop method.

In this method, a well (element of a crystallization tray) is partially filled with a solution of precipitating agents (well solution). A microliter-size drop is made by mixing protein solution with the well solution in a ratio that is usually 1:1 (e.g. 2µL+2µL) but that can vary according to desired conditions. This drop is deposited onto a siliconized glass cover slide that is turned around and used as a lid for the well. The airtightness is ensured with grease (or rubber for models of cover slides that can be screwed on wells). Because the well is closed, it forms an isolated reactor in which the drop contains a less concentrated solution of precipitating agents than the well solution. Since these two solutions are separated by air, the only way for them to equilibrate is that a vapor diffusion occurs from the drop to the well solution (Figure III.1.3).

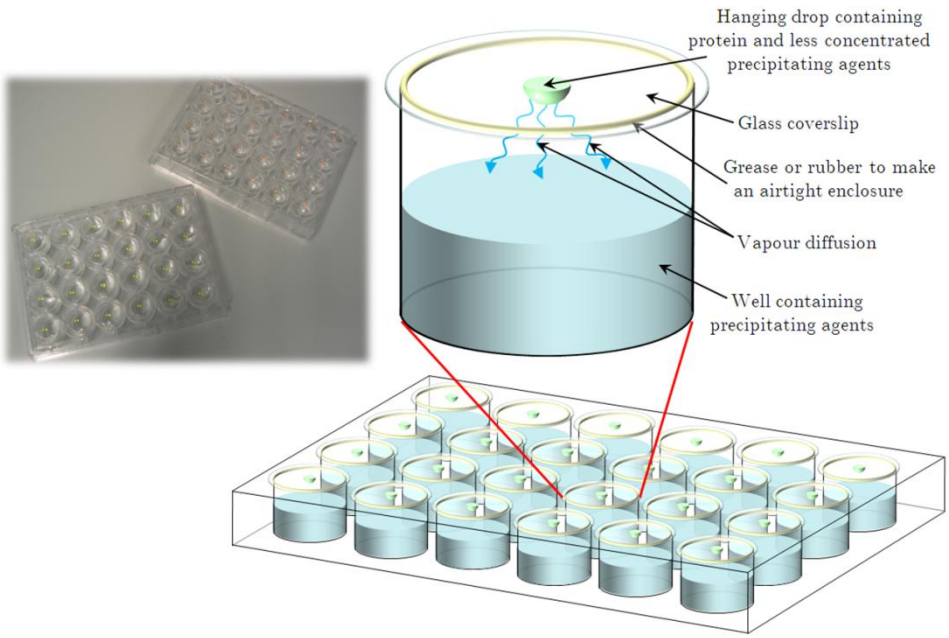

Figure III.1.3 - Photograph of two (Linbro) crystallization trays containing drops of green and red IrisFP (left) and drawing of a 24-well Linbro tray with the detail of a single well (right)

The drop is thus slowly drying, and during this process, the protein molecules get closer to each other, and helped by precipitating agents, may hopefully form a crystal.

b - Streak seeding technique

The first step of the crystallization process is the nucleation. This step is rather slow to occur since the initial components must order into the correct orientation by themselves, while they all are in solution, and form the nucleus. All the heterogeneous components (impurities) may interfere, slow down or even prevent this fragile step. The second step, the crystal growth, is much more rapid since the nucleus is already established and "helps" the other molecules to form a new layer.

In the case of non-reproducible crystals, the seeding technique can help in providing microscopic bits of a crushed crystal (seeds) to a drop already equilibrated in order to facilitate the crystallization.

The streak seeding method (Stura 1999) consists in crushing a crystal (usually of a too low quality) by vortexing it in a few drops of mother liquor thanks to a modified Eppendorf tube containing a hard plastic bead (Figure III.1.4,a). The obtained "seeds" can then be "sown" in a crystallization drop using a tool made from a wand, a pipette tip and a cat whisker (Figure III.1.4,b). The cat whisker is sufficiently rough to retain the seeds when plunged into the tube and to dispense them all along the drop.

a

b

Figure III.1.4 - Tools used to prepare a crystallization experiment by the streak seeding technique
a - tube containing a plastic bead to crush the crystals
b - cat whisker to sow the crystal seeds

3 - Manual and automatic crystallizations

Recently, the developments in high throughput crystallization allowed the installation of two robots, a Cartesian PyxSys 4200™ (Genomic Solutions®, Ann Arbor, USA) located at the Carl-Ivar Bränden Building (CIBB, Grenoble)[23] allowing the preparation of drops with volumes down to 200 nL and a Tecan Genesis™ (Tecan®, Männedorf, Switzerland) located at the Institut de Biologie Structurale (IBS, Grenoble)[24] allowing the preparation of drops with volumes of 1-2 µL. The robots allow the quick test of thousands of crystallization conditions by mixing in small drops the protein with chemicals that are known to usually give a high rate of success and that are available in commercial kits.

At the difference of manual crystallization trials, the drops are not set in Linbro trays that allow to test 24 conditions per tray, but in Greiner trays that allow to pour up to three tiny drops per well (for three different protein concentrations for example) and contain 96 wells, for a total of 288 potential conditions tested per tray in ~20 mn.

All the manual crystallization trials presented in this thesis have been performed in Linbro crystallization trays at the Carl-Ivar Bränden Building (CIBB, Grenoble), Partnership for Structural Biology (PSB, Grenoble). For systematic refinement around a precise condition, some crystallization trials have been performed in Greiner crystallization trays by the crystallization robot located at the Institut de Biologie Structurale (IBS, Grenoble).

[23] http://www-db.embl.de/jss/EmblGroupsGR/g˙241.html

[24] http://robocrist.ibs.fr

Part 2 - Crystallization of proteins presented in this thesis

1 - Crystallization of Dendra2

a - First trials: all that glitters is not gold

The first crystallization trials of Dendra2 were led with a rough high-throughput method. The Tecan crystallization robot of the IBS crystallization platform[25] operated by Delphine Blot. This robot uses Greiner® crystallization trays with sitting drops. Fifteen crystallization screening kits were tested: five crystal screens™ from Hampton research® (I, II, Lite, PEG-Ion and Ammonium Sulfate), eight other screens from Hampton research® (Quick Screen, Screen malonate, Screen formate, PEG 6K, PEG Li-Cl, MPD, MME 5000, Index) and the two wizard screens™ from Emerald Biosystems®. These kits represent 576 different conditions that were tested at three different concentrations of Dendra2: 17, 20 and 23 mg/mL, representing a total of 1728 conditions. The experiments showed several interesting results represented in Figure III.1.5, such as spherulites (a), plate-like crystals (b, e) or needle-shape crystals (c, d, f).

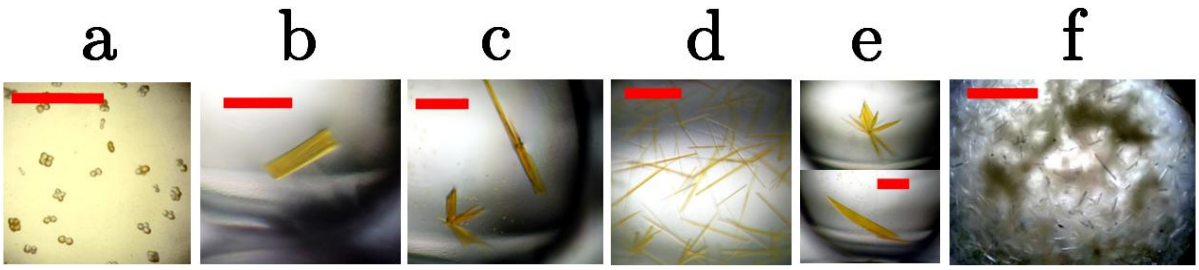

Figure III.1.5 - Some of the first crystallization results obtained for Dendra2. Conditions: (a): 20% PEG 6000, 1 M lithium chloride, 0.1 M Tris pH 8.0 / (b): 0.2 M calcium acetate, 20% PEG 3350, pH 7.5 / (c): 25% PEG 3350, Tris pH 8.5 / (d): 65% MPD, 0.1 M bicine pH 9.0 / (e): 0.2 M magnesium chloride, 25% PEG 3350, 0.1 M HEPES pH 7.5 / (f): 0.26 M magnesium sulfate, 30% PEG 4000. The red scales represent 200 µm.

One might think that crystals shown in Figure III.1.5 (b to e) were nice enough to get a structure... unfortunately, all that glitters is not gold and these crystals displayed low

[25] http://www.ibs.fr/content/ibs˙eng/presentation/Platform/plateform˙Xtallo/

resolution and very twinned diffraction patterns. However, based on these first hits, a semi-rational high-throughput crystallization method was adopted in a narrow pH range.

b - Rationalized high throughput crystallization

Preliminary global tests were performed by mixing the protein with a gradient of three different types of precipitating agents alone: either PEG solutions only, or salts solutions only or other precipitants (mostly volatile compounds). More complex tests were also made by mixing the protein with a combination of two or three of these agents. The tests are summarized in Figure III.1.6 (left) and revealed that while drops containing the protein mixed with only salt or PEG or volatile compounds remained clear, and while the mixing of salts or PEG with volatile compounds mainly formed precipitants, only the combination of salts with PEG gave interesting hits.

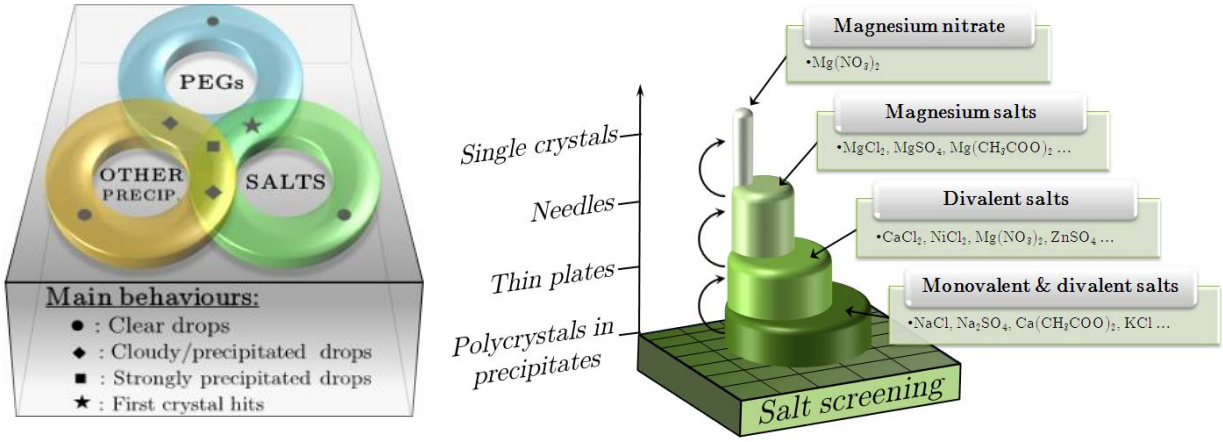

Figure III.1.6 - First screenings used to determine the main crystallizing agents for Dendra2

On the basis of these results, a salt screen (Hampton Research® StockOptions™ Salt-Screen ref. HR2 245) containing 48 different salt types at two different concentrations corresponding to their use as additives, was tested on 288 drops consisting of 96 identical pre-equilibrated drops at three different protein concentrations mixed with the most promising PEG size and concentration. Those 288 conditions were also made using the IBS high-throughput crystallization robot. Those conditions were all different from each other but covered a quite

narrow field of tests in which the salt type was the major variable. This salt screening clearly showed (Figure III.1.6, right) that divalent salts gave better hits than monovalent salts. Among those divalent salts magnesium salts were better and among the latter, magnesium nitrate gave the most promising hits.

A sparse-matrix crystallization method was used to widely scan the pre-selected conditions and find a narrower range of conditions allowing to grow bigger crystals. This sparse-matrix was made of conditions varying in pH, concentrations of magnesium nitrate and PEG 4000 (Figure III.1.6). Very promising hits were quickly found between 30 and 36% PEG as precipitating agent, pH 8.4 to 9.0 and 0.025 to 0.175 M magnesium nitrate as additive. A second matrix was thus made around those conditions with PEG 4000 and PEG 3350, which proved to work better.

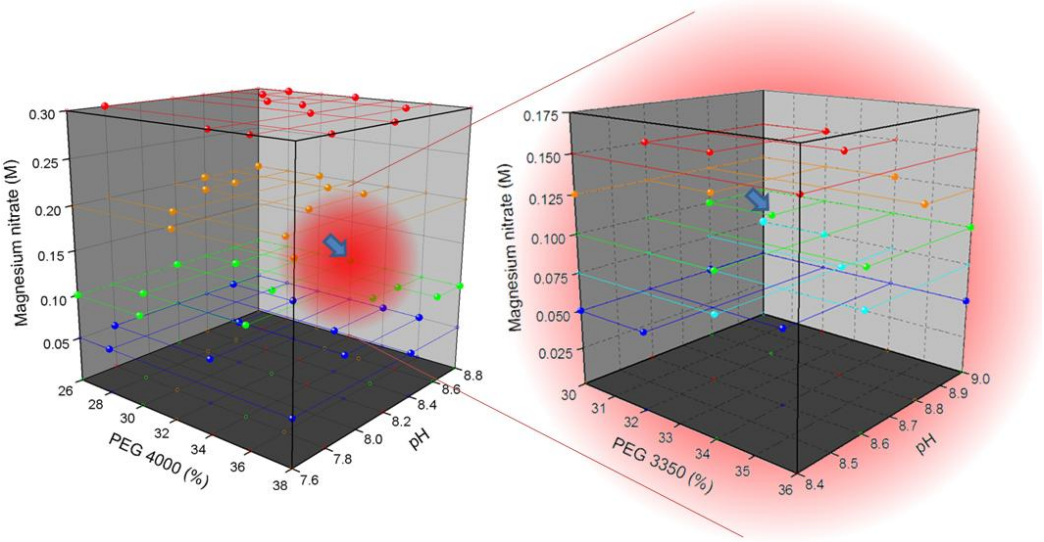

Figure III.1.7 - Sparse-Matrix crystallization of Dendra2. A wide matrix (left) gave rise to some interesting hits (red halo) that were screened in a more restricted matrix (right) to find the crystallization condition (right, blue arrow)

The best hit, in those two subsequent sparse matrices, was found by manually mixing in drops of 2µL+2µL a purified solution of Dendra2 at 17.4 mg/mL with a solution containing 32% PEG 3350, 0.1 M magnesium nitrate, 0.1 M Tris-HCl pH 8.8, using the hanging-drop vapor-diffusion method (cf. Material and methods p.199). A few crystals could be obtained but unfortunately they were too small for X-ray data collections and to be handled easily (Figure

II.1.12, a). Also unfortunately, there was no more protein from the batch used to obtain those crystals and another batch had to be used to upscale the crystallization. When the crystallization was tried with drops of bigger size, no crystals appeared at all but all the protein strongly precipitated. A highly loaded SDS-PAGE of the protein coming from the old batch and the new batch revealed an impurity (in addition to weaker impurities) in the new batch that was not present in the previous one (Figure III.1.8)

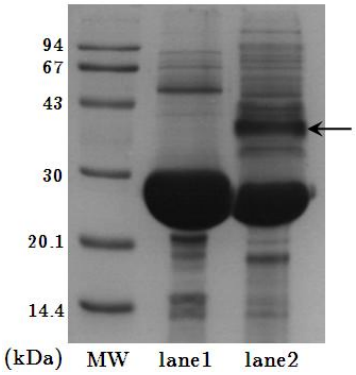

Figure III.1.8 - Low molecular weight SDS-PAGE (15% acrylamide) showing two batches of Dendra2

Lane 1: batch of Dendra2 that gave microcrystals in nitrate magnesium
Lane 2: batch of Dendra2 that failed to give any crystal

We can notice a contaminant (arrow) at ≅40kDa on lane 2

c - Repurification of Dendra2

The impurity described above being the only obvious difference between the two batches, a new purification step was carried out. A Superdex 200 gel filtration column was used to separate the potential contaminant from Dendra2 while the conductivity and absorbance at 280 nm (all proteins), 390 nm and 490 nm (specific of Dendra2) were measured. Fractions of the outflow of this column were analyzed by migration on a SDS-PAGE (Figure III.1.9).

This experiment allowed seeing a gap between the absorbances specific of Dendra2 and the absorbance at 280 nm and corresponding to a band at higher molecular weight than Dendra2. After these fractions, the protein got out of the column and was followed by strange fractions where a band corresponding to the weight of Dendra2 could be detected but the solution only absorbed at 280 nm, as if the chromophore was altered and did not absorb at its specific wavelengths in these fractions. Only the fractions forming the main peak were gathered in a single batch.

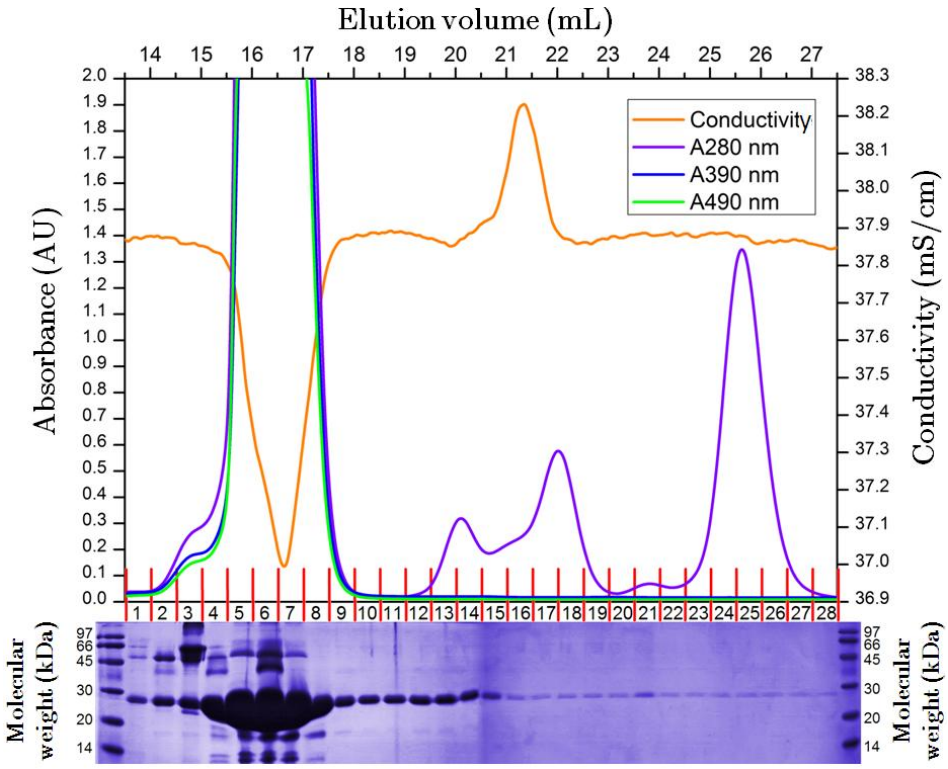

Figure III.1.9 - Re-purification of Dendra2. A chromatogram (up) and the corresponding SDS-PAGE (bottom) for the outflow of a Superdex column are represented

d - Streak seeding

The batch of re-purified protein was used to set new crystallization drops. However, those crystals were still too small to give a suitable diffraction pattern, even on the microfocus beamline ID23-2 (Figure II.1.12, b). Thus, they were crushed and the microscopic resulting seeds were sowed into pre-equilibrated crystallization drops at 20°C containing a solution of 32% PEG 3350, 0.1 M magnesium nitrate, 0.1 M Tris-HCl pH 8.8 and the solution of both Dendra2 before and after the purification described above, using the streak seeding method (cf. Material and methods, p.200). Only in drops containing Dendra2 re-purified, rare single crystals grew after several weeks, of which only two were suitable for X-ray data collection (Figure II.1.12, c). For low-temperature measurements, these crystals were rapidly transferred to a cryoprotectant solution made of the crystallization solution added with 10% glycerol (v/v) before being flash-frozen in gaseous nitrogen at 100 K (Table II.1.3).

2 - Crystallization of EosFP-V123T (d1EosFP)

Crystals of dimeric EosFP have been obtained using the hanging-drop vapor-diffusion method by mixing at a ratio 1:1 a protein solution at 10.3 mg/mL with a crystallizing solution containing 2.2 M ammonium sulphate, 0.1 M Bicine pH 8.6 (Table III.1.12). The final solution contains the addition of 10% glycerol, which allowed obtaining much bigger crystals and avoiding the use of cryoprotectant for X-ray data collections.

3 - Crystallization of EosFP-V123T/T158H (mEosFP)

Crystals of monomeric EosFP have been obtained using the hanging-drop vapor-diffusion method by mixing at a ratio 1:1 a protein solution at 9.2 mg/mL with a crystallizing solution containing 2.2 M ammonium sulphate, 0.1 M Tris/HCl pH 8.5 (Table III.1.12).

Crystal parameters and data collection statistics		
Protein	**mEosFP**	**d1EosFP**
Crystallization		
Crystallization conditions	2.2 M ammonium sulfate, 0.1 M Tris/HCl pH 8.5	2.2 M ammonium sulfate, 0.1 M Bicine pH 8.6, 10% glycerol
Initial protein concentration (mg/mL)	9.2	10.3
Protein:precipitant ratio	1:1	1:1
Cryoprotectant	10% glycerol	none
Content of the unit cell		
Space group	P $2_12_12_1$	P $2_12_12_1$
Cell dimensions		
a; *b*; *c*, Å	86.45; 96.82; 140.43	86.10; 96.71; 140.87
α; β; γ, °	90; 90; 90	90; 90; 90
Solvent content, %	56.31	56.41
Monomers/asymmetric unit	4	4

Table III.1.12 - Crystallization data for monomeric and dimeric variants of EosFP

4 - Crystallization of EosFP-F173S (IrisFP)

We could crystallize the protein EosFP-F173S based on the results obtained for mEosFP and d1EosFP. Crystals were grown at 20°C in 2.4 M ammonium sulfate, 0.1 M Bicine (pH 8.4), using the hanging-drop vapor-diffusion method. Rod-shaped crystals appeared within 24 h and reached their final size of (0.2 x 0.2 x 0.8) μm^3 within a few days. For low-temperature

measurements, crystals were rapidly transferred to a cryoprotectant solution [10% glycerol/2.4 M ammonium sulfate/0.1 M Bicine (pH 8.4)] before being flash-frozen in liquid or gaseous nitrogen at 100 K.

Part 3 - Crystallography and data collection

1 - Basics of X-ray diffraction

X-ray crystallography is a technique allowing to obtain the 3D structure of compounds forming crystalline arrangements at a near-atomic resolution. Such a resolution can currently only be reached by X-ray diffraction, nuclear magnetic resonance (NMR) and neutron diffraction. When exposing a crystal to X-ray radiation, the interaction of the X-ray beam with the crystalline lattice leads to the diffusion of the X-rays, whose constructive and destructive interferences will give rise to the phenomenon of diffraction. These rays are detected thanks to special CCD detectors, forming patterns of spots whose intensity and position are due to diffraction rules (Figure III.1.10).

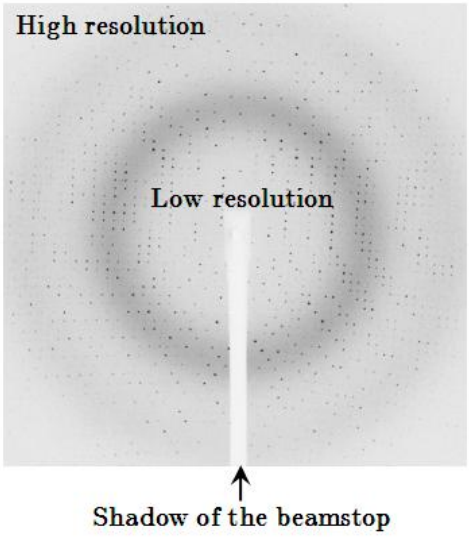

Figure III.1.10 - An example of diffraction pattern obtained at the ESRF beamline ID14-4

The analysis of such diffraction patterns allow the calculation and reconstruction of the repetitive elements (molecules) that diffracted the excitation wave. Nowadays, such experiments are usually performed using monochromatic X-ray wavelengths to simplify the analysis, since the distance that can be measured between two crystal planes is directly proportional to the incident wavelength (Equation III.1). It is also possible to use polychromatic X-ray radiation (Laue crystallography), which allows the requirement of much

shorter data collection times but makes the analysis much more difficult. Since macromolecules are weak objects, X-ray diffraction experiments are mostly performed under low temperature conditions (cryocrystallography), which helps in reducing the radiation damage that can be important when synchrotron sources are used.

When exposing a crystal to X-rays, the electrons of the atoms contained in the crystal will interact coherently with X-rays, diffracting them in precise directions whose angular position can be defined by the Bragg's law:

$$2d_{hkl} \sin \vartheta_B = n\lambda$$

Equation III.1

Where ϑ_B is the scattering (Bragg) angle, *h,k,l* are the Miller indices, λ is the X-ray wavelength and d_{hkl} is the distance between two neighboring planes of the crystal lattice.

In order to determine which lattice planes will give rise to a diffracted signal for a given incident wavelength, one uses the Ewald sphere of reflections. When planes are oriented such as they respect the Bragg condition, the reciprocal lattices intersect the Ewald sphere, whose radius is determined by the inverse of the incident wavelength ($1/\lambda$), and diffraction spots (of coordinates *h,k,l*) appear on the detector plane. The center of this sphere is the source of diffraction (crystal). The intersection of the direct beam with the Ewald sphere defines the origin of a second sphere called "limiting sphere". This second sphere, whose radius is determined by the inverse of the crystal diffraction limit ($1/D_{max}$), has its center that is the origin of the reciprocal space (Figure III.1.11).

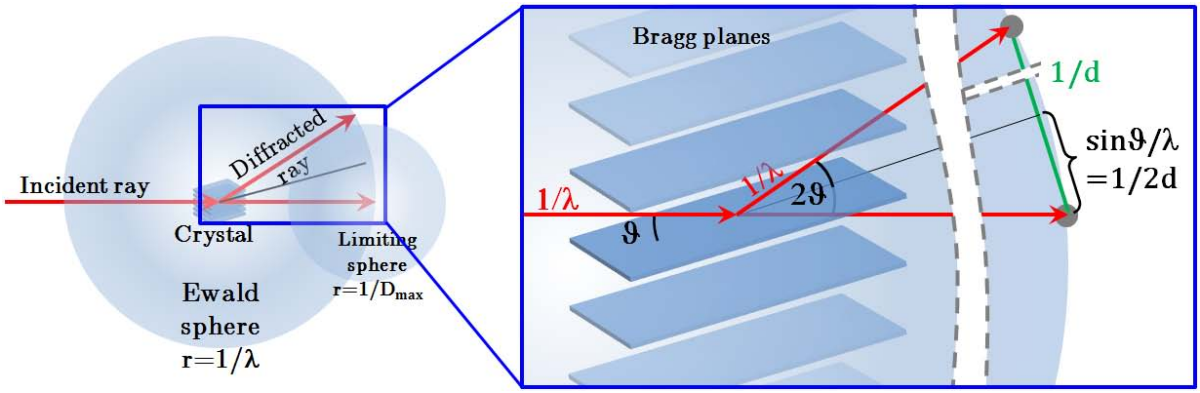

Figure III.1.11 - The Ewald sphere, the limiting sphere and the diffraction condition

The data processing of diffraction patterns is made of several steps : indexation, integration, scaling and calculation of the electron density maps. From then, it is possible to refine the structure so that the model fits correctly in the densities. The indexation step allows the determination of the spacegroup by measuring vectors between diffraction spots (reflections). The integration step allows the measurement of the intensity of diffraction spots. These intensities are scaled, taking into account symmetry-related reflections and redundancy. From this, the structure factors F_{hkl} for each reflection can be calculated since the intensity of the diffraction spots I_{hkl} is proportional to the square of the modulus of the structure factors ($I_{hkl} \propto |F_{hkl}|^2$).

2 - Calculation of electron density maps and refinement

a - Structure factors

For a given crystal lattice, it is possible to define a reciprocal lattice whose unit vectors are:

$$Q_{1=\frac{2\pi}{V}a_2\times a_3}\ ,\ Q_{2=\frac{2\pi}{V}a_3\times a_1}\ ,\ Q_{3=\frac{2\pi}{V}a_1\times a_2}$$

Equation III.2

Where $V = a_2 \cdot [a_2 \times a_3]$ is the unit cell volume.

In a periodic arrangement such as a crystal, for each unit cell of volume V, the electron density of real space coordinates (x,y,z) can be expressed with the following Fourier sum thanks to the structure factors F_{hkl} , the phase ϕ_{hkl} and considering the reciprocal space coordinates (h,k,l):

$$\rho(xyz) = \frac{1}{V}\sum_{h}\sum_{k}\sum_{l} F_{hkl}\, e^{[-2\pi i(hx+ky+lz)+i.\phi_{hkl}]}$$

Equation III.3

The structure factors F_{hkl} can be obtained by integrating all the atomic scattering factors (reverse Fourier transforms) f_j of atoms $j=1...N$ so that:

$$F_{hkl} = \sum_{j=1}^{N} f_j(hkl)e^{[-2\pi i(hx_j+ky_j+lz_j)+i.\phi_{hkl}]} \rightarrow \int_{V} \rho i(xyz)e^{[-2\pi i(hx+ky+lz)+i.\phi_{hkl}]}\, dV$$

Equation III.4

Each reflection (*i.e.* diffraction spot) has coordinates h,k,l in the reciprocal space with particular intensities $I_{(hkl)}$ that one can measure by integrating the volume of each reflection (3D peaks) on each diffraction pattern. The integration of Equation III.3 and Equation III.4 on each unit cell, gives the electron density for each coordinates (x,y,z) in the real space corresponding to each coordinates (h,k,l) in the reciprocal space.

b - Molecular replacement

The phase ϕ_{hkl} cannot be directly measured by diffraction experiments and should be found by other methods such as the SAD, MAD, SIR or MIR techniques that use heavy atoms. However, since these methods were not used during this thesis, they will not be explained here. The phase problem was solved by molecular replacement, which is a method that can generally be used when a 3D structure already solved by afore-mentioned methods, displays more than

25% sequence identity with the protein of interest. In reality the sequence identity is less important than a similar structural folding but since for fluorescent proteins overall structures are always very similar, the molecular replacement is a method of choice. This method consists in determining the correct matrix of orientation (rotation and translation) between the search model and the diffraction data. The phase can then be obtained although it is a bit biased by that of the search model.

c - Refinement and R-factors

During the refinement of a structure, the measured dataset has a set of (observed) structure factors $F_{obs}(h,k,l)$ and their corresponding electron density $\rho_{obs}(x,y,z)$; but the model also brings its own (calculated) structure factors $F_{calc}(h,k,l)$ and so its own electron density $\rho_{calc}(x,y,z)$. A good way to follow the correctness of this refinement is to measure R_{cryst}, the correlation R-factor comparing the observed and calculated structure factors:

$$R_{cryst} = \frac{\sum_{hkl} |F_{obs} - F_{calc}|}{\sum_{hkl} |F_{obs}|}$$

Equation III.5

All along the refinement process, the gap between the observed and calculated structure factors must be, of course, minimized (and the R_{cryst} should decrease) for the model to fit with the measured dataset.

However, by trying to decrease the value of this R-factor, the risk is to produce overfitting, resulting in loss of accuracy of the model. To avoid that, another R-factor has been introduced in 1992 (Brunger 1992) as a routine method to cross-validate the quality of the fit. This R-factor is called R_{free} and its calculation (Equation III.) is performed similarly to the one of the

R_{cryst} factor but it is calculated on a test set of reflections (typically 5 to 10%) that are omitted from the refinement process. These reflections are thus not biased by the refinement and the decrease of both the R_{cryst} and R_{free} values during this process is a sign of good agreement between the data and the model.

$$R_{free} = \frac{\sum_{hkl \subset T} \left| F_{obs} - F_{calc} \right|}{\sum_{hkl \subset T} F_{obs}}$$

Equation III.6

T represents the small fraction of reflections randomly excluded from the refinement process to be part of the test group.

Since these excluded reflections are not biased by the model, the value of the R_{free} factor is higher, and must be higher, than the R_{cryst} value (by a typical order of about 5%)

d - Fourier electron density map and electron density difference maps

In the real space, the difference between the observed and the calculated electron densities is given by:

$$\rho_{obs}(x,y,z) - \rho_{calc}(x,y,z) = \int_{hkl} F_{obs}\, e^{ihr} - \int_{hkl} F_{calc}\, e^{ihr} = \int_{hkl} (F_{obs} - F_{calc})\, e^{ihr}$$

Equation III.7

The representation of the electron density map corresponding to $F_{obs}(h,k,l) + [F_{obs}(h,k,l) - F_{calc}(h,k,l)] = \boxed{2F_{obs}(h,k,l) - F_{calc}(h,k,l)}$ allows the observation of the probability of presence for electrons at a certain threshold. Such a map is generally called Fourier electron density map and is often labeled "$2F_o$ -F_c map".

The representation of the electron density map corresponding to $\boxed{F_{obs}(h,k,l) - F_{calc}(h,k,l)}$ allows the observation of the differences between the model and the measured data. As a consequence, if something is modeled where there is no real density, $F_{obs}(h,k,l) < F_{calc}(h,k,l)$

and a negative density blob appears. At the opposite, if nothing is modeled where there is actually a density, $F_{calc}(h,k,l) < F_{obs}(h,k,l)$ and a positive density blob appears. Such maps are generally called electron density difference maps and are often labeled "F_o -F_c maps".

One of the specificities of this thesis work is to use F'_{obs} -F_{obs} electron density difference maps. The interest of such maps compared to the above-mentioned F_{obs} -F_{calc} difference maps is their very high sensitivity to tiny electron movements between two data sets having observed structure factors F'_{obs} and F_{obs}, respectively. The calculated structure factors F_{calc} being omitted from the calculation of these maps, they are not biased by the model and only electronic differences between the observed data of the two data sets that are compared are observed.

The calculation of these maps is not a routine process and is reserved for cases in which very slight differences between two sets of data are required to be observed, or when only a small fraction of the molecules contained in one of the two samples exhibit a change compared to the other one. We used F'_{obs} -F_{obs} maps during this thesis work especially for the studies about photobleaching because we estimated that only 20% of the molecules exhibited the described distortion of their chromophore and because this distortion was fine.

In order to enhance the signal/noise level of difference densities, a process allowing the weighting of the structure-factors amplitude differences originally developed for the treatment of weak and/or spatially overlapped time-resolved Laue patterns, can be applied. This technique, called q-weighting (Ursby & Bourgeois 1997; Bourgeois 1999) allows to make more evident the actual differences compared to densities that are infact due to noise in the maps.

3 - Softwares used

For all the structures solved and presented in this thesis, the diffraction patterns were indexed and integrated with the XDS program package (Kabsch 1993). When composite datasets were used, the merging of the datasets were made with Pointless. All the data scaling were made with Scala (Evans 2006).

The crystal structures were solved by molecular replacement with Phaser (McCoy 2007), using the coordinates of the green and red forms of EosFP (PDB accession codes 1ZUX and 2BTJ) as search models. Crystallographic refinements were performed with Refmac (Murshudov *et al.* 1997) and Coot (Emsley & Cowtan 2004).

Chapter 2 - The Cryobench laboratory

Résumé en français

Ce chapitre est dédié à la présentation du laboratoire de microspectrophotométrie Cryobench, situé à l'ESRF et où une grande partie des expériences détaillées dans ce volume ont eu lieu. Après une présentation générale du lieu et de l'appareillage, une présentation détaillée est fournie pour les différents modes possibles et utilisés pendant cette thèse: spectroscopie UV/Visible en absorbance et fluorescence, spectroscopie Raman et mesures de temps de vie de fluorescence.

Part 1 - Overview of the facility

PROTEIN X-ray crystallography usually aims at determining the structure of a protein, such as an enzyme, in its resting state, thus yielding only partial information on its mechanism. Proteins are often also active in the crystalline state and reactions can be initiated by a variety of methods, notably making use of light. The study of these reactions directly within crystalline samples is made possible thanks to microspectrophotometers. The first models of spectrophotometers allowing spectroscopic measurements on single protein crystals were designed thirty years ago (Makinen & Fink 1977; Gay & Solomon 1978) and they were used to track spectral changes during time-resolved crystallography experiments (Duke *et al.* 1991; Gouet *et al.* 1996). The development of nitrogen cryostreams, optics and detectors led to the creation of dedicated microspectrophotometers sensitive in the UV/Vis-NIR range, for applications in cryocrystallography (Hadfield & Hajdu 1993; Chen *et al.* 1994; Bourgeois *et al.* 2002; Sakai *et al.* 2002).

The Cryobench[26] is a laboratory located in the ESRF experimental hall (Figure III.2.1) and that allows studying samples by measuring either in solution or directly in a crystalline state the spectroscopic properties of a protein sample. As long as there is enough solvent (which is generally the case for protein crystals) it is possible to initiate reactions in the crystals and follow the reaction pathway by absorbance or fluorescence microspectrophotometry as a function of time or temperature (temperature ramps). With this method, the Cryobench laboratory can be used to detect, and eventually rapidly trap at cryogenic temperatures, reaction intermediate states in the crystal. A protein crystal can be mounted on one of the macromolecular crystallography beamline, the spectroscopic data obtained at the Cryobench laboratory can complement information brought by the structure of the protein, for which the interpretation in the mechanistic role of the protein is often vague. The technique that combines spectroscopic measurements with crystallographic structures made the development of the so-called kinetic crystallography technique easier (Bourgeois & Royant 2005; De la Mora-Rey & Wilmot 2007). For naturally fluorescent proteins for example, it is interesting to observe

[26] http://www.esrf.fr/UsersAndScience/Experiments/MX/Cryobench/

phototransformations induced at controlled temperatures within a crystal and observe the associated structural changes by X-rays diffraction.

The Cryobench microspectrophotometer (Figure III.2.1) is a versatile apparatus that evolved those last years and currently allows the user to measure absorption and/or fluorescence and/or fluorescence lifetime and/or Raman scattering directly in a protein crystal. A single axis goniometer head is installed at the center of three identical objectives (described p. 235) so that light sources from lasers or a deuterium/halogen lamp (DH-2000-BAL, Mikropack GmbH, Ostfildern, Germany) are brought to the mirror-objectives via optical fibers to focus at the loop containing the sample, on a surface of a few µm² (instead of a few mm² for a classical spectrometer).

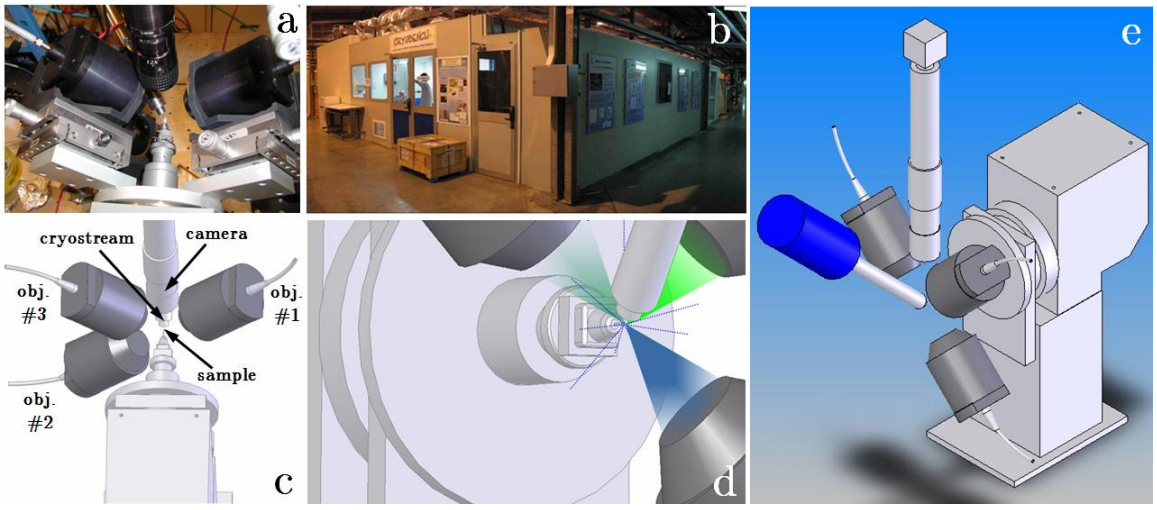

Figure III.2.1 - The Cryobench laboratory. Photograph of the microspectrophotometer (a) located at the Cryobench laboratory (b) and which setup is described (c) as allowing the positioning of a sample at the center of three equivalent objectives (d). A 3D rendering of the apparatus is shown (e)

Two of the objectives are placed face to face for a transmission signal, while the third objective is located at 90° from the two others, allowing fluorescence experiments. One of those objectives sends via an optical fiber the collected signals to a CCD-based spectrometer (HR-2000+, Ocean Optics, Dunedin, USA) where a grating separates the wavelengths. The sample can be kept frozen thanks to a vaporous nitrogen flow, cast by an Oxford cryostream (Oxford Cryosystem Ltd., Oxford, UK) and the sample can be visualized via a videomicroscope.

It is also possible to keep the sample at room temperature by mounting it in a drop kept between two glass coverslides (Figure III.2.14, p.232) or by mounting it in a modified microloop (MicroRT™ from MiTeGen, Ithaca, USA) that can be covered with a very thin-wall transparent polyester tubing (Figure III.2.2, 4).

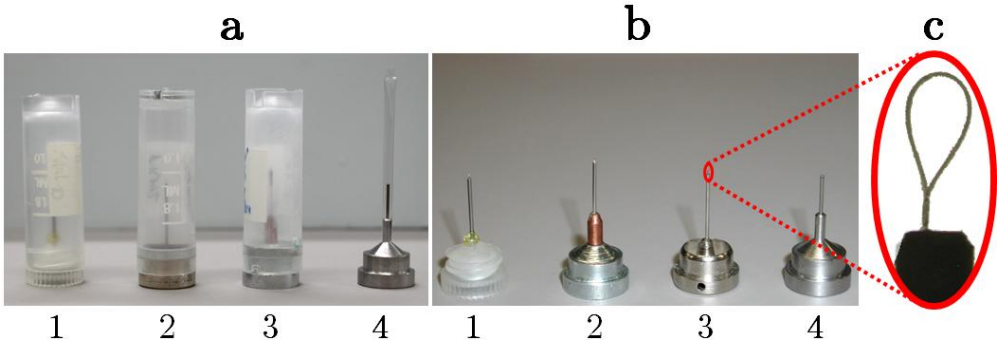

Figure III.2.2 - Different types of microloops for mounting crystals on the Cryobench or beamlines. Loops are shown with (a) and without (b) protective caps. While the cap of number 1 can be screwed, numbers 2 and 3 are maintained by magnets. Number 4 is a loop with a modified base (MicroRT™ from MiTeGen) that can be covered with a polyester capillary to keep crystals wet during room temperature experiments. A microscopic view of a nylon loop is shown in (c)

Several modes of experiments are available at the Cryobench laboratory either for static measurements or after initiation of a reaction, such as for example, a photochemical reaction induced by laser illumination.

Part 2 - The different modes available at the Cryobench

Several types of spectroscopy experiments are possible on the Cryobench microspectrophotometer. The three objectives and the Raman head situated around the sample make this device very versatile. The two objectives that are situated on the same axis can be used for absorption measurements or eventually for fluorescence measurements, using a low pass filter in reception to cut the excitation light. The third objective at 90° from the two others can be used for fluorescence measurements or to photoexcite a sample while its measurement is performed with the other objectives.

1 - Absorbance and fluorescence microspectrophotometries

a - Absorption

Exactly as in a common wet lab, it is possible to take an absorbance spectrum of the studied protein but instead of measuring it in solution in a cuvette (which is also possible at the Cryobench) one can measure it directly in the crystal at any temperature between 100 K and room temperature. To this aim, the two objectives that are placed face to face are used (Figure III.2.3) and the transmitted light is analyzed by the CCD detector.

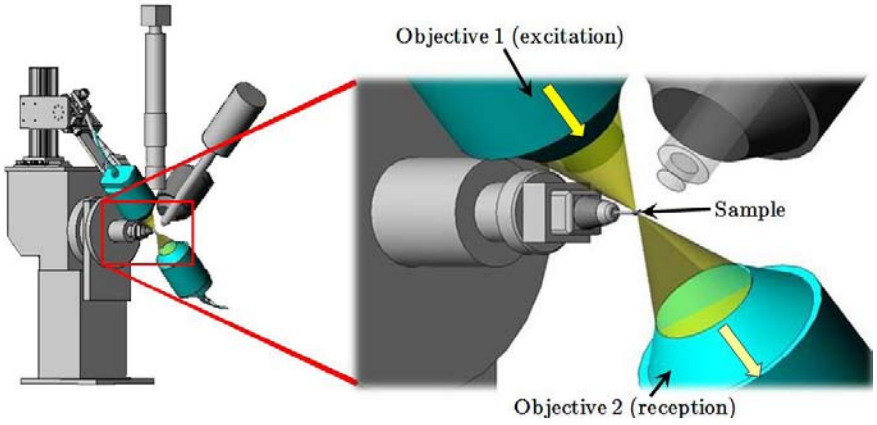

Figure III.2.3 - Sketch of the Cryobench setup for in-crystallo absorption experiments. The nozzle of the nitrogen cryostream is visible in transparency

The absorption spectra are measured thanks to the broadband light sources that cover the whole spectrum from UV to IR. This possibility to study a sample directly in its crystalline state is unique and enables to correlate the modifications occurring within a crystal by spectroscopy and crystallography. The measuring time for an absorption spectrum is typically between 20 ms and a second. A few hindrances have to be noted though: crystals are a very optically dense medium and the rule of Beer-Lambert imposes the use of very crystals with a thin section (optical path) to measure valid absorption spectra.

At most crystal orientations absorbance spectra are completely impossible to measure because no light passes through the sample, due to partial to total reflection of the incident

light on the faces of the crystal. We also observed very often a shifting of a few nanometers of the spectra, depending on the crystal orientation, which is due to the high polarization of molecules in crystalline lattices. A proper orientation has to be found, thus, to be as close as the values obtained in solution.

b - Fluorescence

Fluorescence spectra can also be measured on crystals. This fluorescence is generally induced by lasers, and several lasers covering the whole spectrum from ultraviolet to infrared are available at the Cryobench. It is possible to excite either the endogenous fluorescence of the proteins due to built-in fluorophores or aromatic residues (tryptophanes, tyrosines, chromophores) or exogenous fluorophores (fluorescein, sulforhodamine...) that are soaked in the crystal. Endogenous fluorescence in crystals also allows localizing tiny crystals in cryoloops for crystallographic purposes (Vernede *et al.* 2006). In such cases, the fluorescence signal is generally visualized with the camera or detected at 90° from the excitation (Figure III.2.4).

It is possible, thanks to fluorescence data, to probe several properties of biological samples such as the pH within the crystal, and since some proteins such as the GFPs are naturally highly fluorescent, microspectrofluorometry is a very powerful tool to probe their fundamental properties.

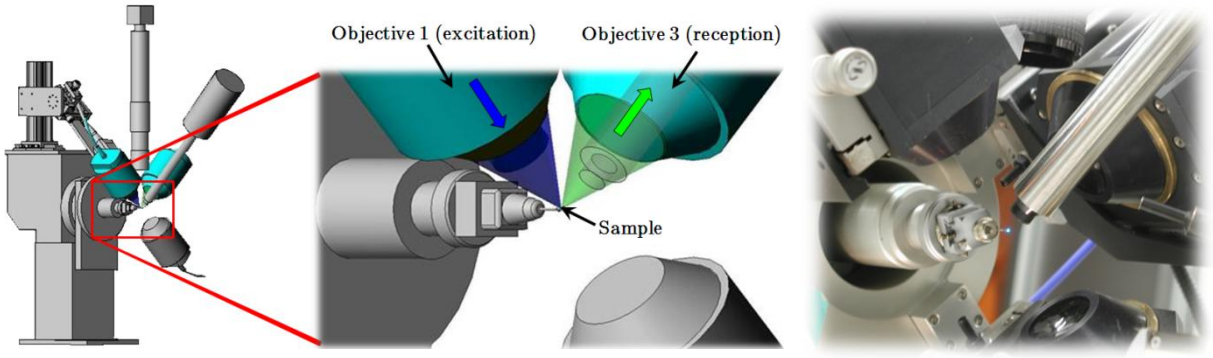

Figure III.2.4 - Sketch of the Cryobench setup for in-crystallo fluorescence experiments (left) and photograph of the real setup with a sample emitting fluorescence (right)

In practice, it is easier to measure a fluorescence spectrum than an absorption spectrum on a crystal at the Cryobench: no baseline correction is required, and the high sensitivity of the microspectrophotometer for photons emitted from the sample allows a measuring time of typically a few milliseconds per spectrum. However, here again, several experimental problems, linked to the study of optically dense samples, can be noted: crystals provoke inner filtering effect so that a part of the emitted light is reabsorbed by the sample, which results in red shifting compared to the measurements performed in diluted solutions. Also, no absolute relation between the measured fluorescence and the concentration is possible.

If the intensity of the fluorescence signal mostly depends on the concentration (which is equivalent to the absorbance) of the fluorescent molecules in very diluted samples, a wider and wider gap in this linearity can be observed with more and more concentrated samples (Figure III.2.5).

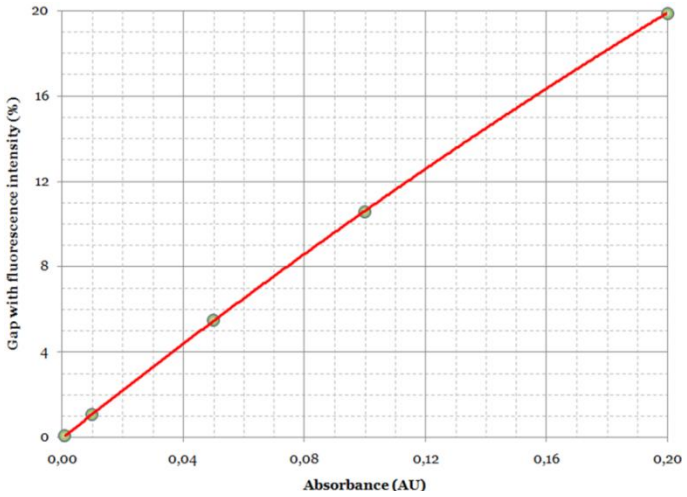

Figure III.2.5 - Increasing gap in the linear relation between the absorbance and the fluorescence intensity of a sample [adapted from (Valeur 2004)]

Consequently, in the case of fluorescent samples in a crystal form (i.e. very concentrated) it is impossible to measure a concentration of fluorophores directly from fluorescence intensity. Even if in practice, it is easier to measure a fluorescence spectrum than an absorption spectrum on crystals at the Cryobench, an emission spectrum contains less quantitative information about the state of the sample.

An important setup that was used at the Cryobench for the experiments described in this thesis is the one allowing the separation between actinic and probe laser excitation (Figure III.2.6). This setup can be used to initiate a photoinduced reaction for a fraction of the

molecules in the sample by a light pulse and measure the fluorescence or absorption spectrum of the sample after this actinic pulse. This setup indeed, allows to alternatively illuminate a sample mounted on the microspectrophotometer with a pulse from a laser (actinic light) and then excite the fluorescence with a pulse from a laser (probe laser) or to measure the absorbance if the laser is replaced by a lamp. This second light source is synchronized with the CCD detector so that only the signal probed by this light source is recorded.

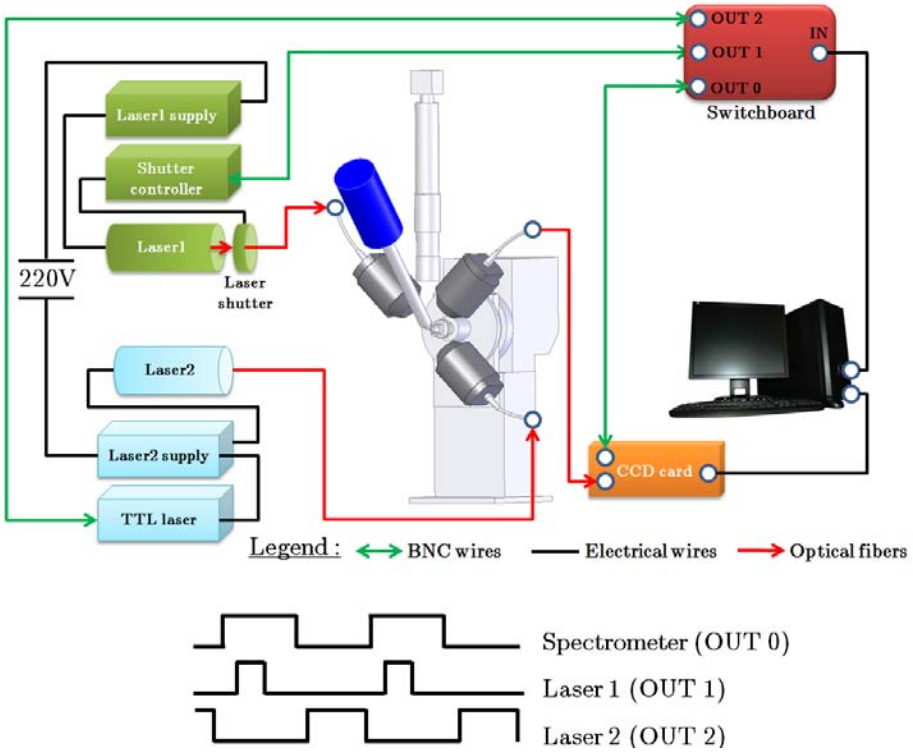

Figure III.2.6 - Cryobench setup allowing the separation between actinic and probe laser excitations

c - Online microspectrophotometer

It is not only possible to perform spectroscopic measurements on protein crystals at the Cryobench laboratory but also directly on one of the MX beamlines (Figure III.2.7). Once the experiments have been carefully prepared "offline" at the Cryobench, direct measurement of spectra is possible during X-ray data collections thanks to the installation on a beamline of a special microspectrophotometer that was developed at the ESRF (McGeehan *et al.* 2009) and whose optical arrangement is very similar to the one of the Cryobench laboratory. Spectroscopic transformations can thus be directly correlated with crystallographic structures.

This device also allows for example to probe spectral changes during X-ray induced transformations such as radiation damage.

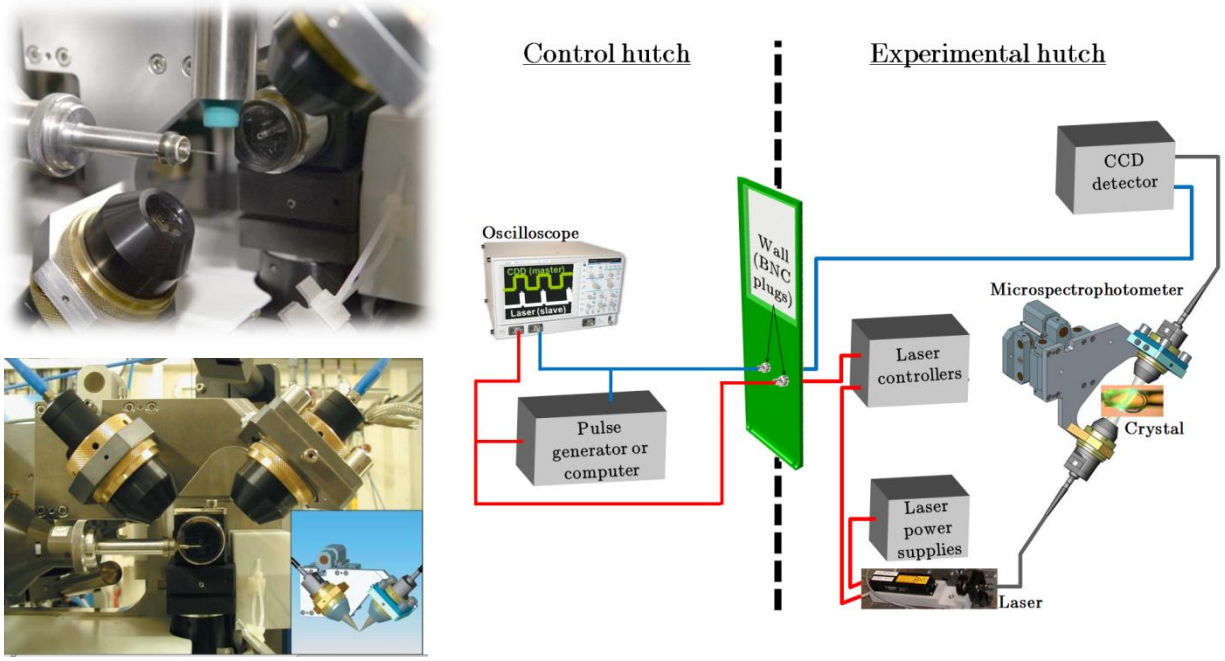

Figure III.2.7 - Photograph of the online microspectrophotometer developed at the ESRF (left) and a prototype with objectives mounted at 90° one another. A general mounting setup of this device on a synchrotron beamline is shown (right)

A routine device, designed to be very compact comprises only two objectives placed face to face, for transmission experiments. Another prototype has been recently developed with the objectives mounted at 90° one another to perform easier fluorescence experiments. Absorption measurements are thus not the only ones that can be made with this device, and fluorescence measurements are also possible. Filters can be installed (like in the objectives of the Cryobench) to cut the excitation wavelength after the sample. The space available, once the apparatus is installed, allows the installation of supplementary devices available at the Cryobench, such as a Raman head for example.

2 - Raman spectroscopy

Raman spectroscopy is a technique allowing the characterization of molecular compounds based on the analysis of their vibrational modes with light scattering, which are fast phenomena (10^{-14} s or less). The adaptation of a commercial Raman spectrometer (Renishaw, Gloucestershire, UK) on the Cryobench, allows characterizing a protein directly within crystals.

a - Theory

The Raman effect has been discovered in 1928 by the Indian physicist Chandrasekhara Venkata Raman (Figure III.2.8) who was awarded the Nobel prize two years later for this discovery. Basically, this effect occurs when photons with an energy $h\nu_0$ interact with a molecule, exciting it into what is described in quantum mechanics as being virtual electronic energy levels (i.e. not real excited electronic states). This interaction can be described in classical mechanics as the perturbation of the molecule's electric field. This perturbation will thus result in vibrational changes of the molecules according to some specific vibrational modes: stretching, bending, librations (Figure III.2.9) that can be detected as peaks in the Raman spectra. The de-excitation of excited molecules can be achieved by several ways explained below.

Figure III.2.8 - Photograph of Sir Chandrasekhara Venkata Raman

The most probable event is that a direct return to the initial level occurs without any energy transfer, resulting in elastic "Rayleigh" scattering of the photon at exactly the same frequency, and thus energy, than the excitation one. In this case, no Raman effect occurs. This phenomenon being extremely probable, the Rayleigh signal is very strong.

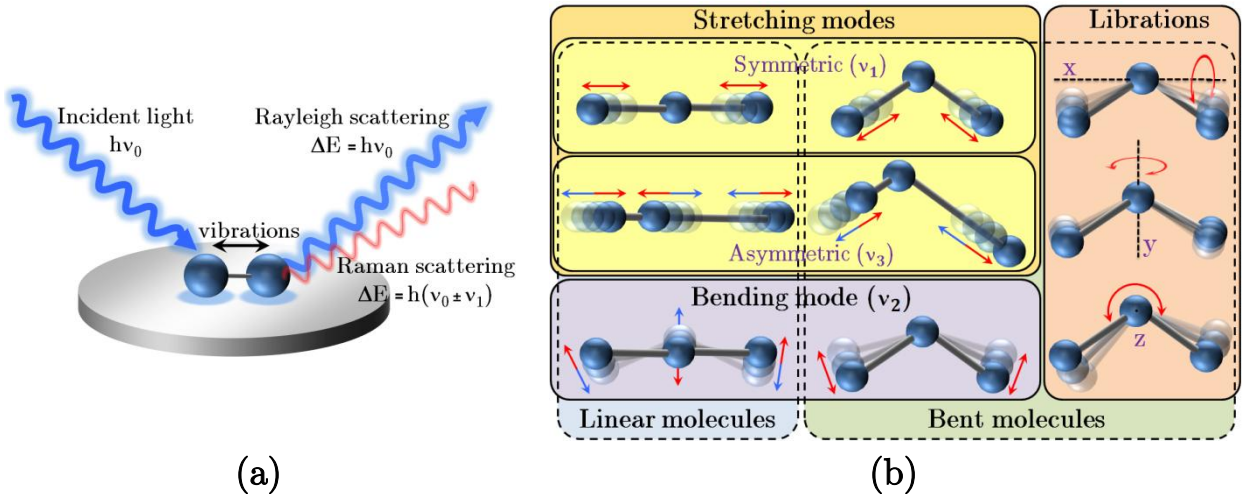

Figure III.2.9 - Principle of Rayleigh and Raman scatterings of light interacting with a vibrating molecule (a) and vibrational modes of linear and bent molecules (b)

After the initial excitation, the molecule can also, with a much lower probability (1 photon out of 10 millions) relax to an elevated vibrational level of the ground state. In such a case, this relaxation will be accompanied by the photon inelastic scattering. The induced small loss of energy corresponds to the created vibration, and is equal to the difference between the initial lowest vibrational level of the ground state and the final elevated vibrational level ($\Delta E=\nu_1$). Overall, the scattered light will have a lower frequency than the incident light ($\Delta E=h(\nu_0-\nu_1)$; this process is called Stokes Raman scattering.

Conversely, the molecule can already be in an elevated vibrational level while interacting with the incident light. In such a case, the interaction with the molecule will cause a net gain for the incident photon and the scattered light will have a higher frequency than the incident light ($\Delta E=h(\nu_0+\nu_1)$; this process is known as Anti-Stokes Raman scattering. Since this elevated vibrational state is less populated, the Anti-Stokes Raman scattering is of a much lower intensity than the Stokes Raman scattering (Figure III.2.10).

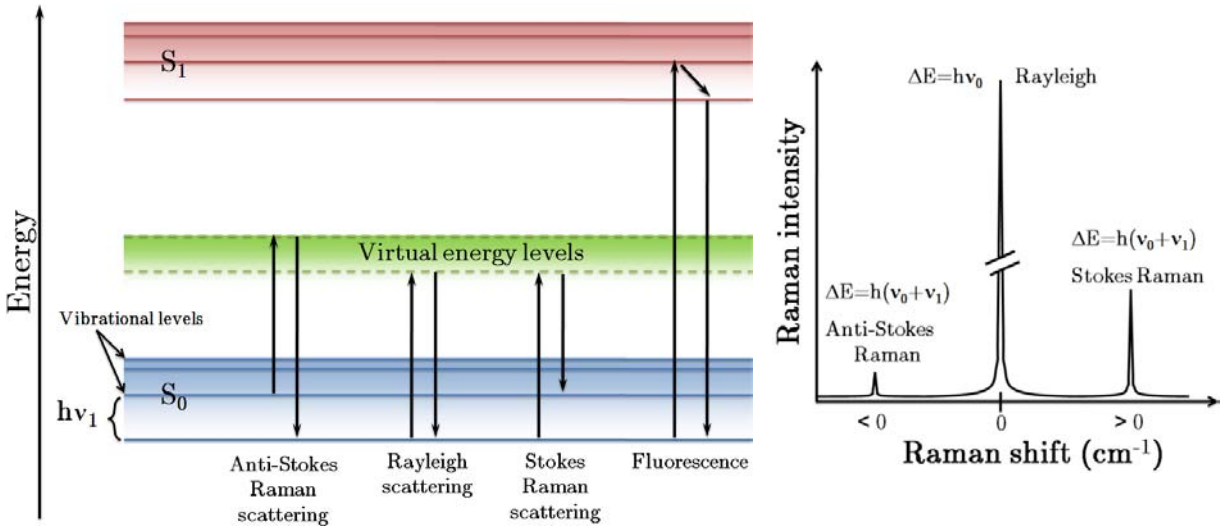

Figure III.2.10 - Left: Diagram representing the Rayleigh and Raman scatterings upon excitation by a light having an energy $\Delta E=h\nu_0$ and their difference with the phenomenon of fluorescence. Right: Simplified representation of the (anti-)Stokes Raman and Rayleigh peaks.

As suggested above, the intensity of a Raman signal depends on the probability of the event to occur and since the anti-Stokes Raman scattering is so low, in Raman spectroscopy we will only follow the Stokes Raman scattering signals for the experiments described in this thesis. The Raman signals that is recorded also depends on the incident wavelengths, since this intensity is proportional to λ^{-4} (Angel & Myrick 1990), which means that the higher the excitation wavelength, the lower the Raman intensity (Figure III.2.11), for this reason, blue lights should *a priori* be preferred to obtain a strong Raman signal. Although most studies in solution are performed in "on-resonance" conditions, in crystals, good signals can be obtained in pre-resonance Raman conditions. Since it has been shown (Carey 1999) that most biological compounds absorb wavelengths below ~650 nm and that above ~800 nm, water molecules absorb, we can perform pre-resonance Raman experiments on crystals by using an

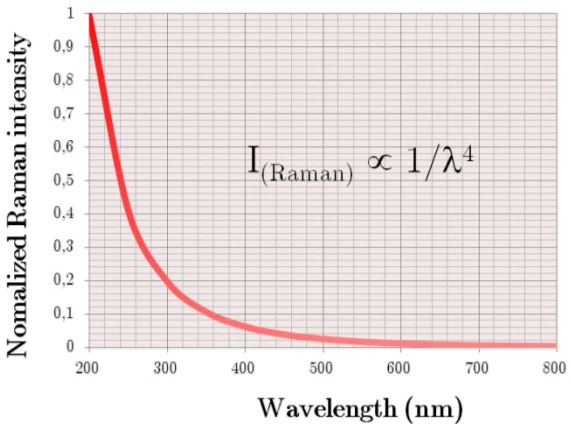

Figure III.2.11 - Raman intensity depends on the excitation wavelength

excitation wavelength situated in the small window between 650 nm and 800 nm, such as lasers emitting at 785 nm. Because of the very weak Raman signals collected when irradiating in the near infrared, recent Raman spectrometers are equipped with high sensitivity detectors and data collections need long exposure times (several minutes).

Depending on the gap between the frequency of the excitation wavelength and the frequency of the absorbing peaks, several types of Raman scattering processes are distinguished. When the energy of the excited virtual states is far below that of the electronic transition, the normal Raman scattering, described previously, occurs. When the gap is smaller and the excitation wavelength tends towards the maximum excitation wavelength, one talks of pre-resonance Raman scattering. Finally, if the incident radiation is of the same energy (or higher) than the maximum excitation peak, the process is termed discrete (or continuum) resonance Raman scattering (Long 2002). This resonance Raman scattering displays only the vibration modes of the excited chromophore but can be 3 to 6 orders of magnitude greater than normal Raman scattering, matching the sensitivity of infrared spectroscopy.

b - Experimental devices

The Raman spectra described in this thesis have been measured on a Renishaw inVia system equipped with three lasers: one emitting at 785 nm and two for resonant Raman applications (emitting at 514 nm and 632 nm) that were not used in this work. The experiments were performed either at the Cryobench laboratory using a classical “offline” setup or on the MX beamline ID23 using an “online” setup.

In the offline mode, a protein crystal is mounted in a microloop and placed at 100K on the goniometer head of the Cryobench microspectrophotometer. Although first trials were made by cryoprotecting the samples with glycerol, this step has quickly been abandoned since glycerol produces a very strong Raman signal that prevented us to observe the signal from the protein. The Raman head probe is focused directly on the sample but because of the geometry imposed by the Cryobench objectives, the Raman head is tilted from the camera axis. Another setup allows the use of a right-angle reflection mirror below the sample. This setup has the advantage

of allowing a very precise centering since the Raman laser beam is in the axis of the camera (Figure III.2.12)

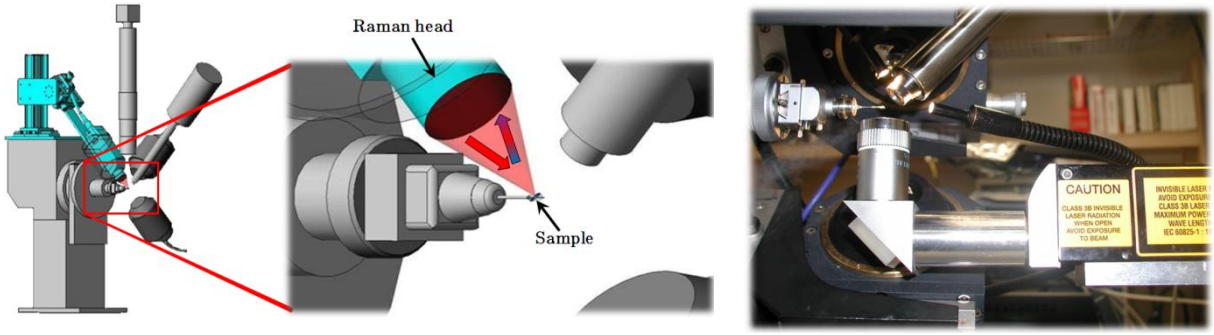

Figure III.2.12 - Sketch of the Cryobench setup for Raman experiments with the Raman head probe mounted directly in the axis of the sample (left), photograph of a variant with right-angle reflection via a mirror (right)

In the online mode, protein crystals were prepared as described above but were mounted on the diffractometer of the beamline ID23-1. Indeed, 50 meter-long optical fibers have been connected from the Cryobench Raman apparatus to the two end stations of the MX beamline ID23 Gemini located in the vicinity of the Cryobench laboratory (Carpentier *et al.* 2007). This setup only requires the installation of the Raman head probe on the beamline (Figure III.2.13). Although being more demanding (long preparation time, need of dedicated beamtime…) and in spite of a lesser signal to noise (~50% weaker compared to the offline mode), this setup allows following Raman signals at the very same and precise location probed by the X-ray beam.

Figure III.2.13 - Photograph of the Raman online setup used on the MX beamline ID23-1

3 - Fluorescence lifetime measurements

A fluorescence emission spectrum is specific of each fluorescent molecule and reflects the probability of transition from the lowest vibration level of the excited state S_1 to the various levels of the ground state S_0.

A very sensitive method to study fluorescence is to measure the fluorescence lifetime (time of residency in the excited state) with the Time Correlated Single Photon Counting (TCSPC) technique. The versatility of the Cryobench allowed to adapt this technique to the microspectrophotometer and measure fluorescence lifetimes in either solution or crystals.

To adapt the Cryobench microspectrophotometer to those kinds of experiments, samples were placed in a drop deposited on a glass coverslip previously glued on a microloop. The airtightness is ensured by a second glass coverslip maintained with silicon grease (Figure III.2.14). The treatment of the fluorescence decays was performed with a software specially developed at the ESRF to this purpose and described in (Royant *et al.* 2007).

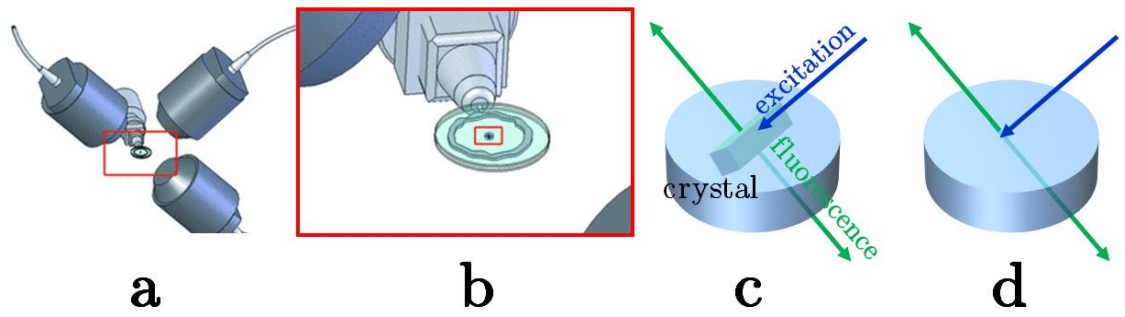

Figure III.2.14 - Experimental setup for TCSPC experiments at the Cryobench laboratory. The drop containing the sample is placed in the microspectrophotometer (a) by mounting the drop containing the sample between two coverslips (b) either in crystal (c) or liquid phase (d)

Chapter 3 - Power densities and quantum yields

Résumé en français

Ce chapitre présente les méthodes utilisées dans cette thèse afin de calculer les densités de puissance d'illumination et les rendements quantiques de phototransformations. Les calculs de densités de puissance sous illumination avec une lumière convergente ou une lumière divergente sont détaillés, ainsi que les calculs ayant permis la modélisation des évolutions de fluorescence suivant des fonctions exponentielles étirées (aussi appelées fonctions de Kohlrausch-Williams-Watts).

Part 1 - Calculating power densities

ALL the direct powers from light sources after the optical fibers (P_0) were measured before an experiment at each wavelength of interest with a laser power/energy meter (FieldMaster GS, Coherent Scientific[27]) in order to be able to calculate the power densities that the samples undergo (after a possible filter).

1 - Case of an experimental setup using a convergent light

a - The objectives used at the Cryobench

To perform microspectrophotometric measurements, we mostly used in this thesis the standard experimental setup of the Cryobench microspectrometer where optical fibers are plugged into objectives (cf. Chapter 2 - The Cryobench laboratory, p. 217). Each objective, made by Optique Peter (Lentilly, France), is based on a Schmidt-Cassegrain system and contains a convex mirror (mirror 1) and a concave mirror (mirror 2) that focus the light from the optical fiber to the plane where the sample is situated (Figure III.3.1).

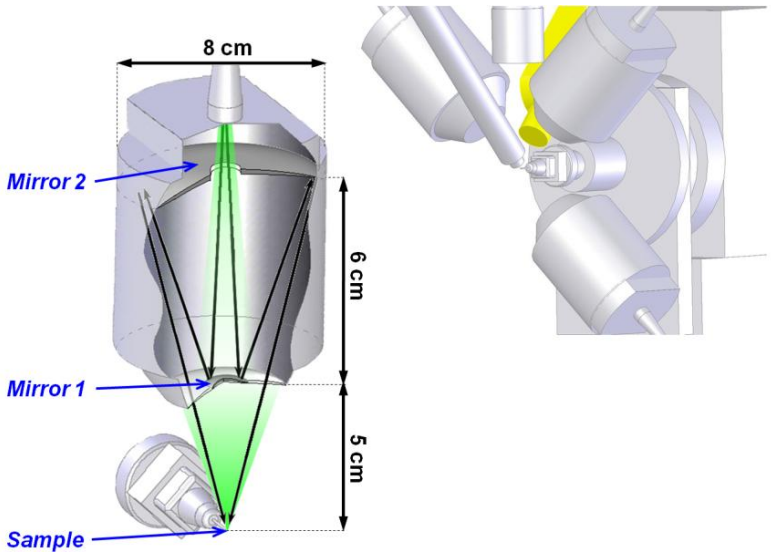

Figure III.3.1 - Optical properties of the objectives used at the Cryobench microspectrophotometer

[27] http://www.coherent.com.au/?div=6&area=products&id=106

A filter can be set between the optical fiber and the mirror 2, if necessary. The magnification is 4, so that the light spot formed on the sample has a diameter that is four times smaller than the diameter of the optical fiber. In this setup, one can calculate the power density of the light disc formed at the sample.

b - General calculations

Considering the variables P_0 and P_1 = light powers before and after a filter in watts, F=filter attenuation in OD units, S = surface in cm² and d_1= diameter of the optical fiber in micrometers, we can calculate the power density in W/cm² (*P.D.*) on a sample placed at the center of the Cryobench microspectrophotometer.

$$P.D. = \frac{P_1}{S} = \frac{P_0 \times 1 \cdot 10^{-F}}{\pi r^2} = \frac{P_0 \times 1 \cdot 10^{-F}}{\pi \times \left(\frac{\frac{d_1}{m} \cdot 10^{-4}}{2}\right)^2}$$

Equation III.8

With m = magnification = 4 for the Cryobench setup

As an example, for an optical fiber having a diameter of 600 µm, P_0 = 20 mW and a filter of OD=1, we find $P.D. = \frac{0.02 \times 1 \cdot 10^{-0.8}}{\pi \times \left(\frac{\frac{600}{4} \cdot 10^{-4}}{2}\right)^2} = 17.9$ W/cm²

2 - Case of an experimental setup using a divergent light

I also used an experimental setup (Figure III.3.2) where an optical fiber was maintained over a plane where the sample was situated, with a filter, if necessary, set in between. Since there is no lens in this setup, the light from the optical fiber diverges toward the plane where the sample is situated.

Once again, in this setup, we can calculate the power density of the light disc formed at the sample level and the homothetic relation between the diameter of the optical fiber and the diameter of this disc.

a - General calculations

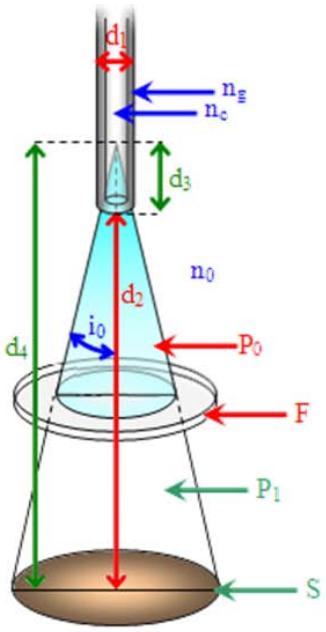

- n_0 *is the refractive index of the medium* ($n_0 = 1$ *for air*)
- n_g *and* n_c *are the refractive indexes of the cladding and core of the optical fibre respectively*
- F *is the filter attenuation, in OD units*
- P_0 *and* P_1 *are the light powers before and after the filter respectively, in watts*
- S *is the surface of the sample that is illuminated, in squared millimeters*
- d_1 *is the diameter of the optical fibre, in micrometers*
- d_2, d_3 *and* d_4 *are the distances* $\overline{S_0O}$, $\overline{OF_p}$ *and* $\overline{S_0F_p} = \overline{S_0O} + \overline{OF_p}$ *respectively, in millimeters. With* S_0 *: sample,* O *: the extremity of the optical fibre and* F_p*: focal point inside the optical fibre*
- i_0 *is the half-angle of aperture, in degrees*

Figure III.3.2 - Drawing of an experimental setup using a divergent light

The numerical aperture ($N.A.$) of the optical fiber is calculated by:

$$N.A. = \sqrt{n_c^2 - n_g^2} = n_0 \times \sin i_0 \rightarrow \boxed{i_0 = \sin^{-1}\left(\frac{N.A.}{n_0}\right)}$$

Equation III.9

We can calculate the diameter (D) of the illuminated area on the sample:

$$\frac{d_1}{D} = \frac{d_3}{d_4} \rightarrow D = \frac{d_1}{\left(\frac{d_3}{d_2 + d_3}\right)} = d_1 \times \left(\frac{d_2}{d_3} + 1\right) = \boxed{d_1 + d_2 \times \frac{d_1}{d_3}} \quad \text{with } d_3 = \left(\frac{\frac{d_1}{2} \cdot 10^{-3}}{\tan i_0}\right) \text{ mm}$$

Equation III.5

With only the values of n_0, d_1, d_2, P_0, F and $N.A.$, we can therefore calculate the power density $P.D.$ (in W.cm^{-2}) of a divergent light, thanks to the following equation:

$$P.D. = \frac{P_1}{S} = \frac{P_0 \times 1 \cdot 10^{-F}}{\pi \times (d_4 \times \tan i_0)^2} = \frac{P_0 \times 1 \cdot 10^{-F}}{\pi \times \left[d_2 \times \tan\left[\sin^{-1}\left(\frac{N.A.}{n_0}\right)\right] + \frac{d_1}{2} \cdot 10^{-3}\right]^2}, \text{with } d_4 = d_2 + d_3$$

Equation III.6

b - Homothetic relations

In Equation III.5, we see that d_3 only depends on the optical fibre diameter d_1 and $\frac{d_1}{d_3}$ only depends on the half-angle of aperture i_0 (or numerical aperture) since

$$\frac{d_1}{d_3} = \frac{d_1}{\left(\frac{\frac{d_1}{2} \cdot 10^{-3}}{\tan i_0}\right)} = 2 \tan i_0 \cdot 10^3$$

In our conditions, we use optical fibers with $i_0 = 12.71°$ ($n_0 = 1 \rightarrow N.A. = 0.22$) and thus, we have

$$\frac{d_1}{d_3} \cong 451 \rightarrow D \cong d_1 + d_2 \times 451$$

Equation III.7

The diameter of a hanging drop (D_{drop}), considered as a half-sphere, can be calculated by:

$$D_{drop} = 2 \times \sqrt[3]{\frac{2 \times V}{4 \cdot \pi / 3}}$$

Equation III.8

Since we classically use crystallization drops with $V \in \{4 \cdot 10^{-9}\ \text{m}^3; 2 \cdot 10^{-9}\ \text{m}^3\}$, we obtain $D_{drop} \in \{2.48\ \text{mm}; 1.97\ \text{mm}\}$ for a range between a non-equilibrated (4 µL) and a fully equilibrated (2 µL) drop respectively.

All the experiments in this thesis, using this setup, were carried out with an optical fiber diameter (d_1) of 600 µm and a distance between the fiber extremity and the drop (d_2) of 4 mm so that $D \cong 2.4\ \text{mm} \cong D_{drop}$

Part 2 - Calculating photoswitching quantum yields

1 - Stretched exponential function

A quantum yield quantifies the efficiency of an event to occur upon the absorption of a photon. For example, the fluorescence quantum yield is defined as the ratio of the number of photons emitted to the number of photons absorbed. As a consequence, for a fluorescence quantum yield of 1 (100%), each photon that is absorbed by the system will give rise to a photon emitted.

Similarly, the photoswitching quantum yield of a fluorescent protein quantifies the molecular fraction of a RSFP that photoswitches upon absorption of a photon. In practice in this work, the time traces of the switching reactions were fitted with stretched exponential functions according to the following equation

$$y = A_1 \cdot \exp\left(-\left(t \times k\right)^{\beta}\right) + A_0$$

Equation III.9

Where β is the stretching parameter and k is the reaction rate τ is the lifetime.

The reaction rate k is the inverse of the lifetime τ, defined as the time at which $\left(A_1 \times \frac{1}{e} + A_0\right)$ percents of the signal is lost or gained.

$$\tau = \frac{1}{k}$$

Equation III.10

This lifetime τ is related to the classical half-time $t^1/_2$ by the relation $t_{1/2} = \ln(2) \times \tau = \frac{\ln(2)}{\langle k \rangle}$

The average time of reaction $<\tau>$ can be calculated from the stretching parameter and the lifetime τ by the Gradshteyn and Rhyzhik integral :

$$\langle \tau \rangle = \frac{\tau}{\beta} \Gamma\left(\frac{1}{\beta}\right)$$

Equation III.11

Where Γ is the Gamma function defined as $\Gamma(z > 0) = \int_0^\infty t^{-1+z} e^{-t} dt$

2 - General formula of the quantum yield

Knowing the illuminated surface *S*, the power *P*, the extinction coefficient *ε*, and the wavelength *λ* used during the experiments, it is possible to calculate a photoswitching quantum yield Φ by the following equation:

$$\Phi = \frac{\frac{1}{\langle \tau \rangle} \times hc \times S \times N_{Av}}{P \times \lambda \times \varepsilon \times \ln 10}$$

Equation III.12

Where
N_{Av} is the Avogadro number = 6.02214179 x 10^{23} mol^{-1}
h is the Planck constant = 6.626068 x 10^{-34} J.s
c is the speed of light 2.99792458 x 10^8 $m.s^{-1}$
$<\tau>$ is the average time of reaction

3 - Example

During an experiment of the red-to-dark switching of IrisFP, we obtained a timetrace (Figure III.3.3) that we can fit with a stretched exponential function that gives k= 0.26 s^{-1} = 15.97 mn^{-1} and β=0.54

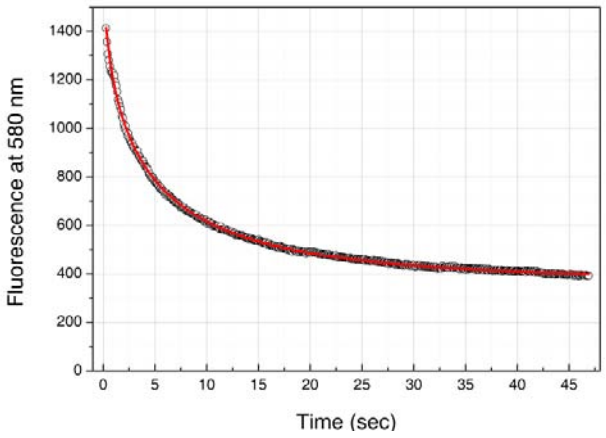

Figure III.3.3 - Timetrace of a fluorescence decay during the red-to-dark photoswitching of IrisFP (black circles) fitted by a stretched exponential function (red curve)

From Equation III.10 and Equation III.11, we find $\tau = 1/k = 3.84$ s and $\langle\tau\rangle = \frac{\tau}{\beta}\Gamma\left(\frac{1}{\beta}\right) = 6.74$ s

Since to perform this experiment we used a cuvette with S = 0.1 cm^2, P = 20 mW, λ = 532 nm and $\varepsilon_{532\,nm}$ = 28400 $M^{-1}.cm^{-1}$, we calculate the quantum yield of photoswitching Φ

$$\Phi = \frac{\frac{1}{\langle\tau\rangle} \times hc \times S \times N_{Av}}{P \times \lambda \times \varepsilon \times \ln 10} \cong 2.5\ 10^{-3}\ (0{,}25\%)$$

Which means that on average, a molecule in switched every 391 photons ($1/\Phi$) absorbed

Chapter 4 - Restraints on the chromophores

Résumé en français

Ce chapitre décrit les méthodes de modélisation et contraintes imposées sur les angles dièdres et la planéité des chromophores des protéines fluorescentes étudiées dans cette thèse.

Les contraintes sont imposées grâces à la constitution d'une bibliothèque sous format CIF généré pour faire correspondre au mieux les divergences de planéité de l'élément chromophore observés dans les différentes structures vertes et rouges des protéines fluorescentes photoactivables. Un effort particulier a en outre été apporté quant à la modélisation des chromophores sous formes cis et trans.

SETTING the geometrical restraints properly for the chromophores is a tricky task that is essential for refinement programs to treat correctly this exogenous component as being part of the protein. For softwares like Refmac (Dodson et al. 1997) or Coot (Emsley & Cowtan 2004), the definition of the restraints is made in a dictionary called Crystallographic Information File or CIF (Hall *et al.* 1991). This file must be carefully checked to avoid problems during the refinement process. In this thesis, the idealized structure files (PDB) for the green and red chromophores of EosFP called CR8 and IEY respectively, have been downloaded from the Hic-Up, Hetero-compound Information Centre[28] (Kleywegt *et al.* 2003). The CIF files with minimal description were then generated from these PDB files with the program Sketcher from the CCP4 suite. During this step, structure regularizations are performed as well as the attribution of bond types (single, double, aromatic...). Finally, a manual edition of the CIF files is performed to modify the labeling of atoms according to the considered structure (EosFP, Dendra2...), the considered form (green or red) and to input the correct restrain values. These modifications are explained hereafter.

1 - Link between the chromophore and the rest of the protein

The declaration of the links is made in the following form:

X.id	X.comp_id_1	X.mod_id_1	X.group_comp_1	X.comp_id_2	X.mod_id_2	X.group_comp_2	X.name

With X: _chem_link, id: label of the linkage, comp_id_n: potential modification before (1) or after (2) the linkage, mod_id_n: label of the modification, group_comp_n: group containing the modification, name: declared name of the linkage

Example:

```
PHE-CR8  PHE      .        .        CR8      .        .     bond PHE-C = CR8-N
CR8-ASN  CR8      .        .        ASN      .        .     bond CR8-C = ASN-N
```

The description of the links in the following form:

X.link_id	X.atom_1_comp_id	X.atom_id_1	X.atom_2_comp_id	X.atom_id_2	X.type	X.value_dist	X.value_dist_esd

With X: _chem_link_bond, link_id: label of the linkage, atom_*n*_comp_id: numbering of the linking atom in the first (*n*=1) or second (*n*=2) fragment, atom_id_*n*: type of the atom *n*, type: type of the bond (single, double…), value_dist: bond length (Å), value_dist_esd: length energy strength

[28] http://xray.bmc.uu.se/hicup/

Example:

```
data_link_PHE-CR8
PHE-CR8  1 C       2 N         single          1.400    0.020
data link CR8-ASN
CR8-ASN  1 C       2 N         single          1.400    0.020
```

2 - Restraints on the torsion angles

The three rings (hydroxyphenyl, imidazolinone and imidazole) of EosFP, IrisFP and Dendra2 were kept extremely flat by setting constraints on all the dihedral angles of the atoms of these cycles as constant terms (CONST_*n*). At the opposite, restraints on the other dihedral angles were set as variable terms (var_*n*). The declaration of torsion angles is made in the following form:

X.comp_id	X.id	X.atom_id_1	X.atom_id_2	X.atom_id_3	X.atom_id_4	X.value_angle	X.value_angle_esd	X.period

With X = _chem_comp_tor, comp_id: label of the component, atom_id_*n*: label of the atom *n* in the considered dihedral angle, value_angle: torsion angle in degrees, value_angle_esd: torsion energy strength, period: number of allowed degrees of freedom (energetic minima)

Example:

```
CR8      CONST_1  O3    C1    C2    C6     180.000    0.000   0
CR8      CONST_2  C1    C2    C6    C7       0.000    0.000   0
CR8      CONST_3  O3    C1    C4    C5     180.000    0.000   0
CR8      CONST_4  C1    C4    C5    C7       0.000    0.000   0
CR8      CONST_5  C4    C5    C7    C8     180.000    0.000   0
CR8      CONST_6  C5    C7    C6    C2       0.000    0.000   0
CR8      var_1    C5    C7    C8    C9     180.000   20.000   1
CR8      var_2    C7    C8    C9    N15    180.000   20.000   1
CR8      CONST_8  C8    C9    C12   O25      0.000    0.000   0
CR8      CONST_9  C8    C9    N15   C14    180.000    0.000   0
CR8      CONST_10 C9    N15   C14   C16    180.000    0.000   0
CR8      CONST_11 N15   C14   N13   C17    180.000    0.000   0
CR8      CONST_12 C14   N13   C12   C9       0.000    0.000   0
CR8      var_3    C14   N13   C17   C      175.000   20.000   1
CR8      var_4    N13   C17   C     O19    175.000   20.000   1
CR8      var_5    N15   C14   C16   C20    175.000   20.000   1
CR8      var_6    C14   C16   N     HN2    175.000   20.000   1
CR8      var_7    C14   C16   C20   C21    175.000   20.000   3
CR8      var_8    C16   C20   C21   N22    175.000   20.000   2
CR8      CONST_13 C20   C21   C23   N11    180.000    0.000   0
CR8      CONST_14 C20   C21   N22   C10    180.000    0.000   0
CR8      CONST_15 C21   N22   C10   N11      0.000    0.000   0
CR8      CONST_16 N22   C10   N11   C23      0.000    0.000   0
CR8      CONST_17 C10   N11   C23   C21      0.000    0.000   0
```

3 - Restraints on the planarity

If some bonds could be modeled as being aromatic or delocalized such as those in the hydroxyphenyl ring, setting the methylene bridge as delocalized bonds force this bridge to be coplanar with the hydroxyphenyl and imidazolinone rings. However, this planarity clearly revealed to be too strong to fit the electron density maps, making appear difference maps that could only be fitted by a slight distortion of the chromophore. Five planes were defined so that rigid groups of atoms (such as cycles along with their coplanar bonds) are kept in a same plane, but allowing these planes to correctly rotate. After a number of attempts, the most satisfying way of setting planes was found to be the one depicted in (Figure III.4.1).

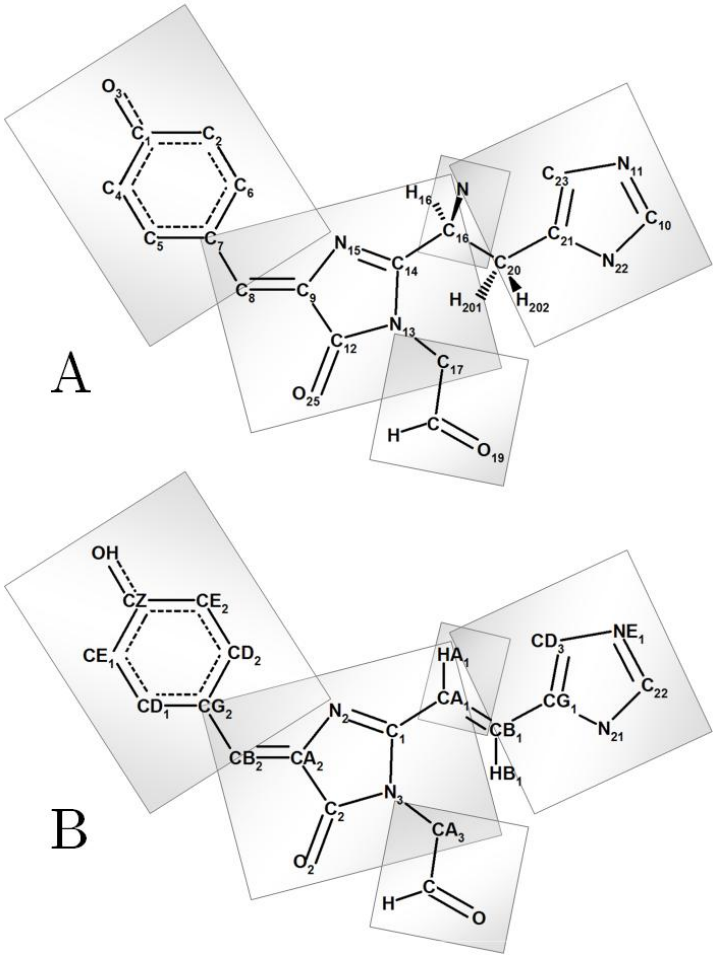

Figure III.4.1 - Constraints used on the planarity of green (A) and red (B) chromophores CR8 and IEY with their corresponding atomic labeling

The numbering shown is that of the green chromophore (A) and the red chromophore (B) and all the planes intercross via one to two common atoms. It is important to note that for the red chromophore, the definition of the phenylalanine amide (NFA) is also needed in the cif file. The declaration of the planarity constraints is made in the following form:

```
X.comp_id    X.plane_id    X.atom_id    X.dist_esd
```

With `X`: `_chem_comp_plane_atom`, `comp_id`: label of the component, `plane_id`: label of the plane, `atom_id`: label of the atom contained in the plane, `dist_esd`: energy strength of the constraint

Example:

```
CR8       plan-1    C          0.020
CR8       plan-1    O19        0.020
CR8       plan-1    C17        0.020
CR8       plan-1    H          0.020
CR8       plan-2    N13        0.020
CR8       plan-2    C17        0.020
                ...
```

The chromophore's planarity in green-cis, green-trans and red-cis forms of IrisFP was assessed by the measurement of the average dihedral angles, over the four monomers, linking atoms N15-C9-C8-C7 (dihedral angle 1) and C9-C8-C7-C5 (dihedral angle 2) of the chromophore. The values for those two dihedral angles for the three chromophores are compiled in Table II.2.8, p.132 and represented in Figure III.4.2.

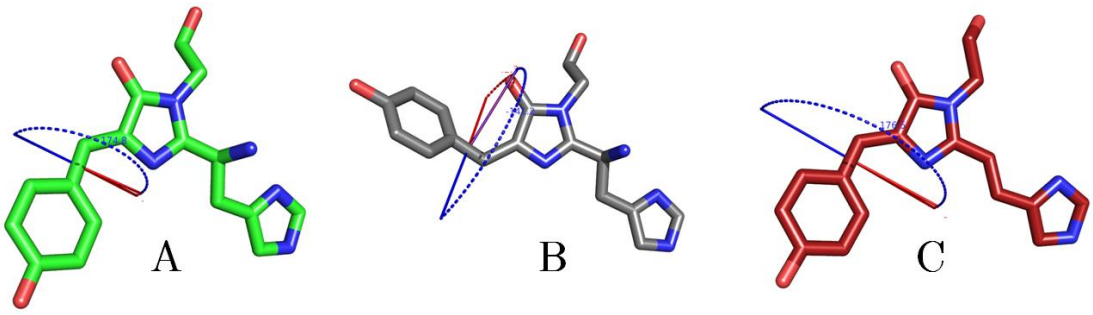

Figure III.4.2 - Torsion of the chromophore in the green-cis (A), green-trans (B) and red-cis (C) forms of IrisFP.

IV. CONCLUSION & PERSPECTIVES

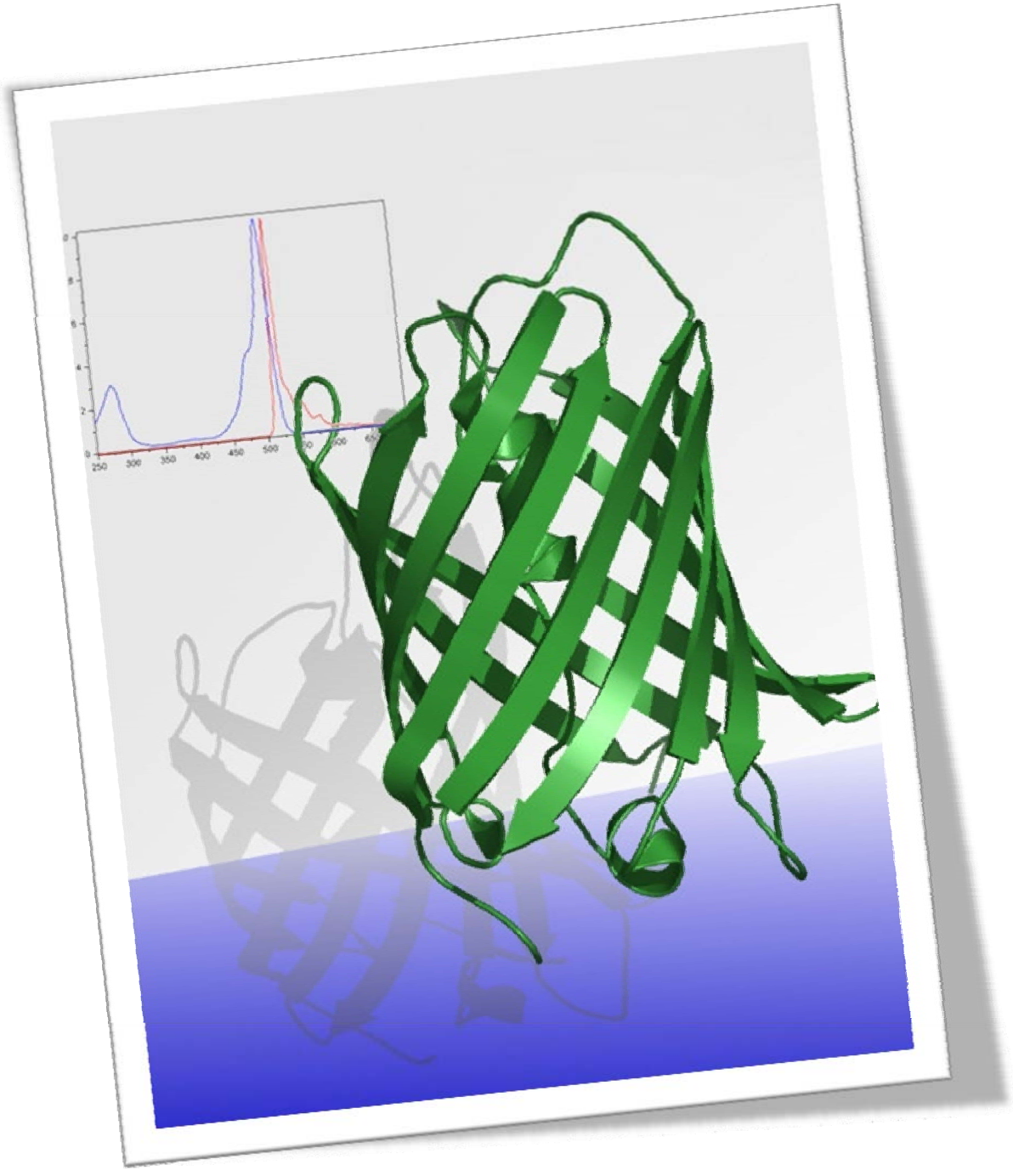

The illustration represents the overall 3D structure of EosFP. Behind are shown the absorption (blue) and emission (red) spectra of the fluorescent protein, measured at the Cryobench laboratory

Chapter 1 - Conclusions

PHOTOACTIVATABLE fluorescent proteins (PAFPs) are a new type of genetically encoded fluorescent markers of an invaluable interest for cell biology. PAFPs can be controlled by actinic illuminations by either photoconverting from an emission color to another (typically from green to red) or by reversibly switching between a fluorescent and a non-fluorescent form. The first kind gathers PAFPs called photoconvertible FPs (PCFPs) and the second type gathers reversibly photoswitchable FPs (RSFPs). At the beginning of this Ph.D. thesis, few things were known and understood about PAFPs, and a little number of these markers existed. We decided to study especially the PCFPs because their number was more important than RSFPs and our collaboration with the University of Ulm (Germany) allowed us to directly start our experiments on the green-to-red photoconvertible EosFP. Our initial aim was to study spectroscopically and structurally the photoconversion mechanism of EosFP and its mutants in order to propose some directions to enhance the protein properties and trap a putative intermediate state of the reaction.

Our collaboration with M. Lelimousin and M.J. Field at the IBS allowed us to go further in the comprehension of the green-to-red photoconversion mechanism of EosFP, by complementing crystallographic and spectroscopic experimental data with quantum and molecular dynamics calculations. We obtained, later, the first 3D structure of Dendra2, a PCFP similar to EosFP that, however, differs in several points and photoconverts more efficiently. The structural and spectroscopic information we could obtain from this protein, gave us a better comprehension of the photoconversion mechanism.

During our experiments on variants of EosFP, we could propose mutations that we estimate crucial to enhance the monomerization of this PCFP, which is an important point to use these naturally tetrameric FPs in imaging applications. We also discovered a fantastic PAFP that we called IrisFP, a mutant of EosFP that displays both the irreversible photoconversion properties of PCFPs and reversible switching properties of RSFPs. This protein represents the first member of this new kind of PAFPs. We hope that this protein will be used soon in dual-color fluorescence microscopy experiments. The great contrast between

green and red forms and the photochromic possibilities of this protein allowed us to give the first proof of principle for the use of PAFPs to optically encode and store data within a single crystal or IrisFP.

Finally, the observations of fluorescence loss, made during a number of experiments, directed our efforts toward the topic of the photobleaching event. This phenomenon is very problematic in fluorescence microscopy but is poorly understood. By using X-rays and UV/Vis sources as tools to generate photobleaching of IrisFP and EosFP, we could propose a structural explanation for one of the pathways leading to photobleaching.

Altogether, our results should lead in a near future to the design of photostable, monomeric and more efficient PAFPs.

A number of questions, however, remain to be answered. The comprehension of the photobleaching, for example, is a very complex topic and if we have proposed here a mechanism for one of the pathways probably existing in FPs, many other pathways certainly coexist and are still to be studied to create better markers in the future. The mechanism for the photoisomerization is still relatively badly understood... although we have proposed an answer, we still need for example to perform more experiments to definitely be sure that photoprotonation precedes the photoizomerization during the switching process.

The mutation of existing PAFPs in order to provide them new capabilities is an exciting task. However, experience shows that such optimizations have been made, in reality, mostly by random mutagenesis approaches, rather than by a rational design. We have to keep in mind that each modification can produce unexpected side effects.

I tried during this work to be as complete as possible on the comprehension of the topics studied and tried to find answers to the ongoing debates about the mechanisms involved for PAFPs phototransformations, but we have not covered, of course, the entire panel of what has to be done on PAFPs. The use of PAFPs as biological tools to track proteins of interest within cells requires taking into account more criteria than the ones that were studied in this thesis.

We have shown that it is possible to make FPs switchable, photoconvert efficiently or be more photostable, but if these proteins do not express properly or display low levels of maturation, their use in imaging applications will be compromised. In other words: the fact that a PAFP shows good quantum yields of fluorescence and phototransformations is not sufficient to make it a good tool for microscopy. We have studied part of this question when we talked about the monomerization of EosFP and Dendra2 but avoiding oligomerization is only one side of the problem of the targeting within cells. For new PAFPs to be used, both their photophysics and biochemical aspects (such as their non-aggregation) have to be optimized.

Since the discovery of the GFP, many fluorescent proteins have been found and the recent discovery of PAFPs opened novel perspectives for the development of new versatile and efficient biological markers. Current efforts to search for new sources of FPs in deep sea and the recent discovery of new types of FPs in unexpected species such as crustaceans, like copepods, and even in the cephalochordate Amphioxus (Deheyn *et al.* 2007), considered as an ancestor of vertebrates, give great hopes for the announcements of many other FPs with new exciting capabilities within the next years.

Chapter 2 - Perspectives

THE interest for fluorescent proteins is currently very high as assessed by the fact that O. Shimomura, M. Chalfie, R. Tsien have been awarded the Nobel Prize in Chemistry 2008 for the discovery, use and development of the GFP. The most evolving and exciting application of PAFPs is probably their use in nanoscopy. This field of science is progressing a lot and super-resolution microscopy techniques such as STED, STORM and PALM have been declared "method of the year 2008" by Nature Methods, which edited a special issue about them. We can expect, thus, a number of new applications to come soon.

The very precise localization of PAFPs that is allowed in nanoscopy and the fast development of better PAFPs permit to think of futuristic perspectives such as in-cell structural biology. This technique would ultimately allow obtaining the structure of all proteins contained in a cell by 3D-nanoscopy. This would make deeply evolve our perception about structural biology, even if it is hardly imaginable to use rather big markers such as FPs to tag macromolecular complexes in-situ. It is indeed unlikely that these complexes would still be functional and the knowledge gained on photoconvertible and photochromic FPs could thus be applied to the development of smaller organic dyes to this aim.

The knowledge acquired during this thesis should now allow me to propose mutations in order to rationally design new kinds of PAFPs. Keeping in mind that, as said previously, such mutations will not be easy, we can for example, based on our structural results, think of enhancing Dendra2 (which is already a very efficient PCFP) by adding photochromic properties. This mutant could even be further improved by making the mutations proposed in this thesis to disrupt the weak interface observed in the structure, so that it would become an even more stable monomer than it is already. Such a stable monomeric protein with high brilliance, high photoconversion efficiency and reversible switching capabilities would be of great interest for dual color super-resolution microscopic applications.

As we saw along the studies performed in this thesis work, the protonation state of the chromophore and immediate environment of PAFPs in given conditions is a crucial information to obtain. These data would indeed allow answering many mechanistic questions. Unfortunately, we are unable with X-ray crystallography to obtain the position of hydrogen atoms in the structures, unless reaching ultra-high resolutions. In the frame of this thesis work, we have established a promising collaboration with Dr. Monika Budayova-Spano and obtained big crystals of EosFP and IrisFP. Our goal is to obtain sufficiently big crystals to obtain the protonated structure of a PAFP by Laue neutron diffraction with the neutron source of the Institut Laue-Langevin (ILL, Grenoble). Our preliminary results are promising for IrisFP and we are now entering a new phase in this project with the imminent perdeuteriation of IrisFP (protein expression in heavy-water conditions, in order to increase the signal of hydrogen atoms by replacing them by deuterium atoms).

Finally, all the fundamental studies performed during my thesis will now allow me to conduct my research toward a more applicative side, with the use of PAFPs in nanoscopy. I should now, in a postdoctoral period, use these proteins on biological projects and try to develop new methods in optics for super-resolution microscopy, still having a foothold in crystallography. I hope that the combination between nanoscopy and crystallography will help both using promising markers such as IrisFP for molecular tagging applications like dual color nanoscopy, and unraveling new mysteries in the mechanistic behaviors of PAFPs.

V. APPENDICES

This page intentionally left blank

Appendix I - DNA and protein sequences

1 - Sequences of wtEosFP & variants m-, d1-, d2-EosFP and IrisFP

```
1   atg agt gcg att aag cca gac atg aag atc aac ctc cgt atg gaa ggc aac gta aac ggg cac cac ttt gtg atc
1   Met Ser Ala Ile Lys Pro Asp Met Lys Ile Asn Leu Arg Met Glu Gly Asn Val Asn Gly His His Phe Val Ile

76  gac gga gat ggt aca ggc aag cct ttt gag gga aaa cag agt atg gat ctt gaa gtc aaa gag ggc gga cct ctg
26  Asp Gly Asp Gly Thr Gly Lys Pro Phe Glu Gly Lys Gln Ser Met Asp Leu Glu Val Lys Glu Gly Gly Pro Leu

151 cct ttt gcc ttt gat atc ctg acc act gca ttc cat tac ggc aac agg gta ttc gcc gaa tat cca gac cac ata
51  Pro Phe Ala Phe Asp Ile Leu Thr Thr Ala Phe His Tyr Gly Asn Arg Val Phe Ala Glu Tyr Pro Asp His Ile

226 caa gac tat ttt aag tcg ttt cct aag ggg tat tcg tgg gaa cga agc ttg act ttc gaa gac ggg ggc att cag
76  Gln Asp Tyr Phe Lys Gln Ser Phe Pro Lys Gly Tyr Ser Trp Glu Arg Ser Leu Thr Phe Glu Asp Gly Gly Ile

301 tgc att gcc aga aac gac ata aca atg gaa ggg gac act ttc tat aat aaa gtt cga ttt cac ggt gta aac ttt
101 Cys Ile Ala Arg Asn Asp Ile Thr Met Glu Gly Asp Thr Phe Tyr Asn Lys Val Arg Phe His Gly Val Asn Phe
                                                                                    Thr

376 ccc gcc aat ggt cca gtt atg cag aag aag acg ctg aaa tgg gag ccc tcc act gag aaa atg tat gtg cgt gat
126 Pro Ala Asn Gly Pro Val Met Gln Lys Lys Thr Leu Lys Trp Glu Pro Ser Thr Glu Lys Met Tyr Val Arg Asp

451 gga gtg ctg acg ggt gat att acc atg gct ttg ttg ctt gaa gga aat gcc cat tac cga tgt gac ttc aga act
151 Gly Val Leu Thr Gly Asp Ile Thr Met Ala Leu Leu Leu Glu Gly Asn Ala His Tyr Arg Cys Asp Phe Arg Thr
                                His                                                                 Ser

526 act tac aaa gct aag gag aag ggt gtc aag tta cca ggc tac cac ttt gtg gac cac tgc att gag att tta agc
176 Thr Tyr Lys Ala Lys Glu Lys Gly Val Lys Leu Pro Gly Tyr His Phe Val Asp His Cys Ile Glu Ile Leu Ser
                                                                  Leu

601 cat gac aaa gat tac aac aag gtt aag ctg tat gag cat gct gtt gct cat tct gga ttg cct gac aat gcc aga
201 His Asp Lys Asp Tyr Asn Lys Val Lys Leu Tyr Glu His Ala Val Ala His Ser Gly Leu Pro Asp Asn Ala Arg

676 cga taa                                                                    (EosFP wt: NCBI Accession AY765217)
226 Arg ochre                                  Green: d1EosFP; Maroon: d2EosFP; Green+Maroon: mEosFP; Red: IrisFP
```

2 - Sequences of wtDendGFP & variants Dendra and Dendra2

```
1   atg aat ctg att aaa gaa gat atg agg gtt aag gtg cat atg gaa ggg aat gta aac ggg cat gct ttt gtg att
1   Met Asn Leu Ile Lys Glu Asp Met Arg Val Lys Val His Met Glu Gly Asn Val Asn Gly His Ala Phe Val Ile

76  gaa ggg gaa gga aaa gga aag ccc tac gaa ggg aca cag acc ttg aac ctg aca gtg aaa gaa ggc gcg cct ctc
26  Glu Gly Glu Gly Lys Gly Lys Pro Tyr Glu Gly Thr Gln Thr Leu Asn Leu Thr Val Lys Glu Gly Ala Pro Leu
                                                        Ala

151 cca ttt tct tac gac atc ttg aca aca gca ttg cac tac gga aac aga gta ttc acc aaa tac cca gaa gat ata
51  Pro Phe Ser Tyr Asp Ile Leu Thr Thr Ala Leu His Tyr Gly Asn Arg Val Phe Thr Lys Tyr Pro Glu Asp Ile
                                      Val

226 ccg gat tat ttc aag cag tcg ttt cct gaa gga tat tcc tgg gaa aga acc atg act tat gaa gac aag ggc att
76  Pro Asp Tyr Phe Lys Gln Ser Phe Pro Glu Gly Tyr Ser Trp Glu Arg Thr Met Thr Tyr Glu Asp Lys Gly Ile
                                                                                Phe

301 tgt acc atc aga agc gac ata agc ttg gaa ggt gac tgc ttt ttc caa aac gtt cgt ttt aat ggg atg aac ttt
101 Cys Thr Ile Arg Ser Asp Ile Ser Leu Glu Gly Asp Cys Phe Phe Gln Asn Val Arg Phe Asn Gly Met Asn Phe
                                                                                Lys     Thr

376 ccc cca aat ggt cca gtt atg cag aag aaa act ttg aag tgg gaa cca tcc aca gag aag ctg cac gtg cgt gat
126 Pro Pro Asn Gly Pro Val Met Gln Lys Lys Thr Leu Lys Trp Glu Pro Ser Thr Glu Lys Leu His Val Arg Asp

451 ggg ttg ctt gtc ggt aat att aac atg gct ctg ctg ctt gaa gga ggt gga cat tac ctg tgt gac ttc aaa act
151 Gly Leu Leu Val Gly Asn Ile Asn Met Ala Leu Leu Leu Glu Gly Gly Gly His Tyr Leu Cys Asp Phe Lys Thr

526 act tac aaa gcg aag aag gtt gtt cag ttg cca gat tat cat ttt gtg gac cat cgc att gag atc ttg agt aat
176 Thr Tyr Lys Ala Lys Lys Val Val Gln Leu Pro Asp Tyr His Phe Val Asp His Arg Ile Glu Ile Leu Ser Asn
                                                Ala                                                 Gly

601 gac agc gat tac aac aaa gtg aag ctg tac gag cat ggg gtt gct cgc tat tct ccg ttg cca agt cag gcc tgg
201 Asp Ser Asp Tyr Asn Lys Val Lys Leu Tyr Glu His Gly Val Ala Arg Tyr Ser Pro Leu Pro Ser Gln Ala Trp
                                                Ala                                                 Val

676 tag
226 amber                    (DendGFP wt: NCBI Accession AF420591) (supp. fig1 Nature biotech. 24, 461-465 (2006))
                                                Blue: Dendra; Blue+Orange: Dendra2
```

Appendix II - Relaxations via nonadiabatic transitions

In quantum mechanics, the definitions of diabatic (from the Greek word διαβαινειν [diabainen] meaning "that can cross") and adiabatic processes that we will consider hereafter are different than their usual acceptation in thermodynamics. In thermodynamics indeed, an adiabatic (or isocaloric) process is a process where the parameters are changed slowly enough for the system to be in equilibrium at any time (constant entropy) and thus, no heat flow is transferred.

In quantum mechanics, a diabatic process is a process in which the conditions are changing so fast that the system is prevented to adapt its configuration so that the system probability density remains unmodified. An easy to understand image could be the case of a pendulum oscillating while its support is suddenly moved; the oscillations will be changed because the movement was too fast for the system to adapt its configuration. At the opposite, in an adiabatic process, the conditions are changing slowly enough for the system to adapt its configuration so that the system probability density is modified by this process, which means that the system will retain its initial character (its eigenstates) and its energy states will not make transitions. In the example of our pendulum, if the support is moved slowly enough, the oscillations will remain essentially unchanged.

The gradually changing parameters, namely the adiabatic parameters, allow the study and the understanding of the static properties of a system on account of the Born-Oppenheimer approximation. In this nonadiabatic approximation, the energy of a system is a function of the varying reaction coordinates of this system so that a potential energy surface (PES) can be calculated. If we consider electrons as our referent, their movement are deconvoluted from those of atomic nuclei that are much slower and the PES represent equilibrated energies at given atomic nuclei positions. Since in linear molecules there are 3N-5 vibrational degrees of freedom for atomic nuclei positions (with N = number of nuclei), for two atoms, only one degree of freedom is available and the PES can be represented in one dimension by a Morse curve. For a protein though, the number of degrees of freedom is so large that the PES

becomes a hypersurface that only can be rendered in 3D by selecting two of its numerous variables (reaction coordinates). Such surfaces (Figure II.2.14) constitute energy landscapes, made of "hills", "valleys" and saddle points, where reactants and products will have to find the minimum energy path for a reaction to occur at a given energy state. Of course, the possibilities to cross some energy barriers will depend on the vibrational energy of the system and this energy landscapes are strongly related with the Perrin-Jabłoński diagram (Figure I.1.1, page 7).

PES can be calculated at any eigenstate of the system ($|S_0\rangle$, $|S_1\rangle$...), however, if the adiabaticity holds in time, no transition will occur at all. Concerning photochemical systems that are excited according to the Frank-Condon principle and relax in a non-radiative way, one thus needs to conceive some breakdowns of this adiabaticity for transitions to occur between different states (Nakamura 2002); those collapses are called nonadiabatic transitions.

In a Franck-Condon excitation, the electron density is modified while the atomic nuclei coordinates do not change. During the following nanoseconds, the nuclei rearrange and either the system comes back to the ground state adiabatically with emission of fluorescence or heat, or via a nonadiabatic transition by slowly continuing to change its atomic coordinates. With such nonadiabatic passages, called Landau-Zener transitions, (Landau 1932; Zener 1932), two PES can intersect (they are said to be degenerate), defining a conical intersection, also known as diabolical conical (Teller 1937; Yarkony 1998) where the diabatic behavior makes that the eigenstates cannot be separated anymore. Those intersections play a major role in non-radiative de-excitation ways like isomerizations (Levine & Martinez 2006) since the system can come back to its ground state by following a PES (surface hopping, (Tully 1990)) by minimizing the energy barriers to cross.

Appendix III - From magnetic to optical memory

The revolution of optical memories that began in the early 1980's allowed the use of versatile data storage devices (until then only magnetic, like floppy discs) as real mass data storage devices comparable with hard-drives. In a world becoming "all digital", the need for big storage capacities became urgent and splicing big files on multiple small capacities floppy discs became more and more difficult. In 1982, Philips Consumer Electronics invented the Compact Disc (CD) that opened the way to new optical mass storage versatile devices. These discs are basically made of a polycarbonate substrate layer with a reflective surface which contains a spiral data track made of tiny holes called "pits". Those pits code for information on a binary system (pit=1, no pit=0) and they are read by an infrared laser beam which gets reflected on the recording surface (Cf. Table V.2.13 and Figure V.2.1-a). The gap between a data track spiral turn and the next one is called "pitch track" and its size is limiting for the laser spot size that can be used to read the data track. On this polycarbonate substrate layer, which measures 0.1 mm thick, a 1.1 mm thick dummy layer is spread for protection and focalization purposes.

Since the invention of the CD, several generations of format standards for laser-based discs have been proposed. Most of them generally failed to have a real success. Nevertheless, the use of red visible lasers (also known as ruby-red) with shorter wavelengths than infrared lasers permitted a narrowing of the data pits size. The Digital Versatile Disc (DVD) using this technology was invented in 1995 by a consortium of major companies like Philips, Sony, Matsushita and Toshiba (Cf. Table V.2.13 and Figure V.2.1-b). It allowed more than a six-fold gain in storage capacity compared to the CD, but the counterpart was the need to improve the optics so that with a wider numerical aperture, the reflective layer has been brought closer to the disc surface (from 1.1 mm to 0.6 mm). The use of blue-violet lasers, allowed once again the writing of more dense information and the release of the so-called High-Density Digital Versatile Disc (HD-DVD) by Toshiba (Cf. Table V.2.13 and Figure V.2.1-c). However, the numerical aperture remained roughly the same (and so the reflective layer position) which did not allow as high performances as what could have been expected. Therefore, the HD-DVD was quickly neglected for the new Blu-ray Disc and finally totally abandoned early 2008.

	CD	*DVD*	*HD-DVD*	*BD*
DISC ARCHITECTURE				
Substrate layer thickness (mm)	0.1	0.6	0.6	1.1
Dummy layer thickness (mm)	1.1	0.6	0.6	0.1
OPTICAL PROPERTIES				
Laser colors	Infrared	Ruby-red	Blue-violet	Blue-violet
Laser wavelength (nm)	780	650	405	405
Numerical Aperture	0.45	0.60	0.65	0.85
Laser spot on recording layer (µm)	1.6	1.1	0.62	0.48
MOLDING				
Track pitch (µm)	1.60	0.74	0.40	0.32
Minimum pit length (nm)	833	440	204	150
Pit width (nm)	500	320	250	250
Pit depth (nm)	125	120	75	?
Data track length (km)	5	11	22	27
DATA STORAGE				
Data density (GB/cm²)	0.17	1.17	3.16	6.21
Total storage capacity (GB)	0.7	4.7	15	25

Table V.2.13 - Physical properties for several generations of optical discs

Blu-ray Discs (BD) were invented in 2004 by a conglomerate called "Blu-ray Disc Association" (Cf. Table V.2.13 and Figure V.2.1-d), they use the blue-violet technology already used for the HD-DVD. Though, like for the evolution from the CD to the DVD, the numerical aperture and lenses were improved so that the reflective layer was brought even closer to the surface (from 0.6 mm to 0.1 mm). This had the big advantage to greatly expand the data storage density but had the major drawback to make the reflective layer highly sensitive to scratches since so close to the surface. This problem was finally solved by the development of new type of ultra-hard resin coatings.

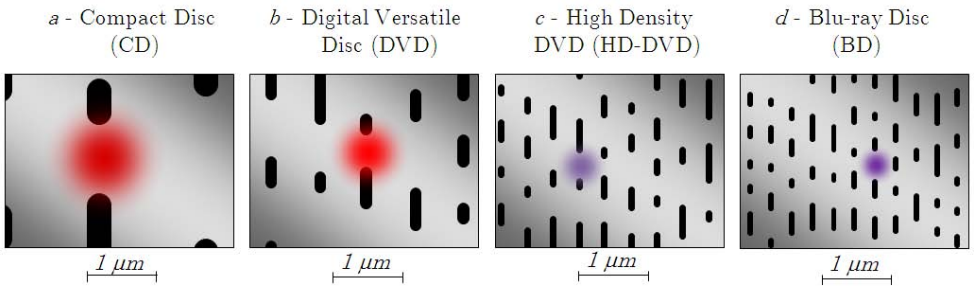

Figure V.2.1 - Representation of recording surfaces details for several generations of laser discs with pits (black) and reading laser spots (colors)

Appendix IV - Phylogeny of cnidarians producing FPs & CPs

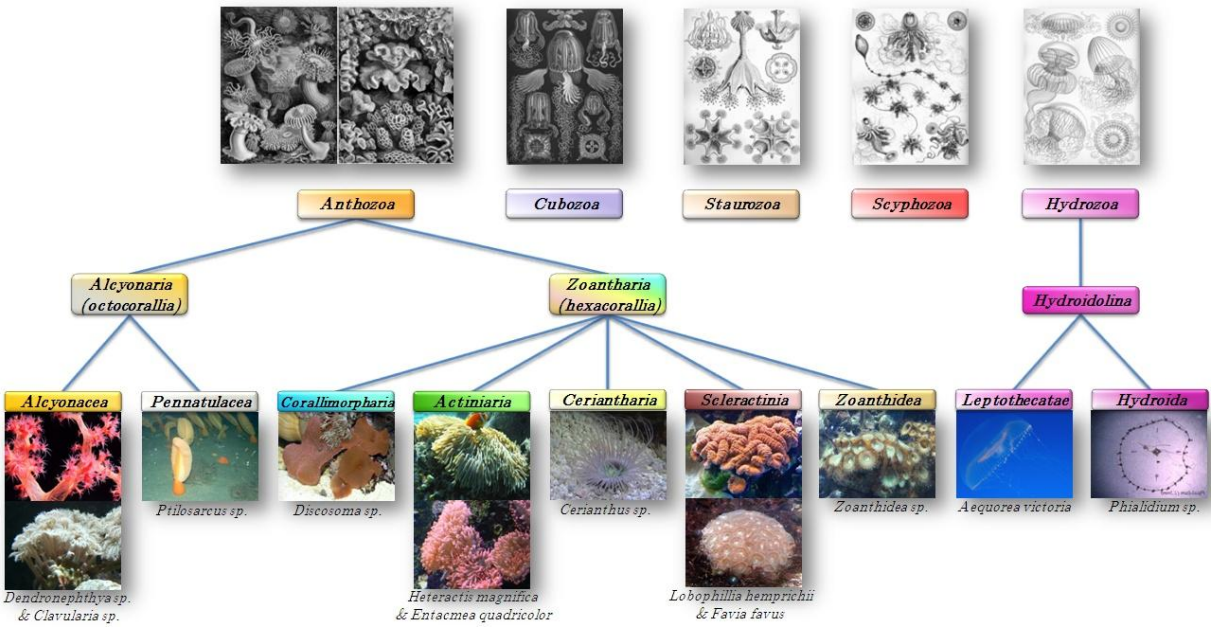

Figure V.2.2 - Illustrated phylogeny of cnidarians with their classis (1st row), subclassis (2nd row) and ordo (3rd row). Photos credits: Wikipedia[29]

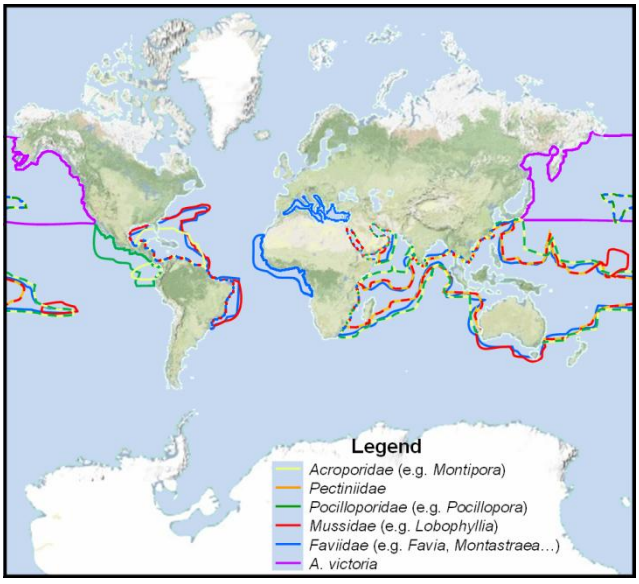

Figure V.2.3 - Map showing the world repartition of main corals producing FPs & CPs and A. victoria [created from (Péron 1809; Lamarck (de Monet de) 1816; Veron 2000a; b; c; d; e; f)]

[29] Wikipedia: The Free Encyclopedia. 23 Oct. 2005. Wikimedia Foundation (http://en.wikipedia.org/)

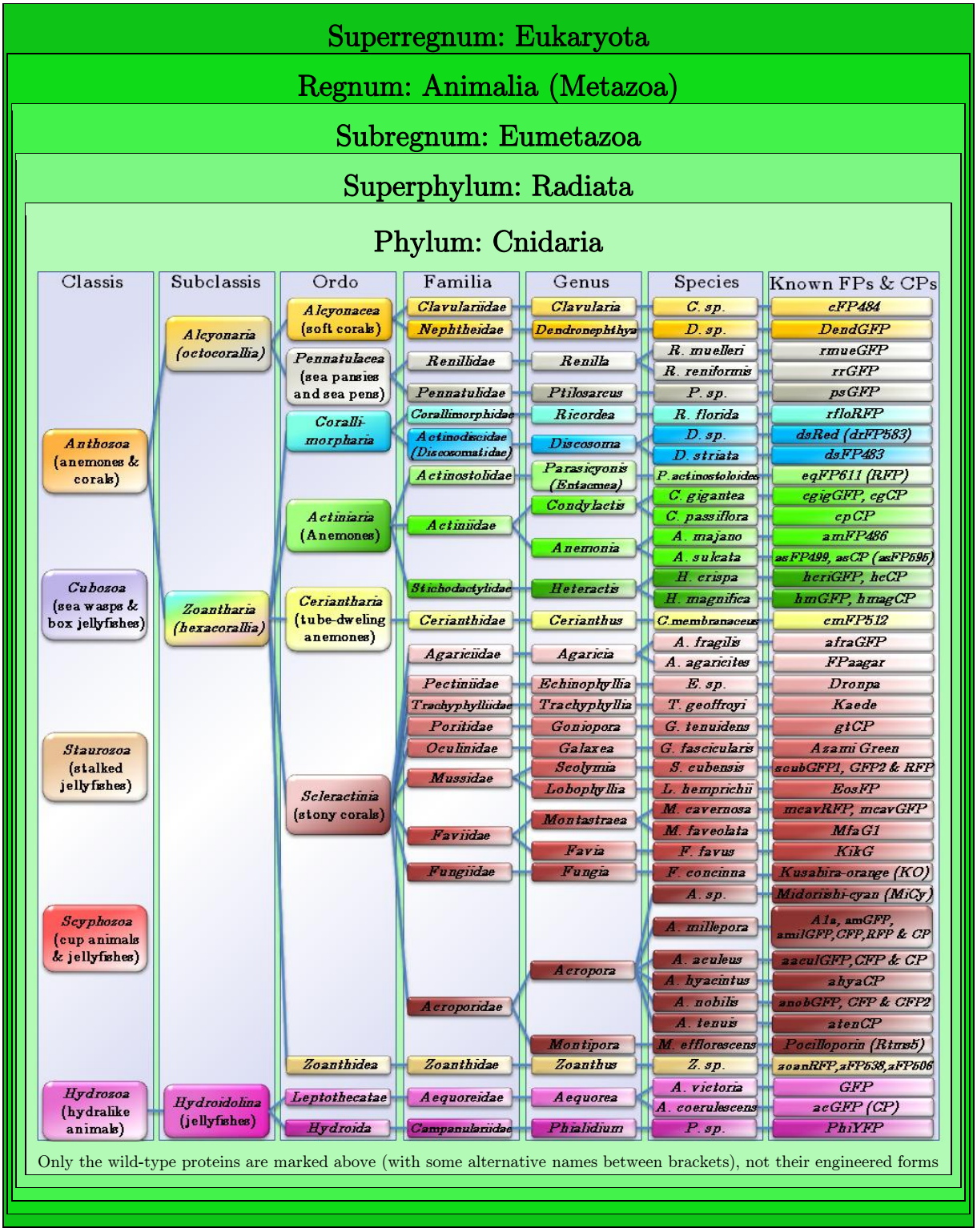

Figure V.2.4 - Complete taxonomy of cnidarian animals producing GFP-like proteins

Appendix V - The European Synchrotron Radiation Facility

The European Synchrotron Radiation Facility (ESRF) is a multinational research institute, situated in Grenoble, France (Figure V.2.5, a) and financed by 19 countries mostly European. The ESRF employs about 600 staff members and is organized as a French "société civile". The working language of the ESRF is English. Research at the ESRF is carried out by several thousand external users each year from universities, public research laboratories and industry, and by the ESRF's own scientists. It operates a powerful synchrotron X-ray source with ~30 beamlines (instruments) covering a wide range of scientific research in fields such as biology & medicine, chemistry, earth & environmental sciences, materials & surface science and physics.

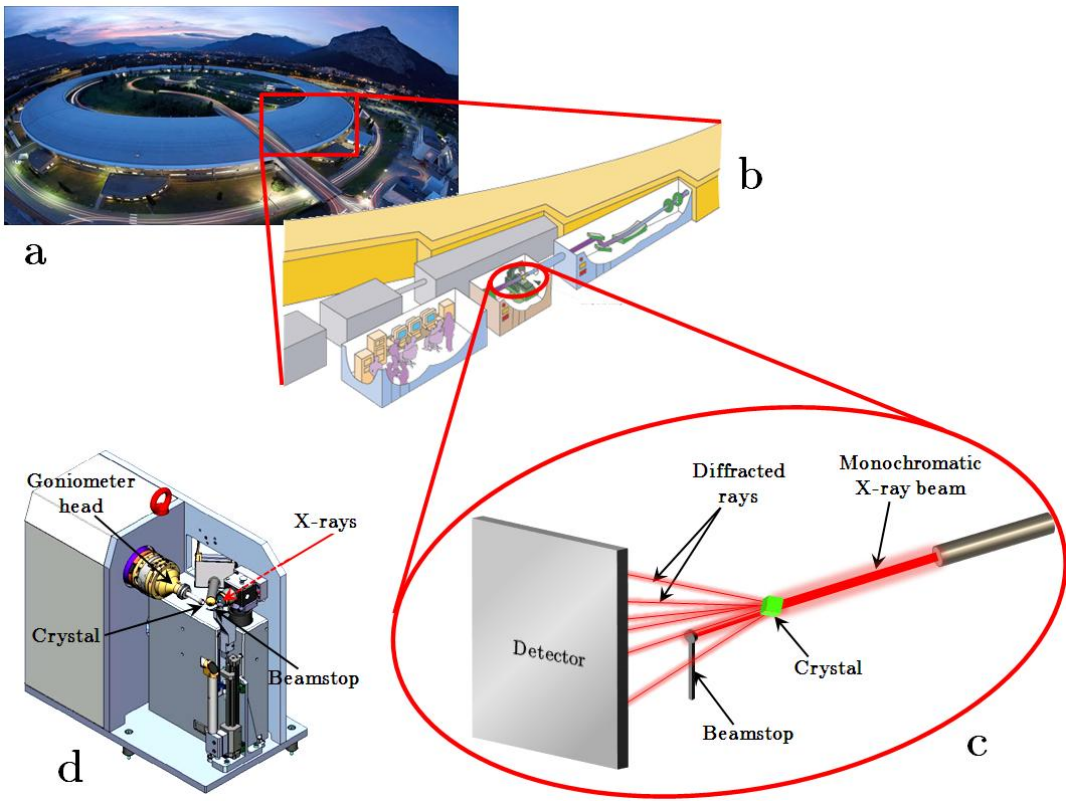

Figure V.2.5 - A classical diffraction experiment at the ESRF.
Inside the ESRF ring (a) the electron storage ring (b, orange) gives rise to X-ray beamlines (b). A crystal is mounted inside the beamline experimental hutch (c) on the goniometer head of a diffractometer (d) that will rotate the crystal in front of a monochromatic X-ray beam. Diffracted X-rays will be collected by a detector while transmitted X-rays will be absorbed by a beamstop

Each beamline (Figure V.2.5, b) is specialized in a particular field of science and its instrumentation differs accordingly. The macromolecular crystallography (MX) group currently owns seven beamlines all over the ESRF ring: ID14-1, ID14-2, ID14-3, ID14-4, ID23-1, ID23-2 and ID29. If certain particularities exist between each of these beamlines, the general principle is the same. In the beamline experimental hutch (Figure V.2.5, c), a crystal is mounted on a goniometer head and the X-ray beam is diffracted by the crystal. The diffracted rays are then detected by a CCD detector. The goniometer is part of a mini- or a micro-diffractometer (Figure V.2.5, d), which is a device that has been standardized on all the MX beamlines and allows the accurate centering of the crystal, its precise rotation and the positioning of several tools such as the nitrogen cryostream nozzle (not shown), the visualizing lamp and the beamstop.

Appendix VI - Publications

During the time of this Ph.D. thesis, I have worked on several projects in parallel. Most of these projects are directly related to the work presented in this volume, while some others are issued from studies I worked on, prior to my thesis, but only finished during it. The outcome of the studies directly in relation with this thesis led to five publications.

Publications directly in relation with the work presented in this thesis:

A. Royant, P. Carpentier, J. Ohana, J. McGeehan, B. Paetzold, M. Noirclerc-Savoye, X. Vernède, V. Adam & D. Bourgeois *"Advances in spectroscopic methods for biological crystals Part I: fluorescence lifetime measurements"* – Journal of Applied Crystallography (2007) **40**, 1105-1112..... 269

V. Adam, M. Lelimousin, S. Boehme, G. Desfonds, K. Nienhaus, M.J. Field, J. Wiedenmann, S. McSweeney, G.U. Nienhaus & D. Bourgeois *"Structural characterization of IrisFP, an optical highlighter undergoing multiple photo-induced transformations"* – Proceedings of the National Academy of Sciences (2008) **105**, 18343-18348..... 277

V. Adam, K. Nienhaus, D. Bourgeois & G.U. Nienhaus *"Structural basis of enhanced photoconversion yield in GFP-like protein Dendra2"* – Biochemistry (2009) **48**, 4905-4915..... 283

M. Lelimousin, V. Adam, G.U. Nienhaus, D. Bourgeois & M.J. Field *"Photoconversion of the fluorescent protein EosFP: a hybrid simulation study reveals intersystem crossings"* – Journal of American Chemical Society (2009) **131**, 16814-16823..... 295

V. Adam, P. Carpentier, S. Violot, M. Lelimousin, C. Darnault, G.U. Nienhaus & D. Bourgeois *"Structural basis of X-ray-induced transient photobleaching in a photoactivatable green fluorescent protein"* – Journal of American Chemical Society (2009) **131**, 18063-18065..... 305

Publications on satellite projects I worked on during the time of this thesis:

F.P. Molina-Heredia, C. Houée-Levin, C. Berthomieu, D. Touati, E. Tremey, V. Favaudon, V. Adam & V. Nivière *"Detoxification of superoxide without production of H_2O_2. Antioxidant activity of superoxide reductase complexed with ferrocyanide"* – Proceedings of the National Academy of Sciences (2006) **103**, 14750-14755

G. Katona, P. Carpentier, V. Nivière, P. Amara, V. Adam, J. Ohana, N. Tsanov & D. Bourgeois *"Raman-assisted crystallography reveals End-on peroxide intermediates in a non-heme iron enzyme"* – Science (2007) **316**, 449-453

A.R. Howard-Jones, V. Adam, A. Cowley, J.E. Baldwin & D. Bourgeois *"Cryophotolysis of a caged oxygen compound for use in low temperature biological studies"* – Photochemical & Photobiological Sciences (2009) **8**, 1150-1156

Publications obtained before starting this thesis:

D. Bourgeois, X. Vernède, V. Adam, E. Fioravanti & T. Ursby *"A microspectrophotometer for UV-visible absorption and fluorescence studies of protein crystals"* – Journal of Applied Crystallography (2002) **35**, 319-332

V. Adam, A. Royant, V. Nivière, F.P. Molina-Heredia & D. Bourgeois *"Structure of superoxide reductase bound to ferrocyanide and active site expansion upon X-ray induced photo-reduction"* – Structure (2004) **12**, 1729-1740

E. Fioravanti, V. Adam, H. Munier-Lehmann & D. Bourgeois *"The crystal structure of Mycobacterium tuberculosis thymidilate kinase in complex with 3'-azidodeoxythymidine monophosphate suggests a mechanism for competitive inhibition"* – Biochemistry (2005) **44**, 130-137

research papers

Journal of
Applied
Crystallography
ISSN 0021-8898

Received 8 April 2007
Accepted 10 September 2007

Advances in spectroscopic methods for biological crystals. 1. Fluorescence lifetime measurements

Antoine Royant,[a,b]* Philippe Carpentier,[a]* Jérémy Ohana,[a] John McGeehan,[c] Bernhard Paetzold,[b] Marjolaine Noirclerc-Savoye,[d] Xavier Vernède,[a] Virgile Adam[b] and Dominique Bourgeois[a,b]

[a]Laboratoire de Cristallogenèse et Cristallographie des Protéines, Institut de Biologie Structurale Jean-Pierre Ebel, CEA–CNRS–Université Joseph Fourier, 41 rue Jules Horowitz, F-38027 Grenoble, France, [b]ESRF, 6 rue Jules Horowitz, BP 220, F-38043 Grenoble Cedex, France, [c]EMBL, 6 rue Jules Horowitz, BP 181, F-38042 Grenoble Cedex 9, France, and [d]Laboratoire d'Ingéniérie Macromoléculaire, Institut de Biologie Structurale Jean-Pierre Ebel, CEA–CNRS–Université Joseph Fourier, 41 rue Jules Horowitz, F-38027 Grenoble, France. Correspondence e-mail: antoine.royant@ibs.fr, philippe.carpentier@ibs.fr

Synchrotrons are now producing thousands of macromolecular structures each year. The need for complementary techniques available on site has progressively emerged, either to assess the relevance of the structure of a protein or to monitor changes that may occur during X-ray diffraction data collection. Microspectrophotometers in the UV–visible absorbance or fluorescence mode have evolved over the past few decades to become the instruments of choice to perform such tests. Described here are recent improvements to the microspectrophotometer of the so-called Cryobench laboratory located at the European Synchrotron Radiation Facility, Grenoble, France. Optical and mechanical properties have been enhanced so as to record better spectra on smaller samples. A device has been implemented to measure the signal decay of fluorescent samples, either in the crystalline or in the solution state. Recording of the fluorescence lifetime in addition to the steady-state fluorescence emission spectrum allows precise monitoring of the fluorescent sample under study. The device consists of an adaptation of a commercially available time-correlated single-photon-counting (TCSPC) system. A method to record and analyze series of TCSPC histograms, *e.g.* collected as a function of temperature, is described. To validate the instruments, fluorescence lifetimes of fluorescent small molecules or proteins in the crystalline or solution state, at room and cryo temperatures, have been measured. Lifetimes of a number of fluorescent proteins of the GFP family were generally found to be shorter in crystals than in solution, and slightly longer at cryo temperatures than at ambient temperature. The possibility of performing fluorescence lifetime measurements on crystals at synchrotron facilities widens the variety of spectroscopic techniques complementing X-ray diffraction on macromolecular crystallography beamlines.

1. Introduction

Single-crystal UV–visible absorbance microspectrophotometry is an invaluable tool for providing X-ray crystallography with a complementary method to assess the relevance of protein structures. Pioneered in the 1970s (Rossi & Bernhard, 1970), this technique has been applied to many proteins containing metal centres or chromophores, in order to compare the properties of macromolecules in their crystalline and solution states (Mozzarelli & Rossi, 1996). Microspectrophotometry has become instrumental in kinetic crystallography studies, where it is used to monitor the build-up of reaction intermediate states within a crystal, particularly for photoactivable or redox proteins (Bourgeois & Royant, 2005). In recent years, it has been realised that X-rays can slightly alter protein structure, especially for coloured proteins, highlighting the need to check that spectroscopic signatures of a given protein in a crystal have not been altered after X-ray data collection (Ravelli & Garman, 2006). In the early 1990s, the emergence of portable microspectrophotometer devices adapted for crystals mounted in nylon loops within a cryogenic stream has contributed to the development of the use of *in crystallo* spectroscopy at synchrotron facilities (Pearson *et al.*, 2004).

Besides UV–visible absorption, fluorescence microspectrophotometry is a promising technique to assess the relevance of the X-ray crystallography-determined structures of proteins containing endo- or exogenous fluorescent groups. Pioneering studies have been performed with non-dedicated spectrometers, both in static and time-resolved modes, on slurries of tRNA crystals (Langlois *et al.*, 1975), on myoglobin single crystals of large dimensions (Willis *et al.*, 1991) and on crystalline GFP (Rosell & Boxer, 2003). The addition of the fluorescence mode to our microspectrophotometer allowed the recording of fluorescence emission spectra of excellent quality on protein crystals of small size, based on single-shot laser excitation and high-sensitivity CCD-based detection (Bourgeois *et al.*, 2002; see also the 4DX microspectrophotometer at http://www.4dx.se). Recently, the feasibility of online fluorescence spectroscopy on the diffractometer of a synchrotron beamline has been demonstrated with the FLUMIX device (Klink *et al.*, 2006).

For crystals of high optical density, fluorescence generally gives a much cleaner signal than absorption, the spectra of which are often flawed by saturated bands. Excitation at wavelengths remote from the peak absorbance may penetrate relatively homogeneously throughout the crystal. However, quantitative assessment of fluorescence emission may be complicated by inner-filtering effects inherent to highly concentrated samples such as protein crystals. Moreover, light scattering and refraction resulting from crystal morphology, as well as geometrical effects observed on microspectrophotometer devices, may slightly alter the fluorescence spectra.

Lifetime measurements are widely used in fluorescence spectroscopy of biological systems. In crystals, they are expected to be less dependent on morphology and concentration than steady-state data, thus providing an easier comparison from crystal to solution and from crystal to crystal. Furthermore, lifetime measurements may allow the deconvolution of contributions from fluorophores present in several copies, such as tryptophan residues. One tryptophan residue can be singled out among other residues, when its lifetime varies upon substrate or cofactor binding, or upon change in solvent environment. In addition, fluorescence lifetime measurements allow differentiation between static and dynamic quenching, which has implications in FRET (Förster resonance energy transfer) data analysis.

Recent work has illustrated the importance of measuring fluorescence lifetimes within a protein crystal (Pascal *et al.*, 2005). The authors have used the FLIM (fluorescence lifetime imaging microscopy) technique to scan the surface of a crystal of the light-harvesting complex II (LHCII) and showed that the chlorophyll fluorescence lifetime was essentially homogenous, with a mean value of 0.89 ns. This result strongly suggested that the published structure of the LHCII complex (Liu *et al.*, 2004) was that of the energy-dissipative oligomeric state, rather than the highly fluorescent trimeric state originally assumed by sole inspection of the crystallographic structure.

Our motivation for developing the fluorescence lifetime measurement option on our microspectrophotometer was to widen the possibilities of *in crystallo* fluorescence spectroscopy in the context of macromolecular crystallography at synchrotron facilities. Our main requirement was that spectroscopic data had to be obtained from crystals maintained in the same conditions as in an X-ray diffraction experiment. Thus, the device was developed to allow measurements from small crystals (~10 µm) mounted in loops at low temperature under a cryogenic stream. Two methods are widely used for measuring fluorescence lifetimes: the frequency- and time-domain methods (Lakowicz, 1999). We chose to use time-correlated single-photon counting (TCSPC), a time-domain method that consists of counting repeatedly the delay between one laser pulse and the generation by the sample of the first fluorescence photon. The number of photons recorded as a function of the time delay eventually builds up a histogram representative of the fluorescence decay.

We describe here improvements to our previous microspectrophotometer setup (Bourgeois *et al.*, 2002), the implementation of the fluorescence lifetime measurement technique, the design of a procedure to record a series of TCSPC histograms as a function of varying parameters (*e.g.* temperature) and an innovative method to analyze the data. The setup is adapted for nanolitre-sized samples that can be easily flash cooled; hence our instrument is perfectly suited for temperature-dependent studies, not only on crystals but also on amorphous solution samples. We provide examples of fluorescence lifetime measurements on protein and DNA crystals, as well as solutions, at low or room temperature. Our data pave the way for future experiments than can probe the effects of temperature, viscosity and crystalline character on the behaviour of fluorescent macromolecules.

2. Description of instruments and methods

2.1. Description of the microspectrophotometer

The original version of our microspectrophotometer (Bourgeois *et al.*, 2002) has been entirely rebuilt with greatly improved characteristics (Figs. 1*a* and 1*b*). Main improvements concern optical and mechanical performances. New reflecting mirror objectives (Optic Peter, Lyon, France) have a focal distance of 50 mm (compared with 26 mm before), thus increasing the available space around the sample. The demagnification ratio has been increased from 2 to 4: light issued from a 100 µm diameter optical fibre is focused on a 25 µm diameter spot. The overall transmittance of the setup (corresponding to the ratio between the intensity of the incoming light on the first objective and the intensity of the outgoing light from the second objective aligned in transmission mode) is now 13% at 280 nm, 25% at 450 and 650 nm, and 28% at 550 nm (compared with the mere 4% of the old setup). Filters and polarizers can be easily inserted in the optical path of each objective. The one-axis goniometer is now motorized and mounted on a stiff granite support greatly enhancing the mechanical stability of the setup. Translation and rotation stages with submicrometre positional accuracy allow precise centring of a sample, and contribute to the stability of the

system (no drift of sample position over days). Space opposite to the goniometer block is fully free so as to allow access for various devices such as the cryogenic cold stream (Oxford Cryosystems, Oxford, UK). Finally, a high-quality sample visualization camera system has been installed: the field of view covers about 400 × 400 µm, with a spatial resolution better than 5 µm at full zoom.

2.2. Description of the fluorescence measurement system

The setup consists of four different elements.

(*a*) A spectrometer for steady-state fluorescence (S2000 board, Ocean Optics Inc.).

(*b*) A pulsed laser diode (Picoquant GmbH, Berlin, Germany): wavelength, 440 nm; average optical power, 1.14 mW at 40 MHz; pulse duration, <300 ps at 1 mW, <90 ps at 0.3 mW.

(*c*) A photomultiplier (PMA-M, Picoquant).

(*d*) An acquisition board (TimeHarp 200, Picoquant).

The instrument is designed to allow the simultaneous recording of steady-state fluorescence spectra and fluorescence decay curves (see Fig. 1*c*). The excitation light from the pulsed laser diode is focused onto the sample by objective 1 *via* an optical fibre of 100 µm diameter, thus illuminating a focal volume smaller than 1 nl. The frequency of the laser can be adjusted between 40 MHz to 2.5 MHz, allowing measurements of fluorescence decays extending from ~100 ps to ~100 ns. Objective 2 collects light at 90° from objective 1 and records steady-state fluorescence emission over a wide spectral range. Objective 3, also in a 90° geometry, collects photons over a narrow wavelength range facilitated by the insertion of a 10 nm bandpass interferential filter selecting a relevant section of the emission spectrum, and guides the photons to the photomultiplier (PM). To ensure proper single-photon counting mode, the PM should not collect more than one photon every 100 cycles. The acquisition board measures the delay between the excitation pulse and the detection of a photon. The information is stored, and the process iterated until a histogram of sufficient signal-to-noise ratio is built up. Histograms with good signal-to-noise ratio are typically collected in one second [for a concentrated fluorophore (a few m*M*)] up to a few tens of seconds [for a diluted fluorophore (a few µ*M*)] in order to accumulate ~10^4 photons on the most densely filled channel.

2.3. Data acquisition

Dedicated software has been written to control the experiment with *LabVIEW* (National Instruments, Austin, TX) from a Windows PC allowing the user to monitor and control all essential parameters of an experiment through a graphical user interface (Fig. 2*a*). The ratio between the PM counting rate and the excitation rate is continuously calculated and the user is warned if the ratio exceeds 1/100. Series of histograms can be recorded either at constant temperature or during a temperature gradient whose rate, and initial and final temperatures can be programmed. Steady-state fluorescence spectra and TCSPC histograms are displayed in real time and can be stored on the control PC hard disk together with the time and temperature courses of the experiment. A complete set of data consists of a series of time points, temperature readings, steady-state fluorescence spectra and TCSPC histograms.

Solution measurements are performed under magic angle conditions by using polarizers rotated by 54.7° from each other. The intensity measured along a given polarization direction is given by:

$$I(t, \beta) \propto N(t)\left[1 + \left(3\cos^2\beta - 1\right)R(t)\right],$$

where β is the angle between the polarizer and the analyser, $N(t)$ the excited-state population and $R(t)$ the anisotropy of the sample defined as:

$$R = \frac{I_{\parallel} - I_{\perp}}{I_{\parallel} + 2I_{\perp}} = R_0 \exp\left(-\frac{t}{\theta}\right),$$

with $I_{\parallel}$ and $I_{\perp}$ being the parallel and perpendicular components of the emission signal, respectively, R_0 the fundamental anisotropy, and θ the rotational correlation time of the fluorophore.

When β is equal to 54.7°, $\cos^2\beta$ = 1/3, and one only measures a signal proportional to the excited-state population decay $N(t)$. These conditions are essential in the case where the fluorophore is expected to tumble on a timescale comparable with the intensity decay. However, if $R(t)$ is zero ($\theta \gg$ fluorescence lifetime τ, *i.e.* for negligible

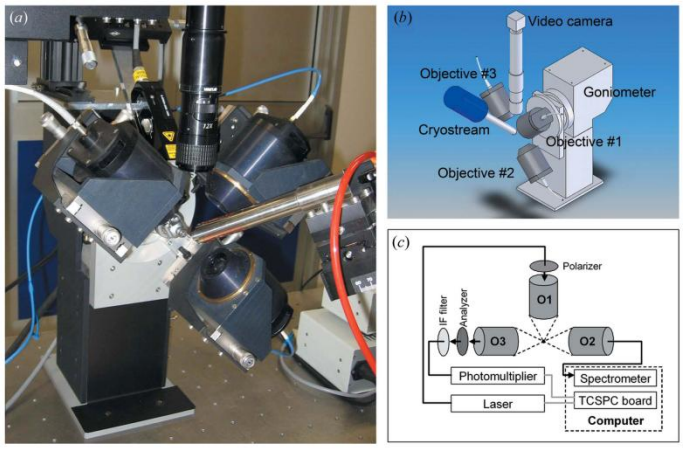

Figure 1
Experimental setup. (*a*) Photograph of the experimental setup. (*b*) Schematic of the Cryobench microspectrophotometer. (*c*) Principle of the TCSPC setup. Connections in black are optical fibres. Connections in grey are high-frequency cables.

viscosity), or constant over the observation time ($\theta \ll \tau$, *i.e.* when the viscosity is quasi-infinite), the magic angle geometry is not necessary. The latter case applies to immobilized fluorophores in a crystal or in a vitreous solution at cryogenic temperatures.

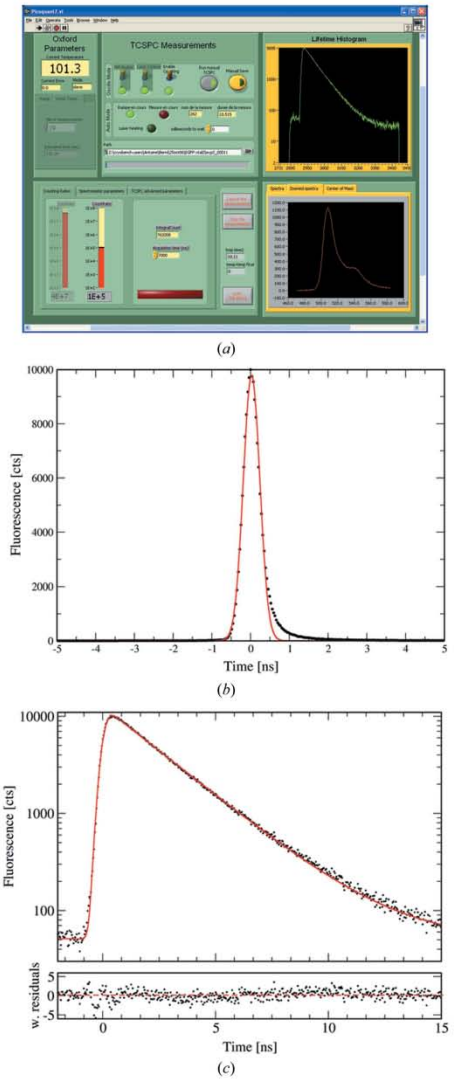

Figure 2
Interfaces used to carry out TCSPC experiments. (*a*) Experiment control software. (*b*) Instrument response function modelled by a Gaussian. (*c*) Fit of the decay curve. The experiment featured is that of an EGFP crystal at room temperature. The weighted residual of the fit is drawn below.

2.4. Data analysis

Ideally, the fluorescence decay upon a Dirac excitation pulse at time t_0 obeys the following multi-exponential behaviour:

$$I(t) = I_0 \sum_{i=1}^{n} \alpha_i \exp\left(-\frac{t - t_0}{\tau_i}\right) H(t - t_0),$$

where τ_i are the various lifetimes with weights α_i, and $H(t)$ the Heaviside function. In practice, the excitation pulse has a given duration, and the response of the instrument is not perfect. This means that the measured signal $I_m(t)$ consists of the convolution of $I(t)$ with the instrumental response function (IRF):

$$I_m(t) \equiv I(t) \otimes \mathrm{IRF}(t).$$

The experimental IRF is classically obtained by recording the TCSPC histogram of a non-fluorescent solution purely scattering the excitation light. However, on a microspectrophotometer, it is difficult to record the IRF accurately, as, for instance, the exact same loop with the same mother liquor, but without the fluorophore, would need to be used. In addition, the IRF needs to be recorded whenever experimental conditions are changed. This is of particular importance during temperature-resolved experiments, where strong changes in laser light scattering occur at temperatures inducing solvent phase transitions (*e.g.* water crystallization), and the IRF is clearly observed to evolve. Thus, the IRF would need to be recorded at each temperature, which is not possible in practice.

We have observed that most of the IRF histograms obtained with our setup are fairly well approximated by a Gaussian curve (areas differing by less than 5%, see Fig. 2*b*). This approximation is an acceptable trade-off, considering the difficulties in measuring the IRF accurately. Murphy *et al.* (1997) have used this approach to model the IRF in neutron time-of-flight experiments as a Gaussian distribution:

$$\mathrm{IRF}(t) = f_0 \exp\left[\frac{-(t - t_0)^2}{2\sigma^2}\right],$$

where σ^2 is the variance of the distribution.

$I_m(t)$ can then be analytically expressed by:

$$I_m(t) = I_{m0} \sum_{i=1}^{n} \alpha_i \exp\left(-\frac{t - t_0}{\tau_i}\right)\left\{1 + \mathrm{erf}\left[\frac{t - t_0 - \sigma^2/\tau_i}{(2\sigma^2)^{1/2}}\right]\right\}.$$

Hence, a TCSPC histogram can be fitted with a least-squares method with five parameters for a monoexponential decay and seven for a biexponential one. The contribution of the τ_i component to the total fluorescence intensity is given by:

$$\%I_i = \alpha_i \tau_i / \sum \alpha_i \tau_i$$

We have written a software program called *FluoTimeFit* to process sequentially collected series of histograms, collected, for instance, as a function of time or temperature (Fig. 2*c*).

2.5. Sample mounting

Room-temperature experiments are performed with two cover slides sandwiching 0.5 µl of solution, and sealed with silicone grease to prevent sample dehydration (Fig. 3) (Smulevich *et al.*, 1990). The drop comes either from a fluorophore solution, or from the mother liquor of a crystal. In the latter case, one crystal, or several, is deposited into the drop.

Experiments at cryogenic temperatures are performed on crystals, or solution films, mounted on cryoloops (Molecular Dimensions or Hampton Research) standing in the stream of a cooling device (Oxford Cryosystems, 600 series cryostream cooler). A cryoprotecting agent is added to the mother liquor when required.

2.6. Fluorophore solution and crystal preparation

2.6.1. DNA–ethidium bromide (EtBr) samples. DNA crystals are of the double-stranded 16-mer 5′-GCTGGAAATTTCCAGC-3′ grown in 34% PEG 200, 600 m*M* $CaCl_2$ and 10 m*M* HEPES pH 8.6 (McGeehan *et al.*, 2007). Conveniently, no additional cryoprotecting agent is required for cryogenic experiments. Interferential filters were chosen according to the fluorescence emission peak position, which varies between 580 and 610 nm depending on conditions, including presence of DNA, solution or crystalline state, and temperature.

2.6.2. EGFP/ECFP. EGFP and ECFP were purified and crystallized as previously described (Hyun Bae *et al.*, 2003; Jain & Ranganathan, 2004). Cryoprotection was ensured by addition of 20% glycerol to the mother liquor. Interferential filters were chosen according to the position of the fluorescence emission maxima, between 500 and 520 nm for EGFP, and between 470 and 500 nm for ECFP.

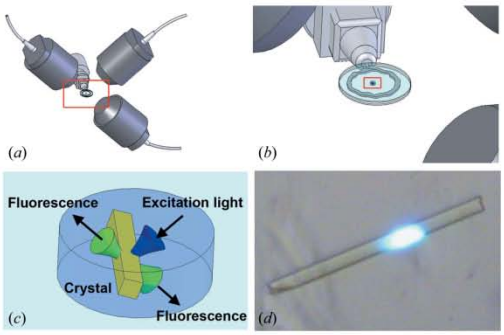

Figure 3
Experimental setup for room-temperature experiments. (*a*) View of the three objectives surrounding the sample. (*b*) Details of the glass slides sandwiching the drop, and sealed by silicone grease. (*c*) Details of a crystal within a mother liquor drop. The blue cone corresponds to the laser light focused onto the sample by the central objective; the two green cones correspond to the fluorescence signals that are gathered by the two objectives placed at 90° from the first one and are used for recording TCSPC histograms and steady-state fluorescence spectra, respectively. (*d*) Photograph of an ECFP crystal under the probing light.

2.6.3. EosFP. EosFP was purified and crystallized as previously published (Nienhaus *et al.*, 2005). Cryoprotection was ensured by addition of 10% glycerol to the mother liquor. Photoconversion was performed with 355 nm laser light. The green fluorescence lifetime was monitored at 520 nm and the red fluorescence lifetime was monitored at 580 nm.

3. Results

We have performed fluorescence lifetime measurements on a series of fluorescent samples in order to validate our instrument. Using an excitation wavelength of 440 nm, several fluorescent proteins as well as DNA oligomers stained with EtBr have been examined both in solution and in crystals, at ambient or cryogenic temperature. Samples were mounted on the microspectrophotometer as described above so that, in all cases, the volume probed by the laser is of the order of 1 nl. These experiments allowed us to investigate the effects of crystallization agents, cryoprotectants, crystalline state and flash cooling of samples on the fluorescence lifetime. Each TCSPC measurement consists of a series of 20–50 consecutively recorded histograms to verify that the laser probe did not have a significant photo-damaging effect on the fluorescence lifetime. For each sample, a steady-state fluorescence emission spectrum was first recorded to identify precisely the position of the emission peak of interest, since this can be affected by experimental conditions (Fig. 4*a*).

3.1. Ethidium bromide

EtBr is a well known fluorescent intercalating agent of DNA, and, as such, is a carcinogenic agent. Its fluorescent properties upon UV light excitation are significantly enhanced upon intercalation between two successive bases. As a result, this molecule has been extensively used for the staining of DNA separation gels and other common molecular biology techniques. We have investigated the mechanism of fluorescence enhancement by comparing the lifetime of EtBr in water to that when EtBr is bound to a 16-mer double-stranded DNA molecule, either in solution or in the crystalline state. Measurements were performed at 100 K or room temperature (298 K), and were compared with data from the literature. Although EtBr fluorescence is usually induced by UV light excitation in order to obtain maximal signal, the high sensitivity of our instrument allows an adequate signal to be measured by excitation at 440 nm.

Previous studies of EtBr complexed to double-stranded DNA in pure water revealed a long fluorescence lifetime of ~22 ns at room temperature, easily distinguishable from the ~1.75 ns lifetime of unbound EtBr (Heller & Greenstock, 1994; Olmsted & Kearns, 1977). The more than tenfold increase in lifetime upon DNA binding was accounted for by the sequestering of the ethidium moiety away from solvent thus preventing a fluorescence quenching mechanism previously attributed to excited-state proton transfer to water molecules (Olmsted & Kearns, 1977). In addition, it was also observed that the fluorescence of the DNA-bound EtBr may

be quenched by unbound EtBr, resulting in a reduction of lifetime down to 15 ns (Heller & Greenstock, 1994).

We first measured the fluorescence lifetime of EtBr in 0.5 µl drops at room temperature under different conditions (Table 1, Fig. 4*b*). A single component lifetime of 1.75 ns was measured in water, in perfect agreement with data from the literature. Addition of DNA, in a 1:16 EtBr–DNA base ratio, resulted in a mixture of a major long lifetime (21.0 ns) and a minor short lifetime (3.5 ns). When EtBr and DNA are only in a 1:37 ratio, the short lifetime disappears, in line with the idea that this stoichiometry ensures complete binding of EtBr to DNA. A solution of 1:16 EtBr–DNA supplemented with 34% PEG 200 and 600 m*M* $CaCl_2$ (crystallization conditions that also ensure cryoprotection) does not show modification of the fluorescence lifetime. DNA crystals soaked in 1 m*M* EtBr and washed twice for 10 min in the crystallization solution, exhibit a biexponential behaviour, with a short lifetime of 2–3 ns, and a long lifetime of 13–15 ns. The long component could be quenched, either by loosely bound or unbound EtBr molecules. The 3 ns component could represent the EtBr molecule bound to the outside of the DNA through electrostatic interactions (Olmsted & Kearns, 1977), as in the case of the solution study with stoichiometry 1:16.

The fluorescence lifetimes of the samples were also measured at 100 K, so as to probe the effect of the flash-cooling procedure typically applied in X-ray crystallography. The fluorescence lifetime of pure EtBr in the cryosolution is 20.5 ns, close to the reported value of 22 ns (±2 ns) (Olmsted & Kearns, 1977). The striking increase of the EtBr fluorescence lifetime upon cooling might be explained by the suppression of excited-state proton transfer in a rigid solvent matrix (Taylor *et al.*, 1969). Upon complexation with DNA, EtBr exhibits a 5–6 ns lengthening of its lifetime after flash cooling, both in solution and in the crystalline form. This lengthening is comparable with the 10 ns lengthening previously observed for polycrystalline samples of DNA–EtBr in glucose-cryoprotected samples (Olmsted & Kearns, 1977).

Table 1
Fluorescence lifetime measurement of ethidium bromide.

All experimental values in this table exhibit a χ^2 value below 2.0. Values in parentheses correspond to the standard deviation of the measurement. Solution samples are in water. Crystal samples are in their mother liquor.

	100 K		298 K	
	Lifetime (ns)	%	Lifetime (ns)	%
EtBr in solution	20.5 (5)	100	1.75 (5)	100
EtBr–DNA in solution (3:7, or 1:37)	n/a	n/a	20.5 (5)	100
EtBr–DNA in solution (1:1, or 1:16)	25.5 (5)	100	21.0 (5)	92 (1)
	–	–	3.5 (1)	8 (1)
EtBr–DNA crystal	20.5 (5)	100	14.0 (10)	91 (4)
	–	–	2.6 (4)	9 (4)

3.2. Fluorescent proteins EGFP, ECFP and EosFP

Enhanced green fluorescent protein (EGFP) and enhanced cyan fluorescent protein (ECFP) are derived from the well known green fluorescent protein from *Aequorea victoria*, and emit maximum fluorescence at 509 (green) and 477 nm (cyan), respectively. 'Eos' fluorescent protein (EosFP) is a protein from the stony coral *Lobophyllia hemprichii* that can be photo-converted from a green to a red fluorescent species upon UV light irradiation (Wiedenmann *et al.*, 2004). This property makes it a promising marker for tracking the movements of biomolecules within the living cell. These three proteins have a characteristic β-can shape and fluorescence arises from an endogenous tripeptide chromophore residing in the centre. The fluorescence decay of EGFP has been shown to be monoexponential with a lifetime of 2.9 ns (Swaminathan *et al.*, 1997) whereas that of ECFP exhibits a biexponential behaviour with lifetimes of 1.1 and 3.7 ns (Borst *et al.*, 2005). EosFP fluorescence has a lifetime of 2.9 ns in the green form and 3.6 ns in the red form (Ivanchenko *et al.*, 2005).

We have performed fluorescence lifetime measurements on nanolitre-sized protein solution samples and checked the agreement with literature

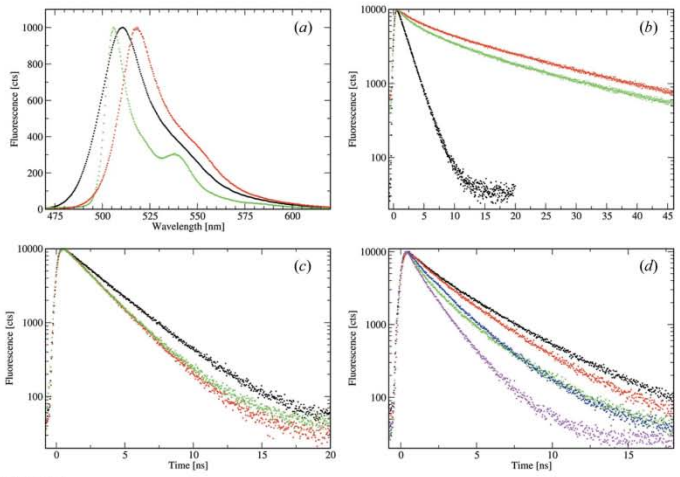

Figure 4
Emission fluorescence spectra and TCSPC histograms of fluorophores in various conditions. (*a*) Emission fluorescence spectra of EGFP (black, 30 µ*M* EGFP solution at room temperature; red, EGFP crystal at room temperature; green, EGFP crystal at 100 K). (*b*) TCSPC histograms of EtBr at room temperature (black, free EtBr in solution; red, EtBr–DNA solution; green, EtBr–DNA crystal). (*c*) TCSPC histograms of EGFP (black, 30 µ*M* EGFP solution at room temperature; red, EGFP crystal at room temperature; green, EGFP crystal at 100 K). (*d*) TCSPC histograms of ECFP [black, 30 µ*M* ECFP solution at room temperature; red, 30 µ*M* ECFP solution supplemented with 50% glycerol at room temperature; green, 30 µ*M* ECFP in mother liquor (24% PEG 8000, HEPES 100 m*M*, pH 7.2) at room temperature; pink, crystal at room temperature; blue, crystal at 100 K].

values. In a second step, we have measured the fluorescence lifetime of the various proteins in the crystalline state at room and cryogenic temperatures (Figs. 4*c* and 4*d*). All results are summarized in Table 2.

First, we have verified that the viscosity of the medium has an influence on fluorescence lifetime by adding increasing amounts of glycerol to ECFP in solution (Borst *et al.*, 2005). Indeed, a higher refracting index (higher viscosity) results in a shortening of the lifetime (black and red histograms in Fig. 4*d*). Then, we observed that crystallized EGFP and ECFP had a fluorescence lifetime decreased by 15–20%, which shows that bringing fluorophores 30–40 Å from each other does not introduce a major quenching effect. The decrease can be explained by the increase of viscosity due to the amount of precipitant, although an additional effect of crystal packing strains on the fluorophore dynamics can be envisaged. Finally, when the crystals are cooled to 100 K the lifetimes increase, which might be related to a decrease of the non-radiative decay when most protein motions are frozen.

Table 2
Fluorescent lifetime measurements of various fluorescent protein samples.

All experimental values in this table exhibit a χ^2 value below 2.0. Values in parentheses correspond to the standard deviation of the measurement. Crystal samples are in their mother liquor, supplemented with 10–20% glycerol for 100 K experiments. ECFP and EGFP solution samples are in 20 m*M* Tris pH 7.5. EosFP solution samples are in 50 m*M* sodium phosphate buffer pH 7.0, 300 m*M* NaCl.

	In a crystal				In solution	
	100 K		298 K		298 K	
Protein	Lifetime (ns)	%	Lifetime (ns)	%	Lifetime (ns)	%
ECFP	2.0 (1)	58 (7)	1.2 (1)	68 (6)	1.4 (1)	19 (2)
	3.7 (2)	42 (7)	3.0 (5)	32 (6)	3.7 (1)	81 (2)
EGFP	2.4 (2)	100	2.3 (1)	100	2.9 (1)	100
EosFP (green)	3.1 (3)	100	2.8 (2)	100	3.4 (1)	100
EosFP (red)	3.4 (3)	100	3.2 (1)	100	3.9 (1)	100

One interesting feature is the presence of two lifetimes for ECFP. It has been shown that ECFP displays structural heterogeneity on a loop separating the chromophore from the bulk solvent (Hyun Bae *et al.*, 2003). It is tempting to propose that a different accessibility of the chromophore to the solvent is responsible for the two lifetimes, by controlling the diffusion of fluorescence quenchers to the chromophore. Inversion of the short and long lifetime contributions may be due to an alteration of the dynamics of the loop responsible for the structural heterogeneity.

For the photoconvertible fluorescent protein EosFP the results show that in all tested conditions, the red form presents a longer fluorescence lifetime than the green form. The solution results (3.4 ns for the green form, 3.9 ns for the red form) compare well with the literature: 2.9 ns for the green and 3.6 ns for the red form (Ivanchenko *et al.*, 2005) given the differences in experimental conditions (excitation and observation wavelengths). As for EGFP and ECFP, the crystalline state introduces a 20% decrease of the green and red lifetime at room temperature, whereas cooling of the crystals to 100 K results in an increase of 10%.

4. Conclusion and perspectives

We have shown that fluorescence lifetimes can be measured from protein or DNA crystals that are endogenously or exogenously fluorescent, using the same experimental conditions as used in standard X-ray crystallography. In particular, one can monitor off-line a potential change in their fluorescence lifetime over an X-ray data collection. An improvement would consist of adapting the setup to the recently designed online microspectrophotometer (Ravelli *et al.*, in preparation). Other spectroscopic techniques, such as UV–visible absorption or Raman spectroscopy (Carpentier *et al.*, 2007) can be used simultaneously.

We have observed that it is necessary to record steady-state fluorescence at the same time as TCSPC histograms since the position of fluorescence emission maxima is sensitive to environmental conditions. Furthermore, this allows monitoring of eventual photobleaching or photoconversion induced by the probing light. Finally, we have shown that our setup is sensitive enough to probe the effects of temperature and viscosity on the lifetime of a fluorophore. Thus, the TDFM (temperature-dependent fluorescence microspectrophotometry) technique might be advantageously complemented by the monitoring of fluorescence lifetimes as a function of temperature, thus providing information on solvent and protein dynamics (Weik *et al.*, 2004).

These studies were carried out using an excitation wavelength of 440 nm; however, the system could be easily adapted to other wavelengths thus opening up the possibility of studying a broader range of fluorophores. In particular, the investigation of fluorescence lifetime of tryptophan residues in protein crystals would open the door to the study of numerous non-coloured proteins. Phosphorescence lifetime measurements on the micro- to millisecond timescale would also be of interest, and could be readily implemented in our system, considering that phosphorescence measurements are more complex than fluorescence ones because of oxygen quenching (Gabellieri *et al.*, 1988). One immediate application would be the fast screening of heavy-atom derivatives in protein crystallography, for example when the heavy atom belongs to the lanthanide family (Horrocks & Albin, 1984). Upon binding to a protein, lanthanide ions lose water from their solvation shell, which has a drastic effect on their luminescence behaviour. However, as lanthanides exhibit very narrow absorption bands, finely tuneable excitation sources would be needed for this application.

In conclusion, the possibility of performing fluorescence lifetime measurements in crystals enlarges the spectroscopic toolbox available to complement X-ray diffraction on synchrotron macromolecular crystallography beamlines.

This work has received financial support from the ESRF and the Ministère de l'Enseignement et de la Recherche, Contrat de plan Etat, Région Rhône-Alpes, France. We thank David Annequin for technical assistance, Karin and Ulrich Nienhaus for providing the protein EosFP, Nediljko Budisa for the gift of the ECFP cDNA, and Jacques-Philippe Colletier, Richard Kahn, Sean McSweeney, Raimond Ravelli, Benoît Sanson, Meike Stelter and Martin Weik for fruitful discussions.

References

Borst, J. W., Hink, M. A., van Hoek, A. & Visser, A. J. (2005). *J. Fluoresc.* **15**, 153–160.
Bourgeois, D. & Royant, A. (2005). *Curr. Opin. Struct. Biol.* **15**, 538–547.
Bourgeois, D., Vernede, X., Adam, V., Fioravanti, E. & Ursby, T. (2002). *J. Appl. Cryst.* **35**, 319–326.
Carpentier, P., Royant, A., Ohana, J. & Bourgeois, D. (2007). *J. Appl. Cryst.* **40**, 1113–1122.
Gabellieri, E., Strambini, G. B. & Gualtieri, P. (1988). *Biophys. Chem.* **30**, 61–67.
Heller, D. P. & Greenstock, C. L. (1994). *Biophys. Chem.* **50**, 305–312.
Horrocks, W. & Albin, M. (1984). *Lanthanide Ion Luminescence In Coordination Chemistry and Biochemistry*, Vol. 31, *Progress in Inorganic Chemistry*, pp. 1–104. New York: Wiley.
Hyun Bae, J., Rubini, M., Jung, G., Wiegand, G., Seifert, M. H., Azim, M. K., Kim, J. S., Zumbusch, A., Holak, T. A., Moroder, L., Huber, R. & Budisa, N. (2003). *J. Mol. Biol.* **328**, 1071–1081.
Ivanchenko, S., Röcker, C., Oswald, F., Wiedenmann, J. & Nienhaus, G. U. (2005). *J. Biol. Phys.* **31**, 249–259.
Jain, R. K. & Ranganathan, R. (2004). *Proc. Natl Acad. Sci. USA*, **101**, 111–116.
Klink, B. U., Goody, R. S. & Scheidig, A. J. (2006). *Biophys. J.* **91**, 981–992.
Lakowicz, J. R. (1999). *Principles of Fluorescence Spectroscopy*, 2nd ed. New York: Kluwer/Plenum.
Langlois, R., Kim, S. H. & Cantor, C. R. (1975). *Biochemistry*, **14**, 2554–2558.
Liu, Z., Yan, H., Wang, K., Kuang, T., Zhang, J., Gui, L., An, X. & Chang, W. (2004). *Nature (London)*, **428**, 287–292.
McGeehan, J. E., Carpentier, P., Royant, A., Bourgeois, D. & Ravelli, R. B. G. (2007). *J. Synchrotron Rad.* **14**, 99–108.
Mozzarelli, A. & Rossi, G. L. (1996). *Annu. Rev. Biophys. Biomol. Struct.* **25**, 343–365.
Murphy, T. J., Chrien, R. E. & Klare, K. A. (1997). *Rev. Sci. Instrum.* **68**, 610–613.
Nienhaus, K., Nienhaus, G. U., Wiedenmann, J. & Nar, H. (2005). *Proc. Natl Acad. Sci. USA*, **102**, 9156–9159.
Olmsted, J. & Kearns, D. R. (1977). *Biochemistry*, **16**, 3647–3654.
Pascal, A. A., Liu, Z., Broess, K., van Oort, B., van Amerongen, H., Wang, C., Horton, P., Robert, B., Chang, W. & Ruban, A. (2005). *Nature (London)*, **436**, 134–137.
Pearson, A. R., Mozzarelli, A. & Rossi, G. L. (2004). *Curr. Opin. Struct. Biol.* **14**, 656–662.
Ravelli, R. B. & Garman, E. F. (2006). *Curr. Opin. Struct. Biol.* **16**, 624–629.
Rosell, F. I. & Boxer, S. G. (2003). *Biochemistry*, **42**, 177–183.
Rossi, G. L. & Bernhard, S. A. (1970). *J. Mol. Biol.* **49**, 85–91.
Smulevich, G., Wang, Y., Mauro, J. M., Wang, J. M., Fishel, L. A., Kraut, J. & Spiro, T. G. (1990). *Biochemistry*, **29**, 7174–7180.
Swaminathan, R., Hoang, C. P. & Verkman, A. S. (1997). *Biophys. J.* **72**, 1900–1907.
Taylor, C. A., El-Bayoumi, M. A. & Kasha, M. (1969). *Proc. Natl Acad. Sci. USA*, **63**, 253–260.
Weik, M., Vernede, X., Royant, A. & Bourgeois, D. (2004). *Biophys. J.* **86**, 3176–3185.
Wiedenmann, J., Ivanchenko, S., Oswald, F., Schmitt, F., Rocker, C., Salih, A., Spindler, K. D. & Nienhaus, G. U. (2004). *Proc. Natl Acad. Sci. USA*, **101**, 15905–15910.
Willis, K. J., Szabo, A. G. & Krajcarski, D. T. (1991). *J. Am. Chem. Soc.* **113**, 2000–2002.

Structural characterization of IrisFP, an optical highlighter undergoing multiple photo-induced transformations

Virgile Adam[a], Mickaël Lelimousin[b], Susan Boehme[c], Guillaume Desfonds[a], Karin Nienhaus[c], Martin J. Field[b], Joerg Wiedenmann[d], Sean McSweeney[a], G. Ulrich Nienhaus[c,e,1], and Dominique Bourgeois[a,b,1]

[a]European Synchrotron Radiation Facility, 6 Rue Jules Horowitz, BP 220, 38043 Grenoble Cedex, France; [b]Institut de Biologie Structurale Jean-Pierre Ebel, Commissariat à l'Energie Atomique, Centre National de la Recherche Scientifique, Université Joseph Fourier, 41 Rue Jules Horowitz, 38027 Grenoble, France; [c]Institute of Biophysics, University of Ulm, Albert-Einstein-Allee 11, 89081 Ulm, Germany; [d]National Oceanography Centre, University of Southampton, Southampton SO14 3ZH, United Kingdom; and [e]Department of Physics, University of Illinois, Urbana, IL 61801

Edited by Hans Frauenfelder, Los Alamos National Laboratory, Los Alamos, New Mexico, and approved October 8, 2008 (received for review June 19, 2008)

Photoactivatable fluorescent proteins (FPs) are powerful fluorescent highlighters in live cell imaging and offer perspectives for optical nanoscopy and the development of biophotonic devices. Two types of photoactivation are currently being distinguished, reversible photoswitching between fluorescent and nonfluorescent forms and irreversible photoconversion. Here, we have combined crystallography and (*in crystallo*) spectroscopy to characterize the Phe-173-Ser mutant of the tetrameric variant of EosFP, named IrisFP, which incorporates both types of phototransformations. In its green fluorescent state, IrisFP displays reversible photoswitching, which involves *cis–trans* isomerization of the chromophore. Like its parent protein EosFP, IrisFP also photoconverts irreversibly to a red-emitting state under violet light because of an extension of the conjugated π-electron system of the chromophore, accompanied by a cleavage of the polypeptide backbone. The red form of IrisFP exhibits a second reversible photoswitching process, which may also involve *cis–trans* isomerization of the chromophore. Therefore, IrisFP displays altogether 3 distinct photoactivation processes. The possibility to engineer and precisely control multiple phototransformations in photoactivatable FPs offers exciting perspectives for the extension of the fluorescent protein toolkit.

fluorescent proteins | microspectrophotometry | photoactivation | photochromism | protein crystallography

In recent years, fluorescent proteins (FPs) from the green fluorescent protein (GFP) family have gained enormous popularity as genetically encoded fluorescence markers (1). They enable the visualization of a broad range of biological processes, including gene expression, protein translocation within cells, and cell movement during development. Photoactivatable FP variants have been recognized as particularly powerful imaging tools. Their fluorescence emission intensity or color can be controlled by irradiation with light of a specific wavelength, which allows selective highlighting of subsets of protein molecules within cells. This capability has been exploited in applications ranging from quantitative studies of protein movements in live cells (2, 3) to optical nanoscopy (4–6), and photoactivatable FPs may even be used in data-storage devices (7).

Two different groups of photoactivatable FPs are presently being distinguished. Members of the first group undergo reversible photoswitching between a fluorescent on state and a nonfluorescent off state (8–10), whereas members of the second group display irreversible photoconversion, either from a nonfluorescent to a fluorescent state (11–13) or between 2 fluorescent states with different emission wavelengths (14–19).

The structural basis of reversible photoswitching has been elucidated by crystallographic studies of several FPs including Dronpa (20), mTFP0.7 (9), and asFP595 (21). In the absence of light, the 4-(*p*-hydroxybenzylidene)-5-imidazolinone chromophores of Dronpa and mTFP0.7 assume a *cis* conformation, in which the anionic, fluorescent state of the chromophore is predominant at physiological pH. Light-induced off-switching of the fluorescence was proposed to arise from a *cis–trans* photoisomerization of the chromophore accompanied by a change of its protonation state (22–24), a loss of chromophore planarity and, for mTFP0.7, a more disordered chromophore structure in the *trans* conformation (9). Alternatively, the loss of fluorescence in the off state was recently explained by light-induced protonation of the Dronpa chromophore, associated with increased chromophore flexibility, which enhances nonradiative deactivation pathways (25). In this scenario, *cis–trans* isomerization may occur as a side effect. In asFP595, the nonfluorescent *trans* state is thermodynamically more stable than the *cis* state, and light irradiation induces a *trans–cis* isomerization to the *cis* state (21), in which a minor, zwitterionic state has been proposed to promote fluorescence (26). When kept in the dark, reversibly photoswitching FPs relax within minutes to several hours to the thermodynamically more stable isomeric state.

For irreversible photoconversion, several mechanisms have been identified. For EosFP, a photoconverting FP that changes its emission color from green to red upon irradiation with violet light (18), the X-ray structures have been determined for the green and red forms (27, 28). They revealed a light-induced extension of the conjugated π-electron system of the chromophore, accompanied by a breakage of the protein backbone between the amide nitrogen and the α-carbon of His-62 (EosFP residue numbering is used throughout this article), with surprisingly little change of the overall protein structure (27). Kaede (29), KikGR (17), and Dendra (14) are further representatives of green-to-red photoconverters that all share the tripeptide His-62–Tyr-63–Gly-64 as the chromophore-forming unit. A β-elimination reaction has been invoked to explain backbone cleavage, which may involve excited state proton transfer (ESPT) from the neutral chromophore to His-62 (27, 29), possibly assisted by dislocation of a water molecule (30). For PA-GFP (11) and PS-CFP (13), irreversible photoactivation

Author contributions: V.A., K.N., G.U.N., and D.B. designed research; V.A., M.L., S.B., and G.D. performed research; M.J.F., J.W., and S.M. contributed new reagents/analytic tools; V.A., M.L., S.B., and G.D. analyzed data; and V.A., M.L., K.N., G.U.N., and D.B. wrote the paper.

The authors declare no conflict of interest.

This article is a PNAS Direct Submission.

Data deposition: The atomic coordinates and structure factors have been deposited in the Protein Data Bank, www.pdb.org (PDB ID codes 2VVH, 2VVI, and 2VVJ).

[1]To whom correspondence may be addressed. E-mail: dominique.bourgeois@ibs.fr or uli@uiuc.edu.

This article contains supporting information online at www.pnas.org/cgi/content/full/0805949105/DCSupplemental.

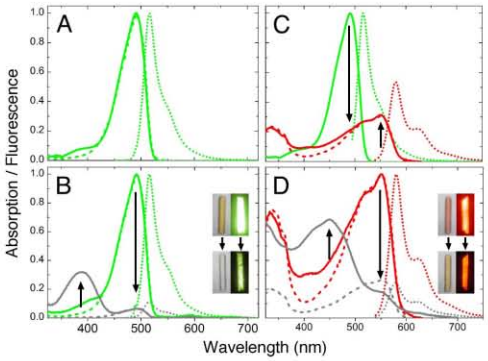

Fig. 1. Spectroscopic characterization of IrisFP. Absorption, excitation, and emission spectra scaled to equal maximum amplitudes are depicted by solid, dashed, and dotted lines, respectively. Emission spectra of green (red) IrisFP were obtained by exciting at 488 (532) nm. Excitation spectra of green (red) IrisFP were obtained by detecting at 550 (620) nm. (*A*) Green IrisFP. (*B*) Green IrisFP before (green lines) and after (gray lines) illumination with 488-nm light. (*C*) Red IrisFP (red lines) after photoconversion of green IrisFP (green lines) with 405-nm light. (*D*) Red IrisFP before (red lines) and after (gray lines) illumination with 532-m light. Spectra were recorded on solution samples in potassium phosphate buffer, pH 9. *Insets* show pictures of green IrisFP crystals before (*B Upper*) and after (*B Lower*) 488-nm illumination and of red IrisFP crystals before (*D Upper*) and after (*D Lower*) 532-nm illumination, respectively. Crystals are shown in bright-field mode (*Insets, Left*) and in fluorescence mode (*Insets, Right*). Detailed experimental procedures are provided in *SI Text*.

arises from stabilization of the anionic chromophore upon irradiation with violet light, presumably due to decarboxylation of Glu-212, as was earlier observed for GFP (31). Irreversible photoactivation has also been noticed for PA-mRFP1 (12) and the asFP595 Ala-148-Gly variant, also known as KFP1 (32); the underlying structural changes have yet to be elucidated.

The presence of structurally diverse photoactivation mechanisms suggests the intriguing possibility that multiple phototransformations can be implemented within a single photoactivatable FP. Such a highlighter would enable sophisticated photoactivation schemes that could help unravel complex protein interaction patterns. Here, we introduce IrisFP, a variant of the tetrameric form of EosFP, which can be switched reversibly between fluorescent and nonfluorescent forms in its green state, then photoconverted from green to red, and finally switched reversibly between fluorescent and nonfluorescent forms in its red state. A structural characterization of IrisFP based on a combination of X-ray crystallography and UV-visible spectrophotometry on crystal and solution samples provides a detailed picture of the different states of IrisFP at near-atomic level.

Results

Spectroscopic Characterization. In the course of random mutagenesis experiments on EosFP, the mutant Phe-173-Ser was generated. We discovered that this mutant undergoes multiple photoactivation processes and, therefore, named it IrisFP (the Greek goddess Iris personifies the rainbow). Optical absorption and emission spectra of IrisFP solution samples and photographs of crystals recorded after exposure to a variety of illumination conditions are shown in Fig. 1. The corresponding spectra measured on single crystals are presented in supporting information (SI) Fig. S1; spectroscopic parameters determined on solution samples are compiled in Table 1. In the green form of IrisFP (Fig. 1*A* and Fig. S1*A*), the main absorption band peaks at 487 nm; it is flanked by a vibronic shoulder at ≈460 nm. A minor absorption band resides at 390 nm. As for EosFP (18), the pH dependence of the absorption spectra (Fig. S2) reveals that the 487- and 390-nm bands are associated with the anionic and neutral states of the chromophore, respectively. Fluorescence emission, peaking at 516 nm, appears upon excitation of the anionic chromophore; the neutral form is only marginally fluorescent. The broader absorption/excitation bands of the anionic species [full width at half maximum (FWHM) 55 nm] as compared with EosFP (FWHM 25 nm) may reflect enhanced conformational freedom of the chromophore in IrisFP, which is also consistent with its decreased fluorescence quantum yield (Φ = 0.43, Table 1).

Illumination of IrisFP solutions or crystals at room temperature by 488-nm light leads to pronounced changes in the optical spectra (Fig. 1*B* and Fig. S1*B*). The absorption band of the anionic species at 488 nm decays rapidly, concomitant with an increase of the band of the neutral species at 390 nm. A crisp isosbestic point at 426 nm (data not shown) suggests a light-driven conversion of the chromophore from anionic to neutral. The resulting species is essentially nonfluorescent. Such experiments are usually difficult to perform with crystals, owing to their high optical density (in IrisFP crystals, the penetration depth is only ≈40 μm at 488 nm). Nevertheless, an almost complete loss of fluorescence can be achieved *in crystallo* because progressive deactivation of layers of molecules in the crystal ensures penetration of the actinic light into the bulk. The nonfluorescent state of the chromophore is very stable; it persists for hours in the dark ($t_{1/2}$ ≈5.5 h in solution). The recovery (on switching) is markedly accelerated by illuminating with 405-nm light, occurring within seconds. The quantum yields for off and on switching are estimated as Φ_{off} = 0.014 and Φ_{on} =

Table 1. Spectroscopic properties of IrisFP in solution

Parameter	Green IrisFP	Red IrisFP	Green EosFP	Red EosFP
$\lambda_{max,\ ex/em}$, nm	488 / 516	551 / 580	506 / 516	571 / 581
ε, M^{-1} cm^{-1}	52,200	35,400	72,000	41,000
$QY_{fluorescence}$	0.43 ± 0.02	0.47 ± 0.02	0.70 ± 0.02	0.62 ± 0.03
$QY_{off\ switching}$*	0.014	0.0020	—	—
$QY_{on\ switching}$*	0.5	0.047	—	—
$QY_{green\text{-}to\text{-}red\ conversion}$	0.0018	—	0.0008	—
Eff_{off}†	≈0.85	≈0.75	—	—
$t_{1/2,\ thermal\ recovery}$, h	5.5	3.2	—	—

Detailed experimental procedures are described in *SI Text*. λ_{max}, peak wavelength; ex, excitation; em, emission; ε, extinction coefficient; QY, quantum yield; $t_{1/2}$, half-life.
*Standard deviations are estimated as 25%.
†Switching efficiencies based on the following illumination conditions: Green IrisFP: 473 nm, 40 mW, ≈10 min. Red IrisFP: 532 nm, 50 mW, ≈10 min.

0.5, respectively. Off/on switching can be repeated several times in solution and in the crystal with minimal loss of fluorescence due to photobleaching (Fig. S3). Overall, the reversible switching behavior of green IrisFP resembles previous observations made with Dronpa (23) or mTFP0.7 (9), which suggests that IrisFP may undergo light-activated chromophore isomerization.

When stimulated by 405-nm laser light, the green IrisFP chromophore turns red (Fig. 1*C* and Fig. S1*C*). This photoconversion process gives rise to changes in the absorption and excitation spectra analogous to those reported earlier for the parent protein EosFP (18). The various bands can be assigned to differently charged chromophore species based on their response to pH changes (Fig. S2) and by comparison with EosFP. The excitation spectrum shows that the anionic species absorbs at 551 nm (with a vibronic shoulder at ≈515 nm) and fluoresces at 580 nm, whereas the neutral species, with a broad absorption feature at ≈450 nm, does not contribute to the fluorescence at 580 nm. Higher-order electronic transitions of the red chromophore are visible in the spectral region <400 nm. Prolonged exposure to violet light results in a slow decay of red fluorescence, possibly due to photobleaching. However, as a result of intramolecular Förster resonance energy transfer (FRET) from green to red subunits within the tetramer, already a moderate 405-nm light exposure yields an almost complete change to red fluorescence. The quantum yield of photoconversion is enhanced as compared with that of the parent protein ($\Phi_{green/red}$ = 1.8×10^{-3}, Table 1).

Exposure of red-converted IrisFP to green light (532 nm) induces yet another photoswitching event, characterized by a decrease in the red fluorescence (Fig. 1*D* and Fig. S1*D*). Concomitantly, absorption at 551 nm decreases and absorption at 450 nm increases, which suggests that a neutral form of the chromophore becomes stabilized. Under our experimental conditions, a maximum switching yield of ≈75% could be achieved (Table 1). In the dark, the new species slowly reverts to the red fluorescent state ($t_{1/2}$ ≈3.2 h). The return is strongly accelerated by exposure to 440-nm light. As for the green species, off/on switching can be repeated several times in solution and in the crystal with minimal loss of fluorescence due to photobleaching (Fig. S3). The quantum yields of photoactivated off and on switching of the red form are estimated to be Φ_{off} = 0.0020 and Φ_{on} = 0.047, respectively. Interestingly, at moderate levels of photoconversion to the red form, off-switching of the red fluorescence results in an increase in green fluorescence (Fig. S4), which arises from the loss of intramolecular energy transfer from green to red monomers within tetrameric molecules.

X-Ray Crystallographic Characterization. To reveal the structural basis of the spectroscopically observed photoactivation processes in IrisFP, we performed X-ray structure analyses on crystals that were exposed to light conditions chosen to enhance particular species. Data collection and refinement statistics are compiled in Table S1. The X-ray structure of the green form of IrisFP, crystallized in the dark, was determined at a resolution of 1.8 Å without prior light exposure. The asymmetric unit consists of a well-defined tetramer. The individual subunits of IrisFP show the classical β-can fold, with no major deviation from the EosFP structure (27), as indicated by the backbone rms deviation of 0.36 Å between the 2 models. The anionic chromophore is slightly nonplanar (Table S1), which may account for the lower fluorescence quantum yield as compared with EosFP (Table 1). The phenolate moiety is stabilized by a hydrogen bond to Ser-142 and 2 water molecules (W-2188 and W-2017, Fig. 2 and S5*A*). The remarkable photoactivation properties of IrisFP result from the replacement of Phe-173 by serine. In EosFP, Phe-173 forces the side chain of Met-159 to establish van der Waals contact with the hydroxybenzylidene moiety (Fig. 2). The smaller Ser-173 side chain in IrisFP reduces these steric constraints, and the Met-159 side chain rotates away from the chromophore. Two cavities are created (total volume ≈13 Å^3), each filled with a water molecule (W-2188 and W-2166, Fig. 2). The less-densely packed chromophore environment of IrisFP may lead to enhanced flexibility of the chromophore, which is in line with the spectroscopic observations that, compared with EosFP, the absorption and emission bands are broader and the fluorescence quantum yield is reduced.

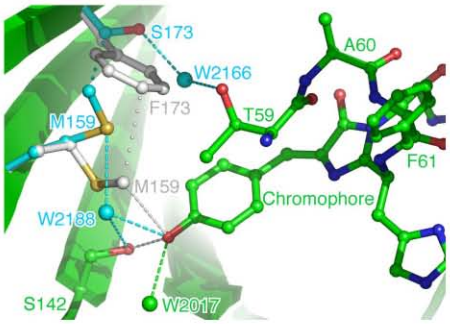

Fig. 2. Changes in the chromophore environment induced by the F173S mutation in EosFP. Common structural elements of EosFP and IrisFP are represented with green carbon atoms. Residues Phe-173 and Met-159 in EosFP are represented with gray carbon atoms, whereas the mutated residue Ser-173 and residue Met-159 in IrisFP are represented with cyan carbon atoms. The 2 water molecules (W-2188 and W-2166) are represented with cyan spheres, and W-2017 is represented with a green sphere. Hydrogen bonds are shown with dashed lines and van der Waals interactions with dotted lines.

To examine the structural basis of photoswitching of the green form of IrisFP, we illuminated a green crystal with 488-nm laser light and flash-cooled it immediately afterward. A diffraction dataset was collected to a resolution of 2.0 Å. An electron density omit map is shown in Fig. S5*B*. From the superposition of the refined models of the fluorescent and nonfluorescent forms in Fig. 3*A*, it is evident that off switching is accompanied by a *cis–trans* isomerization of the chromophore, as was earlier reported for Dronpa (20) and mTFP0.7 (9). The *trans* isomer of the chromophore is nonplanar (Table S1). Substantial rearrangements of residues Ser-142, His-194, Glu-212, Arg-66, and Ile-157 in the chromophore cavity are also apparent (Fig. 3*A*). The hydrogen bond between the phenolate oxygen of the *cis* chromophore and the Ser-142 hydroxyl side chain is removed and Ser-142 achieves a double conformation, either reorienting toward the solvent or H-bonding to His-194 and W-2188. The *trans* chromophore hydrogen-bonds to the presumably deprotonated carboxylate group of Glu-144 and to W-2032, most probably assuming a protonated phenolic form consistent with the observed loss of fluorescence and the increased absorption at 390 nm. The hydrogen-bonding network linking Glu-212 and Glu-144 via His-194 in the *cis* conformation involves Arg-66 in the *trans* conformation, implying large conformational rearrangements of the latter 2 residues similar to those observed in Dronpa (20) or mTFP0.7 (9). In addition, the side chain of Ile-157 undergoes a flip of ≈145°, possibly because of transient repulsion during chromophore isomerization. Based on these structures, the enthalpy difference between the 2 isomeric forms of green IrisFP was estimated from QM/MM molecular dynamics as 68 kJ/mol (*SI Text* and Table S2). This value is substantially smaller than the one estimated for EosFP (114 kJ/mol), assuming a similar *trans* structure. Calculations performed with null atomic charges for Ser-142 suggest that the stability of the *trans* isomeric state largely depends on the electrostatic interactions

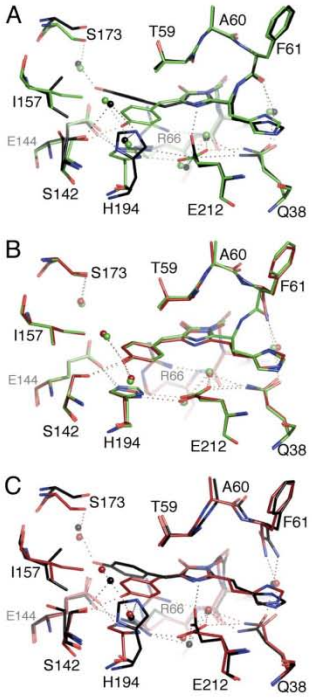

Fig. 3. Structural changes of the chromophore pocket upon phototransformation of IrisFP. (*A*) Superposition of the native green state (green) and the first reversibly switched state (black) obtained upon illumination at 488 nm. (*B*) Superposition of the native green state (green) and the irreversibly photoconverted red state (red) obtained after illumination at 405 nm. (*C*) Superposition of the red state (red) with the second reversibly switched state (black) obtained upon illumination at 405 nm, followed by illumination at 532 nm. In *C*, a putative model of the *trans* state of red IrisFP is shown (black). Hydrogen bonds are shown as dotted lines. Water molecules are shown as spheres.

between this residue and its environment. These interactions are much more favorable in IrisFP than in EosFP (Table S3). Diffraction data collected on a green IrisFP crystal after recovery in the dark from the off state confirmed the reversibility of the *cis–trans* isomerization, as the resulting structure was indistinguishable from the one of the initial fluorescent state (data not shown).

To determine the structure of red IrisFP, a green crystal was illuminated by 405-nm light and flash-cooled to collect a diffraction dataset at 2.0-Å resolution. Backbone cleavage between Phe-61 and His-62 was firmly established on the basis of omit electron density maps (Fig. S5*C*). Except for this modification, the superposition of the modeled chromophore environments of the green and red forms in Fig. 3*B* shows a nearly unperturbed chromophore pocket, as was observed earlier for red EosFP (27). A water molecule proximal to His-62 is dislocated in the red form, as was recently also reported for Kaede (30). These results support the notion of identical green-to-red photoconversion mechanisms for IrisFP and EosFP. Signs of radiation damage that could be caused by the long violet-light exposure of the sample, such as decarboxylation of Glu-212, were not noticeable.

To investigate the structural basis of reversible photoswitching of the red form of IrisFP, a green crystal was irreversibly

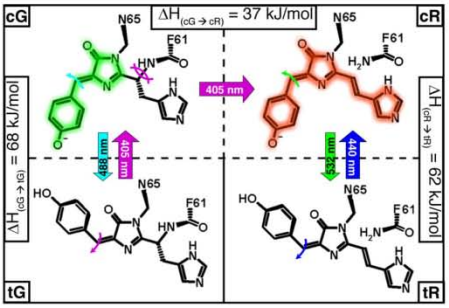

Fig. 4. Photoinduced transformations in IrisFP. Structural motions induced by light are represented by curved arrows of the same color as those used to represent light illumination at specific wavelengths. CG, *cis*-green Iris; tG, *trans*-green Iris; cR, *cis*-red Iris; tR, *trans*-red Iris.

photoconverted to the red form by illumination with 405-nm light and subsequently exposed to 532-nm light to induce reversible switching. After flash-cooling, diffraction data were collected to 2.2-Å resolution. In addition to the features characteristic of green-to-red photoconversion of IrisFP, the electron density map shows the *p*-hydroxybenzylidene ring in both the *cis* and *trans* conformations (Fig. S5*D*). This observation suggests a partial *cis–trans* isomerization of the chromophore, with features similar to those displayed by green off-switched IrisFP (Fig. 3*A*). However, the multiple conformations coexisting in the crystal, possibly as a result of limited penetration of green light within the crystal, made a reliable structural refinement difficult. Thus, assuming a *trans* conformation of the chromophore, only a tentative, energy-minimized model of the off-switched state could be produced (Fig. 3*C* and Fig. S5*D*). Based on this model, the enthalpy difference between the 2 isomeric states of red IrisFP was calculated to be 62 kJ/mol (Table S2). As for the green form, this difference is much higher for wild-type EosFP (122 kJ/mol) because of the less-favorable interactions of Ser-142 with its environment.

Discussion

From the spectroscopic and crystallographic data presented here, it is evident that 2 photoactivation mechanisms occur in IrisFP: reversible photoswitching between a fluorescent and a nonfluorescent state, based on *cis–trans* isomerization of the chromophore, and irreversible green-to-red photoconversion between 2 different fluorescent forms of the chromophore. Fig. 4 summarizes the different optical states of IrisFP, highlighting the richness of its photophysics.

Superposition of the structures of IrisFP, Dronpa, and mTFP0.7 in their fluorescent *cis* and nonfluorescent *trans* states (Fig. S6) suggests that reversible photoisomerization in these proteins proceeds by similar mechanisms. In all 3 proteins, rotation of the chromophore is coupled to concerted motions of His-194 and Arg-66. Glu-212 and Glu-144 act as nanotweezers, providing hydrogen bonds to His-194 in the *cis* configuration and to Arg-66 in the *trans* configuration and, thereby, stabilizing both conformations. However, this common configuration is clearly not sufficient to enable photoswitching, as it is also found in the *cis* state of nonphotoswitchable FPs such as EosFP or Kaede (29). Stabilization of the *trans* conformation of the chromophore requires additional interactions that, in particular, compensate for the cost of breaking the hydrogen bond linking the phenolate oxygen of the benzylidene group to Ser-142 in the *cis* state. Comparison between EosFP and IrisFP allows a precise identification of these additional interactions. Our enthalpy calcu-

lations (Table S3) suggest that an essential factor is the availability of a polar environment around Ser-142 in the *trans* state. In IrisFP, such an environment is provided by the repositioning of Met-159 and by the introduction of water molecule W-2188. As a consequence, Ser-142 may either hydrogen-bond to His-194 and W-2188 or reorient toward the solvent. Our molecular-dynamics simulations suggest that these 2 options are prohibited in EosFP because of the hydrophobic character of Met-159 residing in close vicinity of Ser-142 (Table S2 and Table S3). In Dronpa and mTFP0.7, Ser-142 is also observed to find hydrogen-bonding partners inside the barrel or to reorient toward the solvent in the *trans* configuration of the chromophore. Thus, there are several structural solutions to the problem of stabilizing Ser-142 (Fig. S6): in comparison with EosFP, Dronpa has a valine instead of Ile-157, mTFP0.7 a histidine instead of Met-159, and IrisFP a serine instead of Phe-173.

Another factor contributing to the stability of the *trans* state is the network of interactions available around the phenolic oxygen of the chromophore's benzylidene moiety in this state. In IrisFP, the phenolic oxygen is stabilized by Glu-144 and water molecule W-2032, which both provide hydrogen bonding. Therefore, in contrast to Dronpa and mTFP0.7, the chromophore environment in the *trans* conformation appears largely polar.

Whereas bistability is an essential property of photoswitchable FPs, efficient photoswitching requires a low transition barrier between the 2 isomeric states. Free space around the *p*-hydroxybenzylidene moiety of the chromophore can clearly influence the photoswitching kinetics. The superposition of the *cis* forms of EosFP, Dronpa, and mTFP0.7 (Fig. S6*A*) reveals that these proteins provide rather similar steric environments around the chromophore. In contrast, in IrisFP, the mutation Phe-173-Ser creates significantly more space around the chromophore, notably by displacing Met-159 (Fig. 2). This observation might relate to the exceptional switching quantum yields measured for this protein. Interestingly, the Dronpa mutant Met-159-Thr shows substantially faster photoswitching kinetics than Dronpa (33). Presumably, even more space is freed around the chromophore in this variant, further lowering the transition barrier at the expense of a much reduced fluorescence quantum yield.

It is interesting to note that the 3 proteins compared in Fig. S6 have a different first amino acid in the chromophore-forming triad, namely cysteine in Dronpa, histidine in IrisFP, and alanine in mTFP0.7. Therefore, on/off switching by photoisomerization apparently does not depend on the nature of this amino acid. We also noticed that the carboxylate group of Glu-212 in IrisFP rotates by 90° upon isomerization and forms a hydrogen bond to the presumably unprotonated nitrogen of the chromophore's imidazolinone moiety, contrary to what is observed in Dronpa or mTFP0.7. Therefore, Glu-212 in the neutral *trans* chromophore configuration appears to be protonated. Assuming that this residue is also protonated in the neutral *cis* chromophore configuration, this observation may implicate Glu-212 as a potential donor of a proton in the putative β-elimination reaction leading to green-to-red photoconversion in EosFP-type proteins (27, 29). In the *trans* configuration of green IrisFP, the Glu-212 carboxylate side chain appears too far removed from His-62 for efficient proton transfer (Fig. 3*A*). Therefore, green-to-red photoconversion is unlikely to occur from the neutral *trans* state. Rather, absorption of a violet photon may lead to deprotonation of the phenol oxygen (via excited-state proton transfer), favoring back-isomerization to the *cis* state, from which photoconversion to the red form may readily occur. The excited-state behavior of photoactivatable proteins is to a large extent determined by the protonation states of the chromophore and its environment (23, 26). Therefore, more detailed investigations of these protonation states and their interplay with isomerization will be required to decipher the photoactivation mechanisms of IrisFP.

One could be concerned that the presence of multiple phototransformations in IrisFP would result in poor yields for each of them and in a high susceptibility to photobleaching. However, reversible photoswitching in green IrisFP displays a remarkable efficiency compared with other Dronpa-like proteins. The yield of green-to-red photoconversion is also slightly increased compared with its parent protein EosFP, although red IrisFP appears more susceptible to photobleaching than EosFP. However, upon illumination with violet light, no chromophore photodamage is apparent in our crystal structures.

Our structural data suggest that the mechanisms for reversible photoswitching are essentially the same for green and red IrisFP, although the inhomogeneous chromophore conformation in the X-ray structure of photoswitched red IrisFP still leaves some possibility that isomerization may not be strictly required for switching in this state, as suggested for Dronpa (25). From the backbone breakage next to the chromophore in red IrisFP, which has also been noticed for the photoisomerizable marker protein asFP595 (21), one may expect an enhanced conformational flexibility of the chromophore and thus a facilitated light-induced isomerization. We noticed, on the contrary, that red IrisFP can be photoswitched to the nonfluorescent *trans* form slightly less efficiently than green IrisFP.

Incomplete green-to-red photoconversion may pose some limitations in one or the other marker application. Nevertheless, these adverse effects are greatly alleviated in the tetrameric form of IrisFP if we deliberately choose to only partially photoconvert the marker proteins in the sample. The strong FRET coupling between the chromophores in the tetramer leads to red fluorescence emission upon excitation of the green chromophores even if only 1 of the 4 chromophores is converted into its red fluorescent *cis* form (34). Off switching of the red form then results in the reappearance of green emission because the *trans* configuration of the neutral red chromophore does not absorb green light (Fig. S4). Thus, the partially red-converted tetramer effectively shows an interconversion between 2 bright states, red and green (Fig. S7). Such a mechanism is reminiscent of a technique used in DsRed to induce a color change (35) and also relates to the recently designed protein Phamret (36). It could be exploited further in tandem dimer constructs.

To turn IrisFP into a widely applicable highlighter protein, we aim to develop a monomeric version by introducing similar modifications as in EosFP (18), hoping that it will exhibit the same multiple photoactivation processes that we have observed here for the tetramer.

Conclusions

Photoactivatable FPs hold great promises for applications in cell biology. However, reversibly photoswitchable FPs are not visible in their off state, and photoconvertible FPs are limited by the nonreversible nature of photoconversion. These drawbacks may be alleviated with new highlighters such as IrisFP, which combine the 2 modes of photoactivation. Other applications taking advantage of the multiple phototransformations displayed by IrisFP will undoubtedly emerge, including two-color nanoscopy and sequential photoactivation schemes that can be beneficial for unraveling complex protein–protein interactions. IrisFP also hints at the possibility to combine read-only and rewritable capabilities in future mass storage media.

Materials and Methods

The experimental procedures are briefly sketched in the following; a detailed description is provided as *SI Text*. IrisFP was overexpressed and purified as EosFP (18). Rod-shaped crystals (0.2 × 0.2 × 0.8 mm^3) were grown at 20 °C in 2.4 M ammonium sulfate, 0.1 M bicine (pH 8.4).

X-ray data were collected at 100 K at the European Synchrotron Radiation Facility (ESRF). Crystal structures of IrisFP were solved by molecular replacement using EosFP as a starting model. To induce phototransformations, crystals were illuminated in their crystallization drops before flash-cooling. Illumination conditions are described in *SI Text*.

Spectra on solutions were taken at room temperature, by using protein concentrations of ≈10 μM (absorption) and 1 μM (fluorescence) in 100 mM potassium phosphate buffer (pH 9.0). *In crystallo* spectroscopy was carried out at 100 K by using the microspectrophotometer of the Cryobench laboratory (37).

Enthalpy differences between pairs of phototransformed states in IrisFP and wild-type EosFP were calculated with the *fDynamo* library (38), by using a QM/MM potential. The chromophore and the His-194 and Glu-212 side chains were in the QM region, and the remaining atoms were in the MM region. Enthalpy differences were estimated in 2 ways, by energy minimization of single structures and by Langevin molecular dynamics at 300 K for 100 ps with a time step of 1 fs.

ACKNOWLEDGMENTS. The European Synchrotron Radiation Facility is acknowledged for support of the Cryobench laboratory and for providing in-house beam time on beamlines ID14-3, ID23-1, and ID29. This work was supported by Agence Nationale de la Recherche Grant ANR-07-BLAN-0107-01 (to D.B.), Deutsche Forschungsgemeinschaft Grants NI 291/9 and SFB 497 (to G.U.N.), the Fonds der Chemischen Industrie (G.U.N.), and the Landesstiftung Baden–Württemberg (Elite Postdoc Program) (J.W.).

1. Shaner NC, Patterson GH, Davidson MW (2007) Advances in fluorescent protein technology. *J Cell Sci* 120:4247–4260.
2. Lukyanov KA, Chudakov DM, Lukyanov S, Verkhusha VV (2005) Innovation: Photoactivatable fluorescent proteins. *Nat Rev Mol Cell Biol* 6:885–891.
3. Wiedenmann J, Nienhaus GU (2006) Live-cell imaging with EosFP and other photoactivatable marker proteins of the GFP family. *Exp Rev Proteomics* 3:361–374.
4. Hess ST, Girirajan TP, Mason MD (2006) Ultra-high resolution imaging by fluorescence photoactivation localization microscopy. *Biophys J* 91:4258–4272.
5. Betzig E, *et al.* (2006) Imaging intracellular fluorescent proteins at nanometer resolution. *Science* 313:1642–1645.
6. Hofmann M, Eggeling C, Jakobs S, Hell SW (2005) Breaking the diffraction barrier in fluorescence microscopy at low light intensities by using reversibly photoswitchable proteins. *Proc Natl Acad Sci USA* 102:17565–17569.
7. Sauer M (2005) Reversible molecular photoswitches: A key technology for nanoscience and fluorescence imaging. *Proc Natl Acad Sci USA* 102:9433–9434.
8. Ando R, Mizuno H, Miyawaki A (2004) Regulated fast nucleocytoplasmic shuttling observed by reversible protein highlighting. *Science* 306:1370–1373.
9. Henderson JN, Ai HW, Campbell RE, Remington SJ (2007) Structural basis for reversible photobleaching of a green fluorescent protein homologue. *Proc Natl Acad Sci USA* 104:6672–6677.
10. Lukyanov KA, *et al.* (2000) Natural animal coloration can be determined by a nonfluorescent green fluorescent protein homolog. *J Biol Chem* 275:25879–25882.
11. Patterson GH, Lippincott-Schwartz J (2002) A photoactivatable GFP for selective photolabeling of proteins and cells. *Science* 297:1873–1877.
12. Verkhusha VV, Sorkin A (2005) Conversion of the monomeric red fluorescent protein into a photoactivatable probe. *Chem Biol* 12:279–285.
13. Chudakov DM, *et al.* (2004) Photoswitchable cyan fluorescent protein for protein tracking. *Nat Biotechnol* 22:1435–1439.
14. Gurskaya NG, *et al.* (2006) Engineering of a monomeric green-to-red photoactivatable fluorescent protein induced by blue light. *Nat Biotechnol* 24:461–465.
15. Mizuno H, *et al.* (2003) Photo-induced peptide cleavage in the green-to-red conversion of a fluorescent protein. *Mol Cell* 12:1051–1058.
16. Oswald F, *et al.* (2007) Contributions of host and symbiont pigments to the coloration of reef corals. *FEBS J* 274:1102–1109.
17. Tsutsui H, Karasawa S, Shimizu H, Nukina N, Miyawaki A (2005) Semi-rational engineering of a coral fluorescent protein into an efficient highlighter. *EMBO Rep* 6:233–238.
18. Wiedenmann J, *et al.* (2004) EosFP, a fluorescent marker protein with UV-inducible green-to-red fluorescence conversion. *Proc Natl Acad Sci USA* 101:15905–15910.
19. Ivanchenko S, *et al.* (2007) Two-photon excitation and photoconversion of EosFP in dual-color 4Pi confocal microscopy. *Biophys J* 92:4451–4457.
20. Andresen M, *et al.* (2007) Structural basis for reversible photoswitching in Dronpa. *Proc Natl Acad Sci USA* 104:13005–13009.
21. Andresen M, *et al.* (2005) Structure and mechanism of the reversible photoswitch of a fluorescent protein. *Proc Natl Acad Sci USA* 102:13070–13074.
22. Habuchi S, *et al.* (2005) Reversible single-molecule photoswitching in the GFP-like fluorescent protein Dronpa. *Proc Natl Acad Sci USA* 102:9511–9516.
23. Habuchi S, *et al.* (2006) Photo-induced protonation/deprotonation in the GFP-like fluorescent protein Dronpa: Mechanism responsible for the reversible photoswitching. *Photochem Photobiol Sci* 5:567–576.
24. Fron E, *et al.* (2007) Ultrafast excited-state dynamics of the photoswitchable protein Dronpa. *J Am Chem Soc* 129:4870–4871.
25. Mizuno H, *et al.* (2008) Light-dependent regulation of structural flexibility in a photochromic fluorescent protein. *Proc Natl Acad Sci USA* 105:9227–9232.
26. Schäfer LV, Groenhof G, Boggio-Pasqua M, Robb MA, Grubmüller H (2008) Chromophore protonation state controls photoswitching of the fluoroprotein asFP595 *PLoS Comput Biol* 4:e1000034.
27. Nienhaus K, Nienhaus GU, Wiedenmann J, Nar H (2005) Structural basis for photo-induced protein cleavage and green-to-red conversion of fluorescent protein EosFP. *Proc Natl Acad Sci USA* 102:9156–9159.
28. Nienhaus GU, *et al.* (2006) Photoconvertible fluorescent protein EosFP: biophysical properties and cell biology applications. *Photochem Photobiol* 82:351–358.
29. Ando R, Hama H, Yamamoto-Hino M, Mizuno H, Miyawaki A (2002) An optical marker based on the UV-induced green-to-red photoconversion of a fluorescent protein. *Proc Natl Acad Sci USA* 99:12651–12656.
30. Hayashi I, *et al.* (2007) Crystallographic evidence for water-assisted photo-induced peptide cleavage in the stony coral fluorescent protein Kaede. *J Mol Biol* 372:918–926.
31. van Thor JJ, Gensch T, Hellingwerf KJ, Johnson LN (2002) Phototransformation of green fluorescent protein with UV and visible light leads to decarboxylation of glutamate 222. *Nat Struct Biol* 9:37–41.
32. Chudakov DM, *et al.* (2003) Kindling fluorescent proteins for precise in vivo photolabeling. *Nat Biotechnol* 21:191–194.
33. Stiel AC, *et al.* (2007) 1.8 A bright-state structure of the reversibly switchable fluorescent protein Dronpa guides the generation of fast switching variants. *Biochem J* 402:35–42.
34. Cotlet M, *et al.* (2001) Identification of different emitting species in the red fluorescent protein DsRed by means of ensemble and single-molecule spectroscopy. *Proc Natl Acad Sci USA* 98:14398–14403.
35. Marchant JS, Stutzmann GE, Leissring MA, LaFerla FM, Parker I (2001) Multiphoton-evoked color change of DsRed as an optical highlighter for cellular and subcellular labeling. *Nat Biotechnol* 19:645–649.
36. Matsuda T, Miyawaki A, Nagai T (2008) Direct measurement of protein dynamics inside cells using a rationally designed photoconvertible protein. *Nat Methods* 5:339–345.
37. Bourgeois D, Vernède X, Adam V, Fioravanti E, Ursby T (2002) A microspectrophotometer for UV-visible and fluorescence studies of protein crystals. *J Appl Crystallogr* 35:319–326.
38. Field MJ, Albe M, Bret C, Proust-de-Martin F, Thomas A (2000) The dynamo library for molecular simulations using hybrid quantum mechanical and molecular mechanical potentials. *J Comput Chem* 21:1088–1100.

BIOCHEMISTRY
including biophysical chemistry & molecular biology
Article

Biochemistry **2009,** *48,* 4905 4915 4905
DOI: 10.1021/bi900383a

Structural Basis of Enhanced Photoconversion Yield in Green Fluorescent Protein-like Protein Dendra2[†]

Virgile Adam,[‡,#] Karin Nienhaus,[§,#] Dominique Bourgeois,[‡,∥] and G. Ulrich Nienhaus*[,§,⊥,¶]

[‡]*European Synchrotron Radiation Facility, 6 Rue Jules Horowitz, BP 220, 8043 Grenoble Cedex, France,* [§]*Institute of Biophysics, University of Ulm, Albert-Einstein-Allee 11, 89081 Ulm, Germany,* [∥]*Laboratoire de Crystallogenèse et Crystallographie des Protéines, IBS, Institut de Biologie Structurale Jean-Pierre Ebel, CEA, CNRS, Université Joseph Fourier, 41 Rue Jules Horowitz, F-38027 Grenoble, France,* [⊥]*Institute of Applied Physics and DFG-Center for Functional Nanostructures, University of Karlsruhe (TH), 76128 Karlsruhe, Germany, and* [¶]*Department of Physics, University of Illinois at Urbana−Champaign, 1110 West Green Street, Urbana, Illinois 61801* [#] *V.A. and K.N. contributed equally to this work*

Received March 6, 2009; Revised Manuscript Received April 16, 2009

ABSTRACT: Dendra2 is an engineered, monomeric GFP-like protein that belongs to a subclass of fluorescent proteins undergoing irreversible photoconversion from a green- to a red-emitting state upon exposure to purple-blue light. This photoinduced process occurs only in the neutral state of the chromophore and is known to result from backbone cleavage accompanied by an extension of the delocalized π-electron system. We have measured the X-ray structure of the green species of Dendra2 and performed a comprehensive characterization of the optical absorption and fluorescence properties of the protein in both its green and red forms. The structure, which is very similar to those reported for the closely related proteins EosFP and Kaede, revealed a local structural change involving mainly Arg66 and a water molecule W4, which are part of a charged and hydrogen-bonded cluster of amino acids and water molecules next to the chromophore. Unlike in EosFP and Kaede, Arg66 of Dendra2 does not contribute to negative charge stabilization on the imidazolinone ring by hydrogen bonding to the imidazolinone carbonyl. This structural change may explain the blue shift of the absorption and emission bands, as well as the markedly higher p*K*s of the hydroxyphenyl moiety of the chromophore, which were determined as 7.1 and 7.5 for the green and red species, respectively. The action spectrum of photoconversion coincides with the absorption band of the neutral species. Consequently, its 20-fold enhancement in Dendra2 at physiological pH accounts for the higher photoconversion yield of this protein as compared to EosFP.

The discovery of the green fluorescent protein from the jellyfish *Aequorea victoria* (avGFP) and its further development into a versatile research tool in the life sciences have enabled a vast array of novel approaches to gain insights into biomolecular processes, especially in living cells and organisms (*1*−*4*). Consequently, it was not a surprise that the Nobel Prize in Chemistry 2008 was awarded to Shimomura, Chalfie, and Tsien for the discovery, cloning, and development of avGFP (*5*−*8*). Fluorescent proteins (FPs)[1] from the GFP family have also been found in many other marine animals (*9*−*13*), some of which exhibited entirely new properties that are beneficial for imaging applications, including red-shifted fluorescence and photoactivation. Currently, the search for novel GFP-like proteins is ongoing, driven by the persistent need for advanced and specialized fluorescence labels for cellular imaging.

Although FPs are all structurally similar, their essential optical properties including absorption and emission spectra and fluorescence quantum yields vary greatly (*1*, *2*). Their polypeptide chain consists of 220−240 amino acid residues and folds into a rigid, 11-stranded β-barrel, with a central helix along its axis (*14*, *15*). In the center of the barrel, a fluorescent chromophore forms from the tripeptide X-Tyr-Gly in a posttranslational self-modification process that requires nothing else but molecular oxygen (*16*). The first amino acid, X, may be any amino acid, but the second and third amino acids, tyrosine and glycine, are strictly conserved in nature. The GFP chromophore, 4-(*p*-hydroxybenzylidene)-5-imidazolinone (*p*-HBI), is generated by sequential main-chain cyclization and oxidation−dehydration steps (*17*). For a number of FPs, additional chemical modifications of the chromophore result in substantial changes of the optical properties. Such modifications may occur spontaneously as, for example, the oxidation of the Nα−Cα bond of amino acid X (*18*), yielding the red-emitting 2-imino-5-(4-hydroxybenzylidene)imidazolinone chromophore of orange and red FPs such as DsRed (*19*) and eqFP611 (*20*). Other modifications are photoinduced and require absorption of a photon of suitable energy.

[†]This work was supported by the Deutsche Forschungsgemeinschaft (DGF) and the State of Baden-Württemberg through the DFG-Center for Functional Nanostructures (CFN), by DFG grants NI 291/9 and SFB 497, and by the Fonds der Chemischen Industrie (to G.U.N.). D.B. acknowledges support by the Agence Nationale de la Recherche (ANR-07-BLAN-0107-01).

*To whom correspondence should be addressed. E-mail: uli@uiuc.edu. Phone: +49 (0)731 502 3050. Fax: +49 (0)731 502 3059.

[1]Abbreviations: FP, fluorescent protein; GFP, green fluorescent protein; *p*-HBI, 4-(*p*-hydroxybenzylidene)-5-imidazolinone; ESPT, excited state proton transfer.

Published on Web 04/16/2009

Photoactivation offers an external control over the intensity or color of the fluorescence emission and allows a subset of proteins to be tagged and their subsequent dynamics to be followed within cells, tissues, or entire organisms (*21*, *22*). Moreover, photoactivation forms the basis of novel microscopy concepts featuring image resolutions substantially better than the Abbe (diffraction) limit (*23*−*26*).

Two types of photoactivation are being distinguished. Reversible photoswitching between a fluorescent and a nonfluorescent species involves isomerization of the chromophore, whereas irreversible photoconversion arises from a light-driven covalent modification. For a particular class of photoconvertible FPs, which comprises, among others, EosFP (*27*), mcavRFP (*28*), Kaede (*29*), KikGR (*30*), and Dendra (*31*), irradiation into the ~400 nm band of the neutral chromophore leads to cleavage of the backbone between the Nα and Cα atoms of amino acid X, which is always a histidine in these FPs (*32*−*35*). Concomitantly, a double bond forms between its Cα and Cβ atoms, so that the chromophore π-conjugation is extended to the histidine imidazole ring via an all-trans ethenylene moiety. The new chromophore, 2-[(1*E*)-2-(5-imidazolyl)ethenyl]-4-(*p*-hydroxybenzylidene)-5-imidazolinone, emits fluorescence in the orange-red region of the spectrum.

In this work, we report on structure−function relationships of Dendra2, a variant of Dendra (dendGFP), which was originally cloned from the soft coral *Dendronephthya* sp. from the Anthozoa subclass Alcyonaria (*31*). Like other naturally occurring anthozoan FPs, dendGFP oligomerizes and forms both dimers and tetramers. Dendra2 is an engineered, monomeric variant of dendGFP that was advertised as being photoconvertible by blue (488 nm) light (*36*). Monomerization, which was achieved by the three point mutations Asn121Lys, Met123Thr, and Tyr188Ala (Figure S1, Supporting Information), is crucial for applications as a fusion marker, for which the FP-encoding sequence is linked to the DNA of a protein of interest, thereby adding a fluorescent protein tag for protein visualization and tracking. Dendra2 and EosFP share 69% identical amino acid residues. The X-ray structure of green Dendra2 is overall highly similar to that of EosFP (*32*) but reveals structural differences close to the chromophore. The differences in the optical properties and photoconversion efficiency of Dendra2 and EosFP can be rationalized on the basis of these structural changes.

MATERIALS AND METHODS

Protein Expression and Purification. The pDendra2-B vector was purchased from Evrogen (Moscow, Russia). The sequence coding for Dendra2 was subcloned into a pQE32 expression vector (Qiagen, Hilden, Germany). *Escherichia coli* strain M15[pREP4] was transformed with the recombinant plasmid; protein expression was induced by IPTG. The soluble protein was kept in the dark during purification with a TALON metal affinity resin (BD Biosciences Clontech, Palo Alto, CA). The fraction containing the protein was dialyzed to remove the imidazole present in the elution buffer.

Crystallization. Crystals of Dendra2 were grown at 20 °C by mixing 2 μL of a solution of Dendra2 at 17.4 mg/mL and 2 μL of 30% PEG 4000, 0.2 M magnesium nitrate, and 0.1 M Tris-HCl, pH 8.5, using the hanging-drop vapor-diffusion method. Because the initial crystals diffracted poorly, they were crushed and, using the streak seeding method, transferred into preequilibrated crystallization drops of Dendra2 and a solution containing 32% PEG 3350, 0.1 M magnesium nitrate, and 0.1 M Tris-HCl, pH 8.8. A few single crystals diffracting to 2.0 Å resolution appeared after several weeks. Due to the poor reproducibility of the procedure, crystals of Dendra2 in its red form could not be obtained. For X-ray data collection, crystals of the green form were rapidly transferred to a cryoprotectant solution (10% glycerol/32% PEG 3350, 0.1 M magnesium nitrate, 0.1 M Tris-HCl, pH 8.8) and flash-frozen in a stream of nitrogen gas.

X-ray Data Collection. X-ray diffraction experiments were performed at 100 K on beamline ID14-4 (λ = 0.939 Å) at the European Synchrotron Radiation Facility (ESRF, Grenoble, France). We observed that the diffraction quality of the Dendra2 crystals decayed rapidly upon X-ray exposure. Thus, two crystals were used, and a composite data collection strategy was employed for each of them so as to maximize the completeness (*37*). After individual integration of the two data subsets with the program XDS (*38*), they were scaled and merged with the program XSCALE (*38*). The crystal structure was solved by molecular replacement with Phaser (*39*), using the coordinates of wild-type EosFP (PDB ID code 1ZUX (*32*)) as a search model. Crystallographic refinement was performed with Refmac (*40*) and COOT (*41*). Chromophore restraints were generated in Libcheck (*42*) using idealized coordinates from the Hic-Up database (*43*). The atomic coordinates and structure factors have been deposited in the Protein Data Bank (www.pdb.org, accession code 2VZX).

Optical Spectroscopy. To measure UV/visible spectra, Dendra2 was dissolved to final concentrations of ~10 μM (absorption) and 1 μM (fluorescence) in 100 mM potassium citrate/potassium phosphate (pH < 5), potassium phosphate (5 < pH < 8.5), and potassium carbonate buffers (pH > 8.5), respectively. Absorption spectra were collected at 20 °C on a Cary 1 spectrophotometer (Varian, Darmstadt, Germany) at a resolution of 1 nm. Fluorescence excitation and emission spectra were measured with a SPEX Fluorolog II spectrofluorometer (Spex Industries, Edison, NJ) with the excitation line width set to 2.2 nm; the emission was also recorded with 2.2 nm resolution. Emission spectra were corrected for the detector response.

RESULTS

Overall Structure of Dendra2. Dendra2 crystallized in the *P*1 space group. The structure was determined to 2.0 Å resolution, with a final R_{cryst} of 21.4% and R_{free} of 26.9% (Table 1). The unit cell contains eight protein chains (Figure 1), with little deviation between them (the average rmsd between two protomers in the asymmetric unit is 0.72 ± 0.21 Å). Most amino acids are visible in the electron density, unlike the hexahistidine tag preceding the N-terminus, which apparently is highly disordered. The typical GFP-like β-barrel fold of Dendra2 is shown in Figure 2A, with the nearly planar chromophore (Table 1) held rigidly in the center and shielded from the bulk solvent by the β-barrel and several interconnecting loops.

In a typical tetrameric anthozoan FP, each protomer, denoted A, B, C, and D, is in contact with two neighboring ones so that two subunit interfaces can be distinguished (denoted by A/B and A/C) (*44*). The A and B barrels are oriented in an antiparallel fashion, which produces a meshlike layering of the β-sheets in the A/B interface that is mainly stabilized by hydrophobic interactions. By contrast, in the more hydrophilic A/C interface, the neighboring barrels are rotated against each other to allow for perfect stacking of their β-sheets. Dendra2 was reported to be monomeric in solution (*36*), and its monomeric state may be responsible for the enormous difficulties we encountered

Table 1: Data Collection, Refinement, and Structure Quality Statistics of Dendra2

PDB accession code	2VZX
Data Collection Statistics	
beamline	ESRF/ID14-4
wavelength (Å)	0.939
space group	*P*1
cell dimensions	
a, *b*, *c* (Å)	71.26, 76.85, 92.50
α, *β*, γ (deg)	90.05, 108.17, 106.58
resolution (Å)	33.5−2.0 (2.1−2.0)[a]
R_{merge} (%)[b]	4.7 (17.4)
mean $I/\sigma(I)$	12.15 (4.42)
completeness (%)	94.1 (94.5)
no. of total reflections	220830 (30255)
no. of unique reflections	113215 (16379)
Refinement	
R_{cryst}/R_{free}[c]	0.214/0.269
no. of protein atoms	14474
no. of water	1276
average *B* factor (Å^2)	21.8
chromophore planarity[d]	
dihedral angle 1 (deg)	3.2 ± 1.1
dihedral angle 2 (deg)	8.5 ± 3.6
rms deviation from ideality	
bond lengths (Å)	0.009
bond angles (deg)	1.421

[a] Values in parentheses refer to the highest resolution shell. [b] $R_{merge} = \sum_j\sum_h|I_{h,j} - \langle I_h\rangle|/\sum_j\sum_h I_{h,j}$. [c] $R_{cryst} = \sum_h||F_o| - |F_c||/\sum_h|F_o|$. R_{free} is calculated with a small fraction (5%) of reflections chosen to be part of a test group. [d] Chromophore planarity was assessed by the measurement of the average dihedral angles linking atoms N2−Cα−C*β*−Cγ (dihedral angle 1) and Cα−C*β*−Cγ−Cδ (dihedral angle 2) of the chromophore.

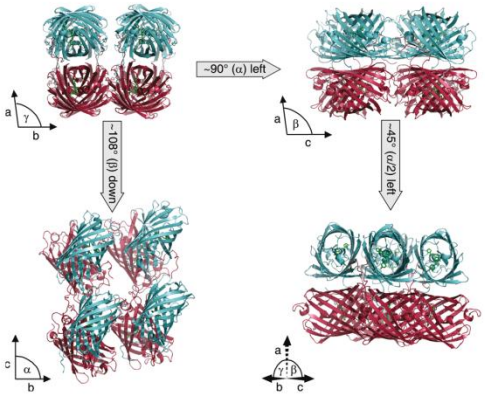

FIGURE 1: Crystal packing of Dendra2, shown along (A) the unit cell axis *c*, (B) the axis *b*, (C), the axis *a*, and (D) at half the angle (~45°) between the *b* and *c* axes. In each unit cell, eight molecules are arranged in four weak dimers; the protomers are colored in cyan and prune. Chromophores are shown as green sticks.

in growing crystals. In crystals, the Dendra2 protomers are observed to form A/C dimers because residual stabilizing interactions promote interface formation at the high protein concentrations present during crystal growth. Two salt bridges exist between Arg149 and Glu96 of each monomer (Figure 3), as in the EosFP A/C interface (*12*). (Here and throughout this paper, we report residue numbers according to Dendra2, as

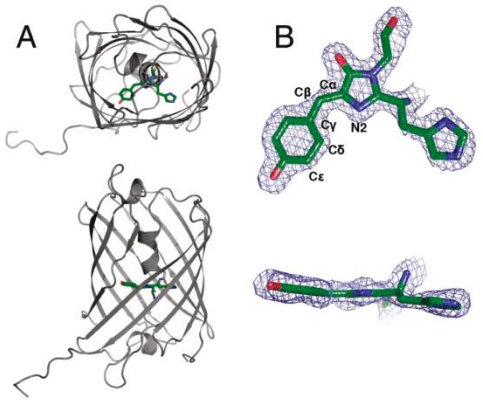

FIGURE 2: (A) Top and side views of the overall fold of a Dendra2 monomer in cartoon representation, with the embedded chromophore shown as sticks. (B) Top and side views of the chromophore. The $2F_o - F_c$ electron density map is contoured at 1.5*σ*.

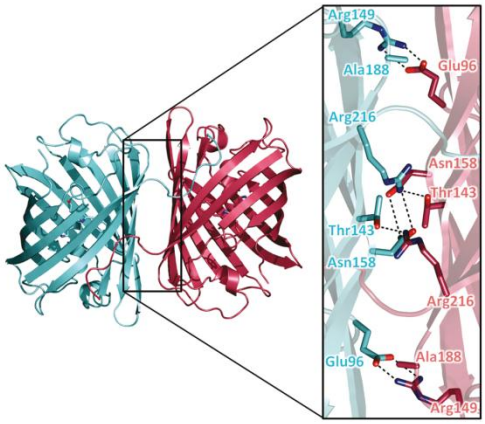

FIGURE 3: (A) Overview of the dimeric structure. (B) Close-up view of the interface. The residues involved in the strongest interactions are shown as sticks.

shown in the alignment in Figure S1, Supporting Information.) Additional interface stabilization is provided by hydrogen bonds within a cluster consisting of Thr143, Asn158, and Arg216 of both monomers. In EosFP, there is also a hydrogen-bonded cluster consisting of Thr143, Arg170, and Asp156. In EosFP, DsRed, and eqFP611, three aromatic residues at positions 188, 190, and 212 of the A and C chains form an additional hydrophobic patch. To generate the monomeric variant Dendra2, one of these residues (Tyr188) was replaced by alanine in the dendGFP sequence, which apparently was sufficient to destabilize the interface at low protein concentrations (*36*).

A typical A/B-type interface is absent in the Dendra2 crystal. Each pair of cyan and prune barrels in the lower left panel of Figure 1 represents an A/C dimer. Thus, A/B dimers would form between barrels of the same color. However, the cyan (prune) barrels plotted side by side are oriented in a parallel fashion, whereas the cyan (prune) barrels plotted above each other (within a column) are oriented in an antiparallel fashion but do not share

an interface. Compared with the wild-type protein, Dendra2 has two point mutations that were introduced to disrupt this interface, Asn121Lys and Met123Thr. The same residues were also modified to destroy the A/B interface in other anthozoan FPs, for example, Val123Thr in EosFP (*12*) and Thr121Arg and Val123Thr in eqFP611 (*44*). The sequence alignment of EosFP and Dendra2 shows that the interface-forming residues of these two proteins are identical except for position 121, at which the histidine of EosFP is replaced by a lysine in Dendra2. In EosFP, the His121 side chains of protomers A and B are π-stacked and, thereby, help to stabilize the interface. In Dendra2, the long lysine side chain may generate steric conflicts, and moreover, the charged amino groups repel each other, so that the interface is completely destabilized.

Chromophore Environment. In all green-to-red photoconvertible FPs, the chromophore forms from the tripeptide His-Tyr-Gly. Indeed, any amino acid replacement of the histidine abolishes photoconversion, suggesting that the imidazole side chain is crucially involved in the photochemical process (*32*). The amino acid preceding the chromophoric triad is a phenylalanine in many FPs including EosFP, Kaede, eqFP611, and avGFP. Interestingly, it is a valine (Val61) in Dendra2. Multiple hydrogen bonds and van der Waals interactions restrain the chromophore in the center of the β-can in an essentially coplanar arrangement of the aromatic imidazolinone and phenyl rings (Figure 2, Table 1). The cis conformation of the *p*-HBI chromophore is stabilized by hydrogen bonds from the tyrosine oxygen atom to the Ser142 oxygen (2.7 Å) and to a water molecule (W5, 2.8 Å). The carbonyl oxygen of the imidazolinone ring hydrogen-bonds with the side chain of Arg91 (2.9 Å).

Glu144, His193, Glu211, Arg66, water molecule W4, and Tyr177 form a planar network beneath the chromophore stabilized by hydrogen bonds and Coulomb interactions (Figure 4A). Similar polar networks, which may provide a rigid scaffold restricting chromophore dynamics, have been noticed for a variety of anthozoan FPs including DsRed (*18*, *19*), eqFP611 (*20*, *45*), zFP538 (*46*), and amFP486 by Henderson and Remington (*47*). The Arg66 side chain is held in place by a salt bridge from Nη_1 to Glu211, a hydrogen bond between Nη_1 and W3, and another hydrogen bond from Nη_2 to W4. It is further stabilized by a weak hydrogen bond between its Nε and the side chain hydroxyl of Thr69 (Figure 5). The same Arg66 stabilization and orientation has been found in amFP486 (*47*), mKO (*48*), and mTFP1 (*49*).

The chromophore environment of EosFP is shown in Figure 4B for comparison. A significant structural difference in the immediate chromophore environment is obvious; namely, water W4 and the Arg66 guanidino group have exchanged their locations. The completely different orientation of the Arg66 side chain in EosFP may originate from the replacement of Thr69 by Ala69 (Figure 5). The small aliphatic side chain cannot form a hydrogen bond to Nε of Arg66. This interaction is also absent in Kaede (*35*) and KikGR (*30*), carrying a valine and an alanine at position 69, respectively; their Arg66 side chains also adopt the EosFP-like position. As a consequence, the carbonyl oxygen of the imidazolinone is only 2.9 Å away from the Nη_1 atom of Arg66 in EosFP (2.8 Å in KikGR, 2.8 Å in Kaede), so that an additional hydrogen bond is established. In contrast, the distance between the Arg66 side guanidine moiety and the carbonyl oxygen is 3.9 Å in Dendra2 (3.9 Å in mTFP1, 3.6 Å in amFP486, 4 Å in mKO) and thus too long for hydrogen bonding. As will be described below, this structural finding bears consequences for the optical properties of Dendra2.

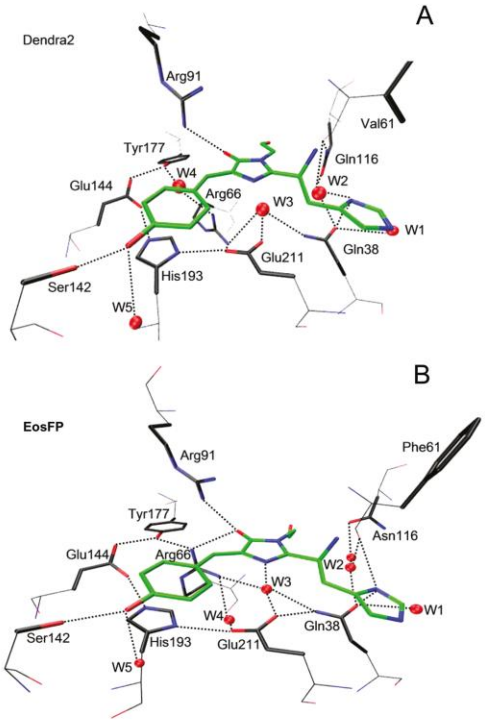

FIGURE 4: Chromophore environment in (A) Dendra2 and (B) EosFP. Water molecules are shown as red spheres. Hydrogen bonds are indicated by dotted lines. Color coding: carbon, black; oxygen, red; nitrogen, blue). The chromophore is shown with green carbon atoms.

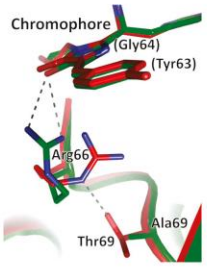

FIGURE 5: In Dendra2 (carbon atoms shown in red), the side chains of Arg66 and Thr69 are connected by a hydrogen bond. In EosFP (carbon atoms shown in green), there is no interaction between the Arg66 and Ala69 side chains.

For light-induced generation of the red 2-[(1*E*)-2-(5-imidazolyl)ethenyl]-4-(*p*-hydroxybenzylidene)-5-imidazolinone chromophore, two key amino acids have been identified, Glu211 and His62. Glu211 has been suggested to act as a base for proton abstraction from His62-Cβ, and indeed, replacement of Glu211 by Gln results in complete loss of photoconversion in EosFP (*12*) and Kaede (*35*). Likewise, mutation of His62 in Kaede (*34*) and EosFP (*27*) to another amino acid completely abolishes formation of the red chromophore. Based on the X-ray structures of

green and red EosFP, we had suggested that the His62 imidazolium may donate a proton to the Phe61 carbonyl, thus rendering the peptide group between Phe61 and His62 an ideal carboximidic leaving group in the β-elimination reaction (*32*). The distances between His62-Nδ and the Phe61 carbonyl are 3.3 Å in EosFP (*32*) and 3.2 Å in Kaede (*35*). In the Dendra2 structure, the corresponding distance between the His62-Nδ and the Val61 carbonyl is significantly larger, 3.8 Å. However, structural readjustments could occur in the excited state that strengthen the interaction and allow proton transfer to take place.

Absorption Spectra of Green Dendra2. The pH-dependent absorption spectra of green Dendra2 are shown in Figure 6A (for additional spectra, see Figure S2, Supporting Information). The two bands at ~385 and ~493 nm are denoted as A and B bands, respectively; they are associated with the neutral (phenol) and anionic (phenolate) forms of the chromophore (*16*, *50*, *51*). The exact peak positions vary with pH and are compiled in Table 2. (The near-UV band at 280 nm results from aromatic amino acid side chain absorption.) With increasing pH, the B band gains amplitude at the expense of the A band. The pH dependence of the transition can be modeled by a single-site protonation, with pK = 7.1 ± 0.1 (Figure 6B). This value is thus significantly higher than the corresponding ones of EosFP (pK = 5.8 (*27*)) and Kaede (pK = 5.6 (*29*)). For EosFP, we observed that replacement of Ala69 by threonine shifted the chromophore pK to ~7 (data not shown). Consequently, stabilization of the proton on the phenyl moiety in Dendra2, which amounts to ~7.5 kJ/mol, may arise from the altered Arg66 side chain conformation due to its interaction with Thr69. The lack of hydrogen bonding between Arg66 and the carbonyl oxygen of the imidazolinone ring results in reduced negative charge stabilization on the ring. The concomitantly enhanced charge density on the hydroxyphenyl moiety may contribute to the stronger proton binding affinity of Dendra2. The same structural difference can also explain the blue shift of the absorption maximum of the anionic green chromophore (492 nm) in Dendra2 with respect to EosFP (506 nm). Upon electronic excitation of the *p*-HBI chromophore, the electron density is known to shift from the phenyl to the imidazolinone (*16*, *52*). The missing charge stabilization on the imidazolinone by Arg66 in Dendra will, therefore, raise the energy of the excited state with respect to the ground state, resulting in a blue shift of the transition. In complete agreement with this explanation, the Thr69Ala mutation indeed turns Dendra2 into a more EosFP-like protein, with the B band red shifted to 502 nm (Table 3), whereas the Ala69Thr mutation of EosFP elicits the opposite effect (data not shown).

Interestingly, in the high-pH regime (pH > 10), the population ratio between the neutral and the anionic chromophore is observed to shift back to the protonated species (Figure S2, Supporting Information). Most likely, the water molecule W5 (Figure 4) that, together with Ser142, stabilizes the negative charge on the phenolate oxygen is exchanged by a hydroxyl ion at high pH, so that the protonated hydroxyphenyl ring becomes energetically favored. At pH 13, a new absorption band at 446 nm appears at the expense of both the A and B bands (dotted line in Figure 6A). For avGFP, a band at a similar position (448 nm) was reported upon base denaturation (*53*), whereas the synthetic analogue of the GFP chromophore, 4-hydroxybenzylidene-2,3-dimethylimidazolinone (HBDI), has an absorption maximum at 425 nm in NaOH. In Dendra2, the 446 nm band subsequently loses intensity, and concomitantly, a new band appears at 347 nm (gray line in Figure 6A). An isosbestic point at 384 nm indicates a two-state transition (Figure S2, Supporting Information); the marked decrease of the wavelength indicates a less delocalized π-electron system in this state. This process is irreversible, suggesting that the chromophore has been destroyed.

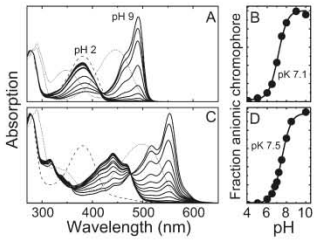

FIGURE 6: Absorption spectra of (A) green and (C) red Dendra2, recorded from pH 4 to pH 10. The spectra of acid/base-denatured Dendra2 are included as dashed/dotted lines. (C) The gray line represents the species which develops at pH 13 with time. (B, D) Symbols: Fraction of deprotonated chromophores as a function of pH. Fit (lines) of the data to a Henderson−Hasselbalch relation.

Table 2: Optical Properties of Dendra2

		neutral chromophore		anionic chromophore	
	pH	$\lambda_{max\,abs}$ (nm/cm^{-1})	$\lambda_{max\,em}$ (nm/cm^{-1})	$\lambda_{max\,abs}$ (nm/cm^{-1})	$\lambda_{max\,em}$ (nm/cm^{-1})
green	1	381.7/26200[a]	–	–	–
	4	378.8/26400	454[b]	–	–
	7	383.1/26100	–	460.8/21700	542.0/18450
				492.6/20300	*504.5/19820*
	9	387.6/25800	–	463.0/21600	542.0/18450
				495.1/20200	504.5/19820
	13	–	–	446 (347)	–
red	1	381.7/26200	–	–	–
	4	393.7/25400	609.7/16400		
		414.9/24100	561.8/17800		
		440.5/22700	516.8/19350		
		471.7/21200	*480.8/20800*		
	10			478.5/20900	675.7/14800
				515.5/19400	619.2/16150
				555.6/18000	*570.5/17530*
	12			499	
				347	

[a] If value is given in both nm and cm^{-1}, peak position was determined by calculating the second derivatives in the wavenumber regime. Estimated error: ±50 cm^{-1}. [b] If value is given only in nm, peak position was obtained by fitting a Gaussian line to the spectrum. Estimated error: ±0.5 nm.

The acid-denatured protein at pH 1 shows an absorption band at 381.7 nm (dashed line in Figure 6A). It is essentially identical to the A band, implying that the neutral green chromophore remains intact even under harsh acidic conditions. HBDI has an absorption maximum at 389 nm upon acidification, which further supports this assertion (*54*).

In addition to the pH-dependent changes in the relative areas of the A and B bands, intrinsic band shifts are visible. Between pH 2 and 9, the A band shifts to the red, from 381.7 to 387.6 nm, and this pH dependence can be described by a pK = 7.1 ± 0.1. A small red shift of the B band from 492.6 nm (shoulder at 460.8 nm) at pH 7 to 495.1 nm (463.0 nm) at pH 9, which is described by pK = 8.0 ± 0.1, is barely visible in the spectra. These band shifts reflect an altered charge distribution around the chromophore, probably caused by deprotonation of an amino acid near the chromophore.

Table 3: Key Properties Related to Blue Shift of Select FPs

FP species	PDB ID	ref	chromophore p*K*	distance $N\eta_{1/2\,Arg91}-O_{imidazolinone}$ (Å)	residue 69	green chromophore $\lambda_{exc}/\lambda_{em}$ (nm)	modified chromophore $\lambda_{exc}/\lambda_{em}$ (nm)
Dendra	2VZX		7.1/7.5	2.9/3.6	Thr	492/505	555/571
zFP538 (immature green)	1XAE	*46*	–	–	Thr	–/506	–
mTFP1	2HQK	*49*	4.3	3.0/3.6	Thr	462/492	–
amFP486	2A46	*47*	< 5	2.7/3.6	Thr	454/486	–
mKO	2ZMU	*48*	5.0	2.8/3.6	Thr	–	548/559
cmFP512	2C9J	*68*	~4	2.7/2.9	Thr	502/512	–
Ala142Ser cmFP512	–	*68*	< 5	–	Thr	486/507	–
EosFP	1ZUX	*32*	5.8	2.6/3.7	Ala	506/516	569/581
Thr69Ala Dendra2	–		–	–	Ala	502/515	565/578
Kaede	2GW3	*35*	5.6	2.7/3.7	Ala	508/518	570/582
mKikGR	2DDC	*30*	6.6/5.2	2.8/3.5	Val	505/515	580/600
Dronpa	2IE2	*69*	5.0	2.8/4.1	Ala	503/518	–

Fluorescence Spectra of Green Dendra2. Figure 7A shows excitation and emission spectra of the neutral green chromophore for different pH values. The excitation spectra were recorded with the emission monochromator set to 450 nm; the emission spectra were collected with 375 nm excitation. To display the different spectra within the same plot and to compare their relative intensities, the excitation and emission spectra were adjusted for slight differences in protein concentration, as judged by the protein absorption at 280 nm. Subsequently, the intensities of the excitation maximum at 378 nm and the emission maximum at 454 nm (at pH 4) were normalized to 1. The remaining spectra were scaled so as to maintain the relative intensities.

In its pH variation, the amplitude of the excitation band scales with that of the corresponding absorption band (pK = 7.1). The 280 nm band is less pronounced in the excitation than in the absorption spectrum, indicating that the probability of transferring the excitation of aromatic amino acids to the chromophore is markedly below 1. Excitation of the neutral chromophore at 375 nm produces weak blue fluorescence at 454 nm, the intensity of which also varies with pH according to pK 7.1 and, consequently, with the population of neutral chromophore (Figure 7A). Upon 375 nm excitation, fluorescence emission of the green anionic chromophore at 504.5 nm is also observed. At pH <5, the population of anionic species is very low (Figure 6B), and therefore, we attribute this emission to a process involving excited-state proton transfer (ESPT) (*50*, *55*−*57*). With increasing pH, emission by the anionic chromophore gets larger, which cannot be explained by ESPT anymore, as the fraction of neutral chromophores decreases. Instead, we record direct excitation of the anionic species even at 375 nm; its excitation band extends to wavelengths as low as 350 nm (Figure 7B). We emphasize here that the overall intensities of the fluorescence spectra in Figure 7A are ~100-fold lower than those in Figure 7B. Excitation (λ_{det} = 520 nm) and emission (λ_{exc} = 480 nm) spectra of the anionic green chromophore are shown in Figure 7B for selected pH values. The pH dependencies of both fluorescence excitation and emission intensities are also well modeled with pK = 7.1 and thus scale directly with the fraction of anionic chromophores.

At pH 7, their maxima are located at 492.6 and 504.5 nm, respectively. Both bands show vibronic structure, with side bands centered on 460.8 and at 542.0 nm. This substructure of both the excitation and emission band indicates a coupling of the chromophore to a vibrational mode with a frequency of 1400 ± 50 cm^{-1}. Völker and co-workers have reported frequencies of

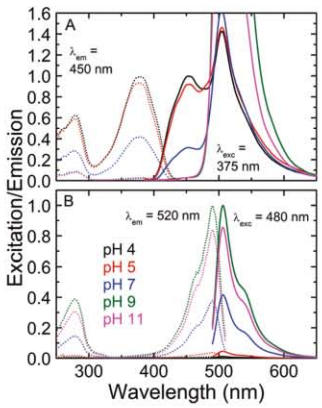

FIGURE 7: Excitation (dotted lines) and emission (solid lines) spectra of green Dendra2 at different pH values. (A) Neutral chromophore. (B) Anionic chromophore.

220, 770, and 1508 cm^{-1} from their spectral hole-burning investigation (*58*), with the latter two frequencies corresponding to local modes of the chromophore coupled to the electronic transition. Indeed, in the resonance Raman spectrum of avGFP, the strongest signal is at ~1560 cm^{-1} (*59*), which has been assigned to a normal mode delocalized over the imidazolinone ring and the exocyclic double bond by isotope labeling studies (*60*).

Photoconversion of Dendra2. Green Dendra2 can be efficiently converted to red Dendra2 by illumination with 405 nm light, as shown in the time sequence of spectra in Figure 8A. To test the hypothesis that photoconversion starts from the neutral green chromophore (*27*, *34*), green Dendra2 at pH 7 was illuminated for 5 min with light of different wavelengths (300−500 nm, 10 nm steps). The achieved increase in fluorescence intensity of the anionic red species (λ_{exc} = 550 nm, λ_{det} = 625 nm) was adjusted for variations in the lamp intensity. In accordance with the findings on EosFP (*27*) and Kaede (*29*), the resulting action spectrum, which describes the efficiency of Dendra2 photoconversion, indeed tracks the absorption band of the neutral green species (Figure 8A).

We also verified that the kinetics of photoconversion in Dendra2 is proportional to the concentration of neutral green chromophores. We illuminated 1 μM solutions of green Dendra2

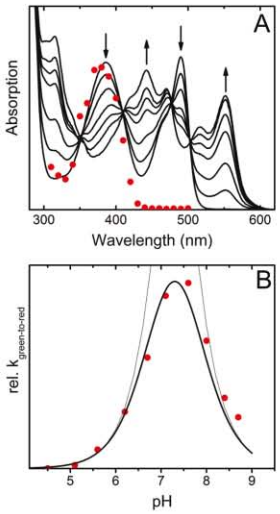

FIGURE 8: (A) Absorption spectra of Dendra2 measured during photoconversion at pH 7 with 405 nm light. Arrows indicate changes with time. Red dots: action spectrum. (B) pH dependence of photoconversion (symbols). The expected pH dependence (thick line) is calculated from the probability for having a neutral green chromophore weighted by the probability to yield a red anionic chromophore (thin lines).

at different pH values with 405 nm light at 1 mW/cm^2 for 300 s. Before and after illumination, we measured the fluorescence intensity at 625 nm. The excitation wavelength was set to 550 nm to only excite the anionic red species (see below). In Figure 8B, the relative increase of the fluorescence intensity is plotted as a function of pH. The solid line indicates the expected fluorescence increase if we assume that only neutral green Dendra2 photoconverts and if we account for the probability to obtain the red anionic species at the selected pH (see below). The good agreement between data and model curve confirms that the rate of photoconversion is indeed proportional to the concentration of neutral green Dendra2.

Absorption Spectra of Red Dendra2. The absorption spectra of red Dendra2 display two sets of bands (Figure 6C), the fractional areas of which change with pH in accordance with a single-site protonation, with pK = 7.5 (Figure 6D), slightly above the pK of 7.1 characterizing the green chromophore. As for the *p*-HBI chromophore of the green species, these bands are also associated with the neutral (A) and the anionic (B) red chromophores. The anionic species peaks at 555.6 nm (Table 2). A pronounced vibronic side band is visible at 515.5 nm; a second one is seen at 478.5 nm. Compared with EosFP, the anionic form of which absorbs at 571 nm, the red form of Dendra2 is markedly shifted to the blue by 15 nm. The shift is thus similar to that of the green species (13 nm) and, as discussed above, may be related to the missing interaction of the charged guanidino group of Arg66 with the imidazolinone carbonyl. A weak shoulder toward the red side of the B band is also visible and can be modeled with a band at 586 nm, which may represent a "super-red" species, similar to the one found in DsRed (*61*, *62*). As for DsRed, the population of this species can be enhanced by intense laser illumination (not shown).

For the neutral red chromophore, the maximum absorbance is located at 440.5 nm. This peak, however, is a vibronic band of the 0-0 transition located at 471.7 nm (see below). Still higher vibronic bands are visible toward the blue side, at 414.9 and 393.7 nm. Less pronounced features between 300 and 380 nm are associated with higher electronic transitions of both the neutral and anionic red chromophore species.

At pH 12, base-denatured Dendra2 has a very broad absorption band with a maximum at 499 nm; minor bands are visible at 330, 347, and 364 nm (dotted line in Figure 6B). Under identical conditions, the absorption spectrum of red EosFP also displays a broad band, with a maximum at 494 nm. By contrast, base-denatured red FPs with a 2-imino-5-(4-hydroxybenzylidene) imidazolinone chromophore such as eqFP611 (*63*) and DsRed (*64*) display an absorption band at 450−460 nm, similar to avGFP (*53*). Apparently, the acylimine of the red chromophore is unstable under these conditions, as was also reported for the chromoprotein RTMS5 at extreme pH values (*65*). As the red chromophores of Dendra2 and EosFP absorb ~50 nm further to the red, the alkenylene extension of the *p*-HBI chromophore is most likely still in place at pH 12.

The band of the acid-denatured red chromophore peaks at 382 nm and looks identical to that of the green chromophore (compare the dashed lines in panels A and B of Figure 6), suggesting a destruction of the alkenylene extension under acidic conditions.

Fluorescence Properties of red Dendra2. Fluorescence excitation and emission spectra of red Dendra2 are compiled in Figure 9 for pH 4, 6, 8, and 10. Excitation spectra were measured with the emission wavelength set close to the emission peaks of the neutral (λ_{det} = 520 nm, black dotted lines) and anionic red chromophores (λ_{det} = 570 nm, red dotted lines). Emission spectra were taken with excitation near the absorption maxima at λ_{exc} = 440 nm and λ_{exc} = 550 nm (solid black and red lines). The spectra were adjusted for slight differences in protein concentration as determined from the absorption at 280 nm.

At pH 4, only the neutral chromophore species contributes to the absorption spectrum (Figure 6C). Hence, direct excitation of the anionic chromophore (λ_{exc} = 550 nm) yields no fluorescence emission because this species is absent at pH 4. The excitation spectrum of the neutral chromophore in Figure 9A, measured with λ_{det} = 520 nm, consists of a series of comparatively well-resolved bands that we assign to the 0-0 transition at 471.7 nm and a progression of vibronic bands, with the largest excitation peak at 440.5 nm, another one at 414.9 nm, and a weak shoulder at 393.7 nm. The energy gap corresponding to the wavelength differences between the bands indicates that an ~1400 cm^{-1} vibrational mode of the chromophore is strongly coupled to the electronic transition, similarly to the observation made in the green state. A remarkably strong excitation band associated with a transition into a higher electronic state is present at 318 nm. The excitation spectra measured with λ_{det} = 480, 520, and 570 nm are identical except for a scale factor accounting for the different amplitudes of the emission spectrum, implying that the emission peaks at 488.8, 516.8, and 561.8 nm (Figure 9A) belong to the same electronic transition. The excitation spectra track the absorption spectrum between 300 and 560 nm; the 280 nm band is lower in the excitation spectrum, however, implying that only a fraction of the excitation of aromatic residues is transferred to the chromophore.

The emission spectrum associated with the neutral red chromophore looks like the mirror image of the excitation spectrum,

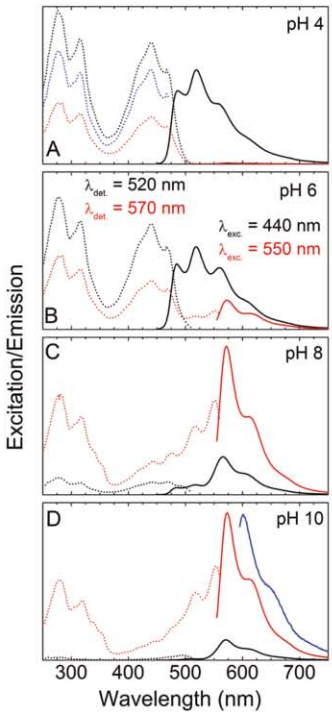

FIGURE 9: Excitation (dotted lines) and emission (solid lines) spectra of red Dendra2 at (A) pH 4, (B) pH 6, (C) pH 8, and (D) pH 10. Emission was excited at 440 nm (black), 550 nm (red), and 590 nm (blue). Excitation spectra were recorded with detection at 480 nm (blue), 520 nm (black), and 570 nm (red).

and the energy separation of the peaks corresponds to a similar vibronic excitation of 1400 cm^{-1} as in the excitation spectra. He et al. have synthesized two compounds, HBMPI and HBMPDI, designed to model the chromophore of DsRed (*66*). Compared to the green model chromophore, they contain one and two additional conjugated double bonds, respectively. Their Raman spectra show that the band assigned to the mode localized over the imidazolinone ring and the exocyclic C=C bond shifts slightly upon extending the conjugated π-system. Our spectral resolution is, however, not sufficient to resolve this difference in the vibrational modes of the green and red chromophores.

We determined the quantum yield (QY) of neutral red Dendra2 at pH 5 as 0.45, which is somewhat lower than the value obtained for the anionic chromophore at pH 9 (QY = 0.61). Unlike neutral Dendra2, the neutral form of red EosFP shows neither appreciable direct fluorescence emission nor emission by the anionic chromophore via ESPT (*27*). Apparently, nonradiative deexcitation pathways are preferred in EosFP, which typically involve rotation of the chromophore around its exocyclic bonds, so that fast radiationless decay can proceed upon crossing of the S_0 and S_1 surfaces (*67*). On the basis of the structure, we may speculate that the tight salt-bridge interaction between Arg66 and Glu211 in Dendra2 (Figure 4A) creates a more rigid environment that maintains the neutral, highly fluorescent red chromophore in a coplanar conformation, which is essential for a high fluorescence quantum yield.

The very low QY of the neutral green chromophore still calls for an explanation. A high fluorescence QY requires that the two rings of the *p*-HBI chromophore are tightly fixed in a coplanar conformation by the surrounding residues and bound water molecules (*68*, *69*). As a matter of fact, the isolated chromophore in solution does not show any fluorescence because it rotates around its exocyclic bonds and undergoes fast radiationless decay by internal conversion upon reaching an avoided crossing of the S_0 and S_1 surfaces (*67*, *70*). A direct coupling between chromophore planarity and QY was reported by Shu et al. for DsRed variants (*71*). The crystal structure reported here, which was determined at pH 8.5, corresponds to the anionic species and, therefore, does not allow us to assess the structure of the neutral species. Presumably, the green neutral chromophore is held in a nonplanar configuration because of restrictions due to the backbone linkage, which are removed in the red species. It is also feasible that the neutral green chromophore experiences increased torsional mobility so that nonradiative deexcitation is enhanced (*70*, *72*).

In the physiological range between pH 6 and 8, both the neutral and anionic species of the red chromophore contribute to the fluorescence spectra (Figure 9B,C). Around pH 10, the chromophore exists only in its anionic form (pK = 7.5, Figure 6D). Its excitation spectrum (λ_{det} = 570 nm) reveals the 0-0 transition at 555.6 nm, a pronounced vibronic side band at 515.5 nm, and a less resolved band at 478.5 nm, indicating again a coupling to a vibrational mode of ~1400 cm^{-1}. Additional bands associated with higher electronic transitions are found at 318, 341, and 355 nm (Figure 9D). The emission spectrum measured with 550 nm excitation has a dominant band at 570.5 nm, with shoulders at 619.2 and 675.7 nm.

In the absorption spectra of red Dendra2, we noticed a broad tail toward the red side of the spectrum, which may indicate an additional band at 586 nm (Figure 8). To further investigate this feature, we collected an emission spectrum with excitation on the red edge of this band. This spectrum, shown in Figure 9D in blue, has its maximum at 600 nm. This observation further supports the notion that a "super-red" species (*61*, *62*) exists in Dendra2.

DISCUSSION AND CONCLUSION

The X-ray structure of Dendra2 reveals a network of salt bridges and hydrogen bonds beneath the chromophore, which is typically found in anthozoan FPs. Compared to EosFP (*32*), Dendra2 shows a pronounced structural difference in this network that involves amino acid residue Arg66 and the water molecule W4. Arg66 does not form a hydrogen bond with the imidazolinone ring of the chromophore and, thus, does not contribute to negative charge density stabilization on the ring. We propose that the absorption and emission bands of Dendra2 are blue shifted from EosFP as a result of this lacking interaction. The Thr69Ala mutation indeed renders Dendra2 EosFP-like and removes the blue shift (Table 3).

Our suggestion is further supported by a comparison with other FPs listed in Table 3. The Dendra2-like orientation of the Arg66 side chain is found in mTFP1 (*49*), amFP486 (*47*), mKO (*48*), zFP538 (*46*), and cmFP512 (*73*), whereas the EosFP-like orientation of the Arg66 side chain is shared by Kaede (*35*), mKikGR (*30*), and Dronpa (*74*). In these latter FPs, the amino acid at position 69 is either an alanine or a valine, which cannot establish a hydrogen-bonding interaction with Arg66 (Figure 5).

A comparison of the excitation and emission maxima of these proteins reveals that the bands of the Dendra2-like FPs are blue shifted by at least 10 nm with respect to the EosFP-type ones (Table 3), with the exception of cmFP512 (*73*). This FP, however, has an alanine instead of a serine at position 142, which compensates the blue shift (*vide infra*). This claim is supported by the blue-shifted bands in cmFP512 mutant Ala142Ser (*73*).

An additional blue shift can be achieved by efficient charge stabilization of the phenolate chromophore, i.e., a low p*K* value. As electronic excitation of the chromophore generates a shift of electron density from the hydroxyphenyl moiety toward the imidazolinone heterocycle (*75*−*77*), an efficient solvation of the phenolate destabilizes the excited state with respect to the ground state. Other Dendra2-like FPs have significantly lower p*K* values of the green chromophore than Dendra2 (Table 3) and a larger blue shift of the absorption/emission maxima (Table 3). In mTFP1, additional stabilization is achieved by His159 (His163 in mTFP1 numbering, Met159 in Dendra2), which is in hydrogen-bonding distance to the hydroxyphenyl moiety (2.6 Å). In mKO, the distance between Ser142 and the hydroxyphenyl moiety is decreased with respect to Dendra2, leading to a stronger hydrogen bond and thus a better stabilization. The Ala142Ser mutant of cmFP512 shows the smallest blue shift with respect to Dendra2, although the anionic chromophore is strongly stabilized by Ser142, Lys159, and a water molecule (*73*). However, the interaction between Arg91 and the imidazolinone heterocycle may be stronger than in the other FPs discussed here, as inferred from the distances between Arg91-Nη_1/Arg91-Nη_2 and the imidazolinone oxygen (Table 3), leading to a more efficient excited-state stabilization and thus to a reduced blue shift. To summarize, the results presented here on Dendra2 and the structural comparison with other FPs strongly suggest that a shift of the green chromophore to the cyan and blue region (and a shift of the red chromophore toward the orange region) can be effected in two ways: (1) by enhancing the charge stabilization on the phenolate oxygen of the anionic chromophore and (2) by reducing charge stabilization of the carbonyl oxygen of the heterocycle.

Remington and co-workers investigated the network of salt bridges and hydrogen bonds beneath the chromophore in the cyan amFP486 and gave an alternative explanation of its blue shift (*47*). They suggested that the His193 side chain carries a positive charge so as to maintain overall charge neutrality of the quadrupole network and argued that the imidazolium side chain stabilizes the charge on the hydroxyphenyl ring of the chromophore. The reduced extent of charge delocalization upon excitation should result in blue-shifted absorption and emission spectra of amFP486. This explanation may be challenged by recent results from another cyan FP, dsFP483 (*78*), which has strongly blue-shifted spectra but a (neutral) threonine instead of a histidine residue at the corresponding position.

Green-to-red photoconversion starts from the neutral green species, as is evident from the pH dependencies of the photoconversion rates and action spectra of EosFP (*27*), Kaede (*29*), and Dendra2 (Figure 8). Because of the higher p*K* of the latter protein, the concentration of the neutral Dendra2 species is 20-fold higher under physiological conditions as compared with EosFP, which enhances the green-to-red photoconversion yield by the same factor. In a confocal microscope, high power densities are available so that photoconversion with blue light (488 nm) is easily observed (*36*). Photoconversion of a bulk sample in a cuvette is, however, much less efficient due to illumination with unfocused light. We note that EosFP can also be photoconverted by 488 nm light in a confocal microscope, as we had shown earlier in Figure 6A in ref *27*, where a few single molecules change their emission wavelengths from green to red while the surface is scanned with 488 nm light. In Dendra2, the red chromophore formed after conversion fluoresces efficiently in both its neutral and anionic forms. In fluorescence imaging applications, both green and red Dendra2 species can be excited efficiently between 450 and 500 nm, e.g., with 473 or 488 nm laser lines, and selective excitation of the red species is achieved by excitation above ~510 nm, e.g., with 532 nm laser lines.

Our structural and spectroscopic investigations on Dendra2 have underscored the similarities among FPs of the green-to-red photoconverting class. Remarkably, the altered optical properties of Dendra2 with respect to its close cousins EosFP and Kaede can be traced to a local structural change near the chromophore. This analysis further contributes to our understanding of structure−dynamics−function relationships in FPs, which is required for a rational engineering of FPs with advanced properties as fluorescence markers.

SUPPORTING INFORMATION AVAILABLE

Amino acid sequence alignment and UV/vis absorption spectra of green Dendra2. This material is available free of charge via the Internet at http://pubs.acs.org.

REFERENCES

1. Shaner, N. C., Patterson, G. H., and Davidson, M. W. (2007) Advances in fluorescent protein technology. *J. Cell Sci. 120*, 4247–4260.
2. Giepmans, B. N., Adams, S. R., Ellisman, M. H., and Tsien, R. Y. (2006) The fluorescent toolbox for assessing protein location and function. *Science 312*, 217–224.
3. Lippincott-Schwartz, J., Snapp, E., and Kenworthy, A. (2001) Studying protein dynamics in living cells. *Nat. Rev. Mol. Cell. Biol. 2*, 444–456.
4. Shcherbo, D., Merzlyak, E. M., Chepurnykh, T. V., Fradkov, A. F., Ermakova, G. V., Solovieva, E. A., Lukyanov, K. A., Bogdanova, E. A., Zaraisky, A. G., Lukyanov, S., and Chudakov, D. M. (2007) Bright far-red fluorescent protein for whole-body imaging. *Nat. Methods 4*, 741–746.
5. Shimomura, O., Johnson, F. H., and Saiga, Y. (1962) Extraction, purification and properties of aequorin, a bioluminescent protein from the luminous hydromedusan, *Aequorea*. *J. Cell. Comp. Physiol. 59*, 223–239.
6. Chalfie, M., Tu, Y., Euskirchen, G., Ward, W. W., and Prasher, D. C. (1994) Green fluorescent protein as a marker for gene expression. *Science 263*, 802–805.
7. Prasher, D. C., Eckenrode, V. K., Ward, W. W., Prendergast, F. G., and Cormier, M. J. (1992) Primary structure of the *Aequorea victoria* green-fluorescent protein. *Gene 111*, 229–233.
8. Nienhaus, G. U. (2008) The green fluorescent protein: a key tool to study chemical processes in living cells. *Angew. Chem., Int. Ed. 47*, 8992–8994. *Angew. Chem. 120*, 4398−4402.
9. Wiedenmann, J. (1997) Patent DE 197 18 640, Deutsches Patent- und Markenamt.
10. Matz, M. V., Fradkov, A. F., Labas, Y. A., Savitsky, A. P., Zaraisky, A. G., Markelov, M. L., and Lukyanov, S. A. (1999) Fluorescent proteins from nonbioluminescent *Anthozoa* species. *Nat. Biotechnol. 17*, 969–973.
11. Wiedenmann, J., Ivanchenko, S., Oswald, F., and Nienhaus, G. U. (2004) Identification of GFP-like proteins in nonbioluminescent, azooxanthellate *Anthozoa* opens new perspectives for bioprospecting. *Mar. Biotechnol. (New York) 6*, 270–277.
12. Nienhaus, G. U., Nienhaus, K., Hölzle, A., Ivanchenko, S., Renzi, F., Oswald, F., Wolff, M., Schmitt, F., Röcker, C., Vallone, B., Weidemann, W., Heilker, R., Nar, H., and Wiedenmann, J. (2006) Photoconvertible fluorescent protein EosFP—Biophysical properties and cell biology applications. *Photochem. Photobiol. 82*, 351–358.
13. Nienhaus, G. U., and Wiedenmann, J. (2009) Structure, dynamics and optical properties of fluorescent proteins: perspectives for marker development. *ChemPhysChem* DOI: 10.1002/cphc.200800839.

14. Yang, F., Moss, L. G., and Phillips, G. N.Jr. (1996) The molecular structure of green fluorescent protein. *Nat. Biotechnol. 14*, 1246–1251.
15. Ormö, M., Cubitt, A. B., Kallio, K., Gross, L. A., Tsien, R. Y., and Remington, S. J. (1996) Crystal structure of the *Aequorea victoria* green fluorescent protein. *Science 273*, 1392–1395.
16. Tsien, R. Y. (1998) The green fluorescent protein. *Annu. Rev. Biochem. 67*, 509–544.
17. Cubitt, A. B., Heim, R., Adams, S. R., Boyd, A. E., Gross, L. A., and Tsien, R. Y. (1995) Understanding, improving and using green fluorescent proteins. *Trends Biochem. Sci. 20*, 448–455.
18. Yarbrough, D., Wachter, R. M., Kallio, K., Matz, M. V., and Remington, S. J. (2001) Refined crystal structure of DsRed, a red fluorescent protein from coral, at 2.0-Å resolution. *Proc. Natl. Acad. Sci. U.S.A. 98*, 462–467.
19. Wall, M. A., Socolich, M., and Ranganathan, R. (2000) The structural basis for red fluorescence in the tetrameric GFP homolog DsRed. *Nat. Struct. Biol. 7*, 1133–1138.
20. Petersen, J., Wilmann, P. G., Beddoe, T., Oakley, A. J., Devenish, R. J., Prescott, M., and Rossjohn, J. (2003) The 2.0-Å crystal structure of eqFP611, a far red fluorescent protein from the sea anemone *Entacmaea quadricolor*. *J. Biol. Chem. 278*, 44626–44631.
21. Lippincott-Schwartz, J., and Patterson, G. H. (2003) Development and use of fluorescent protein markers in living cells. *Science 300*, 87–91.
22. Ivanchenko, S., Glaschick, S., Röcker, C., Oswald, F., Wiedenmann, J., and Nienhaus, G. U. (2007) Two-photon excitation and photoconversion of EosFP in dual-color 4Pi confocal microscopy. *Biophys. J. 92*, 4451–4457.
23. Betzig, E., Patterson, G. H., Sougrat, R., Lindwasser, O. W., Olenych, S., Bonifacino, J. S., Davidson, M. W., Lippincott-Schwartz, J., and Hess, H. F. (2006) Imaging intracellular fluorescent proteins at nanometer resolution. *Science 313*, 1642–1645.
24. Hell, S. W. (2007) Far-field optical nanoscopy. *Science 316*, 1153–1158.
25. Hess, S. T., Girirajan, T. P., and Mason, M. D. (2006) Ultra-high resolution imaging by fluorescence photoactivation localization microscopy. *Biophys. J. 91*, 4258–4272.
26. Hell, S. W. (2009) Microscopy and its focal switch. *Nat. Methods 6*, 24–32.
27. Wiedenmann, J., Ivanchenko, S., Oswald, F., Schmitt, F., Röcker, C., Salih, A., Spindler, K. D., and Nienhaus, G. U. (2004) EosFP, a fluorescent marker protein with UV-inducible green-to-red fluorescence conversion. *Proc. Natl. Acad. Sci. U.S.A. 101*, 15905–15910.
28. Oswald, F., Schmitt, F., Leutenegger, A., Ivanchenko, S., D'Angelo, C., Salih, A., Maslakova, S., Bulina, M., Schirmbeck, R., Nienhaus, G. U., Matz, M. V., and Wiedenmann, J. (2007) Contributions of host and symbiont pigments to the coloration of reef corals. *FEBS J. 274*, 1102–1109.
29. Ando, R., Hama, H., Yamamoto-Hino, M., Mizuno, H. and Miyawaki, A. (2002) An optical marker based on the UV-induced green-to-red photoconversion of a fluorescent protein. *Proc. Natl. Acad. Sci. U.S.A. 99*, 12651–12656.
30. Tsutsui, H., Karasawa, S., Shimizu, H., Nukina, N., and Miyawaki, A. (2005) Semi-rational engineering of a coral fluorescent protein into an efficient highlighter. *EMBO Rep. 6*, 233–238.
31. Labas, Y. A., Gurskaya, N. G., Yanushevich, Y. G., Fradkov, A. F., Lukyanov, K. A., Lukyanov, S. A., and Matz, M. V. (2002) Diversity and evolution of the green fluorescent protein family. *Proc. Natl. Acad. Sci. U.S.A. 99*, 4256–4261.
32. Nienhaus, K., Nienhaus, G. U., Wiedenmann, J., and Nar, H. (2005) Structural basis for green-to-red photoconversion of fluorescent protein EosFP. *Proc. Natl. Acad. Sci. U.S.A. 102*, 9156–9159.
33. Adam, V., Lelimousin, M., Boehme, S., Desfonds, G., Nienhaus, K., Field, M. J., Wiedenmann, J., McSweeney, S., Nienhaus, G. U., and Bourgeois, D. (2008) Structural characterization of IrisFP, an optical highlighter undergoing multiple photo-induced transformations. *Proc. Natl. Acad. Sci. U.S.A. 105*, 18343–18348.
34. Mizuno, H., Mal, T. K., Tong, K. I., Ando, R., Furuta, T., Ikura, M., and Miyawaki, A. (2003) Photo-induced peptide cleavage in the green-to-red conversion of a fluorescent protein. *Mol. Cell 12*, 1051–1058.
35. Hayashi, I., Mizuno, H., Tong, K. I., Furuta, T., Tanaka, F., Yoshimura, M., Miyawaki, A., and Ikura, M. (2007) Crystallographic evidence for water-assisted photo-induced peptide cleavage in the stony coral fluorescent protein Kaede. *J. Mol. Biol. 372*, 918–926.
36. Gurskaya, N. G., Verkhusha, V. V., Shcheglov, A. S., Staroverov, D. B., Chepurnykh, T. V., Fradkov, A. F., Lukyanov, S., and Lukyanov, K. A. (2006) Engineering of a monomeric green-to-red photoactivatable fluorescent protein induced by blue light. *Nat. Biotechnol. 24*, 461–465.
37. Berglund, G. I., Carlsson, G. H., Smith, A. T., Szoke, H., Henriksen, A., and Hajdu, J. (2002) The catalytic pathway of horseradish peroxidase at high resolution. *Nature 417*, 463–468.
38. Kabsch, W. (1993) Automatic processing of rotation diffraction data from crystals of initially unknown symmetry and cell constants. *J. Appl. Crystallogr. 26*, 795–800.
39. McCoy, A. J., Grosse-Kunstleve, R. W., Adams, P. D., Winn, M. D., Storoni, L. C., and Read, R. J. (2007) Phaser crystallographic software. *Acta Crystallogr. D 40*, 658–674.
40. Murshudov, G. N., Vagin, A. A., and Dodson, E. J. (1997) Refinement of macromolecular structures by the maximum-likelihood method. *Acta Crystallogr. D 53*, 240–255.
41. Emsley, P., and Kowtan, K. (2004) COOT version 0.026 model building and molecular graphics system. *Acta Crystallogr. D 70*, 2126–2132.
42. Bailey, S. (1994) The CCP4 suite: programs for protein crystallography. *Acta Crystallogr. D 50*, 760–763.
43. Kleywegt, G. J., and Jones, T. A. (1998) Databases in protein crystallography. *Acta Crystallogr. D 54*, 1119–1131.
44. Wiedenmann, J., Vallone, B., Renzi, F., Nienhaus, K., Ivanchenko, S., Röcker, C., and Nienhaus, G. U. (2005) Red fluorescent protein eqFP611 and its genetically engineered dimeric variants. *J. Biomed. Opt. 10*, 14003.
45. Nienhaus, K., Vallone, B., Renzi, F., Wiedenmann, J., and Nienhaus, G. U. (2003) Crystallization and preliminary X-ray diffraction analysis of the red fluorescent protein eqFP611. *Acta Crystallogr. D 59*, 1253–1255.
46. Remington, S. J., Wachter, R. M., Yarbrough, D. K., Branchaud, B., Anderson, D. C., Kallio, K., and Lukyanov, K. A. (2005) zFP538, a yellow-fluorescent protein from Zoanthus, contains a novel three-ring chromophore. *Biochemistry 44*, 202–212.
47. Henderson, J. N., and Remington, S. J. (2005) Crystal structures and mutational analysis of amFP486, a cyan fluorescent protein from *Anemonia majano*. *Proc. Natl. Acad. Sci. U.S.A. 102*, 12712–12717.
48. Kikuchi, A., Fukumura, E., Karasawa, S., Mizuno, H., Miyawaki, A., and Shiro, Y. (2008) Structural characterization of a thiazoline-containing chromophore in an orange fluorescent protein, monomeric Kusabira Orange. *Biochemistry 47*, 11573–11580.
49. Ai, H. W., Olenych, S. G., Wong, P., Davidson, M. W., and Campbell, R. E. (2008) Hue-shifted monomeric variants of Clavularia cyan fluorescent protein: identification of the molecular determinants of color and applications in fluorescence imaging. *BMC Biol. 6*, 13.
50. Chattoraj, M., King, B. A., Bublitz, G. U., and Boxer, S. G. (1996) Ultra-fast excited state dynamics in green fluorescent protein: multiple states and proton transfer. *Proc. Natl. Acad. Sci. U.S.A. 93*, 8362–8367.
51. Elsliger, M. A., Wachter, R. M., Hanson, G. T., Kallio, K., and Remington, S. J. (1999) Structural and spectral response of green fluorescent protein variants to changes in pH. *Biochemistry 38*, 5296–5301.
52. Voityuk, A. A., Michel-Beyerle, M. E., and Rösch, N. (1998) Quantum chemical modeling of structure and absorption spectra of the chromophore in green fluorescent proteins. *Chem. Phys. 231*, 13–25.
53. Ward, W. W., and Bokman, S. H. (1982) Reversible denaturation of Aequorea green-fluorescent protein: physical separation and characterization of the renatured protein. *Biochemistry 21*, 4535–4540.
54. Webber, N. M., and Meech, S. R. (2007) Electronic spectroscopy and solvatochromism in the chromophore of GFP and the Y66F mutant. *Photochem. Photobiol. Sci. 6*, 976–981.
55. Lossau, H., Kummer, A., Heinecke, R., Pollinger-Dammer, F., Kompa, C., Bieser, G., Jonsson, T., Silva, C. M., Yang, M. M., Youvan, D. C., and Michel-Beyerle, M. E. (1996) Time-resolved spectroscopy of wild-type and mutant green fluorescent proteins reveals excited state deprotonation consistent with fluorophore-protein interactions. *Chem. Phys. 213*, 1–16.
56. Lill, M. A., and Helms, V. (2002) Proton shuttle in green fluorescent protein studied by dynamic simulations. *Proc. Natl. Acad. Sci. U.S.A. 99*, 2778–2781.
57. Stoner-Ma, D., Jaye, A. A., Matousek, P., Towrie, M., Meech, S. R., and Tonge, P. J. (2005) Observation of excited-state proton transfer in green fluorescent protein using ultrafast vibrational spectroscopy. *J. Am. Chem. Soc. 127*, 2864–2865.
58. Creemers, T. M. H., Lock, A. J., Subramaniam, V., Jovin, T. M., and Völker, S. (1999) Three photoconvertible forms of green fluorescent protein identified by spectral hole-burning. *Nat. Struct. Biol. 6*, 557–560.
59. Schellenberg, P., Johnson, E., Esposito, A. P., Reid, P. J., and Parson, W. W. (2001) Resonance Raman scattering by the green fluorescent protein and an analogue of its chromophore. *J. Phys. Chem. B 105*, 5316–5322.

60. He, X., Bell, A. F., and Tonge, P. J. (2002) Isotopic labeling and normal-mode analysis of a model green fluorescent protein chromophore. *J. Phys. Chem. B 106*, 6056–6066.
61. Cotlet, M., Hofkens, J., Habuchi, S., Dirix, G., Van Guyse, M., Michiels, J., Vanderleyden, J., and De Schryver, F. C. (2001) Identification of different emitting species in the red fluorescent protein DsRed by means of ensemble and single-molecule spectroscopy. *Proc. Natl. Acad. Sci. U.S.A. 98*, 14398–14403.
62. Habuchi, S., Cotlet, M., Gensch, T., Bednarz, T., Haber-Pohlmeier, S., Rozenski, J., Dirix, G., Michiels, J., Vanderleyden, J., Heberle, J., De Schryver, F. C., and Hofkens, J. (2005) Evidence for the isomerization and decarboxylation in the photoconversion of the red fluorescent protein DsRed. *J. Am. Chem. Soc. 127*, 8977–8984.
63. Kredel, S., Nienhaus, K., Wolff, M., Oswald, F., Ivanchenko, S., Cymer, F., Jeromin, A., Michel, F. J., Spindler, K.-D., Heilker, R., Nienhaus, G. U., and Wiedenmann, J. (2008) Optimized and far-red emitting variants of fluorescent protein eqFP611. *Chem. Biol. 15*, 224–233.
64. Gross, L. A., Baird, G. S., Hoffman, R. C., Baldridge, K. K., and Tsien, R. Y. (2000) The structure of the chromophore within DsRed, a red fluorescent protein from coral. *Proc. Natl. Acad. Sci. U.S.A. 97*, 11990–11995.
65. Turcic, K., Pettikiriarachchi, A., Battad, J., Wilmann, P. G. Rossjohn, J., Dove, S. G., Devenish, R. J., and Prescott, M. (2006) Amino acid substitutions around the chromophore of the chromoprotein Rtms5 influence polypeptide cleavage. *Biochem. Biophys. Res. Commun. 349*, 1139–1143.
66. He, X., Bell, A. F., and Tonge, P. J. (2002) Synthesis and spectroscopic studies of model red fluorescent protein chromophores. *Org. Lett. 4*, 1523–1526.
67. Kummer, A. D., Kompa, C., Niwa, H., Hirano, T., Kojima, S., and Michel-Beyerle, M. E. (2002) Viscosity-dependent fluorescence decay of the GFP chromophore in solution due to fast internal conversion. *J. Phys. Chem. B 106*, 7554–7559.
68. Prescott, M., Ling, M., Beddoe, T., Oakley, A. J., Dove, S., Hoegh-Guldberg, O., Devenish, R. J., and Rossjohn, J. (2003) The 2.2 Å crystal structure of a pocilloporin pigment reveals a nonplanar chromophore conformation. *Structure (Cambridge) 11*, 275–284.
69. Henderson, J. N., and Remington, S. J. (2006) The kindling fluorescent protein: a transient photoswitchable marker. *Physiology 21*, 162–170.
70. Voityuk, A. A., Michel-Beyerle, M. E., and Rösch, N. (1998) Structure and rotation barriers for ground and excited states of the isolated chromophore of the green fluorescent protein. *Chem. Phys. Lett. 296*, 269–276.
71. Shu, X., Shaner, N. C., Yarbrough, C. A., Tsien, R. Y., and Remington, S. J. (2006) Novel chromophores and buried charges control color in mFruits. *Biochemistry 45*, 9639–9646.
72. Kummer, A. D., Kompa, C., Lossau, H., Pöllinger-Dammer, F., Michel-Beyerle, M. E., Silva, C. M., Bylina, E. J., Coleman, W. J., Yang, M. M., and Youvan, D. C. (1998) Dramatic reduction in fluorescence quantum yield in mutants of green fluorescent protein due to fast internal conversion. *Chem. Phys. 237*, 183–193.
73. Nienhaus, K., Renzi, F., Vallone, B., Wiedenmann, J., and Nienhaus, G. U. (2006) Exploring chromophore−protein interactions in fluorescent protein cmFP512 from *Cerianthus membranaceus*: X-ray structure analysis and optical spectroscopy. *Biochemistry 45*, 12942–12953.
74. Wilmann, P. G., Turcic, K., Battad, J. M., Wilce, M. C., Devenish, R. J., Prescott, M., and Rossjohn, J. (2006) The 1.7 Å crystal structure of Dronpa: a photoswitchable green fluorescent protein. *J. Mol. Biol. 364*, 213–224.
75. Cinelli, R. A., Tozzini, V., Pellegrini, V., Beltram, F., Cerullo, G., Zavelani-Rossi, M., De Silvestri, S., Tyagi, M., and Giacca, M. (2001) Coherent dynamics of photoexcited green fluorescent proteins. *Phys. Rev. Lett. 86*, 3439–3442.
76. Marques, M. A., Lopez, X., Varsano, D., Castro, A., and Rubio, A. (2003) Time-dependent density-functional approach for biological chromophores: the case of the green fluorescent protein. *Phys. Rev. Lett. 90*, 258101.
77. Tozzini, V., and Nifosi, R. (2001) Ab initio molecular dynamics of the green fluorescent protein (GFP) chromophore: an insight into the photoinduced dynamics of green fluorescent proteins. *J. Phys. Chem. B 105*, 5797–5803.
78. Malo, G. D., Wang, M., Wu, D., Stelling, A. L., Tonge, P. J., and Wachter, R. M. (2008) Crystal structure and Raman studies of dsFP483, a cyan fluorescent protein from *Discosoma striata*. *J. Mol. Biol. 378*, 871–886.

J|A|C|S
ARTICLES

Published on Web 11/03/2009

Photoconversion of the Fluorescent Protein EosFP: A Hybrid Potential Simulation Study Reveals Intersystem Crossings

Mickaël Lelimousin,[†,‡,§] Virgile Adam,[||] G. Ulrich Nienhaus,[⊥,#] Dominique Bourgeois,[†,‡,§,||] and Martin J. Field*[,†,‡,§]

CNRS, UMR5075, Institut de Biologie Structurale Jean-Pierre Ebel, 41 rue Jules Horowitz, 38027 Grenoble Cedex 1, France, CEA, DSV, Grenoble F-38027, France, Université Joseph Fourier, Grenoble, F-38000, France, European Synchrotron Radiation Facility, 6 Rue Jules Horowitz, BP 220, 38043 Grenoble Cedex, France, Institute of Applied Physics and Center for Functional Nanostructures, Karlsruhe Institute of Technology, 76131 Karlsruhe, Germany, and Department of Physics, University of Illinois at Urbana−Champaign, 1110 West Green Street, Urbana, Illinois 61801

Received June 30, 2009; E-mail: martin.field@ibs.fr

Abstract: Fluorescent proteins undergoing green to red photoconversion have proved to be essential tools in cell biology, notably in superlocalization nanoscopy. However, the exact mechanism governing photoconversion, which overall involves irreversible cleavage of the protein backbone and elongation of the chromophore π-conjugation, remains unclear. In this paper we present a theoretical investigation of the photoconversion reaction in the fluorescent protein EosFP, using excited-state hybrid quantum chemical and molecular mechanical potentials, in conjunction with reaction-path-finding techniques. Our results reveal a mechanism in which the hydroxybenzylidene moiety of the chromophore remains protonated and there is an excited state proton transfer from His62 to Phe61 that promotes peptide bond cleavage. Excitation of the neutral green form of EosFP to the first singlet excited state is followed by two intersystem crossing events, first to a triplet state and then back to the ground state singlet surface. From there, a number of rearrangements occur in the ground state and lead to the red form. Analyses of the structures and energies of the intermediates along the reaction path enable us to identify the critical role of the chromophore environment in promoting photoinduced backbone cleavage. Possible ways in which photoconvertible fluorescent proteins can be engineered to facilitate photoconversion are considered.

Introduction

During the past 15 years, fluorescent proteins (FPs) have become indispensable tools in cell biology, as their use as markers has revolutionized understanding of cellular processes.[1,2] Some of these proteins can change their photophysical properties on exposure to light. Such modifications in photoactivatable fluorescent proteins include reversible switching between a fluorescent "on" state and a nonfluorescent "off" state and irreversible photoconversion between a green- and a red-emitting state.[3] The structures of the green and red forms of several photoconvertible fluorescent proteins (PCFPs) have been determined by X-ray crystallography, including EosFP,[4] KikGR,[5] Kaede,[6] and IrisFP.[7] Because of the utility of these proteins for investigating movements in live cells[3] or designing super-resolution imaging schemes based on the photoactivated localization microscopy approach,[8] considerable work has gone into optimizing PCFPs. This led to the recent development of the monomeric variants Dendra2,[9] mEos2,[10] and mKikGR,[11] which proved to be more suitable for designing functional fusion constructs.

A conserved triad of residues, His62-Tyr63-Gly64, characterizes the chromophore of PCFPs. As for all members of the GFP family, the chromophore is enclosed in the center of an 11-

† CNRS, Institut de Biologie Structurale Jean-Pierre Ebel.
‡ CEA, Institut de Biologie Structurale Jean-Pierre Ebel.
§ Université Joseph Fourier, Institut de Biologie Structurale Jean-Pierre Ebel.
|| European Synchrotron Radiation Facility.
⊥ Karlsruhe Institute of Technology.
University of Illinois at Urbana−Champaign.

(1) Shaner, N. C.; Patterson, G. H.; Davidson, M. W. *J. Cell Sci.* **2007**, *120*, 4247–4260.
(2) Nienhaus, G. U. *Angew. Chem., Int. Ed.* **2008**, *47*, 8992–8994.
(3) Wiedenmann, J.; Nienhaus, G. U. *Exp. Rev. Proteomics* **2006**, *3*, 361–734.
(4) Nienhaus, K.; Nienhaus, G. U.; Wiedenmann, J.; Nar, H. *Proc. Natl. Acad. Sci. U.S.A.* **2005**, *102*, 9156–9159.
(5) Tsutsui, H.; Karasawa, S.; Shimizu, H.; Nukina, N.; Miyawaki, A. *EMBO Rep.* **2005**, *6*, 233–238.
(6) Hayashi, I.; Mizuno, H.; Tong, K. I.; Furuta, T.; Tanaka, F.; Yoshimura, M.; Miyawaki, A.; Ikura, M. *J. Mol. Biol.* **2007**, *372*, 918–926.
(7) Adam, V.; Lelimousin, M.; Boehme, S.; Desfonds, G.; Nienhaus, K.; Field, M. J.; Wiedenmann, J.; McSweeney, S.; Nienhaus, G. U.; Bourgeois, D. *Proc. Natl. Acad. Sci. U.S.A.* **2008**, *105*, 18343–18348.
(8) Betzig, E.; Patterson, G. H.; Sougrat, R.; Lindwasser, O. W.; Olenych, S.; Bonifacino, J. S.; Davidson, M. W.; Lippincott-Schwartz, J.; Hess, H. F. *Science* **2006**, *313*, 1642–1645.
(9) Gurskaya, N. G.; Verkhusha, V. V.; Shcheglov, A. S.; Staroverov, D. B.; Chepurnykh, T. V.; Fradkov, A. F.; Lukyanov, S.; Lukyanov, K. A. *Nat. Biotechnol.* **2006**, *24*, 461–465.
(10) McKinney, S. A.; Murphy, C. S.; Hazelwood, K. L.; Davidson, M. W.; Looger, L. L. *Nat. Methods* **2009**, *6*, 131–133.
(11) Habuchi, S.; Tsutsui, H.; Kochaniak, A. B.; Miyawaki, A.; van Oijen, A. M. *PLoS One* **2008**, *3*, e3944.

10.1021/ja905380y CCC: $40.75

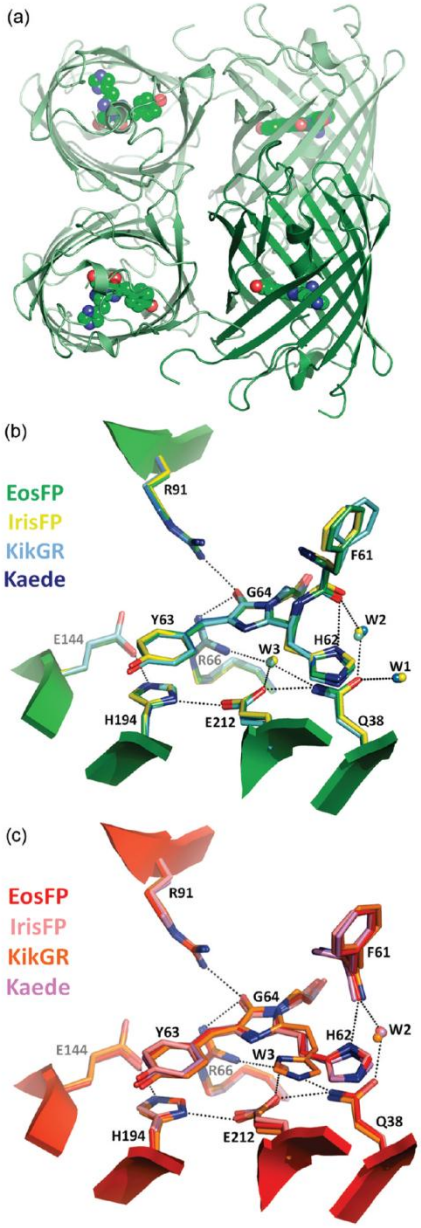

Figure 1. (a) Tetrameric structure of wt-EosFP. Chromophores are shown as van der Waals spheres. (b) Superposition of the chromophore and surrounding residues in the green forms of EosFP, IrisFP, KikGR, and Kaede (hydrogen bonds are indicated by dotted lines). (c) Superposition of the chromophore and surrounding residues in the red forms of EosFP, IrisFP, KikGR and Kaede (hydrogen bonds are indicated by dotted lines).

stranded β-barrel structure (Figure 1a), where it is rigidly held by an environmental network of hydrogen bonds and van der Waals interactions (Figure 1b). The green form of PCFPs arises via autocatalytic maturation in the dark, yielding a 4-(*p*-hydroxybenzylidene)-5-imidazolinone π-conjugated system. Illumination with UV light causes cleavage of the peptide bond between the amide nitrogen of residue 61 and the α-carbon of His62, formation of a double bond on the His62 side chain, and extension of the conjugated system to a 2-[(1*E*)-2-(5-imidazolyl)-ethenyl]-4-(*p*-hydroxybenzylidene)-5-imidazolinone moiety,[4,12] leading to the red-emitting form. Despite these changes, the three-dimensional structure of the protein is almost completely preserved in the red form (Figure 1c). However, a water molecule (W1) that is present in the structures of green EosFP, IrisFP, and Kaede is not observed in the red forms. This water molecule is absent from both the green and red forms of KikGR, which is characterized by an additional isomerization of the His62 side chain.

The basic (anionic) form of PCFP chromophores absorbs around 500 nm, and the acidic (neutral) form around 390 nm. Although it has been reported that very intense illumination at 488 nm converts Dendra2,[9] possibly in the anionic form of the chromophore, it is generally accepted that photoconversion only occurs in the neutral (phenolic) form.[3,11,13−15] The reaction is irreversible: neither keeping the protein in the dark nor under illumination with visible light at any wavelength can restore the green state.[13] Measurements of rate constants for the photoconversion of PCFPs revealed much slower kinetics than for other photoinduced reactions such as photoisomerization.[11,16] As a consequence, the quantum yield of photoconversion in PCFPs is low ($\sim 10^{-3}-10^{-4}$).[5,7,11,13] Photoconversion can be abolished by substitution of His62 with any other amino acid,[12,14] thereby asserting this residue's critical role, and by various other mutations in the chromophore's environment.[12,17]

To date, the exact mechanism of green-to-red photoconversion in PCFPs remains unknown, although several hypotheses have been proposed. Using NMR structures of Kaede, Mizuno et al. suggested initially that the imidazole of His62 could become biprotonated and that this would facilitate backbone cleavage via β-elimination.[12] On the basis of the X-ray crystallographic structures of EosFP in both its green and red states, Nienhaus et al. proposed an excited state proton transfer (ESPT) from the hydroxyl group of Tyr63 to the N_ε of His62, followed by a β-elimination step in which Glu212 acts as a proton acceptor.[4] Finally, Hayashi et al. proposed a water-assisted mechanism to explain the loss of the water molecule W1 in the red form of Kaede.[6]

A detailed experimental investigation of photoconversion is difficult because of its low quantum yield and irreversibility. In contrast, molecular simulation can provide important insights into the photoconversion mechanism. Especially appropriate tools in this endeavor are hybrid quantum chemical/molecular mechanical (QC/MM) potentials because they are well adapted

(12) Mizuno, H.; Mal, T. K.; Tong, K. I.; Ando, R.; Furuta, T.; Ikura, M.; Miyawaki, A. *Mol. Cell* **2003**, *12*, 1051–1058.
(13) Ando, R.; Hama, H.; Yamamoto-Hino, M.; Mizuno, H.; Miyawaki, A. *Proc. Natl. Acad. Sci. U.S.A.* **2002**, *99*, 12651–12656.
(14) Wiedenmann, J.; Ivanchenko, S.; Oswald, F.; Schmitt, F.; Rocker, C.; Salih, A.; Spindler, K. D.; Nienhaus, G. U. *Proc. Natl. Acad. Sci. U.S.A.* **2004**, *101*, 15905–15910.
(15) Adam, V.; Nienhaus, K.; Bourgeois, D.; Nienhaus, G. U. *Biochemistry* **2009**, *48*, 4905–4915.
(16) Dittrich, P. S.; Schafer, S. P.; Schwille, P. *Biophys. J.* **2005**, *89*, 3446–3455.
(17) Nienhaus, G. U.; Nienhaus, K.; Holzle, A.; Ivanchenko, S.; Renzi, F.; Oswald, F.; Wolff, M.; Schmitt, F.; Rocker, C.; Vallone, B.; Weidemann, W.; Heilker, R.; Nar, H.; Wiedenmann, J. *Photochem. Photobiol.* **2006**, *82*, 351–358.

for studying phenomena that require a quantum mechanical description but which occur in large systems. Most reported QC/MM studies of photochemical reactions in proteins concern ultrafast events.[18] Examples include photoisomerization of chromophores in rhodopsins,[19] photoactive yellow protein,[20] and other fluorescent proteins.[21] In this paper, we investigate theoretically the mechanism of the green-to-red photoconversion in EosFP, which is a typical representative of the PCFP family. By employing hybrid QC/MM potentials in conjunction with reaction-path-finding techniques, we propose that two intersystem crossing (ISC) events to the triplet state T_1 and back to the ground state S_0 are critical for forming the red-emitting state. Structural determinants of the EosFP chromophore pocket for efficient photoconversion are also investigated, and general conclusions about PCFPs are drawn.

Methods

All simulations were performed with the fDynamo library.[22] The starting structures for the simulations were those of the tetramers determined by X-ray crystallography for the green (PDB id: 1ZUX) and red (PDB id: 2BTJ) forms of EosFP.[4] The positions of the hydrogen atoms were determined after the protonation states of the residues in the protein had been estimated at a pH of 7.0, using standard Poisson−Boltzmann calculations.[23] All residues were determined to have their expected protonation, with the exception of His194, for which the pK_a calculation and examination of the X-ray crystallographic structures suggested a biprotonation at pH 7.0 (Figure 1b and c). The resulting protein structures were geometry-optimized in vacuum using the OPLS-AA force field.[24] The optimized tetrameric structures were then solvated and optimized in a cubic water box of the appropriate size, employing the TIP3P MM water model.[25] Counterions were added to ensure charge neutrality of the overall system. The final systems comprised approximately 43,100 atoms.

QC/MM simulations were performed starting from the two prepared MM systems. Unless explicitly stated in the text, the QC region consisted of 65 atoms and contained the chromophore and the side chains of two amino acid residues: Glu212, which has been proposed to play an essential role in photoconversion, and His194, which is involved in π-stacking with the hydroxybenzylidene moiety (Figure 1b and c). Atoms in the MM region were treated with the OPLS-AA force field and those in the QC region with either the AM1[26] or the PDDG-PM3[27] semiempirical methods. The results obtained with the two potentials are qualitatively and, in most cases, quantitatively similar, so that we only show the PDDG-PM3 results in the main paper. The AM1 results are given as Supporting Information.

To calculate the energy and atomic forces of the system in both ground and excited states, a standard configuration interaction (CI) method was incorporated into the fDynamo library. The CI method itself permits calculations with a number of possible configuration sets, either all configurations within a given active space (full CI) or a mixture of single and double excitations (CIS, CID, and CISD) from a closed-shell singlet reference state. Gradients of the energy are calculated with the Z-matrix technique.[28,29] Our tests showed that a ten-electron/nine-orbital or [10,9]-CISD approximation gave the best compromise between accuracy and computational time. Sample results for our systems are given in Table S1 (note: all table and figure numbers preceded by "S" are located in Supporting Information). To simplify the discussion, we refer to the [10,9]-CISD(PDDG-PM3)/OPLS and [10,9]-CISD(AM1)/OPLS hybrid potentials as the PDDG and AM1 potentials, respectively.

To assess the accuracy of the semiempirical methods, we also performed time-dependent density functional theory calculations using the ORCA quantum chemical program.[30] Experience showed that the results were more sensitive to the functional that was employed than the basis set. Hence, the calculations reported here are with the BP86 and B3LYP functionals and the SVP (split valence with polarization) basis set.[31]

To investigate the photoconversion reaction, we employed the nudged elastic band (NEB) method[32] to determine minimum energy paths (MEPs) between various, selected reactant and product structures. Although MEPs do not directly give time-scale or thermodynamic information, they can provide useful information about possible mechanisms, including the identity of intermediates, the order in which events occur, and estimates of barrier heights.

All NEB calculations were done using the A monomer of the prepared systems. To reduce the computational expense of the optimization, only the ~840 atoms within 12 Å of the C_α atom of His62 were allowed to move. The remaining atoms were fixed, although their interactions with the mobile atoms were taken into account. The complete photoconversion pathway could not be determined by a single NEB calculation between green and red forms because of the complexity and the multiplicity of the reaction steps and the different electronic states upon which the reaction occurs. Reaction paths were determined between geometry-optimized start and end structures, on either the ground or excited states, and using at least 11 structures along the pathway. Whenever suggested by intersystem crossings, results were refined by recalculating parts of the reaction path between specific intermediates at the appropriate electronic state. In all energy profiles, the labels of intermediate structures are placed above the energy point if the path was minimized in an excited state and below if it was minimized in the ground state. The zero of energy is taken to be the energy of the neutral green form in its ground state. Its vertical excitation to S_1 is estimated to be ~345 kJ/mol for both the QC/MM potentials that were used.

Results and Discussion

Previous Mechanistic Proposals. Scheme 1 provides a summary of the steps putatively involved in the previously proposed photoconversion mechanism of EosFP: an ESPT from the hydroxybenzylidene group of the chromophore to the N_ϵ of His62, followed by a β-elimination reaction in which Glu212 acts as a proton acceptor.[4] The (arbitrary) notation that we use for the various intermediate structures throughout this work is also provided in Scheme 1. Our initial simulations were performed to test the mechanism of Scheme 1 by calculating NEB pathways on the excited state singlet (S_1) for the first step and on the ground state singlet (S_0) surface for all following

(18) Virshup, A. M.; Punwong, C.; Pogorelov, T. V.; Lindquist, B. A.; Ko, C.; Martinez, T. J. *J. Phys. Chem. B* **2009**, *113*, 3280–3291.
(19) Hayashi, S.; Tajkhorshid, E.; Schulten, K. *Biophys. J.* **2009**, *96*, 403–416.
(20) Groenhof, G.; Schafer, L. V.; Boggio-Pasqua, M.; Grubmuller, H.; Robb, M. A. *J. Am. Chem. Soc.* **2008**, *130*, 3250–3251.
(21) Schafer, L. V.; Groenhof, G.; Boggio-Pasqua, M.; Robb, M. A.; Grubmuller, H. *PLoS Comput. Biol.* **2008**, *4*, e1000034.
(22) Field, M. J.; Albe, M.; Bret, C.; Proust-De Martin, F.; Thomas, A. *J. Comput. Chem.* **2000**, *21*, 1088–1100.
(23) Antosiewicz, J.; Mccammon, J. A.; Gilson, M. K. *J. Mol. Biol.* **1994**, *238*, 415–436.
(24) Jorgensen, W. L.; Maxwell, D. S.; TiradoRives, J. *J. Am. Chem. Soc.* **1996**, *118*, 11225–11236.
(25) Jorgensen, W. L.; Chandrasekhar, J.; Madura, J. D.; Impey, R. W.; Klein, M. L. *J. Chem. Phys.* **1983**, *79*, 926–935.
(26) Dewar, M. J. S.; Zoebisch, E. G.; Healy, E. F.; Stewart, J. J. P. *J. Am. Chem. Soc.* **1985**, *107*, 3902–3909.
(27) Repasky, M. P.; Chandrasekhar, J.; Jorgensen, W. L. *J. Comput. Chem.* **2002**, *23*, 1601–1622.
(28) Handy, N. C.; Schaefer, H. F. *J. Chem. Phys.* **1984**, *81*, 5031–5033.
(29) Patchkovskii, S.; Thiel, W. *Theor. Chem. Acc.* **1997**, *98*, 1–4.
(30) Neese, F. ORCA Quantum Chemistry Program. http://www.thch.uni-bonn.de/tc/orca/.
(31) Koch, W.; Holthausen, M. C. *A Chemist's Guide to Density Functional Theory*; Wiley-VCH: New York, NY, 2000.
(32) Galvan, I. F.; Field, M. J. *J. Comput. Chem.* **2008**, *29*, 139–143.

Scheme 1. Hypothetic Photoconversion Mechanism Inspired from Nienhaus et al.,[4] with Intermediate Structures Derived from Simulation[a]

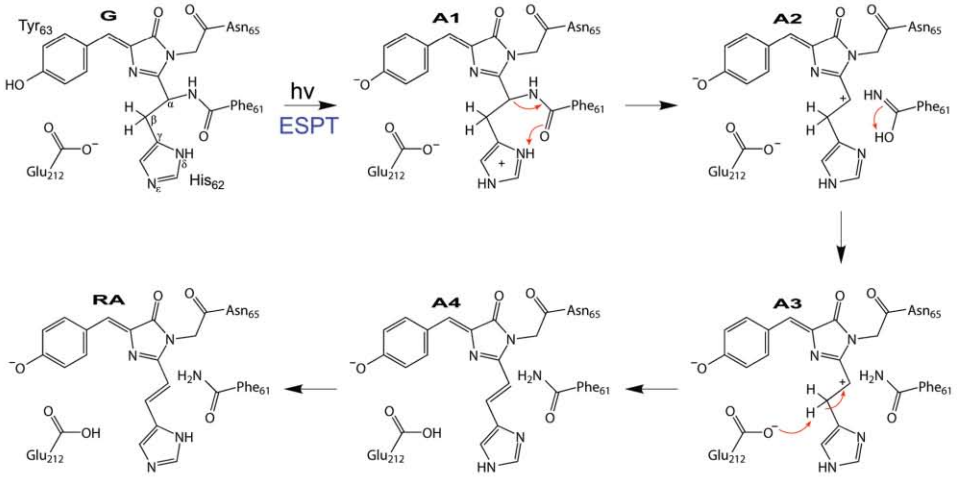

[a] Arrows show the main reaction steps in red (color assigned to the ground state S_0 throughout the paper).

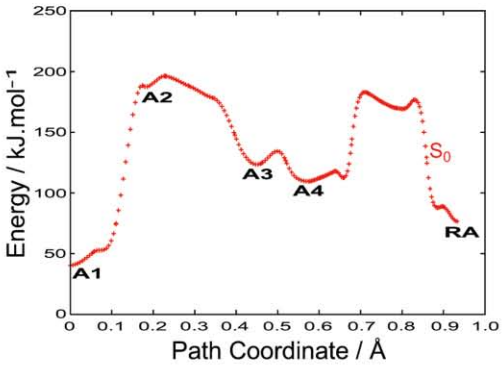

Figure 2. Energy profile of optimized NEB paths from A1 to A4 and from A4 to RA in the ground state S_0 calculated with a PDDG/OPLS hybrid potential.

steps. The energy profiles obtained for these latter are shown in Figures 2 and S1 for the PDDG and AM1 hybrid potentials, respectively. Overall we consider this mechanism unlikely for the reasons given below.

Construction or minimization of NEB pathways between the G and A1 states failed or gave unreasonably high energy barriers (not shown). The occurrence of an ESPT from Tyr63 to His62 in this step was anticipated from the known strong decrease of the hydroxybenzylidene pK_a in S_1.[33] In avGFP, the proton is transferred to Glu222 (corresponding to Glu212 in EosFP) via a hydrogen-bonding network.[34] Such a network between Tyr63 and His62 does not appear to exist in EosFP, based on the crystallographic structures in ground state S_0, and it is difficult to identify a realistic path that could transiently form in S_1, given the essentially identical geometry of our excited-state model and the ~11 Å distance that separates the hydroxyl group of Tyr63 and the N_ε atom of His62 (Figure 1b). Moreover, the N_ε atom of His62 resides in a nonpolar environment unfavorable for protonation.

The next step in the mechanism of Scheme 1 is the cleavage of the C_α–N bond from the imidazolium-based A1 state. This step appears unlikely to occur as it requires crossing an energy barrier approaching 150 kJ/mol. It is followed by an intraresidue proton transfer within Phe61 (A2 to A3) and by the second step of the β-elimination reaction, which involves proton transfer from C_β of His62 to the carboxylate group of Glu212 (A3 to A4). Together, these steps have small energy barriers and result in a large decrease in energy. By contrast, the last step (A4 to RA) again requires crossing a substantial energy barrier of ~75 kJ/mol. This step involves proton transfer from N_ε to N_δ of the imidazole via an intermediate characterized by a sp3-hybridized C_ε. This rearrangement is necessary to restore the hydrogen bond between the carbonyl moiety of Phe61 and the N_δ atom of His62.

A New Proposal. The previously discussed mechanism starts with an ESPT from the hydroxybenzylidene moiety of the chromophore. As an alternative, we propose that the chromophore remains protonated during the entire photoconversion process and that backbone cleavage is a direct consequence of excitation of the neutral chromophore. To investigate this hypothesis, we tested the mechanism shown in Scheme 2, in which Glu212 acts as the proton acceptor in the β-elimination. We started off by optimizing NEB pathways between the G and B4 species on the first singlet excited state (S_1) surface. The resulting energy profiles are shown in Figures 3a and S2a.

The first event along the optimized NEB path is an ESPT from the N_δ atom of His62 to the carbonyl moiety of Phe61. The energy of this proton transfer was determined to be ~25 kJ/mol with the PDDG potential. To our knowledge, an ESPT from the N_δ atom of a neutral imidazole ring has not been reported. However, a fluorophore with an imidazolide ring was

(33) Chattoraj, M.; King, B. A.; Bublitz, G. U.; Boxer, S. G. *Proc. Natl. Acad. Sci. U.S.A.* **1996**, *93*, 8362–8367.
(34) Brejc, K.; Sixma, T. K.; Kitts, P. A.; Kain, S. R.; Tsien, R. Y.; Ormo, M.; Remington, S. J. *Proc. Natl. Acad. Sci. U.S.A.* **1997**, *94*, 2306–2311.

Scheme 2. Suggested Photoconversion Mechanism with Glu212 as Proton Acceptor (B4) and Intermediate Structures Derived from Simulation[a]

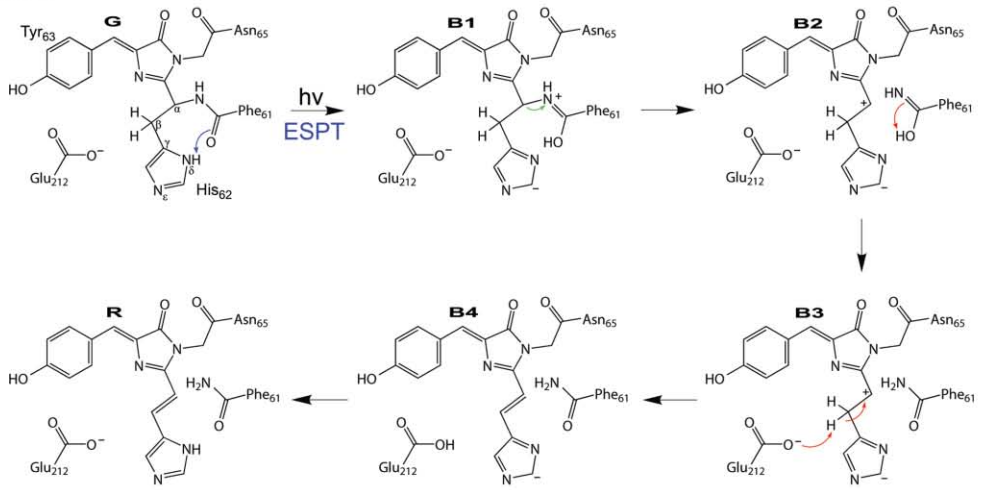

[a] Arrows show the main reaction steps in the color of the electronic state involved: blue for S_1, green for T_1, red for S_0.

recently found under basic conditions,[35] indicating that the usual pK_a of the imidazole ring can be significantly lowered in the presence of certain functionalities. In EosFP, the stereochemical alignment between the N_δ atom of His62 and the carbonyl moiety of Phe61 probably favors ESPT, which may be further facilitated by tunneling effects.[36,37] The occurrence of an ESPT involving an imidazole ring also likely accounts for the fact that His62 is strictly conserved in all PCFPs.

On the S_1 excited state surface, the activation energies for breaking the C_α–N bond is ~110 kJ/mol. This barrier is too high to be crossed, considering the short lifetime of the S_1 state, which is estimated to be of the order of a nanosecond. However, at the B1 intermediate, a conical intersection between the S1 and first excited state triplet (T1) surfaces appears. This conical intersection suggests that, to reach B4 from G, there must be an intersystem crossing from the S_1 to T_1 surfaces, which we denote ISC1 (Figures 3a and S2a).

Making this assumption, we reoptimized NEB pathways for the transition between the B1 and B4 structures of Scheme 2 on the T_1 surface (Figure 3b and S2b). At the B1 intermediate, a positive charge is localized on the nitrogen of the C_α–N bond. As a result, only ~15 kJ/mol are required to activate the C_α–N bond cleavage. At B2, the T_1 and S_0 surfaces become degenerate and remain so until formation of the B3 intermediate, after which the ground state S_0 becomes lower in energy. This suggests a second intersystem crossing, ISC2, occurring between the B2 and B3 intermediates.

We calculated also the minimum energy paths between G and B4 intermediates on the S_0 and T_1 surfaces (Figure S3). In contrast to what was observed for the S_1-optimized pathways (Figures 3a and S2a), cleavage of the C_α–N bond is accompanied by proton transfer from the N_δ atom of His62. Thus, neither a separate B1 intermediate nor an associated conical intersection are observed. To reach B2 from G, activation energies are very high, being ~135 and ~300 kJ/mol on the S_0 and T_1 surfaces, respectively. This implies C_α–N bond cleavage is unlikely in the S_0 and T_1 states, which is supported, at least for the ground state S_0, by the inability of PCFPs to convert in the dark.

Role of Glu212 in the Photoconversion. Glu212 is known to be essential for photoconversion of EosFP, as mutation of this residue to a glutamine (E212Q) abolishes the reaction.[4,17] Nienhaus et al. therefore suggested that the glutamate may act as a proton acceptor,[4] whereas Mizuno et al. proposed that it participates in the stabilization of the transition state.[6]

In our Scheme 2 that implicates Glu212 as a proton acceptor, we found that the proton transfer from C_β of His62 to the Glu212 carboxylate occurs between intermediates B3 and B4 on the S_0 surface (Figures 3b and S2b). To investigate the back proton transfer from Glu212 to the N_δ atom of His62, we optimized NEB pathways on the S_0 surface starting from B4 and going to the final red structure R. The optimized profiles are shown in Figures 3c and S2c. Overall the process is complex and involves a return of the proton to the C_β atom of His62 in a B3-like state, in which the S_0 and T_1 states are degenerate, and with an activation barrier of ~55 kJ/mol. This suggests that B4 may not be involved in the actual photoconversion pathway.

To check if another mechanism is possible that does not involve protonation of Glu212, we optimized NEB pathways from the second intersystem crossing ISC2 to the final red structure on the ground state surface S_0. The full mechanistic pathway is shown in Scheme 3, and the optimized NEB profiles in Figures 4 and S4.

First of all, the B2 intermediate has a carbocation on the C_α atom of His62. This makes the C_β atom very acidic, and delocalized electrons on the imidazolide make the C_γ atom a strong base, much more so than the carboxylate of Glu212. Therefore, in the step from B2 to C3, the proton on C_β is spontaneously transferred to the C_γ of the imidazolide moiety

(35) Berezin, M. Y.; Kao, J.; Achilefu, S. *Chemistry* **2009**, *15*, 3560–3566.
(36) Stoner-Ma, D.; Jaye, A. A.; Ronayne, K. L.; Nappa, J.; Meech, S. R.; Tonge, P. J. *J. Am. Chem. Soc.* **2008**, *130*, 1227–1235.
(37) Violot, S.; Carpentier, P.; Blanchoin, L.; Bourgeois, D. *J. Am. Chem. Soc.* **2009**, *131*, 10356–10357.

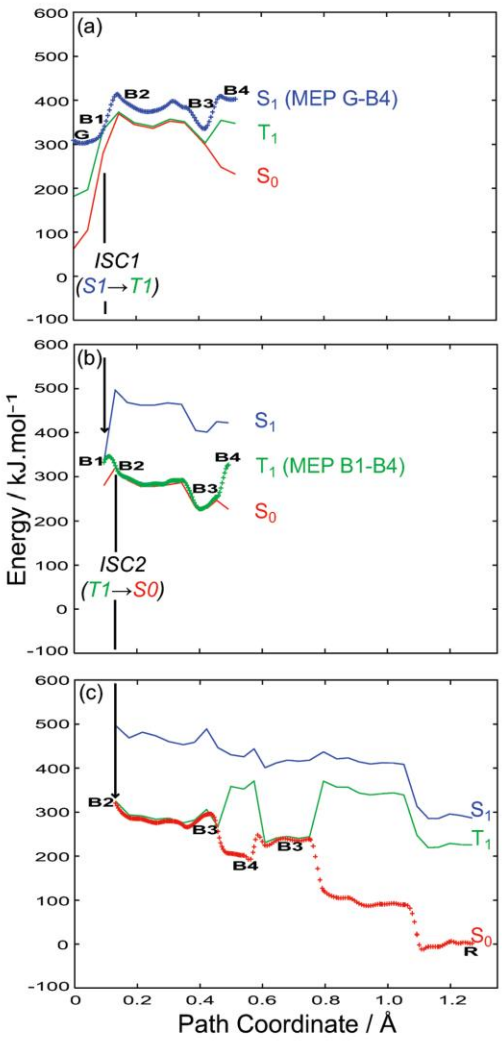

Figure 3. Energy profiles of optimized NEB paths calculated with a [10,9]-CISD(PDDG)/OPLS hybrid potential: (a) from G to B4 in the excited state S_1 (blue plus signs), (b) from B1 to B4 in the excited state T_1 (green plus signs), and (c) from B2 to B4 and from B4 to R in the ground state S_0 (red plus signs). Solid lines in each panel represent the energies of the optimized NEB structures in the electronic states that were not used in the optimization.

and a double bond is formed between C_α and C_β. The same proton is then transferred to the N_δ of His62, and the imidazole ring is reformed. In the last step, the proton on the Phe61 carbonyl rearranges to form the carboxamide. Overall, the complete process is energetically downhill, and the highest energy barrier for any of the proton transfers is ~25 kJ/mol.

KikGR Specificities in the PCFP Family. In the PCFP family, KikGR differs from the other members in that the His62 side chain isomerizes along the photoconversion pathway. The mechanism depicted in Scheme 3 accounts for this specificity. We propose that isomerization of the His62 side chain occurs in the B2 intermediate state, by rotation about the C_α–C_β single bond, taking advantage of the long lifetime of the triplet state before ISC2 takes place. After rotation, formation of the double bond follows and the final proton transfers lead to the red (isomerized) state. In EosFP and Kaede, residue Ile196 in the vicinity of His62 is engaged in hydrophobic interactions with Leu210 and does not leave enough space for isomerization of the His62 side chain (Figure 5a). The situation is different in KikGR, in which Ile196 and Met40 of EosFP are swapped to Met198 and Val40. As a result, Leu212 maintains a hydrophobic interaction with Val40 and leaves Met198 free of interaction. This provides conformational freedom to Met198, which allows His62 isomerization to occur (Figure 5b).

Another specificity of KikGR in the PCFP family is the absence of water molecule W1 in the green form (Figure 5b). For Kaede and EosFP, Hayashi et al. proposed that W1, which disappears in the red form of these proteins (Figure 5a), may assist in photoconversion.[6] In our study, we were unable to find evidence for such involvement of W1. The absence of the water molecule in the crystal structure of KikGR also suggests that it is not essential for the reaction. In our models of green EosFP, W1 is hydrogen-bonded to the side chain oxygen atom of Gln38, to the carbonyl group of Ser39 and, to a lesser extent, to the C_ε atom of His62. The latter two interactions are disrupted during our simulations of photoconversion, and formation of the imidazolide moiety on His62 induces their replacement by hydrogen bonds to the side chains of two neighboring residues (Met40 and Ile10). In our models of red EosFP, because our methods require keeping the same number of atoms throughout the simulations, the hydrogen bonds observed in the green form are restored. We suggest that, in the real mechanism, rearrangements that occur during photoconversion induce transient weakening of the interactions maintained by W1, which leads to the exit of this water molecule from the protein.

Electronic Structure of Intermediates. Figure 6 is a schematic that illustrates the electronic structures of the various intermediates along the photoconversion pathway of Scheme 3 obtained with the PDDG potential. For each intermediate, cartoons of the most important electronic configurations in each electronic state are given, together with images of the orbitals that are involved.

Overall, the majority of the intermediates' electronic states are dominated by a single electronic configuration of the appropriate type. The G electronic states are of simple type except that excitation involves the HOMO-1 rather than the HOMO. As these orbitals are localized on the hydroxybenzylidene-imidazolinone and the His62 imidazole moieties, respectively, the S_1 and T_1 states retain charge density on His62. By contrast, for the B1 intermediate, the excitation to S_1 and T_1 comes from the HOMO even though this orbital and the LUMO have character very similar to those of G. Thus, there is charge transfer between the His62 imidazolide moiety (where the HOMO is localized) and the hydroxybenzylidene-imidazolinone group (where the LUMO is localized), which explains why the S_1 and T_1 states are degenerate, as the two unpaired electrons in the HOMO and the LUMO are in different regions of space and interact only weakly.

At the B2 intermediate, T_1 retains its simple form, although the orbitals involved, the HOMO and LUMO, have electron density concentrated on the imidazolide and imidazolinone moieties but little on the phenol group. S_0 and S_1 are more complicated. S_1 has no compact description, whereas S_0 has

Scheme 3. Photoconversion Mechanism with the Intermediate States (C3, C4) Derived from Simulation[a]

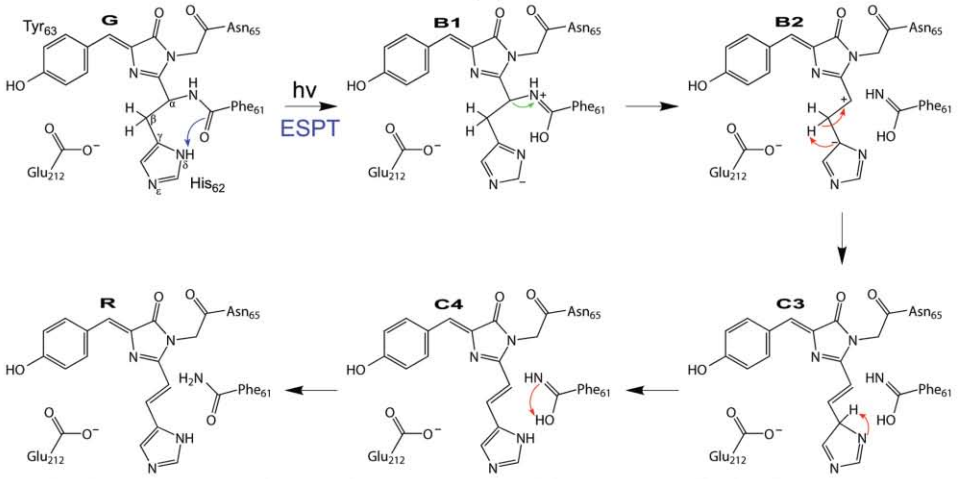

[a] Arrows show the main reaction steps in the color of the electronic state involved: blue for S_1, green for T_1, red for S_0.

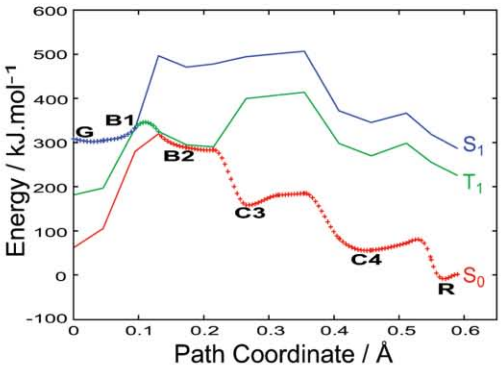

Figure 4. Energy profile of optimized NEB paths calculated with a [10,9]-CISD(PDDG)/OPLS hybrid potential from G to B1 in the excited state S_1 (blue plus signs), from B1 to B2 in the excited state T_1 (green plus signs), and from B2 to R in the ground state S_0 (red plus signs). The solid lines represent the energies of the optimized NEB structures in electronic states that were not used during optimization.

significant contributions from the two closed-shell configurations that are possible by doubly occupying the HOMO and LUMO. These are the same orbitals that are singly occupied in T_1 and indicate why the S_0 and T_1 states are degenerate for this intermediate.

After B2, the mechanism continues on the S_0 surface. The remaining electronic states are all of simple type, except for the S_1 and T_1 states of the red form R, which involve a mixture of two configurations obtained by excitation from the HOMO-1 and the HOMO, respectively.

Anionic Form of PCFPs. Activation with cyan light (~488 nm) of the anionic form of EosFP chromophores does not induce significant photoconversion. To better understand the role of the protonation state, we calculated first the NEB pathways between anionic forms of G and B4 intermediates on the S_1 surface (Scheme 2). The C_α–N bond cleavage is accompanied by proton transfer from the N_δ atom of His62, and the activation energy is very high at ~170 kJ/mol (Figure 7a and S5a). This finding is in agreement with the impossibility of photoconverting anionic forms of EosFP.

As a second test, we recalculated the energy profiles of photoconversion that were obtained for the neutral forms after removing the proton on the chromophore of each structure. The profiles are shown in Figures 7b and S5b. Clearly, the presence of the extra negative charge on the chromophore is likely to stabilize the starting S_1 state of G due to electrostatic interactions between Tyr63 and the cationic His194, while perhaps destabilizing the S_1 state of B1 because formation of the negatively charged imidazolide is less favorable. These trends rationalize why the NEB pathways optimized for cleavage with an anionic chromophore do not go through a B1-like structure, because the putative activation barrier in S_1, approaching 200 kJ/mol (Figures 7b), is larger than for the concerted reaction (Figures 7a).

Even if anionic forms of EosFP underwent the initial ESPT between His62 and Phe61, the expected ISC1 event could not occur since the conical intersection disappears for the B1 structure (Figures 7b). Indeed, T_1 and S_1 excited states of this intermediate are not degenerate since their electronic structure is now markedly different (Figure S6). Overall, these results show the obstacles that exist for a photoconversion pathway involving an anionic chromophore in PCFPs.

Catalytic Effects inside PCFPs. The three-dimensional structure of PCFPs plays a crucial role in the photoconversion mechanism, since denaturated forms of green species cannot be cleaved under UV irradiation.[12] This influence of the protein matrix on the reaction mechanism was investigated by recalculating the energies of the structures along the optimized pathways in vacuo, i.e., by excluding all MM atoms and the side chains of His194 and Glu212. The results are shown in Figures 8a and S7a and indicate a clear stabilization of the S_1 and T_1 (degenerate) states of the B1 intermediate by the protein. The energy difference between the G and B1 species in the S_1 state, which presumably constitutes the most critical activation

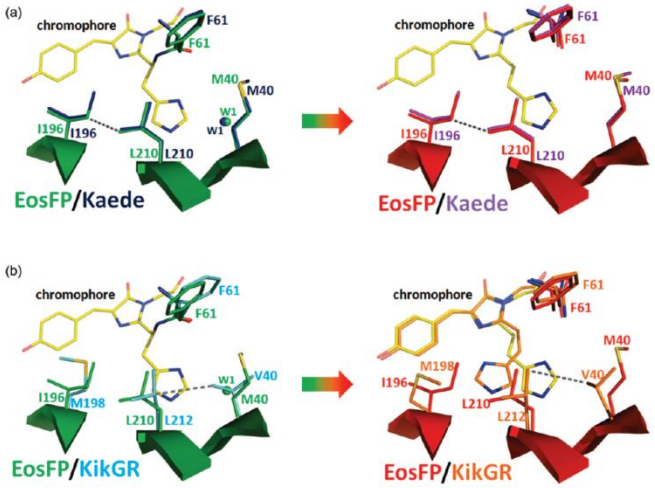

Figure 5. Superposition of structures of EosFP with (a) Kaede and (b) KikGR in the chromophore region before (left) and after (right) photoconversion (hydrophobic interactions are indicated by dashed lines).

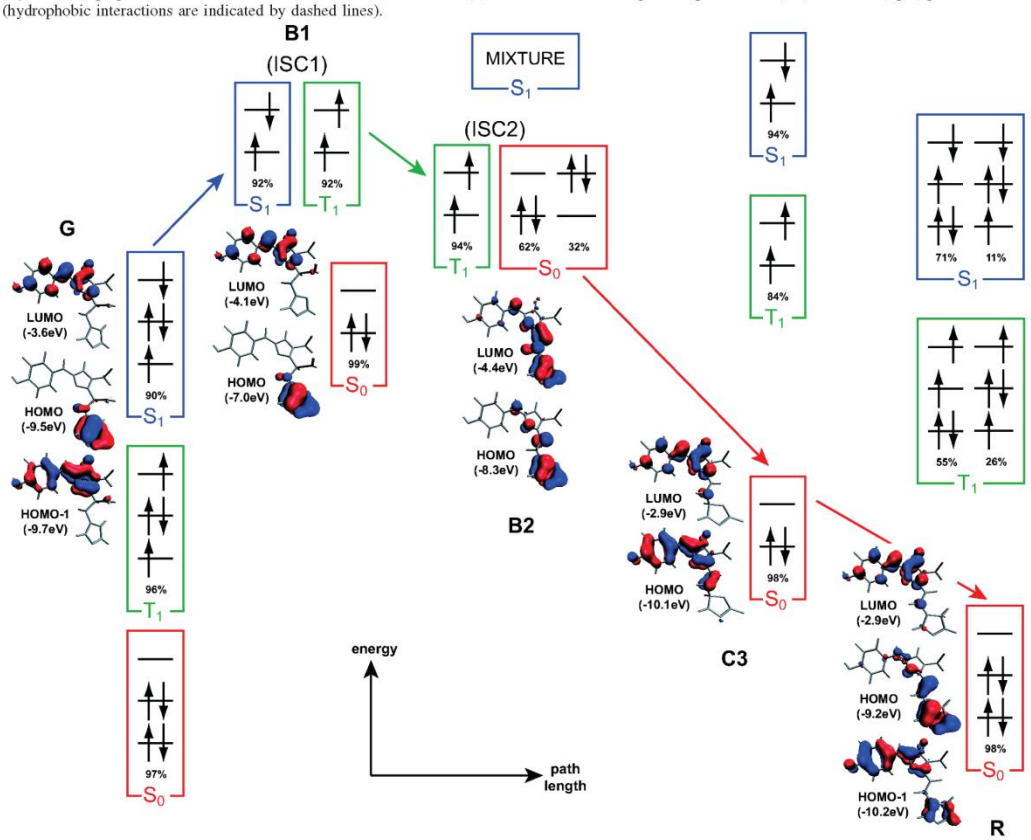

Figure 6. Schematic of the electronic states along the photoconversion path calculated with a [10,9]-CISD(PDDG)/OPLS hybrid potential. For convenience, triplet configurations are represented by a single microstate (S = 1; Sz = +1), as are singlet configurations with two unpaired electrons (electrons with opposing spins in two different orbitals). The fractional weights of the states, however, include contributions from all equivalent configurations. For each structure, only molecular orbitals involved in the excitation are shown.

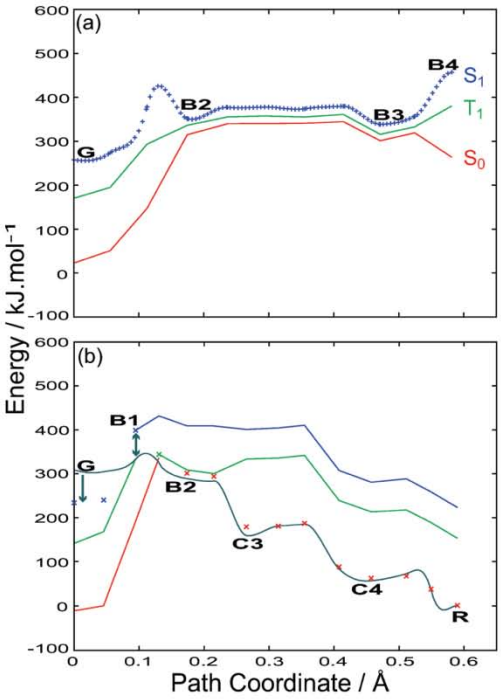

Figure 7. (a) Energy profile of optimized NEB path calculated with a [10,9]-CISD(PDDG)/OPLS hybrid potential between anionic forms of G and B4 in the excited state S_1 (blue plus signs). The solid lines represent the energies of the optimized NEB structures in electronic states that were not used during optimization. (b) Energy profile of the photoconversion pathway obtained with a [10,9]-CISD(PDDG)/OPLS hybrid potential for the neutral structures in which the proton has been removed from the phenol ring of the chromophore. Energies of the resulting anionic structures are calculated in the S_0 (red), T_1 (green), and S_1 (blue) electronic states. Crosses show the energy points along the reaction path; the main deviations to the neutral form profiles (shown in gray) are indicated by arrows. The solid lines represent the energies of the structures in the other electronic states.

barrier to be crossed due to the short lifetime of the excited state, is shifted from ~25 kJ/mol in the protein to ~95 kJ/mol in vacuum.

To more fully understand this catalytic effect, the energies of the structures along the optimized NEB pathways were recalculated with a new QC/MM partitioning in which Glu212 and His194 were excluded from the QC region. The profiles, which are shown in Figure S8, are indistinguishable when superimposed on the optimized ones, suggesting that the role of these residues can equally well be described with a ground-state MM potential. In the same way, the energy profiles in vacuo were recalculated with two different TDDFT methods, in order to check the reliability of our excited state potentials. The profiles, which are shown in Figure S9, are qualitatively similar to those obtained with the semiempirical CI methods.

To probe the specific effects of various residues on the photoconversion mechanism, the profile calculations were repeated by systematically setting the MM charges on each residue within the mobile region to zero. This change has minimal effect on the profiles except for Glu212 and the three

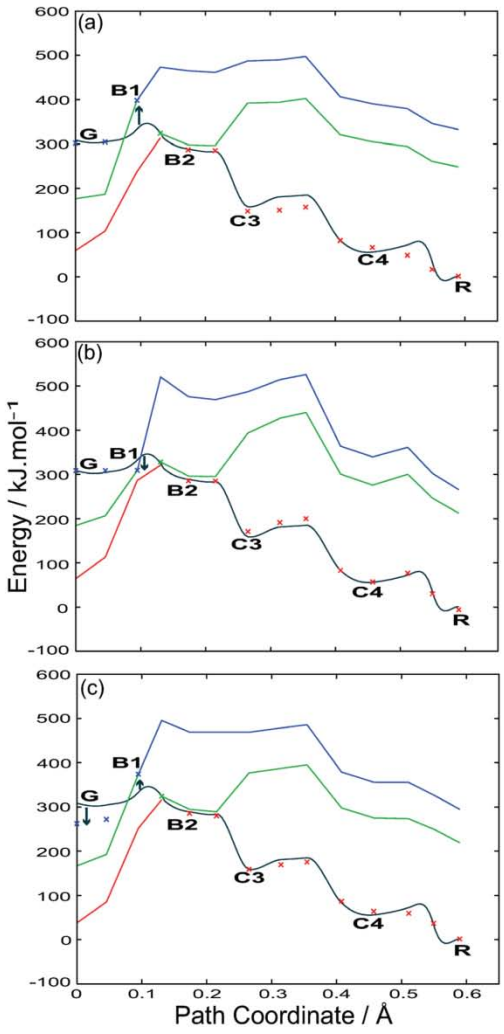

Figure 8. Energy profile of photoconversion calculated: (a) for the chromophore in vacuo with a [10,9]-CISD(PDDG) potential, (b) in protein with null atomic charges (MM) on Glu212, and (c) on His194, with a [10,9]-CISD(PDDG)/OPLS hybrid potential for which His194 and Glu212 are located in the MM region. Energies of structures extracted from the original NEB path (neutral chromophore in protein with the initial QC/MM partitioning) are calculated with the modified potentials in the S_0 (red), T_1 (green), and S_1 (blue) electronic states. Crosses show the energy points along the reaction path; the main deviations to the original profile (shown in gray) are indicated by arrows. The solid lines represent the energies of the structures in the other electronic states.

positively charged residues, His194, Arg66, and Arg91, which are found closest to the hydroxybenzylidene-imidazolinone moiety (Figure 1b).

The profiles with no MM charges on Glu212 are displayed in Figures 8b and S7b. They indicate that removal of the residue's negative charge actually stabilizes the S_1 and T_1 excited states of B1 and has little effect on the remainder of the pathway.

This result is at variance with the suggestion of Hayashi et al. for rationalizing the key role of this residue.[6] The profiles for His194 are shown in Figures 8c and S7c. Both display a stabilization of the green form (structure G) and a destabilization of the B1 intermediate on the S_1 surface. Further analysis shows mainly that the electronic structure of the B1 intermediate is similar to the one of Figure 6 (see Figure S10), although the absence of the positive charge on His194 destabilizes the LUMO that is localized on the hydroxybenzylidene-imidazolinone group, from −4.1 to −3.1 eV (or ~95 kJ/mol), thereby leading to higher energies for S_1 and T_1 (Figures 8c). Consequently, the energy difference between the G and B1 structures in the S_1 state increases from ~25 to ~110 kJ/mol, equivalent to a factor of ~4.5. When compared to His194, the two arginines, Arg66 and Arg91, show similar, but less pronounced, catalytic effects on the photoconversion energy profiles (Figure S11). Clearly, these three positively charged residues, and particularly His194, might have a crucial stabilizing effect on the transition state leading to backbone cleavage.

The results discussed above can also account for the fact that the E212Q variant of EosFP does not undergo photoconversion, even though, according to our results, Glu212 itself does not participate in the reaction. Glu212 hydrogen bonds directly to His194 and indirectly, via a water molecule (W3 in Figure 1b), to Arg66. Hence, it is possible that in the E212Q mutant, His194 can no longer be biprotonated or that, due to the disruption of the hydrogen-bond network around the chromophore, the critical Arg66 residue is displaced, thus impeding photoconversion. This possibility is substantiated by the observation that the E212Q mutation increases the pK_a of Tyr63 by 0.8 unit (6.6 vs 5.8 in wtEosFP), suggesting important modifications in the hydroxybenzylidene-imidazolinone environment.[17] The crucial role of Arg66 in shifting the Tyr63 pK_a found in Dendra2[15] also agrees with this hypothesis. Similar indirect effects could account for the loss of activity reported in other PCFP mutants, such as the A69S variant of Kaede.[12]

Optimization Strategies for PCFPs. Based on our findings, one may speculate that the introduction of additional positively charged residues in the chromophore environment, or of mutations that result in an improved network of positive charges, could facilitate photoconversion. However, whereas lowering the hydroxybenzylidene pK_a, as observed in Dendra2, effectively achieves this goal by increasing the fraction of protonated chromophores at physiological pH,[15] it is expected that the yield of photoconversion cannot be improved to an appreciable extent. In the mechanism proposed in Scheme 3, photoconversion is inherently limited by the two intersystem crossings that lead to transitions between potential energy surfaces.

Overall, we assign the slow kinetics that is experimentally observed in PCFPs to the requirement for two low-yield intersystem crossings events. This also accounts for the somewhat surprising finding that such a low yield process is accompanied by only very small structural changes between the green and red states in PCFPs.

Conclusion

We have investigated the mechanism of photoconversion between the green and red forms of the fluorescent protein EosFP using hybrid QC/MM potentials in conjunction with reaction-path-finding techniques. The preferred pathway identified from our simulations involves excitation of the green protonated form to the S_1 state, followed by two intersystem crossings (ISCs), first to the T_1 state and then to the S_0 ground state. Proton transfer from His62 to the carbonyl group of Phe61 occurs on the S_1 surface, forming an imidazolide ring on His62 side chain. Cleavage of the amide bond between Phe61 and His62 then becomes possible on the T_1 surface. Completion of the red form occurs on the S_0 surface via a series of proton transfers that are downhill in energy, extend the π-conjugated system, and lead to the reformation of the imidazole ring on the His62 side chain.

The occurrence of ISCs is a novel aspect of the photoconversion mechanism in PCFPs and provides an explanation for the observed low quantum yield of the process. The mechanism proposed in this work differs from previous hypotheses in a number of ways: (i) The phenol ring of the chromophore does not undergo an ESPT and remains protonated along the whole reaction pathway. (ii) The essential residue Glu212 remains deprotonated throughout and does not take part in proton transfer. (iii) Water molecules in the vicinity of the chromophore are not involved. An analysis of the structures and energetics of the intermediates along the pathway shows that three cationic residues closest to the chromophore have important catalytic roles, whereas Glu212, which is itself anticatalytic, indirectly serves to maintain the integrity of the chromophore's electrostatic environment. These results suggest that engineering EosFP by reorganizing or introducing extra cationic residues around the chromophore could facilitate photoconversion.

Acknowledgment. We thank Antoine Royant for fruitful discussions. We also thank the Ministère de l'Enseignement Supérieur et de la Recherche, the Centre National de la Recherche Scientifique, the European Synchrotron Radiation Facility, and the Agence Nationale de la Recherche (ANR-07-BLAN-0107-01) for financial support. This work was further supported by the Deutsche Forschungsgemeinschaft (DFG) and the State of Baden-Württemberg through the Center for Functional Nanostructures (CFN) and by DFG grants NI 291/9 and SFB 497.

Supporting Information Available: Table of absorption and emission wavelength predicted by the QC/MM potentials used in this work, additional figures, and comments on alternative reaction pathways. This material is available free of charge via the Internet at http://pubs.acs.org.

JA905380Y

J|A|C|S COMMUNICATIONS

Published on Web 12/01/2009

Structural Basis of X-ray-Induced Transient Photobleaching in a Photoactivatable Green Fluorescent Protein

Virgile Adam,[†] Philippe Carpentier,[‡] Sebastien Violot,[§] Mickaël Lelimousin,[‡] Claudine Darnault,[‡] G. Ulrich Nienhaus,[∥,⊥] and Dominique Bourgeois*[,‡]

European Synchrotron Radiation Facility, 6 rue Jules Horowitz, BP 220, 38043 Grenoble Cedex, France, IBS, Institut de Biologie Structurale Jean-Pierre Ebel, CEA, CNRS, Université Joseph Fourier, 41 rue Jules Horowitz, 38027 Grenoble, France, Laboratoire de Physiologie Cellulaire Végétale, Institut de Recherches en Technologie et Sciences pour le Vivant, CEA, CNRS, INRA, Université Joseph Fourier, 17 rue des Martyrs, F-38054 Grenoble, France, Institute of Applied Physics and Center for Functional Nanostructures (CFN), Karlsruhe Institute of Technology, 76128 Karlsruhe, Germany, and Department of Physics, University of Illinois at Urbana−Champaign, Urbana, Illinois 61801

Received August 28, 2009; E-mail: dominique.bourgeois@ibs.fr

Fluorescent proteins (FPs) are invaluable fluorescent markers in cell biology. Naturally occurring FPs have been optimized to emit bright fluorescence over a wide spectral range, and photoactivatable FPs have recently been developed that enable protein tracking[1] and play a crucial role in super-resolution microscopy.[2] Upon illumination, all FPs undergo transient stochastic switching events to nonfluorescent dark states, a phenomenon known as "blinking".[3] They eventually convert to a permanent off state, which is known as "bleaching". Typically, the 4-(*p*-hydroxybenzylidene)-5-imidazolinone chromophore blinks because of intersystem crossing to the triplet state or excursions to protonated, isomerized, or radical states and emits 10^4-10^5 photons before falling victim to irreversible photodestruction. Although blinking and bleaching can be exploited in certain applications,[4−7] they are generally considered as major nuisances, notably in single-molecule and time-resolved studies, and they limit the achievable resolution in several nanoscopy schemes.

Contrary to organic dyes[8−12] or quantum dots,[13] the details of the molecular mechanisms underlying the transient or permanent loss of fluorescence in FPs have remained largely unexplored, and the development of variants with superior photostability has followed empirical approaches.[14] In organic dyes, electron-transfer reactions have been identified in the formation of transient dark radical states, which constitute important pathways for photobleaching.[8−12] Radical chemistry can also occur in FPs, for example through the Kolbe[15,16] or oxidative "redding"[17] mechanisms. The short-lived nature of radical states in FPs, however, has prevented a structural characterization.

Here we have used X-ray radiolysis as a source of electrons and holes to generate a transient dark state in the photoactivatable fluorescent protein IrisFP,[18] a variant of the fluorescent protein EosFP from *Lobophyllia hemprichii*.[19] We noticed that the fluorescence emission of IrisFP crystals decays very rapidly under a synchrotron X-ray beam, even at 100 K (Figure 1a). This decay occurs at an X-ray dose much lower than that needed to collect a complete diffraction data set (typically 0.5−1.0 MGy) and is mostly reversible, with only a small irreversible component (Figure 1a, inset). The corresponding absorbance decay is composed of a rapid phase followed by a slower phase, is less pronounced at comparable doses, and is also partly reversible [Figure 1a and Figure S1 in the Supporting Information (SI)].

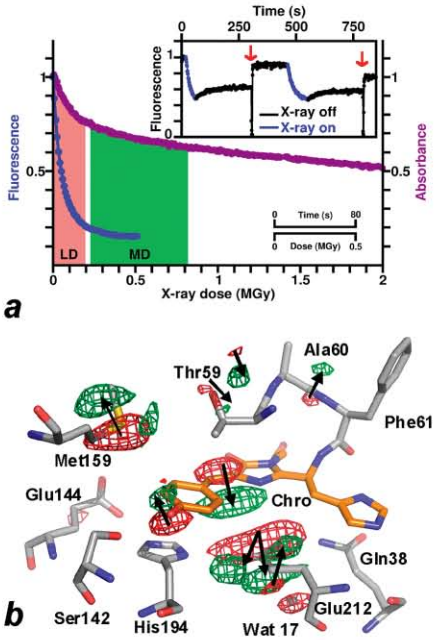

Figure 1. Reversible bleaching of IrisFP in crystallo induced by X-rays at 100 K. (a) Fluorescence (blue) and absorbance (purple) decays due to X-ray irradiation. The doses used for the two composite data sets [low dose (LD) and moderate dose (MD)] are indicated (red and green shading). The inset shows the reversibility of the fluorescence decay. Partial recovery (black) occurs at 100 K, whereas almost complete recovery is rapidly induced by short excursions to room temperature (red arrows at 300 and 780 s). The process can be repeated multiple times. (b) Experimental difference electron density map (red, -9.5σ; green, $+9.5\sigma$) between the LD and MD data sets, overlaid on a model of IrisFP (PDB entry 2VVH). The difference map averaged over the four IrisFP monomers in the crystal asymmetric unit is shown (see the SI). The chromophore is displayed in orange and neighboring residues in gray. Arg66, in contact with the chromophore, has been omitted for clarity. Arrows indicate structural motions.

[†] European Synchrotron Radiation Facility.
[‡] Institut de Biologie Structurale Jean-Pierre Ebel.
[§] Institut de Recherches en Technologie et Sciences pour le Vivant.
[∥] Karlsruhe Institute of Technology.
[⊥] University of Illinois at Urbana−Champaign.

10.1021/ja907296v

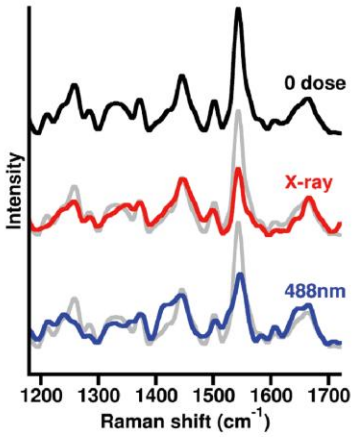

Figure 2. In crystallo Raman spectra of IrisFP. Spectra collected at 100 K are shown before (black and gray lines) and after X-ray irradiation (0.9 MGy; red line), and after 488 nm illumination (26 min at 1.2 kW/cm^2; blue line).

To obtain a structural view of these transient spectroscopic changes, we collected composite X-ray diffraction data sets (see the SI)[20] in order to reconstruct two complete data sets that correspond to the beginning (median dose ~0.1 MGy) and end (~0.5 MGy) of the fast absorbance decay phase (Figure 1 and Table S1 in the SI). The difference electron density map between the two data sets reveals structural changes localized on the chromophore and its immediate environment (Figure 1b). Pairs of negative and positive difference density features show a downward motion of the chromophore's bridging methylene moiety and an upward motion of the benzylidene phenolate oxygen, resulting in a loss of planarity of the chromophore. The motion of the methylene bridge induces a displacement of Glu212 [Glu222 in green fluorescent protein (GFP)] that explores two conformations, with the carboxylate group H-bonded to either His194 or Gln38. The motion of the chromophore phenolate oxygen is accompanied by a shift of the Met159 side chain that is clearly visible because of the heavy sulfur atom. Other structural changes typically observed upon intense X-ray exposure of protein crystals are not visible at the doses employed here (Figure S2 in the SI).

In crystallo Raman spectra of IrisFP collected before and immediately after exposure to a moderate X-ray dose (0.9 MGy) reveal band modifications that are consistent with the observed structural changes (Figure 2; also see the SI). Notably, the band at 1545 cm^{-1}, which is the most strongly resonance-enhanced band in GFP,[21] is significantly reduced. This band has been assigned to a mode that combines stretching of the C_α=C_5 exocyclic double bond (the methylene bridge; Scheme S1 in the SI) and deformation of the imidazolinone moiety of the anionic chromophore.[22] A decrease of the 1545 cm^{-1} band is consistent with a loss of the double-bond character of the methylene bridge, as suggested by the structural data. The 1545 cm^{-1} band is probably converted to a lower-frequency band that cannot be identified in our spectra because it is weak and nonresonant. No other Raman band seems much altered, suggesting that the chromophore does not change its protonation state and that its phenol moiety remains chemically intact (Figure S3).[23] Altogether, the diffraction, UV−vis absorbance, and Raman data indicate that the C_α=C_5 π bond is reversibly altered upon mild X-ray exposure, transiently disrupting the conjugated π-electron system.

Electron difference density maps obtained from data sets collected at moderate and much higher (~20 MGy) X-ray doses, mostly representative of structural changes associated with the slow absorbance decay phase, show a tilted chromophore and a clear decarboxylation of Glu212 (Figure S4), indicative of a permanently bleached state.

Because the reversible loss of color in the crystal is achieved with a number of absorbed X-ray photons orders of magnitude smaller than the number of diffracting protein molecules (see the SI), dark-state formation must result from a secondary radiation damage process.[24] As reactive oxygen species and solvated electrons produced by solvent radiolysis essentially do not diffuse at 100 K, electrons and holes migrating to the chromophore are most likely involved, resulting in protein radical states that eventually lead to permanent photodestruction. The fluorescence decay kinetics is probably accelerated by quenching effects attributable to absorbing radiolysis products (e.g., solvated electrons).[25] Thus, chemically intact chromophores may quickly lose their ability to fluoresce. The absorbance decay, in contrast, correctly accounts for the intrinsic chemical state of the chromophores and therefore can be used to quantitatively evaluate the data. Simple kinetic modeling (see the SI) suggests that upon X-ray exposure, an intermediate state rapidly builds up to a steady-state level of ~20%, characterized by the structural changes shown in Figure 1b. This intermediate, or the starting green-emitting species, infrequently converts to a permanently bleached state (slow phase in the absorbance decay), yielding the structural changes shown in Figure S4. Importantly, the fast buildup of the intermediate, its steady-state level at ~20%, and its slow recovery at 100 K in the absence of X-rays altogether imply that the intermediate is not only induced but also efficiently "repaired" to the initial fluorescent state by X-ray irradiation. Such a repair mechanism probably constitutes a general feature of X-ray-induced radiation chemistry in redox-active biological molecules.

To relate our observations to the mechanism of photodamage induced by visible light, an IrisFP crystal was illuminated at 100 K with 488 nm laser light (see the SI). An irreversible loss of absorbance and fluorescence was achieved, although at short illumination times, a transient rise of the 390 nm absorbance band was also noticed (Figures S5 and S6). We attribute this rise to a photoinduced protonation of the chromophore, possibly involved in the photoswitching mechanism of photochromic FPs, as suggested previously.[26] Raman data collected on a crystal after prolonged illumination by 488 nm light, while also suggesting some photoinduced protonation of the chromophore (see the discussion in the SI), reveal a major decrease of the band at 1545 cm^{-1}, as in the X-ray case (Figure 2). Therefore, like the X-rays, visible photons primarily affect the C_α=C_5 double bond that is key to the chromophore's optical properties.

Absorption of a visible photon in FPs may induce radical species arising from electron transfer in an excited state of the chromophore (Figure 3). As suggested for organic dyes,[8,12] we anticipate that because of its long lifetime, the triplet state T_1 is the most likely starting point for reactions driving the IrisFP chromophore to radical states, although singlet states may also contribute.[9−11] Because of the likely involvement of T_1 and competition with other phototransformation pathways (see the SI), accumulation of a radical state is not expected under visible light at the ensemble level, even at cryogenic temperature. In any case, radical formation by X-rays and visible light proceeds a priori by different mechanisms. We postulate that the strongly reducing electrons and oxidizing holes generated by X-ray-induced solvent radiolysis provide an effective

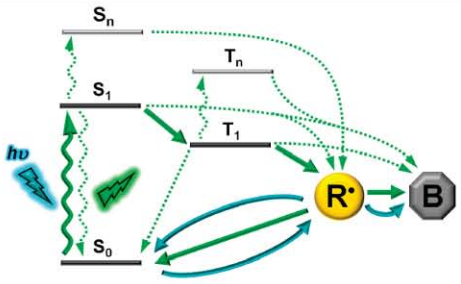

Figure 3. Proposed mechanism for X-ray-induced radical generation in IrisFP and possible photobleaching pathways. Green and blue lines show electron transfer and/or photobleaching pathways induced by visible and X-ray light, respectively. Green dotted lines show other possible pathways not discussed in this article. Notation: R•, radical; B, bleached.

shunt pathway for populating a biologically relevant radical state directly from the ground state.

Our results are in line with recent findings that the fluorescent properties of organics dyes strongly depend on their local redox environment. For example, intermolecular electron transfer from/to reducing/oxidizing agents has been shown to influence the blinking rate of several dyes,[8,9] offering opportunities to scavenge radical states or to precisely control blinking in superlocalization-based nanoscopy.[4] The investigation of similar effects in FPs will be of interest in future studies.

Radical states similar to that observed here may also play important roles in FPs. A radical state has been invoked as a putative intermediate in the oxidative green-to-red photoconversion noticed in some GFP members.[17] The mechanism of superoxide release by the red FP KillerRed is also worth mentioning. It can be speculated that electrons extracted from the excited chromophore can be efficiently transferred out of the protein via a chain of water molecules, allowing reduction of O_2 to $O_2^{\bullet-}$.[27,28]

In organic dyes, a well-known mechanism of photobleaching is the destruction of the chromophore by reactive oxygen species (ROS), which form when molecular oxygen reacts with the excited chromophore. Some evidence exists that such self-sensitization may not be the dominant cause of photobleaching in FPs,[29] as their β-can structure protects the chromophore from the solvent and dissolved O_2. Yet, FPs are typically 1 order of magnitude less resistant to photobleaching than organic dyes. This observation suggests that photobleaching via intramolecular electron transfer might play a comparatively important role in FPs. While the protein matrix tends to protect the chromophore against O_2, it also provides a source of electrons available for redox reactions within the chromophore pocket. In the case of IrisFP (as in GFP[15]), charge transfer from Glu212 to the chromophore may occur upon absorption of a visible photon, leaving an unpaired electron on this residue. This biradical state may then relax back to the ground state or occasionally lead to decarboxylation of Glu212, as observed in this work. More photostable variants could perhaps be designed by insertion of sulfur-containing residues exposed to solvent and linked to the chromophore pocket via electron wires.[27]

Our results underpin the susceptibility of FPs to electron-transfer reactions[17] and reveal the methylene bridge as the Achilles' heel of the chromophore in FPs. Finally, the distortions induced by mild X-ray irradiation observed here for IrisFP suggest that the chromophore geometry in a number of FPs whose structures have been solved using synchrotron radiation may be slightly overbent.

Acknowledgment. We thank M. Weik and A. Royant for insightful discussions. D.B. acknowledges support by ANR-07-BLAN-0107-01. G.U.N. acknowledges support by the State of Baden-Württemberg and the DFG (Grants CFN, NI 291/9, and SFB 497). S.V. was supported by the CEA.

Supporting Information Available: Materials and methods, kinetic model, solution studies, pH-dependent Raman spectra, phototransformations in IrisFP, data collection statistics, and illustrations. This material is available free of charge via the Internet at http://pubs.acs.org.

References

(1) Wiedenmann, J.; Nienhaus, G. U. *Expert Rev. Proteomics* **2006**, *3*, 361.
(2) Hell, S. W. *Nat. Methods* **2009**, *6*, 24.
(3) Dickson, R. M.; Cubitt, A. B.; Tsien, R. Y.; Moerner, W. E. *Nature* **1997**, *388*, 355.
(4) Vogelsang, J.; Cordes, T.; Forthmann, C.; Steinhauer, C.; Tinnefeld, P. *Proc. Natl. Acad. Sci. U.S.A.* **2009**, *106*, 8107.
(5) Folling, J.; Bossi, M.; Bock, H.; Medda, R.; Wurm, C. A.; Hein, B.; Jakobs, S.; Eggeling, C.; Hell, S. W. *Nat. Methods* **2008**, *5*, 943.
(6) Betzig, E.; Patterson, G. H.; Sougrat, R.; Lindwasser, O. W.; Olenych, S.; Bonifacino, J. S.; Davidson, M. W.; Lippincott-Schwartz, J.; Hess, H. F. *Science* **2006**, *313*, 1642.
(7) White, J.; Stelzer, E. *Trends Cell Biol.* **1999**, *9*, 61.
(8) Vogelsang, J.; Kasper, R.; Steinhauer, C.; Person, B.; Heilemann, M.; Sauer, M.; Tinnefeld, P. *Angew. Chem., Int. Ed.* **2008**, *47*, 5465.
(9) Widengren, J.; Chmyrov, A.; Eggeling, C.; Löfdahl, P. A.; Seidel, C. A. M. *J. Phys. Chem. A* **2007**, *111*, 429.
(10) Yeow, E. K.; Melnikov, S. M.; Bell, T. D.; De Schryver, F. C.; Hofkens, J. *J. Phys. Chem. A* **2006**, *110*, 1726.
(11) Hoogenboom, J. P.; van Dijk, E. M.; Hernando, J.; van Hulst, N. F.; Garcia-Parajo, M. F. *Phys. Rev. Lett.* **2005**, *95*, 097401.
(12) Zondervan, R.; Kulzer, F.; Orlinskii, S. B.; Orrit, M. *J. Phys. Chem. A* **2003**, *107*, 6770.
(13) Wang, X.; Ren, X.; Kahen, K.; Hahn, M. A.; Rajeswaran, M.; Maccagnano-Zacher, S.; Silcox, J.; Cragg, G. E.; Efros, A. L.; Krauss, T. D. *Nature* **2009**, *459*, 686.
(14) Shaner, N. C.; Lin, M. Z.; McKeown, M. R.; Steinbach, P. A.; Hazelwood, K. L.; Davidson, M. W.; Tsien, R. Y. *Nat. Methods* **2008**, *5*, 545.
(15) van Thor, J. J.; Gensch, T.; Hellingwerf, K. J.; Johnson, L. N. *Nat. Struct. Biol.* **2002**, *9*, 37.
(16) Bell, A. F.; Stoner-Ma, D.; Wachter, R. M.; Tonge, P. J. *J. Am. Chem. Soc.* **2003**, *125*, 6919.
(17) Bogdanov, A. M.; Mishin, A. S.; Yampolsky, I. V.; Belousov, V. V.; Chudakov, D. M.; Subach, F. V.; Verkhusha, V. V.; Lukyanov, S.; Lukyanov, K. A. *Nat. Chem. Biol.* **2009**, *5*, 459.
(18) Adam, V.; Lelimousin, M.; Boehme, S.; Desfonds, G.; Nienhaus, K.; Field, M. J.; Wiedenmann, J.; McSweeney, S.; Nienhaus, G. U.; Bourgeois, D. *Proc. Natl. Acad. Sci. U.S.A.* **2008**, *105*, 18343.
(19) Wiedenmann, J.; Ivanchenko, S.; Oswald, F.; Schmitt, F.; Rocker, C.; Salih, A.; Spindler, K. D.; Nienhaus, G. U. *Proc. Natl. Acad. Sci. U.S.A.* **2004**, *101*, 15905.
(20) Berglund, G. I.; Carlsson, G. H.; Smith, A. T.; Szoke, H.; Henriksen, A.; Hajdu, J. *Nature* **2002**, *417*, 463.
(21) Schellenberg, P.; Johnson, E.; Esposito, A. P.; Reid, P. J.; Parson, W. W. *J. Phys. Chem. B* **2001**, *105*, 5316.
(22) He, X.; Bell, A. F.; Tonge, P. J. *J. Phys. Chem. B* **2002**, *106*, 6056.
(23) Luin, S.; Voliani, V.; Lanza, G.; Bizzarri, R.; Amat, P.; Tozzini, V.; Serresi, M.; Beltram, F. *J. Am. Chem. Soc.* **2009**, *131*, 96.
(24) Garman, E. F.; Owen, R. L. *Acta Crystallogr., Sect. D: Biol. Crystallogr.* **2006**, *62*, 32.
(25) McGeehan, J.; Ravelli, R. B.; Murray, J.; Owen, R. L.; Cipriani, F.; McSweeney, S.; Weik, M.; Garman, E. *J. Synchrotron Radiat.* **2009**, *16*, 163.
(26) Mizuno, H.; Mal, T. K.; Walchli, M.; Kikuchi, A.; Fukano, T.; Ando, R.; Jeyakanthan, J.; Taka, J.; Shiro, Y.; Ikura, M.; Miyawaki, A. *Proc. Natl. Acad. Sci. U.S.A.* **2008**, *105*, 9227.
(27) Carpentier, P.; Violot, S.; Blanchoin, L.; Bourgeois, D. *FEBS Lett.* **2009**, *583*, 2839.
(28) Pletnev, S.; Gurskaya, N. G.; Pletneva, N. V.; Lukyanov, K. A.; Chudakov, D. M.; Martynov, V. I.; Popov, V. O.; Kovalchuk, M. V.; Wlodawer, A.; Dauter, Z.; Pletnev, V. *J. Biol. Chem.* **2009**, *284*, 32028.
(29) Swaminathan, R.; Hoang, C. P.; Verkman, A. S. *Biophys. J.* **1997**, *72*, 1900.

JA907296V

VI. INDEX AND BIBLIOGRAPHY

This page intentionally left blank

Index

Bibliography

A

Abbe E.K. (1873), *"Beiträge zur Theorie des Mikroskops und der mikroskopischen Wahrnehmung "*, Archiv für Mikroskopische Anatomie **9**: 413-420.

Adam V., Carpentier, P., Violot S., Lelimousin M., Darnault C., Nienhaus G.U. & Bourgeois D. (2009a), *"Structural basis of photobleaching in a photoactivatable green fluorescent protein"*, Proceedings of the National Academy of Sciences USA **131**: 18063-18065

Adam V., Lelimousin M., Boehme S., Desfonds G., Nienhaus K., Field M.J., Wiedenmann J., McSweeney S., Nienhaus G.U. & Bourgeois D. (2008), *"Structural characterization of IrisFP, an optical highlighter undergoing multiple photo-induced transformations"*, Proceedings of National Academy of Science USA **105**(47): 18343-18348.

Adam V., Nienhaus K., Bourgeois D. & Nienhaus G.U. (2009b), *"Structural basis of enhanced photoconversion yield in GFP-like protein Dendra2"*, Biochemistry **48**(22): 4905-4915.

Adam V., Royant A., Niviere V., Molina-Heredia F.P. & Bourgeois D. (2004), *"Structure of superoxide reductase bound to ferrocyanide and active site expansion upon X-ray-induced photo-reduction"*, Structure **12**(9): 1729-1740.

Agmon N. (2005), *"Elementary steps in excited-state proton transfer"*, Journal of physical chemistry A **109**(1): 13-35.

Ai H.W., Henderson J.N., Remington S.J. & Campbell R.E. (2006), *"Directed evolution of a monomeric, bright and photostable version of Clavularia cyan fluorescent protein: structural characterization and applications in fluorescence imaging"*, Biochemical Journal **400**(3): 531-540.

Ai H.W., Olenych S.G., Wong P., Davidson M.W. & Campbell R.E. (2008), *"Hue-shifted monomeric variants of Clavularia cyan fluorescent protein: identification of the molecular determinants of color and applications in fluorescence imaging"*, BMC Biology **6**: 13.

Ando R., Flors C., Mizuno H., Hofkens J. & Miyawaki A. (2007), *"Highlighted generation of fluorescence signals using simultaneous two-color irradiation on Dronpa mutants"*, Biophysical journal **92**(12): L97-99.

Ando R., Hama H., Yamamoto-Hino M., Mizuno H. & Miyawaki A. (2002), *"An optical marker based on the UV-induced green-to-red*
Ando R., Mizuno H. & Miyawaki A. (2004), *"Regulated fast nucleocytoplasmic shuttling observed by reversible protein highlighting"*, Science **306**(5700): 1370-1373.

Andresen M., Stiel A.C., Folling J., Wenzel D., Schonle A., Egner A., Eggeling C., Hell S.W. & Jakobs S. (2008), *"Photoswitchable fluorescent proteins enable monochromatic multilabel imaging and dual color fluorescence nanoscopy"*, Nature biotechnology **26**(9): 1035-1040.

Andresen M., Stiel A.C., Trowitzsch S., Weber G., Eggeling C., Wahl M.C., Hell S.W. & Jakobs S. (2007), *"Structural basis for reversible photoswitching in Dronpa"*, Proceedings of the National Academy of Sciences USA **104**(32): 13005-13009.

Andresen M., Wahl M.C., Stiel A.C., Grater F., Schafer L.V., Trowitzsch S., Weber G., Eggeling C., Grubmuller H., Hell S.W. & Jakobs S. (2005), *"Structure and mechanism of the reversible photoswitch of a fluorescent protein"*, Proceedings of the National Academy of Sciences USA **102**(37): 13070-13074.

Angel S.M. & Myrick M.L. (1990), *"Wavelength selection for fiber optic Raman spectroscopy. Part 1"*, Applied Optics **29**(9): 1350-1352.

Audoin V. (1840), *"Animaux phosphorescents - Remarques sur la phosphorescence de quelques animaux articulés, à l'occasion d'une lettre de M. Forester sur la phosphorescence des lombrics terrestres"*, Comptes rendus hebdomadaires des séances à l'Académie des Sciences, Paris. **11:** 747-749.

Ayoob J.C., Shaner N.C., Sanger J.W. & Sanger J.M. (2001), *"Expression of green or red fluorescent protein (GFP or DsRed) linked proteins in nonmuscle and muscle cells"*, Molecular Biotechnology **17**(1): 65-71.

B

Baird G.S., Zacharias D.A. & Tsien R.Y. (2000), *"Biochemistry, mutagenesis, and oligomerization of DsRed, a red fluorescent protein from coral"*, Proceedings of the National Academy of Sciences USA **97**(22): 11984-11989.

Barondeau D.P., Putnam C.D., Kassmann C.J., Tainer J.A. & Getzoff E.D. (2003), *"Mechanism and energetics of green fluorescent protein chromophore synthesis revealed by trapped intermediate structures"*, Proceedings of National Academy of Sciences USA **100**(21): 12111-12116.

Bates M., Huang B., Dempsey G.T. & Zhuang X. (2007), *"Multicolor super-resolution imaging with photo-switchable fluorescent probes"*, Science **317**(5845): 1749-1753.

Becquerel A.E. (1839), *"Le spectre solaire et la constitution de la lumière électrique"*, Comptes rendus hebdomadaires des séances à l'Académie des Sciences, Paris. **9:** 145.

Bell A.F., Stoner-Ma D., Wachter R.M. & Tonge P.J. (2003), *"Light driven decarboxylation of wild-type green fluorescent protein",* Journal of the American Chemical Society **125**(23): 6919-6926.

Berglund G.I., Carlsson G.H., Smith A.T., Szoke H., Henriksen A. & Hajdu J. (2002), *"The catalytic pathway of horseradish peroxidase at high resolution",* Nature **417**(6887): 463-468.

Betzig E., Patterson G.H., Sougrat R., Lindwasser O.W., Olenych S., Bonifacino J.S., Davidson M.W., Lippincott-Schwartz J. & Hess H.F. (2006), *"Imaging intracellular fluorescent proteins at nanometer resolution",* Science **313**(5793): 1642-1645.

Bourgeois D. (1999), *"New processing tools for weak and/or spatially overlapped macromolecular diffraction patterns",* Acta Crystallographica D **55**(10): 1733-1741.

Bourgeois D. & Royant A. (2005), *"Advances in kinetic protein crystallography",* Current Opinion in Structural Biology **15**(5): 538-547.

Bourgeois D., Vernède X., Adam V., Fioravanti E. & Ursby T. (2002), *"A microspectrophotometer for UV–visible absorption and fluorescence studies of protein crystals",* Journal of Applied Crystallography **35**(3): 319-326.

Boyé S., Brøndsted N.S., Krogh H., Nielsen I.B., Pedersen U.V., Bell A.F., He X., Tonge P.J. & Andersen L.H. (2003), *"Gas-phase absorption properties of DsRed model chromophores",* Physical Chemistry Chemical Physics **5**: 3021-3026.

Boyle R. (1672), *"Some observations about shining flesh, both of veal and of pullet",* Philosophical Transactions of the Royal Society of London **89**.

Boyle R. (1680), *Aerial noctiluca: or some new phenomena, and a process of a factitious self-shining substance*, London, T. Snowden.

Brand A. (1995), *"GFP in Drosophila",* Trends in Genetics **11**(8): 324-325.

Brejc K., Sixma T.K., Kitts P.A., Kain S.R., Tsien R.Y., Ormo M. & Remington S.J. (1997), *"Structural basis for dual excitation and photoisomerization of the Aequorea victoria green fluorescent protein",* Proceedings of the National Academy of Sciences USA **94**(6): 2306-2311.

Brunger A.T. (1992), *"Free R value: a novel statistical quantity for assessing the accuracy of crystal structures",* Nature **355**(6359): 472-475.

Brunger A.T., Adams P.D., Clore G.M., DeLano W.L., Gros P., Grosse-Kunstleve R.W., Jiang J.S., Kuszewski J., Nilges M., Pannu N.S., Read R.J., Rice L.M., Simonson T. & Warren G.L. (1998), *"Crystallography & NMR system: A new software suite for macromolecular structure determination",* Acta Crystallographica D **54**(Pt 5): 905-921.

Bulina M.E., Chudakov D.M., Britanova O.V., Yanushevich Y.G., Staroverov D.B., Chepurnykh T.V., Merzlyak E.M., Shkrob M.A., Lukyanov S. & Lukyanov K.A. (2006a), *"A genetically encoded photosensitizer",* Nature biotechnology **24**(1): 95-99.

Bulina M.E., Chudakov D.M., Mudrik N.N. & Lukyanov K.A. (2002), *"Interconversion of Anthozoa GFP-like fluorescent and non-fluorescent proteins by mutagenesis",* BMC Biochemistry **3**: 7.

Bulina M.E., Lukyanov K.A., Britanova O.V., Onichtchouk D., Lukyanov S. & Chudakov D.M. (2006b), *"Chromophore-assisted light inactivation (CALI) using the phototoxic fluorescent protein KillerRed",* Nature Protocols **1**(2): 947-953.

C

Carey P.R. (1999), *"Raman spectroscopy, the sleeping giant in structural biology, awakes",* Journal of Biological Chemistry **274**(38): 26625-26628.

Carpentier P., Royant A., Ohana J. & Bourgeois D. (2007), *"Advances in spectroscopic methods for biological crystals. 2. Raman spectroscopy",* Journal of Applied Crystallography **40**(6): 1113-1122.

Chalfie M., Tu Y., Euskirchen G., Ward W.W. & Prasher D.C. (1994), *"Green fluorescent protein as a marker for gene expression",* Science **263**(5148): 802-805.

Chattoraj M., King B.A., Bublitz G.U. & Boxer S.G. (1996), *"Ultra-fast excited state dynamics in green fluorescent protein: multiple states and proton transfer",* Proceedings of the National Academy of Sciences USA **93**(16): 8362-8367.

Chen Y., Srajer V., Ng K., Legrand A. & Moffat K. (1994), *"Optical monitoring of protein crystals in time-resolved X-ray experiments: microspectrophotometer design and performance",* Review of Scientific Instruments **65**: 1506-1511.

Chudakov D.M., Feofanov A.V., Mudrik N.N., Lukyanov S. & Lukyanov K.A. (2003), *"Chromophore environment provides clue to "kindling fluorescent protein" riddle",* Journal of Biological Chemistry **278**(9): 7215-7219.

Chudakov D.M., Lukyanov S. & Lukyanov K.A. (2007a), *"Tracking intracellular protein movements using photoswitchable fluorescent proteins PS-CFP2 and Dendra2",* Nature Protocols **2**(8): 2024-2032.

Chudakov D.M., Lukyanov S. & Lukyanov K.A. (2007b), *"Using photoactivatable fluorescent protein Dendra2 to track protein movement",* Biotechniques **42**(5): 553, 555, 557 passim.

Chudakov D.M., Verkhusha V.V., Staroverov D.B., Souslova E.A., Lukyanov S. & Lukyanov K.A. (2004), *"Photoswitchable cyan fluorescent protein for protein tracking",* Nature biotechnology **22**(11): 1435-1439.

Cody C.W., Prasher D.C., Westler W.M., Prendergast F.G. & Ward W.W. (1993), *"Chemical structure of the hexapeptide chromophore of the Aequorea green-fluorescent protein",* Biochemistry **32**(5): 1212-1218.

Cotlet M., Hofkens J., Habuchi S., Dirix G., Van Guyse M., Michiels J., Vanderleyden J. & De Schryver F.C. (2001), *"Identification of different emitting species in the red fluorescent protein DsRed by means of ensemble and single-molecule spectroscopy",* Proceedings of National Academy of Science USA **98**(25): 14398-14403.

Cubitt A.B., Heim R., Adams S.R., Boyd A.E., Gross L.A. & Tsien R.Y. (1995), *"Understanding, improving and using green fluorescent proteins",* Trends in Biochemical Science **20**(11): 448-455.

D

De la Mora-Rey T. & Wilmot C.M. (2007), *"Synergy within structural biology of single crystal optical spectroscopy and X-ray crystallography",* Current Opinion in Structural Biology **17**(5): 580-586.

Dedecker P., Hotta J., Ando R., Miyawaki A., Engelborghs Y. & Hofkens J. (2006), *"Fast and reversible photoswitching of the fluorescent protein Dronpa as evidenced by fluorescence correlation spectroscopy",* Biophysical journal **91**(5): L45-L47.

Deheyn D.D., Kubokawa K., McCarthy J.K., Murakami A., Porrachia M., Rouse G.W. & Holland N.D. (2007), *"Endogenous green fluorescent protein (GFP) in amphioxus",* Biological Bulletin **213**(2): 95-100.

Dickson R.M., Cubitt A.B., Tsien R.Y. & Moerner W.E. (1997), *"On/off blinking and switching behaviour of single molecules of green fluorescent protein",* Nature **388**(6640): 355-358.

Dodson E.J., Winn M. & Ralph A. (1997), *"Collaborative Computational Project, number 4: providing programs for protein crystallography",* Methods Enzymol **277**: 620-633.

Donnert G., Eggeling C. & Hell S.W. (2007), *"Major signal increase in fluorescence microscopy through dark-state relaxation",* Nature Methods **4**(1): 81-86.

Dubois R. (1887), *"Note sur la fonction photogénique chez les Pholades",* Comptes rendus des séances de la Société de Biologie, Paris. **39:** 566.

Duke E.M., Hadfield A., Martin J.L., Clifton I.J., Hajdu J., Johnson L.N., Reid G.P., Trentham D.R., Bruce I. & Fleet G.W. (1991), *"Towards time-resolved diffraction studies with glycogen phosphorylase",* Ciba Foundation symposium **161**: 75-86; discussion 86-90.

Dundas J., Ouyang Z., Tseng J., Binkowski A., Turpaz Y. & Liang J. (2006), *"CASTp: computed atlas of surface topography of proteins with structural and topographical mapping of functionally annotated residues",* Nucleic Acids Research **34**: 116-118.

Dürr H. (1990), *"Definition of photochromism"* in Photochromism: Molecules and Systems. H. Dürr & H. Bouas-Laurent. Amsterdam, Elsevier Science p. 5.

E

Ehrig T., O'Kane D.J. & Prendergast F.G. (1995), *"Green-fluorescent protein mutants with altered fluorescence excitation spectra",* FEBS Letters **367**(2): 163-166.

Elsliger M.A., Wachter R.M., Hanson G.T., Kallio K. & Remington S.J. (1999), *"Structural and spectral response of green fluorescent protein variants to changes in pH",* Biochemistry **38**(17): 5296-5301.

Emsley P. & Cowtan K. (2004), *"Coot: model-building tools for molecular graphics",* Acta Crystallographica D **60**(12): 2126-2132.

Evans P. (2006), *"Scaling and assessment of data quality",* Acta Crystallographica D **62**(Pt 1): 72-82.

F

Flors C., Hotta J., Uji-i H., Dedecker P., Ando R., Mizuno H., Miyawaki A. & Hofkens J. (2007), *"A stroboscopic approach for fast photoactivation-localization microscopy with Dronpa mutants",* Journal of the American Chemical Society **129**(45): 13970-13977.

Follenius-Wund A., Bourotte M., Schmitt M., Iyice F., Lami H., Bourguignon J.J., Haiech J. & Pigault C. (2003), *"Fluorescent derivatives of the GFP chromophore give a new insight into the GFP fluorescence process",* Biophysical journal **85**(3): 1839-1850.

Förster T. (1949), *"Fluoreszenzspektrum und Wasserstoffionen-konzentration",* Naturwissenschaften **36**(6): 186-187.

Förster T. (1950), *"Die pH-Abhaengigkeit der Fluoreszenz von Naphthalinderivaten",* Zeitschrift für Elektrochemie **54**(42): 531-553.

Fradkov A.F., Chen Y., Ding L., Barsova E.V., Matz M.V. & Lukyanov S.A. (2000), *"Novel fluorescent protein from Discosoma coral and its mutants possesses a unique far-red fluorescence",* FEBS Letters **479**(3): 127-130.

Franck J. & Livingston R. (1941), *"Remarks on the fluorescence, phosphorescence and photochemistry of dyestuffs",* Journal of chemical physics **9**(2): 177-184.

Fritzsche M. (1867), *"Sur les carbures d'hydrogène solides tires du goudron de houille",* Comptes rendus hebdomadaires des séances à l'Académie des Sciences, Paris. **64:** 1035-1037.

Fron E., Flors C., Schweitzer G., Habuchi S., Mizuno H., Ando R., Schryver F.C., Miyawaki A. & Hofkens J. (2007), *"Ultrafast excited-state dynamics of the photoswitchable protein Dronpa",* Journal of the American Chemical Society **129**(16): 4870-4871.

G

Garavelli M., Celani P., Yamamoto N., Bernardi F., Robb M.A. & Olivucci M. (1996), *"The structure of the nonadiabatic photochemical trans → cis isomerization channel in all-trans octatetraene",* Journal of American Chemical Society **118**(46): 11656-11657.

Garcia-Parajo M.F., Segers-Nolten G.M., Veerman J.A., Greve J. & van Hulst N.F. (2000), *"Real-time light-driven dynamics of the fluorescence emission in single green fluorescent protein molecules",* Proceedings of National Academy of Science USA **97**(13): 7237-7242.

Gay R.R. & Solomon E.I. (1978), *"Polarized single-crystal spectroscopic studies of oxyhemerythrin",* Journal of American Chemical Society **100**(6): 1972-1973.

Göppert-Mayer M. (1931), *"Über Elementarakte mit zwei Quantensprüngen",* Annalen der Physik **9**: 273-294.

Göppert M. (1929), *"Über die Wahrscheinlichkeit des Zusammenwirkens zweier Lichtquanten in einem Elementarakt",* Naturwissenschaften **17**: 932.

Gouet P., Jouve H.M., Williams P.A., Andersson I., Andreoletti P., Nussaume L. & Hajdu J. (1996), *"Ferryl intermediates of catalase captured by time-resolved Weissenberg crystallography and UV-VIS spectroscopy",* Nature Structural Biology **3**(11): 951-956.

Griesbeck O., Baird G.S., Campbell R.E., Zacharias D.A. & Tsien R.Y. (2001), *"Reducing the environmental sensitivity of yellow fluorescent protein. Mechanism and applications",* Journal of Biological Chemistry **276**(31): 29188-29194.

Gross L.A., Baird G.S., Hoffman R.C., Baldridge K.K. & Tsien R.Y. (2000), *"The structure of the chromophore within DsRed, a red fluorescent protein from coral",* Proceedings of the National Academy of Sciences USA **97**(22): 11990-11995.

Gurskaya N.G., Fradkov A.F., Terskikh A., Matz M.V., Labas Y.A., Martynov V.I., Yanushevich Y.G., Lukyanov K.A. & Lukyanov S.A. (2001a), *"GFP-like chromoproteins as a source of far-red fluorescent proteins",* FEBS Letters **507**(1): 16-20.

Gurskaya N.G., Savitsky A.P., Yanushevich Y.G., Lukyanov S.A. & Lukyanov K.A. (2001b), *"Color transitions in coral's fluorescent proteins by site-directed mutagenesis",* BMC Biochemistry **2**: 6.

Gurskaya N.G., Verkhusha V.V., Shcheglov A.S., Staroverov D.B., Chepurnykh T.V., Fradkov A.F., Lukyanov S. & Lukyanov K.A. (2006), *"Engineering of a monomeric green-to-red photoactivatable fluorescent protein induced by blue light",* Nature biotechnology **24**(4): 461-465.

H

Habibi M.H. & Farhadi S. (1998), *"Photoinduced decarboxylation of ary-substituted carboxylic acids using HGO. A new photo-Kolbe reaction pathway",* Journal of Chemical Research **12**: 776-777.

Habuchi S., Ando R., Dedecker P., Verheijen W., Mizuno H., Miyawaki A. & Hofkens J. (2005a), *"Reversible single-molecule photoswitching in the GFP-like fluorescent protein Dronpa",* Proceedings of the National Academy of Sciences USA **102**(27): 9511-9516.

Habuchi S., Cotlet M., Gensch T., Bednarz T., Haber-Pohlmeier S., Rozenski J., Dirix G., Michiels J., Vanderleyden J., Heberle J., De Schryver F.C. & Hofkens J. (2005b), *"Evidence for the isomerization and decarboxylation in the photoconversion of the red fluorescent protein DsRed",* Journal of American Chemical Society **127**(25): 8977-8984.

Habuchi S., Dedecker P., Hotta J., Flors C., Ando R., Mizuno H., Miyawaki A. & Hofkens J. (2006), *"Photo-induced protonation/deprotonation in the GFP-like fluorescent protein Dronpa: mechanism responsible for the reversible photoswitching",* Photochemical & Photobiological Sciences **5**(6): 567-576.

Hadfield A. & Hajdu J. (1993), *"A fast and portable microspectrophotometer for protein crystallography",* Journal of Applied Crystallography **26**(6): 839-842.

Hall S.R., Allen F.H. & Brown I.D. (1991), *"The crystallographic information file (CIF): a new standard archive file for crystallography",* Acta Crystallographica A **47**: 655-685.

Harvey E.N. (1917), *"Bioluminescence. IV. In Cypridina Hilgendorfii (Japanese Ostracod Crustacean); V. In Firefly; VI. In Cavernularia Haberi (Japanese Pennatulid)",* American Journal of Physiology **42**: 318-358.

Harvey E.N. (1919), *"Chemichal nature of Cypridina luciferin and Cypridina luciferase",* Journal of General Physiology **1**(3): 269-293.

Harvey E.N. (1920), *The nature of animal light*, Philadelphia.

Harvey E.N. (1924), *"Recent advances in bioluminescence",* Physiological Review **4**: 639-671.

Haseloff J. & Amos B. (1995), *"GFP in plants",* Trends in Genetics **11**(8): 328-329.

Hastings J.W. & Morin J.G. (1969), *"Comparative biochemistry of calcium-activated photoproteins from the ctenophore, Mnemiopsis, and the coelenterates Aequorea, Obelia, Pelagia and Renilla",* Biological Bulletin **132**(2): 402.

Haupts U., Maiti S., Schwille P. & Webb W.W. (1998), *"Dynamics of fluorescence fluctuations in green fluorescent protein observed by fluorescence correlation spectroscopy",* Proceedings of National Academy of Science USA **95**(23): 13573-13578.

Haw M. (2003), *"Holographic data storage: The light fantastic",* Nature **422**(6932): 556-558.

Hayashi I., Mizuno H., Tong K.I., Furuta T., Tanaka F., Yoshimura M., Miyawaki A. & Ikura M. (2007), *"Crystallographic evidence for water-assisted photo-induced peptide cleavage in the stony coral fluorescent protein Kaede",* Journal of Molecular Biology **372**(4): 918-926.

He X., Bell A.F. & Tonge P.J. (2002), *"Isotopic labeling and normal-mode analysis of a model green fluorescent protein chromophore",* Journal of Physical Chemistry B **106**: 6056-6066.

He X., Bell A.F. & Tonge P.J. (2003), *"Ground state isomerization of a model green fluorescent protein chromophore",* FEBS Letters **549**(1-3): 35-38.

Heikal A.A., Hess S.T., Baird G.S., Tsien R.Y. & Webb W.W. (2000), *"Molecular spectroscopy and dynamics of intrinsically fluorescent proteins: coral red (dsRed) and yellow (Citrine)",* Proceedings of the National Academy of Sciences USA **97**(22): 11996-12001.

Heim R., Cubitt A.B. & Tsien R.Y. (1995), *"Improved green fluorescence",* Nature **373**(6516): 663-664.

Heim R., Prasher D.C. & Tsien R.Y. (1994), *"Wavelength mutations and posttranslational autoxidation of green fluorescent protein"*, Proceedings of the National Academy of Sciences USA **91**(26): 12501-12504.

Hell S.W. (2003), *"Toward fluorescence nanoscopy"*, Nature biotechnology **21**(11): 1347-1355.

Hell S.W. (2007), *"Far-field optical nanoscopy"*, Science **316**(5828): 1153-1158.

Hell S.W., Jakobs S., Andresen M., Stiel A.C. & Eggeling C. (2007), *"Method and apparatus for storing a three-dimensional arrangement of data bits in a solid-state body"*, http://v3.espacenet.com/textdoc?DB=EPODOC&IDX=EP1763024&F=0, Germany, Max-Planck-Gesellschaft zur Förderung der Wissenschaften. **Patents #US20070047287, DE102005040671, EP1763024**.

Hell S.W., Lindek S., Cremer C. & Stelzer E.H.K. (1994), *"Measurement of the 4Pi-confocal point spread function proves 75 nm axial resolution"*, Applied physics letters **64**(11): 1335-1337.

Hell S.W. & Wichmann J. (1994), *"Breaking the diffraction resolution limit by stimulated emission: stimulated-emission-depletion fluorescence microscopy"*, Optics Letters **19**(11): 780-782.

Helms V., Winstead C. & Langhoff P.W. (2000), *"Low-lying electronic excitations of the green fluorescent protein chromophore"*, Journal of Molecular Structure (Theochem) **506**: 179-189.

Henderson J.N., Ai H.W., Campbell R.E. & Remington S.J. (2007), *"Structural basis for reversible photobleaching of a green fluorescent protein homologue"*, Proceedings of the National Academy of Sciences USA **104**(16): 6672-6677.

Henderson J.N. & Remington S.J. (2005), *"Crystal structures and mutational analysis of amFP486, a cyan fluorescent protein from Anemonia majano"*, Proceedings of the National Academy of Sciences USA **102**(36): 12712-12717.

Henderson J.N. & Remington S.J. (2006), *"The kindling fluorescent protein: a transient photoswitchable marker"*, Physiology (Bethesda) **21**: 162-170.

Henderson R. (1990), *"Cryo-protection of protein crystals against radiation damage in electron and X-ray diffraction"*, Proceedings of the Royal Society of London B **241**(1300): 6-8.

Hirschberg Y. (1956), *"Reversible formation and eradication of colors by irradiation at low temperatures. A photochemical memory model "*, Journal of the American Chemical Society **78**(10): 2304-2312.

Hodgkinson S. (1995), *"GFP in Dictyostelium"*, Trends in Genetics **11**(8): 327-328.

Hofmann M. (2007), *"RESOLFT-Mikroskopie mit photoschaltbaren Proteinen"*, Naturwissenschaftlich - Matermatischen Gemsamtfakultät, Künzelsau, Heidelberg. **Erlangung der Doktorwürde:** 76.

Hoogenboom J.P., van Dijk E.M., Hernando J., van Hulst N.F. & García-Parajó M.F. (2005), *"Power-law-distributed dark states are the main pathway for photobleaching of single organic molecules"*, Physical review letters **95**(9): 097401.097401-097401.097404.

Huang B., Wang W., Bates M. & Zhuang X. (2008), *"Three-dimensional super-resolution imaging by stochastic optical reconstruction microscopy"*, Science **319**(5864): 810-813.

I

Ikawa M., Kominami K., Yoshimura Y., Tanaka K., Nishimune Y. & Okabe M. (1995), *"A rapid and non-invasive selection of transgenic embryos before implantation using green fluorescent protein (GFP)"*, FEBS Letters **375**(1-2): 125-128.

Ivanchenko S., Röcker C., Oswald F., Wiedenmann J. & Nienhaus G.U. (2005), *"Targeted green-red photoconversion of EosFP, a fluorescent marker protein"*, Journal of Biological Physics **31**(3-4): 249-259.

J

Jablonksi A. (1935), *"Über den Mechanismus der Photolumineszenz von Farbstoffphosphoren"*, Zeitschrift für Physikalische Chemie **94**: 38-46.

Jacobson K., Rajfur Z., Vitriol E. & Hahn K. (2008), *"Chromophore-assisted laser inactivation in cell biology"*, Trends in Cell Biology **18**(9): 443-450.

James J. (1976), *Light microscopic techniques in biology and medicine*, The Hague, Martinus Nijhoff Medical Division.

Jimenez-Banzo A., Nonell S., Hofkens J. & Flors C. (2008), *"Singlet oxygen photosensitization by EGFP and its chromophore HBDI"*, Biophysical journal **94**: 168-172.

Jourdan A.J.L. (1837), *"Phosphorescent"* in Dictionnaire raisonné, étymologique, synonymique et polyglotte des termes usités dans les sciences naturelles. Société belge de librairie. Bruxelles, Hauman, Cattoir et comp. p. 472.

Juette M.F., Gould T.J., Lessard M.D., Mlodzianoski M.J., Nagpure B.S., Bennett B.T., Hess S.T. & Bewersdorf J. (2008), *"Three-dimensional sub-100 nm resolution fluorescence microscopy of thick samples"*, Nature Methods **5**(6): 527-529.

K

Kabsch W. (1993), *"Automatic processing of rotation diffraction data from crystals of initially unknown symmetry and cell constants"*, Journal of Applied Crystallography **26**(6): 795-800.

Kaiser W. & Garrett C. (1961), *"Two-photon excitation in $CaF_2:Eu^{2+}$"*, Physical review letters **7**: 229-231.

Karasawa S., Araki T., Nagai T., Mizuno H. & Miyawaki A. (2004), *"Cyan-emitting and orange-emitting fluorescent proteins as a donor/acceptor pair for fluorescence resonance energy transfer"*, Biochemical Journal **381**(Pt 1): 307-312.

Kautsky H. (1939), *"Quenching of luminescence by oxygen"*, Transactions of the Faraday Society **35**: 216-219.

Kellner R.R. (2007), *"STED microscopy with Q-switched microchip lasers"*, Heidelberg, Germany, Combined faculties for the natural sciences and for mathematics of the Ruperto-Carola University. **Ph.D. thesis**.

Kikuchi A., Fukumura E., Karasawa S., Mizuno H., Miyawaki A. & Shiro Y. (2008), *"Structural characterization of a thiazoline-containing chromophore in an orange fluorescent protein, monomeric Kusabira Orange"*, Biochemistry **47**(44): 11573-11580.

Kim J.E., Tauber M.J. & Mathies R.A. (2001), *"Wavelength dependent cis-trans isomerization in vision"*, Biochemistry **40**(46): 13774-13778.

Klar T.A., Engel E. & Hell S.W. (2001), *"Breaking Abbe's diffraction resolution limit in fluorescence microscopy with stimulated emission depletion beams of various shapes"*, Physical Review E, Statistical, Nonlinear and Soft Matter Physics **64**(6 Pt 2): 066613.

Kleywegt G.J., Henrick K., Dodson E.J. & van Aalten D.M. (2003), *"Pound-wise but penny-foolish: How well do micromolecules fare in macromolecular refinement?"*, Structure **11**(9): 1051-1059.

Kneen M., Farinas J., Li Y. & Verkman A.S. (1998), *"Green fluorescent protein as a noninvasive intracellular pH indicator"*, Biophysical journal **74**: 1591-1599.

Kong X., Nir E., Hamadani K. & Weiss S. (2007), *"Photobleaching pathways in single-molecule FRET experiments"*, Journal of American Chemical Society **129**(15): 4643-4654.

Kraeutler B., Jaeger C.D. & Bard A.J. (1978), *"Direct observation of radical intermediates in the photo-Kolbe reaction - heterogeneous photocatalytic radical formation by electron spin resonance"*, Journal of American Chemical Society **100**(15): 4903-4905.

Kubitscheck U., Kuckmann O., Kues T. & Peters R. (2000), *"Imaging and tracking of single GFP molecules in solution"*, Biophysical journal **78**(4): 2170-2179.

L

Labas Y.A., Gurskaya N.G., Yanushevich Y.G., Fradkov A.F., Lukyanov K.A., Lukyanov S.A. & Matz M.V. (2002), *"Diversity and evolution of the green fluorescent protein family"*, Proceedings of the National Academy of Sciences USA **99**(7): 4256-4261.

Lakowicz J.R. (2006), *Principles of fluorescence spectroscopy*, New York, Springer.

Lamarck (de Monet de) J.B. (1816), *Histoire naturelle des animaux sans vertèbres*, Paris.

Landau L. (1932), *"Zur Theorie der Energieubertragung. II"*, Physics of the Soviet Union **2**: 46-51.

Laskowski R.A., Macarthur M.W., Moss D.S. & Thornton J.M. (1993), *"Procheck - a Program to Check the Stereochemical Quality of Protein Structures"*, J Appl Cryst **26**: 283-291.

Lelimousin M., Adam V., Nienhaus G.U., Bourgeois D. & Field M.J. (2009), *"Photoconversion of the fluorescent protein EosFP: a hybrid simulation study reveals intersystem crossings"*, Journal of the American Chemical Society **131**: 16814-16823.

Lenard P. & Wolf M. (1889), *"Zersduben der Körper durch das ultraviolette Licht"*, Wiedemann's Annalen der Physik und Chemie **37**: 455.

Leung K.M. & Holt C.E. (2008), *"Live visualization of protein synthesis in axonal growth cones by microinjection of photoconvertible Kaede into Xenopus embryos"*, Nat Protoc **3**(8): 1318-1327.

Levine B.G. & Martinez T.J. (2006), *"Isomerization through conical intersections"*, Annual Review of Physical Chemistry **58**: 613-634.

Lewis G.N. & Kasha M. (1944), *"Phosphorescence and the triplet state"*, Journal of the American Chemical Society **66**(12): 2100-2116.

Lewis G.N. & Lipkin D. (1942), *"Reversible photochemical processes in rigid media: The dissociation of organic molecules into radicals and ions"*, Journal of the American Chemical Society **64**(12): 2801-2808.

Licetus F. (1640), *"Litheosphorus, sive de Lapide bononiensi lucem in se conceptam ab ambiente claro mox in tenebris mire conservante"*. Nicolai Schiratti, Udine**:** p. 22.

Liu R.S.H. & Asato A.E. (1985), *"The primary process of vision and the structure of bathorhodopsin: a mechanism for photoisomerization of polyenes"*, Proceedings of the National Academy of Sciences USA **82**(2): 259-263.

Long D.A. (2002), *The Raman effect : a unified treatment of the theory of Raman scattering by molecules*, Chichester ; New York, Wiley.

Luin S., Voliani V., Lanza G., Bizzarri R., Amat P., Tozzini V., Serresi M. & Beltram F. (2009), *"Raman study of chromophore states in photochromic fluorescent proteins"*, Journal of American Chemical Society **131**(1): 96-103.

Lukyanov K.A., Chudakov D.M., Lukyanov S. & Verkhusha V.V. (2005), *"Innovation: Photoactivatable fluorescent proteins"*, Nature Reviews. Molecular Cell Biology **6**(11): 885-891.

Lukyanov K.A., Fradkov A.F., Gurskaya N.G., Matz M.V., Labas Y.A., Savitsky A.P., Markelov M.L., Zaraisky A.G., Zhao X., Fang Y., Tan W. & Lukyanov S.A. (2000), *"Natural animal coloration can be determined by a nonfluorescent green fluorescent protein homolog"*, Journal of Biological Chemistry **275**(34): 25879-25882.

M

Maddalo S.L. & Zimmer M. (2006), *"The role of the protein matrix in green fluorescent protein fluorescence"*, Photochemistry and Photobiology **82**(2): 367-372.

Maiti R., Van Domselaar G.H., Zhang H. & Wishart D.S. (2004), *"SuperPose: a simple server for sophisticated structural superposition"*, Nucleic Acids Research **32**: 590-594.

Makinen M.W. & Fink A.L. (1977), *"Reactivity and cryoenzymology of enzymes in the crystalline state",* Annual Review of Biophysics & Bioengineering **6**: 301-343.

Mandzhikov V.F., Murin V.A. & Barachevskii V.A. (1973), *"Nonlinear coloration of photochromic spiropyran solutions",* Soviet Journal of Quantum Electronics **3**(2): 128-129.

Marchant J.S., Stutzmann G.E., Leissring M.A., LaFerla F.M. & Parker I. (2001), *"Multiphoton-evoked color change of DsRed as an optical highlighter for cellular and subcellular labeling",* Nature biotechnology **19**(7): 645-649.

Marckwald W. (1899), Zeitschrift für Physikalische Chemie **30**: 140-145.

Matsuda T., Miyawaki A. & Nagai T. (2008), *"Direct measurement of protein dynamics inside cells using a rationally designed photoconvertible protein",* Nature Methods **5**(4): 339-345.

Matz M.V., Fradkov A.F., Labas Y.A., Savitsky A.P., Zaraisky A.G., Markelov M.L. & Lukyanov S.A. (1999), *"Fluorescent proteins from nonbioluminescent Anthozoa species",* Nature biotechnology **17**(10): 969-973.

Matz M.V., Marshall N.J. & Vorobyev M. (2006), *"Are corals colorful?",* Photochemistry and Photobiology **82**(2): 345-350.

McAnaney T.B., Zeng W., Doe C.F., Bhanji N., Wakelin S., Pearson D.S., Abbyad P., Shi X., Boxer S.G. & Bagshaw C.R. (2005), *"Protonation, photobleaching, and photoactivation of yellow fluorescent protein (YFP 10C): a unifying mechanism",* Biochemistry **44**(14): 5510-5524.

McCoy A.J. (2007), *"Solving structures of protein complexes by molecular replacement with Phaser",* Acta Crystallographica D **63**(Pt 1): 32-41.

McGeehan J., Ravelli R.B.G., Murray J.W., Owen R.L., Cipriani F., McSweeney S., Weik M. & Garman E.F. (2009), *"Colouring cryo-cooled crystals: online microspectrophotometry",* Journal of Synchrotron Radiation **16**: 163-172.

McKinney S.A., Murphy C.S., Hazelwood K.L., Davidson M.W. & Looger L.L. (2009), *"A bright and photostable photoconvertible fluorescent protein",* Nature Methods **6**(2): 131-133.

Mirabella R., Franken C., van der Krogt G.N., Bisseling T. & Geurts R. (2004), *"Use of the fluorescent timer DsRED-E5 as reporter to monitor dynamics of gene activity in plants",* Plant Physiology **135**(4): 1879-1887.

Miyawaki A. (2002), *"Green fluorescent protein-like proteins in reef Anthozoa animals",* Cell Structure and Function **27**(5): 343-347.

Mizuno H., Mal T.K., Tong K.I., Ando R., Furuta T., Ikura M. & Miyawaki A. (2003), *"Photo-induced peptide cleavage in the green-to-red conversion of a fluorescent protein",* Molecular Cell **12**(4): 1051-1058.

Mizuno H., Mal T.K., Walchli M., Kikuchi A., Fukano T., Ando R., Jeyakanthan J., Taka J., Shiro Y., Ikura M. & Miyawaki A. (2008), *"Light-dependent regulation of structural flexibility in a photochromic fluorescent protein",* Proceedings of the National Academy of Sciences USA **105**(27): 9227-9232.

Moerner W.E. (2002), *"Single-molecule optical spectroscopy of autofluorescent proteins",* Journal of chemical physics **117**(24): 10925-10937.

Morin J.G. & Hastings J.W. (1971), *"Energy transfer in a bioluminescent system",* Journal of Cellular Physiology **77**(3): 313-318.

Morise H., Shimomura O., Johnson F.H. & Winant J. (1974), *"Intermolecular energy transfer in the bioluminescent system of Aequorea",* Biochemistry **13**(12): 2656-2662.

Murray J.W., Rudino-Pinera E., Owen R.L., Grininger M., Ravelli R.B. & Garman E.F. (2005), *"Parameters affecting the X-ray dose absorbed by macromolecular crystals",* Journal of Synchrotron Radiation **12**(Pt 3): 268-275.

Murshudov G.N., Vagin A.A. & Dodson E.J. (1997), *"Refinement of macromolecular structures by the maximum-likelihood method",* Acta Crystallographica D **53**: 240-255.

Mutoh T., Miyata T., Kashiwagi S., Miyawaki A. & Ogawa M. (2006), *"Dynamic behavior of individual cells in developing organotypic brain slices revealed by the photoconvertable protein Kaede",* Exp Neurol **200**(2): 430-437.

N

Nakamura H. (2002), *Nonadiabatic transitions: concepts, basic theories and applications*.

Nienhaus G.U., Nienhaus K., Holzle A., Ivanchenko S., Renzi F., Oswald F., Wolff M., Schmitt F., Rocker C., Vallone B., Weidemann W., Heilker R., Nar H. & Wiedenmann J. (2006a), *"Photoconvertible fluorescent protein EosFP: biophysical properties and cell biology applications",* Photochemistry and Photobiology **82**(2): 351-358.

Nienhaus K., Nar H., Heilker R., Wiedenmann J. & Nienhaus G.U. (2008), *"Trans-cis isomerization is responsible for the red-shifted fluorescence in variants of the red fluorescent protein eqFP611",* Journal of the American Chemical Society **130**(38): 12578-12579.

Nienhaus K., Nienhaus G.U., Wiedenmann J. & Nar H. (2005), *"Structural basis for photo-induced protein cleavage and green-to-red conversion of fluorescent protein EosFP",* Proceedings of the National Academy of Sciences USA **102**(26): 9156-9159.

Nienhaus K., Renzi F., Vallone B., Wiedenmann J. & Nienhaus G.U. (2006b), *"Chromophore-protein interactions in the anthozoan green fluorescent protein asFP499",* Biophysical journal **91**(11): 4210-4220.

Nienhaus K., Renzi F., Vallone B., Wiedenmann J. & Nienhaus G.U. (2006c), *"Exploring chromophore--protein interactions in fluorescent protein cmFP512 from Cerianthus membranaceus: X-ray structure analysis and optical spectroscopy",* Biochemistry **45**(43): 12942-12953.

Nienhaus K., Vallone B., Renzi F., Wiedenmann J. & Nienhaus G.U. (2003), *"Crystallization and preliminary X-ray diffraction analysis of the red fluorescent protein eqFP611",* Acta Crystallographica D **59**(Pt 7): 1253-1255.

Niwa H., Matsuno T., Kojima T., Kubota M., Hirano T., Ohashi M., Inouye S., Ohmiya Y. & Tsuji F.I. (1997), *Aequora green fluorescent protein: structural elucidation of the chromophore*, Chichester, Wiley.

Nonell S. & Braslavsky S.E. (2000), *"Time-resolved singlet oxygen detection"*, Methods in enzymology **319**: 37-49.

O

Ohmine I. (1985), *"Mechanisms of nonadiabatic transitions in photoisomerization processes of conjugated molecules: role of hydrogen migrations"*, Journal of chemical physics **83**(5): 2448-2362.

Ormö M., Cubitt A.B., Kallio K., Gross L.A., Tsien R.Y. & Remington S.J. (1996), *"Crystal structure of the Aequorea victoria green fluorescent protein"*, Science **273**(5280): 1392-1395.

Oswald F., Schmitt F., Leutenegger A., Ivanchenko S., D'Angelo C., Salih A., Maslakova S., Bulina M., Schirmbeck R., Nienhaus G.U., Matz M.V. & Wiedenmann J. (2007), *"Contributions of host and symbiont pigments to the coloration of reef corals"*, FEBS Journal **274**(4): 1102-1109.

P

Pakhomov A.A., Martynova N.Y., Gurskaya N.G., Balashova T.A. & Martynov V.I. (2004), *"Photoconversion of the chromophore of a fluorescent protein from Dendronephthya sp"*, Biochemistry (Mosc) **69**(8): 901-908.

Parthenopoulos D.A. & Rentzepis P.M. (1989), *"Three-dimensional optical storage memory"*, Science **245**(4920): 843-845.

Patterson G.H. & Lippincott-Schwartz J. (2002), *"A photoactivatable GFP for selective photolabeling of proteins and cells"*, Science **297**(5588): 1873-1877.

Patterson G.H. & Piston D.W. (2000), *"Photobleaching in two-photon excitation microscopy"*, Biophysical journal **78**: 2159-2162.

Péron F. (1809), in Annales du muséum d'histoire naturelle. Muséum national d'histoire naturelle. Paris.Vol. **14** p. 336.

Perrin F. (1926), *"Polarisation de la lumière de fluorescence. Vie moyenne des molécules dans l'état excité"*, Journal de Physique **7**(12): 390-401.

Perrin F. (1929), *"La fluorescence des solutions. Induction moléculaire. Polarisation et durée d'émission. Photochimie"*, Annales de Physique **10**(12): 169-275.

Peterman J.G., Brasselet S. & Moerner W.E. (1999), *"The fluorescence dynamics of single molecules of green fluorescent protein"*, Journal of physical chemistry A **103**: 10553-10560.

Petersen J., Wilmann P.G., Beddoe T., Oakley A.J., Devenish R.J., Prescott M. & Rossjohn J. (2003), *"The 2.0-A crystal structure of eqFP611, a far red fluorescent protein from the sea anemone Entacmaea quadricolor"*, Journal of Biological Chemistry **278**(45): 44626-44631.

Pieribone V. & Gruber D.F. (2005), *Aglow in the dark - The revolutionary science of biofluorescence*, Harvard, Belknap press.

Pines J. (1995), *"GFP in mammalian cells"*, Trends in Genetics **11**(8): 326-327.

Pletnev S., Shcherbo D., Chudakov D., Pletneva N., Merzlyak E., Wlodawer A., Dauter Z. & Pletnev V. (2008), *"A crystallographic study of bright far-red fluorescent protein mKate reveals pH-induced cis-trans isomerization of the chromophore"*, Journal of Biological Chemistry.

Post J.N., Lidke K.A., Rieger B. & Arndt-Jovin D.J. (2005), *"One- and two-photon photoactivation of a paGFP-fusion protein in live Drosophila embryos"*, FEBS Letters **579**(2): 325-330.

Prasher D.C. (1995), *"Using GFP to see the light"*, Trends in Genetics **11**(8): 320-323.

Prasher D.C., Eckenrode V.K., Ward W.W., Prendergast F.G. & Cormier M.J. (1992), *"Primary structure of the Aequorea victoria green-fluorescent protein"*, Gene **111**(2): 229-233.

Prescott M., Ling M., Beddoe T., Oakley A.J., Dove S., Hoegh-Guldberg O., Devenish R.J. & Rossjohn J. (2003), *"The 2.2 A crystal structure of a pocilloporin pigment reveals a nonplanar chromophore conformation"*, Structure **11**(3): 275-284.

Punge A., Rizzoli S.O., Jahn R., Wildanger J.D., Meyer L., Schonle A., Kastrup L. & Hell S.W. (2008), *"3D reconstruction of high-resolution STED microscope images"*, Microscopy Research and Technique **71**(9): 644-650.

Q

Quillin M.L., Anstrom D.M., Shu X., O'Leary S., Kallio K., Chudakov D.M. & Remington S.J. (2005), *"Kindling fluorescent protein from Anemonia sulcata: dark-state structure at 1.38 A resolution"*, Biochemistry **44**(15): 5774-5787.

R

Ravelli R.B., Haselmann-Weiss U., McGeehan J.E., McCarthy A.A., Marquez J.A., Antony C., Frangakis A.S. & Stranzl G. (2007), *"Plastic-embedded protein crystals"*, Journal of Synchrotron Radiation **14**(Pt 1): 128-132.

Remington S.J. (2006), *"Fluorescent proteins: maturation, photochemistry and photophysics"*, Current Opinion in Structural Biology **16**(6): 714-721.

Remington S.J., Wachter R.M., Yarbrough D.K., Branchaud B., Anderson D.C., Kallio K. & Lukyanov K.A. (2005), *"zFP538, a yellow-fluorescent protein from Zoanthus, contains a novel three-ring chromophore"*, Biochemistry **44**(1): 202-212.

Rosenow M.A., Huffman H.A., Phail M.E. & Wachter R.M. (2004), *"The crystal structure of the Y66L variant of green fluorescent protein supports a cyclization-oxidation-dehydration mechanism for chromophore maturation",* Biochemistry **43**(15): 4464-4472.

Royant A., Carpentier P., Ohana J., McGeehan J., Paetzold B., Noirclerc-Savoye M., Vernède X., Adam V. & Bourgeois D. (2007), *"Advances in spectroscopic methods for biological crystals. 1. Fluorescence lifetime measurements",* Journal of Applied Crystallography **40**(Part 6): 1105-1112.

Rust M.J., Bates M. & Zhuang X. (2006), *"Sub-diffraction-limit imaging by stochastic optical reconstruction microscopy (STORM)",* Nature Methods **3**(10): 793-795.

S

Sakai K., Matsui Y., Kouyama T., Shiro Y. & Adachi S. (2002), *"Optical monitoring of freeze-trapped reaction intermediates in protein crystals : a microspectrophotometer for cryogenic protein crystallography",* Journal of Applied Crystallography **35**(2): 270-273.

Salih A., Larkum A., Cox G., Kuhl M. & Hoegh-Guldberg O. (2000), *"Fluorescent pigments in corals are photoprotective",* Nature **408**(6814): 850-853.

Sato S. (1983), *"Photo-Kolbe reaction at gas-solid interfaces",* Journal of physical chemistry A **87**(18): 3531-3537.

Sato T., Takahoko M. & Okamoto H. (2006), *"HuC:Kaede, a useful tool to label neural morphologies in networks in vivo",* Genesis **44**(3): 136-142.

Sauer M. (2005), *"Reversible molecular photoswitches: a key technology for nanoscience and fluorescence imaging",* Proceedings of the National Academy of Sciences USA **102**(27): 9433-9434.

Schafer L.V., Groenhof G., Boggio-Pasqua M., Robb M.A. & Grubmuller H. (2008), *"Chromophore protonation state controls photoswitching of the fluoroprotein asFP595",* PLoS Comput Biol **4**(3): e1000034.

Schellenberg P., Johnson E., Esposito A.P., Reid P.J. & Parson W.W. (2001), *"Resonance Raman scattering by the green fluorescent protein and an analog of its chromophore ",* Journal of Physical Chemistry B **105**: 5316-5322.

Schenkel M., Sinclair A.M., Johnstone D., Bewley J.D. & Mathur J. (2008), *"Visualizing the actin cytoskeleton in living plant cells using a photo-convertible mEos::FABD-mTn fluorescent fusion protein",* Plant Methods **4**(1): 21.

Schneider M., Barozzi S., Testa I., Faretta M. & Diaspro A. (2005), *"Two-photon activation and excitation properties of PA-GFP in the 720-920-nm region",* Biophysical journal **89**(2): 1346-1352.

Selvin P.R., Lougheed T., Hoffman M.T., Park H., Balci H., Blehm B.H. & Toprak E. (2007), *"Fluorescence imaging with one-nanometer accuracy (FIONA)",* Cold Spring Harbor Protocols: doi: 10.1101/pdb.top1127.

Shagin D.A., Barsova E.V., Yanushevich Y.G., Fradkov A.F., Lukyanov K.A., Labas Y.A., Semenova T.N., Ugalde J.A., Meyers A., Nunez J.M., Widder E.A., Lukyanov S.A. & Matz M.V. (2004), *"GFP-like proteins as ubiquitous metazoan superfamily: evolution of functional features and structural complexity",* Molecular Biology and Evolution **21**(5): 841-850.

Shaner N.C., Campbell R.E., Steinbach P.A., Giepmans B.N., Palmer A.E. & Tsien R.Y. (2004), *"Improved monomeric red, orange and yellow fluorescent proteins derived from Discosoma sp. red fluorescent protein",* Nature biotechnology **22**(12): 1567-1572.

Shaner N.C., Lin M.Z., McKeown M.R., Steinbach P.A., Hazelwood K.L., Davidson M.W. & Tsien R.Y. (2008), *"Improving the photostability of bright monomeric orange and red fluorescent proteins",* Nature Methods **5**(6): 545-551.

Shimomura O. (1985), *"Bioluminescence in the sea: photoprotein systems",* Symposia of the Society for Experimental Biology **39**: 351-372.

Shimomura O., Johnson F.H. & Saiga Y. (1962), *"Extraction, purification and properties of aequorin, a bioluminescent protein from the luminous hydromedusan, Aequorea",* Journal of Cellular and Comparative Physiology **59**: 223-239.

Shu X., Shaner N.C., Yarbrough C.A., Tsien R.Y. & Remington S.J. (2006), *"Novel chromophores and buried charges control color in mFruits",* Biochemistry **45**(32): 9639-9647.

Stark D.A. & Kulesa P.M. (2005), *"Photoactivatable green fluorescent protein as a single-cell marker in living embryos",* Developmental Dynamics **233**(3): 983-992.

Stiel A.C., Andresen M., Bock H., Hilbert M., Schilde J., Schonle A., Eggeling C., Egner A., Hell S.W. & Jakobs S. (2008), *"Generation of monomeric reversibly switchable red fluorescent proteins for far-field fluorescence nanoscopy",* Biophysical journal **95**(6): 2989-2997.

Stiel A.C., Trowitzsch S., Weber G., Andresen M., Eggeling C., Hell S.W., Jakobs S. & Wahl M.C. (2007), *"1.8 A bright-state structure of the reversibly switchable fluorescent protein Dronpa guides the generation of fast switching variants",* Biochemical Journal **402**(1): 35-42.

Stokes G.G. (1852), *"On the refrangibility of light",* Philosophical Transactions of the Royal Society of London(142): 463-562.

Stura E.A. (1999), *"Seeding"* in Protein Crystallization: Techniques, Strategies, and Tips: A Laboratory Manual. T. M. Bergfors, International University Line p. 141-153.

Subach F.V., Patterson G.H., Manley S., Gillette J.M., Lippincott-Schwartz J. & Verkhusha V.V. (2009), *"Photoactivatable mCherry for high-resolution two-color fluorescence microscopy",* Nature Methods **6**(2): 153-159.

Swaminathan R., Hoang C.P. & Verkman A.S. (1997), *"Photobleaching recovery and anisotropy decay of green fluorescent protein GFP-S65T in solution and cells: cytoplasmic viscosity probed by green fluorescent protein translational and rotational diffusion",* Biophysical journal **72**(4): 1900-1907.

T

Teller E. (1937), *"The crossing of potential energy surfaces",* Journal of physical chemistry A **41**: 109-116.

Terskikh A., Fradkov A., Ermakova G., Zaraisky A., Tan P., Kajava A.V., Zhao X., Lukyanov S., Matz M., Kim S., Weissman I. & Siebert P. (2000), *""Fluorescent timer": protein that changes color with time",* Science **290**(5496): 1585-1588.

Thompson R.E., Larson D.R. & Webb W.W. (2002), *"Precise nanometer localization analysis for individual fluorescent probes",* Biophysical journal **82**(5): 2775-2783.

Tomura M., Yoshida N., Tanaka J., Karasawa S., Miwa Y., Miyawaki A. & Kanagawa O. (2008), *"Monitoring cellular movement in vivo with photoconvertible fluorescence protein "Kaede" transgenic mice",* Proc Natl Acad Sci U S A **105**(31): 10871-10876.

Tsien R.Y. (1998), *"The green fluorescent protein",* Annual Review of Biochemistry **67**: 509-544.

Tsien R.Y. (1999), *"Rosy dawn for fluorescent proteins",* Nature biotechnology **17**(10): 956-957.

Tsutsui H., Karasawa S., Shimizu H., Nukina N. & Miyawaki A. (2005), *"Semi-rational engineering of a coral fluorescent protein into an efficient highlighter",* EMBO Reports **6**(3): 233-238.

Tubbs J.L., Tainer J.A. & Getzoff E.D. (2005), *"Crystallographic structures of Discosoma red fluorescent protein with immature and mature chromophores: linking peptide bond trans-cis isomerization and acylimine formation in chromophore maturation",* Biochemistry **44**(29): 9833-9840.

Tully J.C. (1990), *"Molecular dynamics with electronic transitions",* Journal of chemical physics **93**(2): 1061-1071.

Turro N.J. (1991), *Modern molecular photochemistry*, Mill Valley, CA, University Science Books.

U

Ursby T. & Bourgeois D. (1997), *"Improved estimation of structure factor difference amplitudes from poorly accurate data",* Acta Crystallographica A **53**: 564-575.

Usman A., Mohammed O.F., Nibbering E.T., Dong J., Solntsev K.M. & Tolbert L.M. (2005), *"Excited-state structure determination of the green fluorescent protein chromophore",* Journal of the American Chemical Society **127**(32): 11214-11215.

V

Valeur B. (2004), *Invitation à la fluorescence moléculaire*, Bruxelles, De Boeck & Larcier.

van Thor J.J., Gensch T., Hellingwerf K.J. & Johnson L.N. (2002), *"Phototransformation of green fluorescent protein with UV and visible light leads to decarboxylation of glutamate 222",* Nature Structural Biology **9**(1): 37-41.

Vellieux F.M.D. & Dijkstra B.W. (1997), *"Computation of Bhat's OMIT maps with different coefficients",* Journal of Applied Crystallography **30**(3): 396-399.

Vernede X., Lavault B., Ohana J., Nurizzo D., Joly J., Jacquamet L., Felisaz F., Cipriani F. & Bourgeois D. (2006), *"UV laser-excited fluorescence as a tool for the visualization of protein crystals mounted in loops",* Acta Crystallograpica D **62**(Pt 3): 253-261.

Veron J.E.N. (2000a), *"Family Pectiniidae"* in Corals of the World. M. Stafford-Smith. Townsville, Australian Institute of Marine Science.Vol. **2** p. 321-361.

Veron J.E.N. (2000b), *"Genus Favia"* in Corals of the World. M. Stafford-Smith. Townsville, Australian Institute of Marine Science.Vol. **3** p. 100-131.

Veron J.E.N. (2000c), *"Genus Lobophyllia"* in Corals of the World. M. Stafford-Smith. Townsville, Australian Institute of Marine Science.Vol. **3** p. 38-51.

Veron J.E.N. (2000d), *"Genus Montipora"* in Corals of the World. M. Stafford-Smith. Townsville, Australian Institute of Marine Science.Vol. **1** p. 62-167.

Veron J.E.N. (2000e), *"Genus Pocillopora"* in Corals of the World. M. Stafford-Smith. Townsville, Australian Institute of Marine Science.Vol. **2** p. 24-45.

Veron J.E.N. (2000f), *"Genus Trachyphillia"* in Corals of the World. M. Stafford-Smith. Townsville, Australian Institute of Marine Science.Vol. **3** p. 272-273.

Voityuk A.A., Michel-Beyerle M.E. & Rösch N. (1998), *"Quantum chemical modeling of structure and absorption spectra of the chromophore in green fluorescent proteins ",* Chemical physics **231**(1): 13-25.

Voliani V., Bizzarri R., Nifosi R., Abbruzzetti S., Grandi E., Viappiani C. & Beltram F. (2008), *"Cis-trans photoisomerization of fluorescent-protein chromophores",* Journal of Physical Chemistry B **112**(34): 10714-10722.

von Löwenstern-Kunckel J. (1678), *"Oeffentliche Zuschrifft von dem Phosphoro Mirabili und dessen leuchtenden Wunder-Pilulen"*, Leipzig.

W

Wall M.A., Socolich M. & Ranganathan R. (2000), *"The structural basis for red fluorescence in the tetrameric GFP homolog DsRed",* Nature Structural Biology **7**(12): 1133-1138.

Wampler J.E., Hori K., Lee J.W. & Cormier M.J. (1971), *"Structured bioluminescence. Two emitters during both the in vitro and the in vivo bioluminescence of the sea pansy, Renilla",* Biochemistry **10**(15): 2903-2909.

Webber N.M. & Meech S.R. (2007), *"Electronic spectroscopy and solvatochromism in the chromophore of GFP and the Y66F mutant",* Photochemical and photobiological sciences **6**(9): 976-981.

Weber W., Helms V., McCammon J.A. & Langhoff P.W. (1999), *"Shedding light on the dark and weakly fluorescent states of green fluorescent proteins",* Proceedings of the National Academy of Sciences USA **96**(11): 6177-6182.

White J. & Stelzer E. (1999), *"Photobleaching GFP reveals protein dynamics inside live cells",* Trends in Cell Biology **9**(2): 61-65.

Wiedemann E. (1888), *"Über Fluorescenz und Phosphorescenz",* Annalen der Physik **270**(7): 446-463.

Wiedenmann J., Elke C., Spindler K.D. & Funke W. (2000), *"Cracks in the beta-can: fluorescent proteins from Anemonia sulcata (Anthozoa, Actinaria)",* Proceedings of the National Academy of Sciences USA **97**(26): 14091-14096.

Wiedenmann J., Ivanchenko S., Oswald F., Schmitt F., Rocker C., Salih A., Spindler K.D. & Nienhaus G.U. (2004), *"EosFP, a fluorescent marker protein with UV-inducible green-to-red fluorescence conversion",* Proceedings of the National Academy of Sciences USA **101**(45): 15905-15910.

Wiedenmann J. & Nienhaus G.U. (2006), *"Live-cell imaging with EosFP and other photoactivatable marker proteins of the GFP family",* Expert Review of Proteomics **3**(3): 361-374.

Wiedenmann J., Vallone B., Renzi F., Nienhaus K., Ivanchenko S., Rocker C. & Nienhaus G.U. (2005), *"Red fluorescent protein eqFP611 and its genetically engineered dimeric variants",* Journal of Biomedical Optics **10**(1): 14003.

Wilmann P.G., Petersen J., Devenish R.J., Prescott M. & Rossjohn J. (2005), *"Variations on the GFP chromophore: A polypeptide fragmentation within the chromophore revealed in the 2.1-A crystal structure of a nonfluorescent chromoprotein from Anemonia sulcata",* Journal of Biological Chemistry **280**(4): 2401-2404.

Wilmann P.G., Turcic K., Battad J.M., Wilce M.C., Devenish R.J., Prescott M. & Rossjohn J. (2006), *"The 1.7 A crystal structure of Dronpa: a photoswitchable green fluorescent protein",* Journal of Molecular Biology **364**(2): 213-224.

X

Xu C. & Webb W.W. (1996), *"Measurement of two-photon excitation cross sections of molecular fluorophores with data from 690 to 1050 nm",* Journal of the optical society of america B **13**(3): 481-491.

Y

Yang F., Moss L.G. & Phillips G.N., Jr. (1996), *"The molecular structure of green fluorescent protein",* Nature biotechnology **14**(10): 1246-1251.

Yanga D., Xiuyuan Ni X., Chena W. & Weng Z. (2008), *"The observation of photo-Kolbe reaction as a novel pathway to initiate photocatalytic polymerization over oxide semiconductor nanoparticles",* Journal of Photochemistry and Photobiology A **195**(2-3): 322-329.

Yarbrough D., Wachter R.M., Kallio K., Matz M.V. & Remington S.J. (2001), *"Refined crystal structure of DsRed, a red fluorescent protein from coral, at 2.0-A resolution",* Proceedings of the National Academy of Sciences USA **98**(2): 462-467.

Yarkony D.R. (1998), *"Conical intersections: diabolical and often misunderstood",* Accounts of Chemical Research **31**(8): 511-518.

Yildiz A., Forkey J.N., McKinney S.A., Ha T., Goldman Y.E. & Selvin P.R. (2003), *"Myosin V walks hand-over-hand: single fluorophore imaging with 1.5-nm localization",* Science **300**(5628): 2061-2065.

Yildiz A. & Selvin P.R. (2005), *"Fluorescence imaging with one nanometer accuracy: application to molecular motors",* Accounts of Chemical Research **38**(7): 574-582.

Youvan D.C. & Michel-Beyerle M.E. (1996), *"Structure and fluorescence mechanism of GFP",* Nature biotechnology **14**(10): 1219-1220.

Z

Zener C. (1932), *"Non-adiabatic crossing of energy levels",* Proceedings of the Royal Society of London A **137**(6): 696-702.

Zhang L., Patel H.N., Lappe J.W. & Wachter R.M. (2006), *"Reaction progress of chromophore biogenesis in green fluorescent protein",* Journal of the American Chemical Society **128**: 4766-4772.

Zondervan R., Kulzer F., Orlinskii S.B. & Orrit M. (2003), *"Photoblinking of Rhodamine 6G in Poly(vinyl alcohol): Radical Dark State Formed through the Triplet",* Journal of physical chemistry A **107**(35): 6770-6776.

This page intentionally left blank

TITLE

Mechanistic Studies of Photoactivatable Fluorescent Proteins: A Combined Approach by Crystallography and Spectroscopy

ABSTRACT

Since the discovery of the green fluorescent protein (GFP) in 1962, many developments allowed improving the use of this naturally light-emitting protein as a powerful tool for tracking proteins or organelles of interest within living cells and organisms. At the beginning of the 21st century, the discovery of photoactivatable fluorescent proteins (PAFPs), notably from Anthozoan species, triggered a revolution in the field of FP technology. Some PAFPs are capable of being irreversibly photoconverted from a green- to a red-emitting form while other ones can be reversibly switched on and off, depending on specific excitation wavelengths. These proteins are being extensively used in optical microscopy techniques, particularly in "nanoscopy", which provides optical resolution 10 fold beyond the theoretical Abbe limit. In order to further develop these techniques, notably in term of time-resolution, the need to obtain brighter fluorescent probes that photoconvert or photoswitch efficiently is crucial. At the same time, fluorescent highlighters generally need to be monomeric and photostable. In order to better understand the mechanisms of phototransformations in PAFPs, three members of the family have been studied: EosFP, Dendra2 and IrisFP. The phenomena of green-to-red photoconversion, reversible photoswitching and non-reversible photobleaching have been studied by a combination of X-ray crystallography and microspectrophotometry using the Cryobench laboratory of the ESRF/IBS. Together, the results have allowed us to propose a mechanism for the photoconversion of EosFP and Dendra2 and to discover and characterize IrisFP, the first PAFP combining both properties of photoconversion and photoswitching. The structural modifications of the chromophore associated with an X-ray induced radical state, likely to be involved in the photobleaching pathway of PAFPs, were also characterized.

TITRE

Etudes mécanistiques des protéines fluorescentes photoactivables: une approche combinée par cristallographie et spectroscopie

RESUME

Depuis la découverte de la protéine fluorescente verte (GFP) en 1962, de nombreux développements ont permis d'améliorer l'utilisation de cette protéine naturellement luminescente en tant que puissant outil permettant de suivre des protéines ou des organelles d'intérêt dans les cellules ou organismes vivants. Au début du 21ème siècle, la découverte des protéines fluorescentes photoactivables (PAFPs), notamment chez les anthozoaires, a initié une révolution dans le domaine de la technologie des FP. Certaines PAFPs sont capables d'être irréversiblement photoconverties d'une forme fluorescente verte à une forme fluorescente rouge alors que d'autres peuvent être réversiblement commutées entre des formes allumées ou éteintes, selon des longueurs d'onde d'excitation spécifiques. Ces protéines sont intensivement employées pour les techniques de microscopie optique, particulièrement en "nanoscopie", qui permet d'atteindre une résolution optique 10 fois meilleure que la limite théorique d'Abbe. Afin de développer plus en avant ces techniques, notamment en terme de résolution temporelle, la nécessité d'obtenir des sondes fluorescentes plus lumineuses pouvant se photoconvertir ou se photocommuter efficacement est cruciale. Dans un même temps, les marqueurs fluorescents doivent généralement être monomériques et photostables. Afin de mieux comprendre les mécanismes des phototransformations des PAFPs, trois membres de la famille ont été étudiés : EosFP, Dendra2 et IrisFP. Le phénomène de photoconversion du vert au rouge, de photocommutation réversible et de photoblanchiment irréversible ont été étudiés grâce à une combinaison de cristallographie des rayons X et de microspectrophotométrie, en utilisant le laboratoire Cryobench de l'ESRF/IBS. Pris ensemble, les résultats nous ont permis de proposer un mécanisme de photoconversion pour EosFP et Dendra2 et de découvrir et caractériser IrisFP, première PAFP combinant à la fois les propriétés de photoconversion et de photocommutation. Les modifications structurales du chromophore associées à la formation d'un état radicalaire induit par les rayons X, probablement impliqué dans la voie de photoblanchiment des PAFPs, ont aussi été caracterisées.

SCIENTIFIC FIELDS : Crystallography, spectroscopy, biophysics

KEYWORDS : Fluorescent proteins, photoconversion, photoswitching, photobleaching, protein crystallography, microspectrophotometry, synchrotron, Cryobench

MOTS CLES : Protéines fluorescentes, photoconversion, photocommutation, photoblanchiment, cristallographie des protéines, microspectrophotométrie, synchrotron, Cryobench

NAME AND ADDRESS OF THE HOST INSTITUTE :

European Synchrotron Radiation Facility (ESRF)
Macromolecular Crystallography Group
6, rue Jules Horowitz, BP 220 - 38043 Grenoble Cedex - France